

FAA TECHNICAL CENTER
Atlantic City International Airport
New Jersey 08405

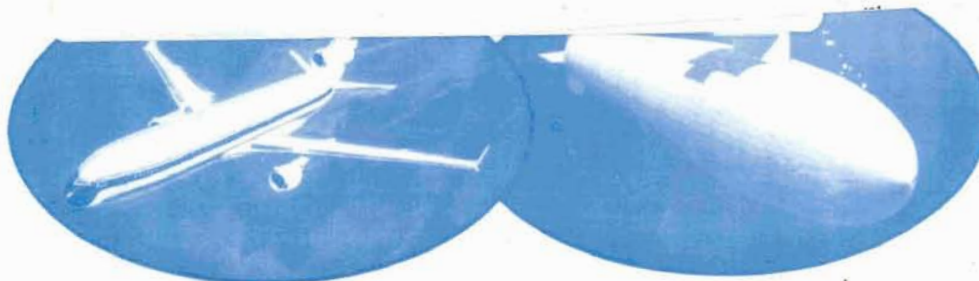
Proceedings Of The Ninth DoD/NASA/FAA Conference On Fibrous Composites In Structural Design

Lake Tahoe, Nevada
November 4-7, 1991

*ANALYTIC
(1+26)*

PSB-NASA-CR

CAT. 24



(NASA-CR-198723) NINTH
DOD/NASA/FAA CONFERENCE ON FIBROUS
COMPOSITES IN STRUCTURAL DESIGN,
VOLUME I (Galaxy Scientific Corp.)
548 p

N95-28420
--THRU--
N95-28446
Unclas

G3/24 0051368



U.S. Department of Transportation
Federal Aviation Administration

FAA TECHNICAL CENTER
Atlantic City International Airport
N.J. 08405

Ninth DoD/NASA/FAA Conference on Fibrous Composites in Structural Design

Compiled by

Joseph R. Soderquist
*Federal Aviation Administration
Washington, DC*

Lawrence M. Neri
*Federal Aviation Administration
Technical Center
Atlantic City International Airport, NJ*

Herman L. Bohon ✓
*Galaxy Scientific Corporation
Hampton, VA*

Proceedings of a conference sponsored by the
Department of Defense, the National Aeronautics
and Space Administration, and the Federal
Aviation Administration, and held in
Lake Tahoe, Nevada on November 4-7, 1991

September, 1992

NOTICE

This document is disseminated under the sponsorship of the U. S. Department of Transportation in the interest of information exchange. The United States Government assumes no liability for the contents or use thereof.

The United States Government does not endorse products or manufacturers. Trade or manufacturers' names appear herein solely because they are considered essential to the objective of this report.

CONFERENCE ORGANIZATION

Joseph R. Soderquist
General Chairman
Federal Aviation Administration
Washington, DC

Lawrence M. Neri
Conference Technical Coordinator
FAA Technical Center
Atlantic City International Airport, NJ

Herman L. Bohon
Technical Chairman
Composites Consultant
Galaxy Scientific Corporation
Hampton, VA

CONFERENCE ORGANIZATION COMMITTEE

Joseph R. Soderquist
James H. Starnes, Jr.
Thomas E. Hess
Donald W. Oplinger
J. David Oetting
Dan E. Good

Federal Aviation Administration
NASA Langley Research Center
Naval Air Development Center
Federal Aviation Administration
Wright Research and Development Center
Army Aviation Applied Technology Directorate

PRIMARY

PREFACE

The Ninth DoD/NASA/FAA Conference on Fibrous Composites in Structural Design is one of a series of conferences jointly sponsored by the Federal Aviation Administration, the National Aeronautics and Space Administration, the U.S. Air Force, the U.S. Army, and the U.S. Navy (Department of Defense). The purpose of this series of conferences is to convene periodically key government and industry research and design engineers to present and discuss the status, problems, and requirements in the technical disciplines related to the design of composite structures. This series of conferences provides a forum for the scientific community to exchange composite structures design and technology.

The Ninth DoD/NASA/FAA Conference on Fibrous Composites in Structural Design was hosted by the Federal Aviation Administration and held at Lake Tahoe, Nevada during November 4-7, 1991. The conference offered 91 presentations by senior managers and experts in the field of composite structures, organized into a total of 11 sessions. These included: one overview session on perspectives in composites; seven discipline sessions in applications (two sessions); innovative design/manufacturing (one session); methodology (two sessions); reliability (one session); damage tolerance (one session); and two focused sessions on thick structures and space structures. The conference also hosted the second industry briefing on the NASA Advanced Composites Technology (ACT) program. This publication contains (in three volumes) the technical material presented in these sessions.

Certain materials are identified in this publication in order to specify adequately which materials were used in the structural design or research efforts. In no case does such identification imply recommendation or endorsement of a product by FAA, NASA, or DoD, nor does it imply that the materials are necessarily the only ones or the best ones available for the purpose. In many cases, equivalent materials are available and would probably produce equivalent results.

The Conference Organizers would like to take this opportunity to thank all the authors and presenters for their outstanding contributions to the conference technical program, as well as the conference attendees whose contributions to the conference discussions helped to make the conference a successful technology exchange forum for current composite structural design issues.

Joseph R. Soderquist
Lawrence M. Neri
Herman L. Bohon

James H. Starnes, Jr.
Thomas E. Hess
Donald W. Oplinger
J. David Oetting
Dan E. Good

TABLE OF CONTENTS

VOLUME I

PREFACE i
CONFERENCE ORGANIZATION iii
TABLE OF CONTENTS v

SESSION I - Perspectives in Composites

Chairman: Joseph R. Soderquist, Federal Aviation Administration

- A. Reliable Composites, Reliable Manufacturing and Materials: A Perspective 30
John C. Halpin, Wright Aeronautical Systems Division
- B. Utilization of Composite Materials by the U.S. Army: A Look Ahead 7-1
Richard Chait, U.S. Army Materiel Command
- C. Benefits and Limitations of Composites in Carrier-Based Aircraft 35-2
Donald P. McErlean, Naval Air Development Center
- D. Advanced Materials Requirements and Needs for Future Aerospace Applications ... 93
Samuel L. Venneri, NASA Office of Aeronautics, Exploration and Technology

SESSION II - Aircraft Design Methodology (A)

Chairman: James H. Starnes, Jr., NASA Langley Research Center

- A. Mechanical Properties of Triaxially Braided Composites: Experimental and Analytical Results NASA 99-3
John E. Masters, Lockheed Engineering and Sciences Company, NASA Langley Research Center; Raymond L. Fay, Lockheed Engineering and Sciences Company, North Carolina A&T State University; and Christopher M. Pastore and Yasser A. Gawayed, North Carolina State University
- B. Mechanisms of Compressive Failure in Woven Composites and Stitched Laminates NASA 125-4
B. N. Cox, M. S. Dadkhah, R.V. Inman, W. L. Morris and S. Schroeder, Rockwell International Science Center
- C. Effect of the Fiber-Matrix Interphase on the Transverse Tensile Strength of the Unidirectional Composite Material 139-5
H. C. Tsai and A.M. Arocho, Naval Air Development Center
- D. The Effect of Material Heterogeneity in Curved Composite Beams for Use in Aircraft Structures NASA 157-6
Brendan J. O'Toole and Michael H. Santare, University of Delaware
- E. Investigation of Static and Cyclic Bearing Failure Mechanisms for GR/EP Laminates 167-7
R. W. Walter and M. M. Tuttle, The Boeing Company
- F. Compression Failure of Angle-Ply Laminates NASA 185-8
L. D. Peel, Mirage Carrier Works; M. W. Hyer, Virginia Polytechnic Institute and State University; and M.J. Shuart, NASA Langley Research Center

SESSION II - Aircraft Design Methodology (A) (continued)

G. Analysis of Composite Structures with Delaminations Under Combined Bending and Compression <i>Han-Pin Kan, Northrop Corporation; Edward Kautz, Naval Air Development Center; and Larry Neri, Federal Aviation Administration Technical Center</i>	197	-9
H. Mechanics of Composites Research at ONR <i>Yapa D. S. Rajapakse, Office of Naval Research</i>	219	-6
I. Post-Buckling Analysis of Curved, Stiffened Composite Panels with Central Cut-Outs <i>U. Mbanefo, Northrop Corporation</i>	223	-6
J. Buckling Behavior of Long Symmetrically Laminated Plates Subjected to Combined Loads <i>Michael P. Nemeth, NASA Langley Research Center</i>	227	-10
K. Compressive Residual Strength of Graphite/Epoxy Laminates After Impact <i>Teresa A. Guy and Paul A. Lagace, Massachusetts Institute of Technology</i>	253	-11

SESSION III - DESIGN APPLICATIONS (A)

Chairman: Dan Good, Aviation Applied Technology Directorate, U.S. Army

A. Application of Advanced Material Systems to Composite Frame Elements <i>Steven Llorente, Pierre Minguet and Russell Fay, Boeing Defense and Space Group; and Steven Medwin, E.I. Du Pont De Nemours and Company (Incorporated)</i>	277	-12
B. Design, Analysis and Testing of a Metal Matrix Composite Web/Flange Intersection <i>S. B. Biggers and N. F. Knight, Jr., Clemson University; S. G. Moran, NASA Headquarters; and R. Olliffe, Lockheed Aeronautical Systems Company</i>	297	-13
C. Characteristics of Laminates with Delamination Control Strips <i>C. T. Sun, Purdue University; J. C. Goering, McDonnell Aircraft Company; and J. M. Alper and L. W. Gause, Naval Air Development Center</i>	329	-14
D. Vibrational Behavior of Adaptive Aircraft Wing Structures Modelled as Composite Thin-Walled Beams <i>O. Song, L. Librescu and C. A. Rogers, Virginia Polytechnic Institute and State University</i>	361	-15
E. Unique Considerations in the Design and Experimental Evaluation of Tailored Wings with Elastically Produced Chordwise Camber <i>Lawrence W. Rehfield, Peter J. Zischka, Michael L. Fentress and Stephen Chang, University of California, Davis</i>	383	-16
F. C-130 Advanced Technology Center Wing Box Conceptual Design/Cost Study <i>R. S. Whitehead, Northrop Corporation; C. R. Foreman, LTV Advanced Products Group; and K. Silva, Wright Laboratories/FIBAC</i>	401	-17
G. Development of Composite Carrythrough Bulkhead <i>R. J. Ehlen, McDonnell Aircraft Company, and M. Libeskind, Naval Air Development Center</i>	421	-18
H. Effects of Floor Location on Response of Composite Fuselage Frames <i>Huey D. Carden and Lisa E. Jones, NASA Langley Research Center, and Edwin L. Fasanella, Lockheed Engineering and Sciences Company</i>	443	-19

SESSION IV - Design Criteria, Reliability, Supportability

Chairman: Thomas E. Hess, Naval Air Development Center

A. A Critical Review of Evolving Qualification Approaches for Contemporary Composite Airframes <i>Keith R. Kedward, University of California; John C. Halpin, Wright Aeronautical Systems Division; and John E. McCarty, Consultant</i>	461	-0
B. Structural Design Optimization with Survivability Dependent Constraints Application: Primary Wing Box of a Multi-Role Fighter <i>Douglas J. Dolvin, Wright Patterson Air Force Base</i>	465	-20
C. Reliability Analysis of Composite Structures <i>Han-Pin Kan, Northrop Corporation</i>	489	-21
D. Uncertainties in Obtaining High Reliability from Stress-Strength Models <i>Donald M. Neal, William T. Matthews and Mark G. Vangel, U.S. Army Materials Technology Laboratory</i>	503	-22
E. Probabilistic Design of Advanced Composite Structure <i>P. M. Gray and M. G. Riskalla, LTV Aerospace and Defense</i>	523	-23
F. Probabilistic Evaluation of Fuselage-Type Composite Structures <i>Michael C. Shiao, Sverdrup Technology, Incorporated, and Christos C. Chamis, NASA Lewis Research Center</i>	535	-24
G. Proof Test Methodology for Composites <i>Edward M. Wu and David K. Bell, Naval Postgraduate School</i>	549	-25
H. Materials and Processes Used for Bonded Repairs of F/A-18 Advanced Composite Honeycomb Sandwich Structures <i>Douglas R. Peri, Naval Aviation Depot North Island</i>	561	-0
I. Navy Composite Maintenance and Repair Experience <i>T. M. Donnellan, R. C. Cochran, E. L. Rosenzweig and R. E. Trabocco, Naval Air Development Center</i>	565	-26

VOLUME II*

SESSION V - NASA Advanced Composites Technology (ACT)

SESSION V-A - Supporting Technology

Chairman: John G. Davis, Jr., NASA Langley Research Center

A. Overview of the ACT Program <i>John G. Davis, Jr., NASA Langley Research Center</i>	577
B. Designers' Unified Cost Model <i>W. Freeman, NASA Langley Research Center; L. Ilcewicz and G. Swanson, Boeing Commercial Airplanes; and T. Gutowski, Massachusetts Institute of Technology</i>	601
C. COINS: A Composites Information Database System <i>Shahid Siddiqi, Louis F. Vosteen, Ralph Edlow and Teck-Seng Kwa, Analytical Services and Materials, Incorporated</i>	621
D. Composite Fuselage Shell Structures Research at NASA Langley Research Center <i>James H. Starnes, Jr. and Mark J. Shuart, NASA Langley Research Center</i>	631
E. Structural Testing of the Technology Integration Box Beam <i>C. F. Griffin, Lockheed Aeronautical Systems Company</i>	659
F. Technology Integration Box Beam Failure Study: Status Report <i>M. J. Shuart, D. R. Ambur, D. D., Davis, Jr., R. C. Davis, G. L. Farley, C. G. Lotts and J. T. Wang, Lockheed Aeronautical Systems Co.</i>	673

* Published in companion document

SESSION V-B. - Stitched RTM Technology

Chairman: Marvin B. Dow, NASA Langley Research Center

- A. Development of Stitched/RTM Composite Primary Structures 689
Susan M. Kullerd, Lockheed Engineering and Sciences Company, and Marvin B. Dow, NASA Langley Research Center
- B. Resin Transfer Molding Technology for Composite Primary 715
Wing and Fuselage Structures
A. Markus, Douglas Aircraft Company
- C. Test and Analysis Results for Composite Transport Fuselage 719
and Wing Structures
Jerry W. Deaton, NASA Langley Research Center; Susan M. Kullerd, Lockheed Engineering and Sciences Company; and Ram C. Madan and Victor L. Chen, Douglas Aircraft Company

SESSION V-C. - Automated Fiber Placement technology

Chairman: William T. Freeman, NASA Langley Research Center

- A. Tension Fracture of Laminates for Transport Fuselage 747
Part I: Material Screening
T. H. Walker, W. B. Avery and L. B. Ilcewicz, Boeing Commercial Airplane Group, and C. Poe, Jr. and C. E. Harris, NASA Langley Research Center
- B. Indentability of Conventional and Negative Poisson's Ratio Foams 789
R. S. Lakes and K. Elms, University of Iowa
- C. Local Design Optimization for Composite Transport Fuselage Crown Panels 795
G. D. Swanson, L. B. Ilcewicz and T. H. Walker, Boeing Commercial Airplane Group, and D. Graesser, M. Tuttle and Z. Zabinsky, University of Washington
- D. Composite Fuselage Crown Panel Manufacturing Technology 815
K. Willden and S. Metschan, Boeing Commercial Airplanes, and C. Grant and T. Brown, Hercules Aerospace

SESSION V-D. - Textile Preform Technology

Chairman: Randall C. Davis, NASA Langley Research Center

- A. Recent Progress in NASA Langley Textile Reinforces Composites Program 845
H. Benson Dexter, Charles E. Harris and Norman J. Johnston, NASA Langley Research Center
- B. Advanced Textile Applications for Primary Aircraft Structures 875
Anthony C. Jackson, Ronald E. Barrie, Bharat M. Shah and Jay G. Shukla, Lockheed Aeronautical Systems Company
- C. Comparison of Resin Film Infusion, Resin Transfer Molding and 903
Consolidation of Textile Preforms for Primary Aircraft Structure
J. Suarez and S. Dastin, Grumman Aircraft Systems
- D. Characterization and Manufacture of Braided Composites for Large 935
Commercial Aircraft Structures
Mark J. Fedro, Boeing Defense and Space Group, and Kurtis Willden, Boeing Commercial Airplane Group

SESSION VI - Damage Tolerance

Chairman: J. David Oetting, Wright Research Development Center

- A. The Use of Impact Force as a Scale Parameter for the Impact 981
Response of Composite Laminates
Wade C. Jackson, U.S. Army Aerostructures Directorate, and C. C. Poe, Jr., NASA Langley Research Center

SESSION VI - Damage Tolerance (continued)

- B. Application of Damage Tolerance Methodology in Certification of the 999
Piaggio P-180 Avanti
Jerry Johnson, Dow-United Technologies Composite Products, Incorporated
- C. Effect of Low-Speed Impact Damage and Damage Location 1013
on Behavior of Composite Panels
Dawn Jegley, NASA Langley Research Center
- D. Impact Damage Resistance of Composite Fuselage Structure, Part I 1037
*E. F. Dost, W. B. Avery, L. B. Ilcewicz and D. H. Grande, Boeing Commercial
Airplane Group, and B. R. Coxon, Integrated Technologies, Incorporated*
- E. Applications of a Damage Tolerance Analysis Methodology in Aircraft Design ... 1071
*M. R. Woodward, S. D. Owens, G. E. Law and L. A. Mignery, General
Dynamics Corporation*
- F. Compressive Strength of Damaged and Repaired Composite Plates 1083
Scott R. Finn and George S. Springer, Stanford University
- G. Post Impact Compressive Strength in Composites 1097
*Edvins Demuts, Raghbir S. Sandhu and John A. Daniels,
Wright Laboratory, U.S. Air Force*
- H. Fundamental Concepts in the Suppression of Delamination 1105
Buckling by Stitching
B. N. Cox, Rockwell International Science Center
- I. Damage Tolerance of a Geodesically Stiffened Advanced 1111
Composite Structural Concept for Aircraft Structural Applications
Marshall Rouse and Damodar R. Ambur, NASA Langley Research Center
- J. Advanced Wing Design Survivability Testing and Results 1123
*J. Bruno, Grumman Aircraft Systems, and M. Tobias,
Naval Air Development Center*
- K. NASA-ACEE /Boeing 737 Graphite-Epoxy Horizontal Stabilizer Service 1139
*J. T. Quinlivan, J. A. Kent and D. R. Wilson, Boeing
Commercial Airplane Group*

VOLUME III*

SESSION VII - Innovative Design/Manufacturing

Chairman: Larry Kelly, Wright Research Development Center

- A. Process and Control Systems for Composites Manufacturing 1153
*T. H. Tsiang and J. L. Wanamaker, Lockheed Aeronautical
Systems Company*
- B. Development of a Low-Cost, Modified Resin Transfer Molding 1163
Process Using Elastomeric Tooling and Automated Preform Fabrication
William J. Doane and Ronald G. Hall, General Dynamics Convair Division
- C. Design of Fabric Preforms for Double Diaphragm Forming 1175
*Steven Luby and Edward Bernardon, Charles Stark Draper
Laboratory, Incorporated*
- D. Static and Fatigue Testing of Full-Scale Fuselage Panels Fabricated Using a 1185
Therm-X® Process
*Albert J. DiNicola, Christos Kassapoglou and Jack C. Chou,
United Technologies-Sikorsky Aircraft Division*
- E. Advanced Tow Placement of Composite Fuselage Structure 1211
Robert L. Anderson and Carroll G. Grant, Hercules Aerospace Company
- F. Service Tough Composite Structures Using the Z-Direction 1223
Reinforcement Process
*Glen Freitas, Constance Magee and Joseph Boyce, Foster-Miller, Incorporated
and Richard Bott, Naval Weapons Center*

* Published in companion document

SESSION VII - Innovative Design/Manufacturing (continued)

- G. Through-the-Thickness® Braided Composites for Aircraft Application 1231
Richard T. Brown, Atlantic Research Corporation
- H. Thermoplastic Pultrusion for Future Aerospace Application 1249
Hsin-Nan Chou, McDonnell Douglas Missile System Company
- I. ACT/ICAPS - Thermoplastic Composite Activities 1253
*M. P. Renieri, S. J. Burpo, L. M. Roundy and S. M. Roundy and S. M. Todd,
McDonnell Aircraft Company*
- J. Composite Intermediate Case Manufacturing Scale-Up for Advanced Engines 1289
Rowena H. Ecklund, Pratt and Whitney Group, United Technologies Corporation
- K. Resin Transfer Molding of Textile Preforms for Aircraft 1303
Structural Applications
*Gregory H. Hasko, Lockheed Engineering and Sciences Company;
H. Benson Dexter, NASA Langley Research Center; and Mark H. Weideman,
Virginia Polytechnic Institute and State University*

SESSION VIII - Design Applications (B)

Chairman: Donald W. Oplinger, Federal Aviation Administration Technical Center

- A. Analysis of Aircraft Engine Blade Subject to Ice Impact 1319
*E. S. Reddy and G. H. Abumeri, Sverdrup Technology, Incorporated
and C. C. Chamis and P. L. N. Murthy, NASA Lewis Research Center*
- B. Application of Fiber-Reinforced Bismaleimide Materials to 1333
Aircraft Nacelle Structures
*Vasilios Peros, John Ruth and David Trawinski, Martin Marietta
Aero and Naval Systems*
- C. Innovative Design and Fabrication of Composite Canopy Frames 1349
*Robert L. Chu and Michael C. Y. Niu, Lockheed Aeronautical
Systems Company*
- D. Assembly Induced Delaminations in Composite Structures 1353
*J. Goering, R. Bohlmann and S. Wanthal, McDonnell Aircraft Company;
E. Kautz, Naval Air Development Center; and L. Neri, Federal
Aviation Administration Technical Center*
- E. Stress Analysis and Failure of an Internally Pressurized 1379
Composite-Jacketed Steel Cylinder
*Peter C. T. Chen, U.S. Army Armament Research, Development
and Engineering Center*
- F. Composite Flight-Control Actuator Development 1389
Richard Bott, Naval Weapons Center, and Fred Ching, HR Textron Incorporated

SESSION IX - Thick Structures Technology

Chairman: Michael F. Card, NASA Langley Research Center

- A. Higher Order Finite Element Analysis of Thick Composite Laminates 1407
J. Goering and H. J. Kim, McDonnell Aircraft Company
- B. An Improved Plate Theory of Order {1,2} for Thick Composite Laminates 1417
A. Tessler, U.S. Army Materials Technical Laboratory
- C. Failure Analysis of Thick Composite Cylinders Under External Pressure 1431
A. Caiazzo and B. W. Rosen, Materials Sciences Corporation
- D. On the Thermally-Induced Residual Stresses in Thick Fiber-Thermoplastic 1447
Matrix (PEEK) Cross-Ply Laminated Plates
Shoufeng Hu and John A. Nairn, University of Uta
- E. Advanced Fabrication Processes for Thick Composite Submarine Structure 1455
*James J. Kelly, DARPA; George Leon, GD/Electric Boat;
and Diana Holdinghausen, McDonnell Aircraft Corporation*
- F. Low-Cost Design and Fabrication of Composite Ship Structures 1459
Milton O. Critchfield and Thomas D. Judy, Davis Taylor Model Basin

SESSION X - Aircraft Design Methodology (B)

Chairman: Donald W. Oplinger, Federal Aviation Administration Technical Center

- A. Analysis of Stresses in Finite Anisotropic Panels with Centrally Located Cut-Outs 1485
Vickie O. Britt, NASA Langley Research Center
- B. The Role of Biaxial Stresses in Discriminating Between Meaningful and Illusory Composite Failure Theories 1507
L. J. Hart-Smith, Douglas Aircraft Company
- C. Static and Dynamic Strain Energy Release Rates in Toughened Thermosetting 1529
Douglas S. Cairns, Hercules Advanced Materials and Systems Company
- D. Analysis Techniques for the Prediction of Springback in Formed and Bonded Composite Components 1539
Michael F. Gasick and Gary D. Ranieri, McDonnell Aircraft Company

SESSION XI - Space Structures

Chairman: Michael F. Card, NASA Langley Research Center

- A. Stiffness and Strength Tailoring in Uniform Space-Filling Truss Structures 1561
Mark S. Lake, NASA Langley Research Center
- B. Design Prediction for Long Term Stress Rupture Service of Composite Pressure Vessels 1589
Ernest Y. Robinson, The Aerospace Corporation
- C. Designing for Time-Dependent Material Response in Spacecraft Structures 1617
M. W. Hyer and Lynda L. S. Oleksuk, Virginia Polytechnic Institute and State University, and D. E. Bowles, NASA Langley Research Center
- D. Composite Flexible Insulation for Thermal Protection of Space Vehicles 1631
S.Amanda Chiu, Sterling Software, Incorporated

SESSION I
PERSPECTIVES IN COMPOSITES

THIS PAGE INTENTIONALLY BLANK

OMIT

**Reliable Composites, Reliable Manufacturing
and Materials: A Perspective**

**John C. Halpin
Wright Aeronautical Systems Division**

THIS PAGE INTENTIONALLY BLANK

THIS PAGE INTENTIONALLY BLANK

THIS PAGE INTENTIONALLY BLANK

P-28

51369

"UTILIZATION OF COMPOSITE MATERIALS BY THE U.S. ARMY ---
A LOOK AHEAD"

PRESENTATION TO NINTH DOD/NASA/FAA CONFERENCE
ON
FIBROUS COMPOSITES IN STRUCTURAL DESIGN

RICHARD CHAIT

It is a pleasure to be with you today to give you some details of the United States Army's Composite Materials Program. My talk is entitled "Utilization of Composite Materials by the U.S. Army ... A Look Ahead." (VG #1)

The message I would like to leave with you is that the Army is very serious about the application of composite materials as it moves to become more and more of a high-tech Army. The value of delivering the right technology at the right time and at an affordable price (VG #2) certainly was brought home during the Gulf Crisis. Prior to detailing the Army's program on composite materials by commodity or mission areas, I would first like to show how composite materials fits into technology planning efforts. I will also cover important efforts to document design allowable information, supporting research, and some notional applications for composite materials. This outline provides the chronological order for the various sections of the talk (VG #3).

Regarding technology planning, the Army has several active efforts, e.g. Tech Base Master Plan (VG #4-6) and the Strategic Technologies for the Army or STAR Study that the National Academy of Sciences has undertaken (VG #7-8). In both instances the importance of advanced materials and particularly composite materials is seen.

One can look at the use of composite materials by commodity or mission area (VG #9). Let's start first by looking at the most important system in the U.S. Army, The Soldier.

SOLDIER -- Today, Kevlar fiber plays a significant role in both vests and helmets used for ballistic protection (VG #10-11). Tomorrow's helmet may be even stronger and lighter with the use of newer fibers such as the SPECTRA 900 fiber (VG #12-13).

GROUND VEHICLES -- Most recognize the Bradley Fighting Vehicle but what is different about this demonstration vehicle is the hull - it is made of fiberglass composite (VG #14-15). Advantages are numerous (VG #16). Plans call for this technology to be utilized in the fabrication of another hull, this time for a heavier vehicle, in the 50-55 ton range (VG #17-18). Other applications of composite

PRECEDING PAGE BLANK NOT FILMED

materials for ground vehicles are the M1A1 driver's seat (VG #19), road wheels (VG #20), turbine engine air plenum assembly (VG #21), power pack container (VG #22), various components of the 5-ton truck (VG #23), bridging (VG #24) and tanker applications (VG #25).

AIRCRAFT -- The use of composite materials is most noteworthy in Army aviation. The full potential of composite materials is realized in the recently awarded LH Comanche RAH-66 program (VG #26). Intense prior planning involved in the Army Modernization Program has paid off handsomely. Technology development such as in the Advanced Composite Airframe Program, played a major role in the LH Program (VG #27). Use of composites in the Comanche is covered in full detail (VG #28-30). It should be noted that a strong in-house research and development capability contributed significantly to the application of composites of Army aircraft (VG #32-33).

MISSILES AND MUNITIONS -- The use of composite materials for application to rocket motor uses, wings, fins and casings is under development (VG #34-36).

Important to the use of composite materials is the ability to obtain and document properties important to design. The Army has been very active in the MIL-HDBK-17 effort to formulate the basis for obtaining design allowable data of important composite materials. Various working groups stress the importance of standardizing mechanical tests, statistical analysis and chemical characterization (VG #37). Three volumes of MIL-HDBK-17 (VG #38) present the guidelines, the data and utilization of the data of various important materials (VG #39).

Complimenting the Army's in-house research to support much of the above developmental work is the effort of the Army Research Office's University Research Initiative program. For example, the URI program at the University of Delaware, developing 2-D cure simulation analysis to predict temperature and degree of cure within given cross-sections (VG #40 & 41), was important to the processing of thick section composite materials for ground vehicle hull application. In addition to awarding graduate fellowships and conducting workshops or symposia (VG #42), the University of Delaware conducts other programs in the area of composite material processing (VG #43-46). Single investigator programs (VG #47), funded by ARO, also contribute significantly to the composite materials knowledge base. Looking into the future for notional applications, one could visualize smart composite materials that would control vibrations in Army Aircraft (VG #48-50).

To summarize (VG #51), composite materials are an important segment of the Army's research, development, and engineering picture. Because of the diverse Army mission, composite materials may find application in any number of mission areas. Because of the uncertain funding profile, it is more important than ever that technology planning provide the basis for effective prioritization and leveraging of the tech base efforts involving advanced materials.

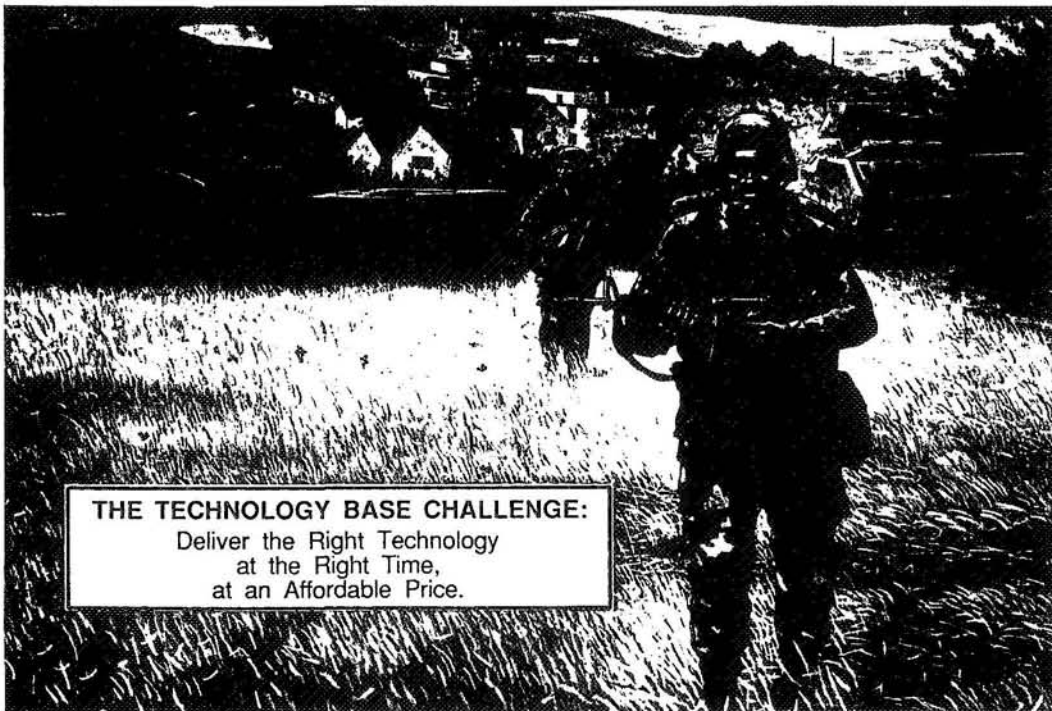


Ninth DOD/NASA/FAA Conference
On
FIBROUS COMPOSITES IN STRUCTURAL DESIGN
November 4 - 7, 1991

UTILIZATION OF COMPOSITE MATERIALS
BY THE U.S. ARMY
... A LOOK AHEAD

Dr. Richard Chait
Chief Scientist
U.S. Army Materiel Command

VG #1



THE TECHNOLOGY BASE CHALLENGE:
Deliver the Right Technology
at the Right Time,
at an Affordable Price.

VG #2



OUTLINE

- I. Introductory Comments
- II. Mission Area Utilization
- III. Design Allowable Handbook
- IV. Supporting Research
- V. Future Concepts
- VI. Concluding Comments

VG #3

ARMY TECHNOLOGY BASE MASTER PLAN

- TECHNOLOGY BASE INVESTMENT STRATEGY
- RESEARCH AND DEVELOPMENT BALANCE
- FOCUS ON CRITICAL/KEY EMERGING TECHNOLOGIES
- SPEEDING TECHNOLOGY TRANSITION
- LEVERAGING SCIENCE AND TECHNOLOGY OUTSIDE THE ARMY
- QUALITY SCIENTISTS AND ENGINEERS

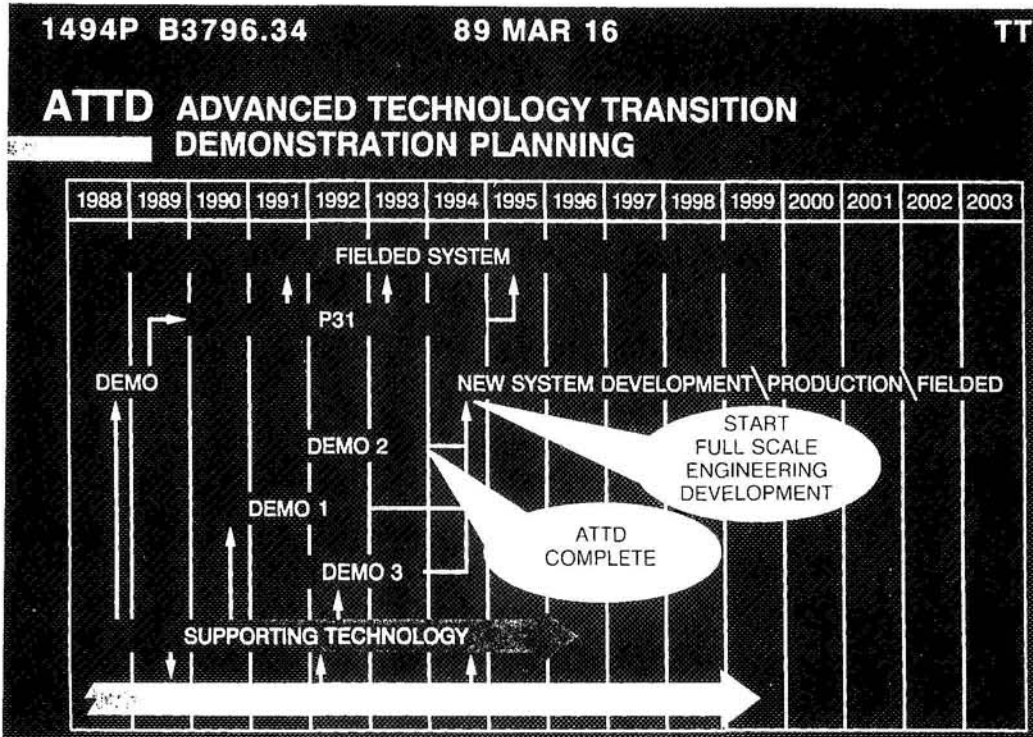
**SCIENCE AND TECHNOLOGY SUPERIORITY:
OUR INVESTMENT IN SHAPING THE FUTURE
AND COMPETING SUCCESSFULLY**

VG #4

TECHNOLOGY BASE MASTER PLAN

CHAPTER I EXECUTIVE SUMMARY	<ul style="list-style-type: none"> DEFENSE GUIDANCE ARMY GUIDANCE THREAT TECH BASE INVESTMENT STRATEGY (TBIS) 	CHAPTER V SYSTEMIC ISSUES	<ul style="list-style-type: none"> CORROSION PREVENTION LIGHTENING THE FORCE LOG R&D SORD BATTLEFIELD SOFTWARE
CHAPTER II SYSTEMS & DEMONSTRATIONS	<ul style="list-style-type: none"> NEXT GENERATION AND FUTURE SYSTEMS ADVANCED TECHNOLOGY TRANSITION DEMONSTRATIONS 	CHAPTER VI SUPPORTING CAPABILITIES	<ul style="list-style-type: none"> SIMULATION/MODELING SOFTWARE SUPPORT TESTING SUPPORT ANALYTICAL SUPPORT
CHAPTER III TECHNOLOGY	<ul style="list-style-type: none"> KEY EMERGING TECHNOLOGIES 	CHAPTER VII INTERFACES	<ul style="list-style-type: none"> LEVERAGE INDUSTRY NATL PROGRAMS DOD EXECUTIVE AGENCY
CHAPTER IV BASIC RESEARCH	<ul style="list-style-type: none"> RESEARCH THRUSTS PERFORMERS 	ANNEXES	<ul style="list-style-type: none"> SCIENCE & TECHNOLOGY OBJECTIVES THREAT

VG #5



VG #6



US ARMY MATERIEL COMMAND
OFFICE OF THE CHIEF SCIENTIST

An Independent Adviser to the Army:

THE BAST

By Mark Bello

Introduction

Advice is not a rare commodity, especially in the nation's capital. The value and usefulness of a specific piece of advice, however, are determined not by its availability, but rather by the quality of its contents.

The main criteria used to judge the quality of advice are the expertise, integrity, and objectivity of the members of an advisory body. High levels of each of these standards are reflected in the composition and activities of the Board on Army Science and Technology (BAST).

A unit of the National Research Council, the service arm of the National Academies of Science and Engineering and the Institute of Medicine, the BAST was formed in 1982 at the request of

James R. Ambrase, recently retired under secretary of the Army. Since then, the independent board, whose members represent a broad range of scientific and engineering expertise, has been called on to study a variety of scientific, technological, and manpower issues confronting the Army.

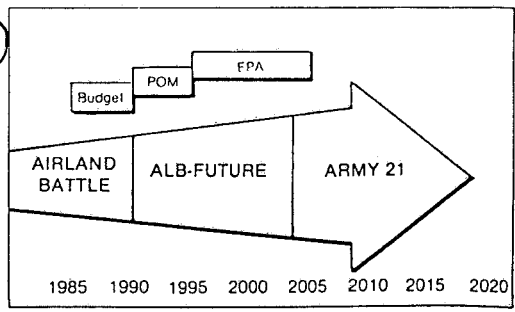
For example, the BAST completed a forecast of the Army's needs for scientific, engineers, and technical personnel through the end of the century, assessed the defense implications of its reliance on foreign suppliers of electronic components

used in weapons systems, and evaluated the adequacy of the Army's research and development program on explosives, propellants, and other energetic materials. Ongoing studies include a continuing review of the congressionally mandated program to dispose of chemical stockpiles by 1994 and a far-reaching assessment that will forecast the strategic technologies critical to ground warfare in the 21st century.

Historical Overview

The BAST's parent organizations, the National Research Council and the National Academy of Sciences, were spawned, in part, by the exigencies of war. Congress created the academy

We need to think beyond the year 2000.

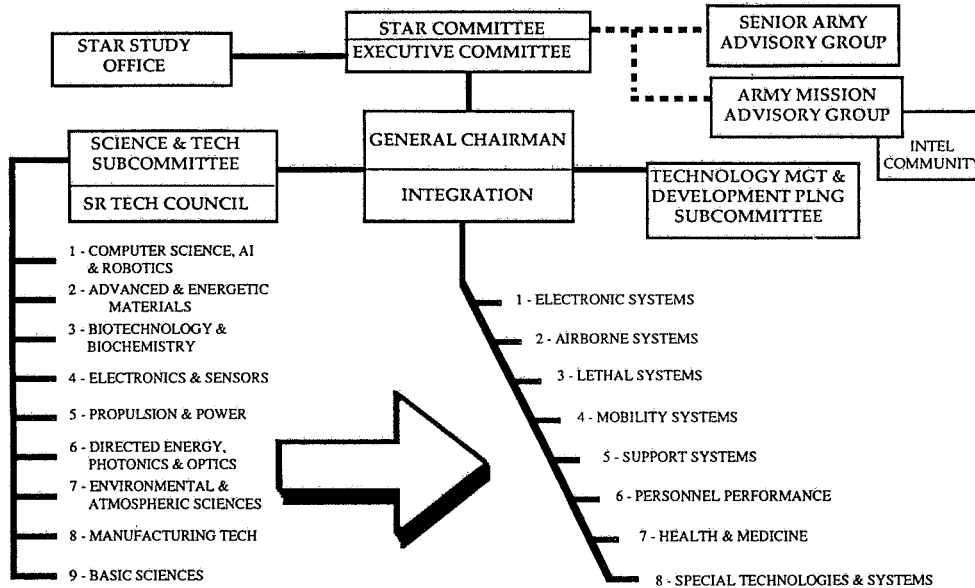


AMC

VG #7



STAR STUDY ORGANIZATION

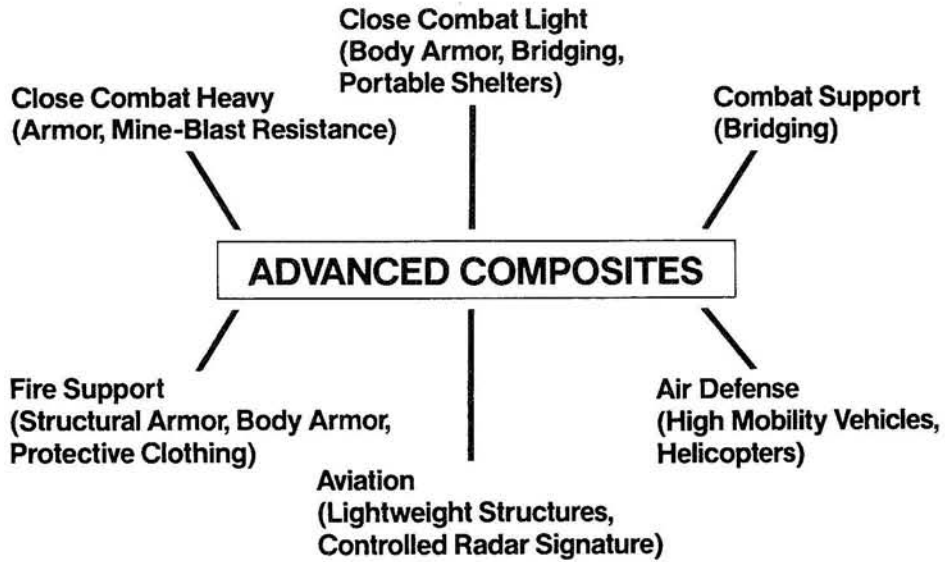


U.S. ARMY MATERIEL COMMAND
OFFICE OF THE CHIEF SCIENTIST

VG #8

LIGHTENING THE FORCE

ARO



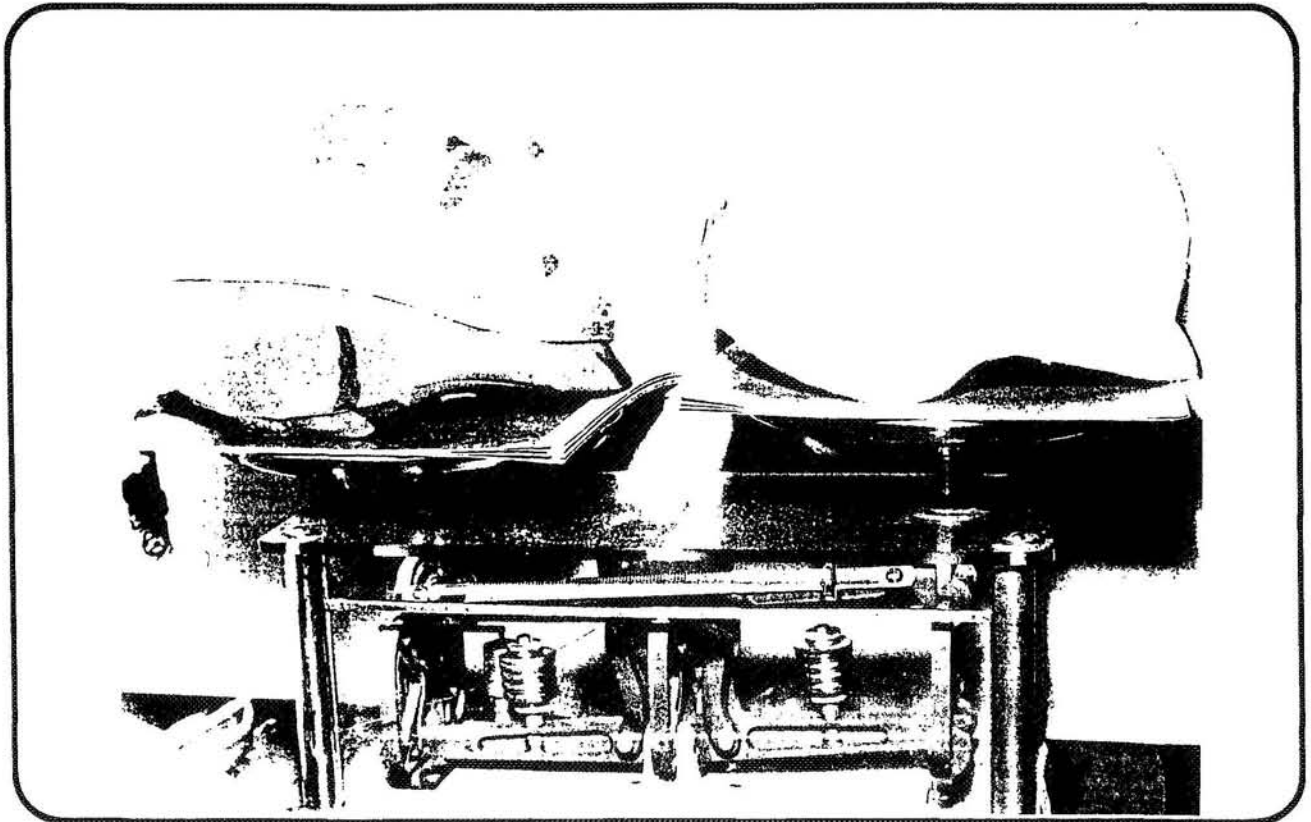
VG #9



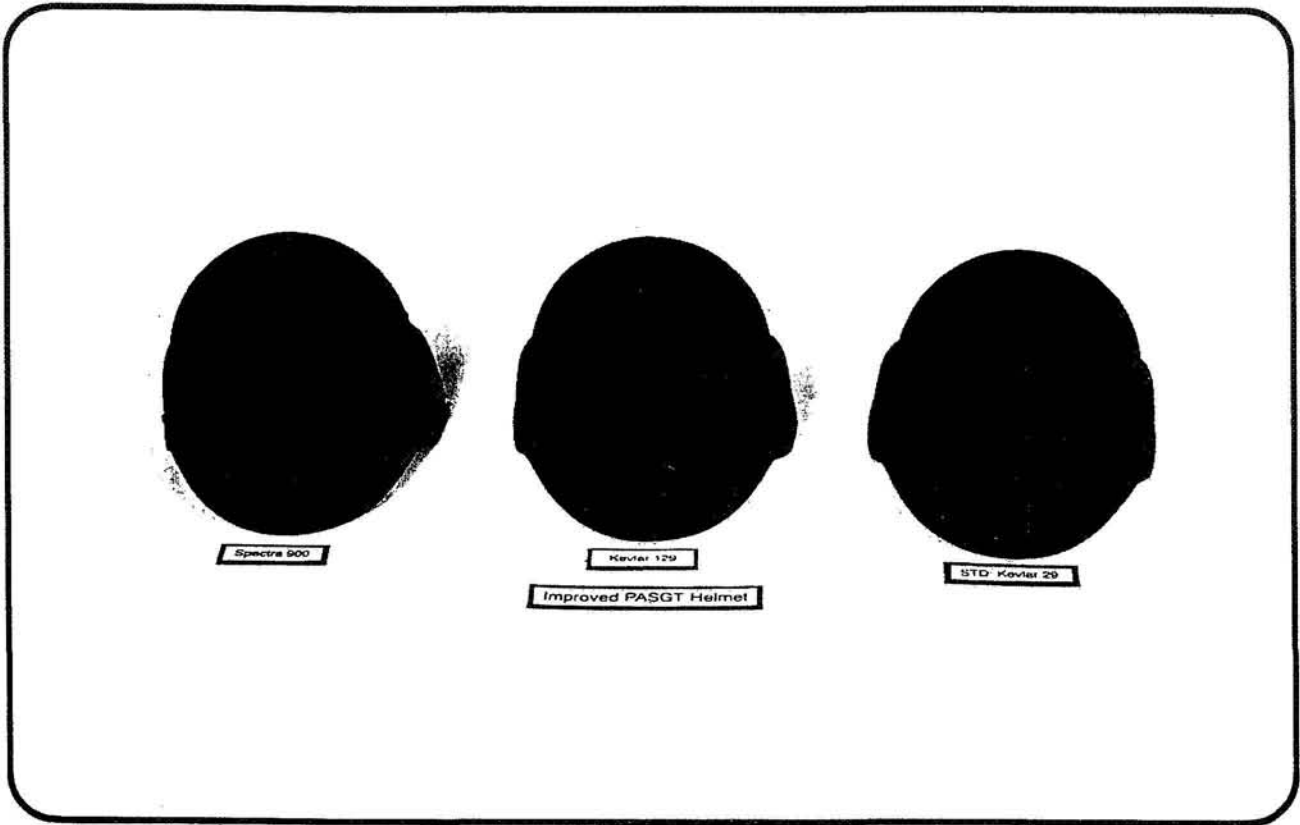
VG #10



VG #11



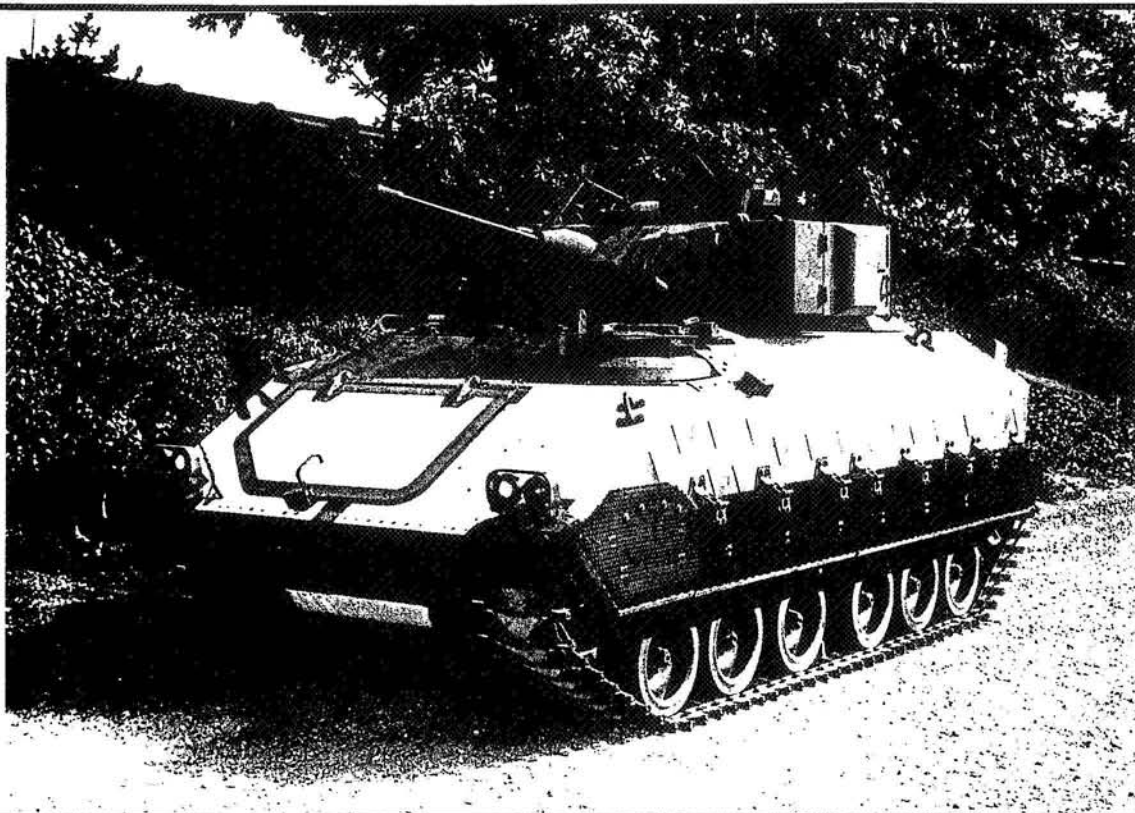
VG #12



VG #13



VG #14



VG #15



MATERIALS ENABLING TECHNOLOGY
COMBAT VEHICLE COMPOSITE HULL



MATERIALS TECHNOLOGY LABORATORY

DESCRIPTION

- THICK-LAMINATE HI-GLASS CONTENT COMPOSITE MOLDED HULL
- 3 STREAMLINED MOLDED PARTS
REPLACE 23 WELDED METAL PLATES
- BLAST-RESIST. COMPOSITE FLOOR
- CERAMIC/COMPOS. & EXPANDED METAL/COMPOS. SIDE ARMOR
- PROGRAM:FABRICATE, 6000 mi. TEST, COST EST., PROVIDE SYSTEMS DEVELOPERS WITH MAT'LS SPECS.

VALUE ADDED

- 25% WT SAVING (hull & armor)
EQUAL BALLISTIC PROTECTION
- REDUCED SPALL (Survivability)
- NO CORROSION (Maintainability)
- SIGNATURE REDUCTION
- REDUCED LIFE CYCLE COST
- LOGISTICS IMPROVEMENTS
MOBILITY
TRANSPORTABILITY
LESS FUEL CONSUMPTION

STATUS

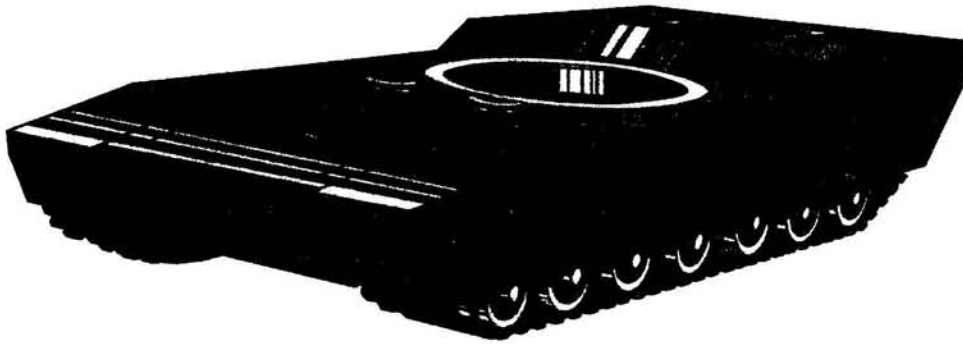
- PH. 1 DONE, ON TIME, IN BUDGET
- STRUCTURAL ANALYSIS DONE, CONCEPT SELECTED: 25% WT SAV.
- FULL-SCALE STRUCT. & BALLISTIC SPECIMENS MET PERFORM. REQUIRE.
- PH. 2 TOOLING DESIGN UNDERWAY

FY89-94 PLANS

- HULL FABRIC. & TEST- mid '89
- FLAMMABILITY CHARACT. - mid '89
- MMT[®] AUTOMATED FABRIC. - FY91
*(not funded)
- INSTALLATION ON VEHICLE FOR 6000 mi. FIELD TEST - mid FY91
- MATERIALS PROCESS. & SPEC. DATA TO TACOM - FY91

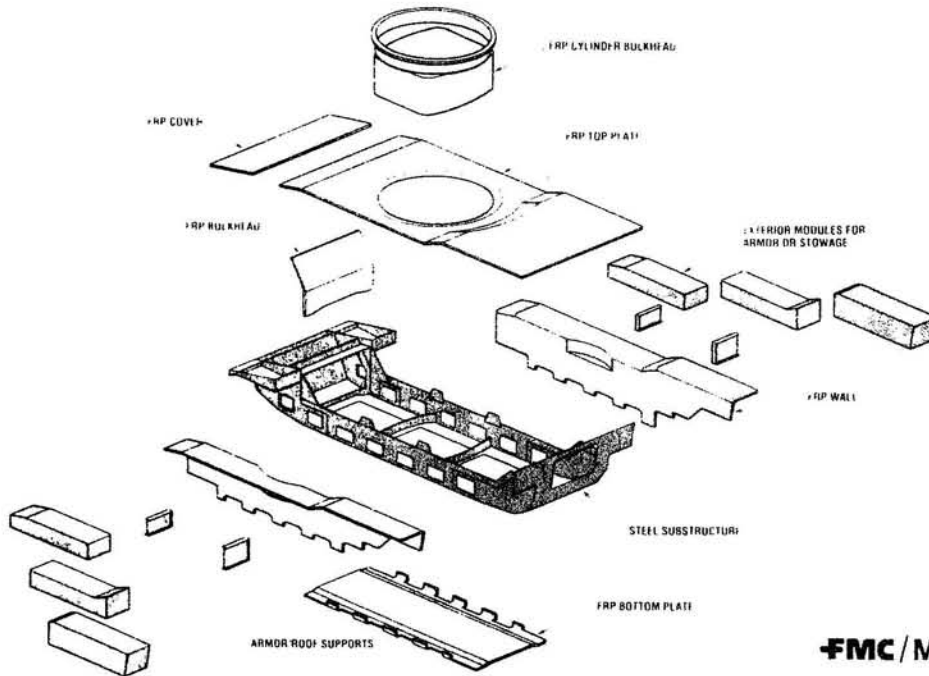
VG #16

Composite Hull Program



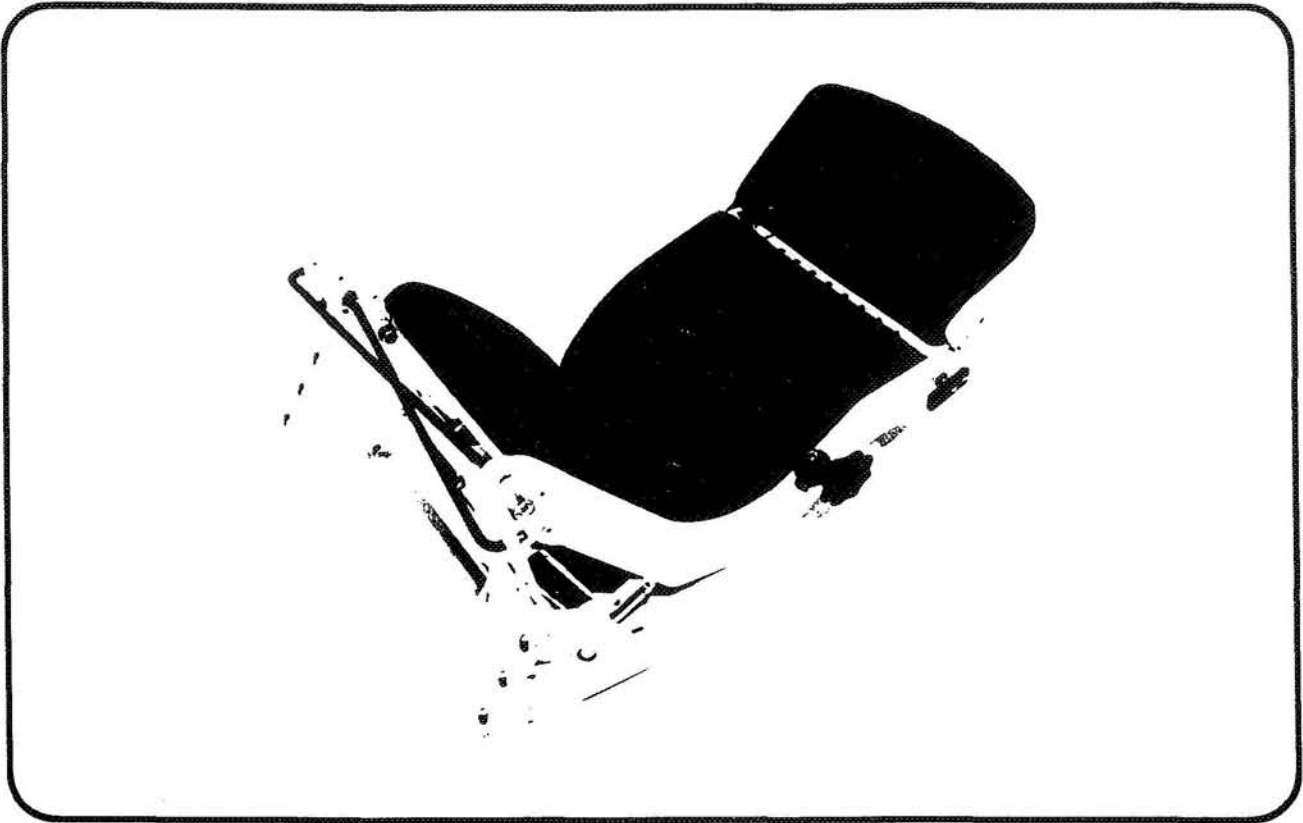
VG #17

COMPOSITE HULL PROGRAM Hull Exploded

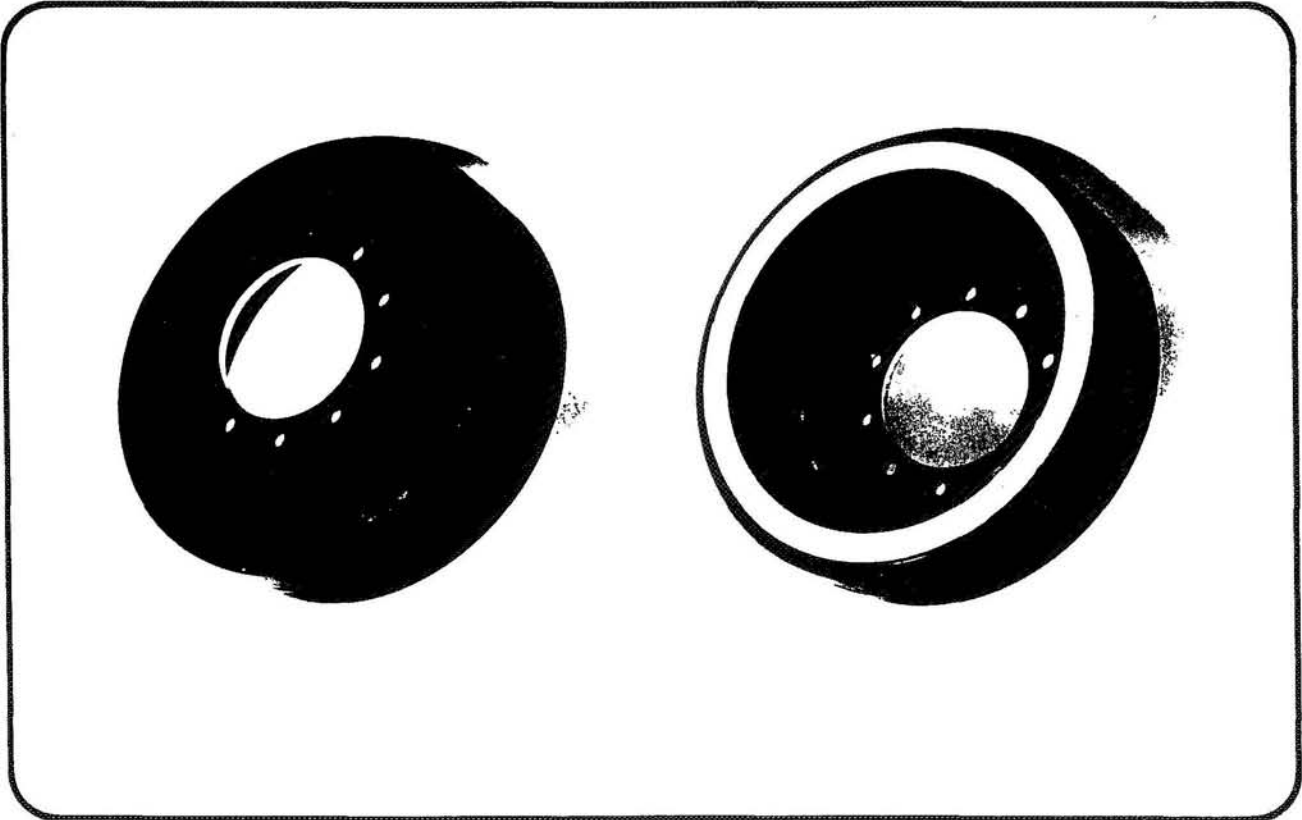


FMC/MTL

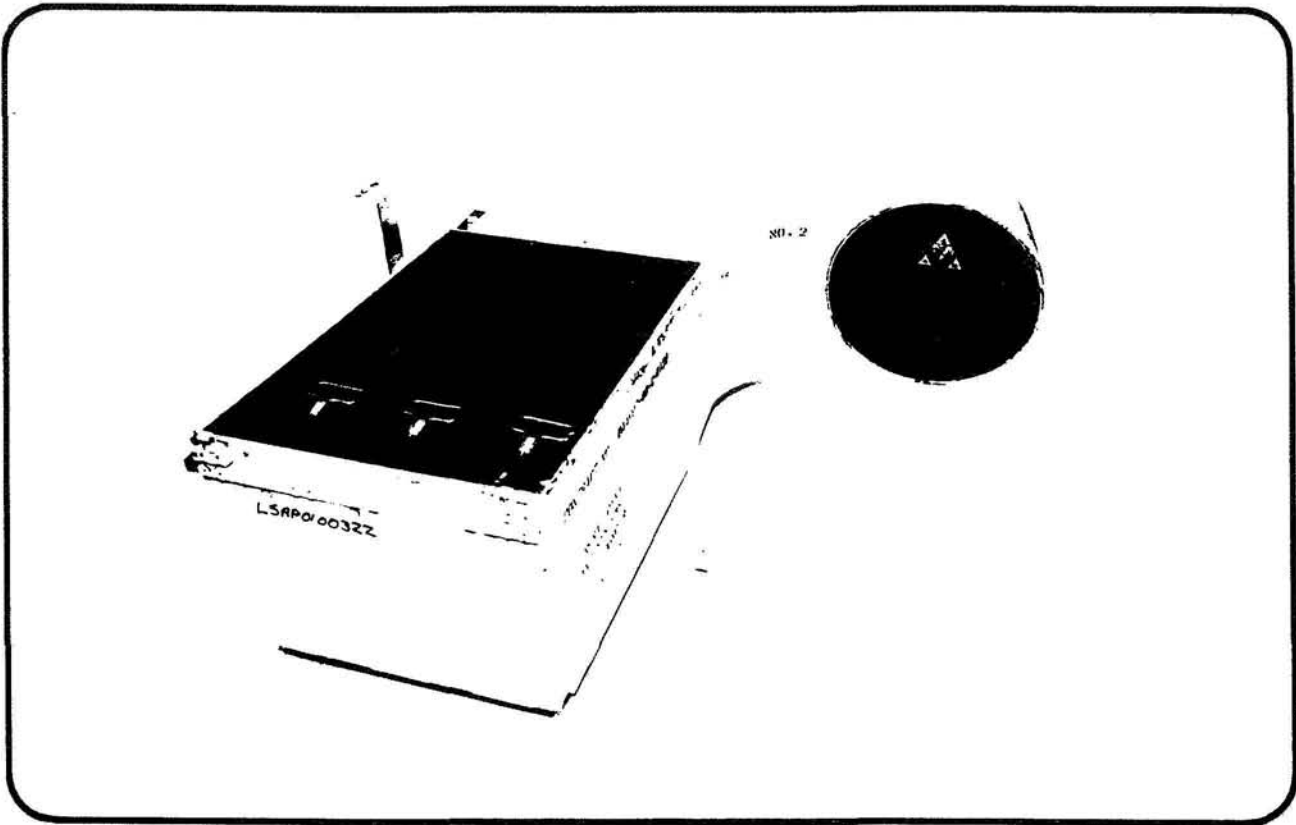
VG #18



VG #19

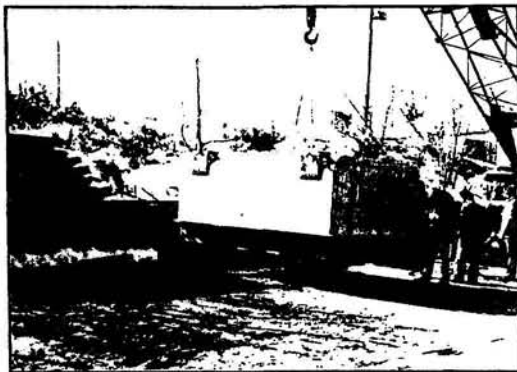


VG #20



VG #21

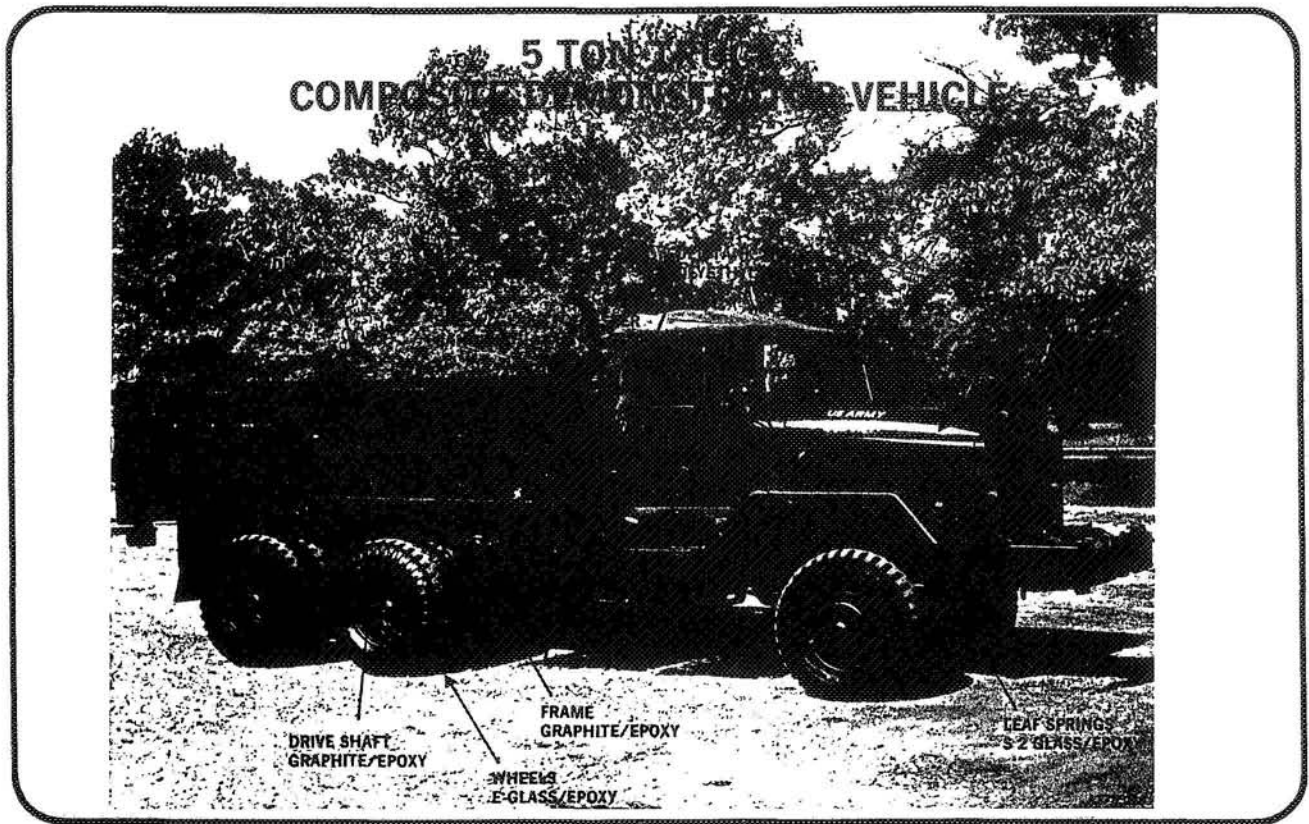
COMPOSITE FULL-UP POWER PACK CONTAINER



2000 POUND WEIGHT SAVINGS
COMPARED TO METAL DESIGN

TAC1434901

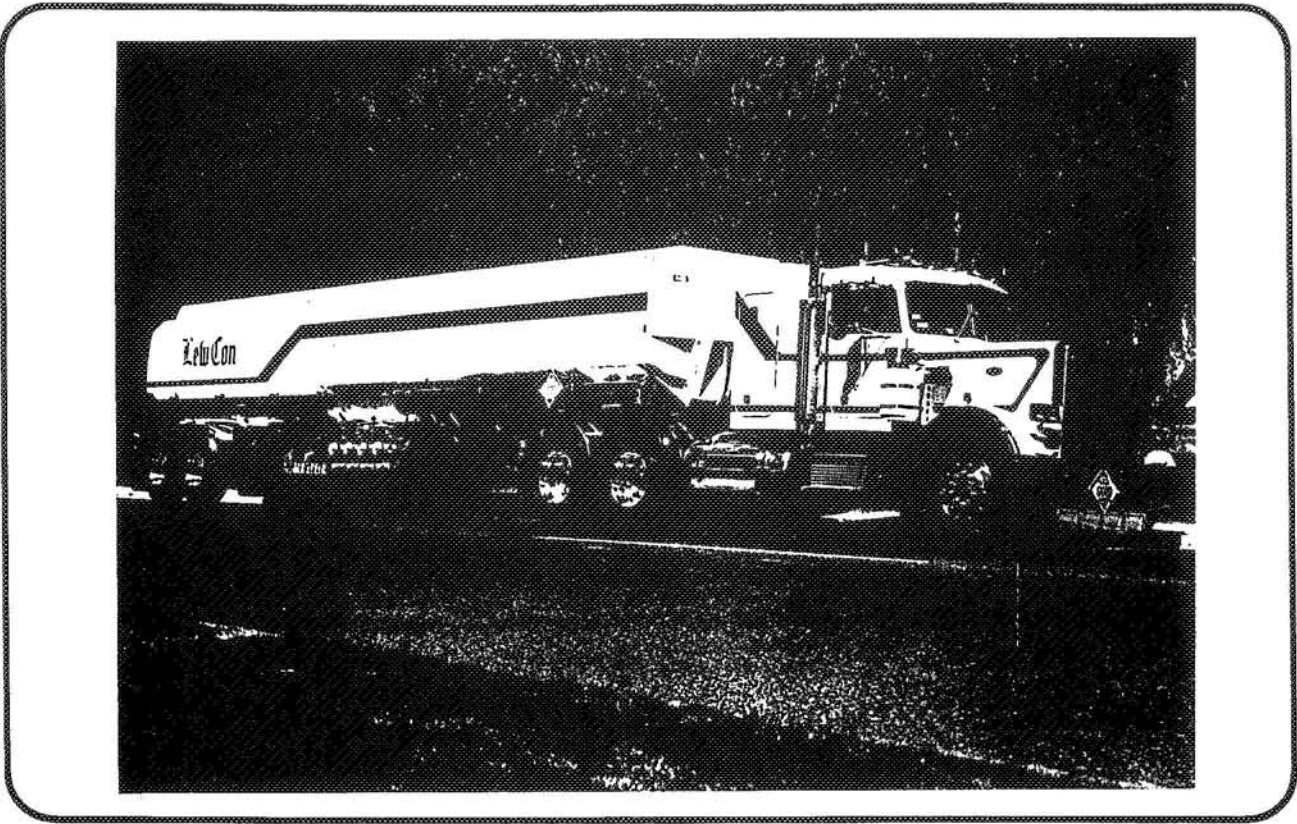
VG #22



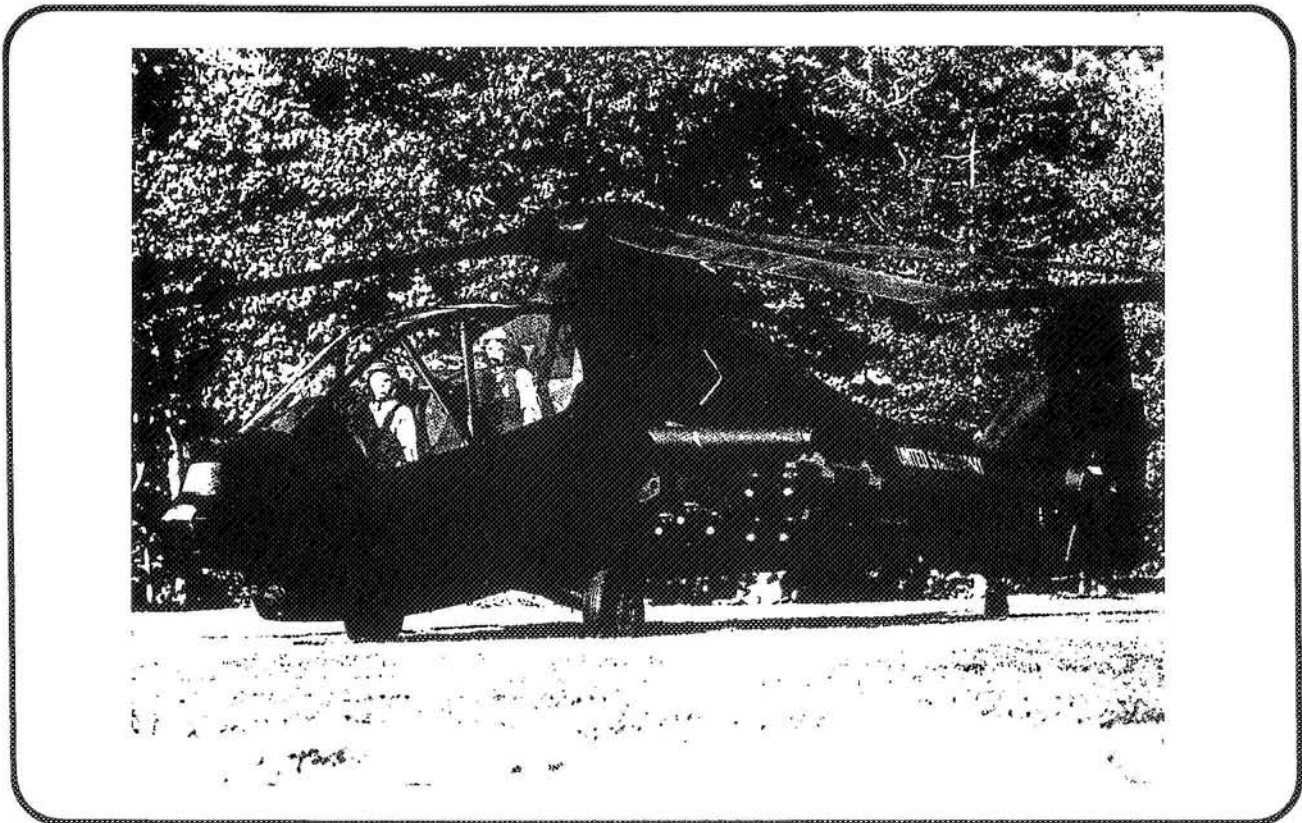
VG #23



VG #24



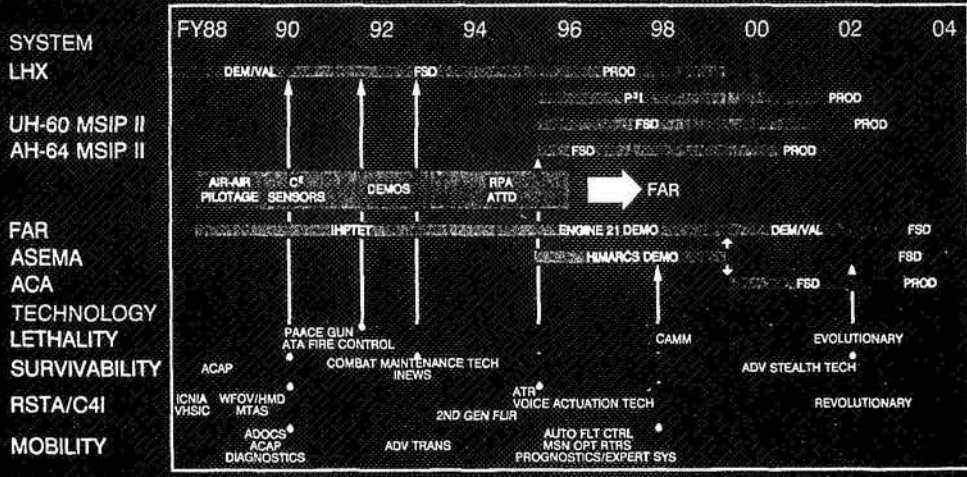
VG #25



VG #26

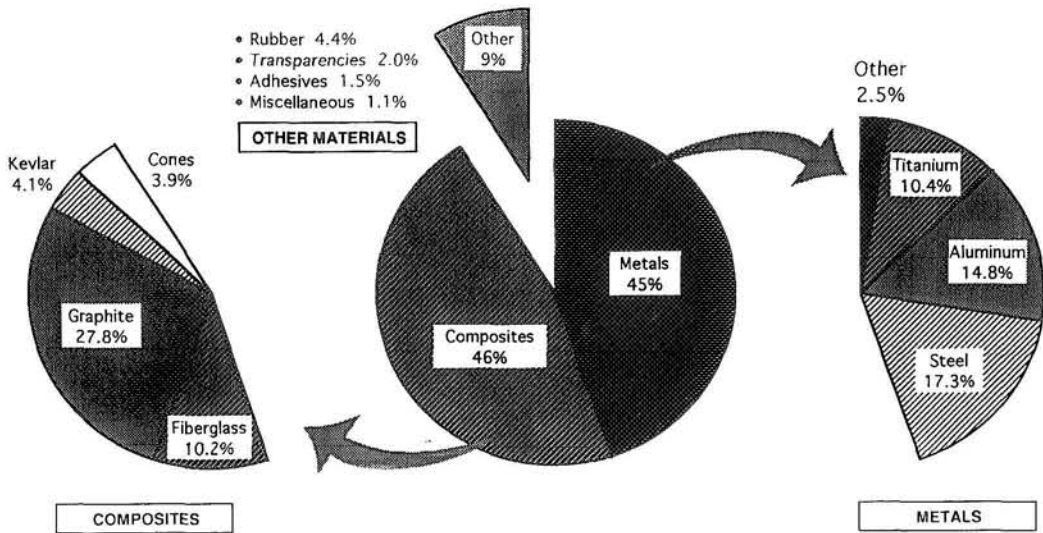
ARMY MODERNIZATION PLAN

AVIATION



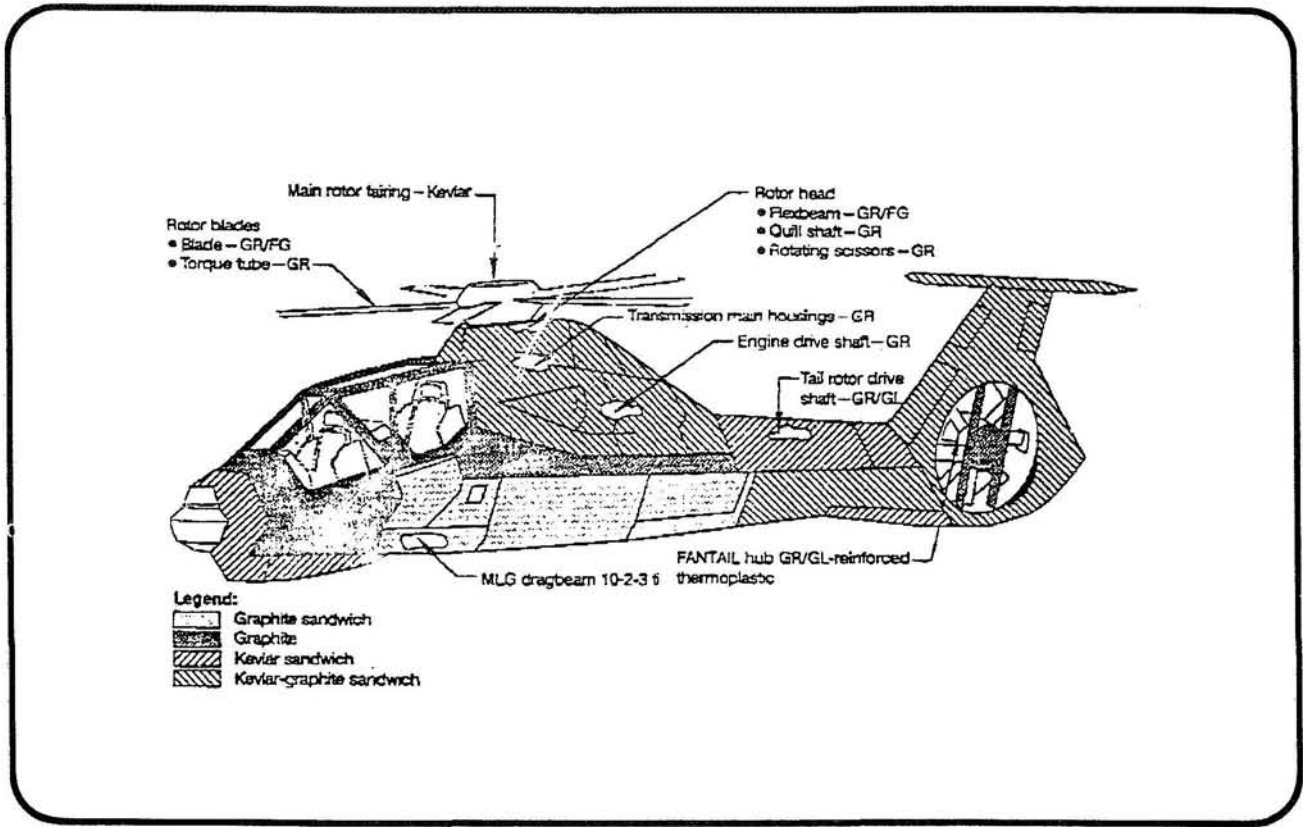
VG #27

LH Material Utilization

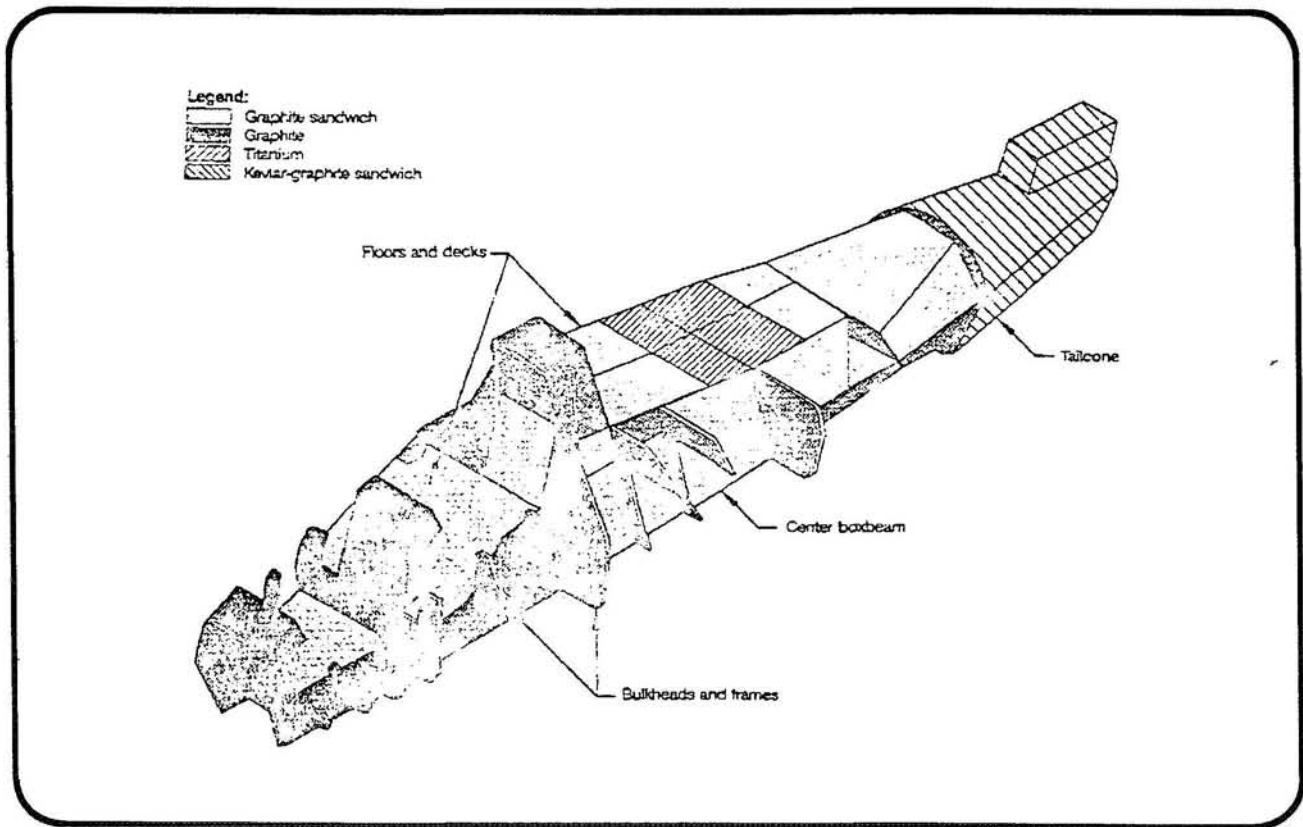


Percentage of Weight of Materials Used (Aircraft Weight)

VG #28



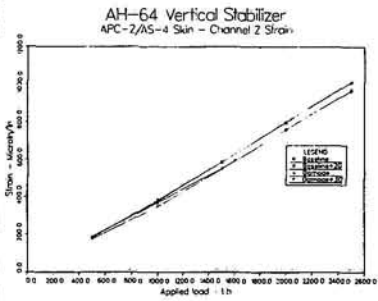
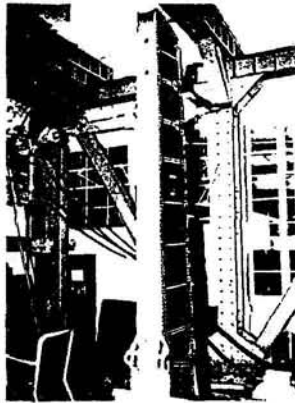
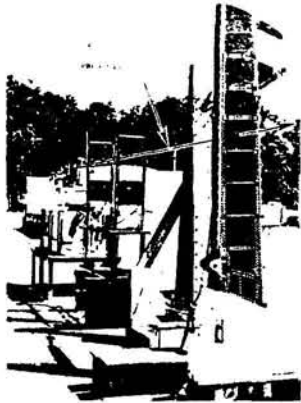
VG #29



VG #30

VERTICAL STABILIZERS TESTS

- Pre Ballistic Fatigue
- Damage (12.7mm)
- Post-Ballistic Fatigue
- Repair
- Post-Repair Fatigue



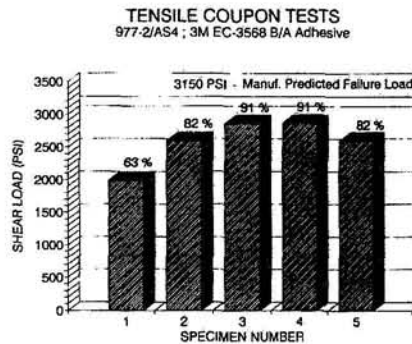
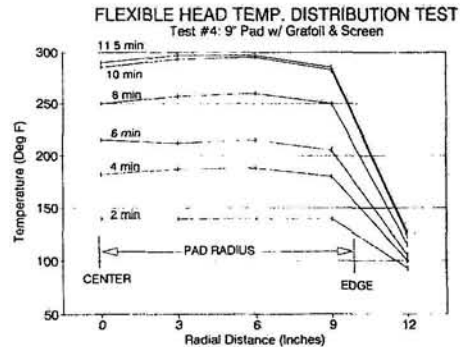
A0368 91 T147 3

VG #32

PORTABLE FIELD REPAIR SYSTEM (CRDA)

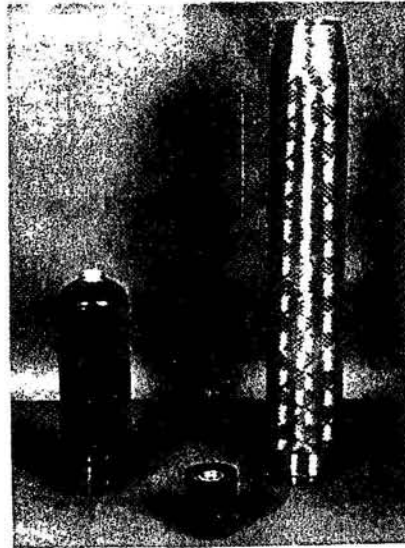
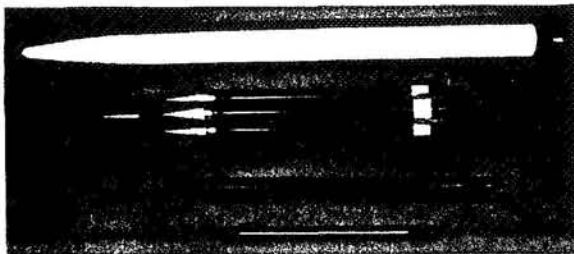
RESULTS:

- **TEMPERATURE DISTRIBUTION TESTS:**
 - UNIFORM TEMPERATURE PROFILE ACROSS PAD
 - RESIDUAL HEATING OUTSIDE PAD REGION
- **TENSILE COUPON TESTING:**
 - SHEAR LOADS UP TO 91% OF ADHESIVE MANUFACTURER'S PREDICTED FAILURE LOAD
- **SHEAR PANEL REPAIR:**
 - REPAIRS WITH INDUCTION HEATING AND HEAT BLANKET TECHNIQUES
 - FAILURE COMPARISONS OF UNDAMAGED, DAMAGED, AND REPAIRED PANELS

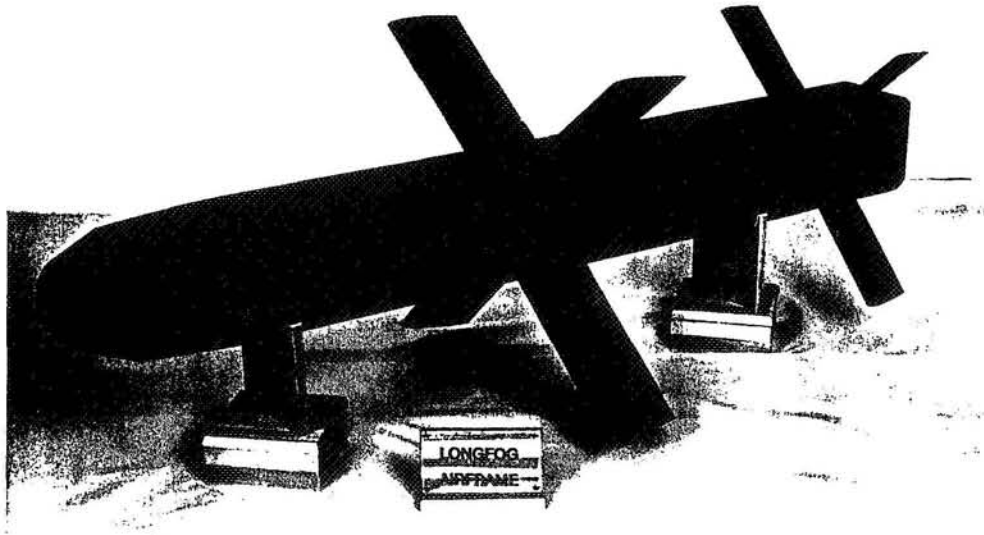


VG #33

- Hypervelocity Structural Development includes a family of Composite Motorcases from SPIKE to ADKEM with velocity capabilities up to 2000 m/s.
- Kinetic Energy Penetrator Lethality Test Vehicles for performing Full Scale Tests.
- Composite Motorcase Development for Insensitive Munitions Tests on SHRIKE, HELLFIRE, and AAWS-M Systems.
- Development of Composite Missile Subsystem Prototypes such as Wings, Fins, Storage Bottles, Blast Shields, and Nozzles.



VG #34

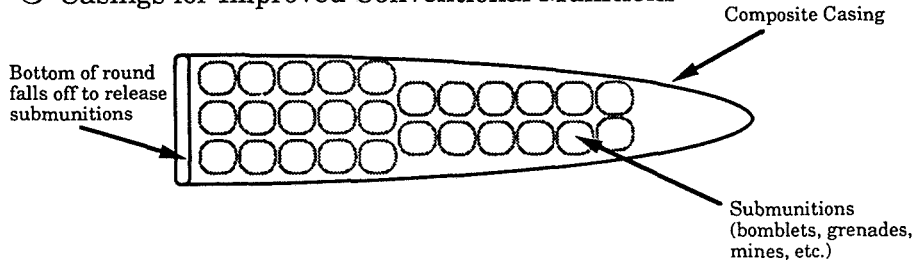


VG #35

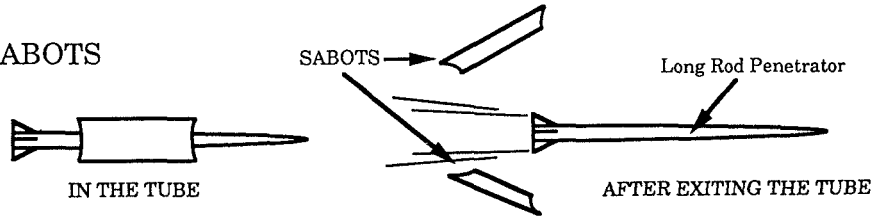


COMPOSITE USE IN MUNITIONS

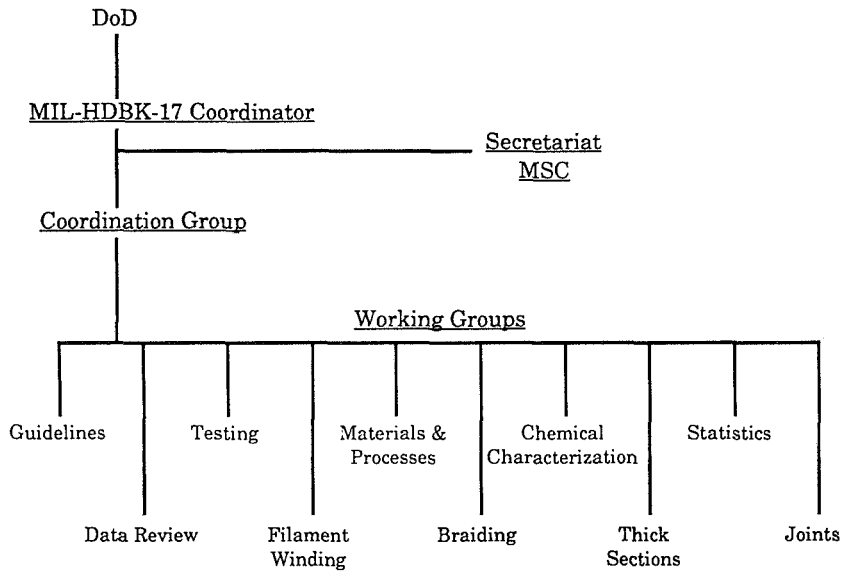
○ Casings for Improved Conventional Munitions



○ SABOTS



VG #36



* September 1991 -- Now

VG #37



MIL-HDBK-17 POLYMER MATRIX COMPOSITES

- MIL-HDBK-17, Guidelines for Generating Material Property Data
 - Release:
 - 90% complete
- MIL-HDBK-17-2B. Material Property Data
 - Release:
 - 13 materials plus all current MIL-HDBK-17A data
- MIL-HDBK-17-3C, Utilization of Data
 - Release:
 - 60% complete

VG #38



VOLUME 2

	Received	Approved
Carbon/Epoxy	39	10
Carbon/Bismaleimide	4	4
Aramid/Epoxy	2	
Glass/Epoxy	1	
Carbon/PEEK	2	1
Carbon/Polyimide	1	1
Quartz/Bismaleimide	1	1
	50	17

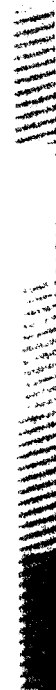
VG #39

GLASS POLYESTER
TEMPERATURE PROFILE



VG #40

GLASS POLYESTER
DEGREE OF CURE PROFILE (%)



VG #41

URI CENTER ON MANUFACTURING SCIENCE, RELIABILITY AND MAINTAINABILITY

RESEARCH ACCOMPLISHMENTS

- STOCHASTIC MODEL FOR PREDICTING CURE IN THICK SECTION COMPOSITES
- PERFORMANCE MAPS FOR DESIGN/MANUFACTURE OF 3-D TEXTILE COMPOSITES
- CONCURRENT ENGINEERING DESIGN METHODOLOGY
- COMPREHENSIVE MODEL FOR THERMO-PLASTIC FILAMENT WINDING

FY 1986 - FY 1991 FUNDING \$(K)

	FY86 - FY90 ACTUAL	FY91 PROJECTED
RESEARCH	\$2,316	\$706
FELLOWSHIPS	\$ 819	\$ 0
EQUIPMENT	\$1,019	\$ 0

TECHNOLOGY TRANSFER

- IMPROVED CURE CYCLE FOR COMPOSITES IN ADVANCED INFANTRY FIGHTING VEHICLE (FMC, MTL)
- CONCURRENT ENGINEERING APPROACH FOR COMPOSITES IN MISSILE COMPONENTS (MICOM)
- DESIGN OF COMPOSITE AIR CREW MASK COMPONENTS (CRDEC)
- COMPOSITE LIGHTWEIGHT TRAILER DESIGN (TACOM, SANDAIRE CORP)

EDUCATION

- 15 GRADUATE FELLOWSHIPS AWARDED
- 6 PHDS, 1 MS EARNED
- OVER 50 RESEARCH PAPERS PUBLISHED
- WORKSHOPS, SYMPOSIUMS, COURSES FOR DOD PERSONNEL
- RESIDENCY PROGRAM FOR ARMY SCIENTISTS
- 3 ARMY OFFICERS PURSUING ADVANCED DEGREES

VG #42

Processing-Induced Stress and Deformation in Thick-Section Thermosetting Composites

T. A. Bogetti (Ph.D. ME) Advisor: J. W. Gillespie, Jr.

RESEARCH GOALS

- Develop a model to study the development of processing induced stress and deformation in thick-section thermosets by modeling the curing process accounting for:
 - Thermo-chemical cure interactions
 - Thermal and cure induced dilation
 - Non-isothermal kinetic-viscoelasticity
 - Arbitrary cross-sectional geometries
- Verify the model's cure simulation, stress and deformation predictions with experiments.
- Optimize cure cycles for thick-section thermosets by retaining processing history to the state of the final component.

VISCOELASTIC STRESS/STRAIN CONSTITUTIVE MODEL

Nonisothermal, anisotropic stress-strain relation:

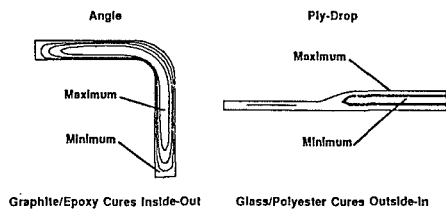
$$\underline{\sigma} = \int_{-\infty}^t \underline{C} [\xi(t) - \xi(\tau)] \frac{\partial}{\partial t} [\xi(\tau) - \alpha(\tau)] d\tau$$

Reduced time accounts for \underline{C} history dependence

$$\xi(t) = \int_0^t \dot{\xi}(\tau) d\tau$$

Where $\dot{\xi}(\tau)$ is temperature and degree of cure dependent.

CONTRASTING DEGREE OF CURE PROFILES (% Cured)



INCREMENTAL FINITE ELEMENT APPROACH

Reduce the viscoelastic solution to the superposition of elastic partial stress components:

$$\underline{\sigma}^{(t)} = \sum_{i=1}^N H_i^{(t)} [\delta \underline{\xi}^{(i)} - \delta \alpha^{(i)}]$$

Where the history dependence is recovered by

$$H_i^{(t)} = \frac{1}{\Gamma_i - 1} \int_{\Gamma_i - 1}^t [\xi(\Gamma_i) - \xi(\tau)] d\tau$$

VG #43

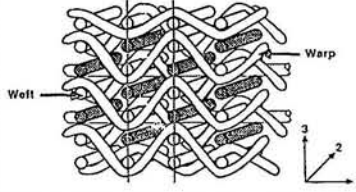
Microstructure-Property-Failure Relationships for 3-D Woven Composites

B. LaMattina (M. ME) Advisor: A. Parvizi-Majidi

OBJECTIVES

- Provide an understanding of the microstructure-property-failure relationships for 3-D woven composites.
- Develop and study RTM processing for 3-D fabric composites.
- Model the impact behavior and damage of fabric composites to provide a tool for the optimization of weave geometry.

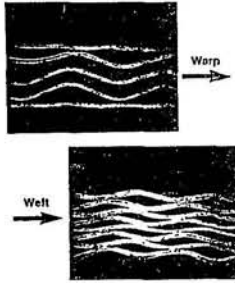
3-D ANGLE INTERLOCK WEAVE



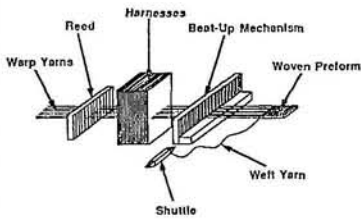
RTM MOLD



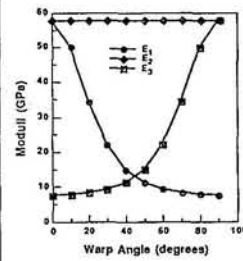
PHOTOMICROGRAPHS



WEAVING LOOM



MODULI VS. WARP ANGLE



VG #44

Design and Automated Fabrication of 3-D Braided Preforms for Structural Composites

T. D. Kostar (M. ME) Advisor: T-W. Chou

BACKGROUND

Three-dimensional braiding offers unique benefits to the science of composite preforming. These include:

- A built in through-the-thickness reinforcement to prevent delamination
- The ability to fabricate both thick and complex shapes
- Net-shape preforming capability

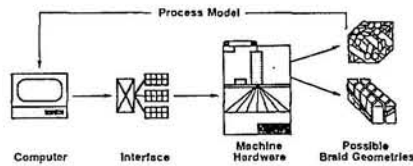
The much needed research in the following areas is under way.

- Automated Preform Fabrication
- Preform Consolidation
- Composite Property Predictions

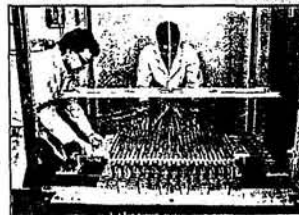
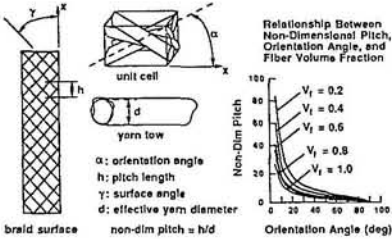
This present research focuses on the automated, intelligent fabrication of three-dimensional braided preforms for composites.

GOALS

- Fully automate the 3-D braiding process.
- Develop process model to relate operating conditions to preform architecture.
- Upgrade control software to allow for tailored design of preform shape and microstructure.



PROCESS MODELING



VG #45

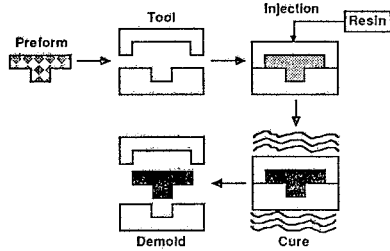
Preform Design and Manufacturing for Liquid Molding

D. A. Steenkamer (Ph.D. ME) Advisor: D. J. Wilkins

OBJECTIVES

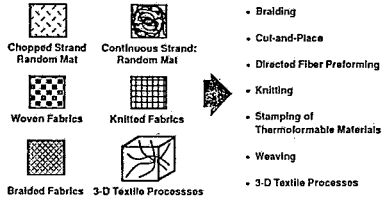
- Define a preform design environment based on the fiber architectures which are attainable with current textile processes.
- Develop analysis tools and processing heuristics to support the preform design environment.
- Devise a technique to efficiently join separate preform sections.

LIQUID MOLDING PROCESS

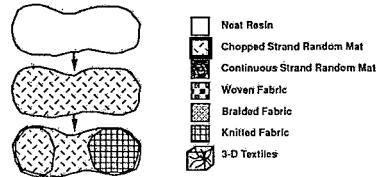


DEVELOPMENT OF PREFORM FIBER ARCHITECTURE FOR LIQUID MOLDING

Fiber Orientation Processes Preform Shaping Processes



PREFORM DESIGN AND ANALYSIS

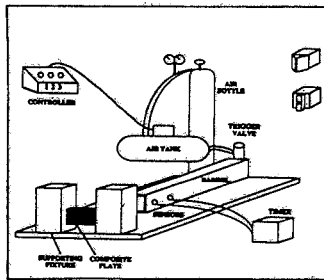


VG #46

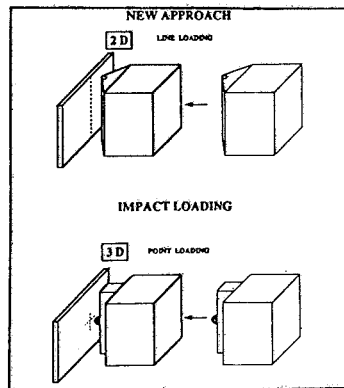
DYNAMIC RESPONSE PROGRAM

The Effects of Curvature and Thickness on Impact Damage in Composite Structures
 Prof. Fu-Kuo Chang, Stanford University

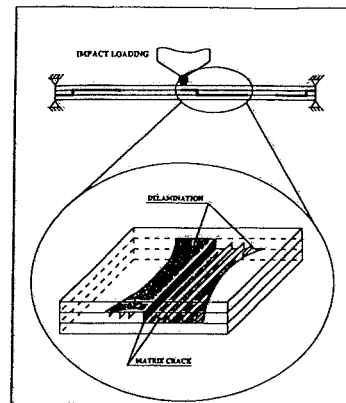
GOAL: Develop an analytical model to predict low velocity impact damage and to study failure mechanisms (cracking, delamination) in composite structures. Conduct experimental validation of the theory.



Impact test facility



Line and point impactors



Typical impact damage pattern in symmetric [0, 90] composites

VG #47

Possible uses for smart materials include "stealthy" submarine skins and composite wings to control vibration in aircraft.

- 1 Incoming sonar wave strikes piezoelectric sensor, generating a voltage pulse, which is then fed to the amplifier.
- 2 The feedback amplifier processes the pulse and sends a voltage to the actuator, causing it to contract.
- 3 As the actuator contracts, it acts like a very soft or compliant material, damping the reflected wave.

When subjected to electrical voltages the particles in electro-rheological fluids are realigned, making the fluid nearly as stiff as a solid. Arranged in alternating layers and controlled by a feedback system, they could be used to fine-tune the flex of an airplane wing.

U.S. ARMY MATERIEL COMMAND
OFFICE OF THE CHIEF SCIENTIST

VG #48

ROBUST CONTROLLERS (to accommodate some delaminations and debonding)

Objective: Controllers designed to reduce the vibrations for a perfect structure may not be used for a delaminated structure may lead to instability?. We would like to design robust controllers that can be effective for delaminated beams as well.

Delaminated Beam

MODAL ACCELERATION

TIME IN SEC

MODAL ACCELERATION

TIME IN SEC

Tip response of a delaminated beam using a controller that is designed for a perfect beam

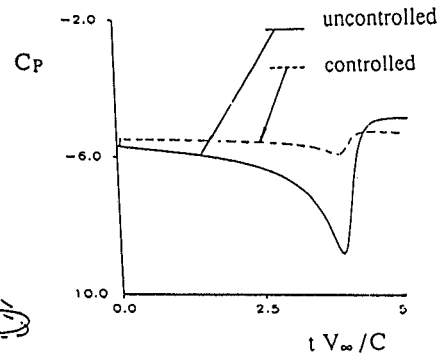
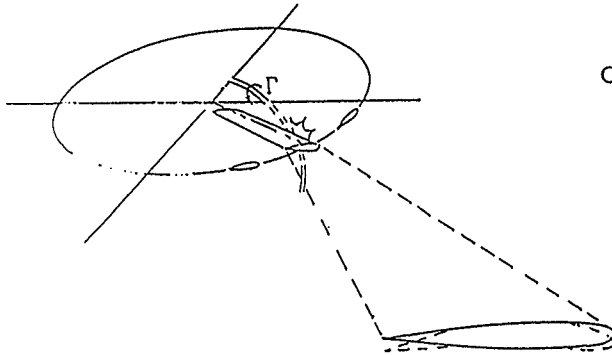
Tip response of a delaminated beam using a robust controller.

Georgia Tech

VG #49

BLADE VORTEX INTERACTION

Objective: We would like to discuss the feasibility of controlling the magnitude of the pressure pulse due to the interaction of the rotor blade with shed vortices of preceding blades, by using actuation that changes the shape of the airfoil.



Active control by the use of shape memory alloys or piezo electric actuators (to change the shape of the airfoil) and optimum control techniques.

Georgia Tech

VG #50

U. S. ARMY MATERIEL COMMAND



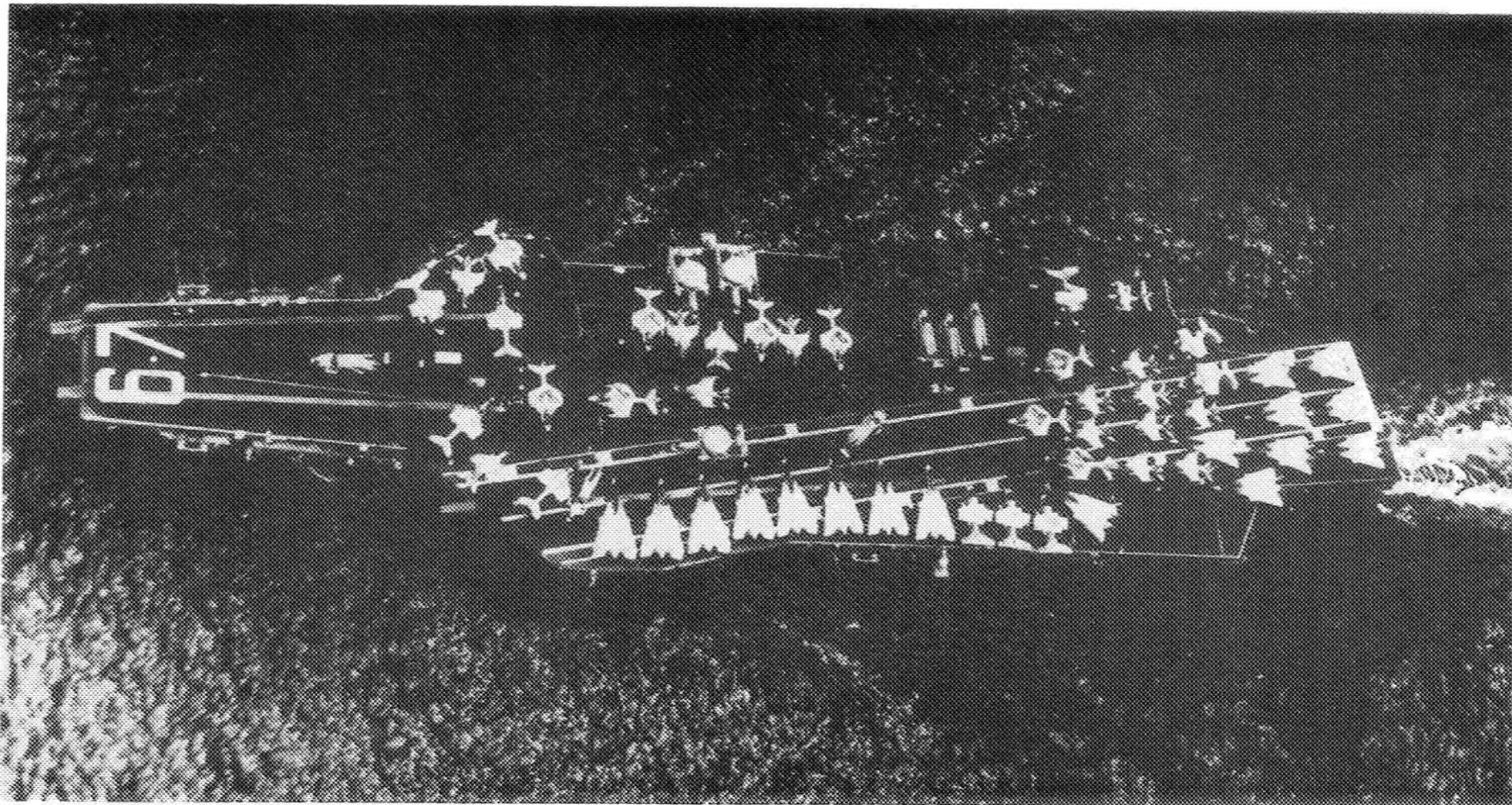
CONCLUDING REMARKS

- Diverse Mission
- Stable Funding For Tech Base
- Need For Advanced Materials
- Need For Composite Materials
- Effective Technical Planning

VG #51



BENEFITS AND LIMITATIONS OF COMPOSITES IN CARRIER-BASED AIRCRAFT



35

NINTH DOD/NASA/FAA CONFERENCE ON FIBROUS COMPOSITES IN STRUCTURAL DESIGN

DR. D. McERLEAN
NAVAL AIR DEVELOPMENT CENTER

5/3/00
P-55

N95-28422

UNIQUE ASPECTS OF NAVAL AIR MISSIONS

THERE ARE MANY UNIQUE ASPECTS OF NAVY AIR MISSIONS THAT LEAD TO THE DIFFERENTIATION BETWEEN THE DESIGN AND PERFORMANCE OF SHIP AND SHORE-BASED AIRCRAFT. WE SHALL DISCUSS THE MAJOR UNIQUE ASPECTS FROM WHICH ESSENTIALLY ALL NAVY AIRCRAFT DESIGN REQUIREMENTS DERIVE.

FIRST: THE FACT THAT NAVY AIRCRAFT OPERATE FROM CARRIERS AT SEA IMPOSES A BROAD SPECTRUM OF PHYSICAL CONDITIONS, CONSTRAINTS AND REQUIREMENTS RANGING FROM THE HARSH AT-SEA ENVIRONMENT, THE SPACE LIMITATIONS OF A CARRIER, TAKE-OFF AND LANDING REQUIREMENTS AS WELL AS A NEED FOR ENDURANCE AT LONG DISTANCES FROM THE CARRIER.

SECOND: BECAUSE THE CARRIER AND ITS AIRWING ARE INTENDED TO BE CAPABLE OF RESPONDING TO A BROAD RANGE OF CONTINGENCIES RANGING FROM CONFRONTATION WITH A MAJOR POWER TO PROVIDING PRESENCE IN THIRD WORLD AREAS, MISSION FLEXIBILITY IS ESSENTIAL. CARRIER BASED AIRCRAFT MUST HAVE MAXIMUM WEAPON CARRIAGE OPTIONS TO MEET CHANGING OR UNKNOWN THREATS, THEY MUST BE CAPABLE OF RAPID RECONFIGURATION, AND MUST HAVE MULTIPLE MISSIONS CAPABILITY TO HANDLE ALL CONTINGENCIES ONCE AIRBORNE.

THIRD: THE EMBARKED AIRCRAFT PROVIDES THE LONG RANGE DEFENSE OF THE BATTLE GROUP AGAINST AIR, SURFACE AND SUBSURFACE LAUNCHED ANTISHIP MISSILES. ALL CAPABILITY MUST BE ORGANIC TO THE BATTLE GROUP.

FOURTH: THE CARRIER AND ITS AIRCRAFT MUST OPERATE INDEPENDENTLY AND OUTSIDE OF NORMAL SUPPLY LINES ANYWHERE ON THE GLOBE. THEREFORE SELF SUFFICIENCY IS ESSENTIAL.



UNIQUE ASPECTS OF NAVAL AIR MISSIONS



- AT SEA/SHIPBOARD OPERATIONS
- MISSION FLEXIBILITY
- SELF-DEFENSE/FLEET DEFENSE A REQUIREMENT
- SELF SUFFICIENCY A REQUIREMENT

NAVAL AIRCRAFT OPERATIONAL ENVIRONMENT

CLEARLY, THE AT-SEA ENVIRONMENT PROVIDES A SIGNIFICANT DIFFERENCE IN AIR OPERATIONS FOR THE NAVY. THE PHOTOGRAPH SHOWS A BOW WAVE ENGULFING AIRCRAFT POSITIONED ON A CARRIER DECK. THIS CORROSIVE ENVIRONMENT REQUIRES MAJOR DIFFERENCES IN MATERIALS AND COATINGS FOR NAVY AIRCRAFT.



SIZE & WEIGHT LIMITS

SIZE LIMITATIONS

- THE CATAPULT TAKEOFF IMPOSES HARD LIMITS ON THE OVERALL LENGTH OF THE AIRPLANE AND THE MINIMUM HEIGHT ABOVE GROUND FOR THE FUSELAGE AND ANY OF ITS ATTACHMENTS, SUCH AS CENTERLINE TANKS OR WEAPONS.
- THE FLIGHT DECK GEOMETRY LIMITS THE WINGSPAN (OR ROTOR DIAMETER).
- THE ELEVATORS REQUIRE THAT HINGES FOR FOLDING THE AIRCRAFT BE EMPLOYED WITH POWER ACTUATION.
- THE HANGAR DECK IMPOSES A HEIGHT LIMIT TO THE VERTICAL TAIL OR TAIL ROTOR, IN THE FOLDED POSITION.

WEIGHT LIMITATIONS

- THE TAKEOFF WEIGHT, FULLY LOADED, IS LIMITED BY THE CAPACITY OF THE CATAPULT (90,000 #).
- THE LANDING WEIGHT, WITH RESERVE FUEL AND UNFIRED WEAPONS, IS LIMITED BY THE ARRESTING GEAR CAPACITY (65,000 #).



SIZE & WEIGHT LIMITS



- CATAPULT LAUNCH
 - OVERALL LENGTH (NOSE TO TAILPIPE)
 - GROUND CLEARANCE HEIGHT
- FLIGHT DECK GEOMETRY
 - WINGSPAN LIMITED FOR CLEARANCE
 - ROTOR DIAMETER ALSO LIMITED FOR CLEARANCE ON SMALLER SHIPS
- ELEVATORS
 - FOLD WINGS, TAILS, NOSE, ROTORS TO FIT (2) AIRCRAFT ON ELEVATOR
- HANGAR DECK
 - HEIGHT OF TAIL, FOLDED WINGS, OR TAIL ROTOR MUST CLEAR OVERHEAD SHIP FRAMES
- TAKEOFF & LANDING WEIGHT
 - THROW CAPACITY OF CATAPULT
 - ENERGY ABSORPTION OF ARRESTING GEAR

NAVY STRUCTURES REQUIREMENTS/CONSTRAINTS

THE DESIGN OF THE STRUCTURE IS DRIVEN BY THE LARGE LANDING SINK RATES AND THE CATAPULT AND ARRESTED LANDING LOADS IMPOSED ON THE AIRFRAME, BOTH STATICALLY AND IN FATIGUE. THE MAGNITUDE AND LOCATION OF THE LOADS INFLUENCE STRUCTURAL CONFIGURATION, LOAD DISTRIBUTION AND MATERIAL SELECTION. THESE HIGHER LOADS IMPOSE SEVERE WEIGHT PENALTIES ON CARRIER BASED AIRCRAFT COMPARED TO LAND BASED AIRCRAFT.

THE SHIPBOARD ENVIRONMENT IMPOSES SEVERE REQUIREMENTS IN AIRFRAME MATERIALS USAGE AND SUPPORTABILITY ISSUES. THE LOGISTICS CONSTRAINTS FOR CARRIER OPERATIONS BEING MUCH MORE SEVERE THAN FOR LAND BASED OPERATIONS, IMPOSE UNIQUE REQUIREMENTS FOR SUPPORTABILITY OF AIRFRAMES. REPAIR MATERIALS REQUIRE LONG SHELF LIFE AT AMBIENT TEMPERATURES. REPAIR PROCEDURES MUST BE COMPATIBLE WITH EQUIPMENT AND FACILITIES ON-BOARD, AND WITHIN THE CAPABILITIES OF FLEET PERSONNEL.

DUE TO THE LIMITED SPACE AVAILABLE BOTH ON THE FLIGHT AND HANGER DECKS, AS WELL AS ELEVATORS, NAVY AIRCRAFT TYPICALLY INCLUDE MECHANISMS TO FOLD OR STOW WINGS, ROTOR BLADES AND TAILS. THE V-22, FOR EXAMPLE, INCORPORATES MECHANISMS TO FOLD ROTOR BLADES, TILT THE NACELLES AND ROTATE THE WING TO A POSITION PARALLEL TO THE FUSELAGE.

VSTOL AIRCRAFT (SUCH AS THE AV-8B) ALSO ENCOUNTER ELEVATED TEMPERATURES AT VARIOUS LOCATIONS ON THE STRUCTURE DUE TO IMPINGEMENT OF HOT EXHAUST GASES FROM THE ENGINE NOZZLES. THIS HAS REQUIRED THE APPLICATION OF SPECIALITY MATERIALS AND HAS RESULTED IN SERVICE PROBLEMS WHICH WILL BE DISCUSSED LATER.

THE MISSIONS FOR CARRIER BASED AIRCRAFT IMPOSE UNIQUE FLIGHT ENVELOPES, FATIGUE SPECTRA, FATIGUE LIFE TRACKING METHODOLOGY, DAMAGE TOLERANCE CRITERIA AND CERTIFICATION REQUIREMENTS. THESE REQUIREMENTS HAVE LED TO THE EVOLUTION OF NAVY DESIGN PHILOSOPHY, CRITERIA, AND CERTIFICATION PROCEDURES. THIS PHILOSOPHY AND CRITERIA ARE SPECIFICALLY USED IN ALL PROGRAMS ADDRESSING STRUCTURAL INTEGRITY ISSUES FOR NAVY/MARINE AIRFRAMES. "TOUGH ENVIRONMENTS REQUIRE TOUGH CRITERIA."



NAVY STRUCTURES REQUIREMENTS/CONSTRAINTS



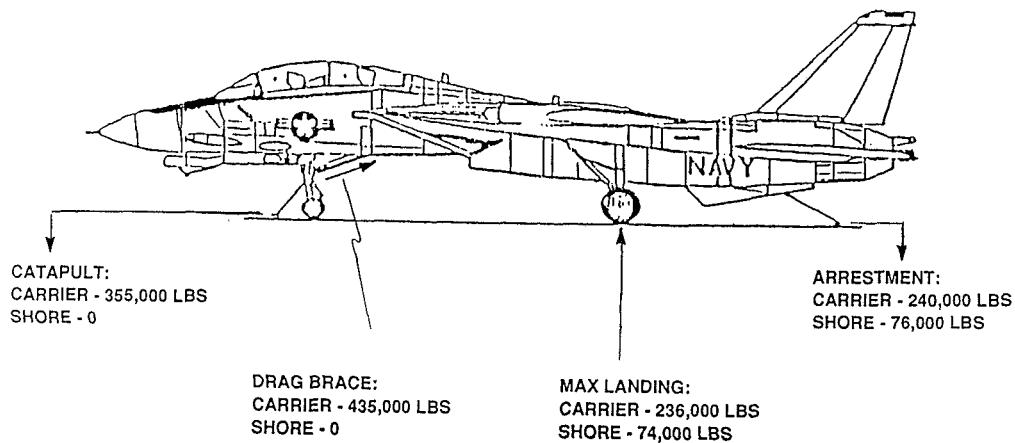
- HIGH SINK RATES
- CATAPULT AND ARREST REQUIREMENTS
- MAINTENANCE LOGISTICS AND SUPPORT EQUIPMENT
- MAINTENANCE AND INSPECTION PROCEDURES
- FOLDING STRUCTURE
- STRUCTURAL TEMPERATURES
- DESIGN PHILOSOPHY AND CRITERIA
- TESTING AND CERTIFICATION REQUIREMENTS
- AIRCRAFT USAGE
- FATIGUE LIFE TRACKING METHODOLOGY

GROUND LOADS COMPARISON CARRIER VS. SHORE BASED

THIS FIGURE DRAMATICALLY ILLUSTRATES THE SIGNIFICANT DESIGN LOAD REQUIREMENTS FOR A TYPICAL NAVY CARRIER BASED AIRCRAFT COMPARED TO A SHORE BASED AIRCRAFT.



GROUND LOADS COMPARISON CARRIER VS. SHORE BASED





NAVY COMPOSITE STRUCTURES EXPERIENCE

THE NAVY HAS 20 YEARS OF COMPOSITE EXPERIENCE. THE NAVY INITIATED THE USE OF ADVANCED COMPOSITES IN PRODUCTION AIRCRAFT DURING THE EARLY 70'S WITH THE USE OF F-14 STABILATORS WITH BORON/EPOXY SKINS OVER A FULL DEPTH HONEYCOMB CORE. DURING DEVELOPMENT OF SUBSEQUENT AIRCRAFT, THE USE OF COMPOSITES INCREASED. THE F-18 DESIGN INCORPORATED GRAPHITE/EPOXY WING SKINS AND HORIZONTAL AND VERTICAL TAILS. THIS WAS A VERY CONSERVATIVE USE OF COMPOSITES. THE PROGRAM SCHEDULE ALSO ALLOWED TIME FOR REDESIGN SHOULD A MAJOR TEST FAILURE OCCUR IN THE COMPOSITE SKINS. THE AV-8B DESIGN WAS MORE AGGRESSIVE IN THE USE OF COMPOSITES AND THE FIRST ALL COMPOSITE WING, FORWARD FUSELAGE AND HORIZONTAL STABILATOR WERE INCORPORATED FOR PRODUCTION. IN THIS AIRCRAFT, THE USE OF COMPOSITES PERMITTED INCORPORATION OF A 15% LARGER SUPERCRITICAL WING WITH A MODERATE WEIGHT SAVINGS OVER THE ORIGINAL METAL AV-8A WING. RECENTLY, THE A-6 RE-WING EFFORT RESULTED IN EXTENSIVE USE OF GRAPHITE FOR THE WING SKINS AND MUCH OF THE SUBSTRUCTURE TO MEET INCREASED FATIGUE AND LOAD REQUIREMENTS AT NO INCREASE IN WEIGHT. AGAIN BECAUSE OF WEIGHT CRITICALITY IN A VSTOL APPLICATION, THE V-22 AIRCRAFT INCORPORATES A NEARLY ALL COMPOSITE WING AND FUSELAGE STRUCTURE.

NAVY COMPOSITE STRUCTURES EXPERIENCE

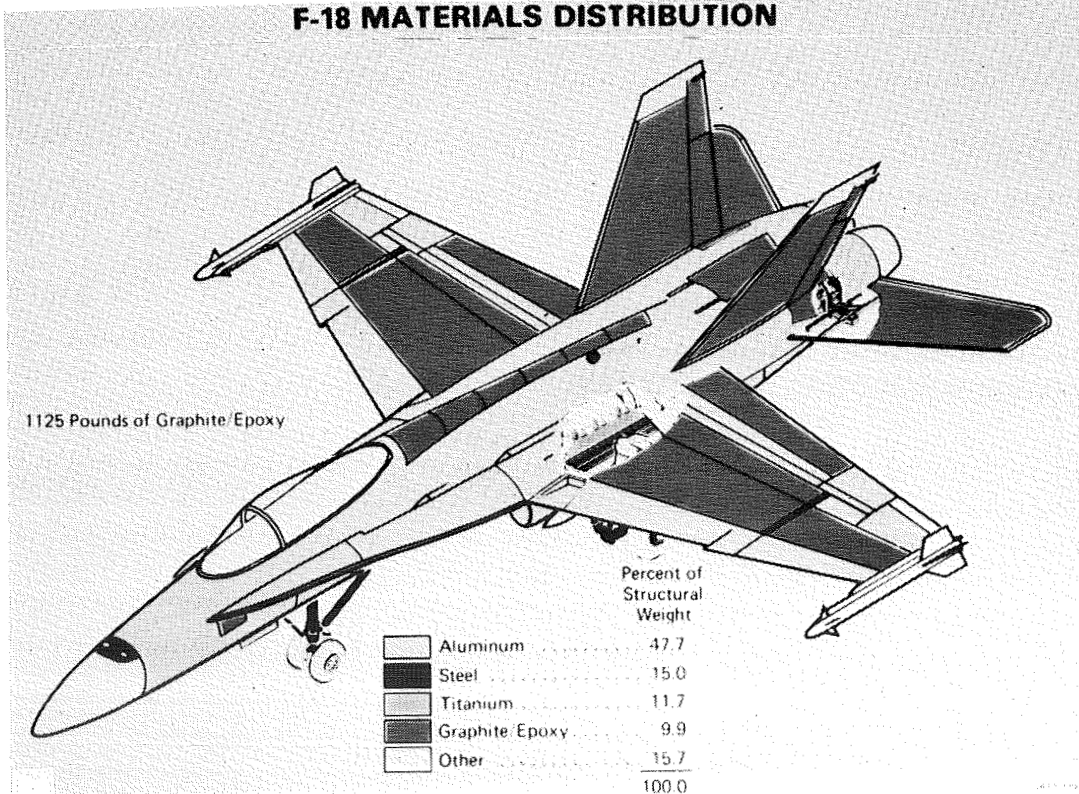
EVOLUTIONARY EXPANSION OF PRODUCTION APPLICATIONS

F-14	1%	1970
F/A-18	10%	1978
AV-8B	26%	1982
A-6 WING	38%	1988
V-22	50%	1990's

F-18 COMPOSITE STRUCTURE

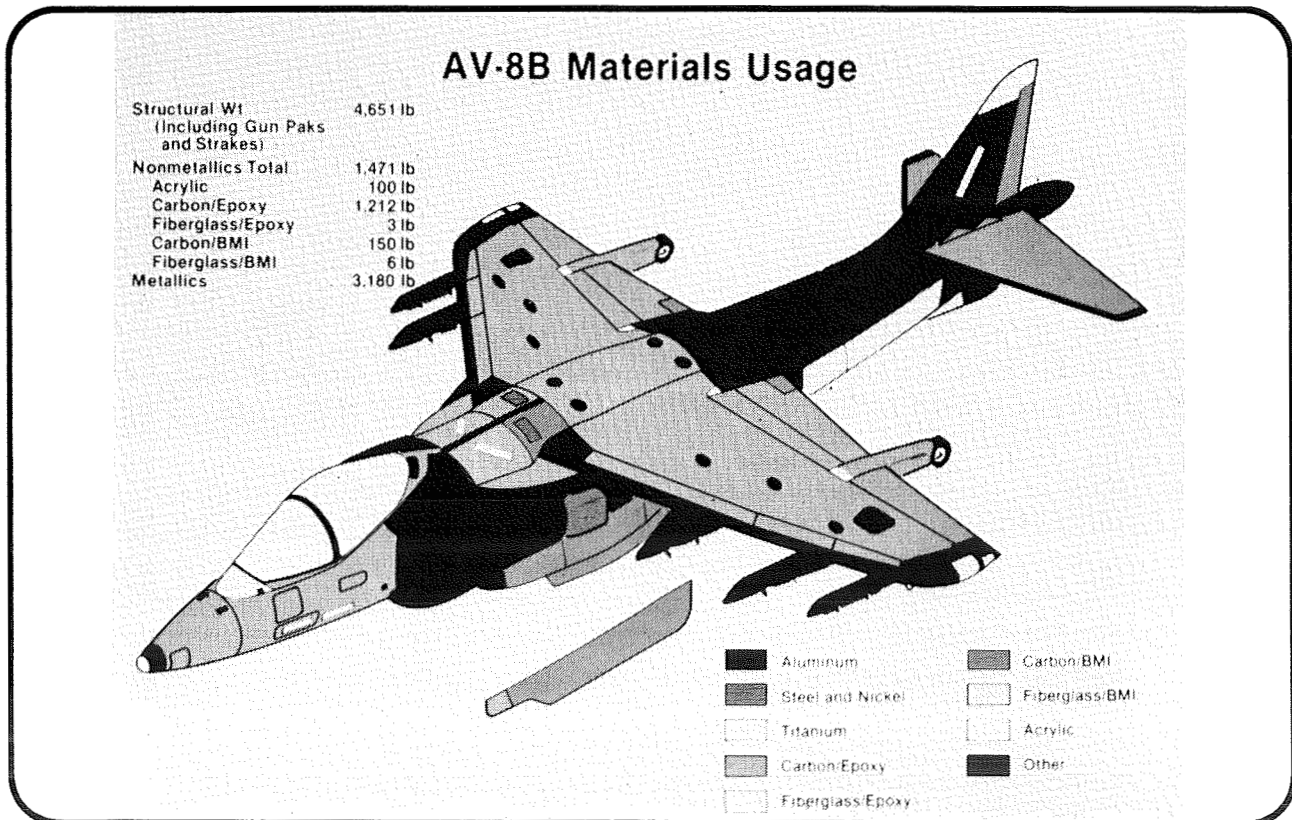
GRAPHITE/EPOXY USED PRIMARILY ON WING AND STABILIZER SKINS AND CENTER FUSELAGE DORSAL FAIRING, SPEED BRAKE AND WING FLAPS.

F-18 MATERIALS DISTRIBUTION



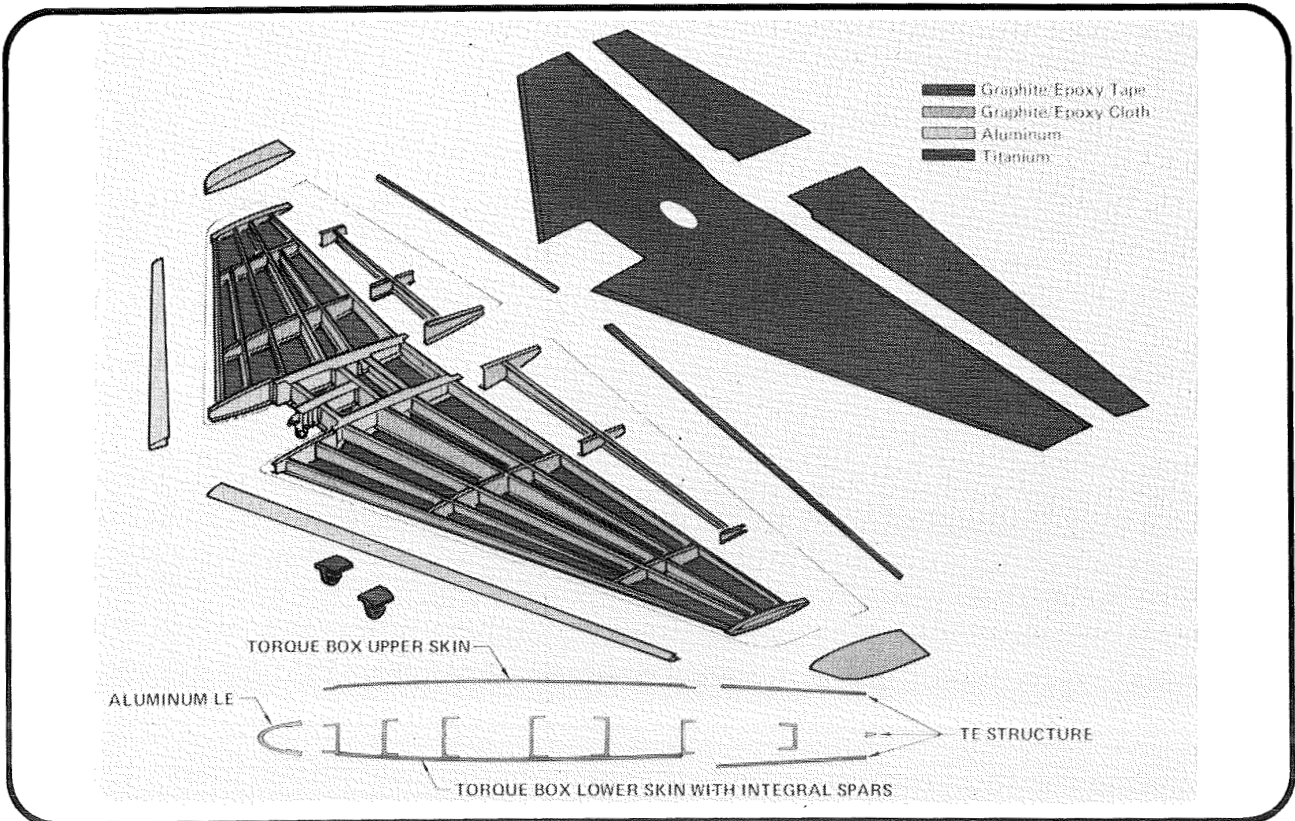
AV-8B COMPOSITE STRUCTURE

GRAPHITE/EPOXY USED IN WING, FUSELAGE, AND TAIL STRUCTURES. WING IS MULTI-SINEWAVE SPAR/RIB SUBSTRUCTURE CONSTRUCTION. GRAPHITE/EPOXY IS ALSO USED IN THE HORIZONTAL STABILIZER AND RUDDER. GRAPHITE/BMI APPLICATIONS INCLUDE STRAKES AND LOWER SKIN OF THE MAIN FLAPS.



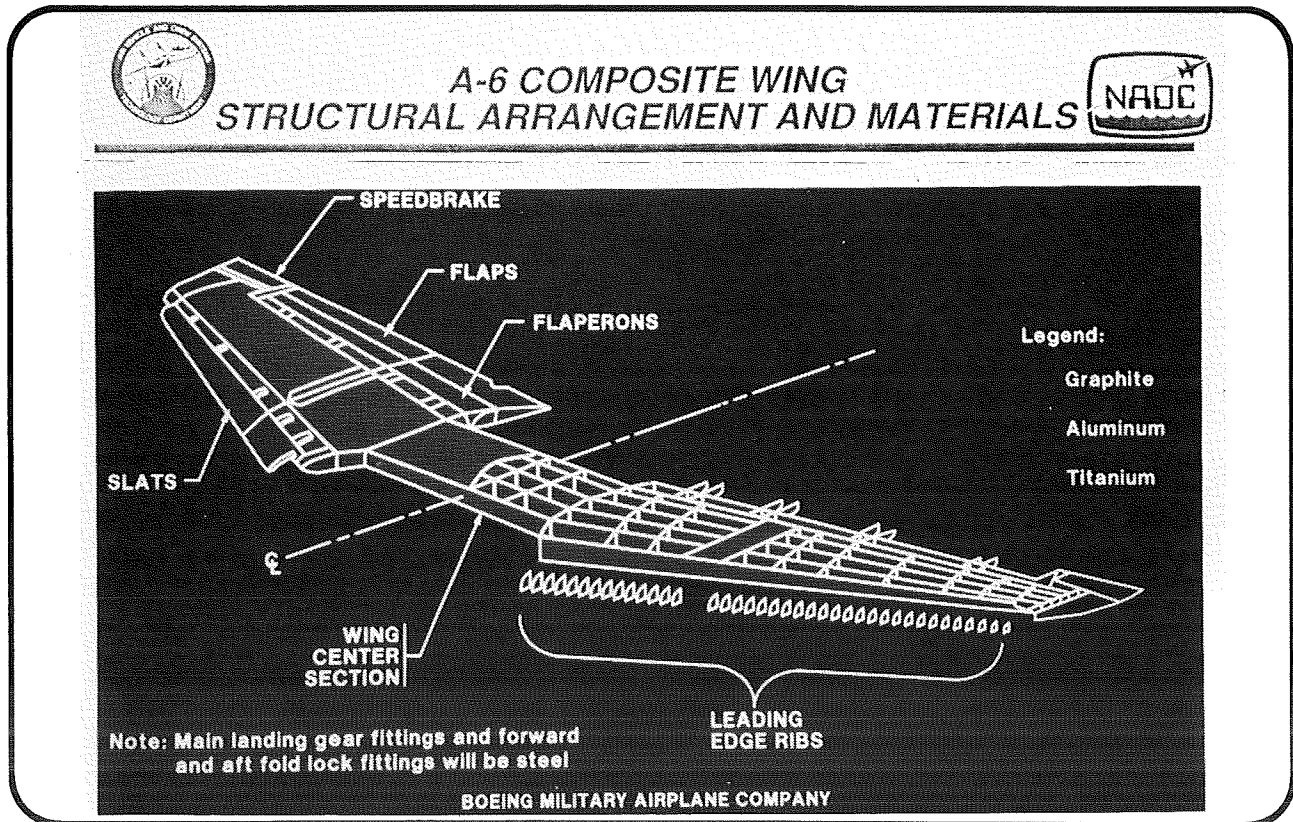
AV-8B HORIZONTAL STABILIZER

SKINS ARE GRAPHITE/EPOXY TAPE. SUBSTRUCTURE IS GRAPHITE/EPOXY CLOTH. SUBSTRUCTURE IS INTEGRAL WITH LOWER SKIN.



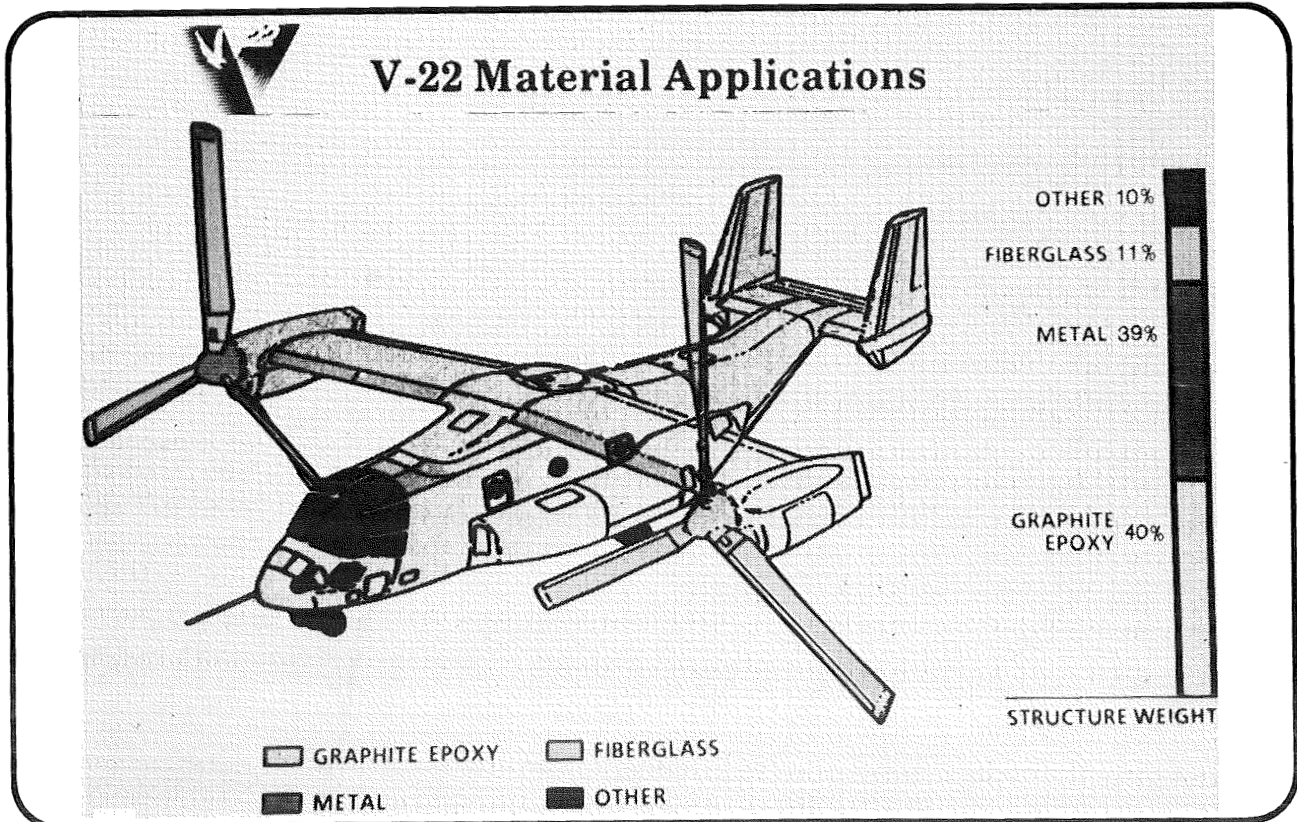
A-6 WING

GRAPHITE/EPOXY IS USED IN THE PLANKED SKINS AND INTERMEDIATE SPARS AND RIBS. ALL BOUNDARY, CLOSE-OUT SUBSTRUCTURE IS TITANIUM.



V-22 COMPOSITE STRUCTURE

GRAPHITE/EPOXY IS USED FOR THE WING AND FUSELAGE. THE WING IS PLANKED SKIN/MULTI-RIB DESIGN. ALL SPARS AND RIBS, WITH THE EXCEPTION OF THE TWO OUTBOARD RIBS, ARE GRAPHITE/EPOXY. FUSELAGE STRUCTURE IS STIFFENED SKIN. THE ROTOR GRIPS ARE FILAMENT WOUND GRAPHITE/EPOXY AND THE YOKE AND ROTOR BLADES ARE WOUND FIBERGLASS.

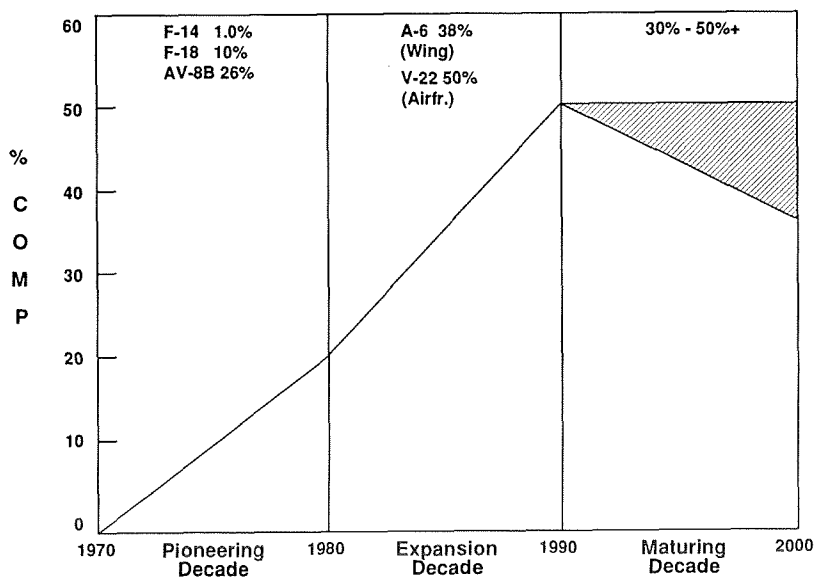


COMPOSITE USAGE IS APPROACHING STABILITY

OVER THE PAST 20 YEARS COMPOSITE USAGE AS A PERCENTAGE OF AIRCRAFT STRUCTURAL WEIGHT HAS BEEN STEADILY INCREASING FROM 1% IN THE F-14 AIRCRAFT TO 50% IN THE V-22. IT APPEARS THAT 50% USAGE IS A MAXIMUM AND IS ONLY APPLICABLE WHERE WEIGHT SAVINGS ARE HIGHLY CRITICAL TO OPERATIONAL CAPABILITY AS IN A VSTOL AIRFRAME. IN THE FUTURE, WITH THE INCREASED EMPHASIS ON CONTROLLING COSTS, USAGE IN THE 30% TO 50% RANGE IS ANTICIPATED.



COMPOSITES USAGE IS APPROACHING STABILITY



SH-60B

COMPOSITES ARE USED IN THE FOLLOWING COMPONENTS OF THE SH-60B

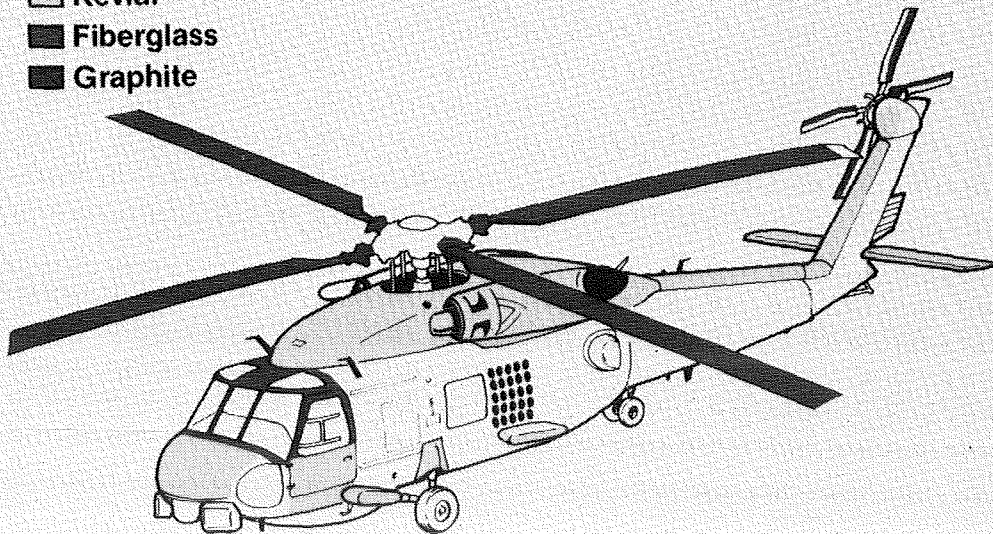
MAIN ROTOR BLADES
TAIL ROTOR BLADES
CABIN FLOOR PANELS
ENGINE COWLING/WORK PLATFORM
RADOME, TRANSMISSION COWLING
TAIL ROTOR DRIVE SHAFT COVER

THE LEADING AND TRAILING EDGES OF THE HORIZONTAL STABILIZER ARE ALL OF COMPOSITE CONSTRUCTION.

FATIGUE RESISTANCE AND CORROSION RESISTANCE WERE THE MAIN REASONS FOR CHOOSING COMPOSITES, ESPECIALLY IN THE ROTOR BLADES.

COMPOSITES USE ON SH-60B

- Kevlar
- Fiberglass
- Graphite



OTHER VEHICLE APPLICATIONS

COMPOSITES ARE USED IN VARIOUS APPLICATIONS ON OTHER HELICOPTER STRUCTURE. BELOW IS A LIST OF VARIOUS HELICOPTERS TOGETHER WITH COMPOSITE USAGE AND REASONS FOR ITS USE.

MAIN ROTOR BLADES - THE MAJORITY OF COMPOSITE BLADES IN USE TODAY ARE MADE WITH FIBERGLASS SKINS OVER A NOMEX HONEYCOMB CORE.

FLOOR PANELS - FIBERGLASS SKINS OVER A NOMEX HONEYCOMB CORE SUCH AS IN THE SH-60B.

IN THE MH-53E, THE COCKPIT, ENGINE AND TRANSMISSION COWLINGS, WORK PLATFORMS, PORTION OF VERTICAL STABILIZER, AND SPONSONS ARE KEVLAR WITH A REINFORCING LAYER OF GRAPHITE.

MH-53E STUB WINGS - KEVLAR SKINS WITH A REINFORCING PLY OF GRAPHITE.

CH-46 STUB WINGS - GRAPHITE/EPOXY SKINS WITH NOMEX HONEYCOMB CORE. COMPOSITE DESIGN/CONSTRUCTION ALLOWS FOR MORE FUEL VOLUME THAN TRADITIONAL METAL SKIN/STIFFENER.

COMPOSITE MATERIALS HAVE BEEN SELECTIVELY APPLIED IN OTHER CLASSES OF FLIGHT VEHICLES CURRENTLY UNDER DEVELOPMENT. THESE VEHICLES INCLUDE SMART WEAPONS (AIWS), RPV'S (PIONEER) AND AIR LAUNCHED MISSILES. FOR APPLICATIONS TO SYSTEMS OF THIS NATURE, EMPHASIS IS PLACED UPON LOW MANUFACTURING COSTS IN CONJUNCTION WITH HIGH PRODUCTION RATES. THIS LEADS TO SEMI-AUTOMATED PROCESSES SUCH AS FILAMENT WINDING, RESIN TRANSFER MOLDING AND COMPRESSION MOLDING. FATIGUE IS NOT AN ISSUE IN THESE APPLICATIONS BECAUSE OF THE VEHICLE'S SHORT SERVICE LIFE.



OTHER VEHICLE APPLICATIONS OF COMPOSITES



HELICOPTERS

SH-60B

MH-53E

AH-1

CH-46

UAV'S

AIWS

RPV'S

AIR LAUNCHED MISSILES

MAJOR BENEFITS TO NAVY

THE NAVY RECOGNIZED EARLY THAT COMPOSITES OFFERED MAJOR BENEFITS TO NAVY/MARINE AIRCRAFT OPERATING IN THE SHIPBOARD ENVIRONMENT. THE REQUIREMENT TO DEVELOP A VSTOL AIRCRAFT IN THE EARLY 70'S REINFORCED THE NEED TO USE COMPOSITES TO REDUCE THE STRUCTURAL WEIGHT FRACTIONS.

SERVICE LIFE REQUIREMENTS HAVE BEEN INCREASING OVER THE YEARS. EARLIER AIRCRAFT HAD DESIGN LIVES OF 4000 HOURS; THE F-18 IS DESIGNED TO 6000 FLIGHT HOURS. THE A-6 COMPOSITE WING HAS A DESIGN LIFE OF 8800 FLIGHT HOURS AND THE V-22 IS DESIGNED TO 10,000 HOURS. THESE INCREASED REQUIREMENTS HAVE PROVIDED ADDITIONAL INCENTIVES FOR THE USE OF ADVANCED COMPOSITES WHICH ARE ESSENTIALLY INSENSITIVE TO FATIGUE.

THE NAVY'S OPERATING ENVIRONMENT MAKES CORROSION CONTROL A HIGH COST MAINTENANCE ITEM. THE FACT THAT COMPOSITES DO NOT CORRODE IS THUS OF EXTREME IMPORTANCE TO THE NAVY.

THESE BENEFITS TAKEN TOGETHER RESULT IN INCREASED PERFORMANCE, LOWER LIFE CYCLE COSTS, AND INCREASED MISSION AVAILABILITY.



MAJOR BENEFITS TO NAVY



- REDUCED WEIGHT
- INCREASED FATIGUE LIFE
- CORROSION RESISTANCE

INCREASED PERFORMANCE
AND AVAILABILITY

THIS PAGE INTENTIONALLY BLANK



MAJOR BENEFITS TO NAVY

- **REDUCED WEIGHT**
- **INCREASED FATIGUE LIFE**
- **CORROSION RESISTANCE**

**INCREASED PERFORMANCE
AND AVAILABILITY**

AIRCRAFT WEIGHT SAVINGS

THIS CHART SHOWS WEIGHT SAVINGS FOR VARIOUS AIRCRAFT WHICH INCORPORATE ADVANCED COMPOSITE MATERIALS. THE PERCENT COMPOSITES BY WEIGHT HAS INCREASED OVER THE YEARS AS CONFIDENCE IN THEIR USE WAS OBTAINED.

CURRENTLY FLYING NAVY AIRCRAFT HAVE SHOWN SIGNIFICANT WEIGHT SAVINGS THROUGH THE USE OF ADVANCED COMPOSITES, THE MOST DRAMATIC OF WHICH IS THE V-22 WHICH SAVED 15% (ALMOST 2000 POUNDS) USING PRIMARILY GRAPHITE EPOXY.

IT IS INTERESTING TO NOTE THAT AS PART OF THE TRADE STUDIES LEADING TO THE FINAL V-22 DESIGN, A COMPARISON WAS MADE BETWEEN THE GRAPHITE/EPOXY WING TORQUE BOX AND AN EQUIVALENT ALUMINUM TORQUE BOX DESIGNED TO THE SAME CRITERIA. IT WAS FOUND THAT THE WEIGHT SAVINGS ACHIEVED THROUGH THE USE OF COMPOSITES WAS 591 POUNDS OR 28% OF THE WEIGHT OF THE METAL TORQUE BOX. THE SAME MATERIALS USED IN THE WING ARE ALSO USED FOR THE FUSELAGE AND EMPENNAGE OF THE V-22.

THE WEIGHT SAVINGS SHOWN FOR THE A-6 WING REQUIRES SOME EXPLANATION.

THE A-6 DESIGN REWING REQUIREMENTS WERE:

- 8800 FLIGHT HOURS INSTEAD OF 6000 FLIGHT HOURS
- 20% INCREASE IN LOADS OVER THE ORIGINAL DESIGN LOADS

THESE INCREASES WERE TO BE ACCOMPANIED BY NO INCREASE IN WING STRUCTURAL WEIGHT. THE 700 POUND WEIGHT SAVINGS SHOWN IS THE WEIGHT SAVED OVER A METAL DESIGN CAPABLE OF TAKING THE SAME LOADS AS THE COMPOSITE.



AIRCRAFT WEIGHT SAVINGS



AIRCRAFT T/M/S	AIRFRAME WEIGHT	% COMPOSITES (BY WEIGHT)	% WEIGHT SAVED	LBS WEIGHT SAVED
F-18	11360	10	5	565
AV-8B	5262	26	10	525
A-6 (WING)	4936	38	14	700
V-22 (WITH ROTOR)	13097	51	15	1962



MAJOR BENEFITS TO NAVY



- **REDUCED WEIGHT**

- **INCREASED FATIGUE LIFE**

- **CORROSION RESISTANCE**

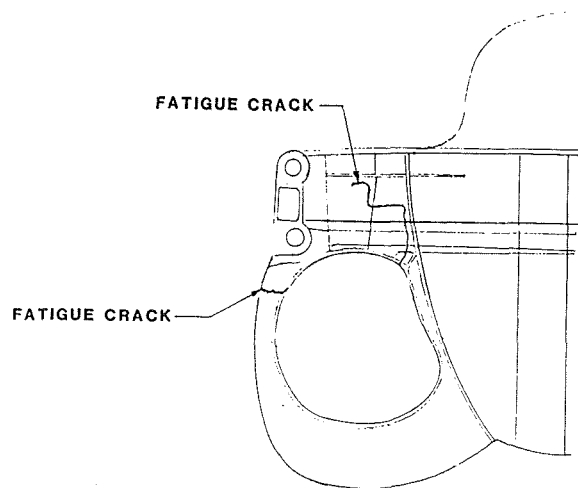
**INCREASED PERFORMANCE
AND AVAILABILITY**

METAL FATIGUE PROBLEMS

THIS SKETCH DEPICTS TYPICAL PROBLEMS ENCOUNTERED WITH METAL STRUCTURE DURING THE FATIGUE TEST OR IN AIRCRAFT SERVICE. IN THE CASE OF THIS ALUMINUM BULKHEAD IN WHICH HIGH LOADS ARE INTRODUCED AT WING AND LANDING GEAR ATTACHMENTS, THE CRACKS OCCURRED DURING THE FULL SCALE FATIGUE TEST. THE CRACKS INITIATED AT HIGH STRESS AREAS DUE TO LOCAL RADII STRESS CONCENTRATIONS. FIXES WERE DEVELOPED AND THE FATIGUE TEST PROGRAM WAS CONTINUED. IN SOME INSTANCES, THESE FATIGUE PROBLEMS ARE NOT DETECTED UNTIL A NUMBER OF AIRCRAFT HAVE ALREADY BEEN DELIVERED TO THE FLEET, AND REWORK, WHICH CAN BE EXTREMELY COSTLY FOR INTERNAL STRUCTURE, IS NECESSARY FOR ALL AIRCRAFT OF THIS TYPE.



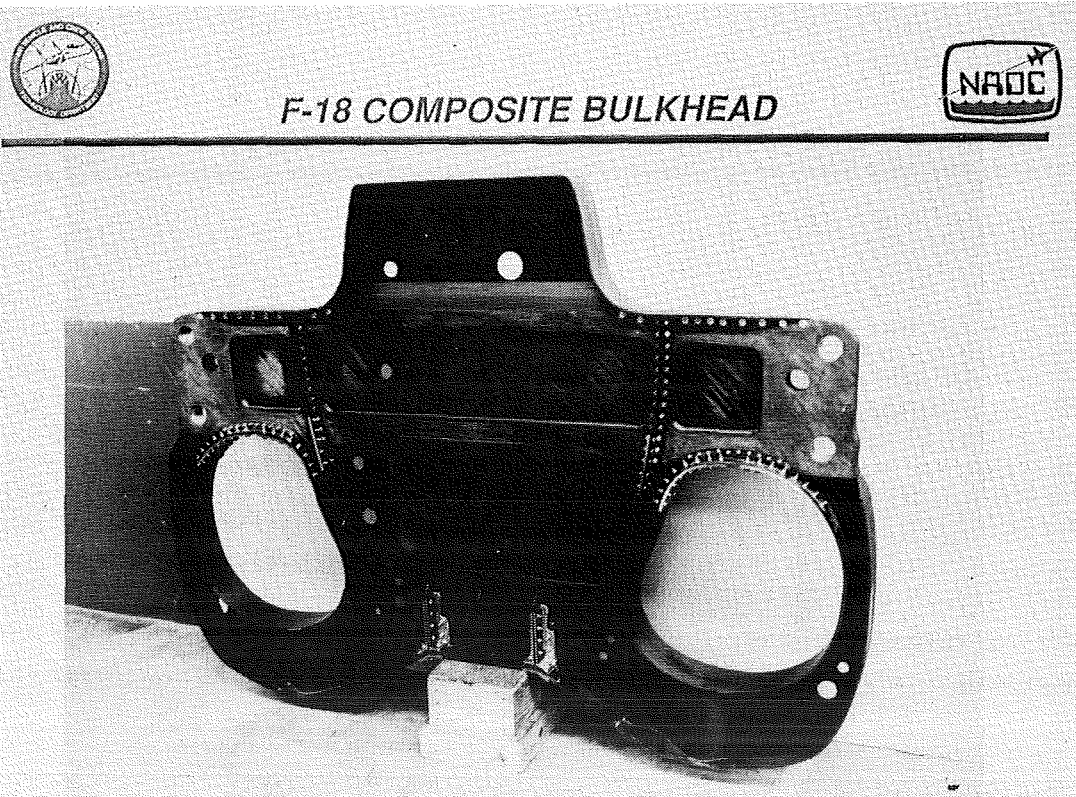
METAL FATIGUE PROBLEMS



PHOTOGRAPH OF F-18 COMPOSITE BULKHEAD

THE NAVAL AIR DEVELOPMENT CENTER AND MCDONNELL AIRCRAFT COMPANY HAVE DESIGNED, FABRICATED AND TESTED A HIGHLY LOADED WING ATTACHMENT BULKHEAD WHICH DEMONSTRATES THE WEIGHT AND FATIGUE ADVANTAGES OF AN ALL COMPOSITE MAJOR LOAD CARRYING COMPONENT. THE BULKHEAD WAS DESIGNED TO MEET THE FORM AND FUNCTIONAL REQUIREMENTS OF THE F-18 FUSELAGE STATION 453 BULKHEAD. TWO ARTICLES WERE FABRICATED: THE FIRST BEING A MANUFACTURING DEMONSTRATION ARTICLE, AND THE SECOND INCORPORATING FABRICATION LESSONS LEARNED, A STRUCTURAL TEST ARTICLE.

FABRICATION OF THE SECOND FULL SCALE ARTICLE, USING IM7/8551-7A GRAPHITE/EPOXY PREPREG, AND TESTING OF THE CARRY-THROUGH BEAM PORTION VERIFIED THE PRODUCIBILITY, STRENGTH AND DURABILITY OF THE DESIGN THEREBY PRESENTING THE OPPORTUNITY FOR USE ON AIRCRAFT UPGRADES AND NEW AIRCRAFT. FOLLOWING TWO LIFETIMES OF ENHANCED, TO ACCOUNT FOR COMPOSITE SCATTER, F-18 WING FATIGUE LOADS THE BULKHEAD WAS SUCCESSFULLY LOADED TO FAILURE WHICH OCCURRED AT 186% DESIGN LIMIT LOAD. A 15% WEIGHT SAVINGS WAS ACHIEVED AND, MORE IMPORTANTLY, THE FATIGUE PROBLEMS THAT NORMALLY PLAGUE METAL BULKHEAD ARE VIRTUALLY ELIMINATED.





MAJOR BENEFITS TO NAVY



- REDUCED WEIGHT
- INCREASED FATIGUE LIFE
- CORROSION RESISTANCE

INCREASED PERFORMANCE
AND AVAILABILITY



ENVIRONMENTAL DEGRADATION



- CORROSION IS A SIGNIFICANT MAINTENANCE ISSUE
- CORROSION ACCOUNTS UP TO 15% OF THE MAINTENANCE MAN-HOURS
- COSTS RELATED TO CORROSION, 900 MILLION DOLLARS FOR NAVAL AIRCRAFT
- COMPOSITE MATERIALS REDUCE MAINTENANCE HOURS

UNSCHEDULED MAINTENANCE EXPENDED ON CORROSION

CORROSION MAINTENANCE MANHOURS REFLECT A GENERAL DECREASING TREND DESPITE AN AGING FLEET DUE TO:

- IMPROVED CORROSION CONTROL PRODUCTS/PROCEDURES
 - UTILIZATION OF IMPROVED MATERIALS SERVING AS BARRIERS; I.E. COATINGS
 - IMPROVED METHODS OF ASSEMBLY
 - PROPER DESIGN CHOICES OF METALLIC MATERIALS
 - IMPROVED SURFACE TREATMENTS
- USE OF POLYMERIC COMPOSITES



UNSCHEDULED MAINTENANCE EXPENDED ON CORROSION



AIRCRAFT	TOTAL MAINTENANCE DMMH/YR THOUSANDS	CORROSION MAINTENANCE DMMH/YR THOUSANDS	% CORROSION MAINTENANCE
A-6	2,251	337	15
E-2	648	99	7.7
P-3	3,143	303	9.6
F-14	2,401	232	9.7
F-18	418	11	2.6

Includes only organizational and intermediate levels
TDMH Direct Maintenance Man-hours

DESIGN DRIVERS ARE INCREASING

EARLY APPLICATIONS OF COMPOSITES WERE CONCERNED PRIMARILY WITH REDUCING STRUCTURAL WEIGHT. THIS WAS THE MAJOR DRIVER FOR THE USE OF COMPOSITES IN THE F-14, F-18 AND AV-8B. IN THESE APPLICATIONS 15-20% WEIGHT SAVINGS WERE ACHIEVED.

RECENT AIRCRAFT PROGRAMS (V-22 & A-6 WING) HAVE INCLUDED DAMAGE TOLERANCE AND SURVIVABILITY REQUIREMENTS. DAMAGE TOLERANCE REQUIREMENTS DIRECTED AT LOW ENERGY IMPACT DAMAGE HAVE BEEN INCLUDED TO CONFORM WITH THE NAVY PHILOSOPHY OF NOT REQUIRING ROUTINE INSPECTIONS. THUS, SERVICE LIFE REQUIREMENTS MUST BE MET WITH THE MOST SEVERE NON-VISIBLE DAMAGE POSSIBLE. SPECIFIED SURVIVABILITY REQUIREMENTS FOR THESE AIRCRAFT WERE A SINGLE HIT BY A 23MM HEI PROJECTILE.

IN THE FUTURE, IT IS ANTICIPATED THAT IN ADDITION TO CURRENT DRIVERS, LOW OBSERVABILITY, QUALITY, COST AND SUPPORTABILITY WILL BE IMPORTANT. IN FACT, IN THE CURRENT CLIMATE OF BUDGET REDUCTIONS, COST CONSIDERATIONS MAY BE OF EQUAL IMPORTANCE TO WEIGHT.



DESIGN DRIVERS ARE INCREASING



PAST (1970'S)

F-14
F-18
AV-8B

WEIGHT

PRESENT (1980'S)

V-22
A-6

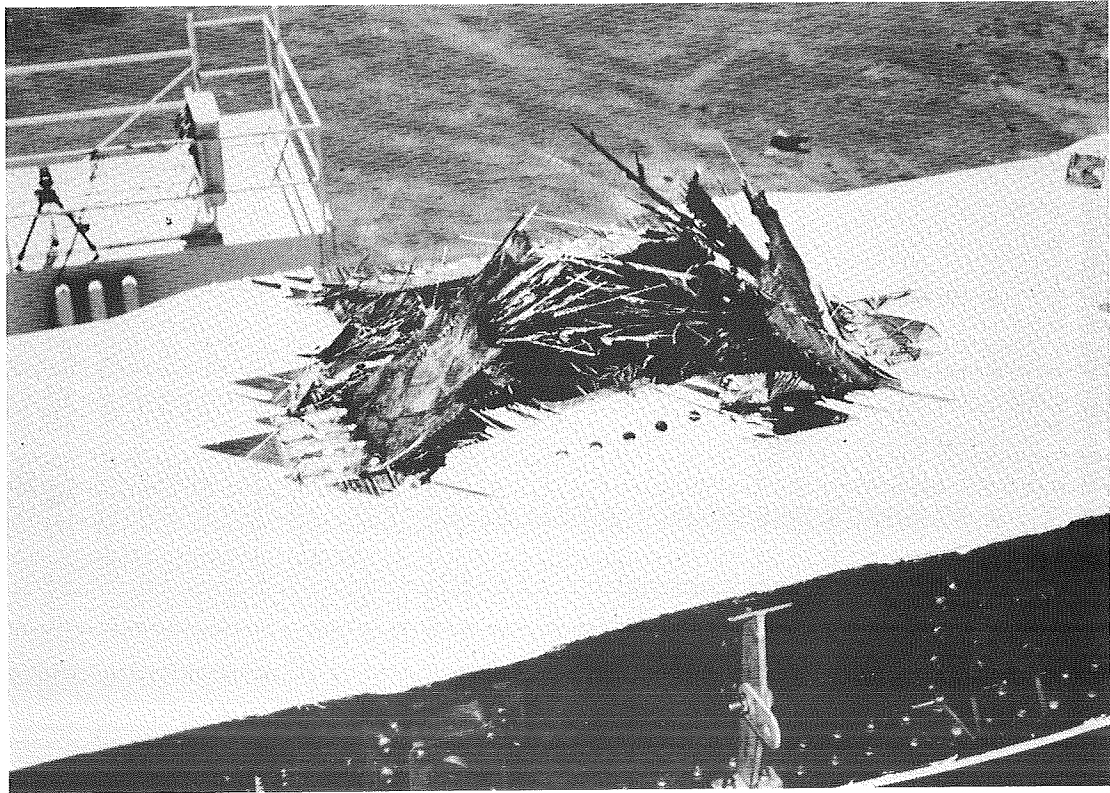
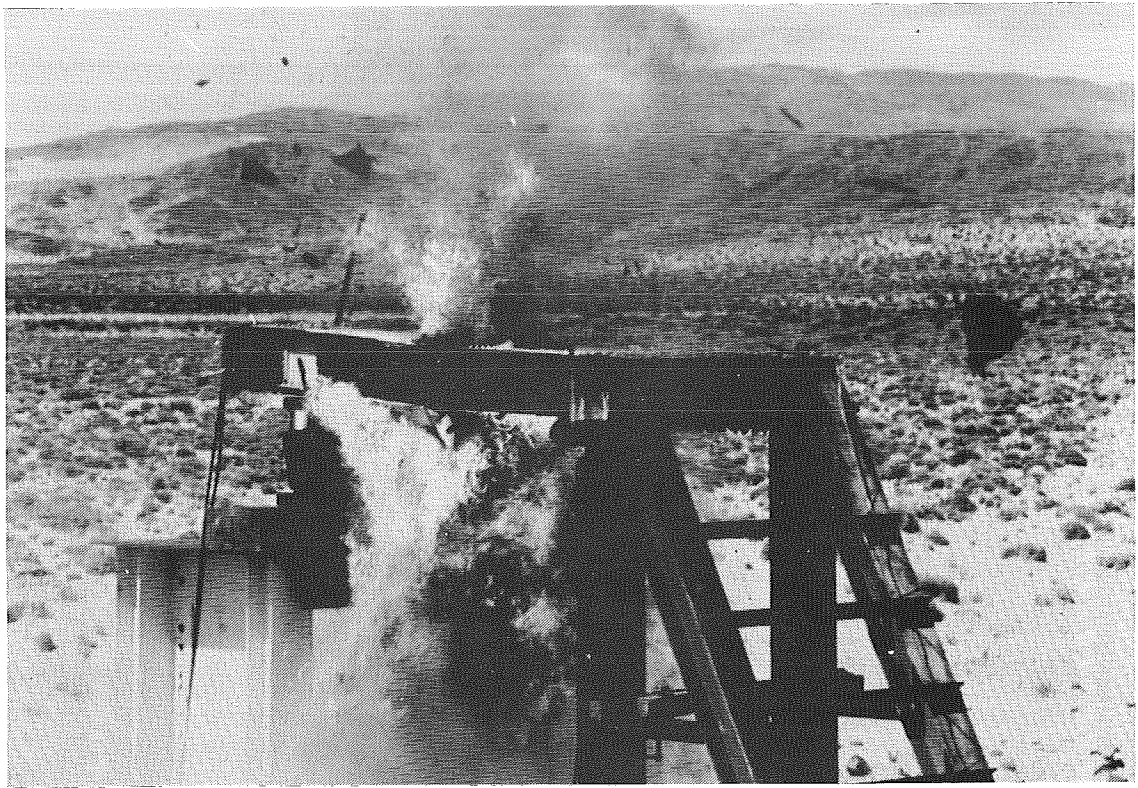
**WEIGHT
DAMAGE TOL.
SURVIVABILITY**

FUTURE (1990'S)

INTERIM F/A
AX
?

**WEIGHT
DAMAGE TOL.
SURVIVABILITY
LOW OBSERV.
QUALITY
COST
SUPPORTABILITY**

INCREASING DEMANDS



NAVY ASSESSMENT OF CURRENT COMPOSITE STRUCTURES

- PERFORMANCE EXPECTATIONS GENERALLY MET

TO DATE, COMPOSITE STRUCTURES EXPERIENCES HAVE BEEN FAVORABLE. IN SERVICE, NO MAJOR STATIC OR FATIGUE FAILURES HAVE OCCURRED. CURRENT FLIGHT TESTING OF THE V-22 HAS NOT REVEALED ANY STRUCTURAL PROBLEMS; HOWEVER, THIS TESTING IS STILL IN ITS EARLY STAGES AND THE FLIGHT ENVELOPE HAS NOT AS YET BEEN EXTENDED TO INCLUDE ALL CRITICAL DESIGN CONDITIONS.

- DEVELOPMENT AND PRODUCTION COSTS HIGH

BECAUSE OF THE LIMITED EXPERIENCE WITH COMPOSITE STRUCTURES WITHIN THE INDUSTRY, RELATIVE TO METALS, AN EXTENSIVE DEVELOPMENT PROGRAM PRIOR TO FULL SCALE TESTING IS CURRENTLY CONSIDERED A NECESSITY. THE COSTS ARE HIGH BUT ARE EXPECTED TO BE PART OF ANY NEW PROGRAM IN THE FORESEEABLE FUTURE. BASIC MATERIAL COSTS ARE HIGH AND CURRENT COMPOSITE MANUFACTURING AND INSPECTION PROCEDURES ARE EXTREMELY LABOR INTENSIVE RESULTING IN HIGH COSTS. THESE COSTS MUST BE REDUCED TO INSURE CONTINUED EXTENSIVE USE OF COMPOSITES IN FUTURE A/C SYSTEMS.

- BASIC MANUFACTURING METHODS USED TO FABRICATE COMPOSITE PARTS HAVE PROGRESSED LITTLE IN THE PAST 20 YEARS.

- MANUFACTURING DISCREPANCIES SUCH AS DELAMINATIONS AND INCLUSIONS REMAIN A PROBLEM IN BOTH PART FABRICATION AND FINAL ASSEMBLY.

- NEW MATERIAL SYSTEMS ARE NEEDED WITH IMPROVED DAMAGE TOLERANCE AND STRENGTH AT CRITICAL ENVIRONMENTS TO BETTER MEET INCREASING DEMANDS OF FUTURE WEAPONS SYSTEMS.

- NO MAJOR PROBLEMS ATTRIBUTED TO THE USE OF COMPOSITES HAVE BEEN ENCOUNTERED IN SERVICE. ALTHOUGH DAMAGE TOLERANCE IS AN ON-GOING CONCERN, EXPERIENCES TO DATE HAVE SHOWN IT TO BE MORE OF A PROBLEM IN THE FACTORY THAN IN OPERATIONAL SERVICE.

- ALTHOUGH FACILITIES AND EQUIPMENT ABOARD THE CARRIER ARE LIMITED, COMPOSITES HAVE BEEN SHOWN TO BE SUPPORTABLE IN THIS ENVIRONMENT.



NAVY ASSESSMENT OF CURRENT COMPOSITE STRUCTURES



- PERFORMANCE EXPECTATIONS GENERALLY MET
- DEVELOPMENT AND PRODUCTION COSTS HIGH
- MANUFACTURING TECHNOLOGY LAGGING
- MANUFACTURING QUALITY CRITICAL ISSUE
- BETTER MATERIALS NEEDED
- SERVICE EXPERIENCE FAVORABLE
- SUPPORTABLE IN CARRIER ENVIRONMENT



NAVY ASSESSMENT OF CURRENT COMPOSITE STRUCTURES



- **PERFORMANCE EXPECTATIONS GENERALLY MET**
- **DEVELOPMENT AND PRODUCTION COSTS HIGH**
- **MANUFACTURING TECHNOLOGY LAGGING**
- **MANUFACTURING QUALITY CRITICAL ISSUE**
- **BETTER MATERIALS NEEDED**
- **SERVICE EXPERIENCE FAVORABLE**
- **SUPPORTABLE IN CARRIER ENVIRONMENT**

PRODUCTION EXPERIENCE

THE NAVY PERIODICALLY CONDUCTS QUALITY AUDITS OF ON-GOING PRODUCTION CONTRACTS. THESE AUDITS, KNOWN AS PRODUCT ORIENTED SURVEYS (POS) HAVE UNCOVERED A NUMBER OF ISSUES RELATED TO MANUFACTURING AND QUALITY ASSURANCE OF COMPOSITE STRUCTURES. MAJOR ISSUES INCLUDE:

ENGINEERING FLOWDOWN - EARLY IN THE DEVELOPMENT PHASE, ENGINEERING IS INTIMATELY INVOLVED IN THE FABRICATION OF PARTS. AS PRODUCTION STARTS, ENGINEERING'S INVOLVEMENT TENDS TO DECREASE. ONCE PRODUCTION IS UNDERWAY, ENGINEERING SUPPORT IS PRACTICALLY NON-EXISTENT. THIS RESULTS, IN SOME CASES, IN CHANGES BEING MADE WITHOUT CONSULTING WITH DESIGN AND STRESS ENGINEERS WHICH MAY EFFECT THE STRUCTURAL INTEGRITY OF THE PART.

TRAINING - IN MANY CASES IT HAS BEEN OBVIOUS THAT TRAINING IN THE PROPER HANDLING AND FABRICATION OF COMPOSITE PARTS IS INADEQUATE. THIS RESULTS IN REDUCED OR UNACCEPTABLE QUALITY PARTS.

PROCESS VERIFICATION & CONTROL - IN MANY INSTANCES IT IS OBSERVED THAT THE CONTRACTOR IS NOT ADEQUATELY INCLUDING PROCESS VERIFICATION PANELS TO ACCOMPANY MAJOR PARTS DURING PROCESSING. THE INTENT OF THESE TRAVELER PANELS IS TO PERFORM DESTRUCTIVE TESTING TO VERIFY MATERIAL QUALITY AND PROCESSING.

FOREIGN MATERIAL INCLUSIONS AND DETECTION - A MAJOR PROBLEM DURING FABRICATION OF COMPOSITE PARTS REMAINS THE INCLUSION OF FOREIGN MATERIALS WITHIN THE LAMINATE. THIS PROBLEM EXISTS AT VIRTUALLY ALL FABRICATION FACILITIES AND RESULTS IN SCRAPPAGE OF MANY PARTS. ALTHOUGH ALL CONTRACTORS ARE AWARE OF THIS PROBLEM, AND EFFORTS ARE UNDERTAKEN TO ELIMINATE IT, IT STILL EXISTS. FURTHER, MANY OF THESE MATERIALS CANNOT BE DETECTED WITHOUT EXTENSIVE NON-DESTRUCTIVE INSPECTIONS.

MACHINING & DRILLING - IN MANY INSTANCES MACHINING AND DRILLING WERE NOT PERFORMED IN ACCORDANCE WITH COMPANY ISSUED SPECIFICATIONS RESULTING IN FIBER BREAKOUT AND DELAMINATIONS.

FIT-UP & ASSEMBLY - MAJOR FIT-UP PROBLEMS BETWEEN SKINS AND SUBSTRUCTURE REMAIN A CRITICAL PROBLEM. EXTENSIVE USES OF LIQUID SHIM ADD COSTS AND WEIGHT TO THE PRODUCT. FAILURE TO PROPERLY SHIM RESULTS IN DELAMINATIONS OCCURRING DURING FINAL ASSEMBLY.



PRODUCTION EXPERIENCE



MAJOR CONCERNS

- ENGINEERING FLOWDOWN

- TRAINING

- PROCESS VERIFICATION AND CONTROL

- FOREIGN MATERIAL INCLUSIONS AND DETECTION

- MACHINING AND DRILLING

- FIT-UP

- ASSEMBLY

MANUFACTURING

DEVELOPMENT OF IMPROVED MANUFACTURING PROCEDURES HAS ADVANCED VERY SLOWLY. BASICALLY, THE SAME TECHNIQUES USED TO FABRICATE THE AV-8B WING ARE STILL BEING USED.

IT IS TIME THAT MAJOR EFFORTS BE UNDERTAKEN TO REDUCE COSTS AND AT THE SAME TIME IMPROVE PART QUALITY. AUTOMATION IS THE OBVIOUS SOLUTION TO THIS PROBLEM. SOME METHODS CURRENTLY BEING EVALUATED INCLUDE TAPE LAYING MACHINES, FIBER PLACEMENT TECHNIQUES, WOVEN PRE-FORMS AND RESIN TRANSFER MOLDING.

NDI METHODS VARY GREATLY THROUGHOUT THE INDUSTRY. CURRENTLY NDI OF ALL PRIMARY COMPOSITE PARTS IS A NAVY REQUIREMENT. CONSISTENT NDI TECHNIQUES MUST BE ESTABLISHED THROUGHOUT THE INDUSTRY.

DUE TO INTERLAMINAR WEAKNESS OF COMPOSITES, ASSEMBLY METHODS THAT DO NOT ACCOUNT FOR POTENTIAL MISMATCHES RESULT IN OUT-OF-PLANE STRESSES WHICH CAUSE DELAMINATIONS. ASSEMBLY METHODS SHOULD ACCOUNT FOR GREATER TOLERANCES WHICH USUALLY OCCUR IN A PRODUCTION ENVIRONMENT.

AND FINALLY, CURRENT TOOLING TECHNIQUES FREQUENTLY RESULT IN INCREASED OUT-OF-TOLERANCE PARTS DURING PRODUCTION NECESSITATING FREQUENT TOOL REPLACEMENTS.



MANUFACTURING



- COMPOSITES MANUFACTURING HAS ADVANCED VERY SLOWLY
- LARGE IMPROVEMENTS ARE NEEDED TO
 - REDUCE COST
 - IMPROVE QUALITY
- AUTOMATED LAY-UP METHODS WILL HELP
- QUALITY SYSTEMS MUST BE ESTABLISHED
 - INSPECTION
 - NDT
 - QUALITY CERTIFICATION
- ASSEMBLY METHODS NEED TO RECOGNIZE INTERLAMINAR WEAKNESS OF COMPOSITES
- TOOLING MATERIALS AND CONCEPTS NEED IMPROVEMENT

THIS PAGE INTENTIONALLY BLANK



NAVY ASSESSMENT OF CURRENT COMPOSITE STRUCTURES



- PERFORMANCE EXPECTATIONS GENERALLY MET
- DEVELOPMENT AND PRODUCTION COSTS HIGH
- MANUFACTURING TECHNOLOGY LAGGING
- **MANUFACTURING QUALITY CRITICAL ISSUE**
- BETTER MATERIALS NEEDED
- SERVICE EXPERIENCE FAVORABLE
- SUPPORTABLE IN CARRIER ENVIRONMENT

PAGE 66 INTENTIONALLY BLANK

PAGE 67 INTENTIONALLY BLANK

67

INCREASED EMPHASIS NEEDED ON MANUFACTURING QUALITY

COMPOSITES ARE HIGHLY SENSITIVE TO MANUFACTURING PROCESS VARIATIONS. IT MUST BE RECOGNIZED THAT WHAT MAY APPEAR TO BE A SMALL CHANGE IN A PROCESSING VARIABLE MAY RESULT IN A SIGNIFICANT CHANGE IN MATERIAL PROPERTIES. THEREFORE, A MANUFACTURING PLAN MUST BE DEVELOPED WHICH RECOGNIZES ANY UNIQUE PROCESSING REQUIREMENTS. THIS PLAN MUST BE AMENABLE TO THE ACTUAL PRODUCTION ENVIRONMENT AND MUST BE VERIFIED DURING FULL SCALE DEVELOPMENT, PRIOR TO PRODUCTION, WITH SUFFICIENT TIME ALLOTTED TO MAKE NECESSARY CHANGES WITHOUT IMPACT TO FULL SCALE TEST AND FLIGHT ARTICLES.

DURING THE SELECTION OF MATERIAL SYSTEMS, QUALITY MUST BE A PRIME CONSIDERATION. SUFFICIENT TIME AND RESOURCES MUST BE ALLOCATED FOR MATERIAL VERIFICATION AND THE DEVELOPMENT OF MANUFACTURING PROCESSES.

DESIGNS ARE USUALLY GENERATED ASSUMING SUPERIOR MANUFACTURING CAPABILITIES FOUND IN THE DEVELOPMENT PHASE OF THE PROGRAM RATHER THAN THOSE EXISTING IN THE PRODUCTION ENVIRONMENT. AS A RESULT, QUALITY IS LESS THAN EXPECTED.

QUALITY SIGNIFICANTLY IMPACTS COST, SCHEDULE, PERFORMANCE AND READINESS/MAINTAINABILITY. IN THE PAST, QUALITY HAS DETERIORATED DURING THE TRANSITION FROM DEVELOPMENT TO PRODUCTION DUE TO USE OF IMPROPERLY TRAINED WORKERS, TOOLING AND PROCESS CHANGES, AND REDUCED ENGINEERING SUPPORT. DURING PRODUCTION, QUALITY FURTHER DETERIORATES DUE TO COST AND SCHEDULE PRESSURES, RELATIVELY LITTLE ENGINEERING ATTENTION AND ADDITIONAL USE OF UNSKILLED WORKERS.

IN ORDER TO INSURE MANUFACTURING QUALITY, A FORMAL METHODOLOGY TO CERTIFY THESE PROCESSES MUST BE DEVELOPED.



INCREASED EMPHASIS NEEDED ON MANUFACTURING QUALITY



- COMPOSITES SENSITIVITY TO MANUFACTURING PROCESS VARIATIONS MUST BE RECOGNIZED
- TIMELY MANUFACTURING DEVELOPMENT MANDATORY - MAY PRECEDE DESIGN
- DESIGN MUST BE MANUFACTURABLE IN PRODUCTION ENVIRONMENT
- INCREASED EFFORT REQUIRED FOR COMPOSITES SHOULD BE RECOGNIZED IN MATERIAL SELECTION, SCHEDULING, RESOURCE, ETC.
- METHODOLOGY TO FORMALLY CERTIFY THE MANUFACTURING/QUALITY PROCESSES NEEDS TO BE DEVELOPED



NAVY ASSESSMENT OF CURRENT COMPOSITE STRUCTURES



- PERFORMANCE EXPECTATIONS GENERALLY MET
- DEVELOPMENT AND PRODUCTION COSTS HIGH
- MANUFACTURING TECHNOLOGY LAGGING
- MANUFACTURING QUALITY CRITICAL ISSUE
- BETTER MATERIALS NEEDED
- SERVICE EXPERIENCE FAVORABLE
- SUPPORTABLE IN CARRIER ENVIRONMENT

MATERIAL IMPROVEMENTS

- **PROPERTIES**
 - FURTHER GAINS IN PERFORMANCE ARE MATERIALS LIMITED
 - HIGHER SPECIFIC STRENGTH AND STIFFNESS
 - IMPROVED COMPRESSION STRENGTH
- **VARIABILITY**
 - REDUCED BATCH TO BATCH VARIATIONS
 - PRE-PREG RESIN CONTENT VARIATIONS
- **PROCESSABILITY**
 - BATCH VARIABILITY, OUT TIME, COMPONENT COMPLEXITY CONTRIBUTES TO PROCESS PROBLEMS
 - KEY TO REPRODUCIBILITY
- **COST**
 - COST OF BASIC MATERIALS (FIBER, RESIN, PREPREG) MUST BE REDUCED
- **SPECIFICATIONS**
 - STANDARD MATERIAL AND PERFORMANCE SPECIFICATIONS WILL IMPROVE REPRODUCIBILITY AND REDUCE COST
- **MATERIAL FORMS**
 - MULTIPLE MATERIAL FORMS IN CONJUNCTION WITH NOVEL PROCESSES OFFER POTENTIAL COST SAVINGS
 - QUALIFICATION OF MULTIPLE FORMS MUST BE ADDRESSED
- **TOUGHER RESINS**
 - DAMAGE TOLERANCE RELIES ON RESIN TOUGHNESS
 - IMPROVEMENTS TRANSLATE INTO STRUCTURAL EFFICIENCY
- **ENVIRONMENTAL RESISTANCE**
 - NAVY HAS AN EXTREMELY AGGRESSIVE ENVIRONMENT
 - MATERIALS MUST PERFORM UNDER EXPOSURE TO HEAT, MOISTURE, SOLVENTS, GALVANIC EFFECTS



MATERIAL IMPROVEMENTS NEEDED



- | | |
|-------------------------|-----------------------------------|
| - PROPERTIES | - TOUGHER RESINS |
| - VARIABILITY | - ENVIRONMENTAL RESISTANCE |
| - PROCESSABILITY | - SPECIFICATIONS |
| - COST | - MATERIAL FORMS |



NAVY ASSESSMENT OF CURRENT COMPOSITE STRUCTURES



- **PERFORMANCE EXPECTATIONS GENERALLY MET**
- **DEVELOPMENT AND PRODUCTION COSTS HIGH**
- **MANUFACTURING TECHNOLOGY LAGGING**
- **MANUFACTURING QUALITY CRITICAL ISSUE**
- **BETTER MATERIALS NEEDED**
- **SERVICE EXPERIENCE FAVORABLE**
- **SUPPORTABLE IN CARRIER ENVIRONMENT**

SERVICE EXPERIENCE

RECURRING DAMAGE AND CAUSES:

- **PUNCTURE OF THIN-SKIN HONEYCOMB STRUCTURE**
 - DROPPED TOOLS/PARTS
 - YELLOW GEAR IMPACT
- **DELAMINATIONS AND DISBONDS**
 - DROPPED TOOLS/IMPACT DAMAGE
- **EDGE CRUSHING**
 - YELLOW GEAR IMPACT
 - AIRCRAFT TO AIRCRAFT CONTACT IN LIMITED CARRIER SPACE
- **HOLE WEAR/DELAMINATION**
 - DUE MAINLY TO REPEATED REMOVAL OF DOORS AND ACCESS PANELS
- **HEAT DAMAGE**
 - AV-8B STRUCTURE EXPOSED TO HOT NOZZLE EXPOSURE. (A DAMAGED STRAKE IS SHOWN IN THE NEXT VIEWGRAPH)
 - CLOSE ENCOUNTER WITH OTHER AIRCRAFT EXHAUST, USUALLY ABOARD THE CARRIERS
 - IN THE CASE OF THE AV-8B, SOME HEAT DAMAGE HAS OCCURRED BECAUSE PILOTS TAXI WITH THEIR FLAPS DOWN WHICH IS AGAINST PROCEDURE AND THE NOZZLE EXHAUST OVERHEATS THE FLAPS.
- **CHAFING**
 - CAUSED BY RUBBING OF MOVABLE PARTS AGAINST ADJACENT STRUCTURE BECAUSE OF OUT-OF TOLERANCE DIMENSIONS
- **OTHER DAMAGE**
 - HAIL DAMAGE - A FEW INCIDENTS HAVE BEEN REPORTED, WITH THE AIRCRAFT HAVING BEEN REPAIRED AND RETURNED TO SERVICE.
 - BIRD STRIKES - SOME INCIDENTS ON AV-8B NOSE CONE, FORWARD FUSELAGE, WINDSHIELD, AND LEADING EDGES
 - CRASH DAMAGE:
 - SEVERAL CRASHED AV-8B'S HAVE BEEN REPAIRED AND RETURNED TO SERVICE
 - V-22 NUMBER 5 CRASHED AND EVEN THOUGH THE DECISION HAS BEEN MADE TO SCRAP IT, THE CRASH WAS SURVIVABLE.

TOM DONNELAN WILL PRESENT A PAPER TUESDAY AFTERNOON ON "NAVY COMPOSITE MAINTENANCE AND REPAIR EXPERIENCE" WHICH WILL GIVE A MORE COMPREHENSIVE SUMMARY OF SERVICE EXPERIENCE.



SERVICE DAMAGE EXPERIENCE



- **FEW RECURRING PROBLEMS ENCOUNTERED**
 - PUNCTURE OF THIN-SKIN HONEYCOMB STRUCTURE
 - DELAMINATIONS AND DISBONDS
 - EDGE CRUSHING
 - HOLE WEAR/DELAMINATION
 - HEAT DAMAGE
 - CHAFING
- **OTHER DAMAGE**
 - HAIL DAMAGE
 - BIRD STRIKES
 - LANDING ZONE DEBRIS
 - CRASH DAMAGE

PHOTO OF HEAT DAMAGED AV-8B STRAKE

THE GUN-PAK STRAKE SHOWN IN THE PHOTO WAS DAMAGED BY REPEATED EXPOSURE TO HEAT FROM THE ENGINE EXHAUST NOZZLES IN THE VERTICAL TAKEOFF AND LANDING MODE. ONLY THE MOST AFT PORTION OF THESE STRAKES HAS EXPERIENCED HEAT DAMAGE.



HEAT DAMAGE AV-8B STRAKE

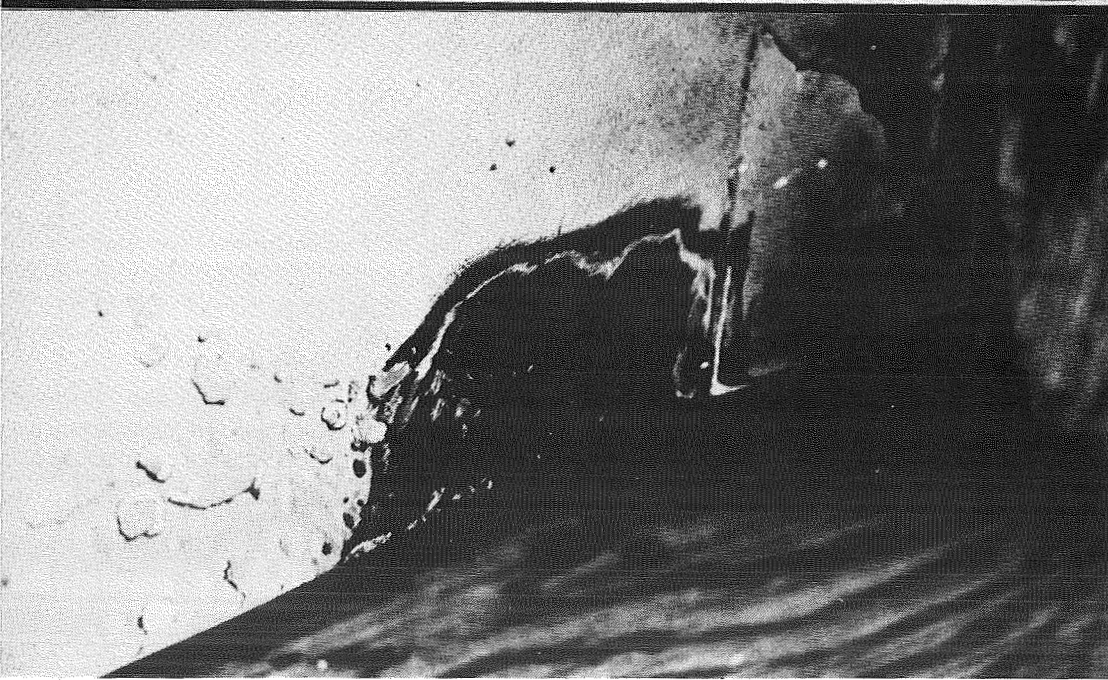


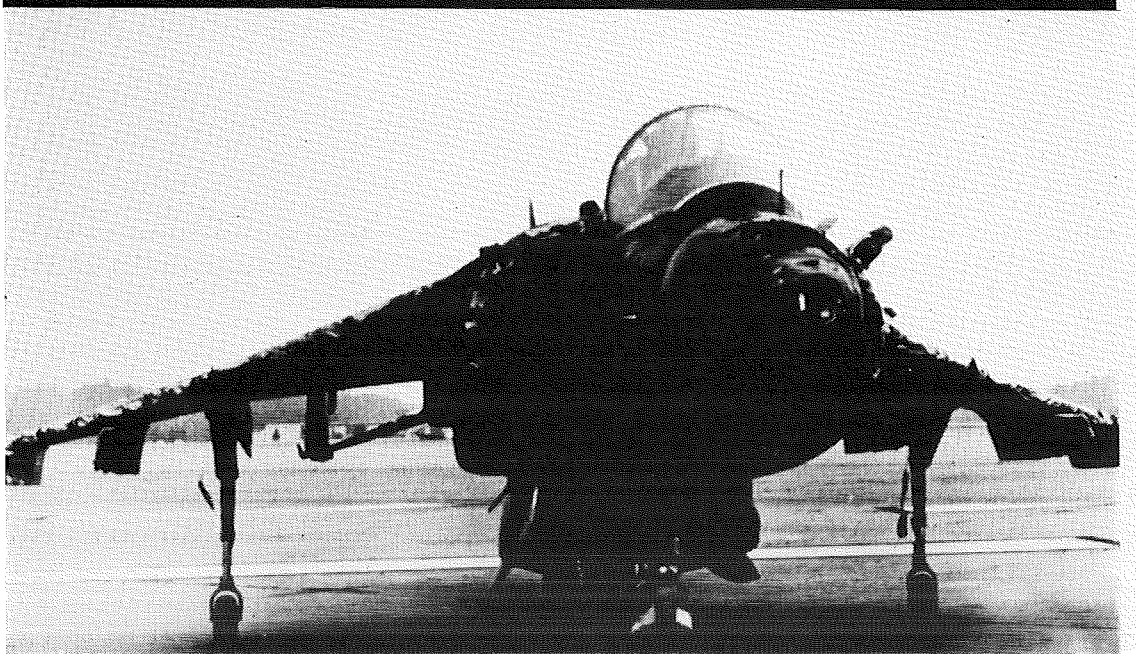
PHOTO OF HAIL DAMAGE

THE NEXT TWO PHOTOS SHOW AN AV-8B THAT WAS DAMAGED IN A HAIL STORM. THE AIRCRAFT WAS FLYING IN FORMATION WITH AN A-4 WHEN THEY INADVERTENTLY FLEW INTO A HAIL STORM. THE AV-8B SUFFERED EXTENSIVE DAMAGE TO ALL LEADING EDGE SURFACES IN ADDITION TO LOSING ITS CANOPY. NOTE THE WINDSCREEN WHICH WAS DESIGNED FOR BIRDSTRIKE IMPACT REMAINED INTACT. ALSO NOTE THE DIFFERENCES IN THE TYPES OF DAMAGE BETWEEN COMPOSITES AND METALS. THE FORWARD FUSELAGE AND NOSE CONE EXCEPT FOR THE METAL TIP ARE CARBON/EPOXY WHILE THE ENGINE INLETS AND WING AND STABILIZER LEADING EDGES ARE ALUMINUM. THE CARBON/EPOXY WING COVERS REMAINED UNDAMAGED.

BOTH AIRCRAFT RETURNED TO BASE SAFELY. AFTER REPLACING THE LIMITED NUMBER OF DAMAGED COMPONENTS, THE AV-8B WAS RETURNED TO SERVICE WHILE THE A-4 WAS SO BADLY DAMAGED THAT IT WAS SCRAPPED.



AV-8B HAIL DAMAGE





AV-8B HAIL DAMAGE

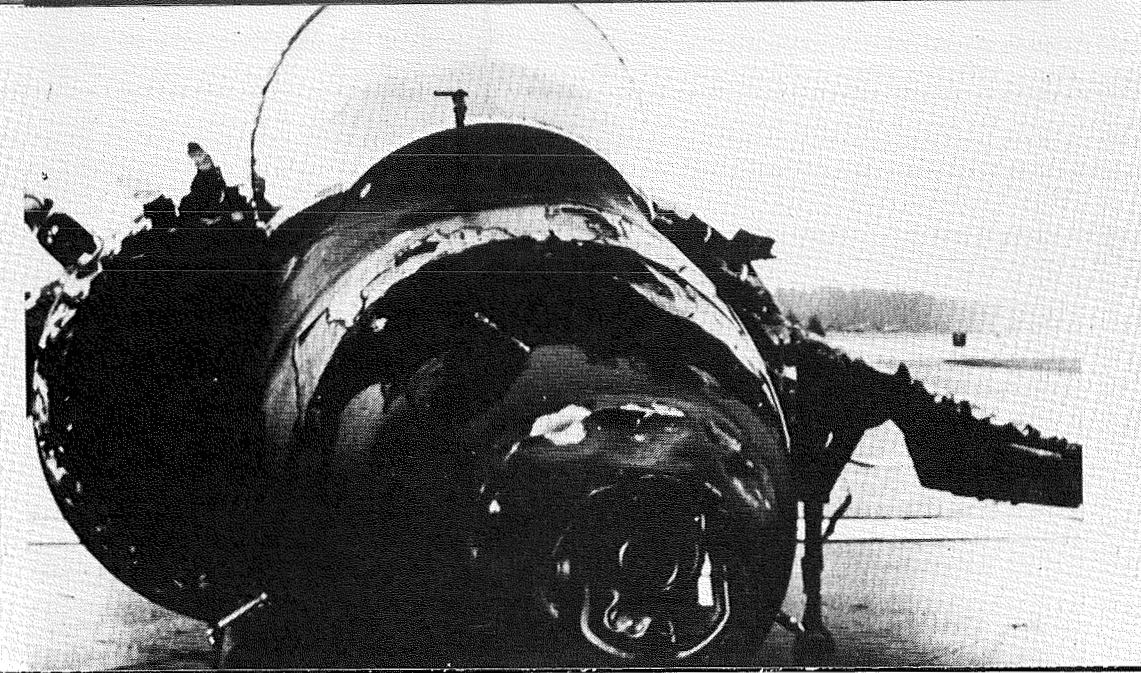
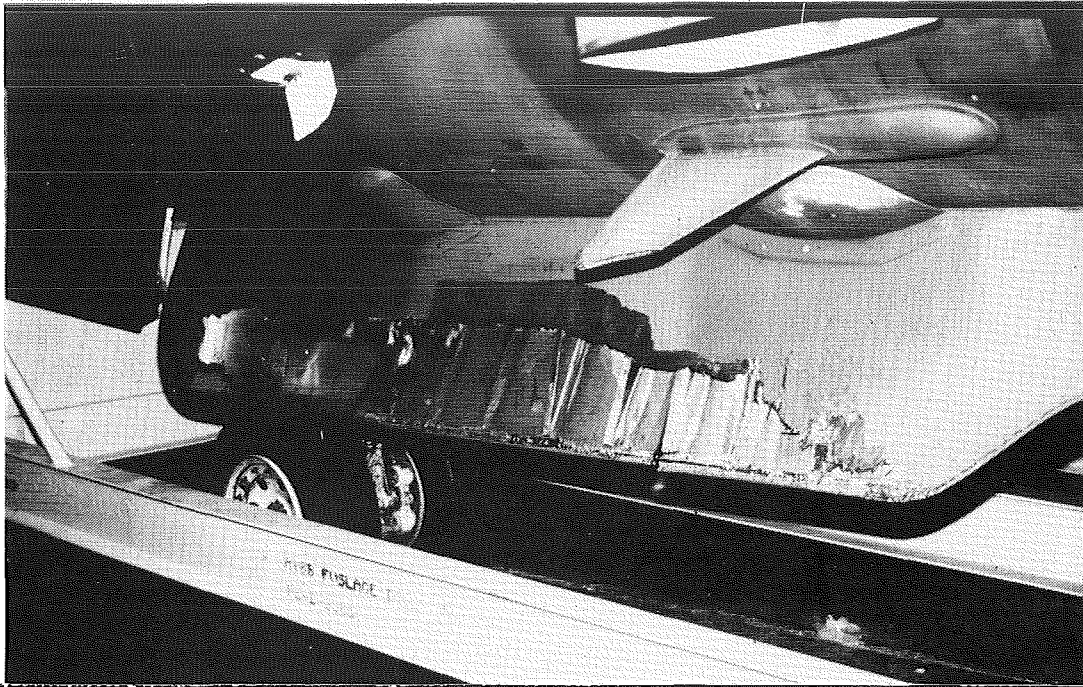


PHOTO OF CRASH DAMAGED TAV-8B STRAKE

THE AIRCRAFT INVOLVED TAXIED AT NIGHT INTO A CONCRETE HIGHWAY BARRIER BEING USED TO BLOCK A CLOSED RUNWAY. THE STRAKE IN THE PHOTO WAS SEVERELY DAMAGED, BUT ACCORDING TO STRUCTURAL ENGINEERS FROM NADEP, CHERRY POINT, THE DAMAGE TO THE STRAKE AND FUSELAGE ATTACHMENT WOULD HAVE BEEN MUCH WORSE IF THE STRAKE HAD BEEN MADE OF ALUMINUM. THE STRAKE WAS REPAIRABLE, BUT IT WAS MORE COST EFFECTIVE IN THIS CASE TO REPLACE IT.



AV-8B CRASH DAMAGE

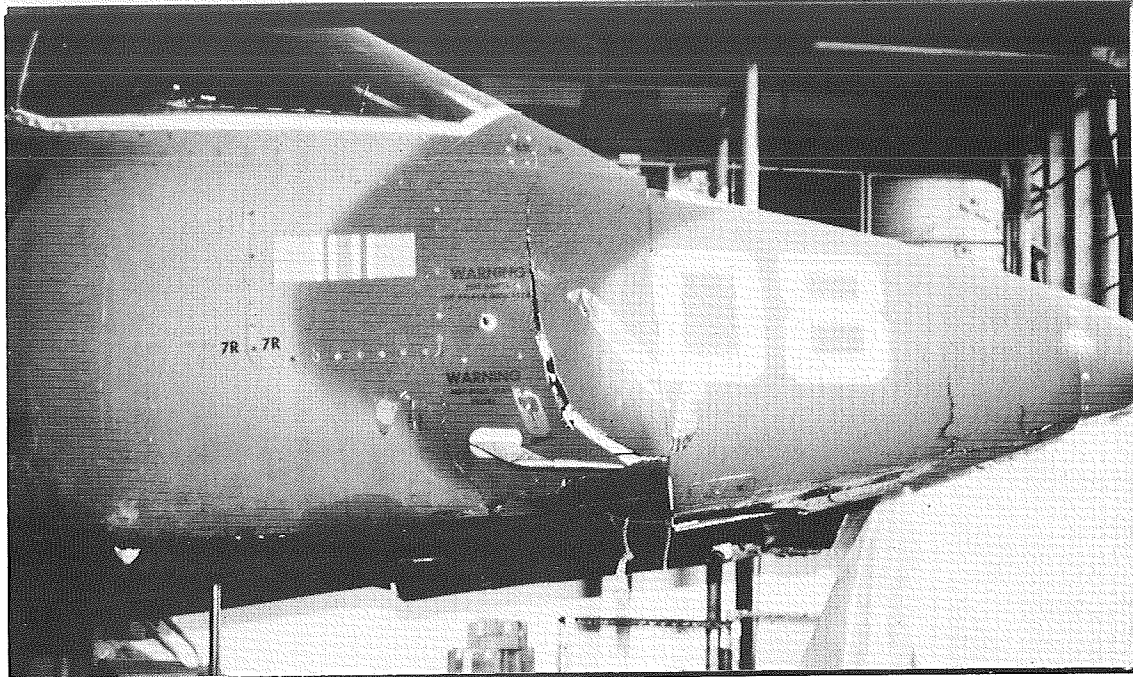


PHOTOS OF AV-8B CRASH DAMAGE REPAIR

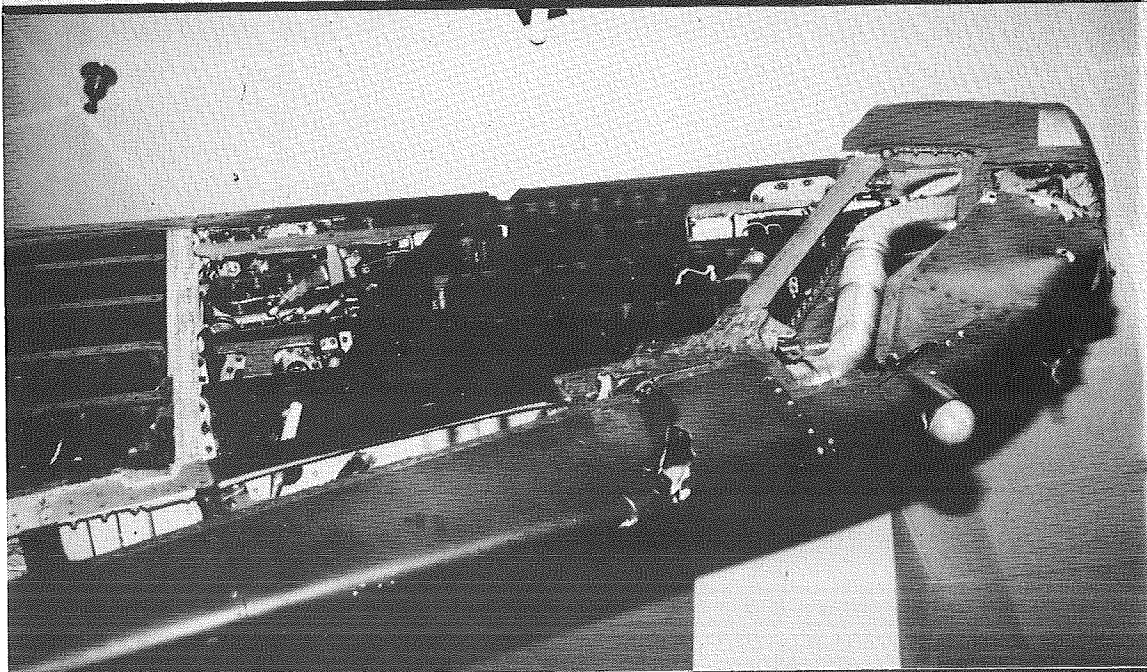
THE AIRCRAFT INVOLVED EXPERIENCED A NOSE WHEEL STEERING MALFUNCTION AND DEPARTED THE RUNWAY AT A HIGH RATE OF SPEED. AFTER THE PILOT EJECTED, THE AIRCRAFT CRASHED INTO A DITCH, SEVERELY DAMAGING THE NOSE SECTION AND WING TIP. IN THE PHOTO, A CRACK CAN BE SEEN THAT EXTENDS THROUGH THE CANOPY RAIL, DOWN THE SIDE OF THE COCKPIT, AND EVENTUALLY THROUGH THE LONGERONS. NO DAMAGE EXTENDED AFT OF THE CRACK. IN THE OPINION OF THE ENGINEERS FROM THE NADEP AT CHERRY POINT, A METAL AIRCRAFT WOULD HAVE BEEN MORE EXTENSIVELY DAMAGED SINCE THE METAL STRUCTURE WOULD HAVE "TELEGRAPHED" THE DAMAGE FURTHER AFT. THE WING TIP SUFFERED DAMAGE TO ITS UPPER AND LOWER SKINS AND THE OUTBOARD PYLON FITTING AND TIP RIB. NADEP CHERRY POINT WAS ABLE TO REPAIR THE AIRCRAFT BY INSTALLING A NEW FORWARD FUSELAGE SECTION OBTAINED FROM MCAIR. REPAIRS WERE ALSO REQUIRED ON THE WING TIP. THE REPAIR SHOWN IN THE NEXT PHOTO OF THE WING IS FROM A DIFFERENT AIRCRAFT BUT IS SIMILAR TO THE DAMAGE SUFFERED BY THIS AIRCRAFT. THE OUTBOARD PYLON FITTING AND TIP RIB WERE REPLACED AND A NEW OUTBOARD SKIN WAS SPLICED INTO THE EXISTING COVER SKIN. THE REPAIR TO THE SKIN SHOWS UP AS THE BLACK SECTION AT THE OUTBOARD END OF THE WING TIP.



AV-8B CRASH DAMAGE

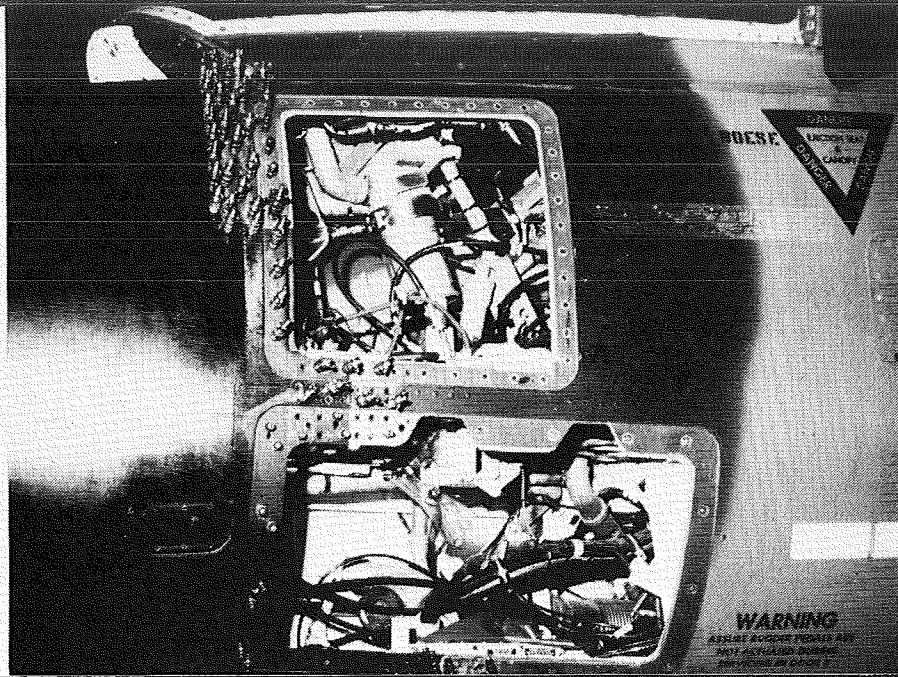


AV-8B CRASH DAMAGE





AV-8B FORWARD FUSELAGE REPAIR



SERVICE RELATED CONCERNS

- **COMPOSITE INDUCED CORROSION**

- **BREAKDOWN IN PROTECTIVE SCHEMES**

- COMPOSITES CAN INDUCE CORROSION OF METALS

- GRAPHITE BASED COMPOSITES CAUSE GALVANIC CORROSION IN SOME AIRCRAFT ALLOYS

- PROTECTION SCHEMES DEVELOPED WHICH REDUCE THE PROBLEM

- BREAKDOWN IN PROTECTION SCHEMES RESULT IN CORROSION OF THE METAL

- IMIDE BASED COMPOSITES REQUIRE STRICT ATTENTION TO GALVANIC CORROSION SINCE COMPOSITES DEGRADE AS CORROSION OCCURS

- **SHELF-LIFE OF COMPOSITE MATERIALS FOR SHIPBOARD REPAIR**

- REFRIGERATED STORAGE ON SHIPS EITHER DOES NOT EXIST OR CANNOT BE COUNTED ON. MOST MATERIALS HAVE LIMITED SHELF LIVES OF ABOUT 1 YEAR. REPAIR MATERIALS WITH SHELF LIVES OF AT LEAST 2 YEARS ARE NEEDED. NADC HAS DEVELOPED INNOVATIVE COMPOSITE REPAIR TECHNIQUES WHICH HAVE DEMONSTRATED THE SHELF LIFE OF MATERIALS TO OVER 18 MONTHS AT AMBIENT CONDITIONS AND ARE EXPECTED TO BE QUALIFIED FOR AT LEAST 2 YEARS SHORTLY.

- **LIGHTNING/EMI PROTECTION SCHEMES INDUCE PENALTIES**

- TYPICAL PROTECTION SCHEMES USING FLAME SPRAY OR EXPANDED COPPER FOIL TO PROVIDE LIGHTNING/EMI PROTECTION ADDS NOT ONLY TO THE WEIGHT AND COST OF THE STRUCTURE, BUT ALSO INCREASES THE SUPPORTABILITY PROBLEMS. BETTER PROTECTION SCHEMES NEED TO BE DEVELOPED.

- **MAINTENANCE PROBLEMS ASSOCIATED WITH HONEYCOMB CONSTRUCTION**

- WATER INTRUSION HAS LONG BEEN A PROBLEM WITH HONEYCOMB STRUCTURES. IN METAL HONEYCOMB IT CAUSES CORROSION, WHILE IN BOTH METAL AND NON-METALLIC HONEYCOMB, IT ADDS WEIGHT AND COMPLICATES THE REPAIR PROCEDURES SINCE THE STRUCTURE MUST BE DRIED BEFORE APPLYING HEAT.



SERVICE RELATED CONCERNS



- **COMPOSITE INDUCED CORROSION**

- **BREAKDOWN IN PROTECTION SCHEMES**

- **SHELF-LIFE OF COMPOSITE MATERIALS FOR SHIPBOARD REPAIR**

- **LIGHTNING/EMI PROTECTION SCHEMES INDUCE PENALTIES**

- **MAINTENANCE PROBLEMS ASSOCIATED WITH HONEYCOMB CONSTRUCTION**

THIS PAGE INTENTIONALLY BLANK



NAVY ASSESSMENT OF CURRENT COMPOSITE STRUCTURES



- PERFORMANCE EXPECTATIONS GENERALLY MET
- DEVELOPMENT AND PRODUCTION COSTS HIGH
- MANUFACTURING TECHNOLOGY LAGGING
- MANUFACTURING QUALITY CRITICAL ISSUE
- BETTER MATERIALS NEEDED
- SERVICE EXPERIENCE FAVORABLE
- SUPPORTABLE IN CARRIER ENVIRONMENT

REPAIRABILITY

- METHODS IN PLACE FOR SHIPBOARD REPAIR

DUE TO THE LIMITED SHIPBOARD SPACE AVAILABLE, REPAIR PROCEDURES HAVE BEEN DEVELOPED THAT MINIMIZE THE NUMBER OF UNIQUE TOOLS, EQUIPMENT AND MATERIALS. THE LACK OF AUTOCLAVES, OVENS AND REFRIGERATED STORAGE HAS DRIVEN THE DEVELOPMENT OF VARIOUS INNOVATIVE COMPOSITE REPAIR TECHNIQUES WHICH HAS EXTENDED THE SHELF LIFE OF MATERIALS TO OVER 18 MONTHS AT AMBIENT CONDITIONS AND PRODUCED HIGH QUALITY REPAIRS.

- REPAIR OPTIONS AVAILABLE

BOTH BOLTED AND BONDED REPAIR TECHNIQUES EXIST TODAY FOR THE REPAIR OF DAMAGED COMPOSITE STRUCTURES. BONDED PROCEDURES HAVE BEEN DEVELOPED FOR BOTH EXTERNAL PATCHES AND FLUSH REPAIRS. MATERIALS/PROCESSES INCLUDE WET LAYUP, PRECURED AND STAGED FORMS.

BOLTED METHODS ARE SIMILAR TO METAL WORKING TECHNIQUES AND CAN UTILIZE ALUMINUM, STEEL OR TITANIUM DEPENDING ON THE PREDICTED LOADS AND FATIGUE REQUIREMENTS.

- SIMPLICITY/REPAIR TIME COMPARABLE TO METAL REPAIRS

THE SKILL LEVEL AND TIME REQUIRED FOR COMPOSITE REPAIRS ARE SIMILAR TO THOSE REQUIRED FOR METAL.

THE NEXT TWO PROGRAMS ARE DESCRIBED IN A LITTLE MORE DETAIL IN THE FOLLOWING VU-GRAPHS.

- MAJOR PROGRAM IN PROGRESS ON THE V-22

THE V-22 COMPOSITE REPAIR DEVELOPMENT (VCRD) (*PRONOUNCED VEE-CARD*) PROGRAM IS CURRENTLY ADDRESSING THE DESIGN OF REPAIRS TO PREDICTED DAMAGE IN 24 AREAS OF THE AIRCRAFT.

- AIRCRAFT BATTLE DAMAGE REPAIR (ABDR) UNDER DEVELOPMENT

THE PURPOSE OF ABDR IS TO RETURN BATTLE DAMAGED AIRCRAFT TO THE BATTLE AS SOON AS POSSIBLE SO THAT THEY MAY HAVE AN EFFECT ON THE OUTCOME OF THE BATTLE. WITH THIS IN MIND, DESIGN AND ANALYSIS TECHNIQUES ARE BEING DEVELOPED THAT WILL USE PERSONAL COMPUTERS TO ANALYZE LARGE SIZE DAMAGE TO COMPOSITE WING STRUCTURE.

- METHODS NEEDED FOR LOW OBSERVABLE STRUCTURE

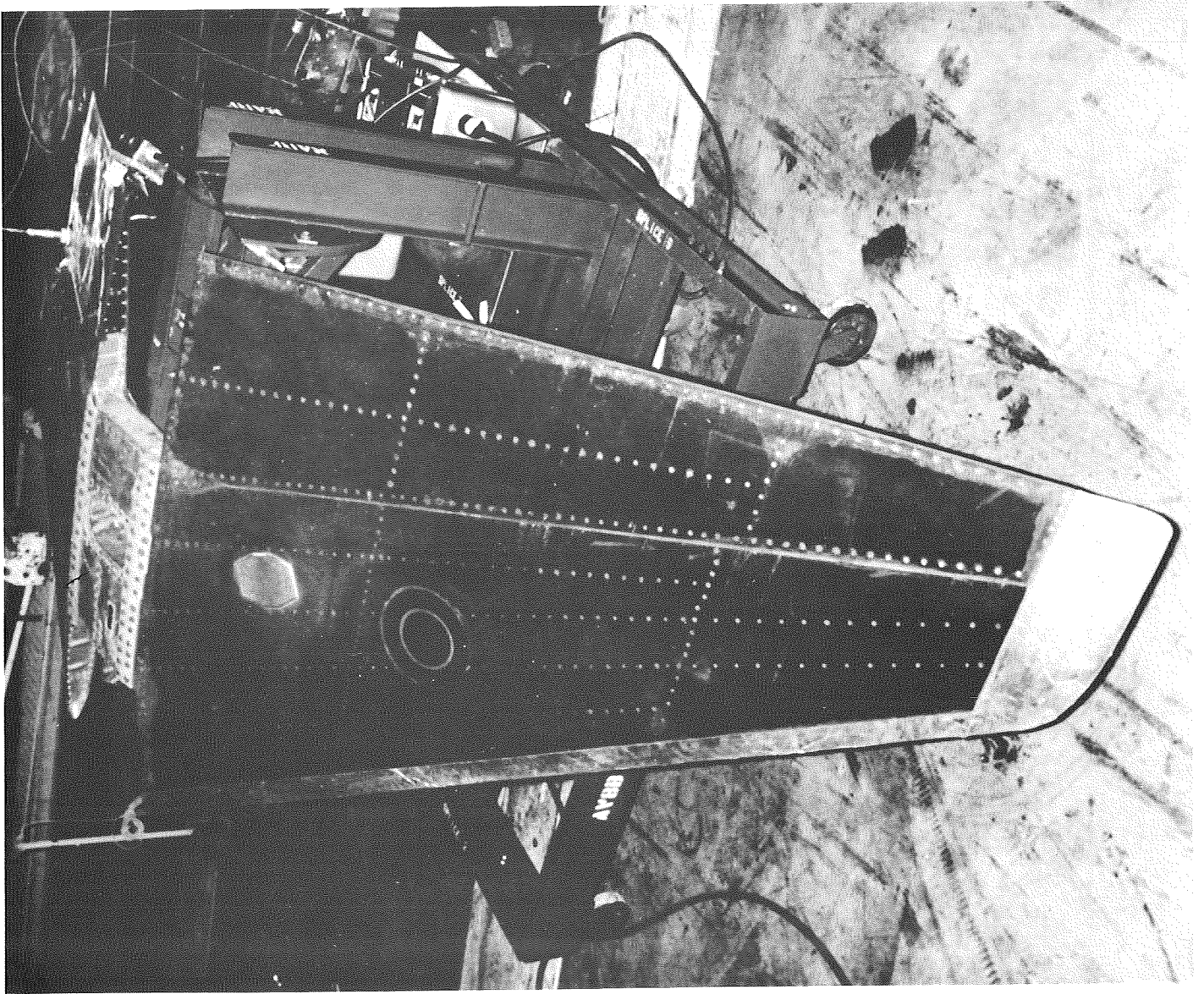
LOW OBSERVABLE STRUCTURES IMPOSE ADDITIONAL REQUIREMENTS. SPECIAL DESIGN AND REPAIR PROCEDURES HAVE TO BE DEVELOPED WHICH DO NOT DEGRADE THE RCS SIGNATURE OF THE AIRCRAFT. WE HAVE JUST RECENTLY INITIATED WORK ON L.O. REPAIRS.



REPAIRABILITY



- METHODS IN PLACE FOR SHIPBOARD REPAIR
 - REPAIR OPTIONS AVAILABLE
 - SIMPLICITY/REPAIR TIME COMPARABLE TO METAL
- MAJOR PROGRAM IN PROGRESS ON V-22
- AIRCRAFT BATTLE DAMAGE REPAIR UNDER DEVELOPMENT
- METHODS NEEDED FOR LOW OBSERVABLE STRUCTURE



AV-8B

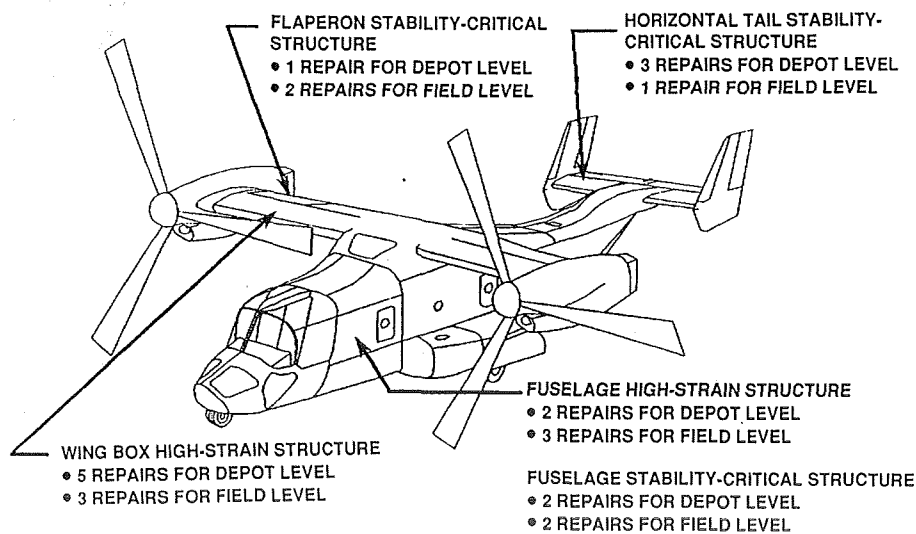
S T A B I L I Z A T O R R E P A I R

THE V-22 COMPOSITE REPAIR DEVELOPMENT PROGRAM

IN THE PAST, LIMITED ATTENTION HAS BEEN PLACED ON COMPOSITE SUPPORTABILITY FOR NEW AIRCRAFT ACQUISITION PROGRAMS. AS A RESULT, LOGISTIC SUPPORT DIFFICULTIES, SUCH AS A LACK OF REPAIR METHODS AND REFRIGERATED MATERIALS HANDLING AND STORAGE, HAVE BEEN EXPERIENCED WHEN INITIALLY FIELDING COMPOSITE STRUCTURES IN THE SERVICE ENVIRONMENT. IN A DEPARTURE FROM PAST EXPERIENCE AND CONCERNED WITH THESE DIFFICULTIES, BOTH THE NAVY AND AIR FORCE LOGISTIC COMMUNITIES JOINTLY INITIATED THE V-22 COMPOSITE REPAIR DEVELOPMENT PROGRAM (VCRD) IN 1989. THE OBJECTIVE OF THIS PROGRAM HAS BEEN TO DEVELOP AND VALIDATE, BY FLEET EVALUATION AND FULL SCALE COMPONENT TESTING, LOGISTICALLY ACCEPTABLE REPAIR METHODS TO RESTORE FULL STRUCTURAL INTEGRITY TO MANY OF THE COMPONENTS EMPLOYING UNIQUE STRUCTURAL CONCEPTS AND MATERIALS. BOTH FIELD AND DEPOT LEVEL REPAIR CONCEPTS ARE UNDER DEVELOPMENT TO ADDRESS VARIOUS LEVELS OF DAMAGE SEVERITY. THE PROGRAM IS SCHEDULED FOR COMPLETION IN 1993 FOLLOWING FULL SCALE VALIDATION TESTING OF REPRESENTATIVE REPAIRED SUBCOMPONENTS AT THE NAVAL AIR DEVELOPMENT CENTER AND BELL HELICOPTER TEXTRON.



V-22 COMPOSITE REPAIR DEVELOPMENT



ABDR

- DEVELOP PC BASED ANALYTICAL TECHNIQUES FOR RAPID REPAIR OF COMPOSITE WING STRUCTURES

THIS COMPUTER CODE WILL PROVIDE AN ANALYTICAL TOOL TO AN AIRCRAFT BATTLE DAMAGE REPAIR ASSESSOR OR ENGINEER TO DETERMINE THE STRUCTURAL CONDITION OF THE UNDAMAGED, DAMAGED, AND REPAIRED STRUCTURE, IN LESS THAN ONE HOUR.

- SIMPLIFIED ANALYSIS FOR RAPID DAMAGE ASSESSMENT/REPAIRS

A PERSONAL COMPUTER BASED ANALYSIS PACKAGE TO ASSESS THE INTEGRITY OF LARGE SCALE RAPID REPAIRS IS BEING DEVELOPED FOR BOTH CURRENT AND EMERGING COMPOSITE WING STRUCTURES IN THE NAVY INVENTORY.

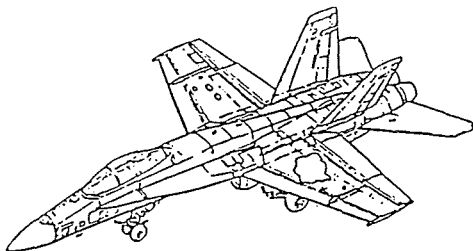
- RAPID ANALYSIS FOR FIELDIED DESIGNS

A STRUCTURAL LIBRARY WILL CONTAIN DETAILED FINITE ELEMENT MODELS OF THE F/A-18, AV-8B, A-6 RETROFIT, AND V-22 WINGS. THE WING MODELS CAN BE MODIFIED INTERACTIVELY TO INCORPORATE LARGE SCALE DAMAGE IN SKINS AND SUBSTRUCTURE. BY USING USER-FRIENDLY AND MENU-DRIVEN INPUTS, REPAIRS CAN BE RAPIDLY DESIGNED FOR THE DAMAGE AT HAND.

THIS ANALYSIS CODE WILL ALLOW THE DESIGN OF SUBSTRUCTURE AND SKIN REPAIRS AND TAKE INTO ACCOUNT THEIR INTERACTION. THE CODE MAY BE EXPANDED TO INCLUDE OTHER COMPOSITE STRUCTURES SUCH AS THE FUSELAGE AND EMPENNAGE.



AIRCRAFT BATTLE DAMAGE REPAIR



- DEVELOP PC BASED ANALYTICAL TECHNIQUES FOR RAPID REPAIR OF COMPOSITE WING STRUCTURE

- SIMPLIFIED ANALYSIS FOR RAPID DAMAGE ASSESSMENT/REPAIR

- REPAIR ANALYSIS FOR FIELDIED DESIGNS

- SKIN/SUBSTRUCTURE INTERACTION

DESIGN ISSUES

THE INHERENT DIFFERENCES BETWEEN METALS AND COMPOSITES NECESSITATES NEW CERTIFICATION REQUIREMENTS.

OUT-OF-PLANE LOADING AND ASSEMBLY INDUCED DELAMINATIONS ARE CRITICAL ISSUES THAT MUST BE DEALT WITH IN DESIGN AND ANALYSIS BECAUSE OF THE LOW INTERLAMINAR STRENGTH OF COMPOSITES. THESE ISSUES ARE BEING WORKED JOINTLY BY THE NAVY AND THE FAA ARE DISCUSSED IN MORE DETAIL IN THE FOLLOWING VIEWGRAPHS.



DESIGN ISSUES



CERTIFICATION REQUIREMENTS

OUT-OF-PLANE LOADING

ASSEMBLY INDUCED DELAMINATIONS

NAVY STRUCTURAL CERTIFICATION METHODOLOGY

CAREFUL PLANNING AND COORDINATION BETWEEN THE NAVY AND THE CONTRACTOR ARE REQUIRED BEGINNING EARLY IN THE AIRCRAFT DEVELOPMENT PROGRAM.

THE DESIGN DEVELOPMENT TEST PROGRAM IS AN INTEGRAL PART OF THE CERTIFICATION PROCESS.

STATIC STRENGTHS GREATER THAN DESIGN ULTIMATE LOAD ARE REQUIRED FOR THE DESIGN DEVELOPMENT TEST SPECIMENS TO ACCOUNT FOR:

- ENVIRONMENTAL STRENGTH DEGRADATION DUE TO TEMPERATURE AND MOISTURE.
- THE INCREASED SCATTER IN MATERIAL PROPERTIES DEMONSTRATED BY COMPOSITES (WHEN COMPARED TO METALS).

FULL SCALE TEST RESULTS MUST CORRELATE WITH DESIGN DEVELOPMENT TEST RESULTS.

- MEASURED STRAINS IN CRITICAL AREAS MUST AGREE.
- FAILURE MODES MUST BE THE SAME.
- STATIC STRENGTH MUST ACCOUNT FOR SCATTER AND ENVIRONMENT.

ADEQUATE TIME AND RESOURCES MUST BE ALLOCATED FOR THE ENTIRE CERTIFICATION PROCESS.

SCHEDULE AND COST RESTRAINTS THAT LIMIT THE SCOPE OF THE DESIGN DEVELOPMENT PROGRAM INCREASE THE RISK OF UNSUCCESSFUL FULL SCALE TESTS.



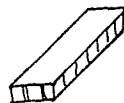
NAVY STRUCTURAL CERTIFICATION METHODOLOGY



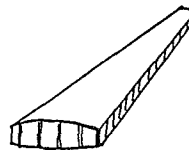
COUPON



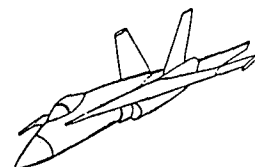
ELEMENT



SUBCOMP



COMPONENT



FULL-SCALE TESTS
STATIC
FATIGUE
FLIGHT

- CERTIFICATION BEGINS EARLY IN DEVELOPMENT PROCESS
- BUILDING BLOCK DEVELOPMENT APPROACH
- CAREFULLY COORDINATED DEVELOPMENT PLANNING
- ADEQUATE TIME AND RESOURCES

AV-8B COMPOSITE WING DEVELOPMENT

AN EXAMPLE OF AN IDEAL DEVELOPMENT PROGRAM IS THE AV-8B COMPOSITE WING. DUE TO THE EXISTENCE OF ADEQUATE TIME AND FUNDING, THE NECESSARY AMOUNT OF DEVELOPMENT AND PRE-PRODUCTION TESTING WAS PERFORMED PRIOR TO THE FABRICATION OF THE FULL STATIC TEST AIRCRAFT. THIS TEST PROGRAM INCLUDED COUPON TESTING TO OBTAIN MATERIAL ALLOWABLES, FOLLOWED BY JOINT AND SKIN PANEL TESTING. ONCE DESIGN PROPERTIES WERE OBTAINED, LARGER SUBSTRUCTURE ELEMENTS AND CRITICAL PORTIONS OF THE TORQUE BOX WERE FABRICATED AND TESTED. THIS APPROACH PROVIDES NECESSARY TEST DATA AND MANUFACTURING EXPERIENCE IN A TIME FRAME WHICH CAN IMPACT THE FINAL DESIGN.

THIS REPRESENTS AN IDEAL DEVELOPMENT PROGRAM FOR COMPOSITE AIRCRAFT STRUCTURE, HOWEVER, SCHEDULE AND COSTS RESTRAINTS OFTEN COMPROMISE THIS APPROACH. ALL EFFORTS SHOULD BE MADE TO FOLLOW THIS APPROACH TO INSURE A SUCCESSFUL FULL SCALE AIRCRAFT TEST.



AV-8B COMPOSITE WING DEVELOPMENT



1974 1975	Preliminary Design	
1975 Thru 1977	Design Allowables	
	Joints	
	Skins	
	Substructure	
	Box Beams	
	Operational Hazards	
1978	Static Wing YAV-83 Flight Demo	
1980 1981	FSD Static Airframe	
1981 1982	FSD Fatigue Airframe	
1984 On	Production Deliveries	

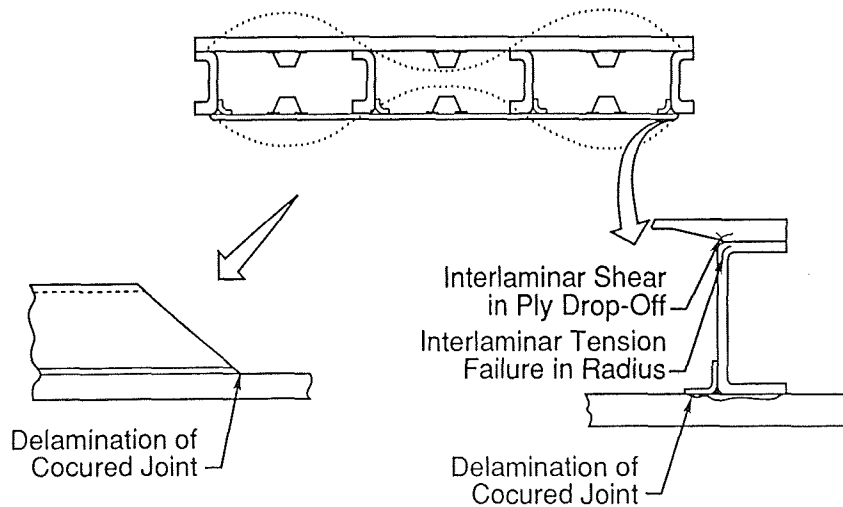
OUT-OF-PLANE ANALYSES

OUT OF PLANE STRESSES ARE AN ISSUE IN COMPOSITES BECAUSE OF THEIR LOW INTERLAMINAR STRENGTH. OUT OF PLANE STRESSES RESULT EITHER DIRECTLY FROM THE APPLICATION OF OUT-OF-PLANE LOADS, SUCH AS FUEL PRESSURE, OR INDIRECTLY, UNDER IN PLANE LOADING, AS A RESULT OF LAMINATE GEOMETRY SUCH AS LAMINATE CORNER RADII, PLY DROP-OFFS, STIFFENER RUN-OUT, AND PANEL BUCKLING DEFORMATION. WHILE THREE DIMENSIONAL FINITE ELEMENT METHODS CAN BE USED TO ANALYZE THESE SITUATIONS, THEY REQUIRE TOO MUCH TIME FOR PRELIMINARY STRUCTURAL SIZING.

IN A JOINT NAVY/FAA PROGRAM, THE PROBLEMS RESULTING FROM OUT-OF-PLANE LOADS WERE INVESTIGATED AND WAYS WERE DEVELOPED FOR AVOIDING FAILURES THAT ARE CAUSED BY THESE LOADS. SIMPLE TWO DIMENSIONAL ANALYSIS METHODS WERE DEVELOPED TO PREDICT OUT-OF-PLANE FAILURE STRENGTH OF COMPOSITE STRUCTURES. ELEMENT TEST DATA WERE USED TO VERIFY THE ANALYSES. THE METHODS AND EXPERIENCE FROM THIS PROGRAM WERE USED TO COMPILE A SET OF DESIGN GUIDES FOR DESIGNERS AND ANALYSTS.



POTENTIAL OUT-OF PLANE FAILURES



ASSEMBLY INDUCED DELAMINATIONS

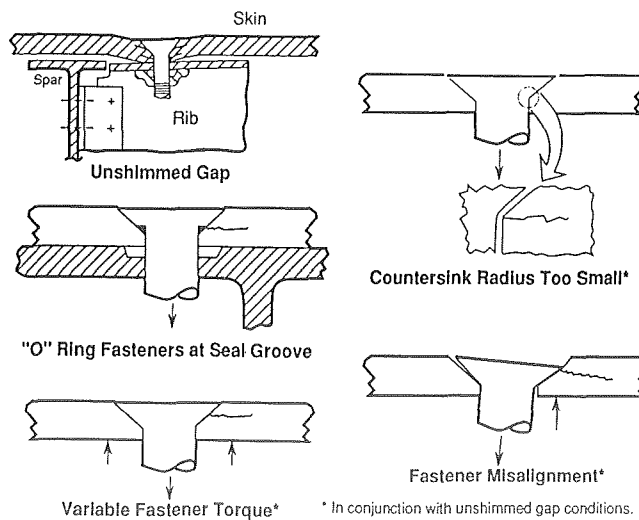
EARLIER, I POINTED OUT A RECURRING PROBLEM IN MANUFACTURING, IN WHICH INTERPLY DELAMINATIONS OF WING SKINS AND SUBSTRUCTURE OCCUR DURING ASSEMBLY. FREQUENTLY THESE DELAMINATIONS ARE ASSOCIATED WITH IMPROPER FASTENER INSTALLATION OR IMPROPER SHIMMING OF MECHANICAL FASTENED JOINTS AS INDICATED ON THIS VU-GRAPH. THESE DELAMINATIONS CAN CAUSE SIGNIFICANT REDUCTION IN THE LOAD CARRYING CAPABILITY OF STRUCTURE, PARTICULARLY IN COMPRESSION STRENGTH AND IN THE STRENGTH OF STRUCTURE SUBJECTED TO OUT-OF-PLANE LOADING. IN ADDITION, THERE IS A POTENTIAL FOR DELAMINATION GROWTH UNDER FATIGUE LOADING, WHICH CAN FURTHER REDUCE LOAD CARRYING CAPABILITY. CURRENTLY, ANALYTICAL METHODS TO ASSESS THE EFFECTS OF THESE DELAMINATIONS DO NOT EXIST. NADC AND THE FAA JOINTLY HAVE INITIATED A PROGRAM TO:

- (1) DEVELOP AND VALIDATE A METHODOLOGY FOR ASSESSING THE SEVERITY OF KNOWN DELAMINATIONS WITH RESPECT TO THEIR EFFECTS ON STRENGTH AND LIFE SO REPAIR/REPLACEMENT DECISIONS CAN BE MADE.
- (2) PROVIDE DESIGN GUIDELINES FOR PREVENTION OF ASSEMBLY INDUCED DELAMINATIONS.

THIS WORK WILL BE REPORTED ON IN DETAIL DURING THIS CONFERENCE.



ASSEMBLY INDUCED DELAMINATIONS



FUTURE COMPOSITE USAGE RATIONALE

IN THE FUTURE THE DRIVER FOR THE SELECTION AND USAGE OF A COMPOSITE MATERIAL WILL NOT BE SOLELY DEPENDENT UPON WEIGHT SAVINGS. OTHER MAJOR DRIVERS SUCH AS COST, MANUFACTURING QUALITY, DAMAGE TOLERANCE, SURVIVABILITY, OBSERVABILITY, SUPPORTABILITY, IN ADDITION TO RISK TO PROGRAM SCHEDULE AND AVAILABLE FUNDING MUST ALL BE TAKEN INTO CONSIDERATION. ONLY APPLICATIONS WHERE THE PAYOFF IS SUFFICIENT TO JUSTIFY THE USE OF ADVANCED COMPOSITES SHOULD BE CONSIDERED. ADDITIONALLY, TO INSURE THAT THESE PAYOFFS ARE REALIZED, BETTER METHODS FOR PREDICTING WEIGHT AND COSTS IN A MANUFACTURING ENVIRONMENT MUST BE DEVELOPED.

THE USE OF IMMATURE MATERIAL SYSTEMS MUST BE AVOIDED. PAST EXPERIENCE HAS SHOWN THAT THE COMMITMENT TO A MATERIAL SYSTEM PRIOR TO ITS COMPLETE CHARACTERIZATION RESULTS IN PERFORMANCE PENALTIES AND COSTLY PROGRAM DELAYS.

BUILDING A MILITARY AIRCRAFT REQUIRES SPECIALIZED EQUIPMENT AND EXPERIENCE RELATED TO COMPOSITE TECHNOLOGY. THE NAVY AND THE CONTRACTOR MUST REALIZE THAT THIS CAPABILITY NEEDS TO EXIST AT THE START OF THE DEVELOPMENT PROGRAM AND CANNOT EXPECT IT TO BE ACQUIRED DURING THE PROGRAM.

APPLICATIONS MUST TAKE ADVANTAGE OF THE AVAILABLE TECHNOLOGY BASE. SHOULD THE TECHNOLOGY FOR A SPECIFIC APPLICATION NOT EXIST AT THE PROGRAM ON-SET, THE RISK OF FAILURE CAN BE SIGNIFICANT.

FINALLY, IT MUST BE REALIZED THAT THE BEST MATERIAL FOR A PARTICULAR APPLICATION MAY NOT BE A COMPOSITE.



FUTURE COMPOSITES USAGE RATIONALE



- ALL KEY DRIVERS - WEIGHT, COST, RISK, ETC.
- PAYOFF VS. APPLICATION
- PROGRAMMATICS - SCHEDULE, FUNDING, ETC.
- MATURITY OF MATERIAL SYSTEMS
- CONTRACTOR EXPERIENCE AND CAPABILITY
- OVERALL TECHNOLOGY BASE VS. APPLICATION
- BEST MATERIAL NOT ALWAYS COMPOSITES

FUTURE PERSPECTIVE

THE NAVY IS COMMITTED TO, AND WILL CONTINUE TO USE, ADVANCED COMPOSITES ON ITS AIRCRAFT. THE MAJOR BENEFITS TO THE NAVY, REDUCED WEIGHT, INCREASED FATIGUE LIFE AND CORROSION RESISTANCE, FAR OUTWEIGH THE LIMITATIONS DISCUSSED. THESE LIMITATIONS ARE NOT CONSIDERED SHOWSTOPPERS AND ARE, AND WILL CONTINUE TO BE, WORKED THROUGH R&D AND MANTECH PROGRAMS. THE TECHNOLOGY WILL CONTINUE TO EVOLVE WITH CONTINUING EMPHASIS ON REDUCING COSTS AND IMPROVING QUALITY THROUGH AUTOMATION. IN ALL CASES THE COSTS ASSOCIATED WITH THE USE OF COMPOSITES MUST BE JUSTIFIED.

IN THE MATERIALS SELECTION AREA, THERMOSETS WILL CONTINUE TO BE THE PRIMARY MATERIAL IN THE FORESEEABLE FUTURE DUE TO THEIR MATURITY AND THE EXISTENCE OF AVAILABLE CAPITAL EQUIPMENT (AUTOCLAVES).

THE ISSUES OF LOW OBSERVABILITY AND SUPPORTABILITY WILL TAKE ON ADDITIONAL IMPORTANCE IN THE FUTURE.



FUTURE PERSPECTIVE



- EVOLUTIONARY DEVELOPMENT OF TECHNOLOGY
- NAVY AIRCRAFT WILL CONTINUE TO USE COMPOSITES
- APPLICATIONS WILL HAVE TO JUSTIFY INCREASED COST
- QUANTUM ADVANCEMENT NEEDED IN MANUFACTURING
- MANUFACTURING QUALITY MUST BE IMPROVED
- THERMOSETS CONTINUE TO BE THE PRIMARY MATERIAL IN THE FORESEEABLE FUTURE
- LOW OBSERVABILITY WILL BE A DESIGN DRIVER
- SUPPORTABILITY WILL BE INCREASINGLY IMPORTANT

MIT

**Advanced Materials Requirements and Needs
for Future Aerospace Applications**

Samuel L. Venneri
National Aeronautics and Space Administration
Office of Aeronautics, Exploration and Technology

THIS PAGE INTENTIONALLY BLANK

Page intentionally left blank

Page intentionally left blank

omit

SESSION II
AIRCRAFT DESIGN METHODOLOGY (A)

PRECEDING PAGE BLANK, NOT FILMED

THIS PAGE INTENTIONALLY BLANK

Mechanical Properties of Triaxially Braided Composites: Experimental and Analytical Results

John E. Masters,
Lockheed Engineering and Science
NASA Langley Research Center

Raymond L. Foye,
Lockheed Engineering and Science
North Carolina A & T State University

Christopher M. Pastore,
and
Yasser A. Gowayed
North Carolina State University

ABSTRACT

This paper investigates the unnotched tensile properties of 2-D triaxial braid reinforced composites from both an experimental and an analytical viewpoint. The materials are graphite fibers in an epoxy matrix. Three different reinforcing fiber architectures were considered. Specimens were cut from RTM composite panels made from each braid. There were considerable differences in the observed elastic constants from different size strain gage and extensometer readings. Larger strain gages gave more consistent results and correlated better with the extensometer readings. Experimental strains correlated reasonably well with analytical predictions in the longitudinal, 0° , fiber direction but not in the transverse direction. Tensile strength results were not always predictable even in reinforcing directions. Minor changes in braid geometry led to disproportionate strength variations.

The unit cell structure of the triaxial braid was discussed with the assistance of computer analysis of the microgeometry. Photomicrographs of braid geometry were used to improve upon the computer graphics representations of unit cells. These unit cells were used to predict the elastic moduli with various degrees of sophistication. The simple and the complex analyses were generally in agreement but none adequately matched the experimental results for all the braids.

INTRODUCTION

Braid reinforced composites are one of the many textile fabric reinforced composites that are under consideration as lower cost and higher impact resistant/tolerant materials for aircraft applications. The wide variety of cross-sectional forms that can be braided promises to reduce fabrication costs for standard and custom made stiffeners, truss members, rotor blade spars, longerons, and frames. However, the analytical tools to evaluate these materials are just now being developed and reliable data bases of fundamental properties are incomplete. Both of these needs are addressed in this investigation.

The specific objective of this study was to understand the role of the braid reinforcement microgeometry in laminate mechanical behavior. This was accomplished through combined analytical and experimental efforts. Fabric preforms were modelled using a process science model. Cured laminates were investigated and their fabric geometries were characterized. The materials' mechanical properties were experimentally measured in unnotched tensile tests and compared to predictions made using analytical models.

A series of three 2-D triaxial braid geometries were investigated in this study. The specimens, which were designed by Boeing and supplied to NASA Langley as part of a joint NASA-Boeing investigation, had a $0/\pm\theta$ braid pattern. The materials' Young's moduli, Poisson's ratios, and ultimate strengths were experimentally determined under in-plane tension load. The sensitivity of these measurements to strain gage size was also studied.

The architecture of the fibers is the key to understanding the mechanical behavior of textile composites. The fabric geometry controls the material response. It must be well understood to interpret the experimental data. Similarly, the ability of any material model to predict material behavior hinges upon the accuracy of its treatment of the fiber geometry.

Graphical modelling of the braided unit cell was carried out using a processing science model coupled with a graphical rendering on a personal computer. This approach permits the construction of a mathematical representation of the surfaces and orientations of the braided yarns within the composite material. The geometric description of the unit cell was validated through optical microscopy and the model was updated to incorporate secondary fabrication effects. Based on the definition of fiber architecture provided by the process science model, it is possible to characterize material properties in local regions within the unit cell.

The analysis of braids is usually based on the use of either a simple diagonal brick model or a more complex inhomogeneous finite element model. Each approach was applied to predict the Young's moduli and the Poisson's ratios of the braided material. In addition, the application of a laminated plate model to these materials was investigated as a simple approximation tool.

MATERIAL SYSTEMS

The materials employed in this study featured triaxially braided AS-4 fabric impregnated with Shell 1895 epoxy resin. A triaxially braided fabric, as shown schematically in Figure 1, consists of three yarns, 0° , $\pm\theta^\circ$, intertwined in a single layer. The fabrics studied were braided in a 2/2 pattern. That is, a $+\theta$ braided tow continuously passes over two $-\theta$ tows and then under two $-\theta$ tows and vice versa. The 0° or longitudinal tows are introduced into the fabric during braiding through stationary guide eyes. These tows are straight (without crimp) and are parallel to the braid axis. Note, the gaps shown between fibers in this schematic are exaggerated for clarity in illustrating the braid pattern.

Three braid geometries were investigated. The braid angle, the yarn sizes, and the longitudinal yarn content were varied to assess material sensitivity to these parameters. The last parameter listed is typically expressed as percentage of 0° yarns. It is the volumetric proportion of longitudinal yarns to total yarn content and is a function of braid angle and yarn size. Yarn size is expressed in terms of the number of filaments per yarn. The longitudinal yarns were larger than the braider yarns in all cases.

The nominal braid configurations are summarized in Table I. In addition to the three parameters listed above, the table also lists the nominal spacings of the longitudinal and braid yarns. Both quantities are expressed in terms of yarn per inch.

Table I. Triaxial Braid Configurations

MATERIAL	BRAID PATTERN	BRAIDER YARN SIZE (Fiber No.)	0° YARN SIZE (Fiber No.)	PERCENT 0° YARNS (%)	0° YARN SPACING (Yarn/in.)	BRAID YARN SPACING (Yarn/in.)
A1	$0/\pm 63^\circ$	12K	24K	31.5	4.17	9.16
B1	$0/\pm 66.5^\circ$	6K	18K	37.6	4.77	11.98
B2	$0/\pm 70^\circ$	6K	18K	34.0	4.37	12.74

Note: K indicates thousands. For the AS-4 yarns, fiber diam. equals 7 microns.

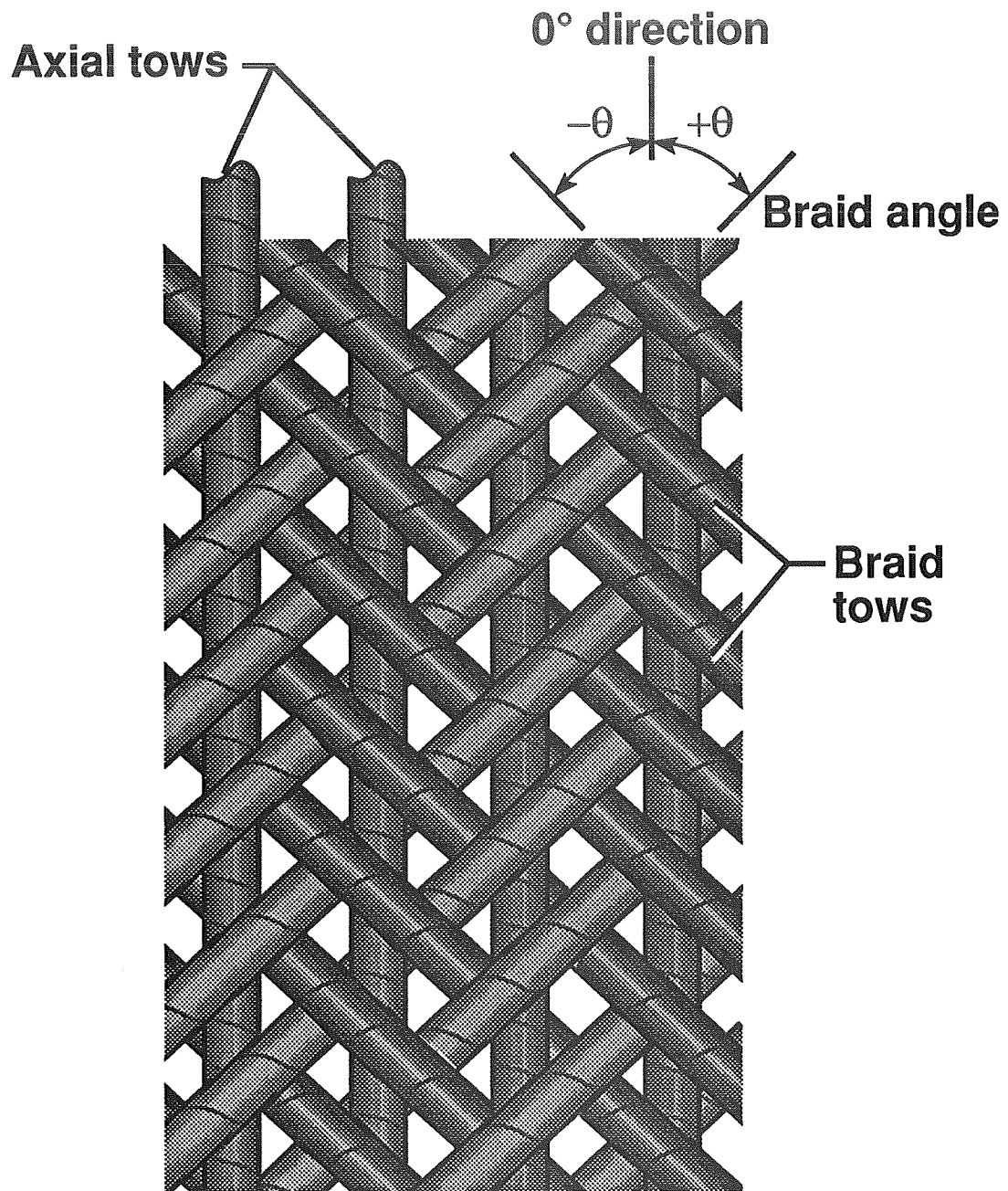


Figure 1. Triaxial braid pattern.

The fabrics investigated in this study were formed with a 144 carrier New England Butt triaxial braider, incorporating 72 longitudinal yarns in a 2/2 regular braid pattern. The braids were formed on cylindrical mandrels, and the desired preform thickness was achieved by over-braiding layers. Since all specimens were to have a nominal thickness of 0.125 in., the number of layers increased as yarn bundle size decreased. Mandrel diameter, D, was also increased to vary longitudinal yarn content.

Table II summarizes the processing parameters employed for each architecture.

Table II. Braid Processing Parameters

MATERIAL	NUMBER OF LAYERS	MANDREL DIAM. (in.)
A1	4	5.5
B1	5	4.8
B2	5	5.25

After braiding, the fabric was cut longitudinally, removed from the mandrel, and border stitched to maintain handleability. The resulting flat pieces of layered fabric were placed in molds and resin was applied through a resin transfer molding (RTM) process.

The braid configurations listed in Table I can be related to the braid process parameters described in the previous paragraphs through mathematical models. A process science model [1] is being developed to relate braid pattern to machine parameters. It also provides a mathematical description of the fiber architecture. This latter aspect of the model will be discussed in the next section, Geometric Modelling.

The models developed to date, however, are approximate because they cannot account for all secondary manufacturing effects which can alter braid architecture. Empirical data, gathered from cured laminates, is required to update these models.

The final fiber architectures of the three braid types were experimentally characterized. The laminates' braid angles, percentage of longitudinal fibers, fiber content, resin content, and their thicknesses were determined.

Digital images of sample specimens from the composite panels were produced and image analysis software was used to calculate braid angles. Each braid was formed with one carrier supplying a nickle coated graphite yarn for post-manufacturing optical and X-ray investigation of the fabric and composite. These yarns were used to verify the placement of yarns in the structure.

Figure 2 shows a scanned image of a typical braided specimen. The nickle coated AS-4 is clearly visible in this scanned image. Samples from different architectures and different panels of the same architecture were scanned for quantification. By tracing the nickle coated yarn, the braid angle was measured for each of the specimens examined. The variation of the braid angle within panels was negligible; the variation of braid angle between panels was found to be less than 1° .

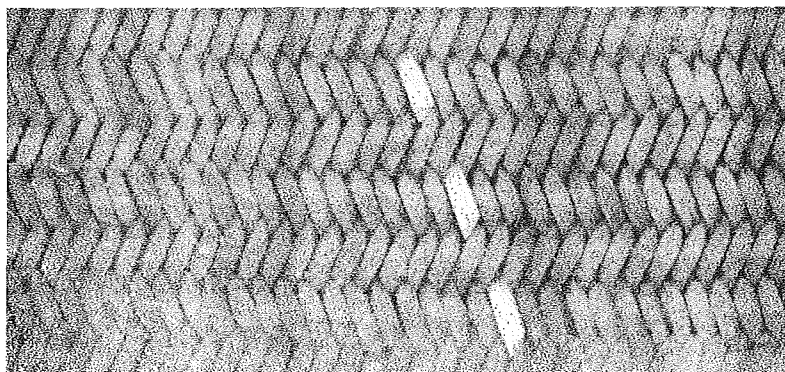


Figure 2. Scanned Surface of Braided Composite Specimen (Type B1) Showing Nickle Coated AS-4 Yarn in Braider Position.

Internal fiber architecture was examined by sectioning and polishing samples of the material. Cross-sectional photomicrographs of the various specimens were also scanned into the computer and examined to determine the placement and frequency of longitudinal yarns. Additionally, the shape of the yarn cross-sections, longitudinal and braid yarn curvatures, and interstitial areas were assessed. Finally, the thickness of the composites was also measured from these micrographs.

The photomicrograph in Figure 3 shows the cross-section of a specimen made from the B2 material. The specimen has been sectioned along the 0° yarns. The three bright horizontal bands that traverse the photomicrographs are sections of axial yarns that intersect the polished surface. The 0° yarns in the two remaining layers did not intersect this plane. The figure illustrates that the inserted 0° yarns exhibit no crimp and are quite straight. Figure 4 contains a photomicrograph of the same material sectioned perpendicular to the 0° yarns.

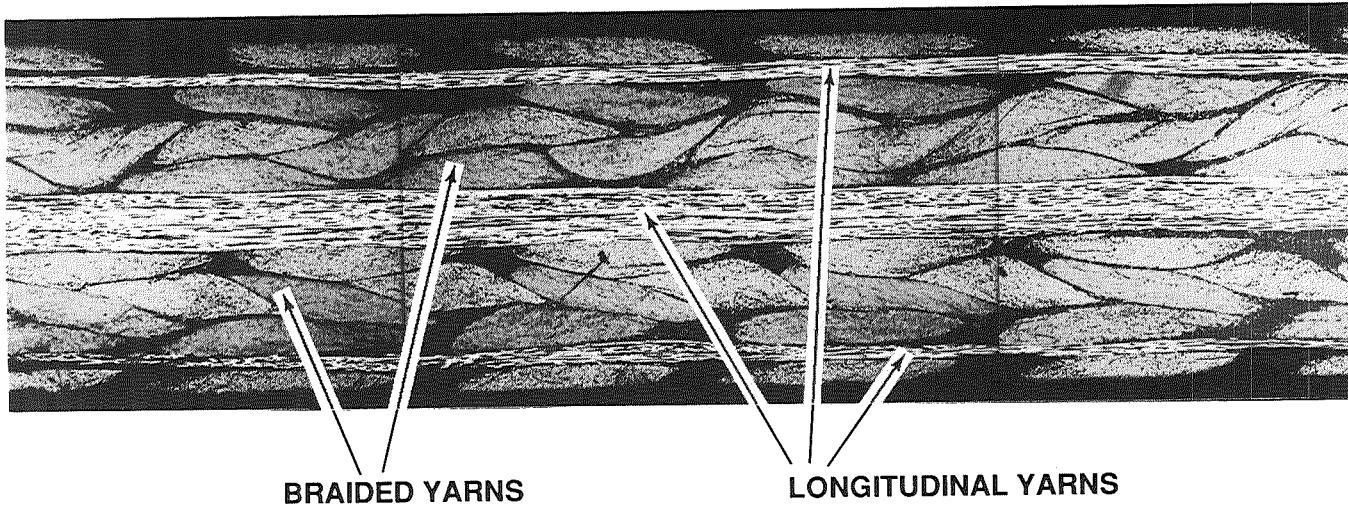


Figure 3. Longitudinal cross-section (20X) of a B2 laminate.

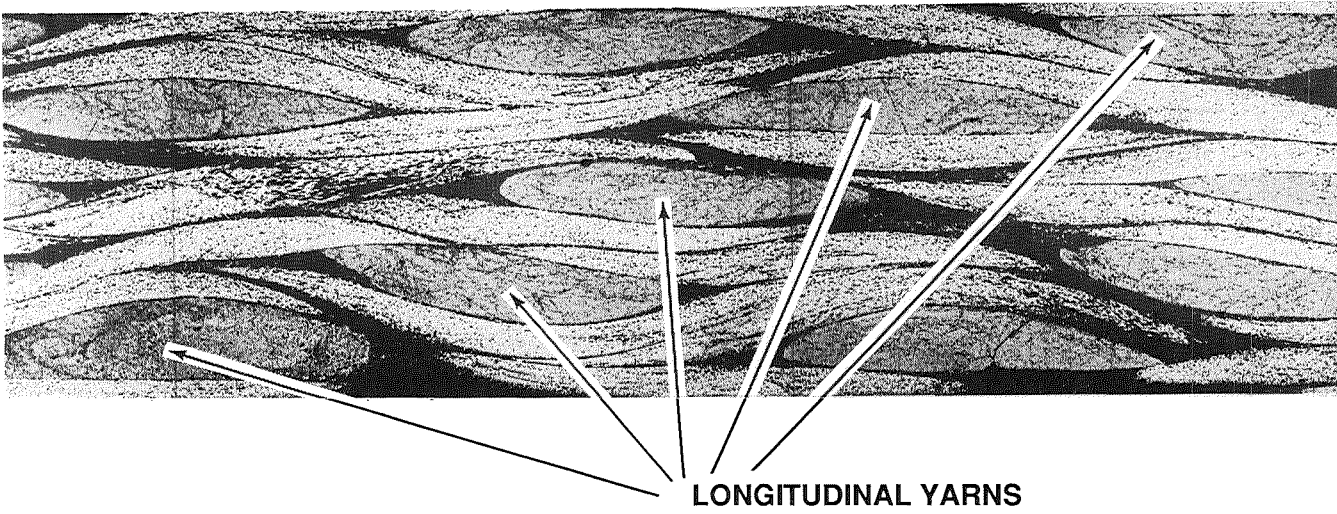


Figure 4. Transverse cross-section (20X) of a B2 laminate.

All five layers of braided preform material can be identified in the figure. The photomicrograph indicates that the axial yarns do not stack on top of one another. Instead, the layers of material nest during the braiding operation. For this reason, only three axial yarns are visible in Figure 3. Finally, the photomicrograph shown in Figure 5 shows the cross-section of a B2 laminate that has been sectioned along the braided yarns. As in the case of the axial yarns, braided yarns for each layer do not appear. The degree of crimp developed in the braided yarns as they intertwine is illustrated in the figure.

The measured braid angles, frequency of longitudinal fibers, and the laminate thicknesses were input to the process science model. The materials' fiber volume fractions and their percentages of longitudinal fibers were predicted with this model using the description of the braiding process as input. The results of the observations and calculations are summarized in Tables III and IV. The physical characteristics and the fiber and resin content were not measured for all panels.

Table III. Physical Characteristics of Test Panels

MATERIAL	PANEL NUMBER	THICKNESS (in.)	BRAID ANGLE (°)	PERCENT 0° YARNS (%)
A1	15L	.135	62.2	31.8
	1U	.137	62.4	31.7
B1	2L	.136	67.1	36.8
	4U	.126	67.7	36.3
B2	10L	.139	68.3	35.7
	11L	.137	67.5	36.5

No significant differences were noted between the nominal braid configurations (Table I) and the measured and calculated physical properties listed in Table III. The braid angles and the ratio of longitudinal yarns to total yarn content showed only minor variations from the nominal values.

Though not listed in the table, the longitudinal yarn spacing was also measured from the photomicrographs. Comparing the measured values to the theoretical yarn spacings listed in Table I indicates negligible lateral expansion/contraction occurred during handling of the cut fabric.

Fiber volume fraction was predicted by the process science model and measured experimentally on specimens cut from the same panels used for tensile test coupons. Experimental measures of fiber and resin content were

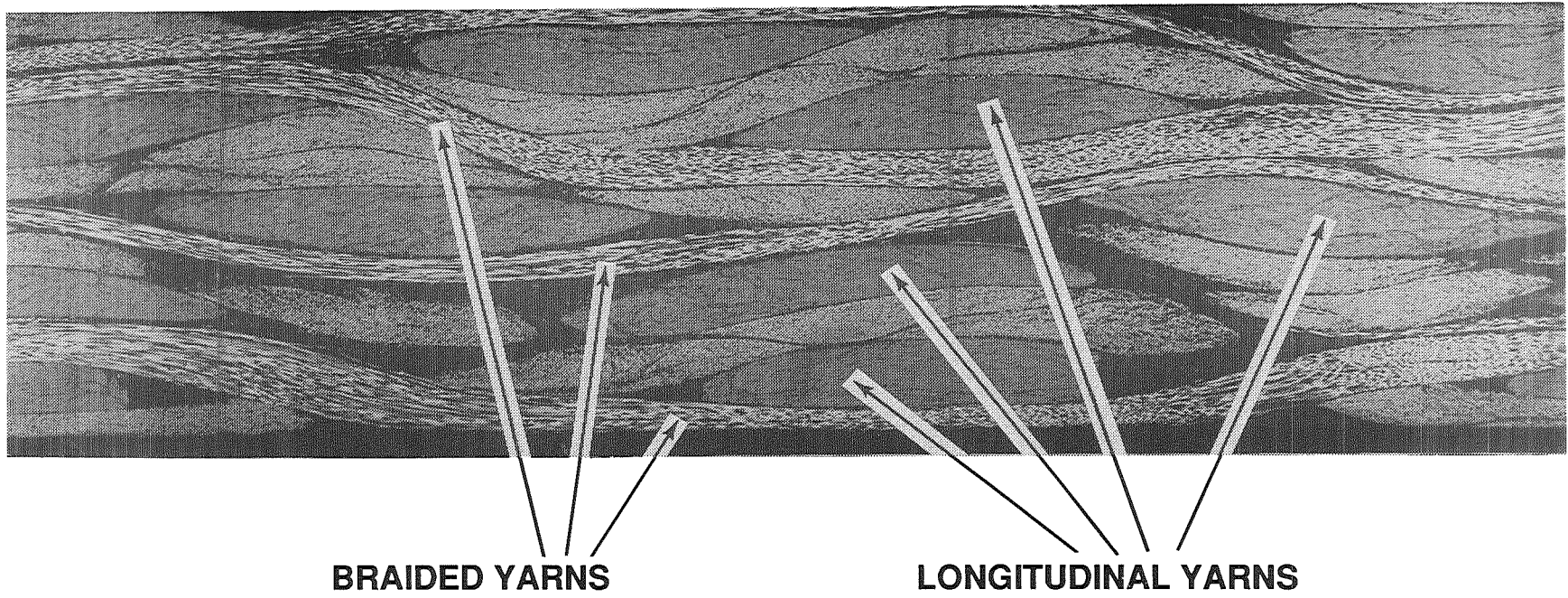


Figure 5. Cross-section of B2 laminate sectioned along braid yarns (20X).

conducted in accordance with ASTM D-3171 [2]. Using this procedure, material samples were digested using concentrated sulfuric acid and 30% hydrogen peroxide. The weight fractions were measured and volume fractions calculated on the basis of density. The density value used for AS-4 was 1.80 g/cc and for the resin was 1.18 g/cc. These results are summarized in Table IV along with the predicted fiber volume fractions.

Table IV. Laminate Fiber and Resin Content

MATERIAL	PANEL NUMBER	DENSITY (g/cc)	THICKNESS (in.)	RESIN VOL. (%)	FIBER VOLUME	
					Measured (%)	Predicted (%)
A1	1U	1.51	.137	45.7	54.0	54.5
	6L	1.51	.137	45.6	54.0	-
B1	2L	1.48	.136	52.8	48.2	50.4
	3U	1.50	.127	47.4	52.3	-
	4U	1.50	.126	46.7	52.8	55.9
B2	11L	1.48	.137	50.9	48.9	46.3
	11U	1.52	.124	44.7	55.2	-

As Tables III and IV indicate, the B1 and B2 materials exhibited a significant panel to panel variation in thickness. Their braid angles and the frequencies of their longitudinal yarns, however, remained relatively constant from panel to panel. Since the fiber preforms did not vary from plate to plate, the thinner laminates contained the same amount of fiber (as the thicker laminates) but less resin. This is reflected in the thinner laminate's lower resin volume percent and, conversely, in their higher fiber volume percent. Consequently, the fiber volume fraction of each individual panel needs to be determined before carrying out analytical modelling.

The correlation between thickness and resin content for panels with the same architecture is apparent. The process science model accurately predicts the fiber volume.

The data in Tables III and IV demonstrate the importance of characterizing material microstructure. Although the braided preforms seem consistent from panel to panel, variations in the RTM process altered the resin content of the panels and changed their fiber volume. Since fiber and resin content effect the material's mechanical response, they should be measured for each panel tested and accounted for in predicting mechanical response.

GEOMETRIC MODELLING

An accurate description of the fiber architecture is required to predict the mechanical properties of textile reinforced composites. The process science model noted earlier provides a three dimensional geometric model of the braided reinforcement. It is used as a front end to other analytical models which predict the material's mechanical properties.

The approach to the geometric modelling consists of three principal steps: i) construction of mean centerline points for each yarn, ii) smoothing the centerlines with a B-spline interpolation to construct a smooth and minimum strain energy curve, and iii) constructing a three dimensional object by sweeping a cross-section along the centerline and forming a surface.

The construction of the mean centerline was carried out on the basis of the processing science model which predicts the ideal architectural arrangement. Since the model cannot account for all secondary manufacturing effects, measured values (braid angle, thickness, distribution of longitudinal yarns, yarn cross-sectional geometry) were used to modify the predicted values. This update creates a good approximation of the actual geometry. Discrepancies between predicted geometries and actual geometries are eliminated prior to performing the mechanical analysis.

Figures 6-8 show the rendered graphics for architectures A1, B1, and B2 respectively. The figures are not drawn to scale.

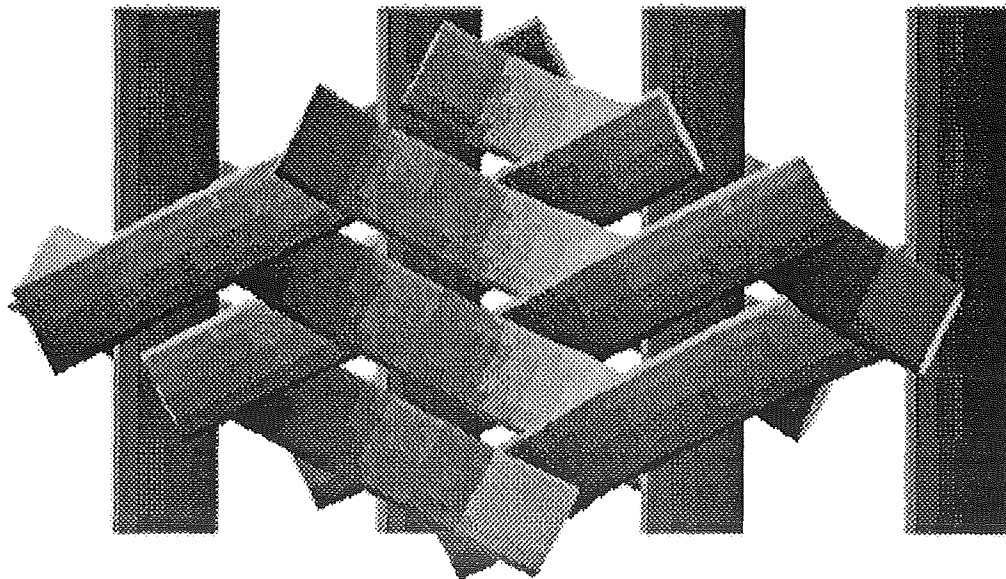


Figure 6. Graphical Rendering of Braid Architecture A1.

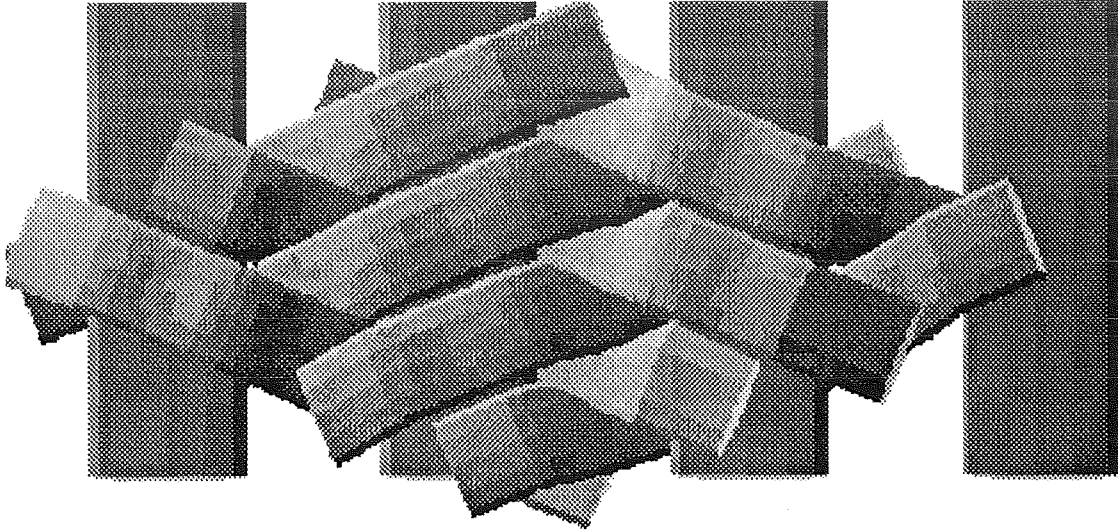


Figure 7. Graphical Rendering of Braid Architecture B1

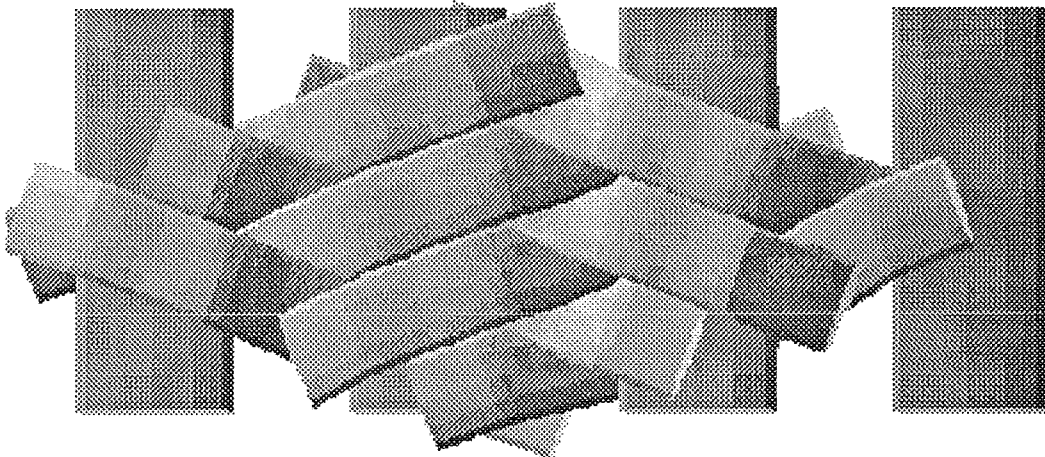


Figure 8. Graphical Rendering of Braid Architecture B2

The graphics can be validated in terms of braid angle, percent longitudinal tows, and fiber volume fraction. In the cases presented above, the renderings were formed based upon these measured values, thus the fit is excellent.

The rhombic frames shown in these figures define unit cells of the three braids studied. A unit cell is a repeatable unit of fabric geometry. It represents the complete yarn or tow intertwinement pattern. It is desirable, for analysis purposes, to define the smallest unit cell possible. Rectangular unit cells are also

preferable. Figure 9 shows the smallest unit cell for a 2/2 triaxial braid. It is contained within the rhombic unit cell.

In a braid, the unit cell width is dependent on mandrel diameter and the number of yarns braided. The height of the unit cell is dependent on the cell width and the braid angle. The sizes of the minimum unit cells for the three braids tested are summarized in Table V. The significance of these dimensions, particularly the width will be discussed further in the following section.

Table V. Summary of Minimum Unit Cell Sizes.

MATERIAL	WIDTH (in.)	HEIGHT (in.)
A1	0.48	0.12
B1	0.42	0.09
B2	0.46	0.08

In addition to the graphic capability illustrated above, the code provides a numerical description of the reinforcing architecture. It is capable of sectioning the unit cells into arbitrarily small volumes and examining the material orientations and proportions within each volume. These volumes can be re-combined using finite elements to predict the mechanical response of the unit cell and to predict the mechanical properties of the braided composite structure [3].

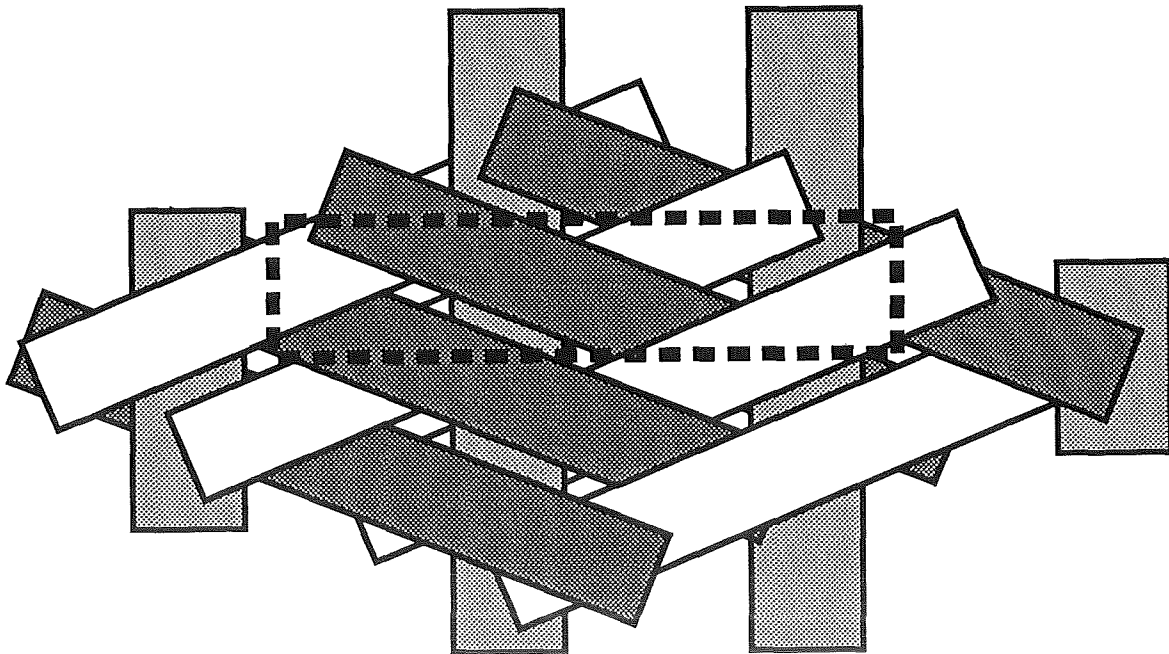


Figure 9. Smallest Unit Cell

EXPERIMENTAL RESULTS

The mechanical properties of the three material systems were experimentally determined in a series of unnotched tensile tests. Test panels were fabricated and machined to permit direct determination of the materials' performance in both the longitudinal direction (parallel to the 0° yarns) and the transverse direction (perpendicular to the 0° yarns). The principal Young's moduli, the Poisson's ratios, and the ultimate tensile strengths were measured in these tests.

All tests were conducted in displacement control (0.01 in/min), on a 50 Kip MTS test machine. The longitudinal or axial tension specimens were 1.5 in. wide and 10.0 in. long. They had 2.25-in.-long fiberglass tabs at the ends yielding a 5.5 in. test section. The transverse tension specimens were 1.5 in. wide and 7.0 in. long. They featured 1.25-in.-long tabs to provide a 4.5 in. long test section.

Axial and transverse strain gages were mounted on each face of the specimen at its center. A range of strain gage sizes was employed to test the sensitivity of the measurements to strain gage size. A $0^\circ/90^\circ$ rosette gage which featured .125 in. square gages, the largest available in stock, was used on all specimens. Sizes of the gages used on the other face of the coupons varied from .062 in. to .187 in. An extensometer with a 1.0 in. gage length was also employed during each test. It was also mounted on the face of the coupon straddling the .125 in. rosette gages.

Thirty-five specimens were tested in the program. Seventeen were loaded to failure to determine ultimate strength, modulus, and Poisson's ratio. Eighteen were loaded to 2000 $\mu\text{in/in}$ of strain to measure modulus and Poisson's ratio only. Stress-strain curves recorded during the strength tests indicated that this strain level was well within the linear range for all of the braids tested.

Results of the strength tests are summarized in Table VI. The table contains the average strengths and ultimate strains (as recorded by the extensometer) for the longitudinal (direction of 0° yarns) and transverse (perpendicular to the 0° yarns) tension tests.

Table VI. Material Strength Test Results

MATERIAL	LONGITUDINAL		TRANSVERSE	
	STRENGTH (KSI)	ULTIMATE STRAIN (%)	STRENGTH (KSI)	ULTIMATE STRAIN (%)
A1	62.6 ± 3.7	1.16 ± .13	35.3	0.67
B1	80.7 ± 1.4	1.36 ± .07	41.7 ± 3.6	0.67 ± .12
B2	57.1 ± 1.7	0.96 ± .12	46.5 ± 5.7	0.70 ± .14

Note: Data in table represents the average for three specimens.
 Results of only two transverse tests on material A1 were available.
 Longitudinal denotes 0° yarn direction; transverse denotes perpendicular direction.

Longitudinal strengths and strains were greater than transverse strengths and strains for all three materials. In fact, transverse strengths and strains showed little sensitivity to fiber architecture. The longitudinal strengths and strains-at-failure showed a range of values, however. For example, the B2 specimens' longitudinal strength was only 20% greater than their transverse strength. The B1 specimens, by comparison, were 50% stronger in the longitudinal direction than they were in the transverse direction.

The most significant result was the difference in longitudinal strength of the B1 and B2 materials, 80.7 ksi vs 57.1 ksi, respectively. The extent of this difference, 41%, is surprising since the materials differ so little. The specimens had comparable fiber architectures: their braid angles differed by only a few degrees; they contained comparable percentages of 0° fibers. The measured fiber volumes of the two materials also showed no significant differences.

Observations of the tests and the failed specimens gave no particular insights into the failure progression. Failures were sudden, catastrophic and somewhat confined to the vicinity of the break. This last observation is more applicable to the transverse specimens than to the longitudinal specimens. Visible surface tow segments gave the appearance of behaving like small structural units that separated from each other. Fracture within tow segments was infrequent. Delaminated tows were always evident adjacent to the fracture site. However, delamination was less extensive in the transverse specimens than in the longitudinal specimens. The extent of delamination in the transverse specimens was on the order of the unit cell dimensions. Delamination in the longitudinal specimens extended over a region of two or three unit cell heights.

As indicated earlier, the three materials' Young's moduli and Poisson's ratios were also measured in these tests. The results of the longitudinal tension

tests are summarized in Table VII. Table VIII lists the transverse tension test results.

Several general observations may be made from these data. There was little difference in the longitudinal and transverse moduli for the A1 and B1 materials. The B2 specimens' average transverse modulus was slightly higher than their average longitudinal modulus. In general, the longitudinal moduli data had less scatter than the transverse moduli data.

The data in the tables may also provide some insight into effective instrumentation practice for future tests. If nonuniform strain fields develop in these materials as a result of their microstructure, then the size and orientation of the gage will have a significant effect on the measured results. Assuming the nonuniformity is on the scale of the smallest unit cell, larger gages, which span larger portions of a unit cell, should have less scatter since they effectively average material response over a larger volume. Ideally, of course, the gage should span several unit cells.

In the longitudinal tests, the axial strain gages are aligned with the short dimension of the unit cells. However, even the longest gage used, 0.187 in. , spanned only two unit cells. The extensometer with its 1.0 in. gage length, on the other hand, spanned several more unit cells in this direction. The general trend in the data indicates that moduli measured using the extensometer strains had less scatter than the results computed from strain gage readings.

By comparison, scatter in the transverse moduli data is larger than the scatter in the longitudinal moduli results. In the transverse direction, (the long dimension of the unit cell), the extensometer spans only about two unit cells (compared to 8 - 12 in the longitudinal direction). The strain gages span less than half a unit cell and their scatter is, likewise, greater.

The longitudinal tension specimens tested were machined from six panels; two for each of the three materials. Although their fiber architectures were comparable, the thicknesses of the B1 and B2 laminates varied. This was reflected in their fiber volume fractions, as noted earlier, and in their moduli. The thinner laminates which had higher fiber volumes had proportionately higher moduli.

The Poisson's ratio data may be subject to the same strain gage and unit cell size interactions suggested above. In general, the data shows that Poisson's ratio increases with strain gage size. This effect was most pronounced in the longitudinal data. The Poisson's ratio measured using .187 in. gages were significantly larger than those measured using .125 in. gages.

Table VII. Longitudinal Modulus and Poisson's Ratio Measurements

MATERIAL	PLATE NO.	THICK. (in.)	MODULUS (MSI)				POISSON'S RATIO		
			.062 Gages	.125 Gages	.187 Gages	Extensometer	.062 Gages	.125 Gages	.187 Gages
A1	15L	.135	-	6.51 ± .49	6.51 ± .58	6.62 ± 0.22	-	.192 ± .026	.300 ± .031
	6L	.137	7.10	6.25	-	6.60	.264	.274	-
B1	2L	.136	-	6.74 ± .68	6.88 ± .61	6.55 ± 0.25	-	.176 ± .018	.268 ± .026
	3U	.127	7.18 ± .06	7.14 ± .21	-	6.88 ± .54	.186 ± .043	.194 ± .036	-
B2	10L	.139	-	6.16 ± .09	6.21 ± .32	6.31 ± .44	-	.150 ± .006	.183 ± .013
	11U	.124	6.24 ± .27	6.47 ± .20	-	6.51 ± .23	.165 ± .018	.151 ± .013	-

115

Table VIII. Transverse Modulus and Poisson's Ratio Measurements

MATERIAL	PLATE NO.	THICK. (in.)	MODULUS (MSI)				POISSON'S RATIO		
			.062 Gages	.125 Gages	.187 Gages	Extensometer	.062 Gages	.125 Gages	.187 Gages
A1	1U	.137	6.26	6.42 ± .92	6.24	6.59 ± .79	.215	.275 ± .040	.307
B1	4U	.126	7.45 ± 1.05	6.13 ± 1.24	6.80 ± .15	6.45 ± .35	.291 ± .022	.163 ± .031	.199 ± .012
B2	11L	.137	7.34 ± 1.79	7.18 ± .88	7.11 ± .68	7.03 ± .62	.161 ± .045	.181 ± .044	.190 ± .008

MECHANICAL PROPERTY PREDICTIONS

The ability to analytically model textile composites and predict their performance is a necessity to the efficient development of these materials and to their effective application.

Linear elastic moduli predictions were made on the basis of four different mechanical models of the various 2-D braid composites tested in the program. These models ranged from simple to complex in the manner in which they represented the fiber architecture. The purpose of this exercise was twofold. The first was to compare the predictions from the various models to each other and to experimental results. The second was to establish the level of accuracy necessary to predict the principal elastic constants of these materials for a typical preliminary design application.

$(0^\circ/\pm\theta^\circ)$ LAMINATE MODEL

The simplest model ignores the out-of-plane undulations of the braided tows and treats each set of tows as if it were a unidirectional ply in a $(0/\pm\theta)$ symmetric laminate. The 0° longitudinal tows are considered to be the 0° unidirectional plies in the laminate. The $\pm\theta$ material corresponds to the braided tows with θ as the average braid angle. When there is a significant percentage of 0° tows in the construction the influence of braid tow undulations may be expected to be minimal. Figures 10 and 11 illustrate the various principal moduli estimates for $(0/\pm\theta)$ laminate as derived from a conventional laminate analysis using the following unidirectional ply properties:

$$E_{11} = 18.0 \text{ MSI} \quad E_{22} = 1.2 \text{ MSI}$$

$$\nu_{12} = 0.3 \quad G_{12} = 0.6 \text{ MSI}$$

where the subscripts 1,2 indicate the fiber direction and the normal to the fiber direction, respectively.

These values correspond to an AS4/epoxy composite with a fiber volume fraction of 52%. Most experimental data for unidirectional AS-4 composite is in the 60 - 65% fiber volume fraction range. Micromechanics estimates of the appropriate corrections factors were applied to the higher fiber volume fraction data in order to obtain the 52% fiber volume fraction values. The three average experimental braid angles of 62.3° , 67.1° , and 67.9° are designated by the vertical lines in Figures 10 and 11. For analysis purposes, the percentage of 0°

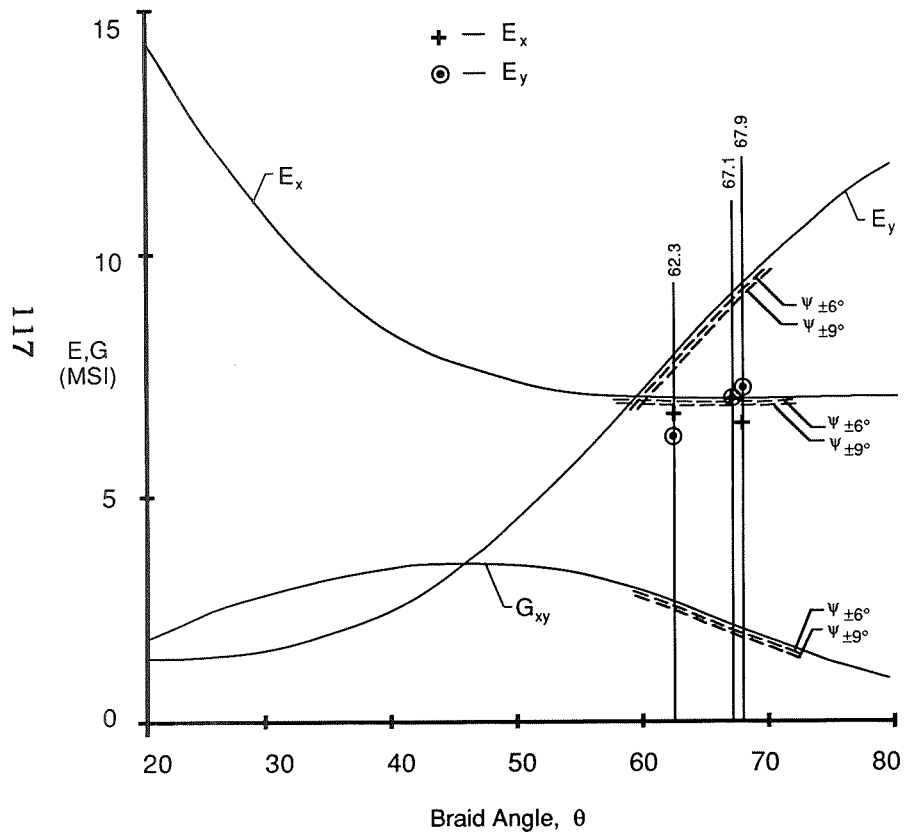


Figure 10: 2-D Braid Modulus Plots

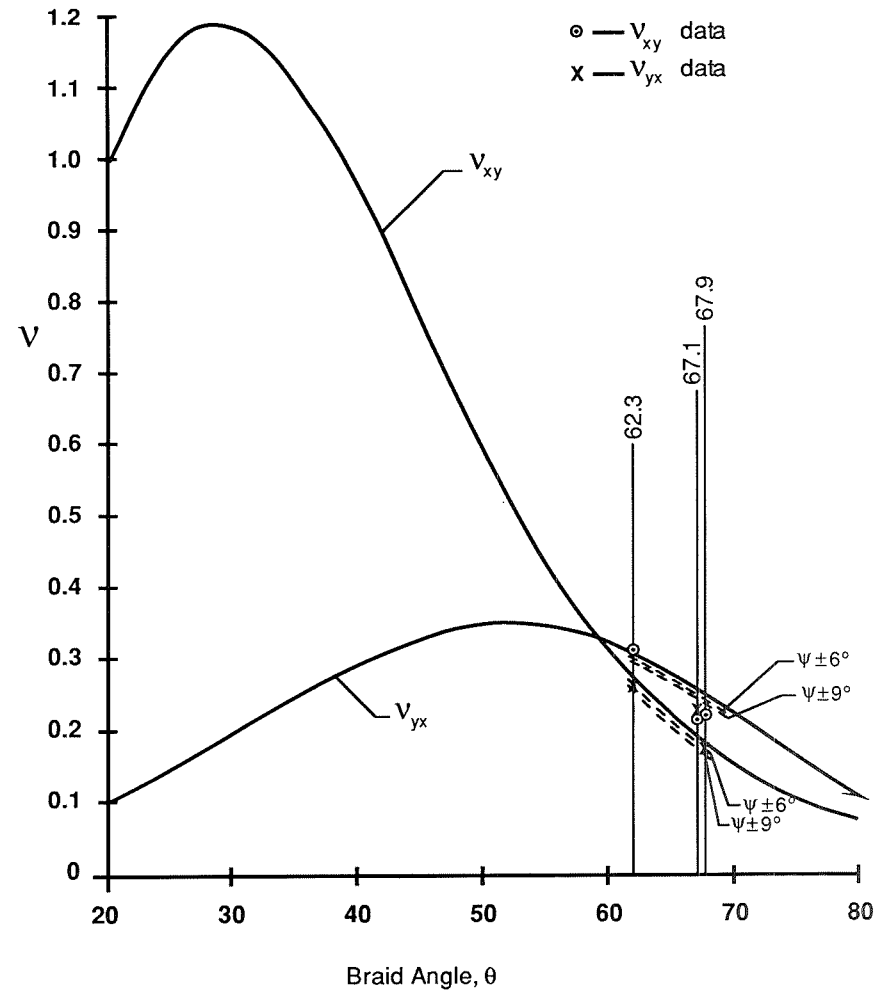


Figure 11: 2-D Braid Poisson Ratio Plots

material in the figures is 34% of the total fiber content. This represents the average for all materials investigated; measured 0° yarn content ranged from 31.7% for an A1 panel to 36.8% for a B1 laminate. Deviations of the individual material averages from this overall average were not more than $\pm 2.8\%$.

A correction factor that accounts for braid undulation can be applied to the laminate analysis. First, an average absolute value of the braid undulation angle, the average out-of-plane angle of the braid tows, ($\pm\psi$) can be obtained by examination of the composite photomicrographs such as Figure 5. Any non-zero ψ should lead to an effective reduction in the longitudinal moduli of the plies representing the two sets of braid tows. The effects on the other principal moduli of these plies should be minimal. The reduction in longitudinal moduli of these plies can be estimated by comparison of the longitudinal modulus of the unidirectional material and the 0° modulus of a $\pm\psi$ symmetric laminate made from the same unidirectional material. This reduction in longitudinal modulus on the braided plies in the original laminate model leads to the corrected estimates of the ($0/\pm\theta$) elastic moduli shown by the dashed lines in Figures 10 and 11. The average braid undulation angles for materials B1 and B2 with the smaller yarns was $\pm 6^\circ$. Material A1, made from the larger tows, had a significantly higher average braid undulation angle of almost $\pm 9^\circ$. The corrected moduli estimates are based on these two observed average undulation angles. The symbols in the figures represent the experimental moduli measured for the three braids. The moduli computed using 0.187 in. strain gages are shown in the figure.

The E_x moduli correlation, where x is the braid direction, was good for all three braids. The E_y moduli correlation, where y is normal to the braid direction, indicated that the analysis was consistently higher than test data. The analytical predictions of the in-plane Poisson's ratio generally followed the trend of the test data. The correction for braid undulations improved the correlation slightly.

DIAGONAL BRICK MODEL

The second mechanical model is based on the concept of the unit cell representation of the composite reinforcing microstructure. The specific model applied here consists of a brick-shaped element of bulk resin with four parallel bar elements along four edges of the brick plus four diagonal bar elements [4]. See Figure 12 for details. The edge bars represent the longitudinal yarns. The main diagonal bars represent the braided yarns. The stiffness of the bar elements (EA/L) are chosen such that they reflect the amount of fiber reinforcement within the unit cell. The dimensions of the brick are determined by the braid angle ($\pm\theta$) and average undulation angle ($\pm\psi$) of the braided yarns.

Table IX compares the moduli predictions from the diagonal brick model with the predictions from the laminate models and the test data for the three different braids. Unlike the results shown in Figures 10 and 11, analytical estimates in Table IX were based on observed fiber volumes, braid angles, undulation angles, and longitudinal yarn content.

The diagonal brick model gave lower Young's moduli estimates than the corrected laminate model resulting in slightly better data correlation. The Poisson's ratio estimates were no better than the laminate analysis.

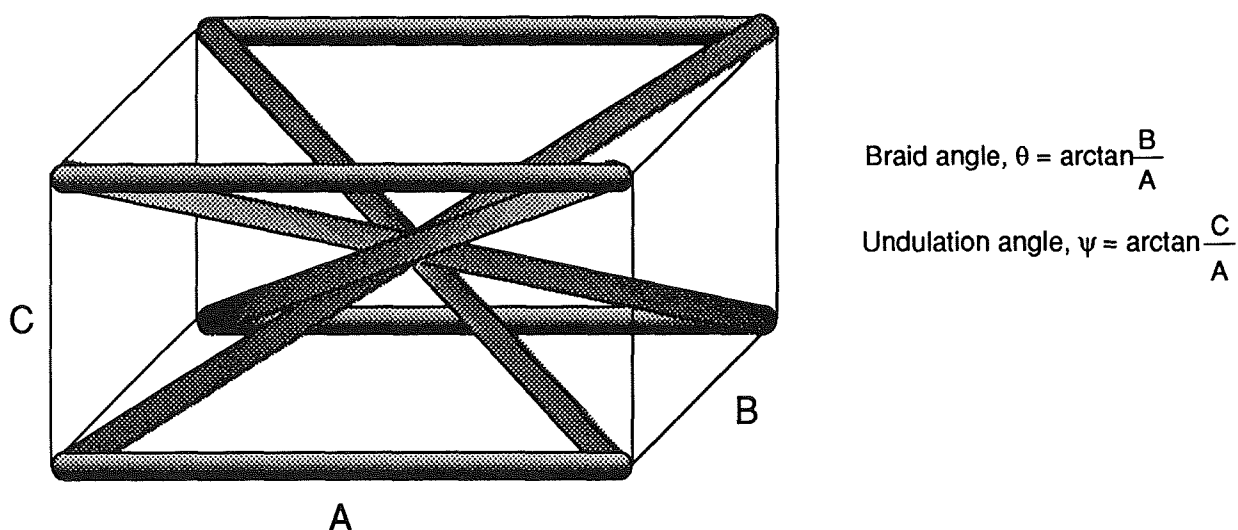


Figure 12. Diagonal Brick Model

FINITE ELEMENT MODEL

Mechanical properties were also predicted using an analytical approach developed by one of the authors [5]. This method, which is shown schematically in Figure 13, analyzes a detailed unit cell of the reinforcing architectures in terms of sub-cells which can be combined in a finite element methodology to predict the unit cell properties. One of the advantages to this approach is that employing sub-cells of arbitrary fine size mitigates the approximation techniques associated with piecewise linear interpretation of the reinforcing geometry.

For the materials under investigation in this paper, the unit cell was constructed with the geometric model described earlier. The unit cell was divided into 9 sub-cells (3 elements per side) and the material properties of each sub-cell were calculated using an inhomogeneous finite element [3]. The

elastic properties of the unit cell were then predicted by creating a stiffness matrix (K) for the structure, and solving unit displacement problems for appropriate boundary conditions.

The results of this analysis are a completed K matrix which can be used to derive elastic properties. For purposes of this evaluation, only E_x and E_y , ν_{xy} , and ν_{yx} are reported. Table IX summarizes the average predicted values for the various materials.

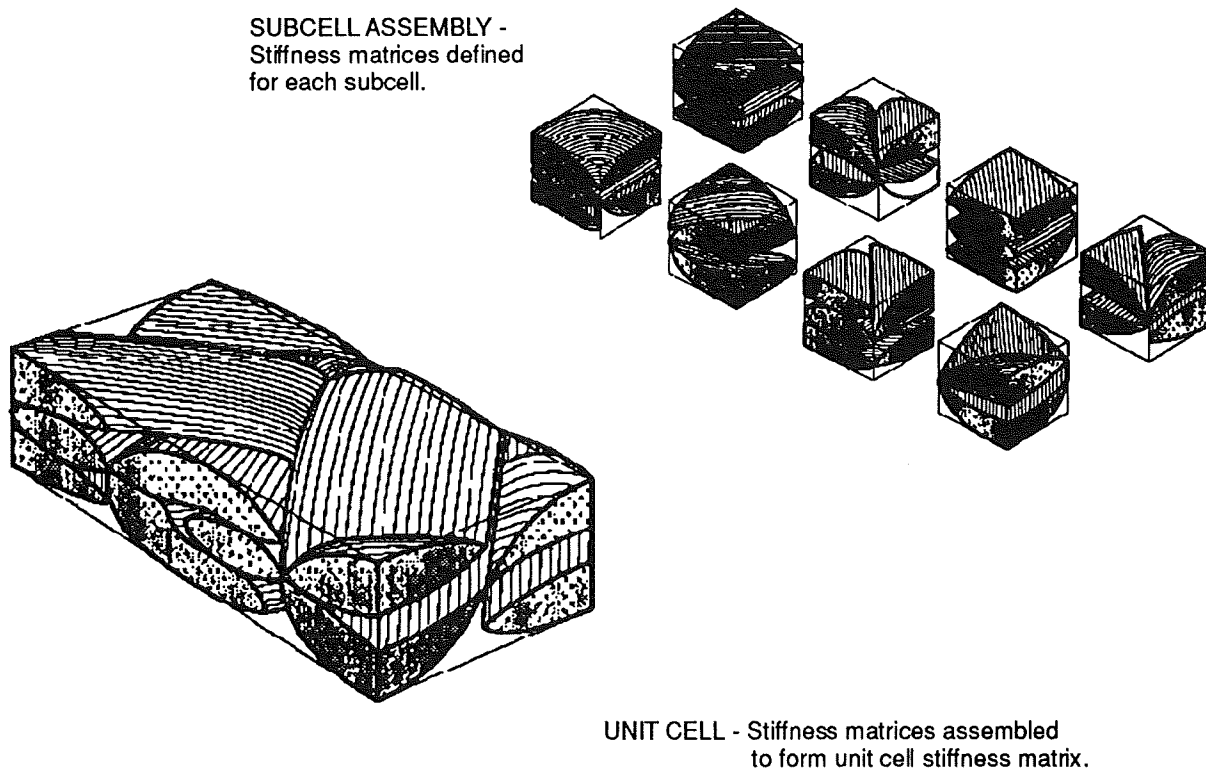


Figure 13. Schematic of Finite Element Approach.

ANALYTICAL CONCLUSIONS

In addition to tabulating the moduli and Poisson's ratios predicted by the various models, Table IX also lists the experimental results obtained using the 0.187 in. strain gages. A column of root mean square (RMS) error values is also included to provide a measure of the agreement of the experimental results to the values predicted by each analytical method.

The data indicate that all the analytical models gave consistent and accurate predictions for the Young's moduli of the three braids in the direction

of the longitudinal tows. The agreement of predicted and experimental transverse moduli values was, however, not as good. Although the RMS values ranged from 25 to 30%, inspection of the data indicates that this was due largely to the models' inability to match the modulus measured for the B1 material. Predicted and experimental results for both the A1 and the B2 materials were in much closer agreement. The reasons for this discrepancy are not fully understood.

Each of the models gave reasonable approximations to the ν_{yx} Poisson's ratio but not the ν_{xy} value. Large disagreements between experimental and measured values for the B1 material again account for most of the RMS error.

In general terms, increasing the rigor with which the model represented the fiber architecture improved the agreement of predicted and experimental results. The diagonal brick model gave a better correlation to the Young's moduli than the corrected or uncorrected laminate analysis. The finite element analysis provided the closest overall agreement although the improvement was not dramatic.

The finite element analysis was marginally better in the sense of minimizing root mean square error of correlation but required more skill in application than is usually available in preliminary design. The main advantage of the finite element model is its generality. It is equally applicable to a wide variety of weaves, braids, or knits.

There is a need for improved methods of analysis and a wider range of test data with regard to braid angles, percent of longitudinal material and fiber content.

SUMMARY REMARKS

Triaxial braid reinforced composites have the potential for improved impact resistance and lower fabrication costs. However, there are problems associated with their application. Their basic design properties have not been adequately characterized. Moreover, the data that is available raises questions regarding the material behavior, the use of standard composite test methods and procedures, and the ability to predict the elastic properties.

Textile reinforced composites must be analyzed and evaluated as a structure and not a material. The fiber architecture plays a more dominant role in these materials than in unidirectional tape materials. It is, therefore, most

important to define the fiber architecture in these composites to interpret experimental results and to form the basis of analytical models.

Table IX. Correlation of Braid Composite Properties

PROPERTY	MODEL	MATERIAL	MATERIAL	MATERIAL	RMS ERROR
		A 1	B 1	B 2	
E _x (MSI)	EXPERIMENT	6.62	6.55	6.31	-
	LAMINATE	6.98	7.22	6.68	7.5%
	LAM. CORR.	6.98	7.22	6.68	7.5%
	DIAG. BRICK	6.61	6.95	6.40	3.6%
	FINITE ELEM.	6.81	6.89	6.32	2.9%
E _y (MSI)	EXPERIMENT	6.59	6.45	7.03	-
	LAMINATE	7.93	9.49	7.97	30.1%
	LAM. CORR.	7.55	9.27	7.75	27.4%
	DIAG. BRICK	7.24	9.07	7.61	24.9%
	FINITE ELEM.	7.71	9.01	7.41	25.1%
V _{xy}	EXPERIMENT	0.300	0.268	0.183	-
	LAMINATE	0.276	0.166	0.181	22.5%
	LAM. CORR.	0.232	0.166	0.182	25.5%
	DIAG. BRICK	0.280	0.162	0.175	23.8%
	FINITE ELEM.	0.259	0.187	0.169	19.6%
V _{yx}	EXPERIMENT	0.307	0.199	0.190	-
	LAMINATE	0.314	0.218	0.216	9.7%
	LAM. CORR.	0.251	0.213	0.211	13.0%
	DIAG. BRICK	0.307	0.212	0.208	6.7%
	FINITE ELEM.	0.305	0.211	0.214	8.1%

Three different triaxial braids were investigated both analytically and experimentally. A process science model was used to create a three dimensional representation of the braid reinforcement. This representation was then used in conjunction with a finite element analysis to predict the materials' mechanical properties. In addition, the ability of a variety of simpler models to predict

performance was also studied. The experimental effort consisted of a series of unnotched tension tests which were run in the two principal directions of material orthotropy.

The process science model, used in conjunction with knowledge of the braid process employed to fabricate the preforms, successfully predicted the braid architecture and the significant braid parameters such as average braid angle, fiber content, unit cell dimensions, tow spacing, and longitudinal/braid yarn ratio.

The test data indicated that the Young's moduli in the 0° direction, the longitudinal direction, were stable (in the sense of varying gradually with small changes in microgeometry) and predictable by any of the common analysis methods. Tensile strength in the same direction was erratic and inexplicable. Young's modulus in the other principal direction, the transverse direction, was stable with reinforcement parameter changes but not predictable analytically. The correlation of predicted and experimental transverse modulus results was acceptable for two of the three materials studied. Strength in the transverse direction was somewhat consistent and intuitively acceptable. Poisson's ratio measurements were reasonable but failed to correlate closely with analysis in the case of contractions in the transverse direction.

The experimental results also indicate the need to carefully consider test methods and procedures in view of the unique aspects of these materials. Inhomogeneities may exist in the strain field due to the intertwining of the fibers. This places increased demand on the instrumentation. The accuracy of the strain readings, for example, is shown to be sensitive to the strain gage size. Results indicate large gage sections were preferable in the braids studied. The extensometer, with its one inch gage length, gave more consistent results than any of the smaller gages. The largest strain gages correlated best with the extensometer readings. In retrospect, significantly larger strain gage sizes and extensometer lengths seem more appropriate to this class of material.

The effects of the fiber architecture on the material response also necessitates an examination of the sizes of the specimens tested. If edge effects are on the order of the unit cell dimensions then 1.5 in. wide specimens may not be wide enough to represent the average material behavior.

The various different analysis models that were applied to the braid reinforced laminates correlated well with each other. The data indicates that the agreement between predicted and experimental values improved as the rigor in which the analyses modeled the fiber architecture increased. For example, incorporating the effect of the braided fiber crimp into the corrected

laminated plate theory improved the agreement between predicted and measured transverse moduli. The diagonal brick model with its more detailed representation yielded even better results. The finite element model yielded the best agreements although the improvements were not large in some cases.

REFERENCES

1. Pastore, C., Gowayed, Y., and Cai, Y. J., "Application of Computer Aided Geometric Modelling for Textile Structural Composites", CADCOMP '90: Computer Aided Design in Composite Material Technology, C. Brebbia, W. de Wilde, W. Blain, Eds., Computational Mechanics Publications, Southampton, U. K., 1990.
2. ASTM D 3171 - 76 (Revised 1990) Standard Test Method for Fiber Content of Resin-Matrix Composites by Matrix Digestion. 1991 Annual Book of ASTM Standards, Volume 15, pp. 123 - 125, American Society for Testing and Materials, Philadelphia, PA.
3. Gowayed, Y. A., "An Integrated Approach to the Prediction of Mechanical and Geometric Properties of Textile Reinforced Composites", Phd Thesis North Carolina State University, Feb 1992.
4. Ma, C-L, Yang, J-M, Chou, T-W, "Elastic Stiffness of Three-Dimensional Braided Textile Structure Composites," Composite Materials: Testing and Design (Seventh Conference), ASTM 893, J. M. Whitney, Ed., American Society for Testing and Materials, Philadelphia, PA, 1986, pp 404-421.
5. Foye, R. L., "The Mechanics of Fabric Reinforced Composites", Fiber-Tex 1988, Proceedings of a conference held in Greenville, SC, Sept 13- 15, 1988. Edited by J. D. Buckley, NASA Conference Publication 3038, 1989.

MECHANISMS OF COMPRESSIVE FAILURE IN WOVEN COMPOSITES
AND STITCHED LAMINATES

B.N. Cox, M.S. Dadkhah, R.V. Inman, W.L. Morris, and S. Schroeder
Rockwell International Science Center
1049 Camino Dos Rios
Thousand Oaks, CA

NASA

54-24

51372

P-14

ABSTRACT

Stitched laminates and angle interlock woven composites have been studied in uniaxial, in-plane, monotonic compression. Failure mechanisms have been found to depend strongly on both the reinforcement architecture and the degree of constraint imposed by the loading grips. Stitched laminates show higher compressive strength, but are brittle, possessing no load bearing capacity beyond the strain for peak load. Post-mortem inspection shows a localized shear band of buckled and broken fibers, which is evidently the product of an unstably propagating kink band. Similar shear bands are found in the woven composites if the constraint of lateral displacements is weak; but, under strong constraint, damage is not localized but distributed throughout the gauge section. While the woven composites tested are weaker than the stitched laminates, they continue to bear significant loads to compressive strains of ~ 15%, even when most damage is confined to a shear band.

1. INTRODUCTION

One of the principal weaknesses of conventional, two-dimensional (2D) polymer composites is their vulnerability to delamination, particularly under compressive loading following impact. This problem has led to the accelerated development of polymer composites reinforced by various three-dimensional (3D) arrangements of fibers, with the general goal of enhancing through-thickness strength without degrading in-plane strength or stiffness (refs. 1-4). All forms of 3D architectures are under study in this quest, including structures manufactured by weaving, stitching, knitting, and braiding; and there has been considerable success in eliminating the delamination problem. Unfortunately, this particular improvement has generally come at the expense of other material properties, such as fatigue resistance and strength.

While there is thus much room for improving 3D composites, there is not yet any understanding of how to set about this systematically. The challenge of choosing from the infinite variety of available reinforcement architectures is compounded by ignorance of how particular geometrical features in the arrangement of fibers might influence failure mechanisms.

This paper begins to address these questions by a comparison of stitched laminates and certain woven composites under monotonic compression. Striking differences are found in the strength and strains to failure for the two classes of material, stitched laminates exhibiting brittle behavior and woven composites ductile behavior. These observations are related to differences in the fiber architecture, suggesting some fundamental concepts for 3D composite behavior, which may guide the way to optimizing strength and damage tolerance and in mapping out failure modes.

2. SPECIMENS

2.1 Stitched Laminates

Stitched laminates were manufactured by Douglas Aircraft Co.† They consist of 48 plies of AS4 carbon fibers in the quasi-isotropic lay-up (+45°/0°/-45°/90°)_{6S}, stitched with carbon, glass, or Kevlar fibers. In fact, each ply is in itself a 2D woven fabric ("uniweave") in which the AS4 fibers have been woven in a plain weave with a small quantity of glass fibers to facilitate handling during stacking and stitching. The AS4 fiber tows serve as warp yarns in this weaving step and constitute 95 percent of the fabric by weight, while the glass fibers are incorporated as fill (weft yarns) and constitute the remainder. Some kinking of the AS4 fibers is inevitable during weaving, but it appears that neither the kinking nor the presence of the woven glass fibers has a strong influence on failure mechanisms (see below). In describing the stacking sequence of the laminate, the angle of each ply refers to the angle of the AS4 fibers.

Following stacking, the lay-up was stitched in rows along both the 0° and 90° directions, using modified lock stitching (Fig. 1). The bobbin threads, which are primarily responsible for 3D reinforcement, consist of one of three kinds of yarn, as listed in Table 1. While in all cases there are nominally 1.6 rows of stitches per cm. (4 per inch) in both the 0° and 90° directions, the number of stitches per cm. within each row varies with stitching direction and from specimen to specimen. Average, measured values are given in Table 1. Table 1 also shows the volume fractions of the stitching fibers (referring only to those segments of stitching tows lying in the through-thickness directions) estimated from these data and specific gravities. The final entry of Table 1 shows the volume fraction of 0° AS4 fibers estimated from micrographs of cross sections.

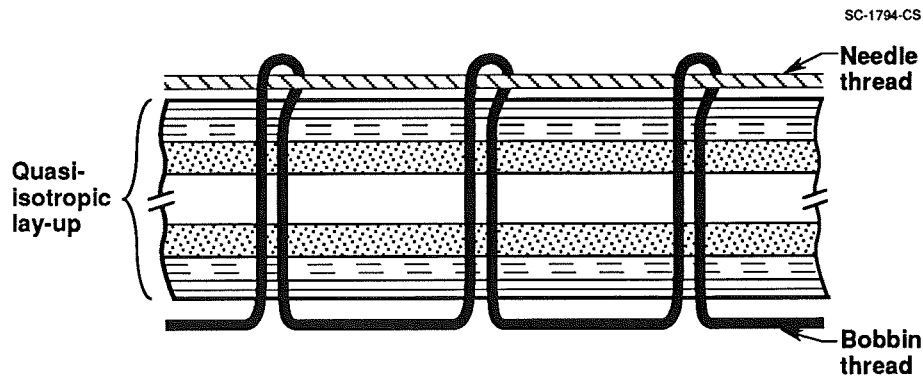


Fig. 1 Schematic of quasi-isotropic laminate reinforced by modified lock stitching.

The stitched preforms were impregnated with 3501-6 resin by resin transfer moulding and the resin was cured (ref. 5).

2.2 Woven Composites

All woven fiber preforms were supplied by Textile Technologies Inc.* They were either through-the-thickness or layer-to-layer angle interlock weaves, as illustrated in Fig. 2. All

†Douglas Aircraft Co., Long Beach, California.

*Textile Technologies, Inc., Hatboro, Pennsylvania.

stuffer (or straight warp) and filler (or weft) fiber tows were 21k denier* AS4 carbon yarns. Warp weaver (or 3D warp) fiber tows were either 9k denier AS4 carbon yarns or 5.95k denier S-2 glass yarns. The stuffers and fillers form a relatively coarse 0°/90° laminate, while the warp weaver tows follow approximately sawtooth paths, binding fillers and therefore stuffers together in the through-thickness direction. Figure 2 shows projections of the weave pattern along the weft direction.

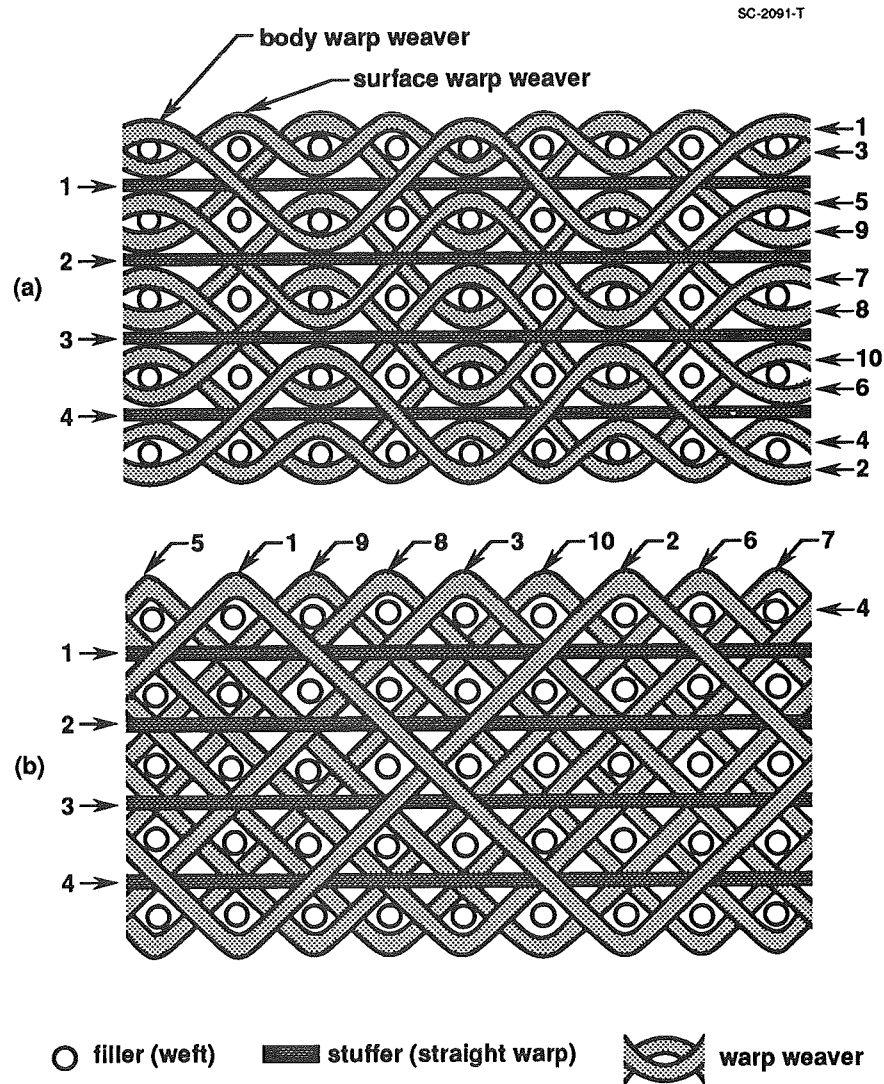


Fig. 2 Schematic of the projection of (a) layer-to-layer and (b) through-the-thickness angle interlock fiber preforms onto a plane normal to the weft tows.

The weaver's nominal specifications of the number of columns of fillers per cm. in the warp direction and the number of columns of stuffers (and therefore pairs or quartets of warp weavers) per cm. in the weft direction are given in Table 2, along with measured thicknesses of the dry preforms. Noting that the density of AS4 carbon is 1.8 g/cm³ and that of S-2 glass 2.48 g/cm³ (e.g. (ref. 6)), and approximating the length of each warp weaver per cm. in the warp direction as $\sqrt{2}$ cm., one can estimate the nominal volume fractions of the various fibers from these data. These results are also shown in Table 2. In the case of the layer-to-layer

*Denier measures the weight in grams of 9000 meters of yarn.

architecture, the volume fraction of warp weavers includes only the body warp weavers of Fig. 2(a).

In practice, considerable deviance from the nominal volume fractions is found in actual specimens, as detailed below. Furthermore, the surface warp weavers in specimens of type A were found not to be curved, as in the specification of Fig. 2(a), but straight. In assessing effects of the volume fraction of fibers aligned along the load axis, they were therefore added to the stuffers in estimating v_s , giving values on average 20% higher than those of Table 2 (see below).

Impregnation and cure of the woven preforms were carried out by the authors, using methods developed *ad hoc*. The matrix in all cases was formed from Tactix 138 resin and H41 hardener (Dow Chemical†). The preform was placed in a reusable aluminum mould, heated to 65°C, and degassed in a vacuum of ~ 1 Torr. The resin was then mixed with the hardener and also heated to 65°C and degassed. The resin and hardener were then poured over the preform (still at 65°C and under vacuum) and the whole assembly was degassed twice again. The first degassing typically resulted in bubbling out of some volatiles followed by apparent boiling of the resin-hardener mixture as the pressure fell further. The pressure was then cycled between 1 Torr and atmospheric pressure to remove small bubbles clinging to the mat. The mould was then closed and the specimen cured, the curing cycle (chosen to maximize resin toughness) comprising 2 hrs at 120°C and 2 hrs at 177°C. All fabrication runs produced 25 cm × 10 cm panels, from which specimens were machined.

There was no visible porosity in any specimen. Furthermore, the only microcracks to be found were confined to surface pockets of resin between tows. Detailed observations of failure mechanisms revealed that these initial surface microcracks have no role in compressive failure.

During impregnation and cure, a small pressure was applied through the thickness of the preform by screwing down the lid of the mould. This pressure was sufficient to ensure firm contact between the mould and the thicker parts of the preform, but not sufficient to maximize fiber packing density elsewhere. It was felt that attempting to do so would have led to fiber kinking where the preform was thickest, which would be likely to degrade compressive strength. If more uniform preforms become available in the future, significant enhancement of the fiber volume fractions should be feasible. It is likely that compressive strength would then also rise.

3. UNIAXIAL COMPRESSION TESTS

The first tests to be described were conducted on cuboidal specimens approximately 2.1 cm long and 1 cm wide, with the thickness being that of the panel. The length of each composite specimen was aligned with the warp direction for woven composites and the 0° ply direction for stitched laminates. The length also coincided with the load axis. Uniaxial compression tests for these specimens were conducted under displacement control in a 20 kip MTS test machine, with the ends of the specimen loaded by flat platens. There was no evidence of slip between the platens and the specimen ends, so that the stress state in the specimens was nonuniform, with deformation near the specimen ends being highly constrained. Results are summarized in Table 3. The epoxy specimens of Table 3 consisted of neat resin cured according to the cycle defined in the preceding section.

Some further tests were conducted for the woven composites using dog-bone specimens with gauge sections 2.4 cm long and 1.1 cm wide. Once again, the load axis and length of the

†Dow Chemical, Freeport, Texas.

dog-bone specimens coincided with the stuffers, while the direction normal to the flat faces of the specimens was that of the through-thickness reinforcement. Loading was effected by a 200 kip hydraulic machine with aligning hydraulic grips.

3.1 Strength and Strain to Failure

Cuboidal Specimen Test Results

Stress-strain curves for cuboidal specimens of stitched laminates and woven composites are shown in Fig. 3. The effective initial composite modulus, the maximum compressive load sustained, the strain ϵ_m at which it occurs, and the strain, $\epsilon_{1/2}$, at which the load had fallen to 50% of its maximum after peak load, are also presented numerically in Table 3.

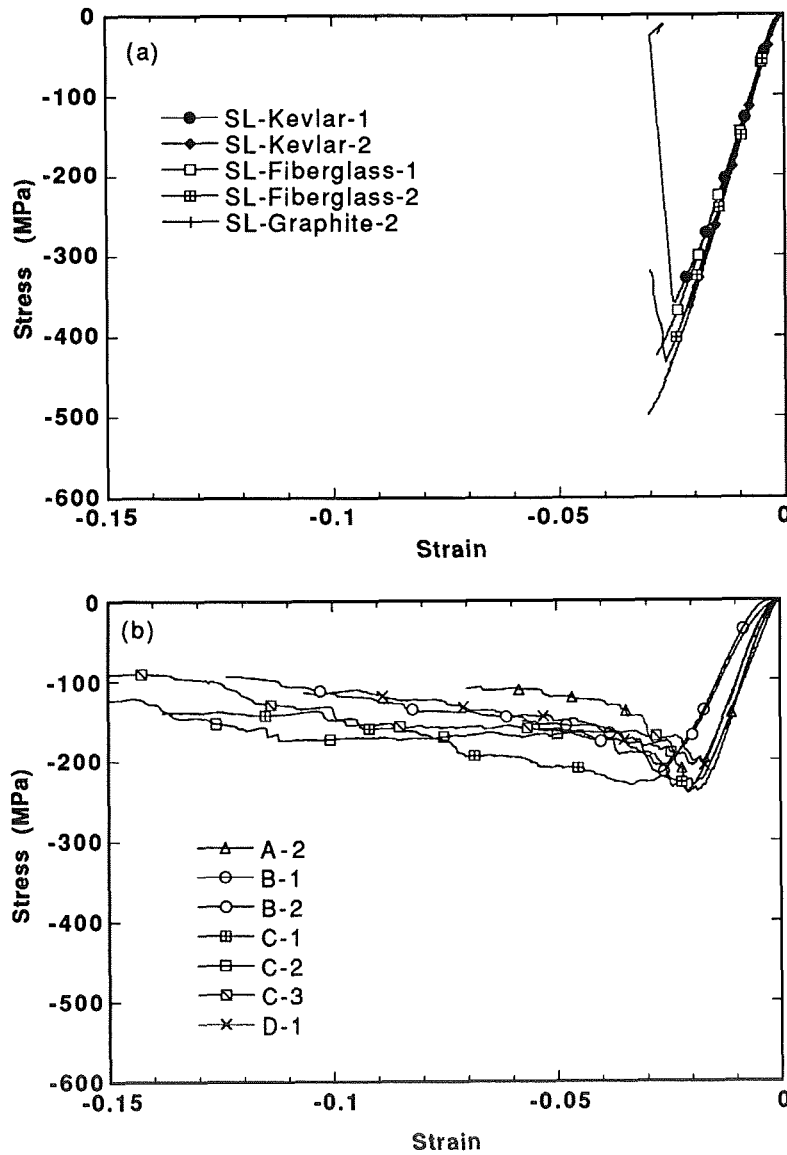
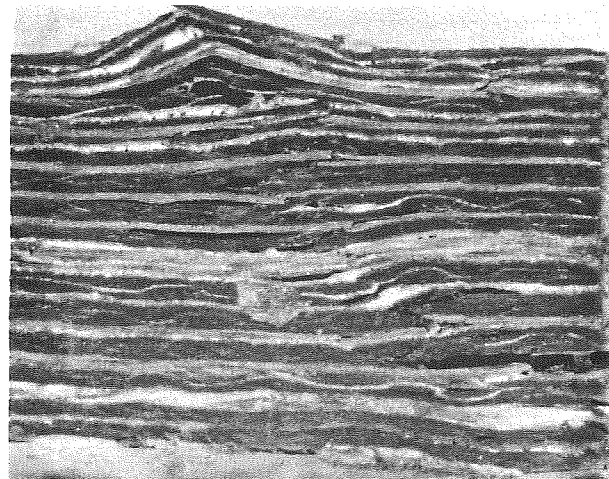
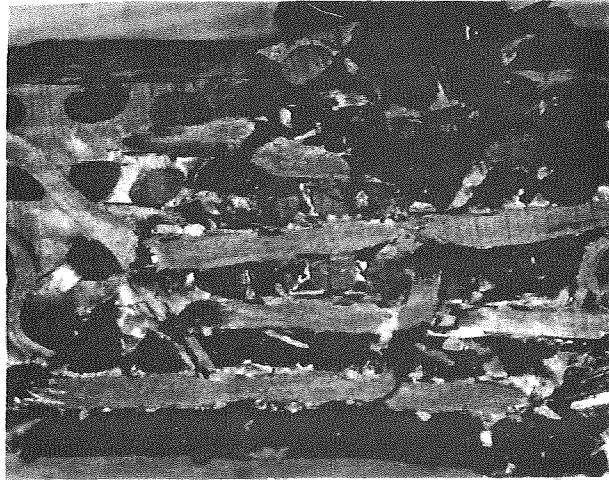


Fig. 3 Strain-load histories for cuboidal specimens under uniaxial compression. (a) Stitched laminates. (b) Woven composites. Legends refer to the nomenclature of Table 3.

For stitched laminates (Fig. 3(a)), the response is initially linear, the apparent non-linearity at very small loads merely reflecting slack space being taken up between the specimens and the platens. (All strains in Table 3 were adjusted to compensate for this effect by extrapolating back from the linear regime to redefine the origin.) There is a moderate decrease in modulus somewhat before failure, which occurs at compressive stresses between 360 and 495 MPa. There is essentially no load bearing capacity at higher strains, indicating that failure is catastrophic. Post-mortem examination reveals the damage typified by Fig. 4(a): damage is confined to a narrow shear band traversing the thickness of the specimen. Within this band, plies are buckled and failed and nearly all plies are delaminated from one another. The damage extends in the 0° ply direction over a distance comparable to the stitching spacing, but the stitches have played no obvious part in initiating or moderating failure.



1 mm



1 mm

Fig. 4 Damage in cuboidal specimens of (a) a stitched laminate (SL-Kevlar-1 of Table 3) and (b) a woven composite (through-the-thickness angle interlock - preform C of Table 1) following failure under uniaxial compression.

For woven composites, the response of the cuboidal specimens is entirely different (Fig. 3(b)). The maximum compressive load still occurs at similar compressive strain, but it is much lower in magnitude. There is substantially more nonlinearity in the stress-strain curve as the maximum load is approached. And, most striking of all, the material continues to bear more than 50% of the maximum load and substantially more than the neat resin out to compressive strains of 15% or more. Post-mortem examination reveals damage typified by Fig. 4(b): there is widespread debonding of warp weavers and stuffers from the surrounding matrix and stuffers have buckled and failed in many places. (Note that so-called debond cracks actually lie entirely within the matrix, rather than consisting even partly of interfacial microcracks between fibers and matrix.) There is no apparent correlation between the locations at which stuffers have failed in any specimen.

There is considerable variation in the strengths of the cuboidal specimens of the woven composites (Table 3). Some of this variation can be correlated with variations in the number of stuffers present in each specimen, as can be seen by comparison with the volume fractions of Table 3, which were estimated by counting stuffers and, for type A specimens, surface warp weavers in each specimen.

For the woven composites, the strain to maximum load, ϵ_m , is remarkably constant ($\pm 3\%$ variance), while there is a larger variation in strength ($\pm 20\%$) and a much larger variation in modulus ($\pm 40\%$). For the stitched laminates, in contrast, both ϵ_m and strength vary by $\pm 20\%$ and are correlated, while the modulus varies by only $\pm 8\%$.

Dog-bone Specimen Test Results

The dog-bone specimens were sufficiently large to allow the use of moiré interferometry to study the localized surface strains that accompany specimen failure. The moiré fringes of Fig. 5 show contours of constant displacement in the load direction for a type C specimen. Even though the strains are all elastic and reversible, since the load in Fig. 5 (80 MPa) is well below the composite yield strength, the influence of stuffers, fillers, and warp weavers is clearly visible. Significant local strain inhomogeneities result.

Figure 6 compares the axial strain from moiré fringes averaged over a 1 cm gauge length (to minimize the effect of inhomogeneity) with strains measured by clip gauges and by an alternative imaging technique. The alternative technique, described fully in (ref. 7), is based on comparing a digitized image taken under load to a reference image taken at zero load. The strains from all three methods are comparable.

Stress-strain histories measured for dog-bone specimens by clip-gauges are shown in Fig. 7 and numerical values of key features are summarized in Table 4. The strengths are smaller than those measured for cuboidal specimens, being comparable to the yield strength on the curves of Fig. 3. Figure 7 also shows a qualitative difference from Fig. 3, since, for all but type D specimens, there is a discontinuous drop in load after the maximum load. As for the cuboidal specimen tests, Table 4 shows remarkable constancy in strain to maximum load.

In all the tests of Table 4, post-mortem inspection of the specimens revealed that final failure was associated with a dominant shear band. This shear band was not as localized as the kink bands observed in cuboidal specimens of stitched laminates; and there was often extensive, ancillary damage visible elsewhere on the gauge section. However, the damage was far more localized than that in cuboidal specimens of woven composites, which always showed damage post mortem over the whole gauge section.

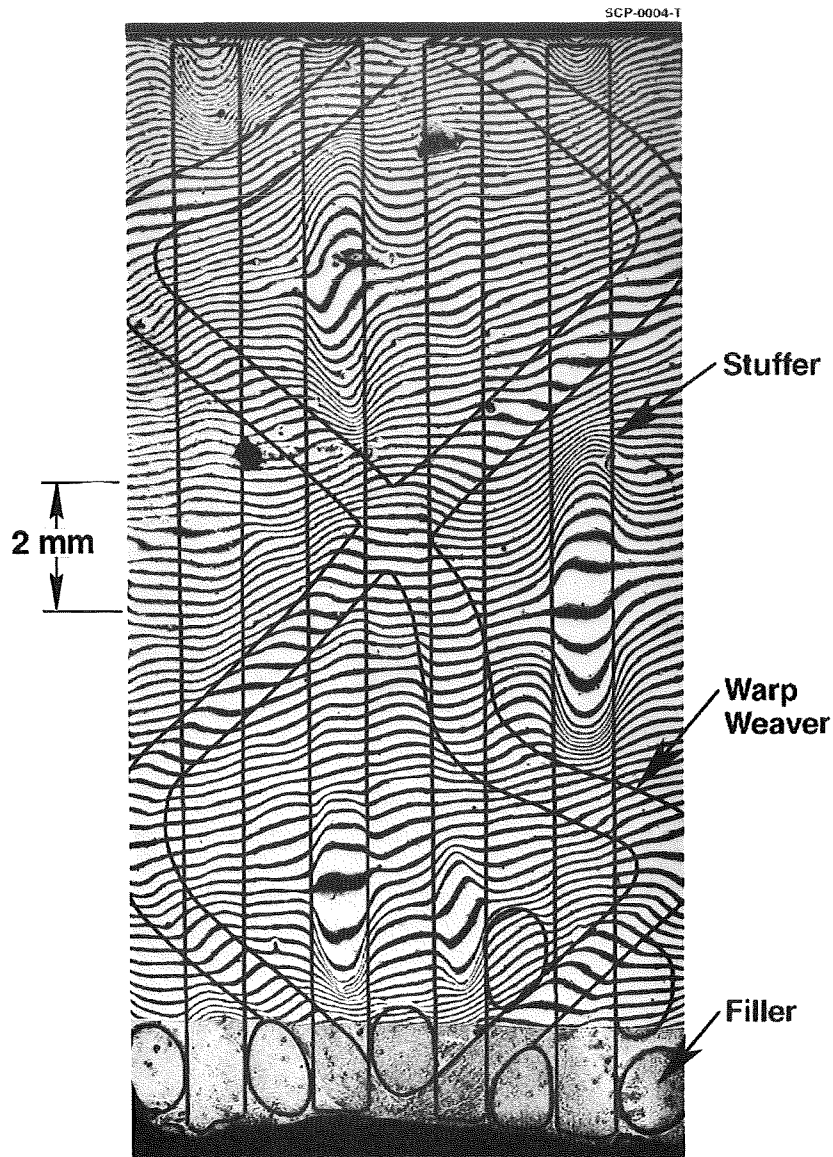


Fig. 5 Contours of constant displacement in the load direction measured by moiré interferometry. Stuffers, warp weavers, and some fillers have been outlined to emphasize their role in determining local strain variations.

3.2 Observations of Microscopic Cracking and Deformation

The digital imaging method was also used to assess local damage before and after the attainment of peak load (and the discontinuous load drop) in type A and C specimens. Observations prior to peak load were consistent with the moiré fringes of Fig. 5. Making measurements after the load drop is not straightforward, because there are many cracks and pieces of the composite move almost independently of one another. Nevertheless, it appears that the first initial deformation is associated with relatively long-ranged buckling of stuffers allowed by extensive systems of cracks aligned parallel to them. This produces a transverse swelling or barrelling of the composite. The buckling of neighboring stuffers shows some correlation, especially for type A specimens (layer-to-layer angle interlock). However, the development of a major shear band of the kind found to dominate the damage post-mortem did not occur until well beyond ϵ_m : at 2% strain for type C specimens and 4% strain for type A. Thus the discontinuous load drop is evidently associated not with a kink band but with the buckling failure of individual stuffers.

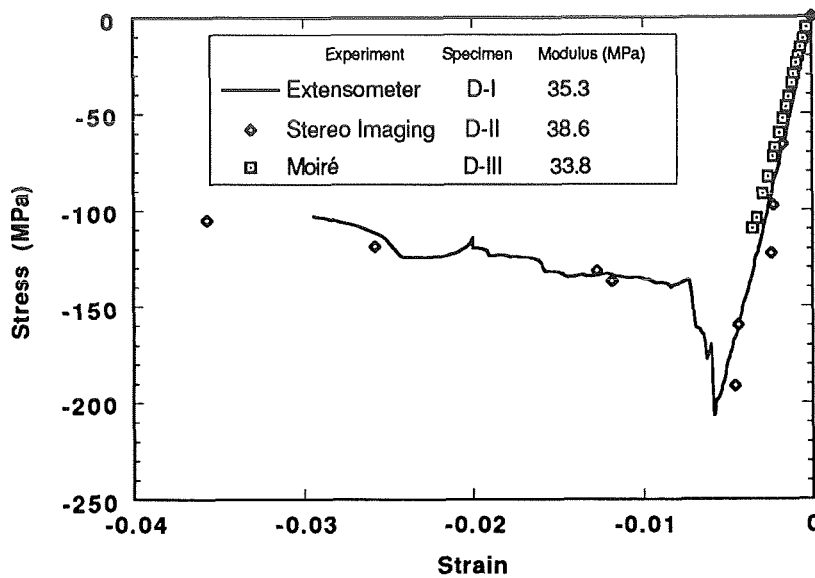


Fig. 6 Strain-load histories for dog-bone specimens of type D woven composites under uniaxial compression measured by several methods.

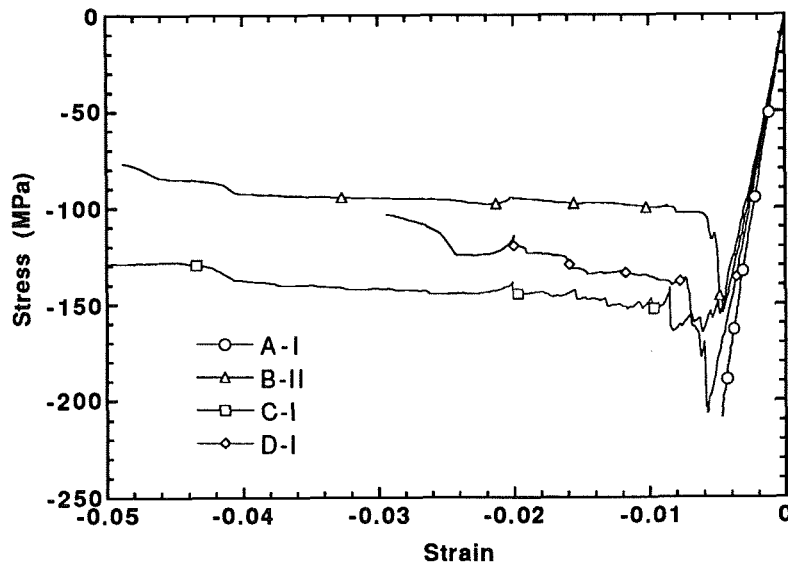


Fig. 7 Stress vs strain for dog-bone specimens.

4. CONCEPTS IN STRENGTH AND DAMAGE TOLERANCE

Comparison of cuboidal specimens of stitched laminates and woven composites under monotonic compression has shown that the former have about twice the strength while the latter have the greater strain to failure by an order of magnitude. Further tests on dog-bone specimens show that in fact woven composites may also exhibit discontinuous load drops, as observed for the stitched laminates, when there is less constraint imposed by the loading grips. But they always retain large strains to total failure. In this section, some mechanistic arguments will be presented to try to account for these observations at least qualitatively. The arguments lead to the interesting prospect of achieving an optimal compromise between strength and damage tolerance by appropriate choice of reinforcement architecture.

4.1 The Role of Fiber Volume Fraction

Consider first the observed relationship between strength and the volume fraction, v_s , of fibers aligned along the stress axis (Tables 1 and 2). Generally speaking, both the modulus and the compressive strength would be expected to increase as v_s increases. Yet $v_s \approx 0.16$ for the stitched laminates (Table 1), which is less than the values for the woven composites (Table 2), while the stitched laminates are far stiffer and stronger. Much of this difference may be attributable to the degree of straightness of the primary load bearing fibers: the coarser fiber architecture of the woven composites probably leads to greater initial curvature of the stuffers than exists in the 0° fibers in the stitched laminates. Further research in which stuffer alignment is controlled more carefully during impregnation and cure is required to quantify this effect.

While fiber volume fraction does not account for the differences between stitched laminates and woven composites, variations of strength within the latter class are correlated with fiber volume fraction, as evidenced by Tables 3 and 4.

4.2 Damage Propagation - The Stability of Kink Bands

The events that follow the buckling and failure of the first stuffer in a woven composite or the first bundle of 0° fibers in a stitched laminate depend on whether neighboring aligned fibers are loaded beyond their failure limit and the degree to which shear displacements are constrained. If the first buckling and failure have occurred at an unusually low stress, neighboring aligned fibers will be less likely to be critically loaded even under the effects of load redistribution; and if shear displacements are constrained, that too will help preserve neighboring fibers by minimizing the stress concentration around the first failure.

In stitched laminates, the first buckling and failure always led in the tests reported here to immediate failure by an unstable kink band. In these materials, the first buckling and failure do not occur at an unusually low stress; the 0° tows are relatively straight and closely packed amongst other plies and the stitching tows are orthogonal to the load axis and do not appear to lower the load at which buckling and failure of 0° fibers occur. Thus the compressive strength is relatively high and, when one bundle of 0° fibers eventually does buckle, the concomitant stress concentration acting on neighboring fibers is sufficient to cause their immediate buckling too, because the applied load is already close to their failure load. Thus a kink band forms and propagates unstably across the whole specimen even for tests of cuboidal specimens, where constraint of the shear displacement required for the kink band to propagate is greatest; the stress-strain history is characteristic of a brittle material. Kink band failure is very common in aligned continuous fibers under compression (see, for example, ref. 8).

In the angle interlock specimens, on the other hand, the relative coarseness of the structure, the presence of thick warp weavers, and the initial curvature of the stuffers all facilitate early buckling failures. The moiré fringes of Fig. 5 clearly show segments of stuffers buckling out of the specimen even in the elastic regime. Such inhomogeneity also implies that, when the first buckling failures of stuffers occur, they will do so at sites uncorrelated with other weak areas - cp. the distribution of early buckling sites in Fig. 5. Furthermore, since the first buckling failures occur at relatively low stresses and stuffers are relatively well separated in the woven structures, adjacent stuffers are not generally loaded above their failure stress in the stress concentration around a failure site. Thus the formation of the eventually fatal shear band is deferred to higher strains.

As for the load, it falls following the first stuffer failures simply because the specimen compliance rises when the volume fraction of intact stuffers is reduced. The stress-strain history is that of a ductile material.

4.3 Possible Design Paths for Future Woven Composites

The overall picture is thus one of compromising strength and strain to failure (or damage tolerance). The open, coarser structure of the woven composites may be considered as containing intrinsic flaws, consisting of fluctuations in geometry that lead to local failure sites. The flaws lead to lower strength, but they tend to cause damage to be spatially distributed, in which case failure is not by the catastrophic mechanism of an unstably propagating kink band, but by the attainment of a critical density of broadly distributed damage.

Since the potency of the flaws is proportional to their size, it can be predicted that, as the scale of the woven architecture becomes finer and finer, e.g. by reducing the denier of all tows, the strength should rise to the limit of that of the stitched laminates while the material should become increasingly brittle. The reduction in the scale of the reinforcement may be thought of as producing a more homogeneous composite populated by flaws of decreasing size.

CONCLUSIONS

Strength and strain to failure under uniaxial compression are strongly influenced by the geometry of the fiber reinforcement in 3D composites and the degree to which lateral displacements are constrained in tests. An open, coarse structure lowers strength but promotes high strain to failure or damage tolerance. In the angle interlock weaves studied, reinforcement inhomogeneity led to early buckling and failure of stuffers. This favored a wide spatial distribution of damage, in contrast to the localized kink bands that always cause failure in stitched laminates. If damage is delocalized, high strain to failure is assured.

ACKNOWLEDGMENTS

Work funded by NASA Langley Research Center under contract number NAS1-18840. The authors are deeply indebted to Dr. David Marshall for many fruitful conversations.

REFERENCES

1. M.B. Dow and D.L. Smith, "Damage Tolerant Composite Materials Produced by Stitching Carbon Fabrics," Int. SAMPE Tech. Conf. Series 21, 595-605 (1989).
2. R.E. Horton and J.E. McCarty, "Damage Tolerance of Composites," in Engineered Materials Handbook, Vol. 1, "Composites," ed. C.A. Dostal, ASM Int., Metals Park, Ohio, 1987.
3. P.J. Smith and R.D. Wilson, "Damage Tolerant Composite Wing Panels for Transport Aircraft," Boeing Commercial Airplane Company, NASA Contractor Report 3951.
4. R. Palmer, M.B. Dow, and D.L. Smith, "Development of Stitching Reinforcement for Transport Wing Panels," in Proc. First NASA Advanced Composites Technology Conference, NASA Conf. Publ. 3104, pp. 621-46.
5. R. Palmer and F. Curzio, "Cost Effective Composites Using Multi-Needle Stitching and RTM/VIM," in Fiber-Tex 1988 Conference, Greenville, South Carolina, September 13-15, 1988. NASA CP-3038, June 1989.
6. M. Piggott, "Load Bearing Fiber Composites," Pergamon, Oxford, 1980.
7. M.R. James, W.L. Morris, and B.N. Cox, "A High Accuracy Automated Strain Field Mapper," Exptl. Mech. 30, 60-67 (1990).
8. N. Fleck and B. Budiansky, "Compressive Failure of Fiber Composites," J. Mech. Phys. Solids, in press.

Table 1
Characteristics of the Stitched Laminates

Material Label	Stitching Tows	Density (g/cm ³)	0° stitches per cm (inch)	90° stitches per cm (inch)	Volume fraction of stitches	v_s (a)
SL-Kevlar	1.5k denier Kevlar-29	1.45	12.7 (5.0)	9.2 (6.0)	0.016	0.16
SL-Fiberglass	3.57k denier S-2 glass	2.48	23 (9.0)	23 (9.0)	0.036	0.16
SL-Graphite	1.44k denier Toray-900 graphite	1.8	20 (8.0)	23 (9.0)	0.019	0.16

(a) Volume fraction of 0° AS4 fibers.

Table 2
Architectures, Materials, and Fiber Densities
in TTI Angle Interlock Preforms

Preform Label	Architecture	Warp Weaver Material	Ends per cm (inch) ^(a)	Picks per cm (inch) ^(b)	Specimen Thickness (cm) ^(c)	v_s (d)	v_f (e)	v_w (f)
A	layer-to layer	AS4	5.1 (13)	4.4 (11.3)	1.26	0.210	0.229	0.064
B	layer-to layer	S-2 glass	5.1 (13)	5.9 (15)	1.24	0.214	0.308	0.031
C	through-the thickness	AS4	4.7 (12)	5.0 (12.7)	1.02	0.240	0.317	0.073
D	through-the thickness	S-2 glass	5.1 (13)	5.0 (12.7)	0.97	0.273	0.334	0.040

- (a) i.e., number of columns of stuffers per inch in weft direction.
 (b) i.e., number of columns of fillers per inch in warp direction.
 (c) in direction normal to warp and weft directions.
 (d) v_s \equiv volume fraction of stuffer (straight warp) tows.
 (e) v_f \equiv volume fraction of filler (weft) tows.
 (f) v_w \equiv volume fraction of body warp weaver (3D warp) tows.

Table 3
Data for Cuboidal Test Specimens

	Specimen Label	Modulus (GPa)	Maximum Compressive Stress (Msa)	$\epsilon_m^{(b)}$		
				$\nu_s^{(b)}$	$\epsilon_m^{(c)}$	$\epsilon_{1/2}^{(d)}$
Woven Composites ^(a)	A-1	14	230	0.28	0.019	0.07
	B-1	11.5	215	0.23	0.020	0.10
	B-2	11	205	0.20	0.020	0.12
	C-1	17	240	0.33	0.020	0.16
	C-2	15	205	0.27	0.020	0.15
	C-3	16	200	0.25	0.019	0.16
	D-1	14.5	240	0.27	0.019	0.1
Tactix 138 epoxy	e-1	2.55	105		0.079	-(e)
	e-2	2.75	115		0.080	-(e)
Stitched Laminates	SL-Kevlar-1	18	360		0.025	-(f)
	SL-Kevlar-2	19.5	380		0.022	-(f)
	SL-Fiberglass-1	17	425		0.028	-(f)
	SL-Fiberglass-2	18.5	430		0.026	-(f)
	SL-Graphite-1	19.5	495		0.03	-(f)

- (a) The letter in labels for woven composites refers to preform label of Table 2.
- (b) Including straight surface warp weavers.
- (c) Compressive strain at maximum load.
- (d) Compressive strain when post-peak load has fallen to half the maximum.
- (e) Test finished with load still exceeding half maximum.
- (f) Essentially identical to ϵ_m .

Table 4
Data for Dog-Bone Test Specimens

Specimen Label	Controlled Parameter	Maximum Compressive Stress (MPa)	Modulus (GPa)	$\epsilon_m^{(b)}$		
				0.5"	0.12"	0.5"
A-I ^(a)	strain	210	41.37	5×10^{-3}		
A-II	load	210	28		1.7×10^{-2}	
B-I	load	140	25	6×10^{-3}		
B-II	strain	155	34.75	5×10^{-3}		5×10^{-2}
B-III	strain	160				
C-I	strain	165	32.4	5.1×10^{-3}		1.4×10^{-1}
C-II	load	150			8.5×10^{-3}	
D-I	strain	205	35.5	6×10^{-3}		3×10^{-2}
D-II	strain	195	38.6	5×10^{-3}		4×10^{-2}

- (a) The letter in the labels refers to the preform labels of Table 2.
- (b) Compressive strain at maximum load.
- (c) Compressive strain when post-peak load has fallen to half of maximum.

EFFECT OF THE FIBER-MATRIX INTERPHASE ON THE
TRANSVERSE TENSILE STRENGTH OF THE UNIDIRECTIONAL
COMPOSITE MATERIAL

H. C. Tsai and A. M. Arocho
Naval Air Development Center
Warminster, PA

55-24
51373

P-17

ABSTRACT

A simple one-dimensional fiber-matrix interphase model has been developed and analytical results obtained correlated well with available experimental data. It was found that by including the interphase between the fiber and matrix in the model, much better local stress results were obtained than with the model without the interphase. A more sophisticated two-dimensional micromechanical model, which includes the interphase properties was also developed. Both one-dimensional and two-dimensional models were used to study the effect of the interphase properties on the local stresses at the fiber, interphase and matrix. From this study, it was found that interphase modulus and thickness have significant influence on the transverse tensile strength and mode of failure in fiber reinforced composites.

INTRODUCTION

Unidirectional fiber reinforced composites have a very low transverse tensile strength. This strength, in general, is much lower than the strength of the pure matrix and limits the performance of the composite system. The transverse tensile strength of a composite is dependent upon the fiber-matrix interfacial bonding strength, matrix strength, transverse fiber strength and stiffness ratio between fiber and matrix, etc. Material defects such as voids in the matrix, broken fibers, microcracks and fiber-matrix disbonds will degrade the transverse tensile strength of composite materials. Conventional analysis methods (Refs. 1-3), which treat the fiber and matrix as two phase, homogeneous and isotropic materials, provide ways to predict the transverse tensile strength of the composite, but the correlation between these analytical results and test results is not satisfactory.

Recently, several researchers (Refs. 4, 5) have suggested that the volume of matrix material immediately surrounding the fiber is significantly different from the bulk matrix. This volume of material is commonly referred to as the interphase. It is believed that the interphase, though small in thickness, has significant effect on the strength and fracture toughness of the composite. To verify this concept, these authors (Ref. 6) have developed micromechanical models which treat the fiber reinforced composite as a three-phase material; namely, fiber, interphase and bulk matrix. Through the analysis of the microdebonding problem, it has been shown that the model including an interphase between fiber and matrix provides a much better prediction of debonding loads than the model without the interphase.

The purpose of this study is to determine the effect of the fiber-matrix interphase on the transverse tensile strength of the composite. Since the transverse tensile strength is very low, there is a potential for engineering material improvements based upon a better understanding of the transverse failure mechanics, so that higher composite transverse tensile strength can be obtained.

In the following discussions, composites without material defects are considered.

METHOD OF ANALYSIS

The composite material is assumed to consist of a square array of unidirectionally elastic circular filaments in an infinite elastic matrix as shown in Figure 1. This simple packing geometry has been known to give satisfactory results (Ref. 7). The filaments are assumed to be perfectly bonded to the matrix. By assuming a square packing arrangement, a repeating unit can be isolated, as indicated by the solid lines a-a-a-a shown in figure 1. For a composite subjected to a remotely applied average tensile stress in the x direction, σ_T , the conditions of symmetry require that boundary lines of this repeating unit in the deformed composite remain parallel to the corresponding lines of the undeformed material, i.e., as shown in Figure 1, line a'-a' is parallel to the corresponding boundary line a-a. This implies that the gross strains over the length 2L in directions x and z remain constant.

$$\frac{1}{2L} \int_{-L}^L \epsilon_x dx = \epsilon_T = \text{constant (at any } z) \quad (1)$$

$$\frac{1}{2L} \int_{-L}^L \epsilon_z dz = \epsilon_z = \text{constant (at any } x) \quad (2)$$

Also, at any section across the element 2L the conditions of force equilibrium require that

$$\sigma_T = \frac{1}{2L} \int_{-L}^L \sigma_x dz \quad (3)$$

$$0 = \frac{1}{2L} \int_{-L}^L \sigma_z dx \quad (4)$$

Having established the assumptions of square packing, gross strain and stress conditions, the physical problem can be formulated as follows:

ONE-DIMENSIONAL PREDICTION METHODOLOGY

The repeating unit to be modeled which includes the interphase is shown in Figure 2. The basic concept for the one-dimensional model is shown in Figure 3. The material response to the external transverse tensile stress, σ_T , can be approximated by the response of a one-dimensional series spring system.

In the region consisting of fiber, interphase and matrix, there will be three distinct stiffnesses corresponding to each constituent. In the region consisting of interphase and matrix, there will be two distinct stiffnesses corresponding to interphase and matrix. At the region $Z \geq R + t_i$, there will be only one stiffness, namely, stiffness of matrix. From the basic concept, we can conclude that

$$\begin{aligned} \sigma_f = \sigma_i = \sigma_m = \sigma_L & \quad 0 \leq Z \leq R \\ \sigma_m = \sigma_i = \sigma_L & \quad R \leq Z \leq R + t_i \end{aligned} \tag{5}$$

where $\sigma_f, \sigma_i, \sigma_m$ = stress in the fiber, interphase and matrix respectively

σ_L = local stress

Based on this concept, the local stress at three regions can be derived as follows:

(1) $0 \leq Z \leq R$

This region includes three phases; namely, fiber, matrix and interphase. The total displacement, as shown in figures 2 and 3, at $x = L$, can be written as

$$U = \epsilon_f \cdot \overline{AB} + \epsilon_i \cdot \overline{BC} + \epsilon_m \cdot \overline{CD} \tag{6}$$

where

ϵ_f = strain in the fiber

ϵ_i = strain in the interphase

ϵ_m = strain in the matrix

Divide both sides of equation (6) by L. We have

$$\epsilon_T = \epsilon_f k_f + \epsilon_i k_i + \epsilon_m (1 - k_f - k_i) \tag{7}$$

From Reference 8, we have

$$\begin{aligned} k_f &= \left(\frac{4V_f}{\pi} \right)^{\frac{1}{2}} \left\{ 1 - \left(\frac{Z}{R} \right)^2 \right\}^{\frac{1}{2}} \\ k_i &= \left(\frac{4V_f}{\pi} \right)^{\frac{1}{2}} \left\{ \left[\left(1 + \frac{t_i}{R} \right)^2 - \left(\frac{Z}{R} \right)^2 \right]^{\frac{1}{2}} - \left[1 - \left(\frac{Z}{R} \right)^2 \right]^{\frac{1}{2}} \right\} \end{aligned}$$

$$k_m = 1 - k_f - k_i$$

$$V_f = \text{volume fraction of the fiber} \quad (8)$$

From the stress-strain relationship, we have

$$\epsilon_f = \frac{\sigma_f}{E_f}$$

$$\epsilon_i = \frac{\sigma_i}{E_i} \quad (9)$$

$$\epsilon_m = \frac{\sigma_m}{E_m}$$

Substituting equation (9) into (7) and making use of equation (5), the local stress, σ_L , in this region can be expressed as follows

$$\sigma_L = \epsilon_T \frac{1}{\frac{k_f}{E_f} + \frac{k_i}{E_i} + \frac{(1 - k_f - k_i)}{E_m}} \quad (10)$$

$$(2) \quad R \leq Z \leq R + t_i$$

This region includes matrix and interphase. The total displacement, as shown in figure 2, contributed from these constituents can be written as follows:

$$U = \epsilon_i \cdot \overline{EF} + \epsilon_m \cdot \overline{FG} \quad (11)$$

Divide both sides of equation (11) by L, we have

$$\epsilon_T = \epsilon_i k_i + \epsilon_m (1 - k_i) \quad (12)$$

where

$$k_i = \left(\frac{4V_f}{\pi} \right)^{\frac{1}{2}} \left\{ \left(1 + \frac{t_i}{R} \right)^2 - \left(\frac{Z}{R} \right)^2 \right\}^{\frac{1}{2}} \quad (13)$$

By this same token, the local stress, σ_L , in this region can be written as follows

$$\sigma_L = \epsilon_T \frac{1}{\left\{ \frac{k_i}{E_i} + \frac{(1 - k_i)}{E_m} \right\}} \quad (14)$$

$$(3) \quad R + t_i \leq Z \leq l$$

This region consists of matrix material only. By the same token, the local stress, σ_L , in the region can be expressed as

$$\sigma_L = \epsilon_T \left(\frac{1}{E_m} \right) \quad (15)$$

If ϵ_T is known, then the local stress, σ_L , can be obtained from equations (10), (14) and (15) for the corresponding region.

In the case where only the applied transverse tensile stress, σ_T , is known, then equation (3) will be used to obtain the local stress.

From reference 8, the local stress, σ_L , can be expressed as follows:

$$\sigma_L = \sigma_T \left(\frac{E_m}{E_T} \right) \frac{1}{[1 - k_f (1 - E_m/E_f) - k_i (1 - E_m/E_i)]} \quad 0 \leq Z \leq R \quad (16)$$

$$\sigma_L = \sigma_T \left(\frac{E_m}{E_T} \right) \frac{1}{[1 - k_i (1 - E_m/E_i)]} \quad R \leq Z \leq R + t_i \quad (17)$$

$$\sigma_L = \sigma_T \left(\frac{E_m}{E_T} \right) \quad R + t_i \leq Z \leq L \quad (18)$$

where

$$\frac{E_T}{E_m} = \frac{1}{L} \left\{ \int_0^R \frac{dz}{[1 - k_i (1 - E_m/E_i) - k_f (1 - E_m/E_f)]} + \int_R^{R+t_i} \frac{dz}{[1 - (1 - E_m/E_i) k_i]} + L - (R + t_i) \right\} \quad (19)$$

Equation (19) can be solved through numerical integration

Define

$$\text{S.C.F.} = \text{stress concentration factor} = \frac{\sigma_L}{\sigma_T} \quad (20)$$

Making use of equations (16) through (20), we can obtain S.C.F. at any location in the composite material.

TWO DIMENSIONAL MODEL

The basic concept, which was originated from reference 2, will be adopted in this paper as shown in Figure 4. The solution procedure can be divided into two parts. One is to solve the two-dimensional plane strain problem with $U = \Delta U$ at $x = \pm L$, and $V = 0$, at $Z = \pm L$; the other is to solve the two-dimensional plane strain problem with $V = \Delta V$ at $Z = \pm L$, $U = 0.0$ at $x = \pm L$. The final solution will be the linear combination of these two solutions so that equations (3) and (4) will be met. The detailed derivation is in Reference 8.

Only one quadrant of the circular fiber cross section and the surrounding interphase and matrix material needs be analyzed due to symmetry. The finite element model used in this study is shown in Figure 5. The mesh refinement at the fiber-matrix interfacial region is evident. The 'ABAQUS' computer code was used to solve this two-dimensional plane strain problem.

VALIDATION OF ANALYTICAL METHODS

In this analysis, it is assumed that an individual point failure immediately causes failure of the whole material. We recognize that, depending upon the failure locations and the properties of the constituents, this assumption may not be true. Yet the presence of an individual point failure suggests failure of the whole material and provides a conservative prediction. A maximum normal stress failure criterion will be used to determine the failure of the individual point in the material. According to this criterion, fracture is assumed to have occurred if any one of the three principal stresses at this individual point reach the ultimate strength of the corresponding constituent.

VALIDATION OF ONE-DIMENSIONAL MODEL

The comparison between the theoretical and experimental transverse stress distribution is shown in Figure 6. The test-theory correlation for the maximum stress concentration is shown in Figure 7.

The test data (Ref. 1) were obtained from transverse tensile loading tests on plates containing aluminum inclusions imbedded in epoxy resin. As shown in figure 6, both one-dimensional theories, with and without interphase, provide accurate predictions as compared with test data. The model including interphase predicts better results than the model without interphase. Matching analytical results to test data requires that the interphase modulus be seven times smaller than matrix modulus and the interphase thickness be about 1.5 percent of the radius of the fiber.

Figure 7 shows the maximum transverse tensile stress, which occurs at $Z = 0.0$ as a function of the volume fraction of the fiber. Both one-dimensional theories provide very good predictions. The interphase modulus and thickness are assumed the same for all fiber volume fractions. As shown in Figure 7, the inclusion of the interphase in the model does not seem to provide better results than the model without interphase for $V_F = 0.65$. This is

because as V_f increases the plane strain condition becomes more evident. The one-dimensional model does not include the effect of the plane strain condition. In the next section, it can be seen that the two-dimensional model including the interphase provides much better results than the two-dimensional model without interphase.

Another example to verify the accuracy of the one-dimensional theory is shown in Figure 8. The test data were obtained from Reference 9. The correlation between analytical results and test results is reasonably good. Since most test data is above the curve with $E_m/E_i = 1.0$, this may suggest that the interphase is a soft interphase.

VALIDATION OF TWO-DIMENSIONAL MODEL

The same composite as shown in Figures 6 and 7 is modelled, with the same interphase modulus and thickness as used in the one-dimensional model. The comparison between the theoretical and experimental transverse stress distribution is shown in Figures 9 and 10. The test-theory correlation for the maximum transverse stress is shown in Figure 11. Again, as shown in figures 9 and 10, both two-dimensional models predict good results as compared with the test data. The two-dimensional model with interphase predicts better results than the model without interphase. Figure 11 shows the merit of the two-dimensional model. By using the same interphase modulus and thickness as used in the one-dimensional model, the two-dimensional model with interphase predicts the best results among all models.

COMPARISON OF ONE-DIMENSIONAL AND TWO-DIMENSIONAL RESULTS

Table I shows the stress concentration factor of the composite, with $E_f/E_m = 21.3$, $V_f = 0.65$, $t_i/R = .015$. The agreement between the one-dimensional model and two-dimensional model is excellent.

From the above comparisons, we conclude that the one-dimensional model is accurate enough to be used to predict the local stress of the composite under transverse loading. Also, the one-dimensional model can be used as a first approximation to estimate the interphase modulus and thickness. By using an iteration scheme and two-dimensional analysis, accurate interphase modulus and thickness estimates of the composite can be obtained.

APPLICATIONS

The one-dimensional model has been verified in the previous section as an adequate model to predict the local stress of the composite. Unless otherwise noted, the following analyses are based on one-dimensional theory.

Effect of Interphase Moduli and Thickness on Stress Concentration Factors of the Composite

Equation (16) was used to calculate the stress concentration factor at $Z = 0$, for various E_m/E_i and t_i/R . Figures 12 and 13 show the results.

Certain conclusions can be drawn: (1) with fixed t_i/R the softer the interphase, the lower the stress concentration factor, (2) with softer interphase and E_m/E_i fixed, the larger the interphase thickness the lower the stress concentration factor. For stiffer interphase (i.e., $E_m/E_i \leq 1.0$), the smaller the interphase thickness, the less the stress concentration factor.

Effect of E_f/E_m and E_m/E_i on the Maximum Stress Concentration Factor of the Composite

From Figure 14, one can see that the higher the E_f/E_m , the larger the stress concentration for all kinds of interphases. But, the degree of influence is decreased as the interphase becomes softer.

The Shift of the Critical Location and the Optimal Interphase (or Coating)

Equations (16), (18) and (19) were used to calculate the stress concentration factors at $Z = 0.0$ and $R + t_i \leq Z \leq L$, the results are shown in Figure 15. $\theta = 0^\circ$ represents the line $Z = 0$, while $\theta = 90^\circ$ represents line $X = 0.0$ and $R + t_i \leq Z \leq L$. As one can see from this figure, curve (S.C.F.) $\theta = 0^\circ$ and (S.C.F.) $\theta = 90^\circ$ intersect at $E_m/E_i = (E_m/E_i)_c$ and

$$(S.C.F.)_{\theta = 0^\circ} \geq (S.C.F.)_{\theta = 90^\circ}, \text{ for } E_m/E_i \leq (E_m/E_i)_c$$

$$(S.C.F.)_{\theta = 0^\circ} \leq (S.C.F.)_{\theta = 90^\circ}, \text{ for } E_m/E_i \geq (E_m/E_i)_c$$

Also, the two-dimensional analysis shows that for $E_m/E_i \geq (E_m/E_i)_c$ σ_L^{\max} occurs at "b" as shown in Figure 16, where from Reference 8, $(E_m/E_i)_c$ can be expressed as follows

$$(E_m/E_i)_c = 1.0 + [1 - (E_m/E_f)] / (t_i/R) \quad (21)$$

Two-dimensional analysis had been performed in reference 8 and confirmed the transition of the critical location. From equation (21), one can conclude that (1) failure will occur at $\theta = 0^\circ$, if $E_m/E_i \leq (E_m/E_i)_c$; (2) for $E_m/E_i \geq (E_m/E_i)_c$, failure will occur at $\theta = 90^\circ$ and $Z = R + t_i$; (3) for $E_m/E_i = (E_m/E_i)_c$, failure will occur at $\theta = 0^\circ$ and 90° simultaneously. Figure 16 shows the critical stress concentration factors at these three regions. It is evident that $E_m/E_i = (E_m/E_i)_c$ is the optimal interphase modulus to ensure the least stress concentration factor. Figure 17 shows curves of critical stress concentration factor for various interphase thicknesses. Curve a b c d constitutes the optimal interphase for the composite with fiber volume fraction equal to .65 and $E_f/E_m = 25.0$. For varying fiber volume fraction, the curves for optimal interphase are shown in Figure 18. These curves can be used to design the interphase or coating to obtain the maximum transverse tensile strength of the composite. Figure 19 shows how the interphase affects the transverse tensile strength as compared with the transverse tensile strength of the composite without interphase for various fiber volume fractions. It can be seen that the transverse tensile strength, for the composite with $E_f/E_m = 21.3$ and $t_i/R = .0286$, can be increased as much as 43%, 38% and 34% for $V_f = .65, .57$ and $.502$ respectively.

Effect of Interphase Properties on the Transverse Failure Modes of the Composite

One-dimensional models can not detect the location of failure because the local transverse tensile stress is assumed to be the same in the fiber, interphase and matrix at constant Z and any X as expressed in equation (5). For this purpose, the two-dimensional model must be used. Figure 20 shows the stress distribution in the interphase and matrix at $Z = 0$ as a function of interphase modulus. As shown in this figure, the assumption that the stress at the matrix and interphase is equal for one-dimensional theory is approximately correct. Also, for $1.0 \leq E_m/E_i \leq 5.0$, the local transverse tensile stress in the matrix is higher than in the interphase. Thus, in this range, matrix cracking is the failure mode. For $5.0 \leq E_m/E_i$, the stress in the interphase or interface is higher than the stress in the matrix. Thus, in this range, failure will occur either in the interphase or at the interface. Based on this idea, one can obtain the critical stress concentration factor and failure mode of the composite as a function of interphase modulus and thickness as shown in Figures 21 and 22.

Notice that the above results are based on the assumption that the strength in matrix, interphase and interface is the same. If the tensile strength of the matrix and interphase (or coating), and the disbonding strength of the interface are known, then similar design curves as shown in Figures 21 and 22 can also be produced to determine the transverse tensile strength and the failure mode as the function of interphase modulus and thickness.

CONCLUSIONS

Interphase thickness and modulus have significant influence on the transverse tensile strength of unidirectional fiber reinforced composites. A soft interphase is shown to reduce the stress concentration factor, hence increasing the transverse tensile strength of the composite. In order to increase transverse tensile strength of a composite, the interphase modulus should be decreased and/or the thickness of the interphase should be increased. The location for maximum stress concentration factor varies with interphase modulus and thickness, hence the mode and location of failures may be changed by changing these parameters.

RECOMMENDATIONS

It is recommended that micromechanical models, which include the interphase be further developed for composites with initial microcracks or fiber-matrix disbands. These models can be used to determine: (1) the transverse tensile strength of the composite with existing microcracks or interface disbands, (2) the effect of the interphase (or coating) on the fracture resistance of the composite, (3) the favorable failure mode (or failure location) by adjusting interphase properties so that the crack propagation can be arrested or slowed down. Also, we recommend that elastic-plastic matrix and interphase behavior should be included in the micromechanical models to determine the combined effects of interphase and material nonlinearity of the matrix on the transverse tensile strength of the composite.

REFERENCES

1. L. B. Greszczuk, "Theoretical and Experimental Studies on Properties and Behavior of Filamentary Composite," Society of Plastics Industry, 21st Annual Conference, Washington, D.C., 1966.
2. D. F. Adams and D. R. Doner, "Transverse Normal Loading of a Unidirectional Composite," Journal of Composite Materials, 1,152, 1967.
3. D. F. Adams, "A Micromechanics Analysis of the Influence of the Interface on the Performance of Polymer Matrix Composites," proceedings of the American Society for Composites, First Technical Conference, 1986.
4. L. T. Drzal, "Tough Composite Materials: Recent Developments," Noyes, Park Ridge, New Jersey, pp. 207-222, 1985.
5. M. R. Piggott, "Polymer Composite," B(5), pp. 291-296, 1987.
6. H. C. Tsai, A. M. Arocho, L. W. Gause, "Prediction of Fiber-Matrix Interphase Properties and Their Influence on Interface Stress, Displacement and Fracture Toughness of Composite Material," Journal of Materials Science and Engineering, A126, pp. 295-304, 1990.
7. D. F. Adams, and S. W. Tsai, "The Influence of Random Filament Packing on the Transverse Stiffness of Unidirectional Composite," Journal of Composite Materials, Volume 3, pp. 368-381, July 1969.
8. H. C. Tsai and A. M. Arocho, "Effect of the Fiber-Matrix Interphase on the Transverse Tensile Strength and Fracture Resistance of Composite Materials," NADC Technical Report, to be published.
9. A. M. Skuda, "Micromechanics of Failure of Reinforced Plastics," Failure Mechanics of Composites, p. 18, Volume 3, Handbook of Composites, North-Holland, 1986.

Table I - Comparison of 1-D and 2-D Analytical Results

($E_f/E_m = 21.3$, $V_F = 0.65$, $t_f/R = .015$)
S.C.F

Em/Ei	1.0	10.0	15.0	20.0	30.0	40.0	50.0
METHOD							
1-D	1.905	1.651	1.582	1.531	1.460	1.410	1.371
2-D	2.019	1.716	1.643	1.592	1.519	1.459	1.412
1-D/2-D	.944	.962	.963	.962	.961	.966	.971

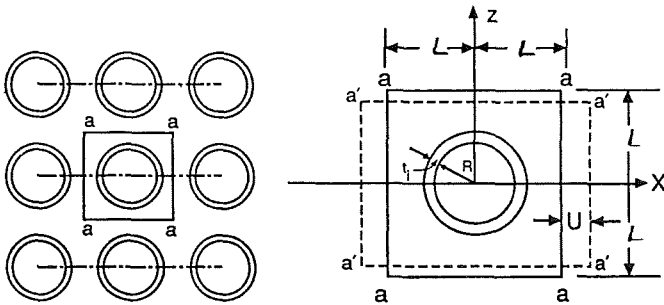


Figure 1 - Fiber Packing Geometries

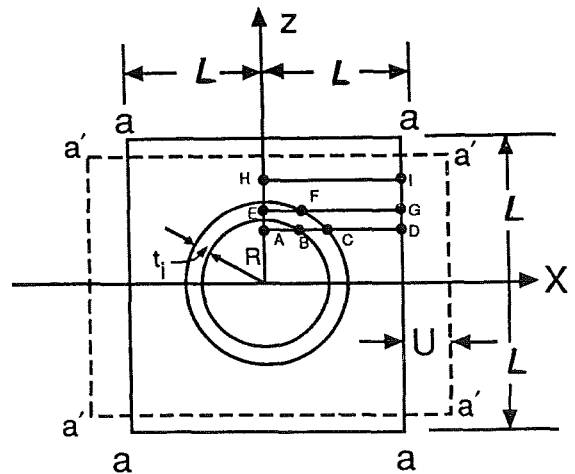


Figure 2 - One-Dimensional Model for the Composite Under Transverse Tensile Loading

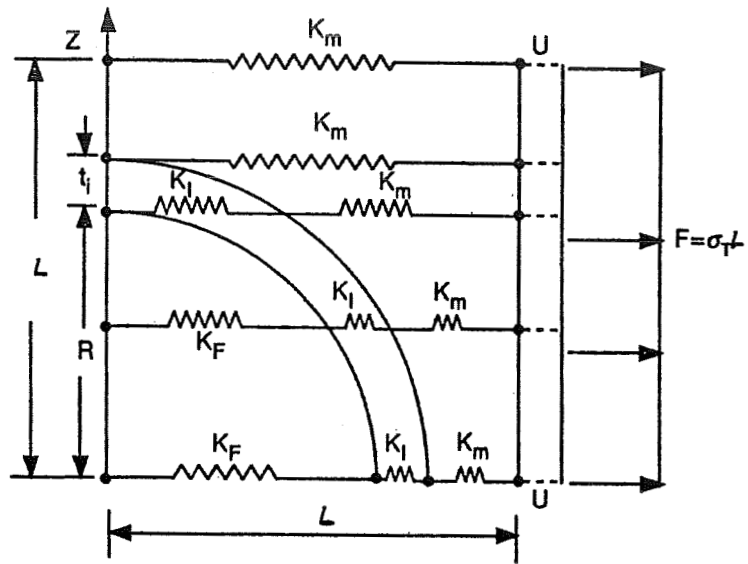


Figure 3 - Basic Concept for One-Dimensional Model

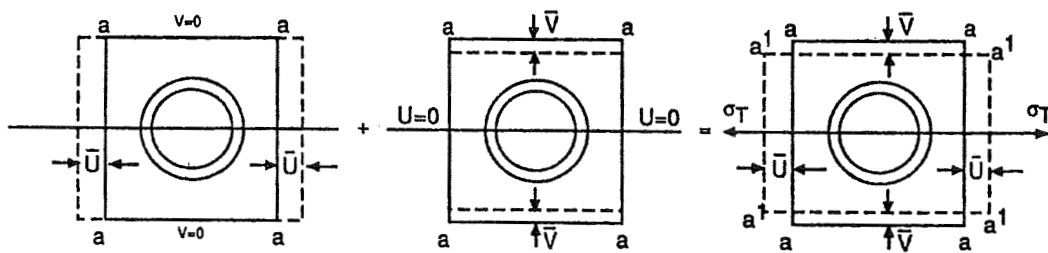


Figure 4 - Basic Concept for Two-Dimensional Model

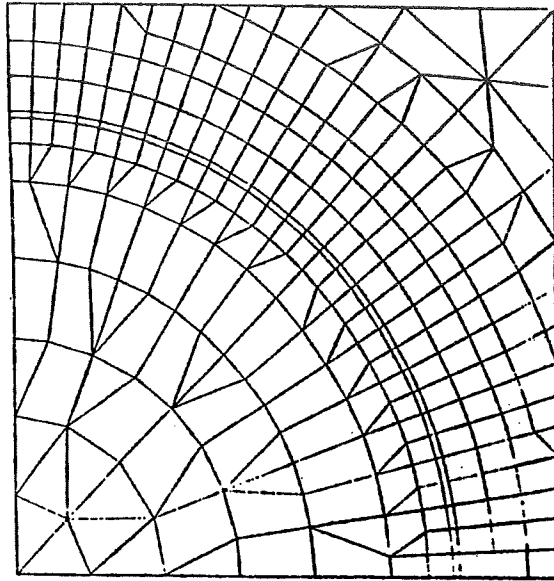


Figure 5 - Two-Dimensional Finite Element Model

A_L/E_p
 $E_f = 10.0 \times 10^6 \text{ psi}$, $\nu_f = 0.31$ $V_f = 0.502$
 $E_m = 0.47 \times 10^6 \text{ psi}$, $\nu_m = 0.36$

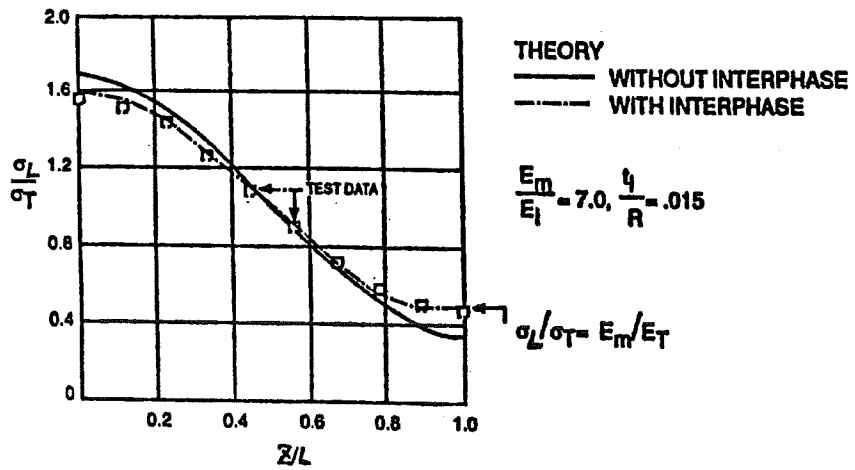


Figure 6 - Transverse Tensile Stress Distribution Along $X = L$; Test vs. One-Dimensional Theory

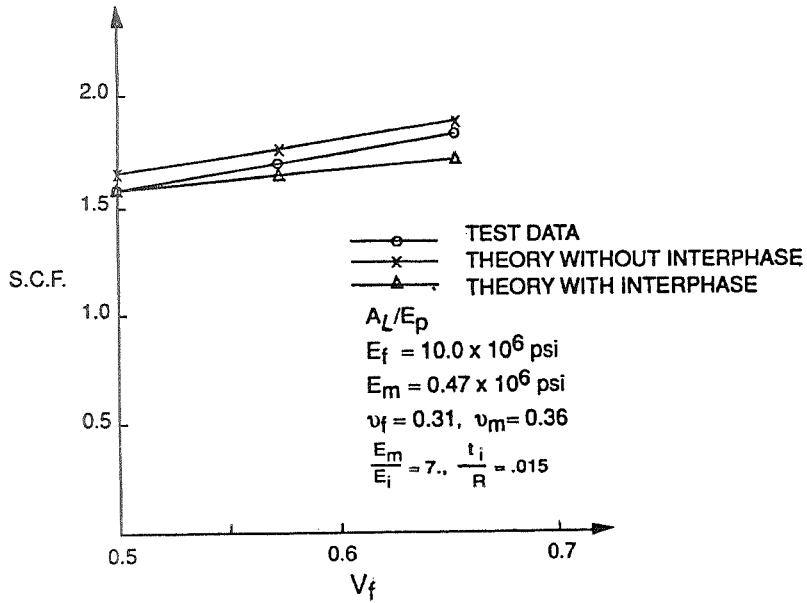


Figure 7 - Maximum Transverse Tensile Stress; Theory vs. Test

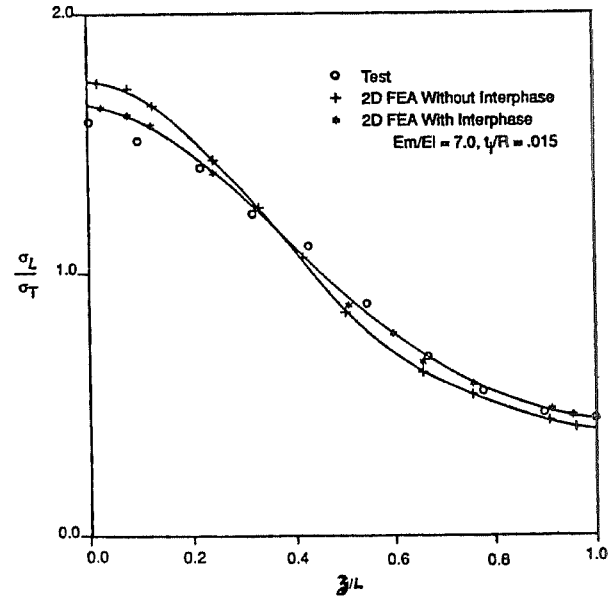


Figure 9 - Transverse Tensile Stress Distribution Theory vs. Test, $V_f = .502$

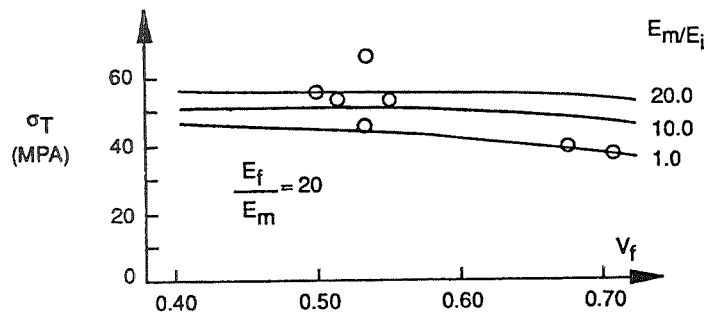


Figure 8 - Correlation of 1-D Theory With Test Data For GI/Ep Composite

$(\sigma_{mu} = 74.2 \text{ MPA}, \frac{t_i}{R} = .0286)$

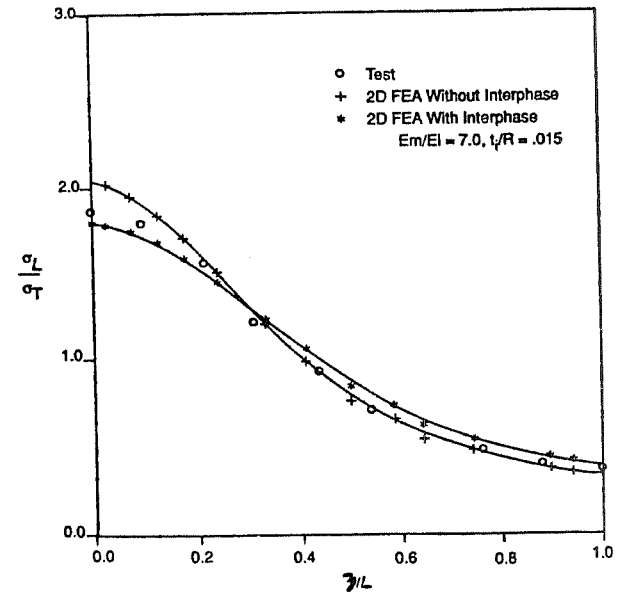


Figure 10 - Transverse Tensile Stress Distribution Theory vs. Test, $V_f = .65$

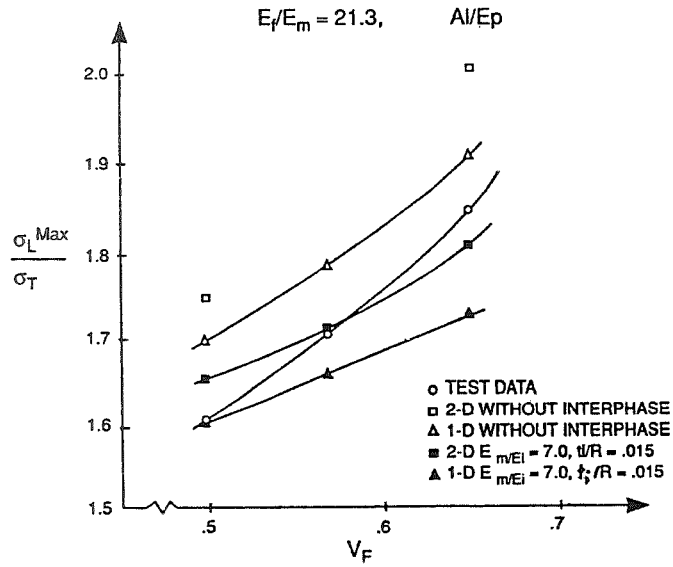


Figure 11 - Maximum Transverse Tensile Stress Theories vs. Test

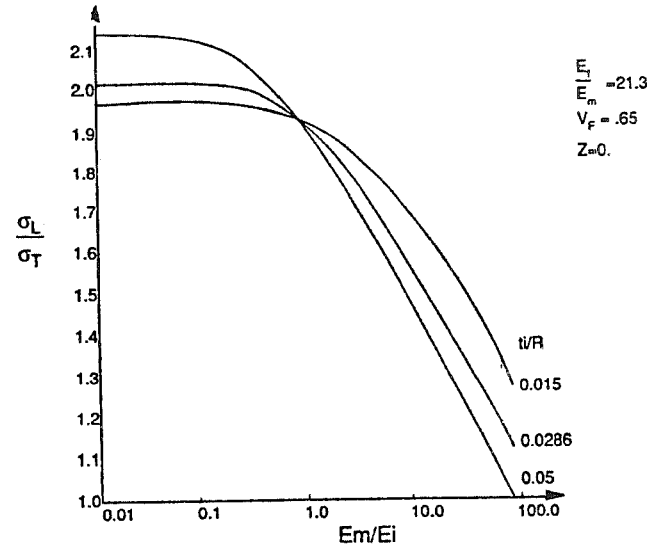


Figure 13 - $\frac{\sigma_L}{\sigma_T}$ vs. $\frac{E_m}{E_i}$ With Various Interphase Thickness

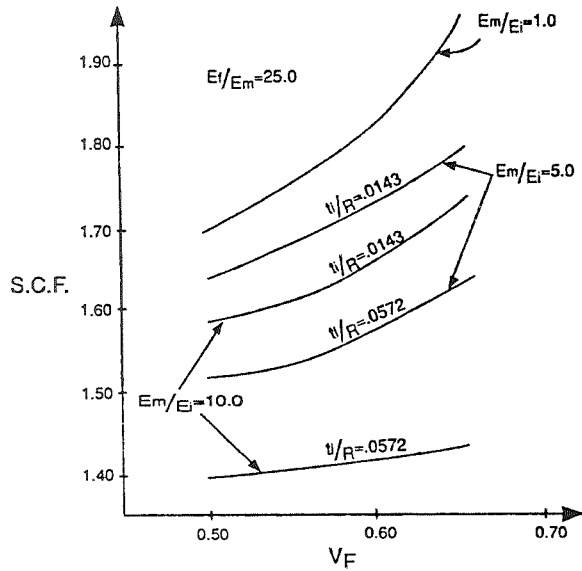


Figure 12 - Effect of Interphase Moduli and Thickness on S.C.F. of the Composite

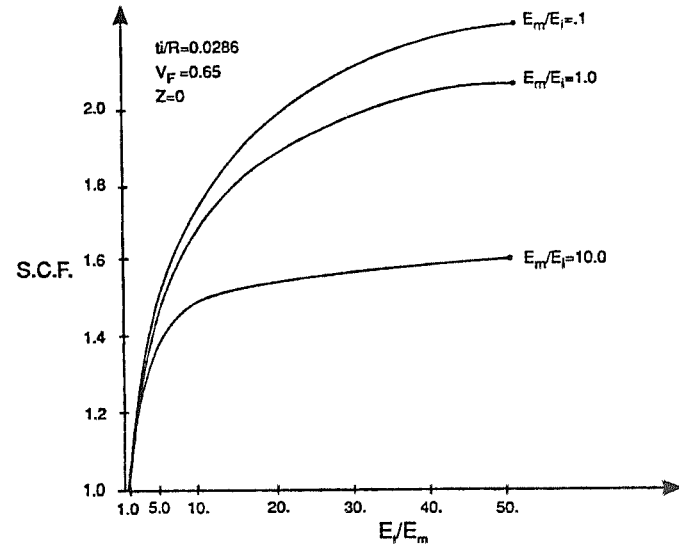


Figure 14 - Effect of E_f/E_m and E_m/E_i on the Maximum Stress Concentration Factor

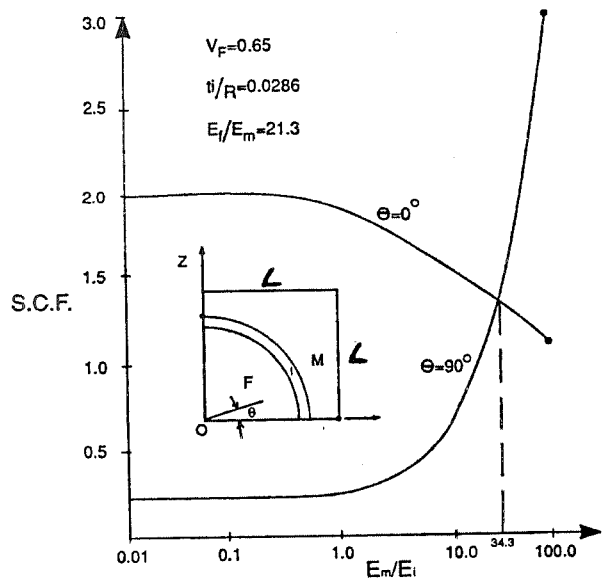


Figure 15 - The Shift of the Critical Location

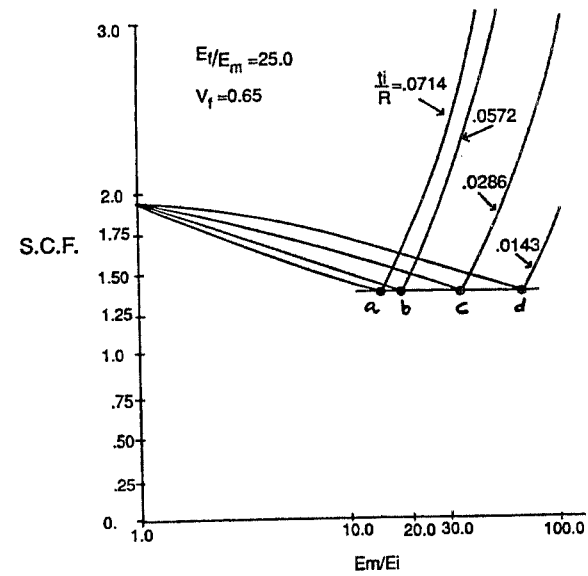


Figure 17 - Critical Stress Concentration Factors As Functions of Interphase Moduli and Thickness

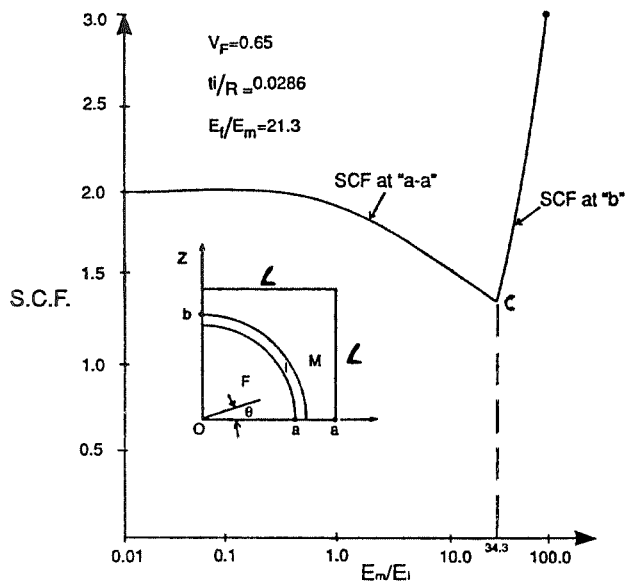


Figure 16 - Critical Stress Concentration Factors As Functions of Interphase Moduli

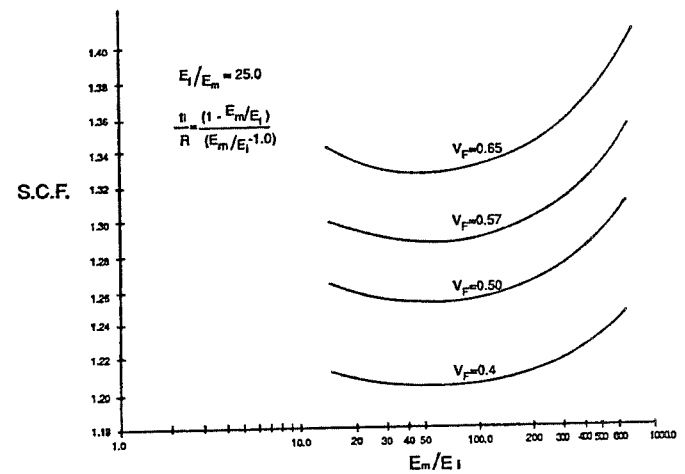


Figure 18 - Design Curves for Optimal Interphase Modulus and Thickness

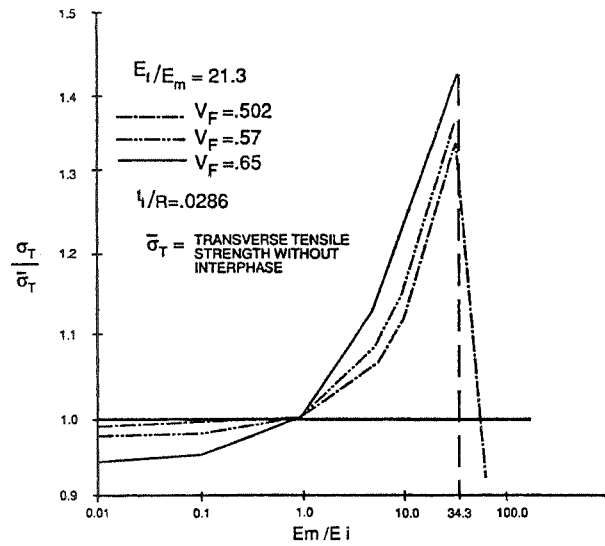


Figure 19 - Effect of Interphase Moduli on the Transverse Tensile Strength of Composite Material

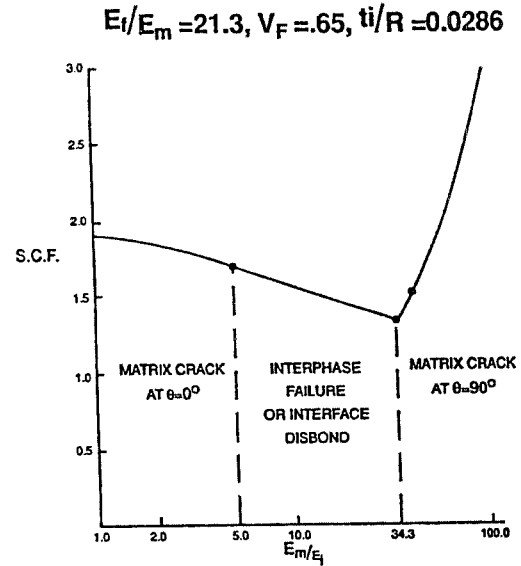


Figure 21 - Design Curve for Transverse Tensile Failure of the Composite Material

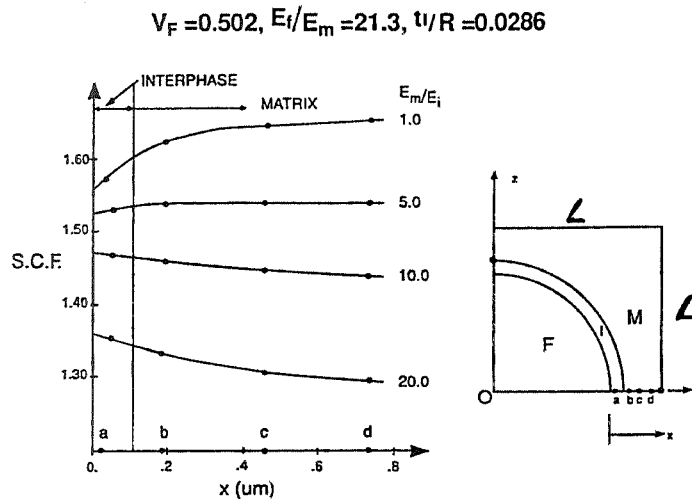


Figure 20 - Stress Distribution in the Interphase and Matrix at $Z = 0.0$, As Function of Interphase Moduli

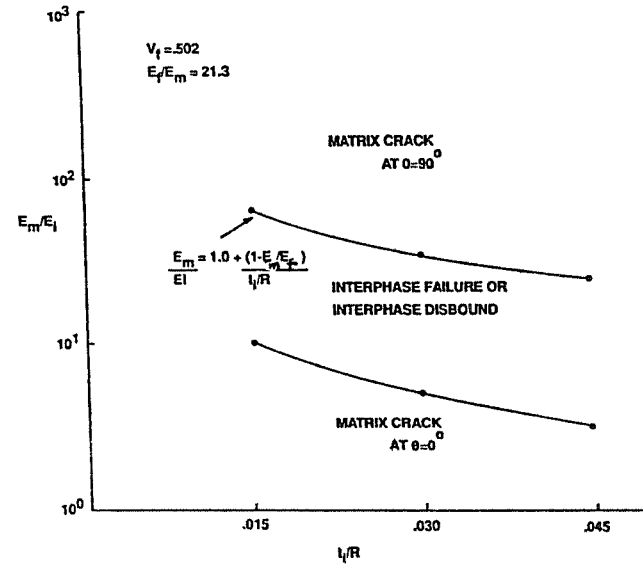


Figure 22 - Effect of Interphase Modulus and Thickness on the Transverse Failure Mode of the Composite

THIS PAGE INTENTIONALLY BLANK

NASA

56-24

57374

P-10

THE EFFECT OF MATERIAL HETEROGENEITY
IN CURVED COMPOSITE BEAMS
FOR USE IN AIRCRAFT STRUCTURES¹

Brendan J. O'Toole and Michael H. Santare

Department of Mechanical Engineering and the Center for Composite Materials
University of Delaware, Newark DE

ABSTRACT

A design tool is presented for predicting the effect of material heterogeneity on the performance of curved composite beams for use in aircraft fuselage structures. Material heterogeneity can be induced during processes such as sheet forming and stretch forming of thermoplastic composites. This heterogeneity can be introduced in the form of fiber realignment and spreading during the manufacturing process causing a gradient in material properties in both the radial and tangential directions. The analysis procedure uses a separate two-dimensional elasticity solution for the stresses in the flanges and web sections of the beam. The separate solutions are coupled by requiring that forces and displacements match at the section boundaries. Analysis is performed for curved beams loaded in pure bending and uniform pressure. The beams can be of any general cross-section such as a hat, T-, I-, or J-beam. Preliminary results show that the geometry of the beam dictates the effect of heterogeneity on performance. Heterogeneity plays a much larger role in beams with a small average radius to depth ratio, R/t , where R is the average radius of the beam and t is the difference between the inside and outside radius. Results of the analysis are in the form of stresses and displacements, and they are compared to both mechanics of materials and numerical solutions obtained using finite element analysis.

INTRODUCTION

The use of composite materials in commercial aircraft has been focused on secondary structures such as control surfaces and trailing edge panels. Breakthroughs in manufacturing techniques, materials, and structural concepts are needed so that more primary structures can be produced from composites resulting in structural weight savings, part count reduction, and cost reduction. This research investigates the possibilities of combining a new material system of long discontinuous fibers in a thermoplastic matrix with fabrication techniques such as sheet forming and stretch forming to produce curved beams for use as primary structures in commercial aircraft.

Manufacturing processes such as sheet forming and stretch forming can be used to produce several types of composite parts [1, 2]. The use of a long discontinuous fiber material system allows for material stretching over complex curvature parts while maintaining a high percentage of the continuous fiber material properties [3]. Combination of these forming methods and material system allows the production of complex structures such as curved beams as shown in Figure 1. The microstructure of a curved beam is sensitive to the production method and gradients in material properties are expected in both sheet formed [4] and stretch formed [2] beams. Schematic examples of two types of heterogeneity are shown in Figure

¹ NASA Contract NAS1-18758 Program Monitor: Dawn Jegley

2; analysis of these types of beams can be useful in determining the effect of such property gradients on the overall performance of a given beam.

Two separate analyses were conducted. The first uses a closed form stress potential approach to investigate the effect of radial heterogeneity on curved beams loaded in pure bending. The stress state is found for beams which can have several different geometries including I, J, T, and rectangular cross-sections. Material properties can be specified independently for each section of the beam, i.e., flange and web can have different properties. Each section of the beam is treated as an individual curved rectangular beam loaded in pure bending and with a constant distributed load on the curved surfaces. Superposition is used to combine the results of the individual sections into the total beam solution. Details of the analysis are provided and results are shown for comparison with known solutions.

The second analysis technique uses a Rayleigh-Ritz approach to solve the minimum potential energy equation in a circular ring loaded with an internal and external pressure. This is an approximate solution which uses an assumed series formulation of the displacement field. The advantage of this method is that it allows for any type of material heterogeneity and can be used to solve other relevant problems such as tensile loaded beams or beams with geometric stress concentrations such as cutouts.

Analysis results are compared to solutions found by using mechanics of materials and finite element analysis. The mechanics of materials solutions are useful for comparing results for beams with homogeneous material properties and the finite element analysis is necessary to solve the problem when the beam has heterogeneous material properties. The first type of analysis has been incorporated into a design tool for analyzing curved beams loaded in pure bending. A wide range of geometric parameters and material properties can be analyzed with relative ease. The second type of analysis is being developed so that a similar tool can be used to analyze curved beams with different loading conditions or geometric configurations.

ANALYSIS PROCEDURES

Radial Heterogeneity Analysis

The state of stress and strain is determined for a curved beam loaded in pure bending which has any of the following cross-sections; I-beam, T-beam, J-beam, etc. The solution is found by separating the beam into three sections; each with an applied bending moment and distributed load. A stress potential approach is used to solve the two-dimensional problem in each section. The constitutive relations take the form

$$\epsilon_i = \alpha_{ij} r^{-n} \sigma_j ; \quad i, j = 1, 2 \quad (1)$$

where ϵ is the two-dimensional strain vector in polar coordinates, σ is the corresponding stress vector, r is the radial position, and α_{ij} are the base values of the elements of the compliance matrix;

$$\alpha_{11} = a^n/E_{11} \quad , \quad \alpha_{12} = \alpha_{21} = -\nu_{12} a^n/E_{12} \quad , \quad \alpha_{22} = a^n/E_{22} \quad , \quad (2)$$

and a is the inside radius of the beam. The degree of radial heterogeneity, n , allows for a property gradient in the radial direction of the beam. A positive ' n ' defines a beam which is stiffer with increasing radius, a negative ' n ' defines a beam which is more compliant with increasing radius and homogeneous material properties are specified by letting $n = 0$. Base values for the material properties are defined along the inside radius of the beam. This constitutive relation, together with equilibrium and compatibility can be combined to form the equation

$$\nabla^4 \phi = 0 \quad (3)$$

where ϕ is the stress potential. We can solve for ϕ by applying boundary conditions to the two-dimensional curved beam as shown in Figure 3; the tractions along the straight edges are represented by a bending moment, M , and the curved surfaces are traction free. The resulting stresses are [5]:

$$\begin{aligned}\sigma_r &= -\frac{M}{b^2hg} \left[\frac{c^t - c^{n+1}}{c^s - c^t} \rho^{s-1} + \frac{c^{n+1} - c^s}{c^s - c^t} \rho^{t-1} + \rho^n \right], \\ \sigma_\theta &= -\frac{M}{b^2hg} \left[\frac{c^t - c^{n+1}}{c^s - c^t} s \rho^{s-1} + \frac{c^{n+1} - c^s}{c^s - c^t} t \rho^{t-1} + (n+1) \rho^n \right],\end{aligned}\quad (4)$$

where,

$$g = \frac{(c^t - c^{n+1})(1 - c^{s+1})}{c^s - c^t} \frac{s}{s+1} + \frac{(c^{n+1} - c^s)(1 - c^{t+1})}{c^s - c^t} \frac{t}{t+1} + \frac{(n+1)}{(n+2)} (1 - c^{n+2}), \quad (5)$$

$$\begin{pmatrix} s \\ t \end{pmatrix} = \frac{1}{2} \left(n \pm \sqrt{n^2 + 4 \gamma_n} \right), \quad \gamma_n = \frac{(\alpha_{11} + n \alpha_{12})}{\alpha_{22}}, \quad (6)$$

and h is the beam thickness, c is the ratio of the inside radius to the outside radius ($c = a/b$), and ρ is the ratio of radial position to outside radius ($\rho = r/b$). Notice that the solution is axisymmetric and $\sigma_{r\theta} = 0$ everywhere.

Another loading condition that produces an axisymmetric state of stress in a curved beam is the classic Lamé's problem, which is a circular cylinder with an internal and external pressure. The stresses in such a cylinder are [5]:

$$\begin{aligned}\sigma_r &= -P c \frac{\rho^{s-1} - \rho^{t-1}}{c^s - c^t} + Q \frac{c^t \rho^{s-1} - c^s \rho^{t-1}}{c^s - c^t} \\ \sigma_\theta &= -P c \frac{s \rho^{s-1} - t \rho^{t-1}}{c^s - c^t} + Q \frac{s c^t \rho^{s-1} - t c^s \rho^{t-1}}{c^s - c^t}\end{aligned}\quad (7)$$

where P is the internal pressure, Q is the external pressure, and all the other variables are the same as in the pure bending case. When looking at a section of the cylinder, as shown in Figure 4, the straight edges are not traction free; the tractions can be represented by an end moment and an end load analogous to hoop stress found in a thin walled cylinder. The end load, L , is determined by integrating the tangential stress across the depth of the beam and the end moment, M_L , is found by integrating the tangential stress times the radius across the depth of the beam.

The displacements for both of these loading conditions are found using a two step procedure. The first step finds the radial and tangential strains by substituting equations (4) and (7) into equation (1). Then the expressions for the displacements can be found by applying the strain displacement relations [5].

Superposition of Two-Dimensional Solutions

Now that the solution for the stresses has been established in each individual section under the general loading shown in Figure 5, superposition is used to find the solution of the entire beam. The

curved I-beam, for example, loaded with a bending moment, M , is separated into three sections with the following bending moments and distributed loads: $M_1, M_2, M_3, P_2, P_3, Q_1$, and Q_2 , as shown in Figure 5. Applying superposition; the sum of the moments on the ends must be equal to M :

$$M_1 + M_2 + M_3 + M_{L1} + M_{L2} + M_{L3} = M \quad (8)$$

where M_1, M_2 , and M_3 are applied bending moments and M_{L1}, M_{L2} , and M_{L3} are the bending moments due to the applied distributed loads Q_1, P_2 and Q_2 , and P_3 , respectively.

Six more equations are necessary to solve this problem. The sections must be in equilibrium where they meet, therefore the radial loads must be equal resulting in the following relations:

$$P_2 h_2 = Q_1 h_1 \quad \text{and} \quad P_3 h_3 = Q_2 h_2 \quad (9)$$

where h_1, h_2 , and h_3 are the thickness of each section and the P 's and Q 's are the applied pressures. The final equations are found by requiring the continuity of the displacements at the section boundaries. The radial and tangential displacements of section 1 must be equal to the corresponding displacements of section 2 at the section boundary where $r = b$. Similar conditions hold at the other section boundary where $r = c$.

$$\begin{aligned} u_r^{(1)} &= u_r^{(2)}, \quad \text{at } r = b & u_r^{(2)} &= u_r^{(3)}, \quad \text{at } r = c \\ u_\theta^{(1)} &= u_\theta^{(2)}, \quad \text{at } r = b & u_\theta^{(2)} &= u_\theta^{(3)}, \quad \text{at } r = c. \end{aligned} \quad (10)$$

Equation (8) which is the superposition equation, equations (9) which are the two equilibrium equations, and equations (10) which are the four continuity equations are solved simultaneously for the seven unknowns; $M_1, M_2, M_3, P_2, P_3, Q_1$, and Q_2 . The stresses, strains and displacements can be found in each section based on these loading conditions.

Rayleigh-Ritz Structural Analysis

This method is used to solve the problem of a circular ring loaded by internal and external pressure. It makes use of an assumed displacement field which can also be used to solve several other problems [6]. This method allows for the calculation of stresses in components without the need for elaborate pre- and post-processing; which is especially convenient for parts with complex heterogeneous material properties and geometry.

The principle of minimum potential energy states that of all displacement fields which satisfy the prescribed constraint conditions, the correct state is that which makes the total potential energy, Π , of the structure a minimum [7]. The potential energy of the structure is the sum of the elastic strain energy, U , and the potential of the external forces, V . The minimum potential energy is found by setting its first variation equal to zero, $\delta \Pi = \delta U + \delta V = 0$; which can be expanded to

$$\int_A \delta \{\epsilon\}^T \{N\} dA - \int_S \delta \{u\}^T \{t\} dS = 0. \quad (11)$$

where,

- $\{\epsilon\}$ = strain vector
- $\{N\}$ = stress resultant vector
- $\{u\}$ = displacement vector
- $\{t\}$ = applied surface traction vector

and A is the area of the circular ring and S is the curve which defines its boundary. We assume the following form of the displacement field,

$$u_r = \sum_{j=0}^N \sum_{k=1}^M q_j^k r^{2(k-M)+1} \cos(2j\theta) \quad , \quad u_\theta = \sum_{j=0}^N \sum_{k=1}^M q_j^{M+k} r^{2(k-M)+1} \sin(2j\theta) \quad , \quad (12)$$

where u_r and u_θ are the displacement components and q_j^k are unknown parameters. This displacement field satisfies symmetry conditions and, for the case of an isotropic circular ring loaded by internal and external pressure, it converges to the exact solution with very few terms of the series; $j=0$ and $k=2$. Substituting this equation into the principle of minimum potential energy, equation (11), leads to a system of $M(2N+1)$ linear equations which are solved simultaneously for the unknown parameters, q_j^k . A detailed description of the solution procedure is presented by Russell [6].

RESULTS

The superposition model, which is used to find stresses and displacements in a curved beam loaded in pure bending, has been verified by comparing results with mechanics of materials and finite element analysis solutions. Several example problems of isotropic beams having I-, T-, or rectangular cross-sections have been examined and the difference between the superposition and mechanics of materials solutions is less than 1% for all cases. Two-dimensional finite element analysis is used to compare results for a curved heterogeneous anisotropic J-beam. The heterogeneity is introduced into the finite element analysis by varying the material properties in each element of the model. Table 1 compares the superposition results with those found using finite element analysis for a beam with the following dimensions: inside radius is 37.4 inches, the outside radius is 39.9 inches, the lower flange is 0.49 inches wide, the upper flange is 0.89 inches wide and the web and flanges are 0.06 inches thick. The flanges are incorporated into the finite element model by setting the thickness of the inside and outside row of elements accordingly. Three different constitutive relations are examined; the degree of radial heterogeneity, n , is set equal to -2, 0, and +2, where an 'n' value of -2 corresponds to a beam which is approximately 20% stiffer on the inside radius, an 'n' value of +2 is roughly equivalent to a beam which is 20% stiffer on the outside radius, and an 'n' value of zero means the beam is homogeneous. The finite element analysis results are within 3.4% of the superposition results as shown in Table 1.

The validity of the model has been demonstrated and the effect of radial heterogeneity on beam performance can now be determined. The maximum tangential stress and maximum displacement versus heterogeneity are found for a curved J-beam loaded in pure bending. These maximum values are plotted for several different beam geometries in Figure 6. The degree of heterogeneity is varied from -2 to +2 corresponding to approximately a 20% decrease or 20% increase in stiffness, respectively. The effect of material heterogeneity is highly dependent on the beam geometry which is characterized by the average radius to depth ratio, R/t ; where $R = (r_i + r_o)/2$ and $t = r_o - r_i$. Heterogeneity has a considerable effect on the maximum tangential stress in beams with a small curvature, $R/t = 1$, while it has virtually no effect on the stresses in beams with a large curvature. The maximum displacement is effected by heterogeneity for all beam geometries considered, but, the effect is again seen more drastically in beams with small curvature.

This analysis procedure can be used as a simple tool for preliminary design of curved beams. Given the basic beam dimensions, i.e., inner and outer radii, a range of values for all other dimensions can be selected. Flange widths and thicknesses can be varied independently as well as the material properties and degree of heterogeneity in each section. The results of a sample preliminary design are presented in Table 2. Two types of beams are analyzed; a J-beam with an R/t ratio of 14.5 and a channel beam with an R/t ratio of 6.7. The table shows the change in maximum and minimum tangential stress as well as the

maximum deflection for a range of several variables. These variables are the degree of radial heterogeneity which is varied from -2 to +2 for isotropic and unidirectional beams, the inner flange thickness, h_1 , which is varied from 0.09 to 0.89 inches, and the web thickness, h_2 , which is varied from 0.04 to 0.1 inches.

Table 1: Comparison of Superposition and Finite Element Analysis Results for a Heterogeneous, Anisotropic J-Beam Loaded in Pure Bending

Solution Procedure	Degree of Heterogeneity (n)	Maximum Displacement (in)	Maximum Stress (psi)	Minimum Stress (psi)
FEA	-2	7.08 E-5	5.14	-3.50
Superposition	-2	7.21 E-5	5.17	-3.54
% Difference	---	1.8 %	0.6 %	1.1 %
FEA	0	6.53 E-5	5.01	-3.57
Superposition	0	6.76 E-5	5.04	-3.63
% Difference	---	3.4 %	0.6 %	1.7 %
FEA	2	6.23E-5	4.89	-3.67
Superposition	2	6.34 E-5	4.91	-3.71
% Difference	---	1.7 %	0.4 %	1.1 %

Table 2: Design Study Results

Beam Type	Material	Variable Parameter	% Change in Max. Stress	% Change in Min. Stress	% Change in Max. Deflection
J-Beam	Uni-Directional	n = -2 to +2	6.7	6.1	12.8
J-Beam	Isotropic	n = -2 to +2	6.7	6.1	12.8
J-Beam	Uni-Directional	$h_1 = .09$ to $.89$	49.7	20.1	37.4
J-Beam	Uni-Directional	$h_2 = .04$ to 0.1	33.9	26.7	31.1
C-Beam	Uni-Directional	n = -2 to +2	16.5	14.3	28.4
C-Beam	Isotropic	n = -2 to +2	16.3	14.0	28.2
C-Beam	Uni-Directional	$h_1 = .15$ to $.45$	26.2	10.1	18.7
C-Beam	Isotropic	$h_1 = .15$ to $.45$	26.1	10.2	19.6

The Rayleigh-Ritz technique is used to solve the problem of a curved beam loaded by internal and external pressure. Solutions are compared with exact results for isotropic and axisymmetric anisotropic beams [5], and the difference is within 0.1%. This solution technique is also verified by solving the problem of an infinite plate with a centrally located hole loaded only by an internal pressure where the principal material directions are along the cartesian axes. This problem is modeled by letting $r_i = 1$ inch, $r_o = 30$ inches, $P_i = 1$ psi, and $P_o = 0$ psi. The stress concentrations found at $\theta = 0^\circ$ and 90° are within 1% of those found by Lekhnitskii [5]. A carbon reinforced thermoplastic composite ring with an inner radius of 6

inches and an outer radius of 8 inches is analyzed for two different fiber arrangements; one with tangentially oriented fibers and the second with fibers aligned in the x-direction. The stress distribution is axisymmetric in the ring with tangentially oriented fibers as shown in Figure 7a while the ring with straight fibers in the x-direction has a slight stress concentration at approximately $\theta = 45^\circ$ as shown in Figure 7b. These results are evidence that the tangential heterogeneity due to non-axisymmetric fiber distribution can affect the stresses in a curved beam loaded by internal and external pressure.

DISCUSSION

A closed form elasticity solution can be used to solve for the stresses and displacements in a heterogeneous anisotropic curved beam loaded in pure bending. The elasticity analysis, based on the superposition of several two-dimensional solutions, provides results which are in very good agreement with those found from mechanics of materials and finite element analysis. The heterogeneity is introduced into the model by defining the material properties as an exponential function of the radius, while the actual heterogeneity due to fiber realignment during forming can be determined using enhanced ultrasonic C-scanning techniques.

The effect of radial heterogeneity on curved beams loaded in pure bending depends on the geometry of the beam. The maximum stress and deflection in beams with a small average radius to depth ratio is significantly affected by heterogeneous material properties. A beam whose stiffness decreases by 20% from the inside to outside radius (i.e., $n = -2$), shows a 28% increase in the maximum tangential stress and a 75% increase in the maximum deflection when compared to a homogeneous beam if $R/t = 2$, but only a 1% and 4% increase, respectively, if $R/t = 10$. It is unlikely that radial heterogeneity affects the performance of most beams used in transport aircraft fuselage applications since they have an $R/t > 10$; but this heterogeneity could play a part in the performance of beams used in other applications.

The superposition elasticity analysis has been incorporated into a computer program which can be used for design studies of curved beams. Several of the beam parameters can be varied to determine their overall effect on maximum tensile and compressive stresses, as well as maximum deflections. The variable parameters are the thickness and depth of the flange and web along with their material properties and degree of radial heterogeneity. This provides a quick and easy way to perform initial beam sizing calculations.

The Rayleigh-Ritz analysis can be used to solve problems with both radial and tangential heterogeneity. The importance of this ability is demonstrated by the results of the pressurized ring problem. Isotropic and axisymmetric anisotropic rings have an axisymmetric state of stress when pressurized. Rings with tangential heterogeneity, however, do not have an axisymmetric state of stress when pressurized. Stress concentrations develop which are a function of both the material properties and the heterogeneity. This type of analysis is currently being used to study the effect of heterogeneity on curved beams subject to several different loading conditions; pure bending, internal and external pressure, and end loading. Geometric heterogeneity, such as a notch or cut-out, is also under investigation. Future work includes applying an appropriate failure criterion to the results of these analyses and comparisons with experimental data.

REFERENCES

- [1] C.M. O'Bradaigh, R.B. Pipes and P.J. Mallon. Issues in Diaphragm Forming of Continuous Fiber Reinforced Thermoplastic Composites. *Polymer Composites*, Vol. 12, no. 4, 1991, pp 246-256.
- [2] S. Medwin. Long Discontinuous Ordered Fiber Structural Parts. 34th International SAMPE Symposium and Exhibition, Reno, NV, May 8-11, 1989.

- [3] J.F. Pratte, W.H. Krueger, and I.Y. Chang. High Performance Thermoplastic Composites With Poly Ether Ketone Matrix. 34th International SAMPE Symposium and Exhibition, Reno, NV, May 8-11, 1989.
- [4] R.B. Pipes, M.H. Santare, B.J. O'Toole, A.J. Beaussart, D.C. DeHeer, and R.K. Okine. Long Discontinuous Fiber Composite Structure - Forming and Structural Mechanics. Proceedings of the First NASA Advanced Composites Technology Conference, Seattle, Washington, Oct. 29-Nov. 1, 1990, pp 247-270.
- [5] S.G. Lekhnitskii. Theory of Elasticity of an Anisotropic Body. Mir Publishers, 1981.
- [6] S.G. Russell. A Rayleigh-Ritz Analysis Methodology for Cutouts in Composite Structures. Proceedings of the First NASA Advanced Composites Technology Conference, Seattle, Washington, Oct. 29-Nov. 1, 1990, pp 901-920.
- [7] T.R. Tauchert. Energy Methods in Structural Mechanics. McGraw-Hill, 1974, pp 72-76.



Figure 1: Thermoplastic Composite Curved Beam

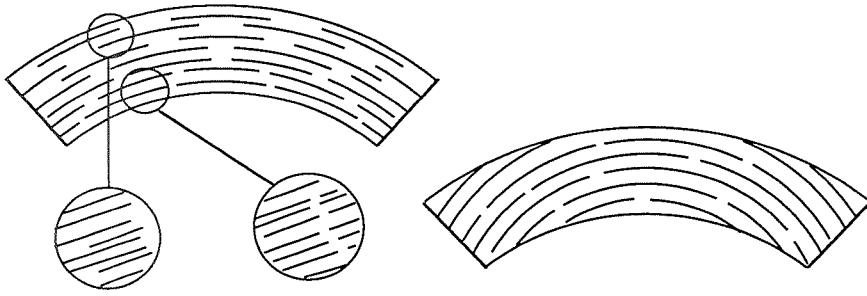


Figure 2: Different Types of Material Heterogeneity

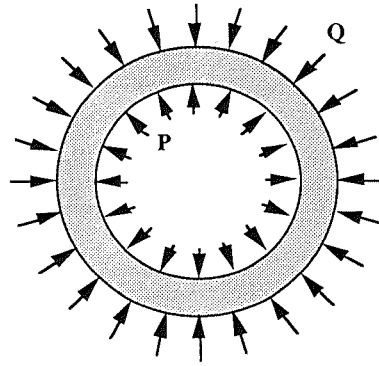


Figure 4: Lamé's Problem

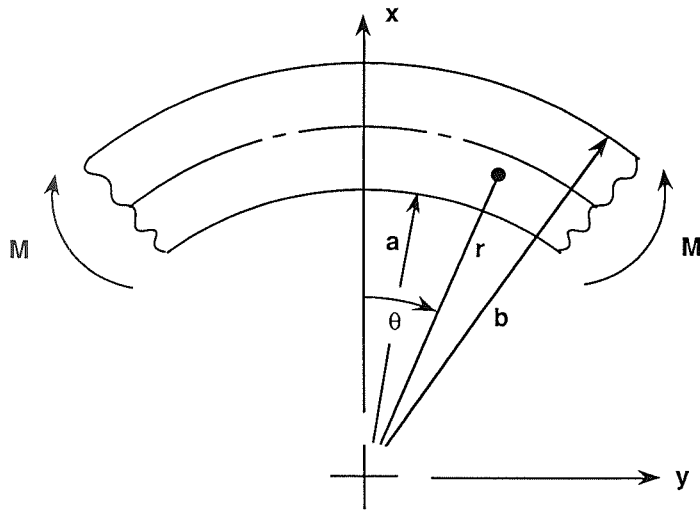
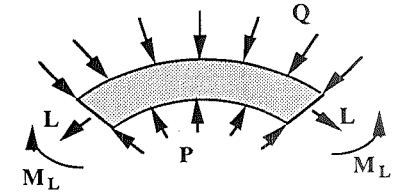


Figure 3: Pure Bending Load Case

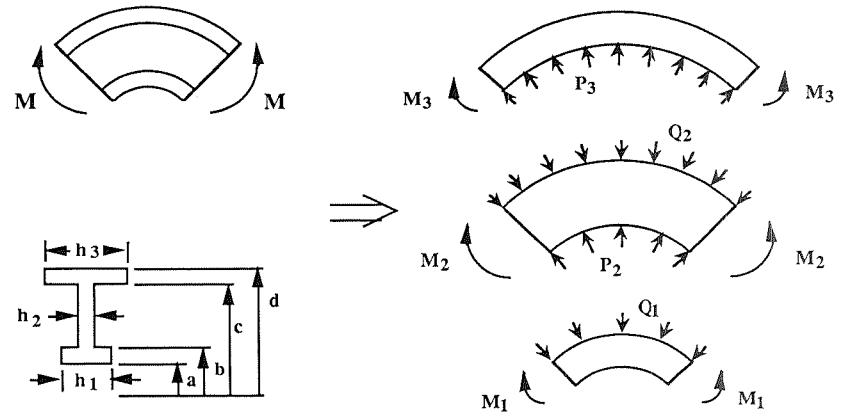


Figure 5: Superposition Analysis

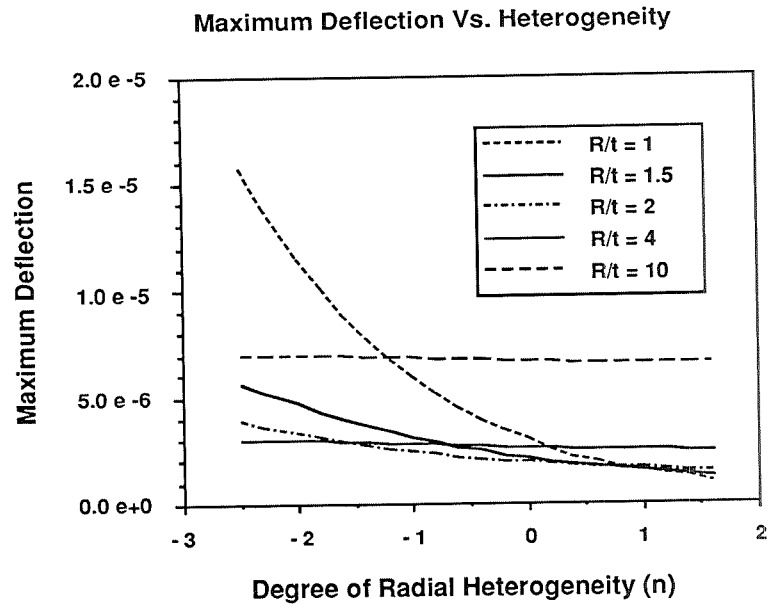
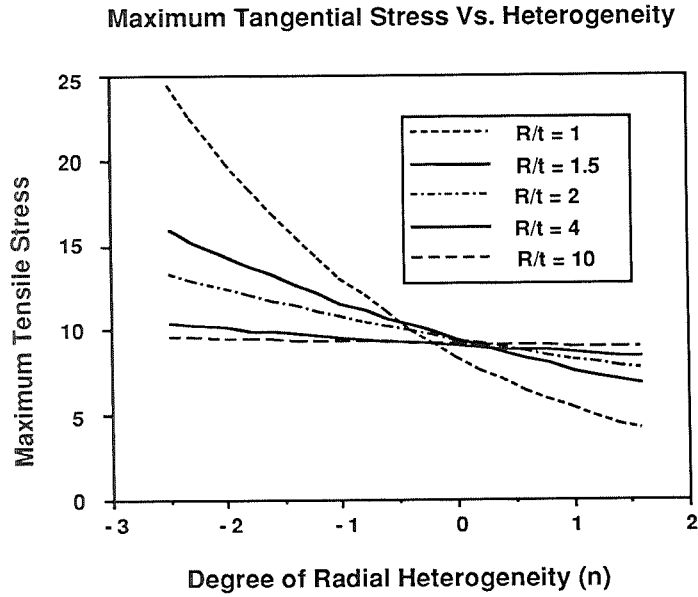


Figure 6: Maximum Tangential Stress vs. Heterogeneity and Maximum Displacement vs. Heterogeneity

Lines of Constant Tangential Stress, Units in psi.

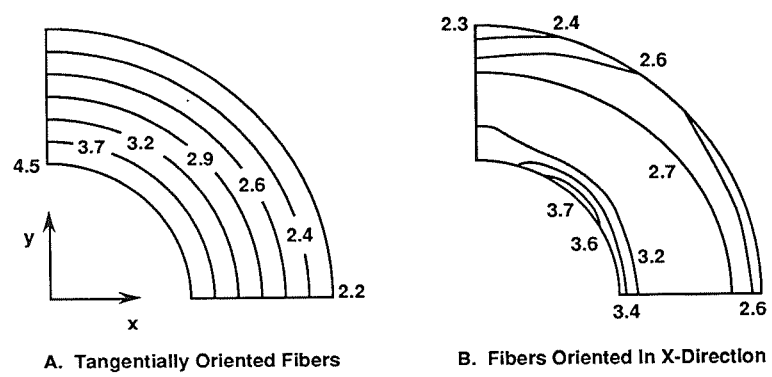


Figure 7. Tangential Stress Contours in a Circular Ring Loaded by an Internal Pressure, $P_1 = 1$ psi.

INVESTIGATION OF STATIC AND CYCLIC BEARING

FAILURE MECHANISMS FOR GR/EP LAMINATES

R. W. Walter and M. M. Tuttle
The Boeing Company
Defense and Space Group
Military Airplane Division
Seattle, Washington

57-24
P18

51375

SUMMARY

Static, cyclic load (fatigue), and residual strength testing of graphite-epoxy and aluminum pin bearing joints was completed to investigate bearing failure mechanisms. Parameters investigated included static strength, failure mode, fatigue life, hole growth, joint stiffness, and residual strength. Comparative evaluation of these results show that the MIL-HDBK-5 convention for the definition of bearing strength can be used for GR/EP materials while maintaining the same, or improved, level of structural integrity demonstrated for metal joints.

INTRODUCTION

The determination of bearing strength design allowables for advanced composite primary aircraft structure surfaced many questions and concerns. There was no industry accepted consensus or standard for defining bearing strength for GR/EP materials. Also, the permissibility of local damage and the influence of cyclic loading above a load level that created initial damage on structural integrity was a concern.

Bearing allowables that did not permit local damage were initially defined. However, these allowables precluded the potential strength capability and structural efficiency of GR/EP structures from being realized.

Early work was directed toward joints with relatively low e/D ratios typical of splice details. Evaluation of proposed GR/EP structures showed that attachments with high e/D ratios typical of brackets, rib-to-cover, and chord-to-web details had significant impact on structural weight. Consequently, failure mechanisms and allowables for the high e/D details received attention in this evaluation.

A detailed study was initiated to investigate the bearing static strength and cyclic performance. Results of this study were then used to establish a procedure for defining bearing allowables.

SYMBOLS

D Fastener diameter (inches)
e End margin; distance from center of hole to end of specimen (inches)
e/D Ratio of end margin to fastener diameter
FBR Bearing Stress (KSI)
KSI Stress (KIPS per square inch)
P Load (KIPS)
RTD Room Temperature Dry
t Thickness (inches)
W Width (inches)
W/D Ratio; specimen width to fastener diameter

APPROACH

Definition of the procedures to be used for defining GR/EP bearing strength allowables included 1) a review of existing and proposed bearing strength definitions and then 2) completing a test program to evaluate concerns and potential problem areas.

No industry standards are available which can be used to assess the acceptability of the proposed definition of bearing failure and the resulting design allowables. For this study, standard was selected as the performance level demonstrated by 2024-T3 aluminum. This material has an extensive background of allowables development and successful service experience in the aircraft industry.

Tests for the aluminum material were completed to define a baseline for comparison. Results for the GR/EP material were then compared to those for the aluminum. If the GR/EP performs equal to or better than the known successful aluminum standard, the performance of the GR/EP material should also be acceptable.

The test program was designed to evaluate several concerns. These include:

- 1) No catastrophic failure at ultimate load
- 2) Acceptable deformation up to ultimate load
- 3) No detrimental damage at limit load
- 4) Acceptable fatigue performance
- 5) Acceptable residual strength after cyclic loading
- 6) Acceptable hole growth
 - No joint leaks after cycling
 - Maintain "tight joint"
- 7) Acceptable change in joint stiffness
 - Maintain design load distribution

The GR/EP material used in this program was T300/934 tape and fabric. Layups consisted of quasi isotropic, 25/50/25, as well as 0/100/0 and 50/0/50. These layups represent a wide range of laminate design and behavior.

CANDIDATE BEARING STRENGTH DEFINITIONS FOR GR/EP MATERIAL

Many proposed definitions for GR/EP bearing strength were investigated. Those considered most viable are summarized in Figure 1. A brief description of these and concomitant advantages and disadvantages are presented in Figures 2 through 5.

TEST PLAN

Specimen geometry and the number and type of tests completed in this program are shown in Figure 6. The geometry selected permits direct comparison between the data generated during this study and bearing strength data generated for other materials in separate test efforts.

The test plan is illustrated in Figure 7. Static test data include failure loads, failure modes, and the load deflection curves to failure. Similar data were obtained for the cyclic test specimens. Load-deflection curves from zero to the maximum cyclic load were periodically recorded. These recordings were typically made at the cyclic lives noted in Figure 7. This information was used to obtain joint stiffness (slope of the elastic portion of the load-deflection curve) and permanent hole deformation.

Special attention was directed to eliminating extraneous variables from influencing test results. Specimen fabrication was monitored carefully. All specimens were tested in the same machine by the same operator. Specimen temperature was continually monitored and cyclic rate controlled to keep the local specimen temperature below 120°F. One engineer monitored all tests and reduced all data.

Steel loading fixtures and a steel pin were used to apply the bearing test load. This is consistent with the ASTM E-238 (Ref 1) test procedure and MIL-HDBK-5 (Ref 2). However, the steel pin (bolt) was installed "finger tight". This provided some restraint to resist "brooming" of the GR/EP laminate at the high bearing area. However, it did not provide any capability to transfer load by friction; all load was transferred by bearing. This provides more representative strength for the GR/EP material than results from the truly untorqued configuration defined in ASTM E-238 (Ref 3). It also provided a configuration that could be used for the cyclic testing thus eliminating a test variable.

A cyclic stress ratio ($R = f_{\min}/f_{\max}$) of 0.06 was selected for test. This provided the largest stress excursion while eliminating cyclic test problems encountered with load reversal and specimen stability.

It is recognized the load reversal can have a significant effect on fatigue performance and hole growth. However, since cyclic data from this testing will be evaluated on a comparative basis only, the relative performance of the materials should be similar.

A maximum cyclic life of 10,000 cycles was chosen for this test. Since most of the cyclic load levels in this investigation are approaching or above limit stress (67 percent of ultimate), this is considered a severe and sufficient number of cycles.

TEST RESULTS

Influence of Material

A comparison of bearing load-deflection behavior of the investigated GR/EP laminates and aluminum materials is presented in Figure 8. Data are presented in two formats: 1) load vs deflection and 2) percent of typical static failure load vs. deflection. The maximum load sustained by the specimen was considered failure load.

The load-deflection curves shown are for the material test specimens which had the most representative behavior and strength of those tested. Strength and load-deflection performance for each test group were consistent.

As shown in Figure 8, the load-deflection curves for all materials tested were similar. The maximum load capability of the aluminum specimen was low because of the lesser relative specimen thickness (See Figure 6).

Comparison of the normalized load-deflection performance shows similar behavior for all materials. The aluminum experiences non-linear behavior at a lower percentage of ultimate load than do the GR/EP laminates.

Influence of End Margin (e/D)

Load deflection and strength comparisons for a 25/50/25 GR/EP laminate are shown in Figure 9. The load required to obtain permanent deformation is about the same for all end margins tested. However, maximum load carrying capability and deformation at failure increases as the end margin increases.

Influence of Cyclic Loading

Influence of cyclic loading on bearing strength integrity is shown in Figures 10 through 16 for the materials, lay-ups, and end margins investigated. Loads are defined as a percent of the typical ultimate load capability.

A typical load-deflection curve for each material and end margin is shown. The bearing proportional limit and the .02D offset loads are defined. Typical ultimate load is 100 percent; typical limit load can be considered to be 67 percent.

Fatigue test data points are also shown. Fatigue specimens which did not fail prior to 10,000 cycles were tested in static tension to obtain tension residual strength. Specimens experiencing bolt failures were not tested for residual strength.

Hole growth data were reduced and plotted in an S-N curve format. These data show cycles required at a given load level to grow the hole to a deformation defined as a percentage of the fastener diameter.

Bearing stiffness (slope of the elastic portion of the bearing load-deflection curve) was determined. Comments relating relative change of stiffness as a function of cyclic loading are presented.

A summary of the cyclic loading behavior for the investigated materials is presented in Figure 17. This comparison is for a maximum cyclic load which is the lowest of 1) two percent diameter off-set or 2) 67 percent of maximum static load. This can be considered equivalent to a limit load level for a structure designed to the MIL-HDBK-5 allowable bearing stress guidelines.

The GR/EP materials have a higher relative allowable bearing load (based on ultimate load) than do the 2024 material. Consequently, for the cyclic comparison, the GR/EP materials are loaded at a higher percentage of their ultimate load capability than the aluminum material.

Results of this comparison show that all materials have good fatigue performance. No fatigue failures were experienced during 10,000 cycles of limit load.

The GR/EP materials typically did not experience any reduction in residual strength after cycling. The 2024 and 0/100/0 fabric ($e/D=8.0$) did experience minor residual strength reductions. However, the number of data points available to support this observation is limited.

Cycles required to grow the hole a distance of 0.04 diameters was significantly greater for GR/EP than for the 2024 aluminum. No growth was experienced on the 50/0/50 or the 25/50/25 GR/EP laminates for end margins of 2.5 diameters.

Bearing stiffness for the aluminum was found to increase with cycling. No significant change in stiffness was noted for the GR/EP laminates.

COMPARISON OF BEARING SPECIMEN AND JOINT SPECIMEN STRENGTH

A limited test effort was conducted to assess the applicability of using bearing allowables derived from untorqued specimens for defining strength of torqued joints typical of aircraft structure.

Results presented in Figure 18 show that the torqued joint exhibits higher bearing stress than the non-torqued bearing specimen. This increased strength is probably due to the added local stability and friction load carrying capability provided by the torque-up. This should provide a small amount of conservatism in joints sized with allowables determined from non-torqued test specimens.

CONCLUSIONS

A wide range of GR/EP laminates was tested to define bearing strength. The resulting strength values were assessed to compare performance relative to 2024-T3 aluminum. Results of this study show that:

- a) The bearing behavior of GR/EP is dependent on laminate design and end-margin (e/D).
- b) Using MIL-HDBK-5 (Ref 2) definition of bearing, the GR/EP laminates can be designed to a higher percentage of their ultimate strength capability than can 2024-T3 aluminum.

- c) Fatigue performance of GR/EP laminates loaded in bearing is equal to or better than that of 2024 aluminum.
- d) Hole growth for GR/EP laminates subjected by cyclic loading is less than that for 2024 aluminum.
- e) Residual strength of GR/EP laminates does not decrease during 10,000 cycles of design limit bearing load.
- f) Bearing stiffness of GR/EP does not change significantly with cyclic loading.
- g) Fully torqued joints designed for bearing failure exhibit slightly higher load carrying capability than untorqued joints.

Based on these findings, the following conclusion is derived.

The MIL-HDBK-5 (Ref 2) convention for defining bearing strength for metals can be used for GR/EP materials while maintaining the same, or improved, level of structural integrity demonstrated for metal joints.

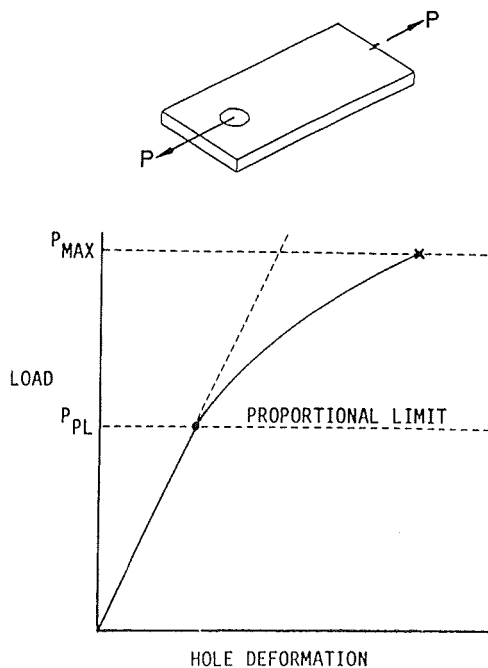
The results of the testing was specifically directed to Fiberite T300/934 GR/EP material, manufactured by Fiberite Corporation. Other material systems may behave in a different manner and should be investigated. The presented scheme for comparison of significant design parameters against known successful production material is recommended for that determination.

REFERENCES

1. Standard Method for Pin-Type Bearing Test of Metallic Materials
ASTM Designation: E238-84. Part 3 of Annual Book of ASTM
Standards, 1984.
2. Military Handbook-5E, June 1987, Metallic Materials & Elements
for Aerospace Vehicle Structures
3. Standard Test Method for Bearing Strength of Plastics ASTM
Designation: D953-84, Part 8 Annual Book of ASTM Standards,
1984

CRITERIA OR METHOD	REFERENCE	CRITERIA LOAD FOR	
		YIELD	ULTIMATE
PROPORTIONAL LIMIT	-	P @ BEARING PROPORTIONAL LIMIT	P _{MAX}
ASTM STANDARD FOR PLASTICS	ASTM D953-84a (REF. 3)	-	P AT 4% DIA. TOTAL BEARING DEFORMATION
VARIATION OF ASTM STANDARD FOR PLASTICS	-	-	P AT 4% DIA. PLASTIC BEARING DEFORMATION
MIL-HDBK-5 STANDARD FOR METALLIC STRUCTURES	MIL-HDBK-5 SECTION 1.4.7.2 (REF. 2) (REF. 1)	P AT 2% DIA. PLASTIC BEARING DEFORMATION	P _{MAX}

FIGURE 1. SUMMARY - BEARING STRENGTH CRITERIA



CRITERIA

(1) DETERMINE PROPORTIONAL LIMIT AND P_{MAX} FROM LOAD DEFORMATION CURVE

(2) DESIGN FOR f_{BR_ULT} AS LOWEST OF:

$$\bullet f_{BR_ULT} = P_{MAX} / tD$$

$$\bullet f_{BR_ULT} = [P_{PL} / tD] \times 1.5$$

ADVANTAGE

(1) MINIMUM LAMINATE DAMAGE AT LIMIT LOAD

DISADVANTAGES

(1) RELATIVELY LARGE VARIATION IN DETERMINING PROPORTIONAL LIMIT

(2) PROVIDES CONSERVATIVE (LOW) VALUES FOR LAMINATES WITH HIGH e/D VALUES OR HIGH PERCENTAGE OF ± 45 DEGREE PLYS

FIGURE 2. PROPORTIONAL LIMIT BEARING STRENGTH METHOD

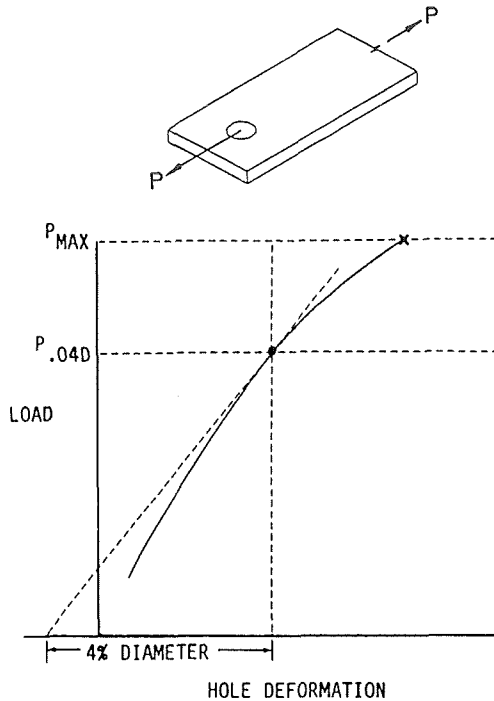


FIGURE 3. ASTM D953-84A BEARING STRENGTH METHOD

CRITERIA

- (1) DETERMINE LOAD AT WHICH BEARING HOLE DEFORMATION IS 4% OF HOLE DIAMETER
- (2) DESIGN FOR f_{BR_ULT} AS:

$$f_{BR_ULT} = P_{.04D} / tD$$

ADVANTAGES

- (1) ATSM STANDARD D953-84A (REF. 3) THAT CONSIDERS TOTAL HOLE DEFORMATION
- (2) LIMITS TOTAL DEFORMATION OF HOLE

DISADVANTAGES

- (1) DOES NOT CONSIDER ELASTIC DEFORMATION
- (2) PROVIDES CONSERVATIVE (LOW) VALUES FOR LAMINATES WITH HIGH e/D VALUES OR HIGH PERCENTAGE OF ± 45 DEGREE PLYS

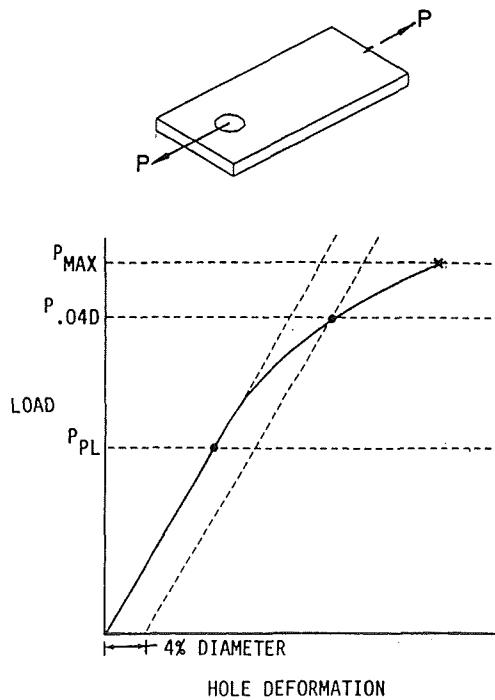


FIGURE 4. FOUR PERCENT OFFSET BEARING STRENGTH METHOD

CRITERIA

- (1) DETERMINE MAX FAILURE LOAD AND LOAD AT PLASTIC HOLE DEFORMATION EQUAL TO 4% OF FASTENER DIAMETER
- (2) DESIGN FOR f_{BR_ULT} AS LOWEST OF:

$$f_{BR_ULT} = P_{MAX} / tD$$

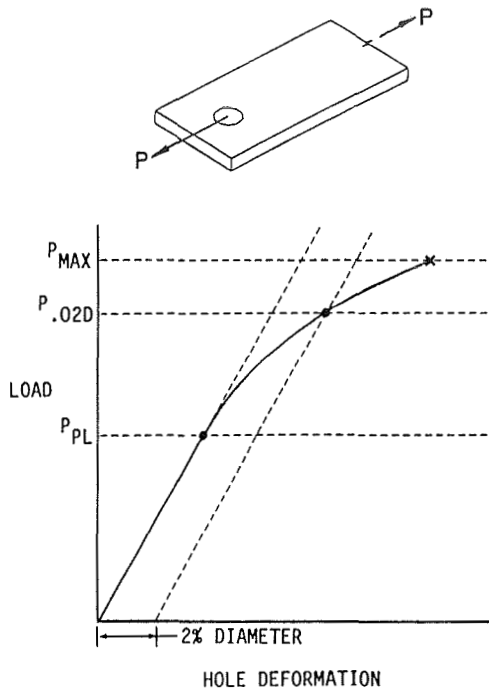
$$f_{BR_ULT} = P_{.04D} / tD$$

ADVANTAGE

- (1) RECOGNIZES ELASTIC CAPABILITY OF MATERIAL
- (2) LIMITS PLASTIC DEFORMATION OF HOLE

DISADVANTAGES

- (1) RELATIVELY LARGE VARIATION IN DETERMINING PROPORTIONAL LIMIT
- (2) PROVIDES CONSERVATIVE (LOW) VALUES FOR LAMINATES WITH HIGH e/D VALUES OR HIGH PERCENTAGE OF ± 45 DEGREE PLYS



CRITERIA

- (1) DETERMINE MAX FAILURE LOAD AND LOAD AT PLASTIC HOLE DEFORMATION EQUAL TO 2% OF FASTENER DIAMETER
- (2) DESIGN FOR f_{BR_ULT} AS LOWEST OF:

- $f_{BR_ULT} = P_{MAX} / tD$
- $f_{BR_ULT} = 1.5P_{.02D} / tD$

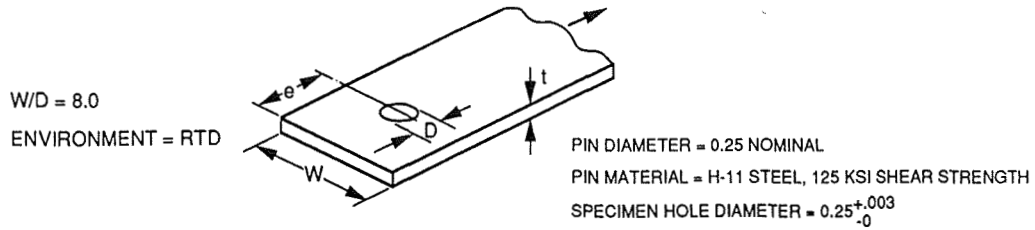
ADVANTAGE

- (1) RECOGNIZES ELASTIC CAPABILITY OF MATERIAL
- (2) LIMITS PLASTIC HOLE DEFORMATION AT LIMIT LOAD
- (3) ACCEPTED MIL-HDBK-5 STANDARD (REF. 2) FOR METALLIC MATERIALS

DISADVANTAGES

- (1) NO LIMIT FOR MAX HOLE DEFORMATION AT ULTIMATE LOAD

FIGURE 5. MIL-HDBK-5 BEARING STRENGTH METHOD



MATERIAL	NOMINAL t (IN)	e/D	NUMBER OF TEST SPECIMENS		
			STATIC	FATIGUE	RESIDUAL ¹
ALUMINUM 2024-T3	0.10	2.5	3	3	2
2024-T3	0.10	4.0	3	3	3
GRAPHITE/EPOXY ²					
25/50/25 TAPE	0.25 ³	2.5	8	3	1
50/0/50 TAPE	0.25 ³	2.5	3	3	2
0/100/0 TAPE	0.25 ³	2.5	6	4	3
0/100/0 FABRIC	0.25 ⁴	2.5	6	4	2
0/100/0 FABRIC	0.25 ⁴	8.0	3	5	3
TOTAL			32	25	16

- ¹ RESIDUAL STRENGTH TESTS CONDUCTED ON SELECTED FATIGUE TEST SPECIMENS
- ² FIBERITE T300/934 MATERIAL (TAPE 1/PLY = .0078, FABRIC 1/PLY = .0156)
- ³ 28 PLYS OF TAPE; SUFACE PLYS ARE FABRIC (t = .2496)
- ⁴ 16 PLYS OF FABRIC (t = .2496)

FIGURE 6. STATIC AND FATIGUE TEST SPECIMENS

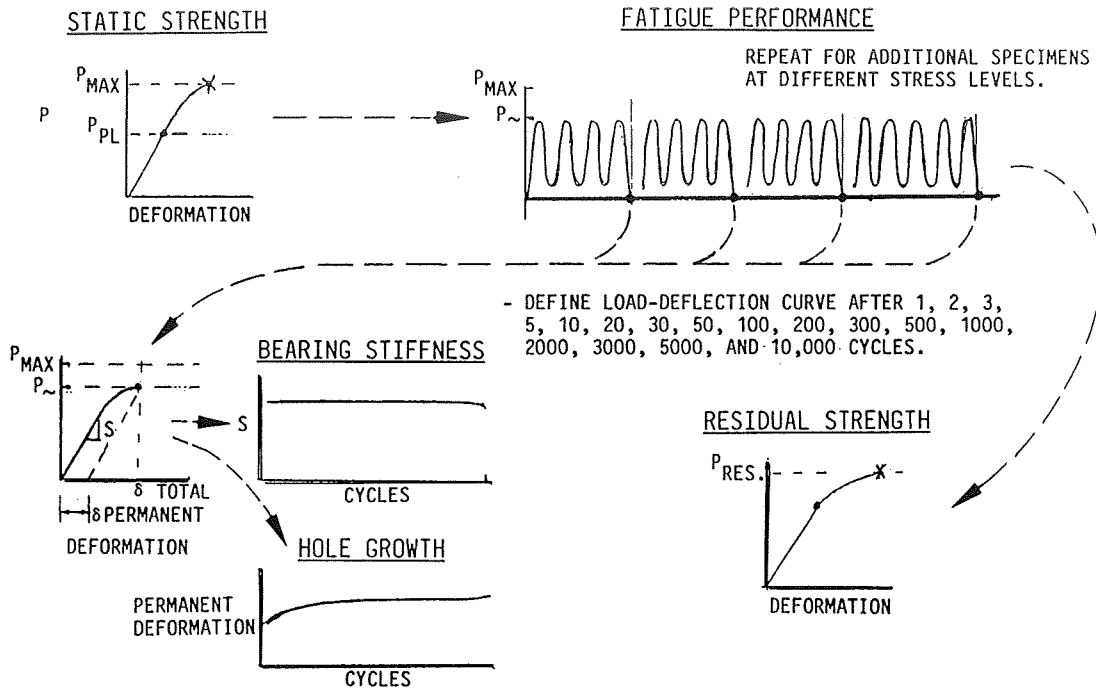


FIGURE 7. TEST PLAN

ENVIRONMENT = RTD
DIA = 0.25
e/D = 2.5
W/D = 8.0

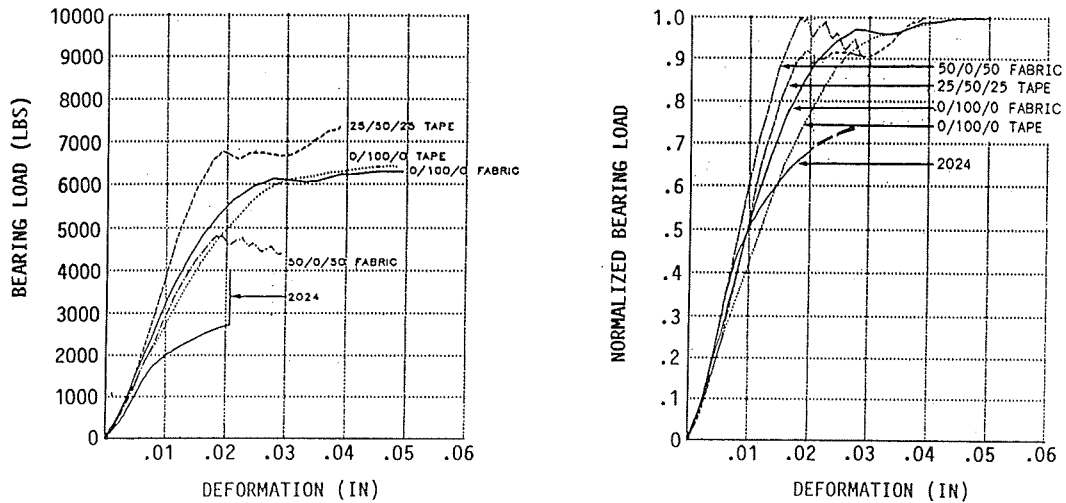
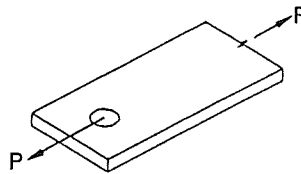


FIGURE 8. BEARING STATIC STRENGTH BEHAVIOR MATERIAL COMPARISON

LAMINATE DESIGN = 25/50/25
 ENVIRONMENT = RTD
 DIA = 0.25
 $e/D = 2.5 \sim 5.0$
 $W/D = 8.0$

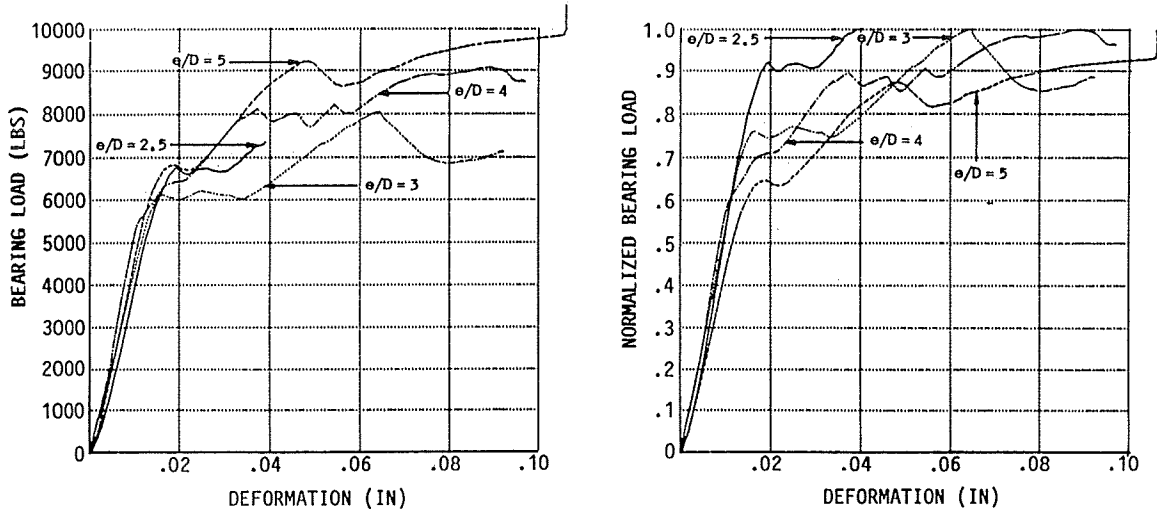
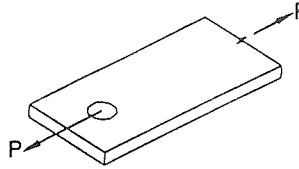
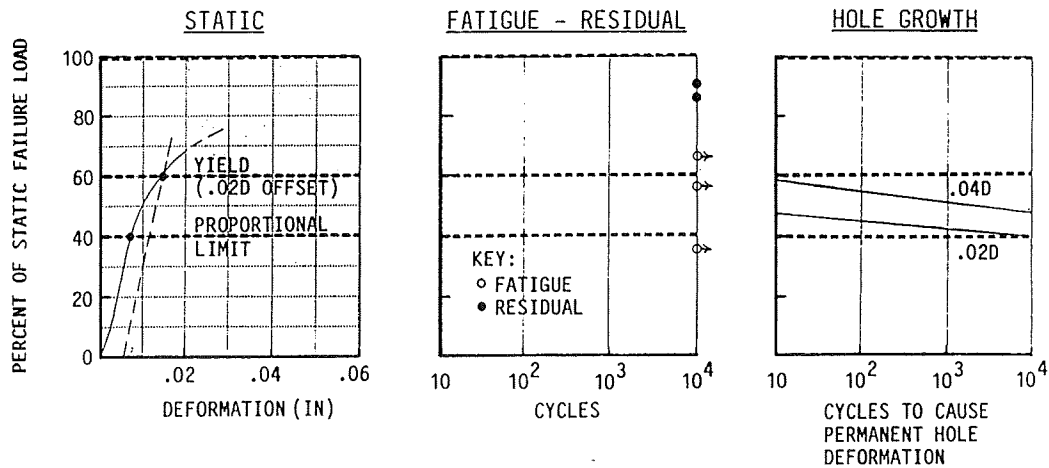
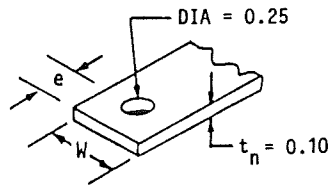


FIGURE 9. BEARING STATIC STRENGTH BEHAVIOR e/D COMPARISON

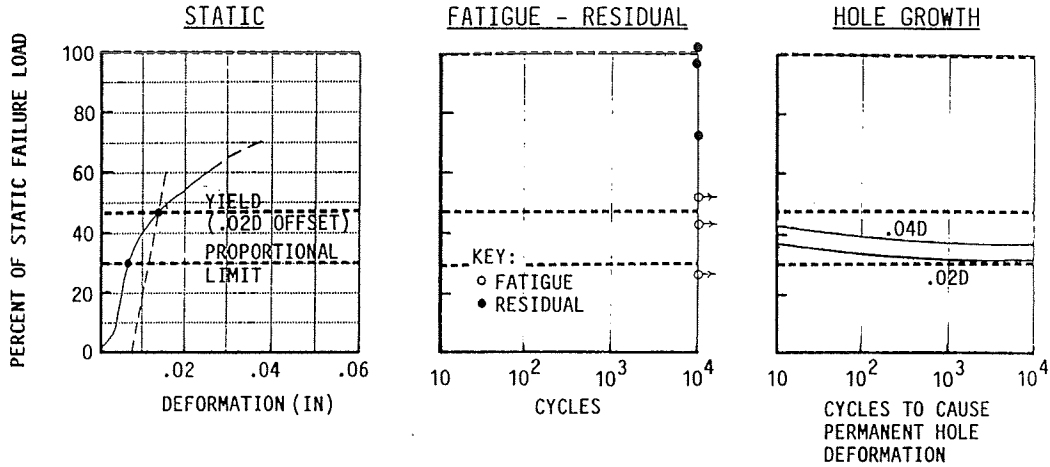
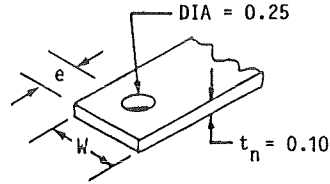
MATERIAL: 2024-T3
 e/D : 2.5
 W/D : 8.0
 ENVIRONMENT: RTD



- BEARING STIFFNESS INCREASED DURING CYCLIC TESTING

FIGURE 10. BEARING BEHAVIOR, 2024-T3, $e/D = 2.5$

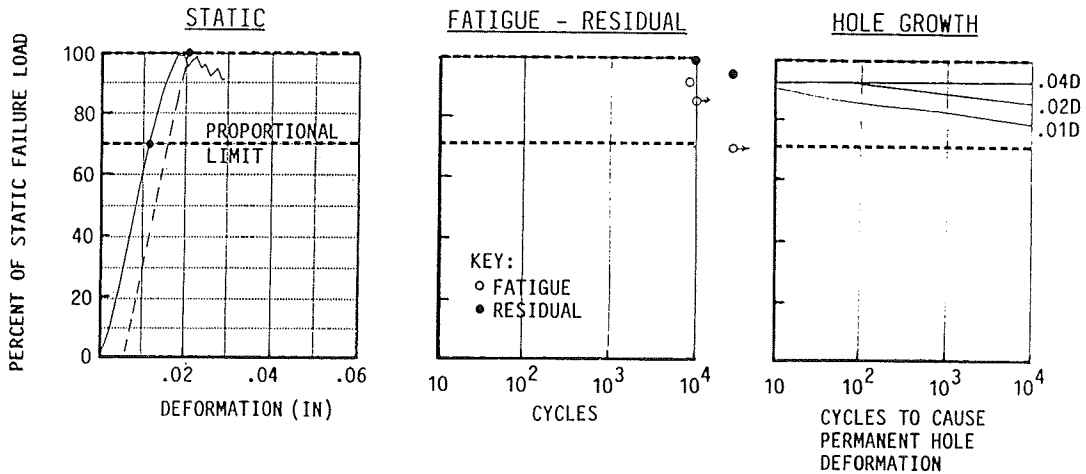
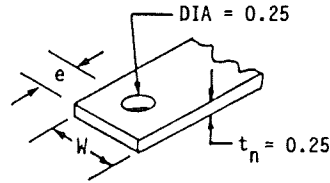
MATERIAL: 2024-T3
 e/D: 4.0
 W/D: 8.0
 ENVIRONMENT: RTD



- BEARING STIFFNESS INCREASED DURING CYCLIC TESTING

FIGURE 11. BEARING BEHAVIOR, 2024-T3, e/D = 4.0

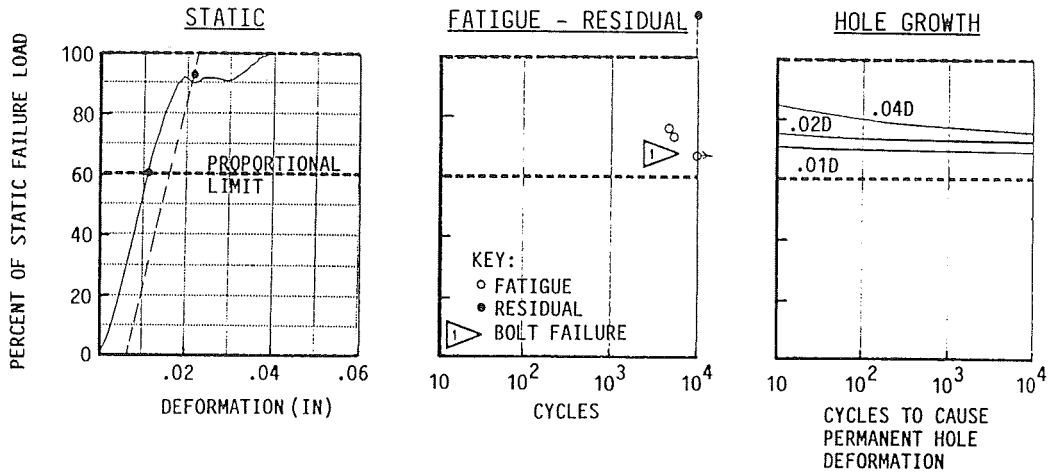
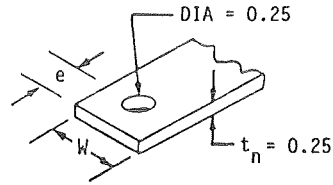
MATERIAL: 50/0/50 FABRIC
 e/D: 2.5
 W/D: 8.0
 ENVIRONMENT: RTD



- BEARING STIFFNESS DID NOT CHANGE SIGNIFICANTLY DURING CYCLIC LOADING.

FIGURE 12. BEARING BEHAVIOR, 50/0/50 FABRIC, e/D = 2.5

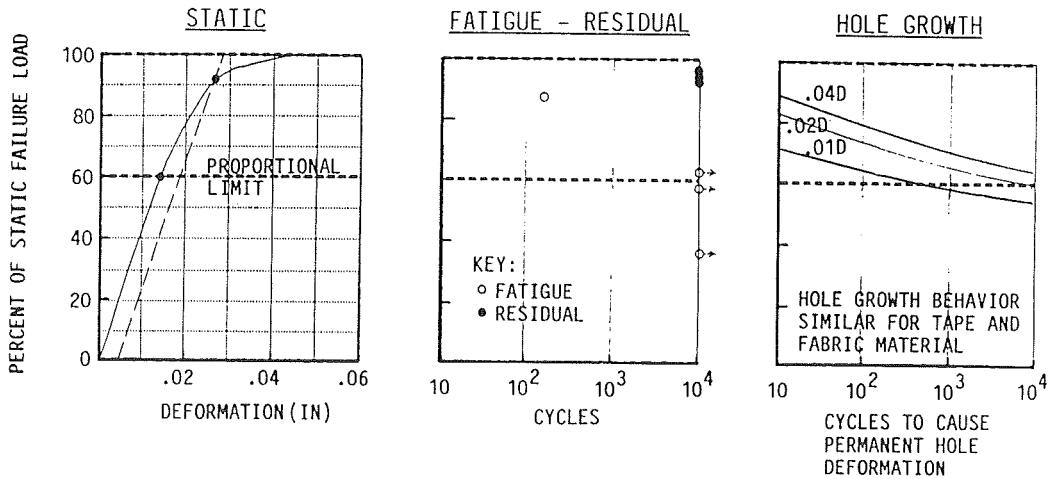
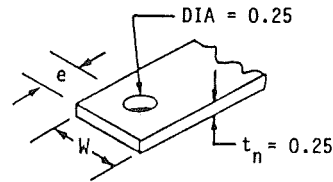
MATERIAL: 25/50/25 TAPE
 e/D: 2.5
 W/D: 8.0
 ENVIRONMENT: RTD



- BEARING STIFFNESS DID NOT CHANGE SIGNIFICANTLY DURING CYCLIC LOADING.

FIGURE 13. BEARING BEHAVIOR, 25/50/25 TAPE, e/D = 2.5

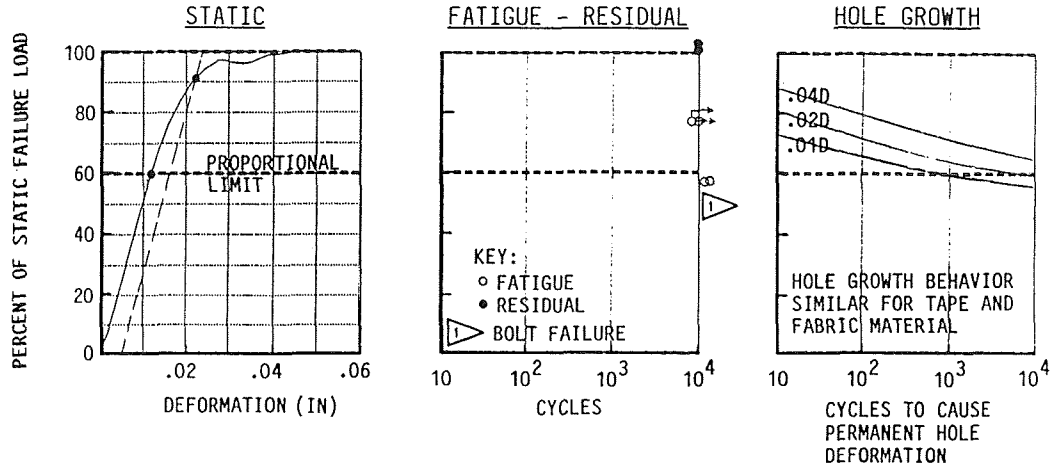
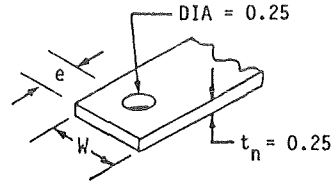
MATERIAL: 0/100/0 TAPE
 e/D: 2.5
 W/D: 8.0
 ENVIRONMENT: RTD



- BEARING STIFFNESS DID NOT CHANGE SIGNIFICANTLY DURING CYCLIC LOADING.

FIGURE 14. BEARING BEHAVIOR, 0/100/0 TAPE, e/D = 2.5

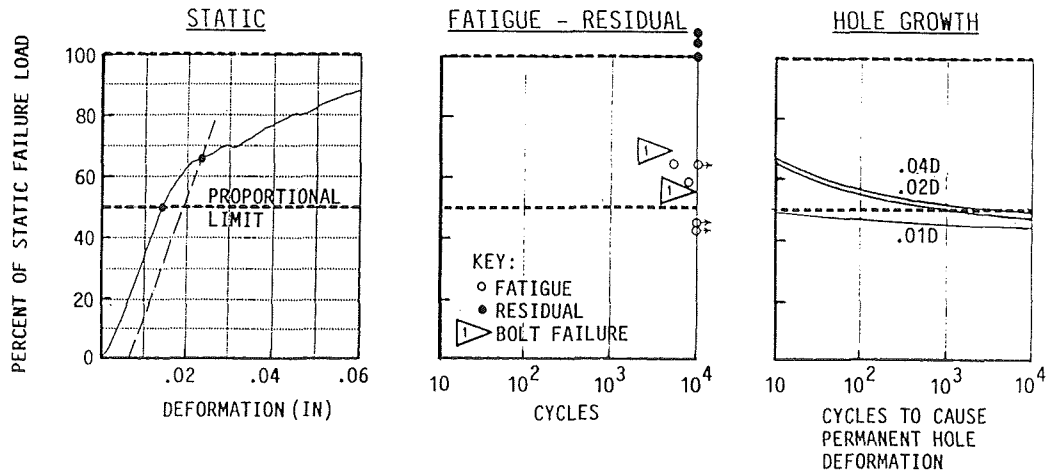
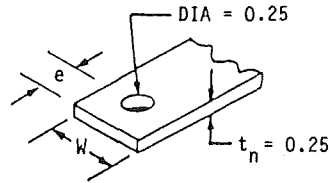
MATERIAL: 0/100/0 FABRIC
 e/D: 2.5
 W/D: 8.0
 ENVIRONMENT: RTD



- BEARING STIFFNESS DID NOT CHANGE SIGNIFICANTLY DURING CYCLIC LOADING.

FIGURE 15. BEARING BEHAVIOR, 0/100/0 FABRIC, e/D = 2.5

MATERIAL: 0/100/0 FABRIC
 e/D: 8.0
 W/D: 8.0
 ENVIRONMENT: RTD



- BEARING STIFFNESS DID NOT CHANGE SIGNIFICANTLY DURING CYCLIC LOADING.

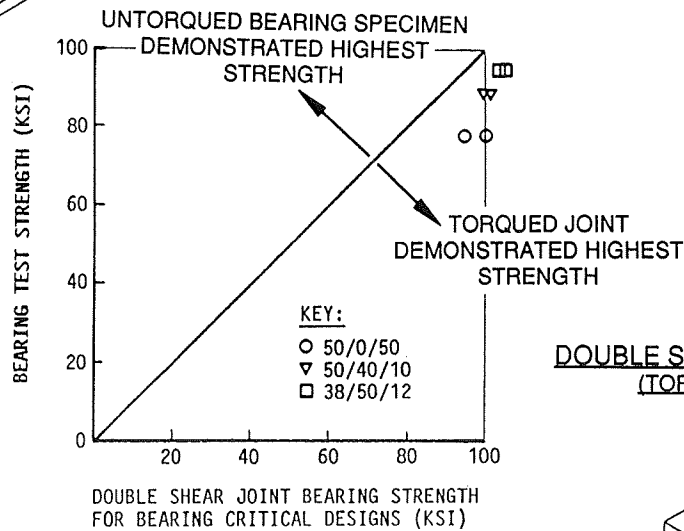
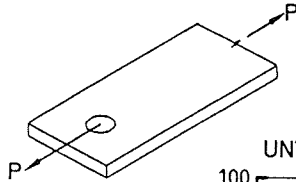
FIGURE 16. BEARING BEHAVIOR, 0/100/0 FABRIC, e/D = 8.0

PERFORMANCE AT LOWEST OF 2% DIAMETER OFF-SET LOAD OR 0.67 x MAX STATIC LOAD						
MATERIAL OR GR/EP LAMINATE DESIGN	e/D	LOAD LEVEL (% OF MAX STATIC)	FATIGUE FAILURES BEFORE 10,000 CYCLES	RESIDUAL STRENGTH REDUCTION AFTER 10,000 CYCLES	CYCLES TO GROW HOLE TO .04 DIA	BEARING STIFFNESS CHANGE AFTER 10,000 CYCLES
2024-T3	2.5	60	NO	YES (10%)	<10	INCREASE
2024-T3	4.0	47	NO	NO	<10	INCREASE
50/0/50 FABRIC	2.5	67	NO	NO	>>10,000	NONE
25/50/25 TAPE	2.5	67	NO	NO	>>10,000	NONE
0/100/0 TAPE	2.5	67	NO	YES (5%)	1,000	NONE
0/100/0 FABRIC	2.5	67	NO	NO	1,000	NONE
0/100/0 FABRIC	8.0	66	NO	NO	10	NONE

ENVIRONMENT: RTD
W/D: 8.0

FIGURE 17. SUMMARY - BEARING BEHAVIOR OF GR/EP AND 2024 ALUMINUM MATERIALS

BEARING TEST SPECIMEN
(UNTORQUED FASTENERS)



DOUBLE SHEAR JOINT SPECIMEN
(TORQUED FASTENERS)

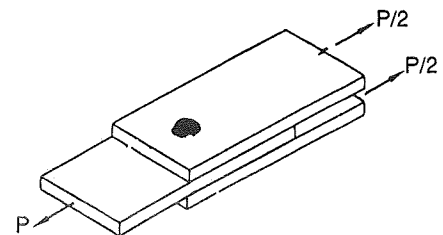


FIGURE 18. COMPARISON OF BEARING STRENGTH FOR BEARING AND JOINT TEST SPECIMENS

COMPRESSION FAILURE OF ANGLE-PLY LAMINATES

L.D. Peel¹
Mirage Carriage Works
West Valley, UT

M.W. Hyer²
Department of Engineering Science and Mechanics
Virginia Polytechnic Institute and State University
Blacksburg, VA

M.J. Stuart³
Aircraft Structures Branch
NASA-Langley Research Center
Hampton, VA

NASA
58-24
51376
P12

ABSTRACT

Test results from the compression loading of $(\pm \theta / \mp \theta)_{8S}$ angle-ply IM7-8551-7a specimens, $0 \leq \theta \leq 90^\circ$, are presented. The observed failure strengths and modes are discussed, and typical stress-strain relations shown. Using classical lamination theory and the maximum stress criterion, an attempt is made to predict failure stress as a function of θ . This attempt results in poor correlation with test results and thus a more advanced model is used. The model, which is based on a geometrically nonlinear theory, and which was taken from previous work, includes the influence of observed layer waviness. The waviness is described by the wave length and the wave amplitude. The theory is briefly described and results from the theory are correlated with test results. It is shown that by using levels of waviness observed in the specimens, the correlation between predictions and observations is good.

INTRODUCTION

The compression loading of composite structures continues to present an interesting challenge to the designer. Unlike tensile loading, the seemingly simple task of testing for allowable levels of compressive stress often leads to results that are open to question. A number of methods for determining compression strength are available [1]. However, different fixture and specimen designs can lead to different results for supposedly identical materials. Aside from the issue of allowable stress levels, there is also the question of what really is the loading on a structure. Eccentricities can cause a loading to be one of compression plus bending, when the intent was to have a purely compressive load. In addition, fabrication of the structure can lead to defects and variations in the material that could well control failure. Nonuniform resin distribution, broken fibers, dropped plies, and ply waviness are but a few of the imperfections that find their way into actual composites. To make progress in understanding the broad issue of compression failure, narrower and more focused topics should be studied. This paper presents the results of an experimental and theoretical investigation

¹ Former graduate student, Department of Engineering Science and Mechanics, Virginia Polytechnic Institute and State University

² Professor

³ Assistant Branch Head

of the compression failure of angle-ply laminates. A fixture that loads specimens in an end-loaded fashion was used to study the failure of $(\pm \theta / \mp \theta)_{65}$ laminates as a function of the off-axis angle θ , $0 \leq \theta \leq 90^\circ$. The material considered was IM7-8551-7a. The failure stresses, failure strains, and failure modes were examined for three replicate specimens at each angle. In an effort to understand the failures, the failure data at specific off-axis angles, as determined from the testing, and from published results, were used in conjunction with classical lamination theory and the maximum stress criterion [2] to predict the relation between failure stress and off-axis angle. Prediction of the mode of failure as well as the magnitude of the failure stress were of interest. Unfortunately, the correlation between the predictions and experimental results was not good. For low off-axis angles, $0 \leq \theta \leq 15^\circ$, the predictions were roughly a factor of two higher than the experimental results. For off-axis angles in the range $15 \leq \theta \leq 45^\circ$ the discrepancy was not as severe. For $\theta > 45^\circ$, a range that represents a less useful class of laminates, the correlation was good. Based on observations of the laminates tested, and the observations of other similar laminates [3], it was postulated that ply waviness was responsible for the discrepancies. Work of this nature had been done before both with flat laminates [4] and in the context of pressure-loaded cylinders [5]. To address the issue of waviness in these compression-loaded angle-ply specimens, an analytical model was proposed that was based on previous work [4]. The results of this model were used in conjunction with the maximum stress criterion to predict the observed test results. To follow is a summary of the test results, a brief explanation of the analytical model, and predictions of failure that are based on the model. These predictions are compared with the test results from the angle-ply specimens.

TEST RESULTS

The short-block compression fixture used in the testing phase of the study is shown in fig. 1. The fixture consists of two identical halves and in the figure a specimen is positioned in the bottom half of the fixture. It is seen that a sliding portion of the fixture can be made to snug against each end of the specimen to prevent end-brooming. Each specimen was gaged with 4 strain gages mounted back-to-back and side-to-side to measure axial strain, and to aid in assuring a uniform compression loading. A fifth transverse gage measured Poisson effects. A direct current displacement transducer (DCDT) was used to measure the overall change in length of the specimen.

The stress vs. strain relations for a 0° , a 20° , and a 45° specimen are shown in figs. 2, 3, and 4, respectively. In each figure the average response of the four axial strain gages, the response of the transverse gage, and the overall strain response as measured by the DCDT are shown. The strain response of the transverse gage was actually negative. These strains are on the horizontal axis. The vertical axis represents the nominal stress normalized by Young's modulus for the specimen in the direction of loading. As can be observed, the stress-axial strain response for the 0° specimen was nearly linear to failure. There was an offset in the relation as measured by the DCDT but this was due to the usual slack that is present when measuring displacements. If this offset is removed by manipulating the data, then the axial strain as measured by the gages and the axial strain as measured by the DCDT would agree quite well. The slopes of the two stress-strain relations were nearly identical. For the 20° specimen the response was also reasonably linear to failure. The 45° specimen showed considerable nonlinearity, the stress-axial strain relation exhibiting a definite knee and being practically bilinear. The erratic vertical line indicates failure of the strain gages due to the strains becoming excessive. The strain as measured by the DCDT continued past that point, however. These three figures exemplify the range of stress-axial strain behavior observed for these specimens. For off-axis angles $\theta > 45^\circ$, the stress-axial strain relations

were decreasingly nonlinear as θ approached 90° . The strains to failure, however, became greater and greater as the off-axis angle increased.

The relation between compression strength, based on an average of the three replicate tests, and off-axis angle is shown in fig. 5. In the range $0 < \theta < 10^\circ$ the strength was practically independent of θ . For $10 < \theta < 45^\circ$ the strength decreased steadily with θ , while for $\theta > 45^\circ$ the strength was again independent of θ . As important as the magnitude of the failure stress is the failure mode. In the range $0 < \theta < 10^\circ$ classic kink band formation was observed, along with inplane transverse tension failure (splitting) or inplane shearing failure. Both inplane transverse tension failure and inplane shearing failure can result in a clean break within a layer parallel with the off-axis fiber direction. This clean break was observed. The clean break indicated that either the strength of the matrix or the strength of the fiber-matrix interface, or both, controlled failure. However the kink band indicated fiber compression failure was also involved. In the range $15 < \theta < 30^\circ$ a clean break along the off-axis fiber direction in the absence of kink band formation was observed. This indicates that the strength in this range of θ relied solely on matrix strength and/or fiber-matrix interface strength. For $\theta > 45^\circ$ failure was also along lines parallel with the off-axis fiber direction. Due to the softening nature of the material at these off-axis angles, there was not the clean break, however. For this range of θ some delamination was also observed. This could have occurred after the initial inplane failure.

Table 1 summarizes the important specimen responses measured during the testing. The numerical values in Table 1 are the average of the repeat tests at a given off-axis angle. Note that the calculation for Poisson's ratio, ν_{xy} , was made at 40% of the maximum load. Erratic and nonlinear response of the transverse gage at low and high load levels led to this approach.

COMPARISON WITH CLASSICAL THEORY

Though the experimental data were important in their own right, it was also important to be able to predict failure. In particular, it was important to be able to use data from external sources, or data from the tests themselves, to construct a failure theory that correlated well with observations. In that regard, failure stresses from the 45° and 90° specimens, and data from ref. 6 were used with stress calculations based on classical lamination theory and the maximum stress criterion in an attempt to predict failure over the range of θ . The elastic and strength properties used in these calculations are indicated in Table 2. The correlation between the classical theory and test results are indicated in fig. 6. In the figure there are several predicted failure loci, each locus representing a different failure mode. The test results are represented by closed circles and the predictions by various other closed symbols, the triangles representing failure due to fiber compression, the squares representing failure due to inplane normal stresses transverse to the fiber, and the diamonds representing failure due to inplane shear stresses. In the theory transverse tension occurs for $\theta < 45^\circ$, while transverse compression occurs for $\theta > 45^\circ$. As can be observed, for low off axis angles correlation was quite poor. Obviously failure mechanisms or laminate characteristics not represented by the classical theory were present and not being accounted for. These effects appear to be very important at the low off-axis angles and less important at the higher off-axis angles.

Scraps of the panels from which the specimens were machined were examined for any anomalies or unusual characteristics. The examination revealed a number of anomalies, including layer waviness. The waviness was on the order of 10 to 20 layer thicknesses in length and 0.2 to 0.5 layer thicknesses in amplitude. It was assumed that waviness was present in

the specimens themselves, though it would be difficult to prove a posteriori. With a compressive loading, layer waviness would seem to be a serious issue. Waviness could produce an eccentricity in the loading in particular layers, the eccentricity overloading the layers, generating unwanted interlaminar shear stress, or simply leading to layer level instabilities. In regard to this latter point, a laminate can be considered as a group of stiff, parallel, fiber-dominated plates connected to each other through soft, matrix-dominated interlaminar layers. With a compressive loading the stiff plates (layers) can buckle, either individually, or as a group, depending on the mechanics of layer to layer interaction. Due to the interaction between layers, any buckling that is likely to occur would be of the short wavelength type, as opposed to overall Euler buckling. The wavelength of the short wavelength buckling mode could well be in the range of the length of the waviness observed in the specimen panels. A useful calculation would be to determine the short wavelength values for the laminates.

In this context, then, a previously developed model was called upon to evaluate the role of waviness on the compression strength of the angle-ply laminates. Each layer was modelled as a stiff plate which was assumed to obey the Kirchhoff hypothesis. Geometric nonlinearities, in the sense of von Karman, were included in the analysis of each plate. Adjacent plates were connected by a matrix-dominated layer. The displacements in these layers were controlled by the displacements of the adjacent plates. Essentially, the matrix layers were modelled by a simple shear lag theory. The assemblage of plates was assumed to be compressed by a uniform inplane strain, each plate being compressed the same amount. All four edges of each plate were assumed to be simply supported. This assumption does not match the boundary conditions for the test fixture shown in fig. 1. However, it was anticipated that the short wavelength buckling mode would result in wave lengths in the individual layers of no more than 50 layer thicknesses in length. This would result in a large number of wavelengths in both the lengthwise and widthwise directions of the laminate, large enough so that the actual boundary conditions would not influence the calculation of stresses and deformations within a single wave.

The geometrically nonlinear model described above was used to derive the linearized buckling equations for the assemblage of plates, and the equations governing the compressive response in the presence of layer waviness. Layer waviness was assumed to consist of an initial sinusoidal half-wave out-of-plane deformation of the layers. The wavelength λ and the amplitude δ of the half-wave imperfection were considered known. Wavelengths equal to the critical buckling wavelength and wavelengths representative of the anomalous waviness observed in the panel scraps were considered. The critical buckling wavelengths were determined from the linearized buckling model. The geometrically nonlinear analysis used the wave length and wave amplitude information to compute the response of the laminate with wavy layers to the applied compressive loading. The computation of response relied on using the Kantorovich method and a numerical scheme to solve the governing equations. Further details of the model can be found in ref. 4.

The stresses computed with the advanced theory were used with the maximum stress criterion to predict failure. In addition, an interlaminar shear strain criterion was used to evaluate the possibility of interlaminar failure. The shear strain of interest was in the plane that is perpendicular to the laminate, and parallel to the direction of loading.

COMPARISONS WITH THE ADVANCED THEORY

The comparison between the numerical predictions from the advanced theory and the observations from the tests are illustrated in figs. 7, 8, and 9. Focusing on fig. 7, the predictions from the advanced theory are shown as nonfilled triangles, squares, and diamonds. The predictions from the classical theory are also included for comparison and these are shown, as they were in fig. 6, as closed triangles, squares, and diamonds. The test data are shown as closed circles. Shown is the predicted compressive strength as a function of off-axis angle. An imperfection with a wavelength equal to 20 times a layer thickness and a wave amplitude equal to 0.1 of a layer thickness, t ; i.e., $\lambda = 20t$ and $\delta = 0.1t$, was used to produce the numerical results. Including the predictions based on the classical theory provides an indication of the influence of waviness on compressive response and strength.

Figure 7 is quite complex. Considerable failure information is shown. Specifically, for each mode of failure, i.e., fiber compression, inplane shear, etc., a failure locus is shown. For the advanced theory each locus was generated by computing the response of the angle-ply specimens as a function of off-axis angle and determining the applied stress level that caused failure for that mode. Clearly, for any given off-axis angle only one mode is important, that mode being the one that results in the lowest compressive stress. However, it is interesting to see how waviness influences the mechanics of the problem to change the dominance of one mode over the others. The calculations are not a continuous function of off-axis angle because the numerical calculations are computer-intensive, and hence expensive, as they are based on a nonlinear theory. Therefore the calculations were done for 5° increments of the off-axis angle. Two levels of interlaminar failure shear strain, $(\gamma_{IL})_{\max}$, are included because of the range of values reported in the literature (see, for example, ref. 7).

Examining fig. 7 in detail, it is seen that layer waviness strongly influences failure due to excessive fiber compressive stresses. The open triangles, which represent the fiber failure mode in the presence of waviness, are at a much lower stress level than the closed triangles, the symbols representing fiber failure stresses for the perfectly flat laminate, i.e., the classical theory. For low off-axis angles, waviness of the level used in the calculations could well explain the differences observed between the classical predictions and the test results. Continuing with an examination of fig. 7, for the range $15^\circ \leq \theta \leq 30^\circ$, the open squares with crosses, the symbols representing inplane failure transverse to the fibers, correlate well with the test data. The locus for this mode of failure based on the classical theory is represented by the closed squares. It can be seen that the inplane transverse stress locus is influenced by waviness. Regarding failure for any given mode, it should be noted that since waviness can introduce bending in the specimen, the failures predicted by the advanced theories for the various modes do not occur in every off-axis layer simultaneously. The bending causes the stresses on one side of the specimen, and indeed, on one side of each layer, to be different than the stresses on the other side of the specimen and layer. For the classic theory, where the specimen is assumed perfectly flat, failure in a given mode occurs in every layer at the same time. It is interesting to note in fig. 7 that interlaminar shear effects become important at low off-axis angles. However, for this level of waviness the interlaminar failure mode does not appear as important as the fiber compression failure mode.

The influence of the wavelength of the initial waviness is illustrated in fig. 8. In that figure calculations for a wavelength half that used in fig. 7, but with the same wave amplitude, are shown. Specifically, fig. 8 illustrates the influence of waviness with the parameters $\lambda = 10t$ and $\delta = 0.1t$. Comparing fig. 8 with fig. 7, it is seen that wavelength appears to have a significant influence on controlling the failure mechanisms at low off-axis angles. The fiber compression mode locus, represented by the open triangles, is traced out at very low stress

levels. The transverse tension mode locus, represented by the open squares with crosses, has dropped relative to the longer wavelength case; and for that matter, relative to the classic case. Also, the interlaminar shear strain failure locus using $(\gamma_{IL})_{max}=0.025$ begins to match the test data. This degree of waviness is felt to be quite severe. The linearized buckling analysis indicated that for low off-axis angles, the critical short wave length, λ_{cr} , is about 25 layer thicknesses in length. For high off-axis angles, $\lambda_{cr} = 10t$.

The influence of wave amplitude on the predicted failure characteristics is shown in fig. 9. In this figure $\lambda=20t$ and $\delta=0.2t$. This represents a wave amplitude twice that used in fig. 7, the wave length being the same. Focusing again on low off-axis angles and using fig. 7 for comparison, it is seen that the increased wave amplitude has a detrimental effect on the fiber compression failure mode. Relative to the lower amplitude wave of fig. 7, the locus for the fiber compression mode is considerably lower. Comparing the influence of decreasing the wave length by a factor of two, fig. 8, to increasing the wave amplitude by a factor of two, it is clear the failure locus for fiber compression failure is much more sensitive to the wavelength parameter. In addition, the inplane transverse tension locus seems to be more sensitive to wave length than wave amplitude, though that distinction is not as dramatic as the influence on the fiber compression locus. On the other hand, relative to the case of fig. 7, the interlaminar failure mode seems to be influenced equally as much by wave length as by wave amplitude. Observations such as these have led some researchers to characterize the effects of waviness by a single imperfection parameter defined as the ratio of wave amplitude to wave length, i.e.,

$$I = \frac{\delta}{\lambda}. \quad (1)$$

For the cases of fig. 8 and fig. 9 $I=0.01$. Based on this observation, and similar observations for results not shown, it appears that the interlaminar shear failure locus, and the inplane shear failure locus, depend only on the value of this ratio rather than the individual values of λ or δ . For the fiber compression locus, however, it is evident such a parameter may not have as much significance.

As the severity of the wave increases, say, by considering the case $\delta=0.2t$ and $\lambda=10t$, the inplane transverse tension and the inplane shear loci actually drop below the fiber compression locus. Thus shear in these specimens, be it inplane or interlaminar, can actually control the response over a significant range of θ .

SUMMARY AND CONCLUSIONS

Presented has been a discussion of the influence of layer waviness on the compression strength of angle ply laminates. The work was motivated by discrepancies between test results and predictions based on simple theory. From the results presented it can be concluded that there is an influence of waviness on the predicted compression strength. As with any study there are a number of issues that are still left unanswered by the proposed theory. Brooming of the ends of the specimens could be an alternative explanation for the discrepancies. However, what is important is that the proposed theory indicates that compression strength is sensitive to a number of factors, including the possibility of interlaminar shear failure in supposedly flat specimens, or inplane transverse tensile failure at low off-axis angles. That these mechanisms are possible is important because they must be included in other models.

ACKNOWLEDGMENTS

The work reported on was supported by Grant NAG-1-343, the NASA-Virginia Tech Composite Program, from NASA Langley Research Center's Aircraft Structures Branch to Virginia Tech. The financial support is greatly appreciated.

REFERENCES

1. Schoeppner, G.A. and Sierakowski, R.L., "A Review of Compression Test Methods for Organic Matrix Composites," *J. Composites Technology and Research*, vol. 12, no. 1, pp. 3-12, 1990.
2. Jones, R.M., Mechanics of Composite Materials, McGraw-Hill, Inc., 1975.
3. Shuart, M.J., "Failure of Compression-Loaded Multidirectional Composite Laminates," *AIAA Journal*, vol. 19, no. 9, pp. 1274-1279, 1989.
4. Shuart, M.J., "Short-Wavelength Buckling and Shear Failures for Compression-Loaded Composite Laminates," NASA TM 87640, 1985.
5. Telegadas, H.K. and Hyer, M.W., "The Influence of Layer Waviness on the Stress State in Hydrostatically Loaded Cylinder: Further Results," *J. Reinforced Plastics and Composites*, vol. 9, no. 5, pp. 503-518, 1990.
6. Hercules Internal Report No. H050-347, pp. 8-9, available Hercules, Inc., Magna, UT, 1989.
7. Cogull, S.L. and Adams, D.F., "Mechanical Properties of Several Neat Polymer Matrix Materials and Unidirectional Carbon Fiber-Reinforced Composites," University of Wyoming Report UW-CMRG-R-88-114, 1988.

Table 1 - Tabulated IM7/8551-7a Test Results

Angle	$\sigma_{x, failure}$ (ksi) ^a	$\epsilon_{x max}$ ($\times 10^{-3}$)		E_x (Msi)	ν_{xy} (@ 40% max. load)
		gage strain	DCDT strain		
0	114 ^b	5.91 ^b	7.20 ^b	21.0 ^b	0.323 ^b
5	113	6.16	8.26	20.2	0.446
10	111	6.82	8.21	18.8	0.609
15	102	6.95	8.06	16.3	0.813
20	70.7	5.97	6.80	12.8	1.037
30	44.0	7.21	8.26	7.49	1.439
45	34.4	c	128	2.46	0.876
60	33.2	c	56.2	1.47	0.334
70	33.2	c	45.9	1.39	0.154
75	33.3	c	42.0	1.32	0.0844
80	32.5	36.6	39.0	1.32	0.0502
85	32.0	37.3	34.5	1.29	0.0249
90	31.4	35.3	33.1	1.28	0.0160

a – P/A_{nom} b - average values from multiple specimens c - strain gage reached upper limit

Table 2 - IM7/8551-7a Elastic Properties and Strengths

Compression Elastic Properties				Strengths		
E_{11}	21.0*	Msi		S_f	240.0 ⁶	ksi
E_{22}	1.28*	Msi		S_2^c	31.4*	ksi
G_{12}	0.707*	Msi		S_2^t	7.70 ⁶	ksi
ν_{12}	0.360 ⁶			S_{12}	17.2*	ksi
E neat resin	0.590 ⁷	Msi				
G neat resin	0.260 ⁷	Msi				
ν neat resin	0.360 ⁷					

* from present experiments

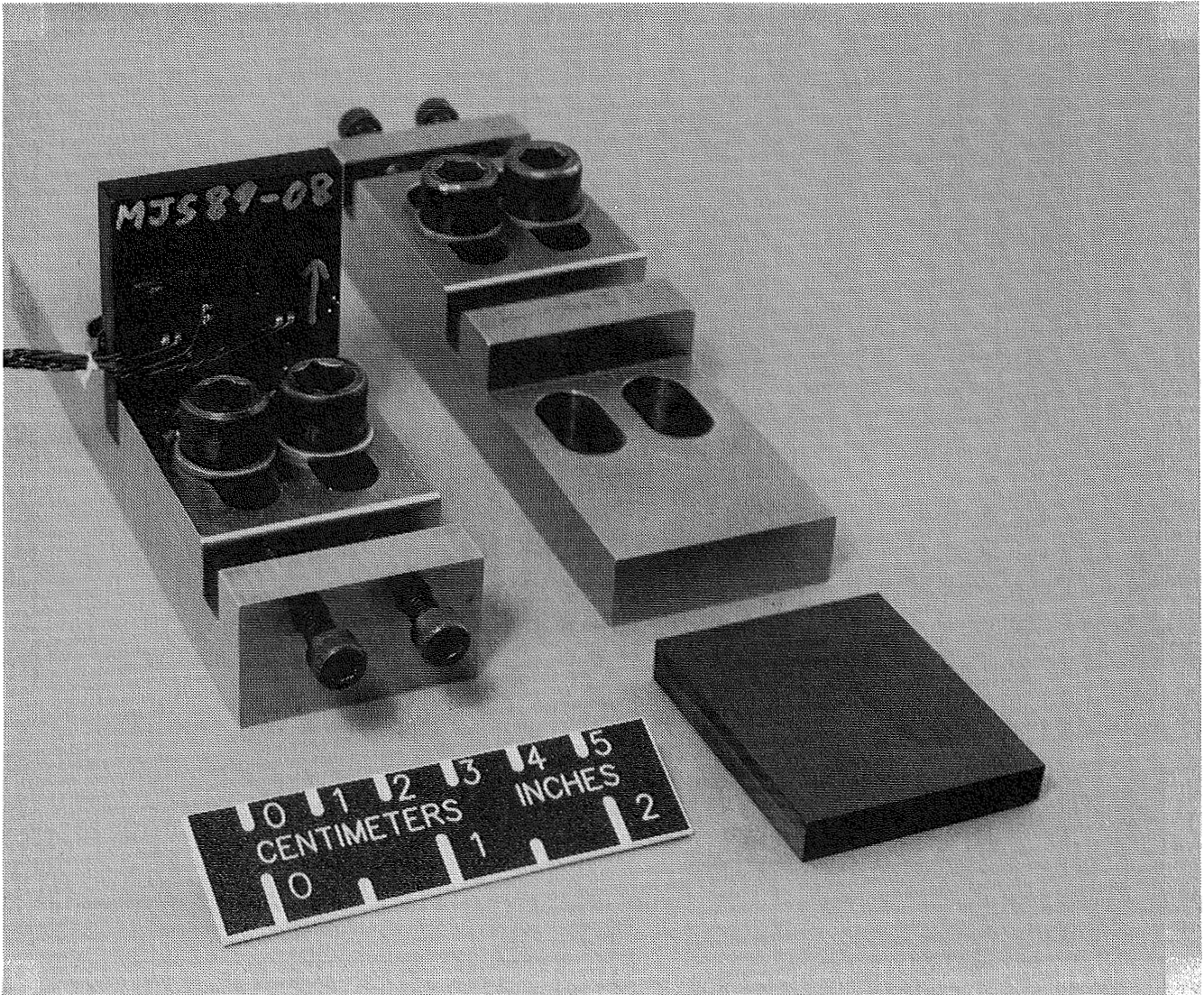


Fig. 1 - Short-Block Compression Fixture.

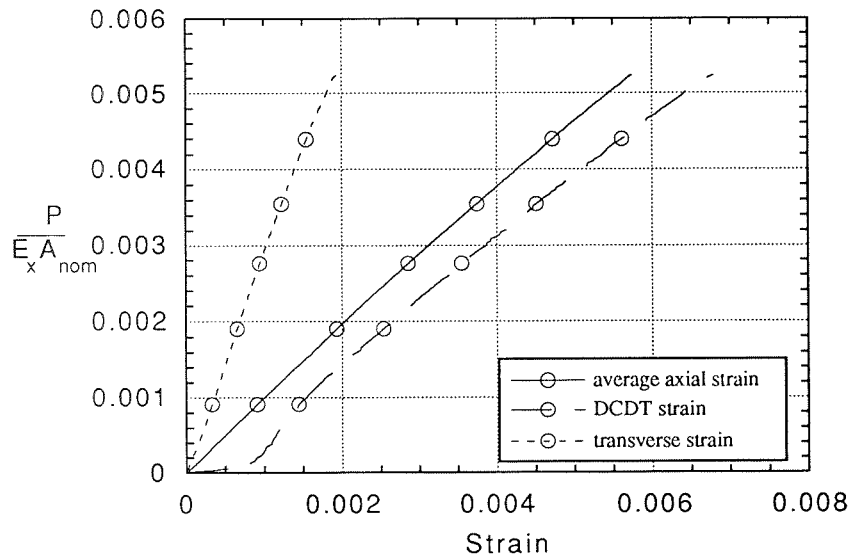


Fig. 2 - Stress - Strain Relations for 0° Specimens.

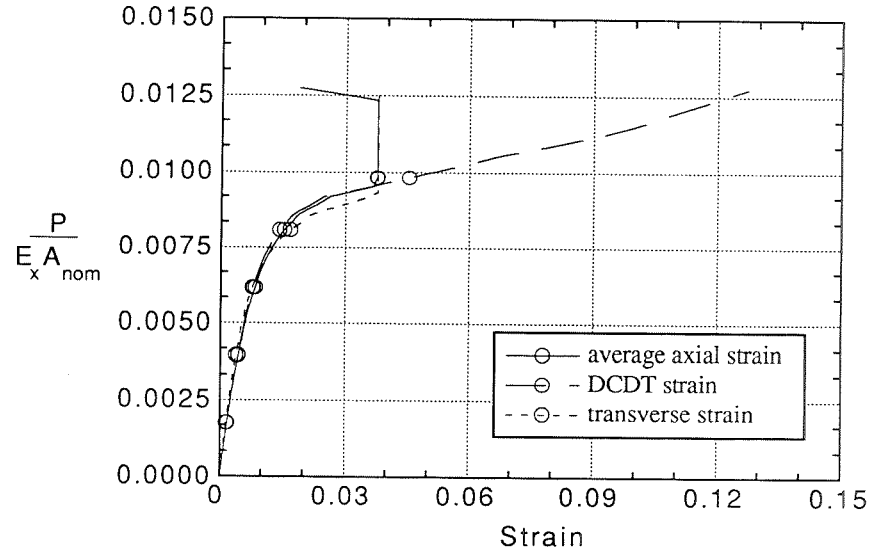


Fig. 4 - Stress - Strain Relations for 45° Specimens.

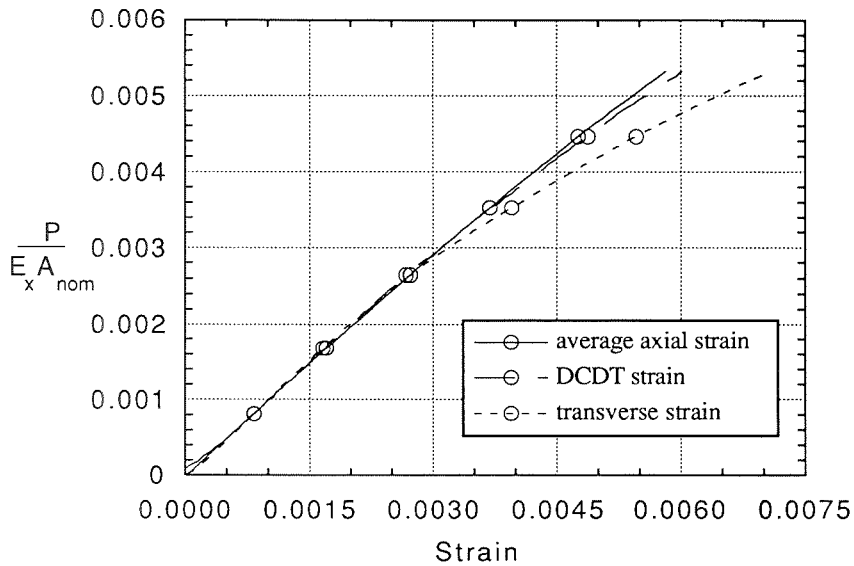


Fig. 3 - Stress - Strain Relations for 20° Specimens.

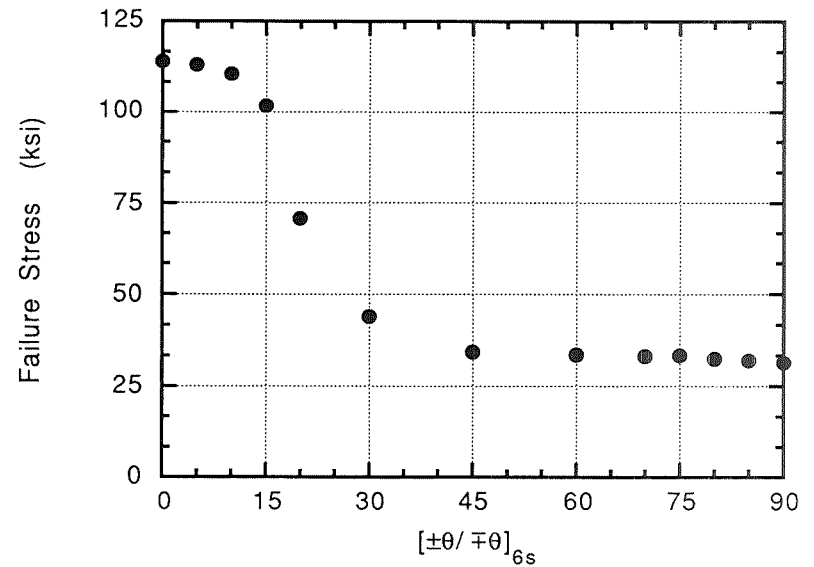


Fig. 5 - Compression Strength as a Function of Off-Axis Angle.

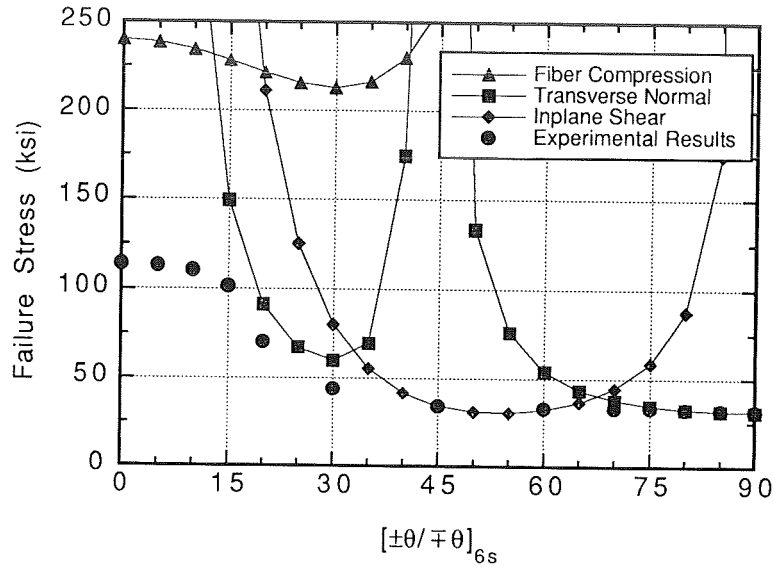


Fig. 6 - Comparison between Predictions Based on the Classical Theory and Test Results.

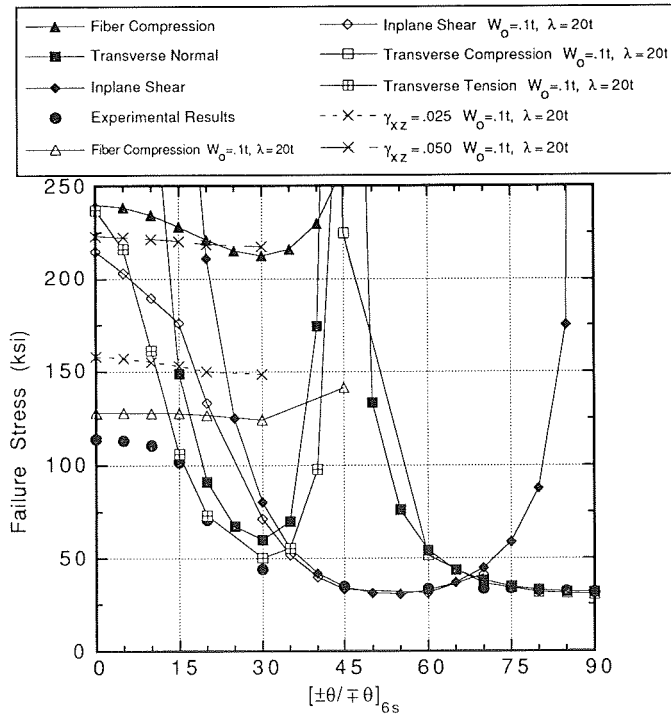


Fig. 7 - Comparison between Predictions Based on the Advanced Theory and Test Results, $\lambda = 20t$ and $\delta = 0.1t$.

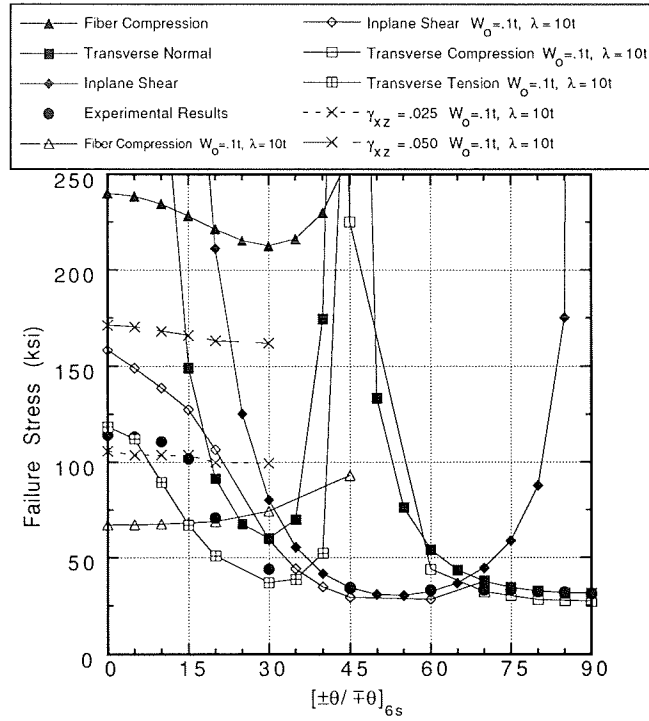


Fig. 8 - Comparison between Predictions Based on the Advanced Theory and Test Results, $\lambda = 10t$ and $\delta = 0.1t$.

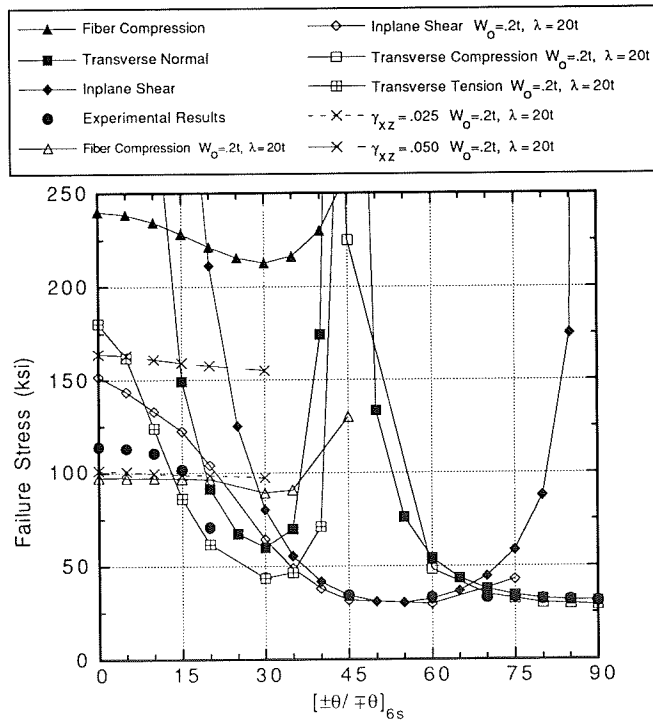


Fig. 9 - Comparison between Predictions Based on the Advanced Theory and Test Results, $\lambda = 20t$ and $\delta = 0.2t$.

ANALYSIS OF COMPOSITE STRUCTURES WITH DELAMINATIONS UNDER COMBINED BENDING AND COMPRESSION¹

Han-Pin Kan
Northrop Corporation, Aircraft Division
Hawthorne, California

59-24

Edward Kautz
Naval Air Development Center
Warminster, Pennsylvania

51377
P-22

Larry Neri
FAA Technical Center
Atlantic City Airport, New Jersey

ABSTRACT

A methodology has been developed for strength prediction of composite structures with delaminations under combined bending and compression loads. The methodology is an extension of the delamination analysis method developed under the USAF/Boeing/Northrop "Damage Tolerance of Composites" program. Delamination buckling and strain energy release rate analyses are used as basic tools in the strength prediction. In addition, failure mode interaction and structural configuration effects are taken into consideration. The influence of fasteners on the strength of a delaminated structure is incorporated to evaluate assembly-caused delaminations. The capabilities and limitations of the analysis method are demonstrated by correlating the analytical results with existing experimental data. The failure load, failure mode and failure sequence of a structure containing delaminations are predicted and the analytical results are compared with test data.

INTRODUCTION

The current trend in aircraft design is to use advanced composite materials in primary and secondary structure, wherever possible, in order to reduce weight and increase performance. During assembly of these structures, interply delamination of composites can occur. When an assembly utilizes bolts, for example, delaminations can occur when torquing the bolts causes mating parts to be forced together due to the existence of an unshimmed gap between those parts. Delaminations occurring during final assembly are of particular concern because final assemblies are not generally subjected to non-destructive inspection, and, even if an inspection is performed, not all areas are accessible after final assembly. These delaminations can cause

¹ This work was performed under NADC/FAA/Northrop Contract N62269-90-C-0282, entitled "Delamination Methodology for Composite Structures."

significant reduction in the load carrying capability of structure, particularly in compression strength and in the strength of structure subjected to out-of-plane loading. In addition, there is a potential for delamination growth under fatigue loading, which can further reduce load carrying capability. Therefore, it is very important to have a validated methodology for assessing the severity of known delaminations with respect to their effects on strength and life so repair/replacement decisions can be made.

In recent years, considerable effort has been devoted to the development of delamination analysis methods for composite structures. These analyses have been of two types: (1) one-dimensional analyses for through-the-width delaminations in composite structural members and (2) two-dimensional analyses that focus on a delaminated region in a composite plate. The two-dimensional analyses have been developed for specialized delamination geometries (e.g., circular, elliptical, or rectangular delaminations).

One-dimensional analysis methods are given in References 1 through 9. With the exception of References 2 and 6, which are based on a finite element approach, each of the one-dimensional methods provides closed-form results using a beam-column model. Two-dimensional delamination analysis methods are given in References 1 and 10 through 19. References 14, 15, and 18 are based wholly or partially upon finite element analysis. The remaining analyses are based upon classical plate methods or Rayleigh-Ritz approaches applied to circular or elliptical delaminations in a composite panel.

The effects of delamination on the static strength and fatigue life are experimentally examined in References 1, 3, 4, 10 and 20 through 23. An extensive database was generated in Reference 1. The parameters investigated in this reference include material, test environment, laminate thickness and layup, delamination size and location, and structural configuration. A systematic review of experimental data was also conducted in Reference 1.

The objective of the present paper is to develop an analysis method for strength and failure mode prediction of composite structures containing assembly caused delaminations. To achieve this objective, the methodology developed in Reference 1 is first extended to include the effects of out-of-plane bending on the strength of delaminated composite laminate. This analysis method is then modified to accommodate the presence of a hole and a torque-up fastener.

ANALYSIS DEVELOPMENT

The analysis method developed in Reference 1 is used in the present work as a baseline methodology. In the reference, a three-part analysis was developed. These are: (1) delamination buckling analysis, (2) strain-energy-release-rate computation, and (3) failure predictions. This analytical procedure is discussed in the following paragraphs.

Delamination Buckling Analysis

Laminate with an Elliptical Delamination Subjected to Combined Bending and Compression Loads. Consider a composite laminate with an elliptical delamination subjected to combined bending moment and axial compression as shown in Figure 1. The delaminated layer (layer 1 in the figure) consists of n plies with thickness t_1 . This layer is treated as a thin, elastic, orthotropic, elliptical plate with major and minor axes a and b , respectively. The plate boundary is considered to be between simply supported and fully clamped. A boundary fixity coefficient $0.0 \leq \alpha \leq 1.0$ is used to describe the boundary condition. The value of α is 0 when the boundary is fully clamped and $\alpha = 1.0$ for a simply supported boundary.

Under combined loading, the strain due to axial force (ϵ^A) and the strain due to bending moment (ϵ^B) are obtained from the classical lamination theory. These strains are given by

$$\epsilon^A = -\frac{N}{A_{11}} \quad (1)$$

and

$$\epsilon^B = \frac{My}{D_{11}} \quad (2)$$

where M is the bending moment per unit width of the laminate
 N is the axial compression per unit width of the laminate
 A_{11} is the axial stiffness of the laminate
 D_{11} is the bending rigidity of the laminate
 y is the distance from the neutral axis of the laminate to the point of interest

The buckling load of the delaminated layer is obtained using the method of Reference 1 and is given by:

$$N_{\text{crd}} = \frac{1}{a^2} \left[(12-8\alpha)D_{11d} + 8 \left(\frac{a}{b} \right)^2 D_{12d} + (12-8\alpha) \left(\frac{a}{b} \right)^4 D_{22d} + 16 (1-\alpha) \left(\frac{a}{b} \right)^2 D_{66d} \right] \quad (3)$$

where D_{11d} , D_{12d} , D_{22d} and D_{66d} are the bending rigidities of the delaminated layer.

The buckling load of the delaminated layer is obtained by equaling the total force in the layer to the critical load given in equation (3).

The total force in the delaminated layer is computed by summing the forces in each ply of the layer. This force is given by

$$N_d = \frac{N}{A_{11}} \sum_{i=1}^{n_d} A_i + \frac{M}{D} \sum_{i=1}^{n_d} A_i y_i \quad (4)$$

where the summation is over the n_d plies.

At buckling $N_d = N_{crd}$, or the right hand side of equation (3) is equal to the right hand side of equation (4).

Laminate with an Elliptical Delamination Around A Fastener Subjected to Combined Bending and Compression Loads. A second delamination configuration considered here is used to simulate the assembly-caused delamination in built-up composite structures. The delamination configuration considered is illustrated in Figure 2. The analysis method is an extension of the energy method developed in Reference 1. The displacement function for the current method is assumed to be

$$w = A \left(1 - \frac{x^2}{a^2} - \frac{y^2}{b^2}\right)^2 \left(1 - \frac{x^2+y^2}{R^2}\right)^2 \quad (5)$$

where

A is an undefined coefficient

a and b are the major and minor axes of the elliptical delamination

R is the radius of the fastener hole

The displacement function defined in equation (5) represents a simply supported boundary around the delamination as well as around the hole. Thus, the clamp-up effect of the fastener head is conservatively approximated by the zero displacement around the hole. With this displacement function, the buckling load can be determined by the energy method. The strain energy is given by

$$U = \frac{1}{2} \iint [D_{11}w_{xx}^2 + 2D_{12} w_{xx} w_{yy} + D_{22} w_{yy}^2 + 4D_{66} w_{xy}^2] dx dy \quad (6)$$

where

D_{11} , D_{22} , D_{12} , and D_{66} are the plate (delamination) bending rigidities and subscripts x and y denote partial differentiations.

The double integral in equation (6) covers the area within the ellipse outside of the fastener hole, as shown by the shaded region in Figure 1. The delamination buckling load is obtained by letting the variation of the total potential energy equal to zero, that is

$$\delta (U - W) = 0 \quad (7)$$

where W is the work done by the external load. In the present problem

$$W = \frac{1}{2} \iint N_x w_x^2 \, dx dy \quad (8)$$

Substituting equation (5) into (6) and (8) resulting in 127 integrals in the general form of:

$$I = f(a, b, R) \left\{ \int_{-b}^{-R} \int_{-c_1}^{c_1} x^m y^n \, dx dy \right. \\ \left. + \int_R^b \int_{c_2}^{c_1} x^m y^n \, dx dy + \int_{-R}^{-R} \int_{-c_1}^{c_2} x^m y^n \, dx dy \right. \\ \left. + \int_{-R}^R \int_{c_2}^{c_1} x^m y^n \, dx dy \right\} \quad (9)$$

where m and n are positive integers $0 \leq m, n \leq 14$

$$c_1 = \frac{a}{b} \sqrt{b^2 - y^2}$$

$$c_2 = \sqrt{R^2 - y^2}$$

$f(a, b, R)$ is a polynomial in terms of a , b and R .

These lengthy algebraic manipulations were carried out and the results were coded into a computer program operational on personal computers.

Strain Energy Release Rate Computation

The value of the strain energy release rate (G) for an elliptical delamination varies around the periphery of the delamination front. This has

been shown in Reference 1 for laminates with a delamination loaded in compression. The analysis method of Reference 1 is used here for strain energy release rate computation. This method is applicable to both delamination configurations shown in Figures 1 and 2. In Reference 1, the strain energy release rate is computed based on the assumption that the inplane displacement along the lines AA and BB (see Figure 1) is constant through the width of the laminate. The strain energy release rate at a point y on the delamination front due to compression is then given by

$$G_A = \frac{1}{2} N_y (N_y - N_{cr}) \left[\frac{1}{E_{xs} t_s} - \frac{1}{E_x t} \right] \quad (10)$$

where N_y is determined based on the assumption that AA and BB remain straight under applied load. The relationship between N_y and the applied compression N is given by

$$N_y = \frac{\frac{aN}{t_2 E_{x2}} - (a-d) N_{cr} \left[\frac{1}{t_2 E_{x2}} - \frac{1}{t E_x} \right]}{\frac{d}{t_2 E_{x2}} + \frac{a-d}{t E_x}} \quad (11)$$

where

$$d = \frac{a}{b} (b^2 - y^2) \quad (12)$$

is the distance from the delamination centerline to the point of interest along the loading direction.

Similarly, the strain energy release rate due to applied bending moment is given by

$$G_B = \frac{1}{2} \left\{ \left(\frac{M_y - M_{cr}}{D_{11s}} \right)^2 \sum A_{11i} y_{si}^2 + \frac{M_{cr} (M_y - M_{cr})}{D_{11} D_{11s}} \sum A_{11i} y_{si} \right. \\ \left. - \left[\left(\frac{M_y}{D_{11}} \right)^2 - \left(\frac{M_{cr}}{D_{11}} \right)^2 \right] \sum A_{11i} y_i^2 \right\} \quad (13)$$

In equation (13) M_y , the effective moment, depends on the location of the point of interest. M_y is related to the applied bending moment (M) as

$$M_y = \frac{\frac{aM_{y_{si}}}{D_{11s}} - (a-d) M_{cr} \left[\frac{y_{si}}{D_{11s}} - \frac{y_s}{D_{11}} \right]}{\frac{dy_{si}}{D_{11s}} + \frac{(a-d) y_s}{D_{11}}} \quad (14)$$

where D_{11} is the bending rigidity of the laminate
 D_{11s} is the bending rigidity of the remaining layer (layer 2 in Fig. 1)
 y_s is the distance of the first ply beneath the delamination to the laminate neutral axis
 y_{si} is the distance of the first ply beneath the delamination to the neutral axis of the remaining layer

The total strain energy release rate is then given by

$$G_T = G_A + G_B \quad (15)$$

Failure Prediction

It was recognized early in the analysis development of Reference 1 that delaminations can cause several different failure modes which all have to be accounted for to predict residual strength correctly. Figure 3 summarizes the six potential failure modes for delaminated laminates. To account for these failure modes, it is necessary to predict:

1. Compression strength of a laminate with delaminations
2. Initial buckling strength
3. Local buckling strength
4. Global buckling strength
5. Laminate compression strength

These strengths are then plotted as a function of the delamination size. From such a plot, the overall laminate strength as a function of delamination size can be determined.

An example of such a plot is shown in Figure 4. In this example, it is assumed that the compression strength of the undamaged laminate is lower than the global buckling strength of the laminate. That is, when there is no delamination present in the laminate, the laminate failure mode is compression failure. When a delamination is introduced, both the failure mode and the failure strength depend on the delamination size. In Figure 4, the lower bound failure strength as a function of the delamination size is shown by a solid line, which can be divided into three regions. In Region I the size of the delamination is small, the initial buckling strength is high, and the failure strength equals the undamaged laminate compression strength (Failure Mode 1). In Region II the initial buckling strength is lower than the

undamaged laminate compression strength. The failure is initiated by initial buckling of the delamination followed by stress redistribution until finally, the compression stress in the remaining layer exceeds its compression strength (Failure Mode 2). In Region III the delamination size is large, the failure starts as initial buckling, and is followed by local buckling of the remaining layer (Failure Mode 5). In addition, the delamination may grow under static loading because of released strain energy (Failure Mode 6). As a result of delamination growth, the laminate may fail in either Mode 2, 4, or 5. Clearly, it is important to account for competing failure mode effects in the analysis of delaminated composite structures.

NUMERICAL RESULTS

A 24-ply, $(\pm 45/90/0/\pm 45/0_2/\pm 45/0_2)_s$ laminate is used as an example for numerical analysis. Results for both solid laminates with an elliptical delamination (Figure 1) and elliptical delamination around a clamp-up fastener hole are obtained. Initial buckling load, strain energy release rate and failure prediction for each delamination configuration are presented below.

Elliptical Delamination

The initial buckling load for the 24-ply $(\pm 45/90/0/\pm 45/0_2/\pm 45/0_2)_s$ laminate is shown in Figure 5. The figure shows the initial buckling load for the laminate with a 4-ply deep circular delamination with a boundary fixity coefficient of 0. Buckling loads (N_{cr}) for the N/M ratio of 10, 20, 50 and ∞ are shown in the figure. As can be seen in the figure, the buckling load depends on the axial force to bending moment ratio. The results of Reference 1 are recovered for $N/M = \infty$ (pure compression).

As stated earlier, the value of the strain energy release rate (G) varies around the delamination front. Only the maximum values are shown here, because those values control the growth of the delamination. The maximum strain energy release rate occurs at points along the delamination centerline normal to the loading direction. This result indicates that delamination growth would initiate in the direction normal to the applied load. In other words, the aspect ratio of the delamination (a/b) will decrease as delamination grows. Typical maximum strain energy release rates (G_{max}) are shown in Figures 6 and 7. In these figures the values of G_{max} , under constant laminate load, are plotted as a function of delamination radius. Figure 6 shows the values of G_{max} for a laminate subjected to pure bending with the delamination on the compression side. The values of G_{max} for the 24-ply laminate subjected to compression dominated loading ($N/M=50$) are shown in Figure 7. Both Figures 6 and 7 show similar trends for the value of G_{max} as a function of delamination size. That is, G_{max} remains zero when the applied load is below delamination buckling load. The value of G_{max} increases sharply following the initial buckling and stabilizes as the delamination size becomes larger.

The variation of G around the delamination front is shown in Figure 8. This figure shows that the variation of G around the delamination is more significant for increased bending (decreased N/M ratio).

The failure load, failure mode and failure sequence of the 24-ply laminate with a 4-ply circular delamination under combined load ($N/M=50$) are shown in Figure 9. The figure shows the results for a delamination with a boundary fixity coefficient of 0. It can be seen from the figure that, depending on the delamination size, there are four different failure modes. For small delamination, ($R \leq 0.65$ in) the delamination buckling load is high and laminate strength controls the failure of the damaged laminate. As the size of the delamination increases ($0.65 < R < 0.7$), the delamination buckled before failure occurs. However, no delamination growth takes place and the failure is controlled by the undamaged laminate strength. Further increases in delamination size ($0.7 \leq R < 0.85$), buckling and delamination growth take place prior to final laminate failure. For large delamination ($R \geq 0.85$ in) the failure load is controlled by the strength of the remaining layer. Failure occurs after buckling of the delaminated region and significant growth of the delamination.

Comparisons of observed (Reference 1) and predicted failure strains are shown in Figures 10 through 12. Figure 10 shows the effects of delamination size, shape and depth location on the residual strength of the laminate. The analysis correctly predicted the failure sequence and reasonably predicted the failure strain, except for the 4-ply deep 1.0-inch diameter delamination. For this delamination type, no delamination buckling was predicted. Experimental data, however, showed that buckling occurred at approximately 80% of the failure load. This deficiency may be due to the value of the boundary fixity coefficient chosen in the analysis (0.33).

The influence of the multiple delaminations on the residual strength of the laminate is shown in Figure 11. The figure shows that the analysis overpredicted the failure strain for specimens with three delaminations when $\alpha=0.33$ was used for all delaminations. However, if the inner sublaminates separated by the near surface and the mid-plane delaminations assumed a less constrained fixity the correlation can be significantly improved. The prediction agrees with experimental data for $\alpha = 0.7$ as shown in Figure 11.

The influence of laminate thickness on residual strength is shown in Figure 12. The analytical correlations are not conclusive because of the large number of tab failures during test of the thicker specimens. However, the predictions are conservative when compared with data for specimens with no tab failure.

Elliptical Delamination Around a Clamped Fastener Hole

The buckling load for an elliptical delamination around a clamped fastener hole (Figure 2) is obtained by using equation (7). After lengthy algebraic manipulations equation (7) is coded into a computer code operational on personal computers. Typical buckling loads based on this analysis method are shown in Figure 13. The figure shows the buckling loads for the 24-ply laminate with a 4-ply deep delamination around a 0.25 in. diameter fastener hole.

Figure 13 shows that the buckling load for this delamination configuration is very high, as compared to the buckling load for a circular delamination of equal size in a solid laminate (also shown in the figure for comparison purposes). This is an indication that for this laminate, smaller delaminations (smaller than 1.5 inches in diameter) failure is controlled by the effects of stress concentration of a filled fastener hole. The effects of delamination on the failure strength is small.

Failure of delaminations around fastener holes are similar to that in a solid laminate. However, because of the stress concentration effects induced by the fastener hole, a hole failure criterion must be used in the failure prediction. The average stress (strain) criterion proposed in Reference 24 with a filled hole correction factor is used in the present program. The average stress criterion predicts the failure stress (strain) of a laminate with an open hole. For a fastener hole with fastener installed, a correction factor of 1.15 is applied. This value of filled hole correction factor is obtained by comparing experimental data generated under a Northrop IRAD program (Reference 25).

The failure analysis method, the buckling analysis method and the strain energy release rate computation technique were integrated into a computer code for strength prediction. Typical results obtained from the computer program are summarized in Figure 14.

Figure 14 shows that the failure mode depends on the delamination size. For a delamination radius from 0.5 to 2.5 inches, there are three distinct failure modes. At a delamination radius up to 1.3 inch, the delamination buckling strength is high, failure of the laminate is governed by the filled hole strength of the delaminated plate. Failure may initiate in the delamination layer or the remaining layer, depending on the stress concentration factor of the respective layer. At a delamination radius of 1.4 inch, the delamination layer buckling strength is lower than the laminate strength. Thus, buckling occurs before the final failure. After the delamination buckled, release of strain energy takes place. However, for this delamination size, the energy release is not sufficient for delamination growth. The laminate failed in the remaining layer without delamination propagation. As the delamination size further increased, delamination growth occurs at load level N_G before the final failure at the filled hole in the remaining layer.

Results for the 24-ply laminate with 1-, 2-, 4- and 6- ply deep delamination are shown in Figure 15. The figure shows that for each delamination depth, there is a clear transition in failure mode. At a smaller delamination size, the failure mode is a filled hole strength failure with no buckling or delamination growth (mode 1 in Figure 14). With larger delamination, the mode of failure becomes a remaining layer hole failure after delamination buckling (with or without delamination growth, mode (2) or (3) in Figure 14).

SUMMARY

A methodology has been developed for strength prediction of composite structures with imbedded delaminations under combined bending and compression loads. The methodology is further modified to accommodate the presence of a fastener through an elliptical delamination by modelling the effects of fastener clamping force. Limited data correlation indicates that the methodology correctly predicts the failure load and failure sequence of delaminated composite laminates. Further verification of the methodology is currently being conducted under a NADC/FAA/Northrop contract N62269-90-C-0282, entitled "Delamination Methodology for Composite Structures".

REFERENCES

1. Horton, R. E., Whitehead, R. S., et al, "Damage Tolerance of Composites" AFWAL-TR-87-3030, Vol. I, II, and III, July 1988.
2. Kachanov, L. M., "Separation Failure of Composite Materials," Polymer Mechanics, Vol. 12, 1976, pp. 812-815.
3. Whitcomb, J. D., "Finite Element Analysis of Instability-Related Delamination Growth," Journal of Composite Materials, Vol. 15, September 1981, pp. 403-426.
4. Whitcomb, J. D., "Strain-Energy Release Rate Analysis of Cyclic Delamination Growth in Compressively Loaded Laminates," Effects of Defects in Composite Materials, ASTMSTP 836, American Society for Testing and Materials, 1984, pp. 175-193.
5. Chai, H., Babcock, C. D., and Knauss, W. G., "One Dimensional Modelling of Failure in Laminated Plates by Delamination Buckling," International Journal of Solids and Structures, Vol. 18, 1981, pp. 10.
6. Wang, S. S., Zahlan, N. M. and Suemasu, H., "Compressive Stability of Random Short-Fiber Composites, Part II - Experimental and Analytical Results," Journal of Composite Materials, Vol. 19, July 1985, pp. 317-333.
7. Ashizawa, M., "Fast Interlaminar Fracture of a Compressively Loaded Composite Containing a Defect," Proceedings of the Fifth DOD/NASA Conference on Fibrous Composites in Structural Design, New Orleans, Louisiana, January 1981.
8. Simitzes, G. J., Sallam, S., and Yin, W. L., "Effect of Delamination of Axially Loaded Homogeneous laminated Plates," AIAA Journal, Vol. 23, 1985, pp. 1437-1444.
9. Sallam, S., and Simitzes, G. J., "Delamination Buckling and Growth of Flat, Cross-Ply Laminates," Composite Structures, Vol. 4, 1985, pp. 361-381.
10. Konishi, D. Y., and Johnson, W. R., "Fatigue Effects on Delaminations and Strength Degradation in Graphite/Epoxy Laminates," Composite Materials: Testing and Design Fifth Conference, ASTM STP 674, American Society for Testing and Materials, 1979, pp. 597-619.
11. Chai, H., "The Growth of Impact Damage in Compressively Loaded Laminates," PhD Thesis, California Institute of Technology, March 1982.
12. Chai, H., and Babcock, C. D., "Two-Dimensional Modelling of Compressive Failure in Delaminated Laminates," Journal of Composite Materials, Vol. 19, January 1985, pp. 67-98.

13. Webster, J. D., "Flaw Criticality of Circular Disbond Defects in Compressive Laminates," Center for Composite Materials Report No. 81-03, 1981.
14. Shivakumar, K. N., and Whitcomb, J. D., "Buckling of a Sublaminar in a Quasi-Isotropic Composite Laminate," Journal of Composite Materials, Vol. 19, January 1985, pp. 2-18.
15. Whitcomb, J. D., and Shivakumar, K. N., "Strain Energy Release Analysis of a Laminate With a Postbuckled Delamination," Fourth International Conference on Numerical Methods in Fracture Mechanics, Pineridge Press, 1987, pp. 581-605.
16. Yin, W. L., "Axisymmetric Buckling and Growth of a Circular Delamination in a Compressed Laminate," International Journal of Solids and Structures, Vol. 21, 1985, pp. 503-514.
17. Fei, Z., and Yin, W., "Postbuckling Growth of a Circular Delamination in a Laminate Under Compression and Bending," Proceedings of SECTAM XII, Vol. II, May 1984, pp. 130-134.
18. Whitcomb, J. D., "Instability-Related Delamination Growth of Embedded and Edge Delaminations," NASA TM 100655, August 1988.
19. Marshall, R. D., Sandorff, P. E., and Laruaitis, K. N., "Buckling of a Damaged Sublaminar in an Impacted Laminate," Journal of Composites Technology and Research, Vol. 10, No. 3, 1988, pp. 107-113.
20. Ramkumar, R. L., "Fatigue Degradation in Compressively Loaded Composite Laminates," NASA CR 165681, April 1981.
21. Ramkumar, R. L., "Performance of a Quantitative Study of Instability-Related Delamination Growth," NASA CR 166046, March 1983.
22. Byers, B. A., "Behavior of Damaged Graphite/Epoxy Laminates Under Compression Loading," NASA CR 159293, August 1980.
23. Porter, T. R., "Compression and Compression Fatigue Testing of Composite Laminates," NASA CR 168023, 1982.
24. Whitney, J. M. and Nuismer, R. J., "Stress Fracture Criteria for Laminated Composites Containing Stress Concentrations," Journal of Composite Materials, Volume 8, 1974.
25. Whitehead, R. S., et al., "Advanced Material Development Program," Northrop IRAD D-1913, 1986-1991.

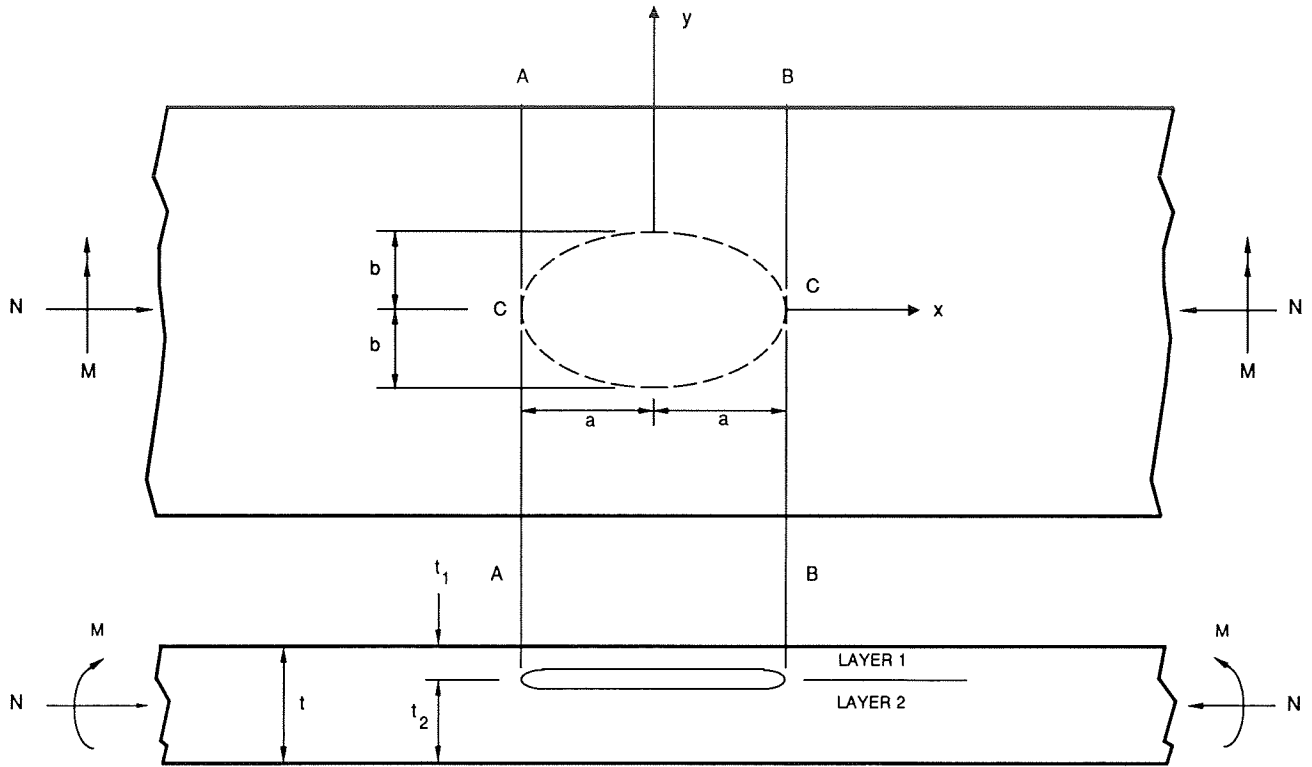


Figure 1. Laminate With an Elliptical Delamination.

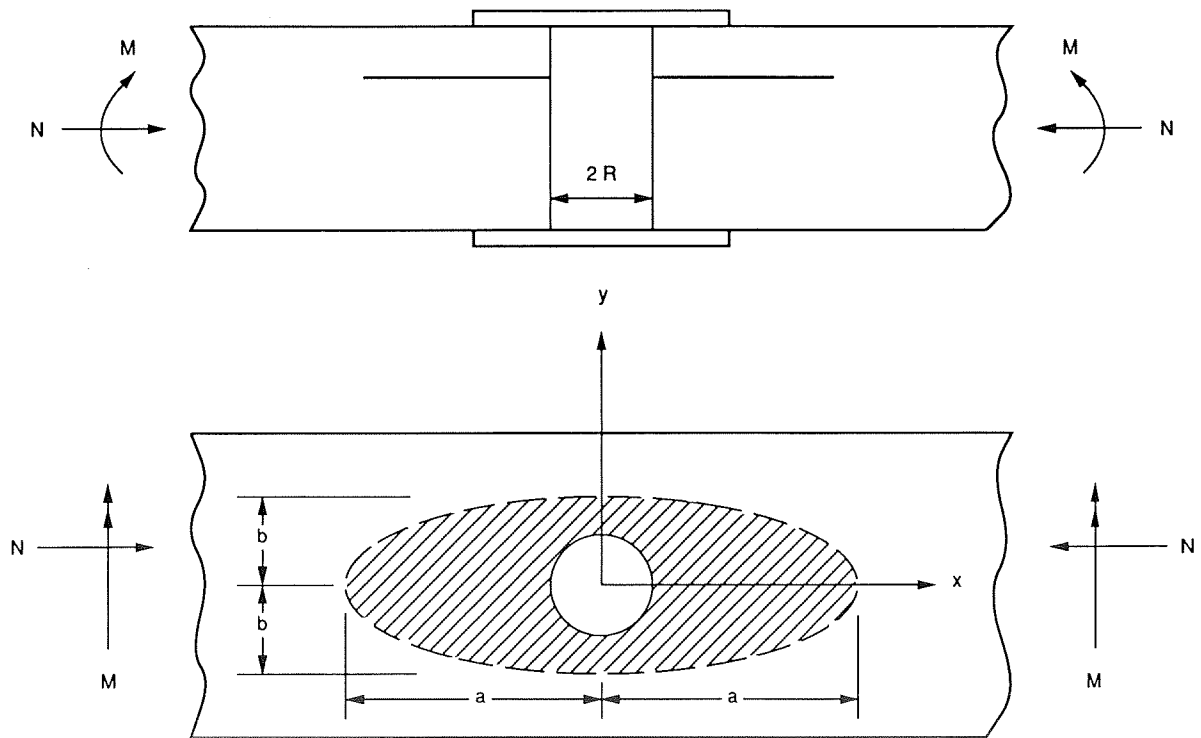
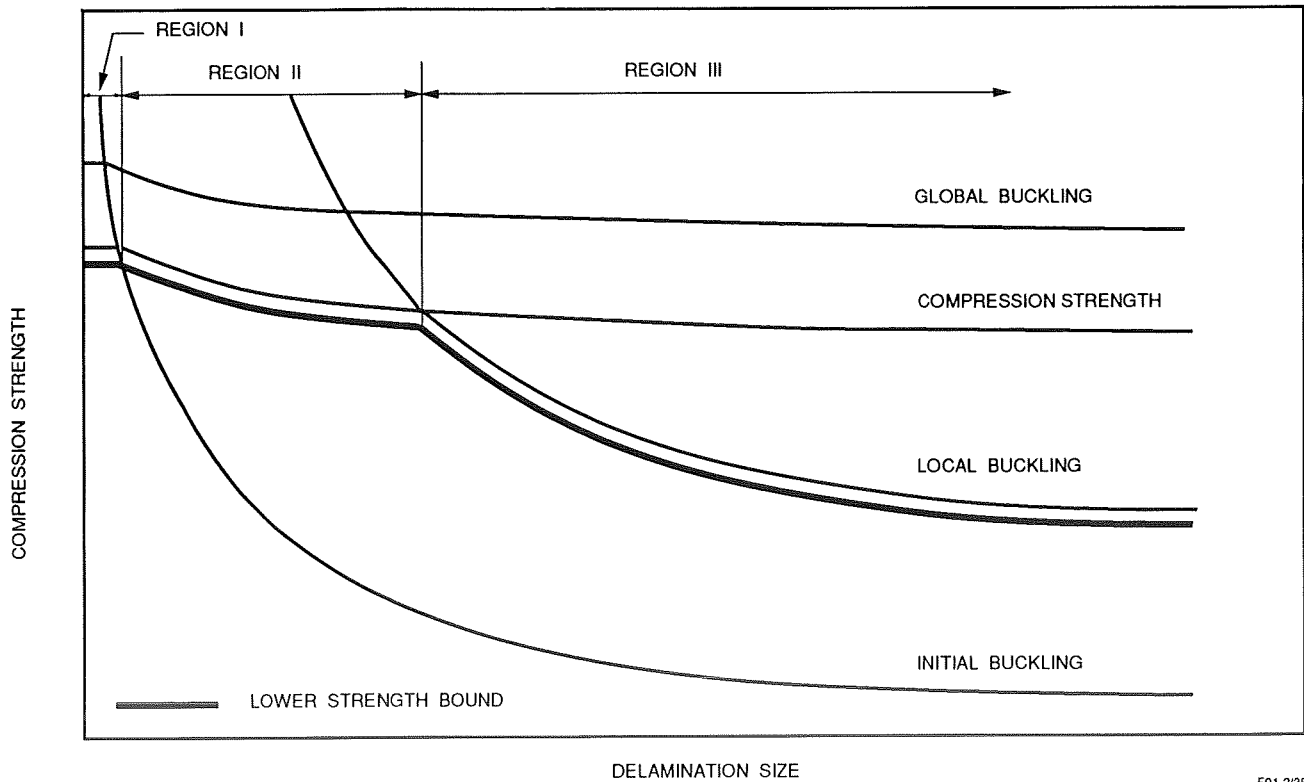


Figure 2. Delamination Around a Fastener Hole.

FAILURE MODE	DESCRIPTION
1	<p>INITIAL DELAMINATION COMPRESSION FAILURE GROSS COMPRESSION FAILURE</p>
2	<p>INITIAL DELAMINATION INITIAL BUCKLING COMPRESSION FAILURE INITIAL BUCKLING OF THE DELAMINATION FOLLOWED BY COMPRESSION FAILURE</p>
3	<p>INITIAL DELAMINATION GLOBAL BUCKLING</p>
4	<p>INITIAL BUCKLING INITIAL DELAMINATION INITIAL BUCKLING OF THE DELAMINATION FOLLOWED BY GLOBAL BUCKLING</p>
5	<p>INITIAL DELAMINATION LOCAL BUCKLING INITIAL BUCKLING OF THE DELAMINATION FOLLOWED BY LOCAL BUCKLING OF THE REMAINING LAYER</p>
6	<p>INITIAL DELAMINATION DELAMINATION GROWTH INITIAL BUCKLING OF THE DELAMINATION FOLLOWED BY DELAMINATION GROWTH AND EVENTUALLY FAILURE BY MODE 2, 4 OR 5</p>

F91-2/37

Figure 3. Static Failure Modes for a Laminate With Delamination.



F91-2/38

Figure 4. Failure Mode and Failure Strength Dependence on Delamination Size.

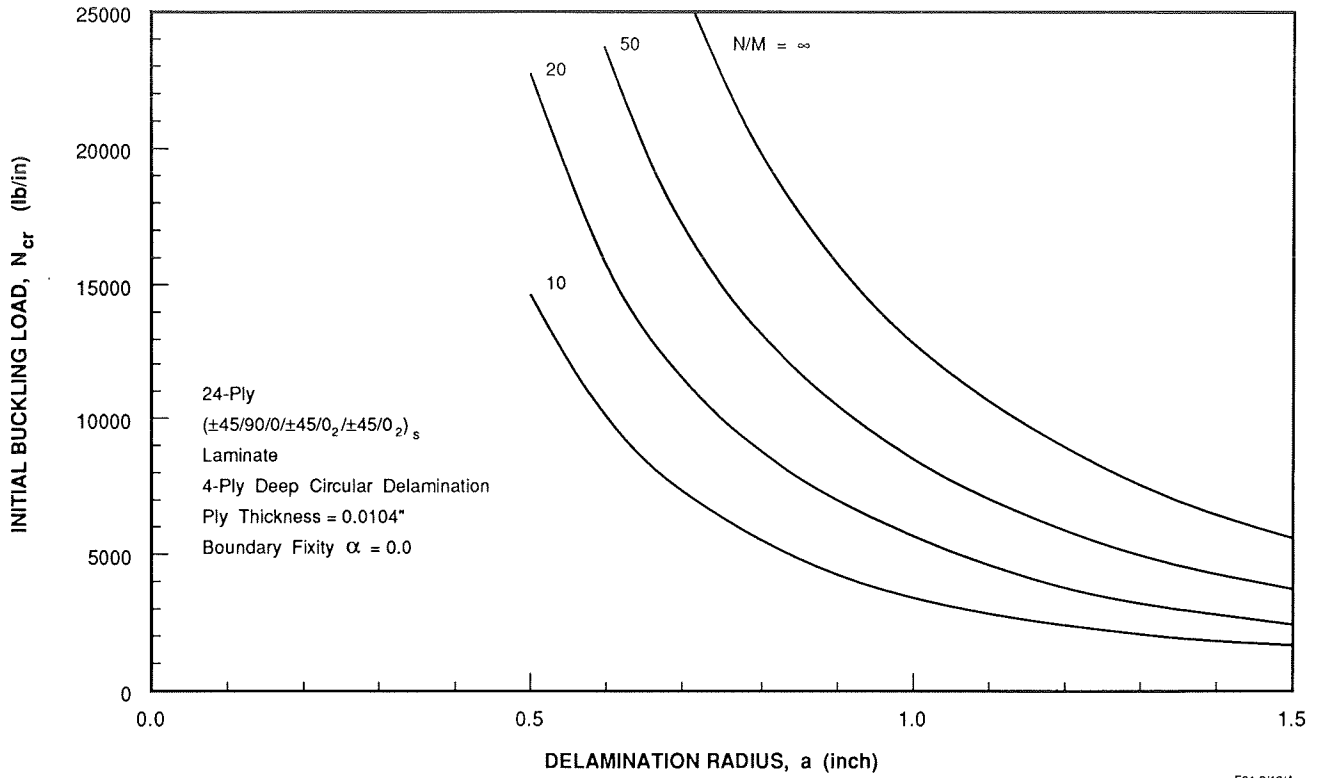


Figure 5. Initial Buckling Load for a 24-Ply Laminate With a Circular Delamination.

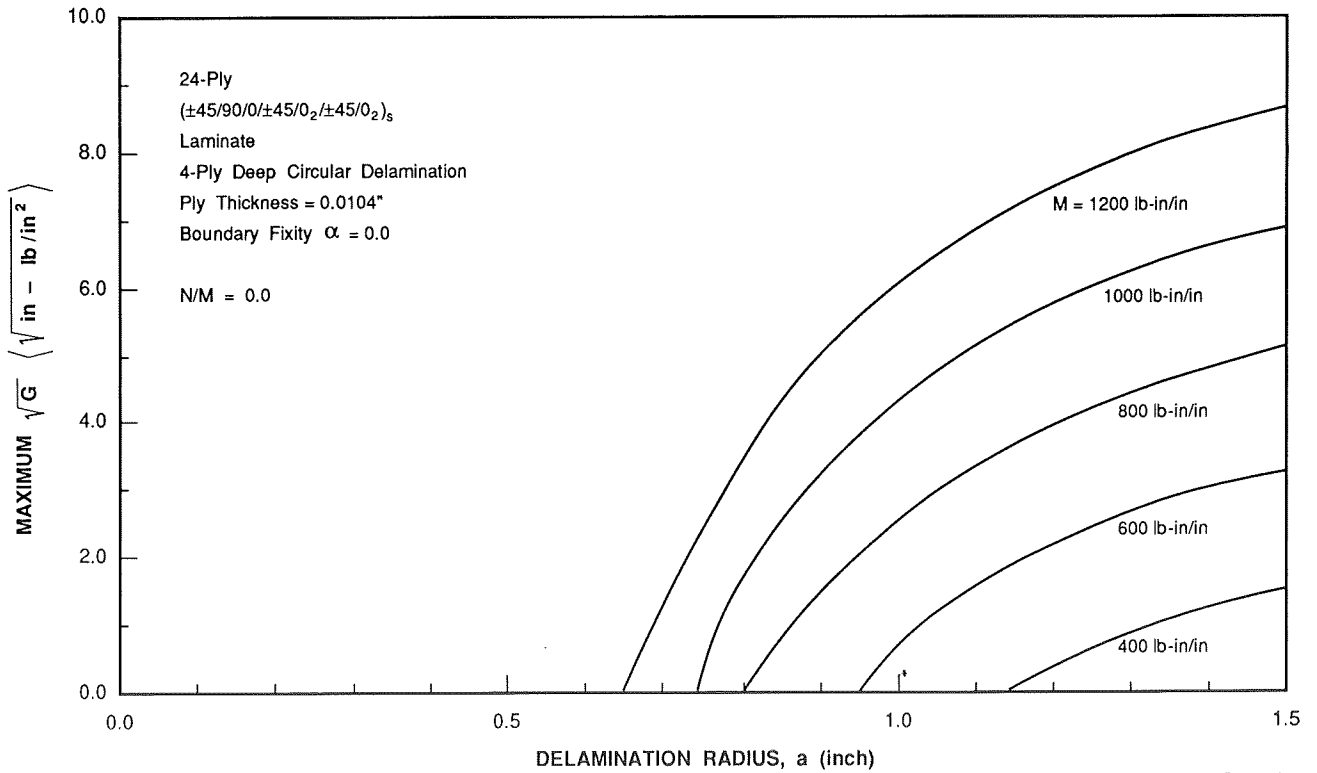


Figure 6. Strain Energy Release Rate for a 24-Ply Laminate With a Circular Delamination – Pure Bending.

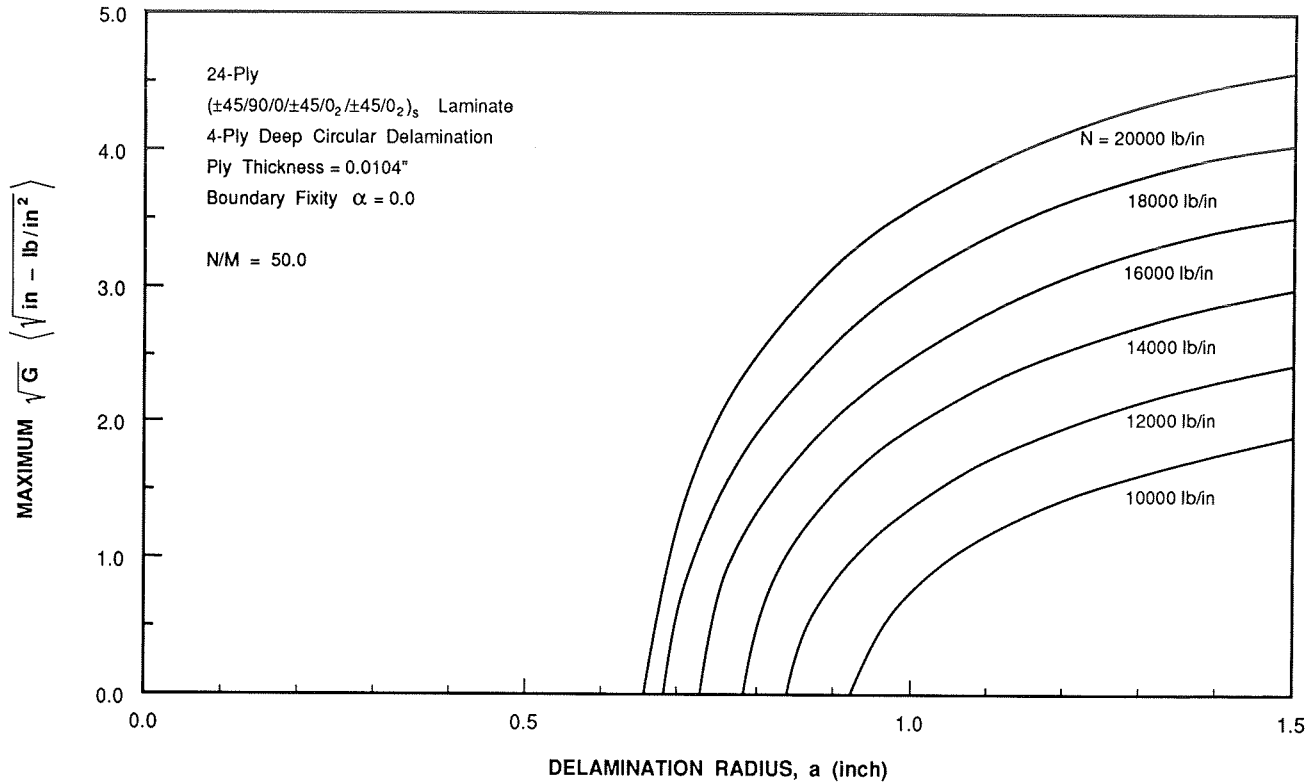


Figure 7. Strain Energy Release Rate for a 24-Ply Laminate With a Circular Delamination Under Combined Compression and Bending Loads – $N/M = 50.0$.

F91-2/14/A

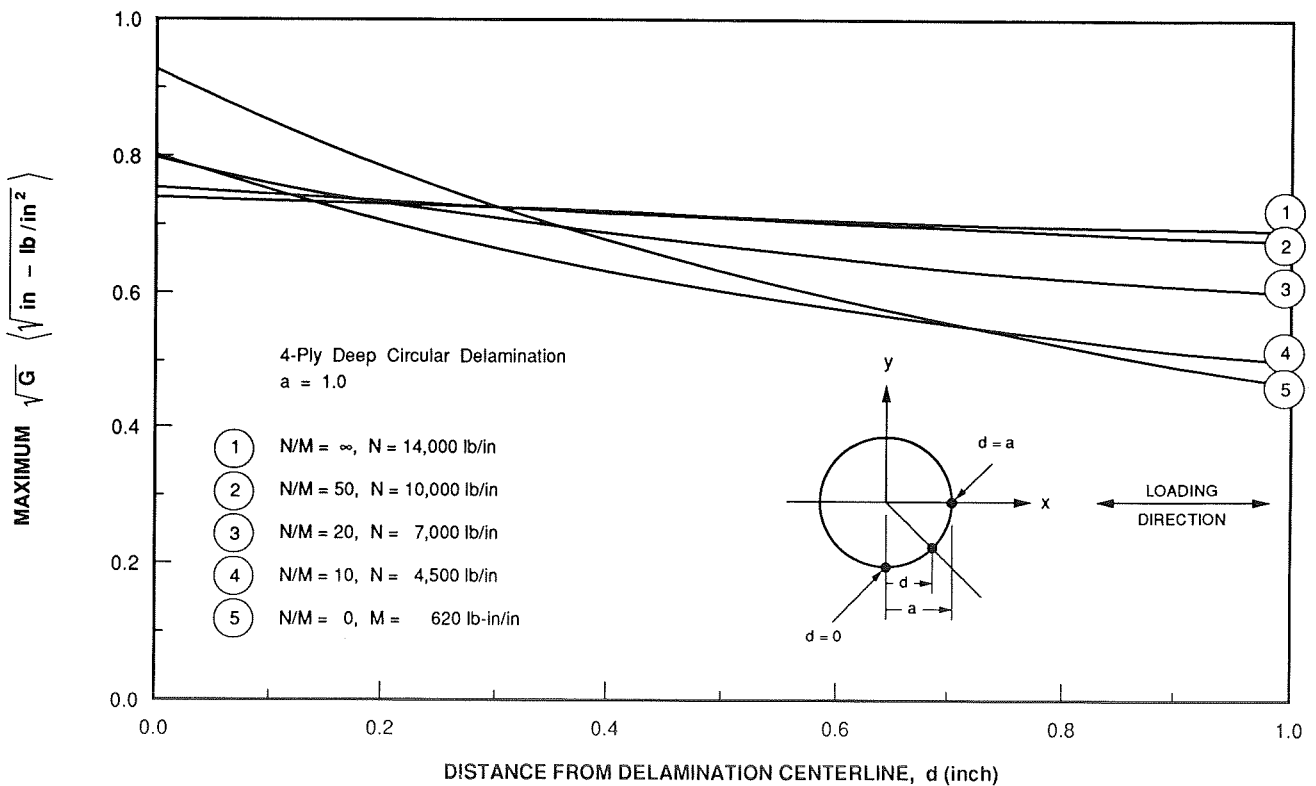


Figure 8. Strain Energy Release Rate Around the Periphery of a Circular Delamination.

F91-2/21/A

DELAMINATION RADIUS R (in)	BUCKLING LOAD N_{cr} (lb/in)	FAILURE LOAD N_f (lb/in)	FAILURE MODE
0.5	29,074	17,800	(1)
0.6	20,191	17,800	(1)
0.65	17,204	17,800	(2)
0.7	14,834	17,800	(3) $N_G = 16,239$
0.8	11,357	17,800	(3) 13,035
0.9	8,974	17,337	(4) 10,893
1.0	7,269	16,924	(4) 9,394
1.1	6,007	16,618	(4) 8,307
1.2	5,048	16,385	(4) 7,493
1.3	4,301	16,204	(4) 6,868
1.4	3,708	16,061	(4) 6,379
1.5	3,230	15,945	(4) 5,987
1.6	2,839	15,850	(4) 5,669
1.7	2,515	15,771	(4) 5,408
1.8	2,243	15,706	(4) 5,190
1.9	2,013	15,650	(4) 5,006
2.0	1,817	15,602	(4) 4,850
2.1	1,648	15,561	(4) 4,716
2.2	1,502	15,526	(4) 4,601
2.3	1,374	15,495	(4) 4,500
2.4	1,262	15,468	(4) 4,412
2.5	1,163	15,444	(4) 4,334

UNDAMAGED LAMINATE STRENGTH: $N = 17,800$ lb/in, $M = 356$ lb-in/in

UNDAMAGED REMAINING LAYER STRENGTH: $N = 15,160$ lb/in, $M = 303$ lb-in/in

FAILURE MODES:

- (1) NO BUCKLING, NO DELAMINATION GROWTH, FAILED BY LAMINATE STRENGTH.
- (2) DELAMINATION BUCKLED, NO DELAMINATION GROWTH, FAILED BY LAMINATE STRENGTH.
- (3) DELAMINATION BUCKLED AND GROWN AT N_G , FAILED BY REMAINING LAYER STRENGTH.

F91-2/40

Figure 9. Failure Load and Mode of the 24-Ply Laminate With a 4-Ply Deep Circular Delamination Under Combined Loads ($N/M = 50$).

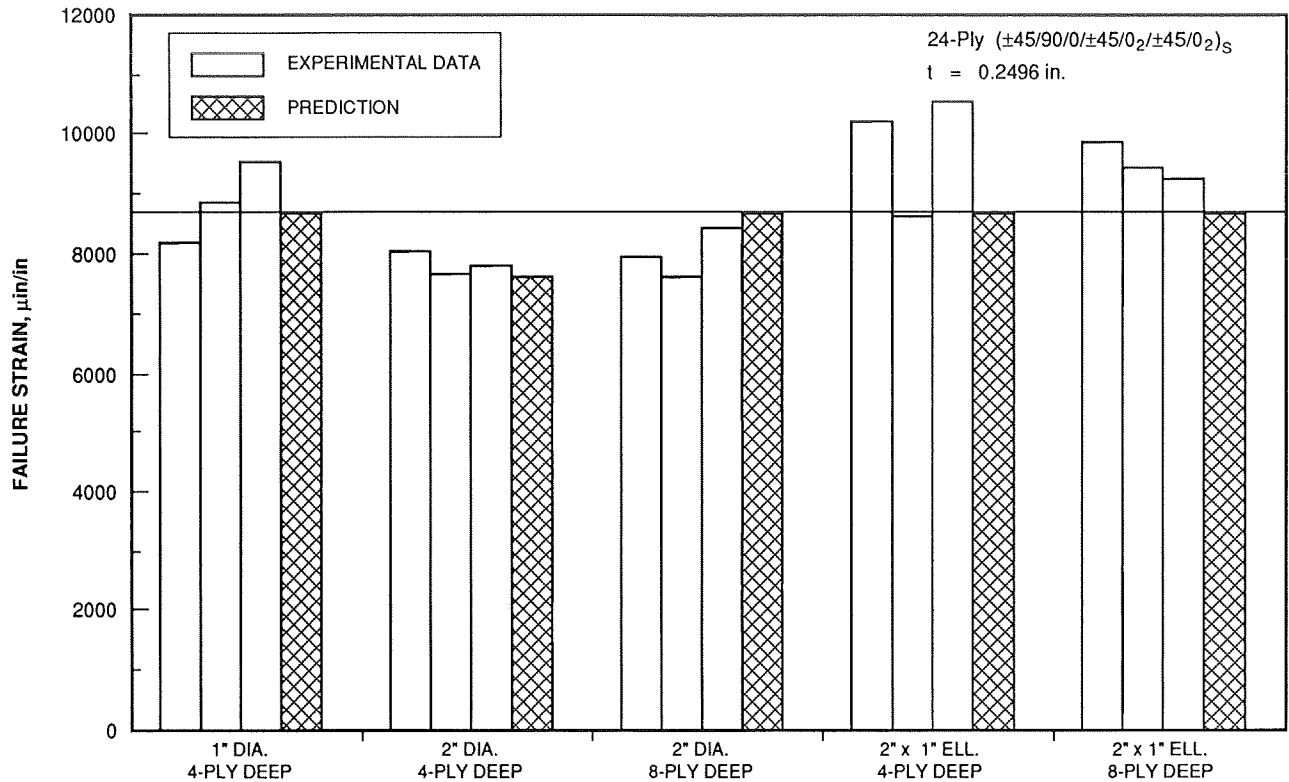


Figure 10. Comparison of Observed and Predicted Failure Strain of a 24-Ply Laminate With Single Circular or Elliptical Delamination.

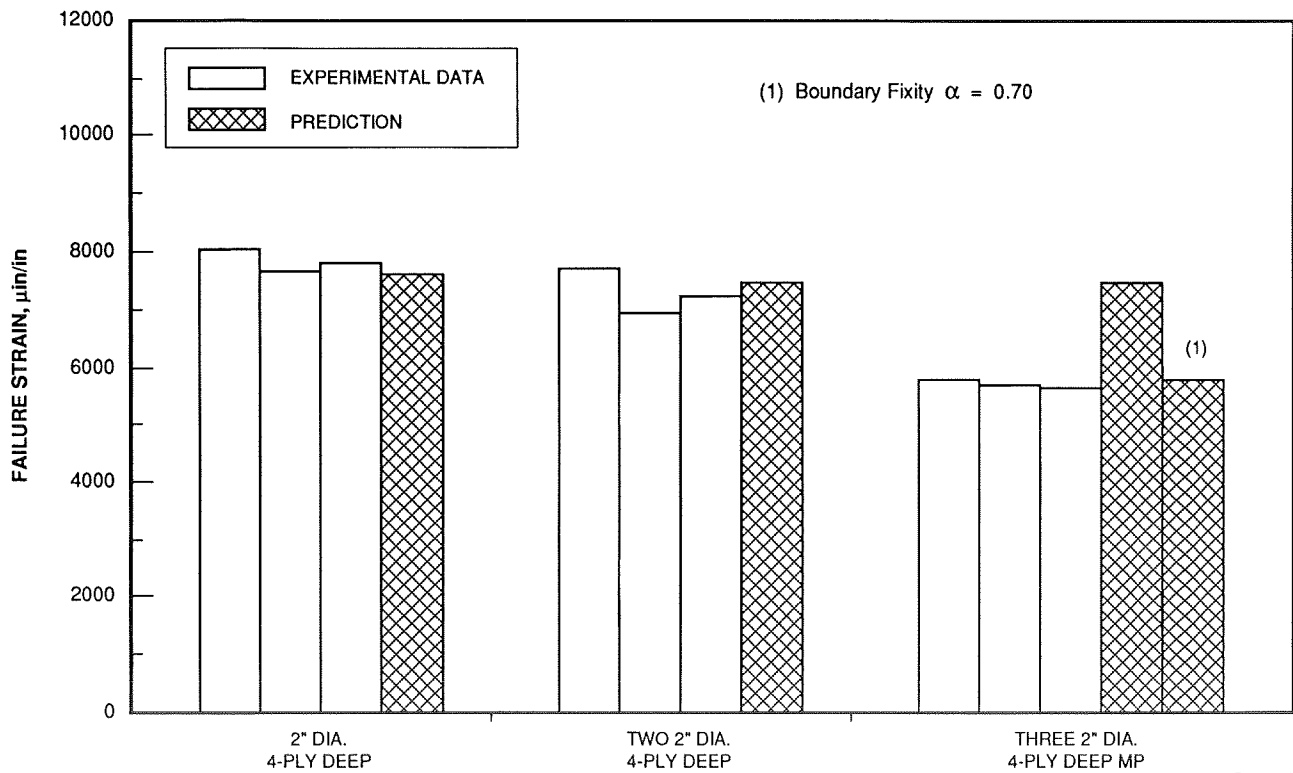


Figure 11. Comparison of Observed and Predicted Failure Strain of a 24-Ply Laminate With Multiple Delaminations.

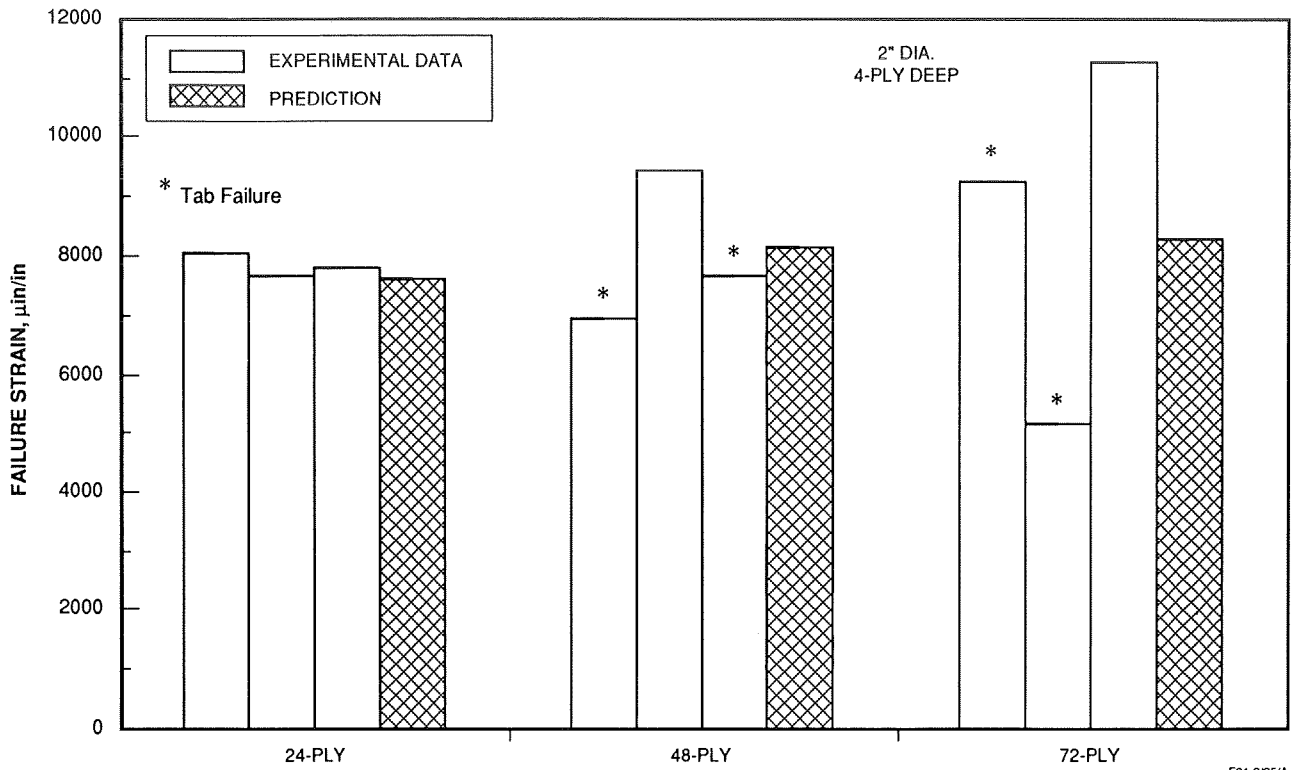


Figure 12. Comparison of Observed and Predicted Failure Strain for Laminate With 4-Ply Deep Circular Delamination.

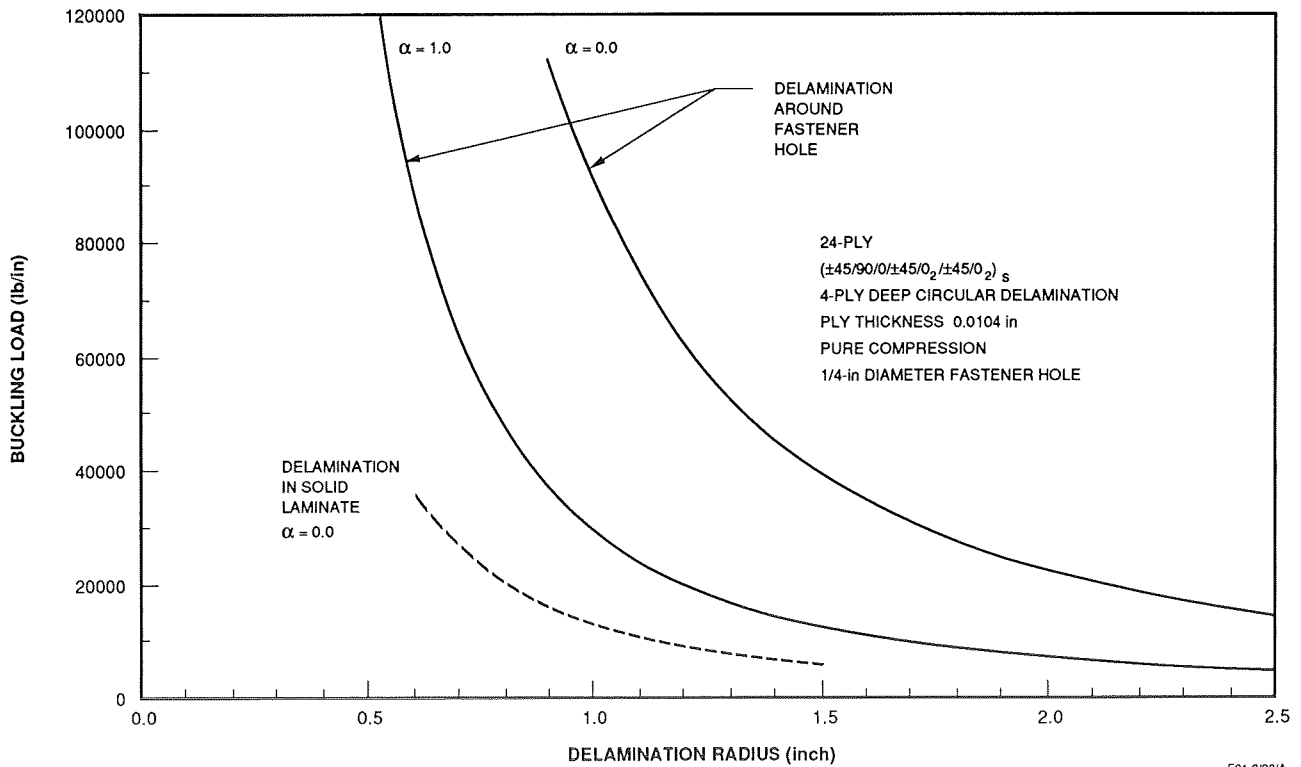


Figure 13. Initial Buckling Load for Delamination Around a Fastener Hole.

DELAMINATION RADIUS R (in)	BUCKLING LOAD N_{cr} (lb/in)	FAILURE LOAD N_f (lb/in)	FAILURE MODE
0.5	129,220	16,455	(1)
0.6	86,590	16,455	(1)
0.7	62,320	16,455	(1)
0.8	47,090	16,455	(1)
0.9	36,880	16,455	(1)
1.0	29,690	16,455	(1)
1.1	24,420	16,455	(1)
1.2	20,450	16,455	(1)
1.3	17,380	16,455	(1)
1.4	14,950	15,590	(2)
1.5	13,000	15,440	(3) $N_G = 14,630$
1.6	11,410	15,310	(3) 13,210
1.7	10,100	15,210	(3) 12,060
1.8	8,998	15,120	(3) 11,120
1.9	8,069	15,050	(3) 10,340
2.0	7,278	14,980	(3) 9,688
2.1	6,597	14,930	(3) 9,140
2.2	6,008	14,880	(3) 8,676
2.3	5,494	14,840	(3) 8,279
2.4	5,044	14,810	(3) 7,937
2.5	4,647	14,780	(3) 7,640

LAMINATE STRENGTH: SOLID 25,920 lb/in
 FILLED HOLE 16,600 lb/in
 FILLED HOLE WITH DELAMINATION 16,455 lb/in

REMAINING LAYER STRENGTH: SOLID 22,700 lb/in
 FILLED HOLE 14,410 lb/in

FAILURE MODE:

- (1) NO BUCKLING, NO DELAMINATION GROWTH, FAILURE DUE TO STRESS CONCENTRATION AT FILLED HOLE.
- (2) DELAMINATION BUCKLED, NO DELAMINATION GROWTH, FAILURE AT FILLED HOLE IN THE REMAINING LAYER.
- (3) DELAMINATION BUCKLED AND GROWN AT N_G THAN FAILED AT FILLED HOLE IN THE REMAINING LAYER.

F91-2/39

Figure 14. Results of Failure Analysis.
 4-Ply Deep Circular Delamination in 24-Ply Laminate
 0.25 in Diameter Fastener Hole

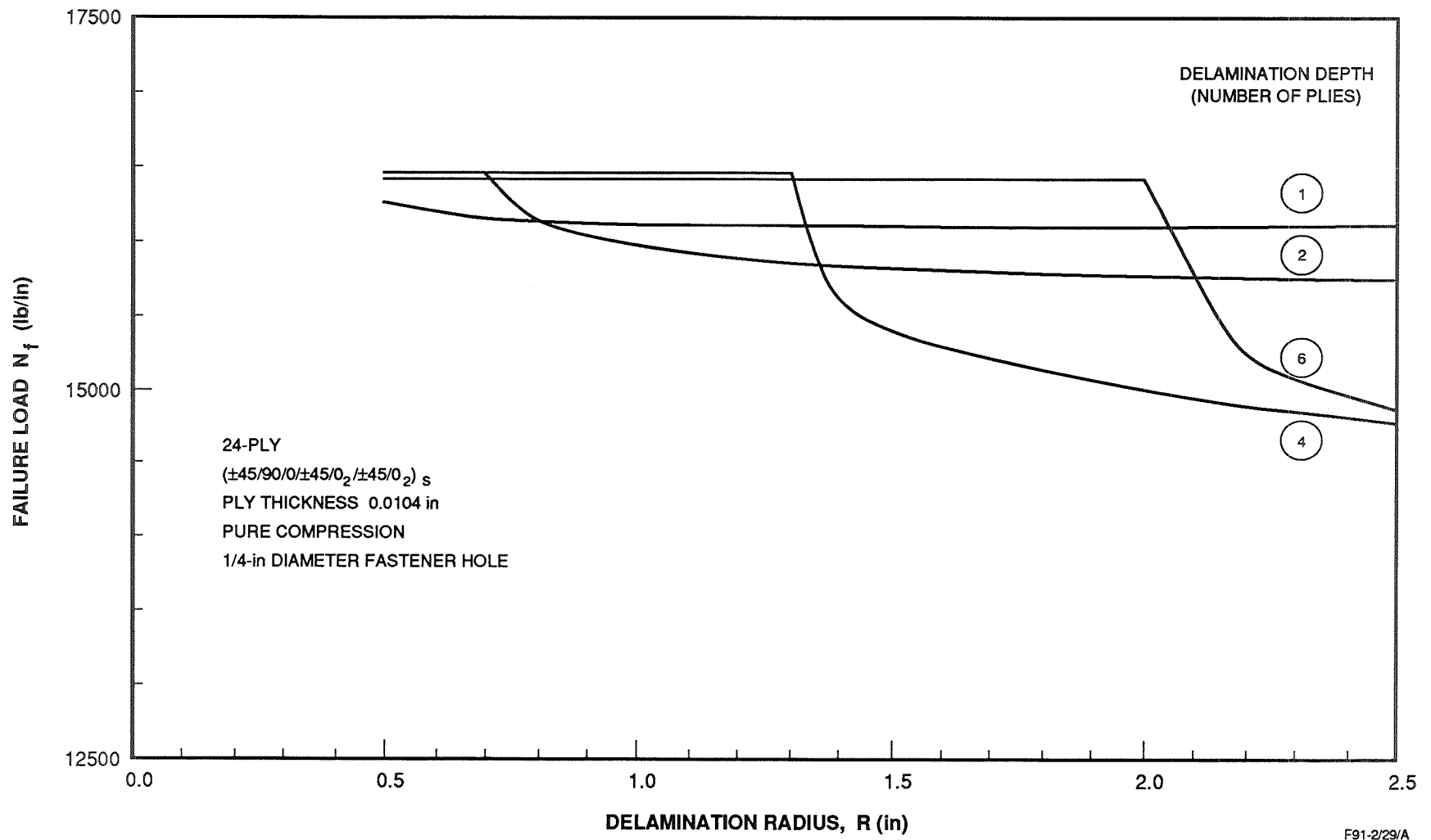


Figure 15. Failure Load of Laminate With Circular Delaminations Around a Fastener Hole.

omit

Mechanics of Composites Research at ONR

Yapa D. S. Rajapakse
Office of Naval Research

THIS PAGE INTENTIONALLY BLANK

Page intentionally left blank

Page intentionally left blank

omit

**Post-Buckling Analysis
of Curved, Stiffened Composite Panels
with Central Cut-Outs**

U. Mbanefo
Northrop Corporation

THIS PAGE INTENTIONALLY BLANK

Page intentionally left blank

Page intentionally left blank

Buckling Behavior of Long Symmetrically Laminated Plates
Subjected to Combined Loads

Michael P. Nemeth*
Structural Mechanics Division
NASA Langley Research Center
Hampton, Virginia

NASA

310-24

51378

P-26

ABSTRACT

A parametric study of the buckling behavior of infinitely long symmetrically laminated anisotropic plates subjected to combined loadings is presented. The loading conditions considered are axial tension and compression, transverse tension and compression, and shear. Results obtained using a special purpose analysis, well suited for parametric studies are presented for clamped and simply supported plates. Moreover, results are presented for some common laminate constructions, and generic buckling design charts are presented for a wide range of parameters. The generic design charts are presented in terms of useful nondimensional parameters, and the dependence of the nondimensional parameters on laminate fiber orientation, stacking sequence, and material properties is discussed.

An important finding of the study is that the effects of anisotropy are much more pronounced in shear-loaded plates than in compression-loaded plates. In addition, the effects of anisotropy on plates subjected to combined loadings are generally manifested as a phase shift of self-similar buckling interaction curves. A practical application of this phase shift is that the buckling resistance of long plates can be improved by applying a shear loading with a specific orientation. In all cases considered in the study, it is found that the buckling coefficients of infinitely long plates are independent of the bending stiffness ratio

$$(D_{11}/D_{22})^{1/4}.$$

INTRODUCTION

Buckling behavior of laminated plates is a topic of fundamental importance in the design of aerospace vehicle structures. Often, the sizing of many subcomponents of these vehicles is determined by stability constraints in addition to other constraints such as stiffness and strength. One typical subcomponent that is of great practical importance in structural design is the long rectangular plate. These plates routinely appear as subcomponents of stiffened panels used for wings, ribs, and spars. In addition, long plates commonly appear as subcomponents of semi-monocoque shells used for fuselage structure, liquid-propellant booster tankage, and booster interstage structure. Buckling results for infinitely long plates are important because they provide a lower bound on the behavior of finite-length rectangular plates, and provide information that is useful in explaining the behavior of finite-length plates.

Understanding the buckling behavior of symmetrically laminated plates is an important part of the search for ways to exploit plate orthotropy and anisotropy to reduce structural weight of aircraft and launch vehicles. Symmetrically laminated plates can exhibit anisotropy in the form of material-induced coupling between pure bending and twisting deformations. This coupling generally yields buckling modes

* Senior Research Engineer, Aircraft Structures Branch.

that are skewed in appearance, as depicted in figure 1. The effects of anisotropy on the buckling behavior of these compression-loaded plates are well known (e.g., references 1 and 2). However, the effects of anisotropy on symmetrically laminated plates subjected to shear loadings and various other combined loadings are generally not as well understood.

Symmetrically laminated plates can have many different constructions because of the wide variety of material systems, fiber orientations, and stacking sequences that can be used to construct a laminate. Thus, it is extremely useful for the designer to have a means of assessing the performance of various laminated plates on a common, and unbiased, basis. The use of nondimensional parameters can provide this means for assessing laminate performance. Moreover, the use of nondimensional parameters permits buckling results to be presented in a concise manner as a series of generic curves, on one or more plots, that span the complete range of plate dimensions, loading combinations, boundary conditions, laminate construction, and material properties. An added benefit is that the generic curves also furnish the designer with an overall indication of the sensitivity of the structural response to changes in the design parameters. Examples of generic design charts, for buckling and postbuckling of orthotropic plates, that use nondimensional parameters are presented in references 3 and 4.

The major objectives of the present paper are to indicate the effects of plate bending orthotropy and anisotropy on the buckling of plates subjected to combined loads, and to present generic design charts that indicate the buckling behavior of long plates for a wide range of parameters in a concise manner. The loading conditions considered in this paper are axial tension and compression, transverse tension and compression, and shear loadings. Results are presented herein for plates with the two opposite long edges clamped or simply supported. A substantial number of generic buckling curves are presented in the present paper that are applicable to a wide range of laminate constructions.

SYMBOLS

A_m, B_m	displacement amplitudes (see eq. (8)), in.
b	plate width (see fig. 1), in.
$D_{11}, D_{12}, D_{22}, D_{66}$	orthotropic plate bending stiffnesses, in.-lb
D_{16}, D_{26}	anisotropic plate bending stiffnesses, in.-lb
E_1, E_2, G_{12}	lamina moduli, psi
K_x, K_y, K_s	nondimensional buckling coefficients associated with axial compression, transverse compression, and shear loadings
m	laminate stacking sequence number
N_x, N_y, N_{xy}	membrane prebuckling stress resultants (see fig. 1), lb/in.

$N_x^{cr}, N_y^{cr}, N_{xy}^{cr}$	values of the membrane stress resultants at buckling, lb/in.
\bar{p}, \bar{p}_{cr}	nondimensional loading parameter and corresponding value at buckling
x, y	plate coordinate system (see fig. 1), in.
w_N	out-of-plane displacement field at buckling (see eq. (8)), in.
$\alpha, \beta, \gamma, \delta$	nondimensional parameters defined by eqs. (1) through (4)
λ	half-wave length of buckling mode (see fig. 1), in.
$\eta = y/b, \xi = x/\lambda$	nondimensional plate coordinates
ν_{12}	lamina major Poisson's ratio
Φ_m, Ψ_m	kinematically admissible basis functions (see eq. (8))
θ	fiber orientation angle (see fig. 1), deg.

APPROACH

The objectives of the present study are achieved herein in two different ways. In the first way, the effects of plate orthotropy and anisotropy are presented in an implicit manner for symmetrically laminated angle-ply plates. This family of laminates is denoted herein by the symbols $[(\pm\theta)_m]_s$, where θ is the fiber orientation angle shown in figure 1 (given in units of degrees) and m is the stacking sequence number that indicates the number of times the plies in parentheses are repeated. This family of laminates was chosen since varying the laminate parameters θ and m encompasses a wide range of plate bending orthotropy and bending anisotropy. The term implicit is used above to reflect the fact that for the angle-ply laminates, as well as for all other laminates, the plate orthotropy and anisotropy are implicit functions of laminate fiber orientation and stacking sequence and do not typically vary independently. This implicit way of assessing plate behavior is generally the approach that is the most familiar to aerospace vehicle designers.

A second way to characterize the effects of plate orthotropy and anisotropy uses the nondimensional parameters presented in reference 1. These nondimensional parameters are used in the present paper to show the effects of plate orthotropy and anisotropy on buckling behavior in a somewhat more explicit manner. For example, buckling results are presented in the present paper as a function of two parameters that characterize plate orthotropy and two parameters that characterize plate anisotropy. By varying each parameter in a systematic manner, the effects of orthotropy and anisotropy on buckling can be assessed independently. An important step in this assessment is to establish an understanding of how laminate fiber orientation, stacking sequence, and material properties affect the values of the

nondimensional parameters. Thus, results are also presented herein that indicate the effects of laminate construction on the nondimensional parameters for a few selected laminates. Material properties considered herein are representative of high-strength graphite-epoxy material, ultra-high-modulus graphite-epoxy material, S-glass-epoxy material, Kevlar-epoxy material, boron-epoxy material, and boron-aluminum material.

ANALYSIS DESCRIPTION

Often in preparing generic design charts for buckling of a single plate element, a special purpose analysis is preferred over a general purpose analysis code, such as a finite element code, due to the cost and effort involved in generating a large number of results with a general purpose analysis code. The results presented in the present paper have been obtained using such a special purpose analysis. A brief description of the analysis is presented subsequently.

The buckling analysis used in the present study is based on the classical Rayleigh-Ritz variational method, and is derived explicitly in terms of the nondimensional parameters defined in reference 1. Deriving the analysis in this manner inherently makes the resulting computer code well suited for parametric studies. The nondimensional parameters used are given by

$$\alpha = \frac{b}{\lambda} (D_{11}/D_{22})^{1/4} \quad (1)$$

$$\beta = \frac{D_{12} + 2D_{66}}{\sqrt{D_{11}D_{22}}} \quad (2)$$

$$\gamma = \frac{D_{16}}{(D_{11}D_{22})^{1/4}} \quad (3)$$

$$\delta = \frac{D_{26}}{(D_{11}D_{22})^{1/4}} \quad (4)$$

where λ is the half-wave length of the buckle mode and b is the plate width shown in figure 1. The subscripted D terms appearing in the equations are the plate bending stiffnesses of classical laminated plate theory. The parameters α and β characterize plate bending orthotropy, and the parameters γ and δ characterize plate bending anisotropy. The parameters defined by equations (2) through (4) depend only on the plate bending stiffnesses, whereas the parameter α depends on the buckle aspect ratio λ/b also. Without loss of generality, and as a matter of convenience, the nondimensional parameter $(D_{11}/D_{22})^{1/4}$ is used in the present study in the place of the parameter α to assess plate bending orthotropy.

In addition to $(D_{11}/D_{22})^{1/4}$, β , γ , and δ ; three additional nondimensional quantities are used to characterize buckling resistance. The quantities are given by

$$K_x = \frac{N_x^{cr, 2}}{\pi^2 \sqrt{D_{11} D_{22}}} \quad (5)$$

$$K_y = \frac{N_y^{cr, 2}}{\pi^2 D_{22}} \quad (6)$$

$$K_s = \frac{N_{xy}^{cr, 2}}{\pi^2 (D_{11} D_{22})^{1/4}} \quad (7)$$

The quantities K_x , K_y , and K_s are referred to herein as the axial compression buckling coefficient, the transverse compression buckling coefficient, and the shear buckling coefficient, respectively. Each of the loading conditions associated with these buckling coefficients is shown in figure 1. The positive-valued compressive stress resultants and shear stress resultant corresponding to the loadings are denoted by N_x , N_y , and N_{xy} respectively. The stress resultants appearing in the buckling coefficients correspond to critical values associated with the onset of buckling.

In the buckling analysis, the infinitely long plates are assumed to have uniform thickness and material properties that do not vary along the plate length and width. In addition, the uniform biaxial and shear loadings, and the boundary conditions do not vary along the plate length. Under these conditions, infinitely long plates have periodic buckling modes that exhibit either inversion symmetry or inversion antisymmetry with respect to a given reference point. The buckling mode depicted in figure 1 corresponds to either inversion symmetry or antisymmetry depending on the selection of the reference point. The presence of the periodicity and inversion symmetry or antisymmetry in the plate buckling mode aids in simplifying the buckling analysis.

An important characteristic of an infinitely long plate that possesses a periodic buckling mode is that a basic repetitive buckle pattern can be identified from which the overall buckling mode can be constructed by axial translation of the pattern. The selection of the basic repetitive buckle pattern is not unique, and thus one may choose it to simplify the buckling analysis further. In the present study, the basic repetitive buckle pattern was chosen such that it possesses inversion symmetry about its geometric center. This simplification is important in that it permits the elimination of superfluous terms in the kinematically admissible series used to describe the buckling mode, which in turn simplifies the ensuing analysis and reduces the number of computations required to obtain an accurate result. The mathematical expression used in the variational analysis to describe the buckle pattern is given by

$$w_N(\xi, \eta) = \sin \pi \xi \sum_{m=1}^N A_m \Phi_m(\eta) + \cos \pi \xi \sum_{m=1}^N B_m \Psi_m(\eta) \quad (8)$$

where $\xi = x/\lambda$ and $\eta = y/b$ are nondimensional coordinates (see figure 1), w_N is the out-of-plane displacement field, and A_m and B_m are the unknown displacement

amplitudes. In accordance with the Raleigh-Ritz method, the basis functions $\Phi_m(\eta)$ and $\Psi_m(\eta)$ are required to satisfy the kinematic boundary conditions on the plate edges at $\eta = 0$ and 1. For the simply supported plates, the basis functions used in the analysis are given by

$$\Phi_m(\eta) = \sin 2m\pi\eta \quad (9a)$$

$$\Psi_m(\eta) = \sin(2m-1)\pi\eta \quad (9b)$$

for values of $m = 1, 2, 3, \dots, N$. Similarly, for the clamped plates, the basis functions are given by

$$\Phi_m(\eta) = \cos(2m-1)\pi\eta - \cos(2m+1)\pi\eta \quad (10a)$$

$$\Psi_m(\eta) = \cos 2(m-1)\pi\eta - \cos 2m\pi\eta \quad (10b)$$

Algebraic equations governing buckling of long plates are obtained by substituting the series expansion for the buckling mode given by equation (8) into the second variation of the total potential energy and then computing the integrals appearing in the second variation in closed form. The resulting equations constitute a generalized eigenvalue problem that depends on the aspect ratio of the buckle pattern λ/b (see figure 1) and the nondimensional parameters defined by equations (1) through (4). The inplane loadings are expressed in terms of a loading parameter \tilde{p} that is increased monotonically until buckling occurs. The smallest eigenvalue of the problem \tilde{p}_{cr} corresponds to buckling and is found by specifying a value of λ/b and solving the corresponding generalized eigenvalue problem for its smallest eigenvalue. This process is repeated for successive values of λ/b until the absolute smallest eigenvalue is found. The absolute smallest eigenvalue corresponds to \tilde{p}_{cr} .

Results obtained using the analysis described in the present paper were compared to results for isotropic and specially orthotropic plates published in the technical literature for several loading cases and boundary conditions (see references 4 through 10). Results for anisotropic plates were also compared to results obtained using the computer code VIPASA (see reference 11). In all comparisons, results obtained from the analysis used in the present study were found to be within a few percent of the results published in references 4 through 10 and the VIPASA results.

LAMINATE CONSTRUCTION AND NONDIMENSIONAL PARAMETERS

To characterize plate buckling behavior in terms of nondimensional parameters, it is important to understand how laminate fiber orientation, stacking sequence, and material properties affect their values. To accomplish this task and to determine the numerical range of the nondimensional parameters for typical balanced symmetric laminates, results are presented in this section for $[(+\theta)_m]_s$ angle-ply laminates, $[(+45/0/90)_m]_s$ and $[(0/90/+45)_m]_s$ quasi-isotropic laminates, and $[(+45/0_2)_m]_s$ and $[(+45/90_2)_m]_s$ laminates typically referred to as orthotropic

laminates. Each of these laminates possess specially orthotropic membrane deformation states prior to buckling (i.e., the A_{16} and A_{26} laminate constitutive terms are zero-valued).

Effects of Fiber Orientation and Stacking Sequence

Values of the nondimensional parameters β , γ , δ , and the parameter $(D_{11}/D_{22})^{1/4}$ are shown in figures 2 and 3 for $[\pm\theta]_s$ and $[(\pm 45)_m]_s$ angle-ply laminates, respectively. Similar results are presented in figure 4 for $[(\pm 45/0/90)_m]_s$ and $[(0/90/\pm 45)_m]_s$ quasi-isotropic laminates, and in figure 5 for $[(\pm 45/0_2)_m]_s$ and $[(\pm 45/90_2)_m]_s$ laminates. All results presented in these figures are for laminates with plies made of a typical graphite-epoxy material, having a longitudinal modulus $E_1 = 18.5 \times 10^6$ psi, a transverse modulus $E_2 = 1.6 \times 10^6$ psi, an inplane shear modulus $G_{12} = 0.832 \times 10^6$ psi, major Poisson's ratio $\nu_{12} = 0.35$, and a nominal ply thickness of 0.005 in.

For the angle-ply laminates, the anisotropic parameters γ and δ have maximum values at $\theta = 39$ and 51 degrees, respectively (see figure 2), and their values diminish monotonically as the number of plies increases (see figure 3). Between the values of 39 and 51 degrees, values of γ (and similarly δ) vary by only a couple of percent. The orthotropic parameters β and $(D_{11}/D_{22})^{1/4}$ have maximum values at $\theta = 45$ and 0 degrees, respectively, and their values remain constant as the number of plies increases.

For the $0/45/90$ family of quasi-isotropic laminates, the anisotropic parameters γ and δ shown in figure 4 asymptotically approach zero from above as the number of plies increases. The solid lines and dashed lines shown in figure 4 indicate results for the $[(0/90/\pm 45)_m]_s$ and $[(\pm 45/0/90)_m]_s$ laminates, respectively. The results in figure 4 indicate that the orthotropic parameters β and $(D_{11}/D_{22})^{1/4}$ for the $[(\pm 45/0/90)_m]_s$ laminates asymptotically approach the value of one from above as the number of plies increases. The values of β and $(D_{11}/D_{22})^{1/4}$ for the $[(0/90/\pm 45)_m]_s$ laminates asymptotically approach the value of one from above and below, respectively, as the number of plies increases. A value of one for β and for $(D_{11}/D_{22})^{1/4}$, and a value of zero for γ and for δ represent pure isotropy associated with a plate made from an essentially homogeneous material like wrought aluminum plate.

The results presented in figure 5 for the $[(\pm 45/0_2)_m]_s$ and $[(\pm 45/90_2)_m]_s$ laminates indicate that anisotropic parameters γ and δ also asymptotically approach zero from above as the number of plies increases. The solid lines and dashed lines shown in figure 5 indicate results for the $[(\pm 45/0_2)_m]_s$ and $[(\pm 45/90_2)_m]_s$ laminates, respectively. The results in figure 5 indicate that both laminate families have the same value of the orthotropic parameter β for a given number of plies, and that β decreases monotonically to an asymptotic value as the number of plies increases. In contrast, the $[(\pm 45/0_2)_m]_s$ laminates have larger

values of $(D_{11}/D_{22})^{1/4}$ than the $[(+45/90_2)_m]_s$ laminates. Moreover, the values of $(D_{11}/D_{22})^{1/4}$ for the $[(+45/90_2)_m]_s$ and $[(+45/0_2)_m]_s$ laminates diminish and increase monotonically, respectively, as the number of plies increases.

Effects of Varying Material Properties

Results showing the effects of varying material properties on the nondimensional parameters for $[\pm\theta]_s$ angle-ply laminates are presented in figures 6 through 9. In these figures, results are presented for laminates made of high-strength graphite-epoxy material, ultra-high-modulus graphite-epoxy material, S-glass-epoxy material, Kevlar-epoxy material, boron-epoxy material, and boron-aluminum material. The moduli ratios E_1/E_2 and E_2/G_{12} , and the major Poisson's ratio ν_{12} for these materials are given in Table 1.

The results presented in figure 6 show that maximum values of the orthotropic parameter β occur at $\theta = 45$ degrees for all the material properties considered. The largest values of β are, for most of the range of fiber orientation angles, exhibited by laminates made of ultra-high-modulus graphite-epoxy material, followed by laminates made of Kevlar-epoxy material, boron-epoxy material, high-strength graphite-epoxy material, S-glass-epoxy material, and boron-aluminum material. The results presented in figure 7 indicate that the largest value of $(D_{11}/D_{22})^{1/4}$ is also exhibited by laminates made of ultra-high-modulus graphite-epoxy material for values of $0 \leq \theta \leq 45$ degrees. The next highest values of $(D_{11}/D_{22})^{1/4}$ in the range of $0 \leq \theta \leq 45$ degrees are exhibited by laminates made of Kevlar-epoxy material, high-strength graphite-epoxy material, boron-epoxy material, S-glass-epoxy material, and boron-aluminum material. In the range of $45 \leq \theta \leq 90$ degrees, the trend reverses.

The results presented in figures 8 and 9 indicate that the largest values for the anisotropic parameters γ and δ are also exhibited by laminates made of ultra-high-modulus graphite-epoxy material followed by laminates made of Kevlar-epoxy material, boron-epoxy material, high-strength graphite-epoxy material, S-glass-epoxy material, and boron-aluminum material; i.e., the same trend as exhibited by the orthotropic parameter β . The maximum values of γ and δ for each material system ranges between $\theta = 31$ and 59 degrees. For example, γ is a maximum at $\theta = 31$ degrees ($\gamma = 0.13$) and δ is a maximum at $\theta = 59$ degrees ($\delta = 0.13$) for laminates made of boron-aluminum material. For laminates made of ultra-high-modulus graphite-epoxy material, γ is a maximum at $\theta = 40$ degrees ($\gamma = 0.68$), and δ is a maximum at $\theta = 50$ degrees ($\gamma = 0.68$).

The results discussed in this section indicate a practical range of the numerical values of the nondimensional parameters. In subsequent sections of this paper, generic buckling results are presented for $0.2 \leq \beta \leq 3.0$, $0.5 \leq (D_{11}/D_{22})^{1/4} \leq 3.0$, $0 \leq \gamma \leq 0.8$, and $0 \leq \delta \leq 0.8$. Negative values for γ and δ are possible for some laminates (e.g., $[\bar{+}45]_s$ laminates), but are not considered in the present paper. An important physical consideration to keep in mind when using the nondimensional parameters in an arbitrary manner to generate buckling design charts is that together they must satisfy the condition that the strain energy of the plate be positive valued. This condition is due to the thermodynamic

restrictions that define the admissible range of lamina material properties, and hence define the range of admissible plate bending stiffnesses. This condition was enforced in the buckling analysis and accounts for the fact that some of the curves shown on the generic buckling design charts presented herein do not span the entire range of the nondimensional parameters specified herein.

BUCKLING RESULTS AND DISCUSSION

Results are presented in this section for clamped and simply supported plates loaded by either axial compression or shear. In addition, results are presented for plates subjected to combined loading of axial tension or compression and shear, transverse tension or compression and shear, and transverse tension or compression and axial compression. In each of the loading cases involving shear, a distinction between positive and negative shear loadings is made whenever anisotropy is present. A positive shear loading corresponds to a shear stress acting on the plate edge $y = b$ (see figure 1) in the positive x -coordinate direction. For each of the loading cases considered in the present paper, results are first presented for the familiar angle-ply laminates, and then generic results are presented in terms of the nondimensional parameters described herein. The results presented for the angle-ply laminates are calculated using lamina material properties of a typical graphite-epoxy material. The properties used are the same ones that were used to calculate the nondimensional parameters shown in figure 2.

Axial-Compression-Loaded Plates

Nondimensional buckling coefficients K_x are presented in figure 10 for infinitely long clamped and simply supported $[\pm\theta]_s$ plates loaded in axial compression, as a function of the fiber orientation angle θ . The 4-ply $[\pm\theta]_s$ laminates are limiting cases, but they are useful in the present study since they exhibit the highest degree of anisotropy of the angle-ply laminates. Similar results are presented in figure 11 for $[(\pm 45)_m]_s$ plates for $m = 1, 2, \dots, 12$. The solid lines shown in figures 10 and 11 correspond to results for which anisotropy is included in the analysis. The dashed lines in the figures correspond to results for which the D_{16} and D_{26} anisotropic constitutive terms are neglected. The buckling coefficients shown in figure 10 were calculated for increments in θ equal to 1 degree. Similar sets of results for square finite-length plates are presented in reference 1.

The results presented in figure 10 indicate that neglecting plate anisotropy in the analysis always overestimates the plate bending stiffness, and thus always yields nonconservative estimates of the buckling resistance. The largest buckling coefficients for the orthotropic plates occur at $\theta = 45$ degrees, whereas the largest ones for the anisotropic plates occur at slightly less than 45 degrees. The largest difference between the orthotropic and anisotropic solutions for both clamped and simply supported plates is about 25% of the corresponding orthotropic solution.

The results presented in figure 11 indicate that the anisotropic solutions for both clamped and simply supported plates converge monotonically from below to the specially orthotropic solutions as the number of plies in the $[(\pm 45)_m]_s$ laminates increases. The largest difference between the anisotropic and orthotropic solutions occurs for $m = 1$, and is approximately 25% of the corresponding

orthotropic solution. The difference is approximately 5% for $m = 2$, and less than 1% for $m = 6$.

Generic buckling results for clamped compression-loaded plates are presented in figures 12 through 14 for a wide range of values of the four nondimensional parameters. The results presented in figure 12 show buckling coefficients of clamped plates as a function of the parameter $(D_{11}/D_{22})^{1/4}$ for $\beta = 3$. Buckling curves are presented in this figure for discrete values of $\gamma = \delta$ ranging from 0 to 0.8. The $[\pm 45]_s$ laminates made of a typical graphite-epoxy material and an ultra-high-modulus graphite-epoxy material have values of γ and δ equal to 0.52 and 0.68, respectively. Thus, a value of 0.8 corresponds to an extremely anisotropic plate. The lines shown in figure 12 are parallel to the abscissa axis and thus indicate that the buckling coefficients are independent of the parameter $(D_{11}/D_{22})^{1/4}$ for the entire range of anisotropy shown in the figure. Similar plots were made for clamped and simply supported plates in which the orthotropic parameter β was varied and unequal values of γ and δ were used. The additional results also show the buckling coefficients to be independent of the parameter $(D_{11}/D_{22})^{1/4}$. This finding is consistent with the observation that plots of buckling coefficient versus plate aspect ratio (length over width), for finite-length plates, attenuate to constant values as the plate aspect ratio becomes large. More specifically, in a finite-length plate, the bending stiffness ratio $(D_{11}/D_{22})^{1/4}$ influences the size and number of buckles that occur along the plate length. The number of buckles that occur along the plate length, in turn, directly affects the value of the buckling coefficient for a given plate (as indicated by the festoon nature of the buckling curves for finite-length plates). For an infinitely long plate, the bending stiffness ratio $(D_{11}/D_{22})^{1/4}$ still influences the size of the buckles, with respect to the basic periodic unit of an infinitely long plate, but the number of buckles that occurs along the plate length becomes meaningless. This independence of K_x with respect to $(D_{11}/D_{22})^{1/4}$ represents an important simplification in that the buckling coefficients of long plates can be represented by a single orthotropic parameter, namely β . However, the parameter $(D_{11}/D_{22})^{1/4}$ is important since it does affect the aspect ratio of the buckle pattern, and is useful in determining when classical plate theory becomes insufficient and transverse shear deformation must be included in buckling analyses.

Buckling coefficients are presented in figure 13 for clamped compression-loaded plates as a function of the orthotropic parameter β for values of $\gamma = \delta$ ranging from 0 to 0.8. Using the result that the buckling coefficients are independent of $(D_{11}/D_{22})^{1/4}$, results corresponding to particular laminates made of a typical graphite-epoxy material and an ultra-high-modulus graphite-epoxy material are also shown in figure 13 and are indicated by symbols. Symbols that represent several laminates indicate that all of the laminates have the same buckling coefficient. The results presented in this figure indicate that anisotropy can significantly reduce buckling resistance, and that the effect of anisotropy tends to diminish somewhat as β increases (i.e., the curves become spaced closer together as β increases). Similar results were obtained for simply supported

plates. These results indicate the same trends, and indicate that the effects of varying β are slightly more pronounced for the clamped plates (i.e., the linear portions of the curves for the clamped plates generally had a higher slope than the corresponding curves for the simply supported plates).

Results are presented in figure 14 for clamped compression-loaded plates in which the anisotropic parameters γ and δ are varied independently. Curves are also presented in this figure for values of γ and δ ranging from 0 to 0.8. Moreover, two sets of curves are shown in figure 14 corresponding to values of the orthotropic parameter β equal to 1 and 3. The results presented in this figure indicate that the buckling coefficients are more sensitive to the parameter δ than to γ . This observation can be seen by comparing the differences in the values of the buckling coefficients in which γ is held constant and δ is varied and vice versa. The results also support the previous statement presented herein that the effect of anisotropy tends to diminish somewhat as β increases. A set of results similar to those presented in figure 14 were obtained for simply supported plates. These results indicate the same trends, and indicate that the effects of varying β , γ , and δ are also slightly more pronounced for the clamped plates.

Shear-Loaded Plates

Shear buckling coefficients K_s are presented in figure 15 for infinitely long clamped and simply supported $[\pm\theta]_s$ plates, as a function of the fiber orientation angle θ . Similar results are presented in figure 16 for $[(\pm 45)_m]_s$ plates for $m = 1, 2, \dots, 12$. The solid and dotted lines shown in figures 15 and 16 correspond to results for which anisotropy is included in the analysis. The solid lines correspond to a positive shear loading, and the dotted lines correspond to a negative shear loading. The dashed lines in the figures correspond to results for which anisotropy is neglected, and no distinction between positive and negative shear is necessary. The buckling coefficients shown in figure 15 were calculated for increments in θ equal to 1 degree.

The results presented in figure 15 indicate that neglecting plate anisotropy in the analysis yields nonconservative estimates of the buckling resistance of plates loaded in positive shear, and yields conservative estimates for the plates loaded in negative shear. Moreover, the plates loaded in negative shear exhibit the most buckling resistance. The largest buckling coefficients for the orthotropic plates occur at $\theta = 45$ degrees, whereas the largest buckling coefficients for the anisotropic plates loaded in negative shear are slightly more than 45 degrees. The largest buckling coefficients for the clamped plates loaded in positive shear occur at $\theta = 0$ and 90 degrees, and those for the corresponding simply supported plates occur at 20 degrees. The largest difference between the orthotropic and anisotropic solutions for both clamped and simply supported plates is approximately 48% of the corresponding orthotropic solution. This difference is nearly twice that of the corresponding compression-loaded plates.

The results presented in figure 16 indicate that the anisotropic solutions for both clamped and simply supported plates converge monotonically to the specially orthotropic solutions as the number of plies in the $[(\pm 45)_m]_s$ laminates increases. The plates loaded by negative shear converge from above, and the plates loaded by positive shear converge from below. The largest difference between the anisotropic and orthotropic solutions occurs for $m = 1$, and is approximately 48% of the corresponding orthotropic solution. The difference is approximately 7% for

$m = 6$ and approximately 3.5% for $m = 12$. Comparing the results presented in figures 11 and 16 indicates that the effects of anisotropy are much more pronounced in shear-loaded plates than in compression-loaded plates.

Generic buckling results for clamped and simply supported shear-loaded plates are presented in figures 17 through 19 for a wide range of values of the nondimensional parameters. The results presented in figure 17 show buckling coefficients of clamped plates as a function of the parameter $(D_{11}/D_{22})^{1/4}$ for $\beta = 3$. Buckling curves are presented in this figure for values of $\gamma = \delta$ ranging from 0 to 0.8. The results presented in figure 17 indicate that, like the compression-loaded plates, the buckling coefficients are independent of the parameter $(D_{11}/D_{22})^{1/4}$ for the entire range of anisotropy. Similar results were obtained for clamped and simply supported plates in which the orthotropic parameter β was varied. The additional results also show that the buckling coefficients are independent of the parameter $(D_{11}/D_{22})^{1/4}$. The parameter $(D_{11}/D_{22})^{1/4}$ was found, however, to affect the aspect ratio of the buckle pattern.

Buckling coefficients are presented in figure 18 for clamped shear-loaded plates as a function of the orthotropic parameter β . Curves are also presented in this figure for values of $\gamma = \delta$ ranging from 0 to 0.8. Applying the simplification that the buckling coefficients are independent of $(D_{11}/D_{22})^{1/4}$, results corresponding to particular laminates made of a typical graphite-epoxy material and an ultra-high-modulus graphite-epoxy material are indicated in the figure by symbols. Like the compression-loaded plates, the results presented in this figure indicate that anisotropy can significantly reduce buckling resistance of shear-loaded plates, and that the effects of anisotropy tend to diminish somewhat as β increases. Similar results were obtained for simply supported plates. These results also indicate the same trends, and indicate that the effects of varying β are slightly more pronounced for the clamped plates.

Results are presented in figure 19 for clamped shear-loaded plates as a function of the anisotropic parameters γ and δ with values ranging from 0 to 0.8, and for a value of $\beta = 3$. The results presented in figure 19 indicate the same trend shown in figure 14 for the compression-loaded plates; i.e., the buckling coefficients are more sensitive to the parameter δ than to γ . Similar results were obtained for $\beta = 1$. These results also indicate that the effects of anisotropy tend to diminish somewhat as β increases. Results similar to those presented in figure 19 were obtained for simply supported plates with $\beta = 1$ and 3. These results indicate the same trends, and once again indicate that the effects of varying β , γ , and δ are slightly more pronounced for the clamped plates than for the simply supported plates.

Plates Subjected to Combined Loadings

Results are presented in this section for plates subjected to combined loadings. First, results are presented for plates subjected to axial tension or compression loadings combined with shear loading. Next, results are presented for plates subjected to transverse tension or compression loadings combined with shear loading. The last set of results presented are for plates subjected to axial compression combined with either transverse tension or compression.

Axial Tension or Compression and Shear Loading

Buckling interaction curves are presented in figure 20 for infinitely long clamped $[\pm\theta]_s$ plates subjected to axial tension or compression and shear loadings for several values of fiber orientation angle θ . The dashed lines shown in figure 20 correspond to results for which anisotropy is included in the analysis. The solid lines in the figures correspond to results for which the D_{16} and D_{26} anisotropic constitutive terms are neglected. Negative values of K_x correspond to axial tension loadings, and negative values of K_s correspond to negative shear loadings. Points of intersection of the interaction curves shown in the figure with a straight line emanating from the origin of the plot constitute constant values of $N_{xy}/N_x (D_{11}/D_{22})^{1/4}$ and are depicted in the figure for convenience.

The results presented in figure 20 indicate that the effects of anisotropy manifest themselves as a phase shift of self-similar curves in the K_x - K_s plane. The self-similar nature of the curves suggests that it may be possible to obtain simple buckling interaction formulas like those existing for isotropic plates (see reference 5). For plates loaded in positive shear, neglecting plate anisotropy in an analysis yields buckling coefficients substantially larger than those corresponding to the anisotropic solution. For plates loaded in negative shear, however, this trend is reversed. Similar results were obtained for corresponding simply supported plates, and these results exhibit exactly the same trends. In addition, the results in figure 20, and the corresponding results for simply supported plates, suggest that the buckling resistance of a compression-loaded plate can be improved by applying a negative shear loading. For the plates with $\theta = 45$ degrees, the improvement is approximately 20% and 25% of the K_x values corresponding to pure axial compression loading for the clamped and simply supported plates, respectively. The results presented in figure 20 also indicate that laminates with $\theta = 45$ degrees yield the most buckling resistant interaction curves for both of the cases in which anisotropy is included and neglected. This trend is also exhibited by the simply supported plates.

Generic buckling results for clamped and simply supported plates subjected to combined axial and shear loadings are presented in figures 21 through 23 also for a wide range of values of the nondimensional parameters. Additional results were obtained for both boundary condition cases and several values of β , γ , and δ . These additional results indicate that the buckling interaction curves, such as those presented in figures 21 through 23, are independent of the parameter $(D_{11}/D_{22})^{1/4}$.

Buckling interaction curves are presented in figure 21 for clamped and simply supported plates and for several values of the orthotropic parameter β . The curves appearing in this figure are for values of $\gamma = \delta = 0$. Using the simplification that the buckling interaction curves are independent of $(D_{11}/D_{22})^{1/4}$, results corresponding to particular laminates can be obtained once the value of β for the specific laminate is known, provided the corresponding nondimensional anisotropic parameters are zero-valued. Good estimates of buckling resistance can be obtained for laminates with small values of the nondimensional anisotropic parameters compared to unity. For example, the curves with $\beta = 1$ correspond to solutions for isotropic plates, and give good approximations to the

results for $[(+45/0/90)_m]_s$ quasi-isotropic laminates with 32 or more plies made of a typical graphite-epoxy material. An important result shown in figure 21 is that substantial gains in buckling resistance can be obtained by tailoring laminate construction to increase the parameter β .

Results are presented in figure 22 for clamped and simply supported plates with values of $\gamma = \delta$ ranging from 0 to 0.8 and for a value of $\beta = 3$. These results also show that anisotropy is generally manifested as a phase shift of the interaction curves in the $K_x - K_s$ plane, and support the statement given previously in the present paper that the buckling resistance of a compression-loaded plate can be improved by applying a negative shear loading (as was seen for the angle-ply laminates). For extremely anisotropic plates with $\gamma = \delta = 0.8$, the improvement indicated by these results is approximately 90% and 85% of the K_x values corresponding to pure compression loading for the clamped and simply supported plates, respectively. The results presented in figure 22 also indicate that plates with $\gamma = \delta = 0$ are the most buckling resistant of the plates loaded by positive shear forces, whereas the plates with $\gamma = \delta = 0.8$ are the most buckling resistant of the plates loaded by negative shear forces. This trend is also exhibited by the simply supported plates.

Results are presented in figure 23 for clamped plates with $\beta = 1$ as a function of the anisotropic parameters γ and δ . Curves are shown in this figure for values of $\gamma = 0$ and 0.4, and values of δ ranging from 0 to 0.6. The results presented in figure 23 indicate the same trend shown in figure 14 for the axial compression-loaded plates and in figure 19 for the shear-loaded plates; i.e., the buckling coefficients are more sensitive to the anisotropic parameter δ than to γ .

Transverse Tension or Compression and Shear Loading

Buckling interaction curves are presented in figure 24 for infinitely long clamped $[\pm\theta]_s$ plates subjected to transverse tension or compression and shear loadings for several values of fiber orientation angle θ . The dashed lines shown in figure 24 correspond to results for which anisotropy is included, and the solid lines correspond to solutions for which it is neglected. Negative values of K_y correspond to transverse tension loadings, and negative values of K_s correspond to negative shear loadings. Points of intersection of the interaction curves shown in the figure with a straight line emanating from the origin of the plot constitute constant values of $N_y/N_{xy} (D_{11}/D_{22})^{1/4}$. The horizontal straight-line portions of the buckling interaction curves indicate values of the buckling coefficients for which a plate buckles into a wide column mode ($K_y = 4$ for clamped plates). For this mode, the half-wave length λ shown in figure 1 approaches infinity in the analysis.

The results presented in figure 24 indicate that the effects of anisotropy also manifest themselves as a phase shift of self-similar curves in the $K_s - K_y$ plane for these loading conditions. For plates loaded in positive shear, neglecting plate anisotropy in an analysis yields buckling coefficients substantially larger than those corresponding to the anisotropic solution. In addition, the value of K_s at which the plate buckles into a wide column mode is significantly overestimated. For plates loaded in negative shear, this trend is

reversed. The coalescence of all the curves shown in figure 24 into the same horizontal line segment at $K_y = 4$ indicates that anisotropy is unimportant for plates that buckle into a wide column mode; i.e., the transverse loading N_y forces the plate to assume a deformation state that is not skewed (or it is skewed at $x = \pm$ plus and minus infinity). Similar results were obtained for corresponding simply supported plates, and these results exhibit exactly the same trends. The simply supported plates buckle into a wide column mode at $K_y = 1$.

Generic buckling results for clamped and simply supported plates subjected to combined axial and shear loadings are presented in figures 25 through 27. Additional results were obtained for both boundary condition cases and several values of β , γ , and δ . These additional results indicate that the buckling interaction curves for this combination of loadings are also independent of the parameter $(D_{11}/D_{22})^{1/4}$.

Buckling interaction curves are presented in figure 25 for clamped and simply supported plates with several values of the orthotropic parameter β and with $\gamma = \delta = 0$. Once again, the fact that the buckling interaction curves are independent of $(D_{11}/D_{22})^{1/4}$ permits results for particular laminates with zero-valued (or small compared to unity) anisotropic parameters to be obtained directly from figure 25 once the value of β for the specific laminate is known. The results shown in figure 25 indicate that substantial gains in buckling resistance can be obtained by tailoring laminate construction to increase the parameter β .

Generic buckling results are presented in figure 26 for clamped and simply supported plates with values of $\gamma = \delta$ ranging from 0 to 0.8 and for a value of $\beta = 3$. These results also confirm the results presented in figure 24 that show that the anisotropy is generally manifested as a phase shift of the interaction curves in the $K_s - K_y$ plane, and that anisotropy does not affect the wide column buckling mode. The results presented in figure 26 also indicate that plates with $\gamma = \delta = 0$ are the most buckling resistant of the plates loaded by positive shear forces, whereas the plates with $\gamma = \delta = 0.8$ are the most buckling resistant of the plates loaded by negative shear forces.

Results are presented in figure 27 for clamped plates with $\beta = 3$ in which the anisotropic parameters γ and δ are varied independently. Buckling interaction curves are shown in this figure for values of $\gamma = 0$ and 0.6, and values of δ ranging from 0 to 0.6. The results presented in figure 27 indicate the plates loaded by transverse tension or compression and shear are also more sensitive to the anisotropic parameter δ than to γ .

Axial Compression and Transverse Tension or Compression Loading

Buckling interaction curves are presented in figure 28 for infinitely long clamped and simply supported $[\pm\theta]_s$ plates subjected to transverse tension or compression and axial compression loadings for several values of fiber orientation angle θ . The dashed lines shown in figure 28 correspond to results for which anisotropy is included in the analysis, and the solid lines correspond to results for which it is neglected. Points of intersection of the interaction curves shown in the figure with a straight line emanating from the origin of the plot constitute constant values of $N_y/N_x (D_{11}/D_{22})^{1/2}$. The horizontal straight-line portions of

the buckling interaction curves indicate values of the buckling coefficients at which a plate buckles into a wide column mode.

The results presented in figure 28 indicate that the effects of anisotropy for plates subjected to these loading conditions also generally manifest themselves as a phase shift of self-similar curves in the $K_x - K_y$ plane. Neglecting plate anisotropy in an analysis always yields buckling coefficients larger than those corresponding to the anisotropic solution. Similar to the plates loaded by shear and transverse compression, the value of K_x at which the plate buckles into a wide column mode is substantially overestimated when anisotropy is neglected.

Generic buckling results for clamped and simply supported plates subjected to combined axial and transverse loadings are presented in figures 29 through 31. Additional results were obtained for both boundary condition cases and several values of β , γ , and δ . These additional results indicate that the buckling interaction curves for this combination of loadings are also independent of the parameter $(D_{11}/D_{22})^{1/4}$.

Buckling interaction curves are presented in figure 29 for clamped and simply supported plates with several values of the orthotropic parameter β and with $\gamma = \delta = 0$. Since the buckling interaction curves are independent of $(D_{11}/D_{22})^{1/4}$, results for particular laminates with zero-valued (or small compared to unity) nondimensional anisotropic parameters can be obtained directly from figure 29 once the value of β for the specific laminate is known. The results shown in figure 29 indicate that substantial gains in buckling resistance can be obtained when β increases.

Generic buckling results are presented in figure 30 for clamped plates with values of $\gamma = \delta$ ranging from 0 to 0.6. Two sets of curves are shown in the figure. The solid and dashed lines correspond to values of $\beta = 3$ and 1, respectively. These results also show a phase shift due to anisotropy, and show that the effects of anisotropy are more pronounced for plates with $\beta = 1$ than for plates with $\beta = 3$. The results presented in figure 30 also indicate that plates with $\gamma = \delta = 0$ are the most buckling resistant of the plates when nonzero axial loading is present.

Results are presented in figure 31 for clamped plates with $\beta = 3$ as a function of the anisotropic parameters γ and δ . Curves are shown in this figure for values of $\gamma = 0$ and 0.6, and values of δ ranging from 0 to 0.6. The results presented in figure 31 indicate the plates loaded by transverse tension or compression and axial compression are also generally more sensitive to the parameter δ than to γ .

CONCLUDING REMARKS

A parametric study of the buckling behavior of infinitely long symmetrically laminated anisotropic plates subjected to combined loadings has been presented. Loading conditions consisting of axial tension and compression, transverse tension and compression, and shear were investigated for clamped and simply supported plates. Results are presented that were obtained using a special purpose analysis that was derived in terms of useful nondimensional parameters. The analysis was found to be well suited for parametric studies. Buckling results are also presented for some common laminate constructions, and generic buckling design charts have been presented for a wide range of parameters. The generic design charts are presented in terms of useful nondimensional parameters, and the

dependence of the nondimensional parameters on laminate fiber orientation, stacking sequence, and material properties is discussed.

The results presented in the present paper show that nondimensional parameters can be very useful in presenting results in a concise manner for a wide range of loading conditions, boundary conditions, and laminate constructions. Results are presented that show that the effects of anisotropy are much more pronounced in shear-loaded plates than in compression-loaded plates. In addition, the effects of anisotropy on plates subjected to combined loadings are shown to be generally manifested as phase shifts of self-similar buckling interaction curves. These results indicate that the buckling resistance of long compression-loaded highly anisotropic plates can be improved significantly by applying a shear loading with a specific orientation. Moreover, it is shown that anisotropy reduces the buckling resistance of biaxially compressed plates.

A substantial number of generic buckling results are presented in the present paper for a wide range of values of the nondimensional parameters. In all cases considered in the study, it is shown that the buckling coefficients of infinitely long plates are independent of the bending stiffness ratio $(D_{11}/D_{22})^{1/4}$. It is also shown that large increases in buckling resistance can be obtained by tailoring the laminate construction to increase the parameter $\beta = (D_{12} + 2D_{66})/(D_{11}D_{22})^{1/2}$, and that the importance of anisotropy generally diminishes as β increases. Results are also presented that show the buckling coefficients to be generally more sensitive to the anisotropic parameter $\delta = D_{26}/(D_{11}D_{22})^{1/4}$ than to the anisotropic parameter $\gamma = D_{16}/(D_{11}D_{22})^{1/4}$ for the entire range of loadings and boundary conditions considered.

REFERENCES

1. Nemeth, M. P.: Importance of Anisotropy on Buckling of Compression-Loaded Symmetric Composite Plates. AIAA Journal, Vol. 24, No. 11, November 1986, pp. 1831-1835.
2. Grenestedt, J. L.: A Study on the Effect of Bending-Twisting Coupling on Buckling Strength. Composite Structures, Vol. 12, No. 4, 1989, pp. 271-290.
3. Johns, D. J.: Shear Buckling of Isotropic and Orthotropic Plates, A Review. A.R.C. R&M No. 3677, 1970.
4. Stein, M.: Postbuckling of Orthotropic Composite Plates Loaded in Compression. Presented at the AIAA/ASME/ASCE/AHS 23rd Structures, Structural Dynamics, and Materials Conference, New Orleans, Louisiana, May 10-12, 1982. AIAA Paper No. 82-0778.
5. Gerard, G. and Becker, H.: Handbook of Structural Stability. Part I - Buckling of Flat Plates. NACA Technical Note 3781, July 1957.
6. Stowell, E. Z.: Critical Shear Stress of an Infinitely Long Flat Plate with Equal Elastic Restraints Against Rotation Along the Parallel Edges. NACA Wartime Report ARR 3K12, November 1943.

7. Stowell, E. Z. and Schwartz, E. B.: Critical Stress for an Infinitely Long Flat Plate with Elastically Restrained Edges Under Combined Shear and Direct Stress. NACA Wartime Report ARR 3K13, November 1943.
8. Batdorf, S. B. and Houbolt, J. C.: Critical Combinations of Shear and Transverse Direct Stress for an Infinitely Long Flat Plate with Edges Elastically Restrained Against Rotation. NACA Report No. 847, 1946.
9. Batdorf, S. B., Stein, M. and Libove, C.: Critical Combinations of Longitudinal and Transverse Direct Stress for an Infinitely Long Flat Plate with Edges Elastically Restrained Against Rotation. NACA Wartime Report ARR L6A05a, March 1946.
10. Housner, J. M. and Stein, M.: Numerical Analysis and Parametric Studies of the Buckling of Composite Orthotropic Compression and Shear Panels. NASA Technical Note D-7996, October 1975.
11. Wittrick, W. H. and Williams, F. W.: Buckling and Vibration of Anisotropic or Isotropic Plate Assemblies Under Combined Loadings. International Journal of Mechanical Sciences, Vol. 16, 1974, pp. 209-239.

Table 1. Stiffness ratios and major Poisson's ratio for common lamina material systems.

Material system	E_1/E_2	E_2/G_{12}	ν_{12}
High-strength graphite-epoxy material	11.6	1.9	.35
Kevlar-epoxy material	13.8	2.7	.34
S-glass-epoxy material	4.4	2.1	.25
Ultra-high-modulus graphite-epoxy material	50.0	1.5	.26
Boron-epoxy material	10.0	4.3	.21
Boron-aluminum material	1.6	3.0	.23

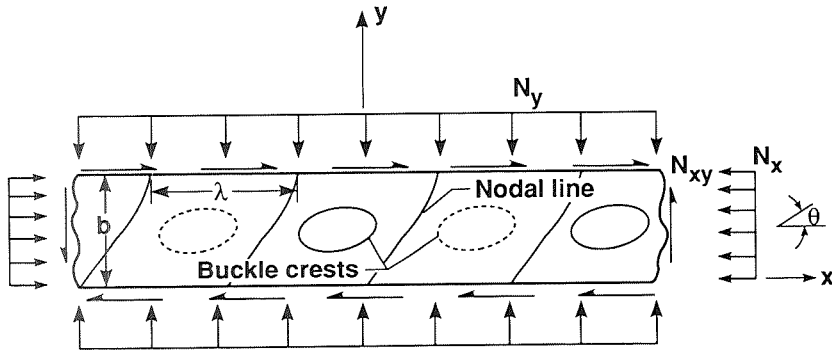


Figure 1. Geometry of a buckled plate subjected to biaxial compression and shear loadings.

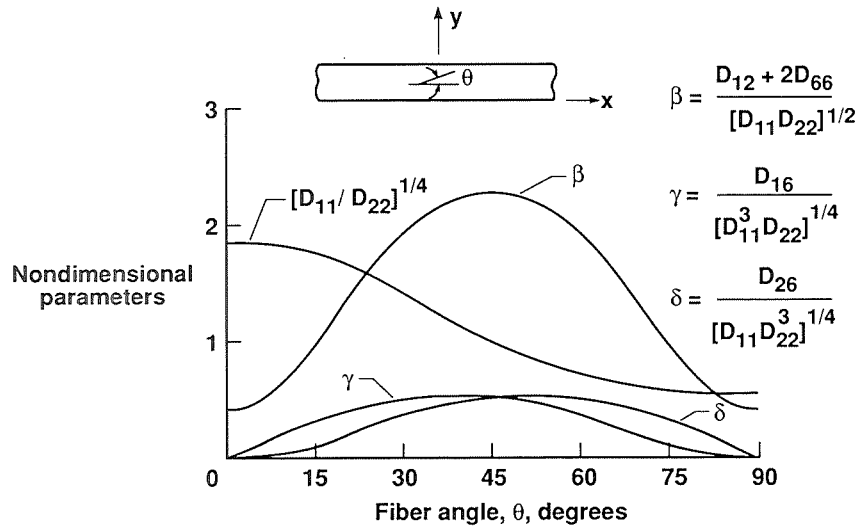


Figure 2. Nondimensional parameters for $[\pm\theta]_s$ graphite-epoxy laminates.

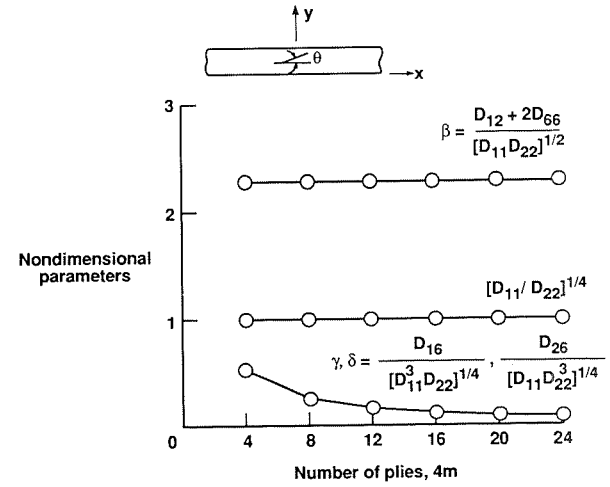


Figure 3. Nondimensional parameters for $[(+45)_m]_s$ graphite-epoxy laminates.

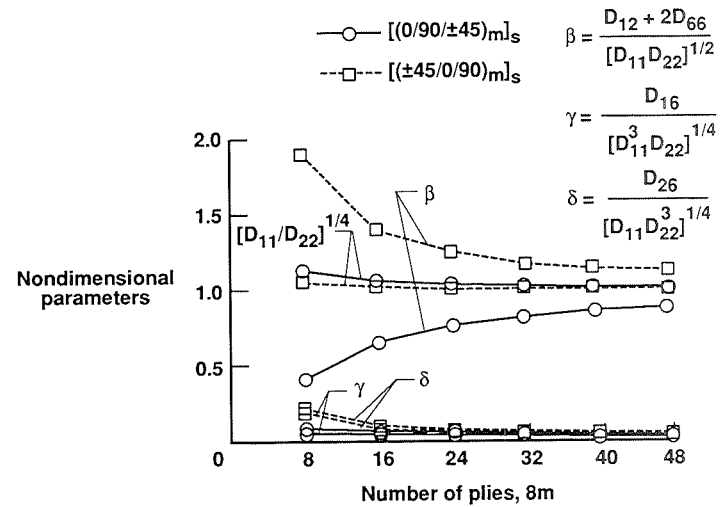


Figure 4. Nondimensional parameters for quasi-isotropic graphite-epoxy laminates.

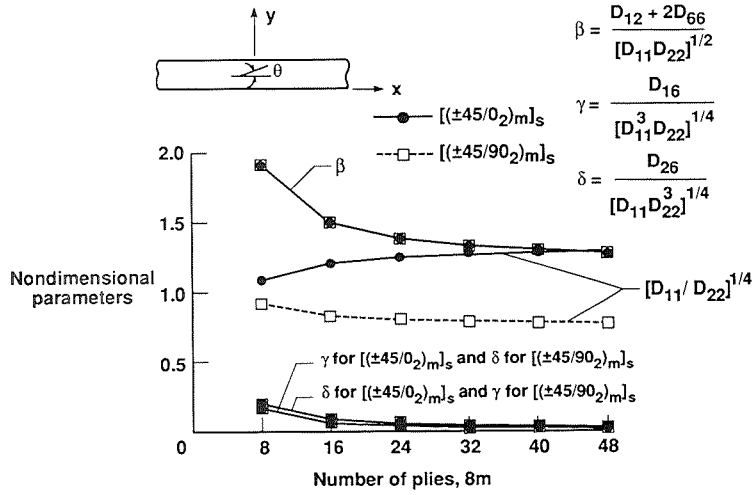


Figure 5. Nondimensional parameters for $[(\pm 45/0_2)_m]_s$ and $[(\pm 45/90_2)_m]_s$ graphite-epoxy laminates.

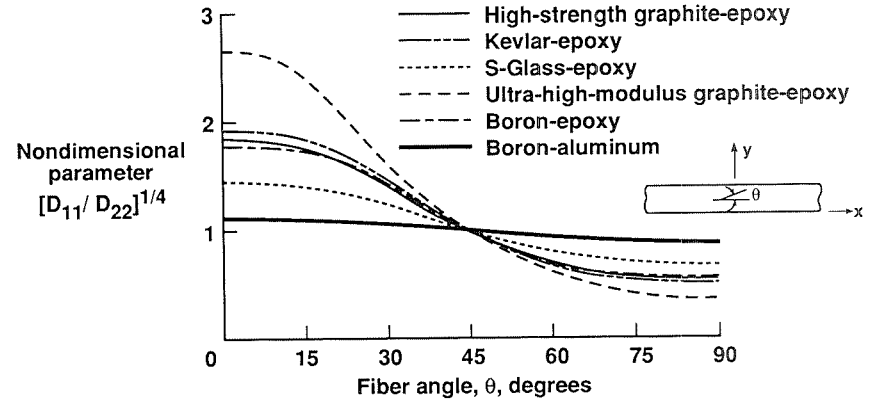


Figure 7. Effect of lamina material properties on the parameter $(D_{11}/D_{22})^{1/4}$ for $[\pm\theta]_s$ laminates.

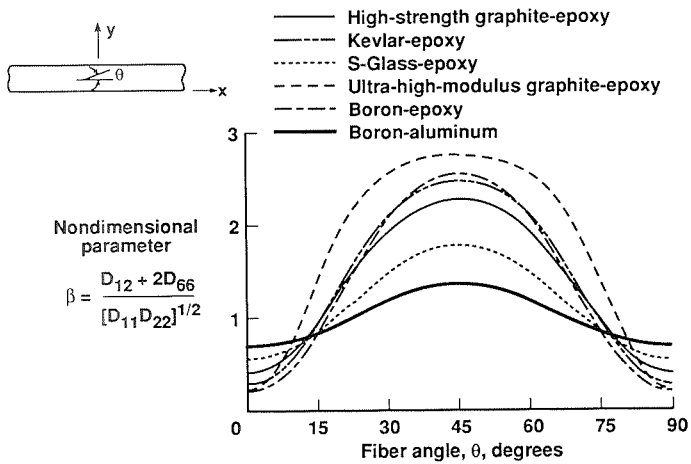


Figure 6. Effect of lamina material properties on the nondimensional orthotropic parameter β for $[\pm\theta]_s$ laminates.

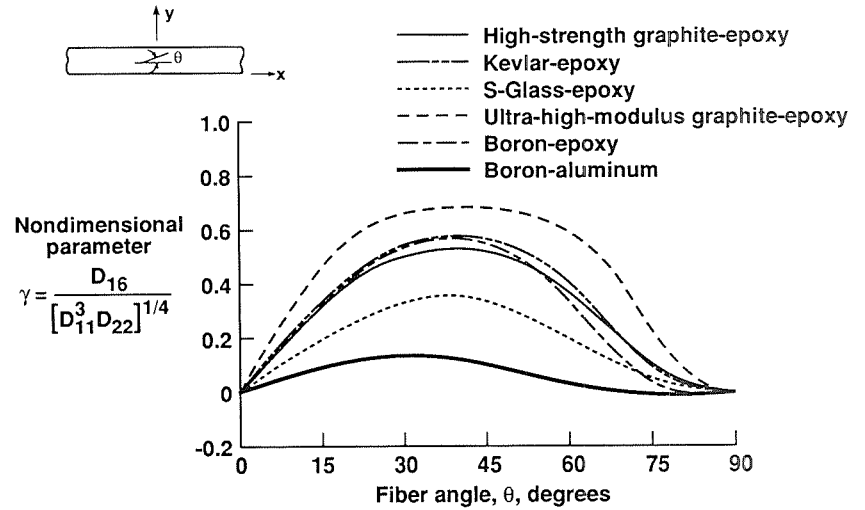


Figure 8. Effect of lamina material properties on the nondimensional anisotropic parameter γ for $[\pm\theta]_s$ laminates.

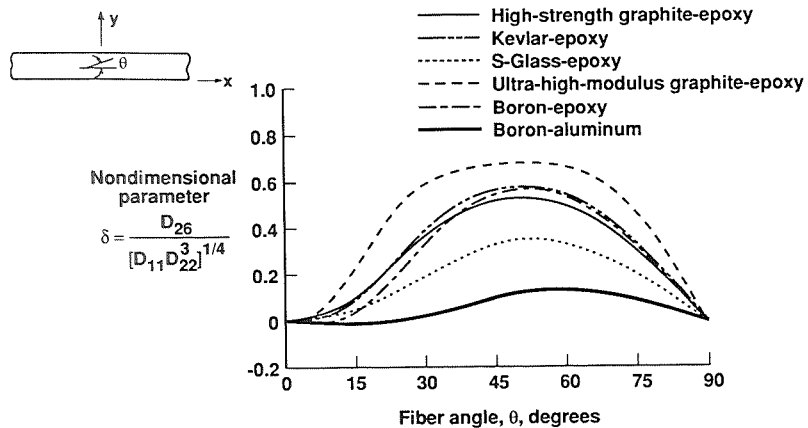


Figure 9. Effect of lamina material properties on the nondimensional anisotropic parameter δ for $[+\theta]_s$ laminates.

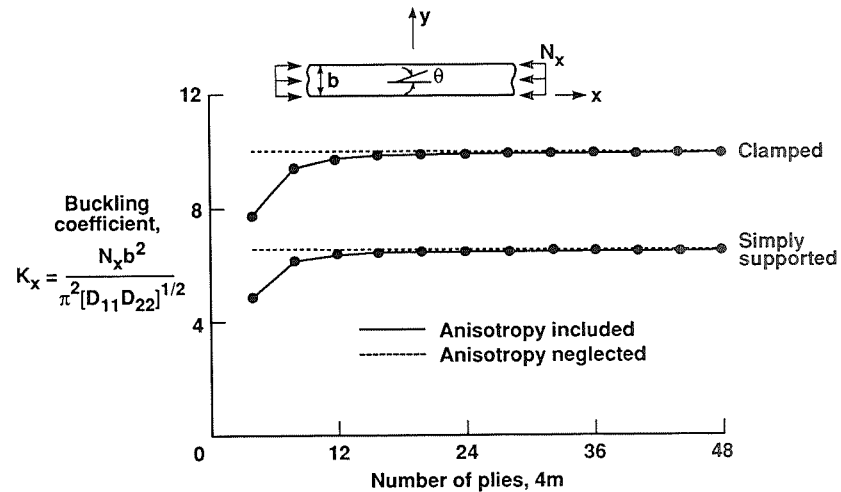


Figure 11. Buckling coefficients for axial-compression-loaded $[(+45)_m]_s$ graphite-epoxy laminates.

247

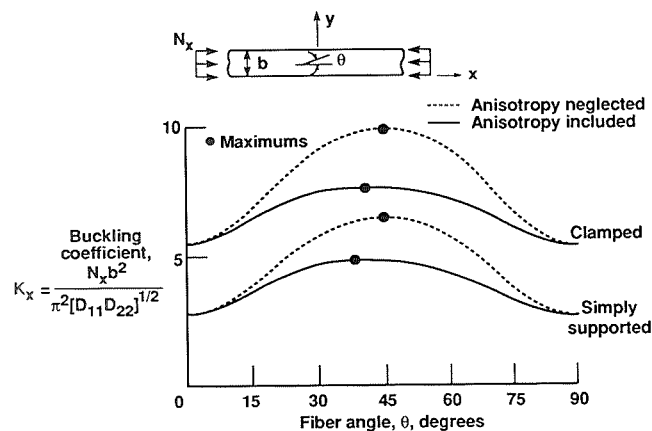


Figure 10. Buckling coefficients for axial-compression-loaded $[+\theta]_s$ graphite-epoxy laminates.

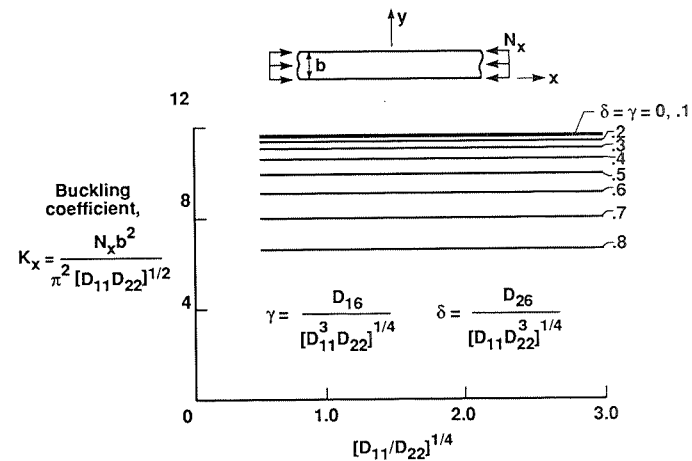


Figure 12. Effects of $(D_{11}/D_{22})^{1/4}$ and anisotropic parameters γ and δ on buckling coefficients for axial-compression-loaded clamped plates ($\beta = 3$).

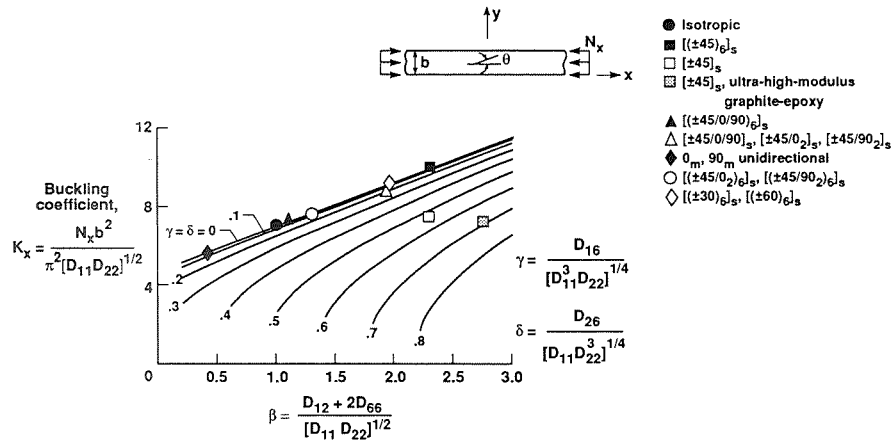


Figure 13. Effects of orthotropic parameter β and anisotropic parameters γ and δ on buckling coefficients for axial-compression-loaded clamped plates. All laminates shown are made of typical graphite-epoxy material unless otherwise noted.

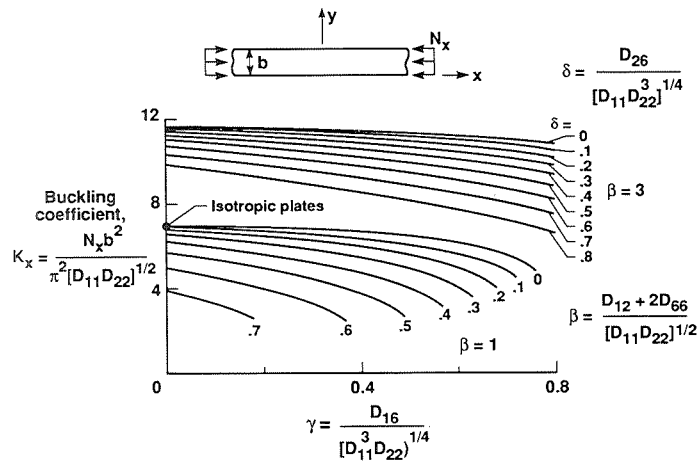


Figure 14. Effects of anisotropic parameters γ and δ on buckling coefficients for axial-compression-loaded clamped plates.

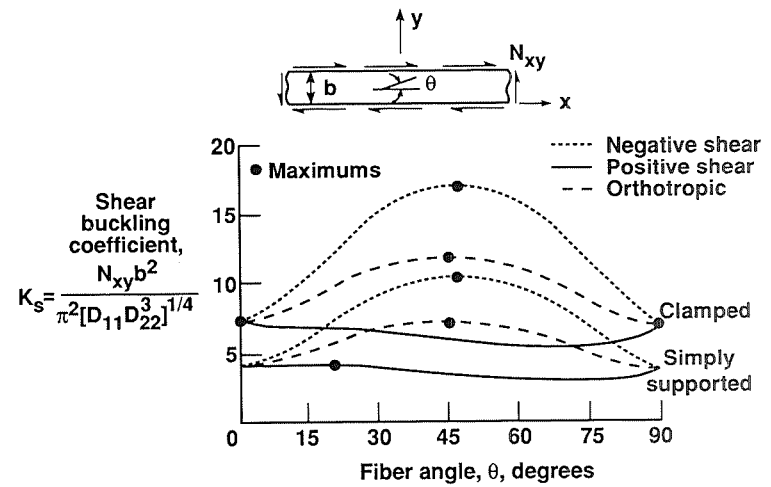


Figure 15. Buckling coefficients for shear-loaded $[\pm\theta]_S$ graphite-epoxy laminates.

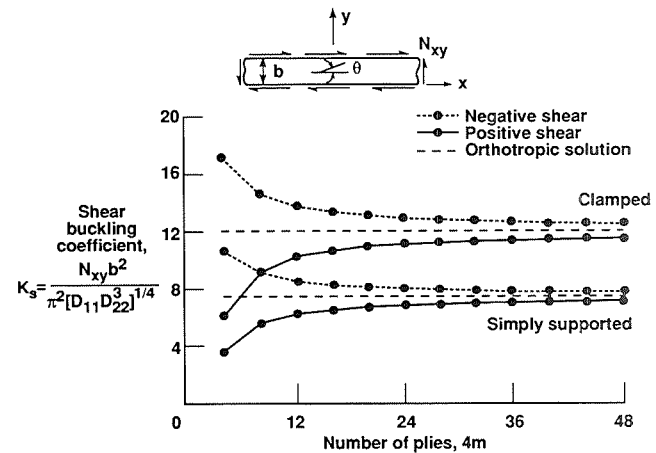


Figure 16. Buckling coefficients for shear-loaded $[(\pm 45)_m]_S$ graphite-epoxy laminates.

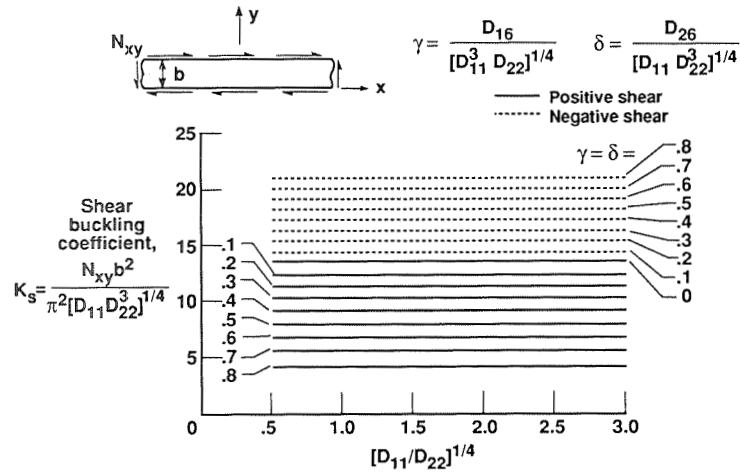


Figure 17. Effects of $(D_{11}/D_{22})^{1/4}$ and anisotropic parameters γ and δ on buckling coefficients for shear-loaded clamped plates ($\beta = 3$).

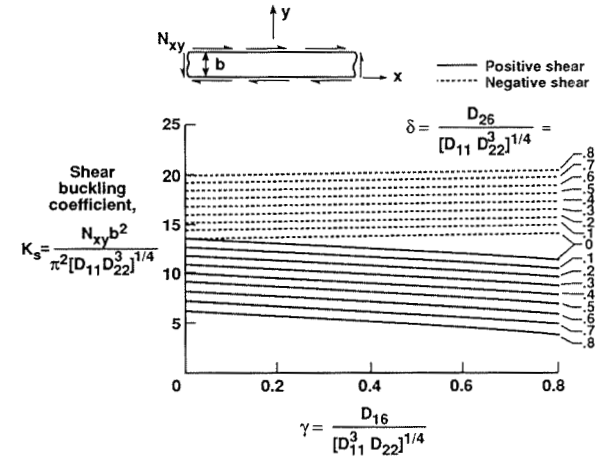


Figure 19. Effects of anisotropic parameters γ and δ on buckling coefficients for shear-loaded clamped plates ($\beta = 3$).

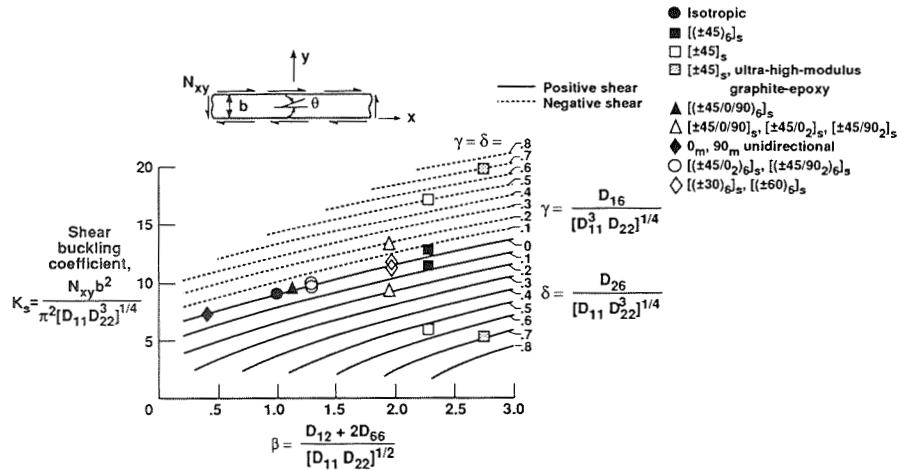


Figure 18. Effects of orthotropic parameter β and anisotropic parameters γ and δ on buckling coefficients for shear-loaded clamped plates. All laminates shown are made of typical graphite-epoxy material unless otherwise noted.

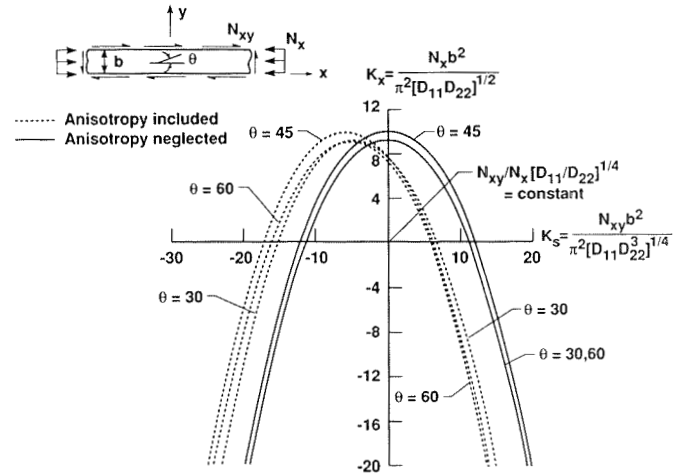


Figure 20. Buckling interaction curves for clamped \$[+\theta]_s\$ graphite-epoxy laminates subjected to axial tension or compression and shear.

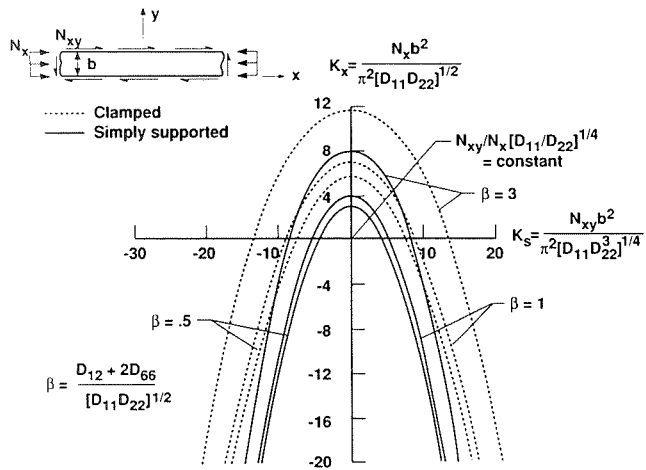


Figure 21. Effect of orthotropic parameter β on the buckling interaction curves for specially orthotropic laminates ($\gamma = \delta = 0$) subjected to axial tension or compression and shear.

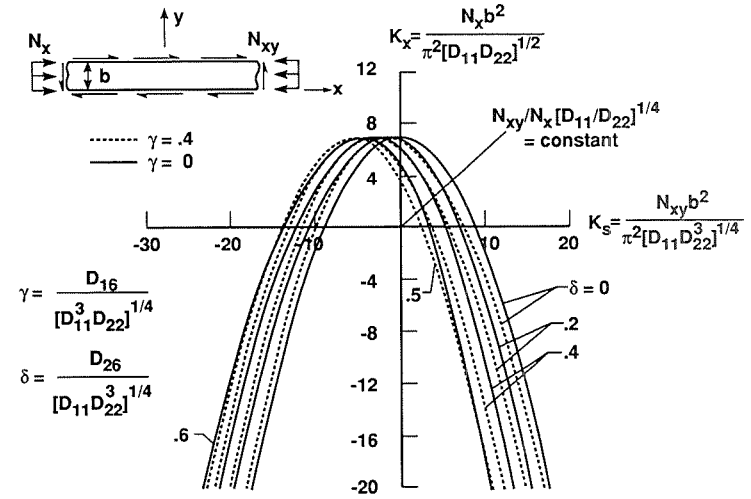


Figure 23. Effect of anisotropic parameters γ and δ on the buckling interaction curves for clamped laminates subjected to axial tension or compression and shear ($\beta = 1$).

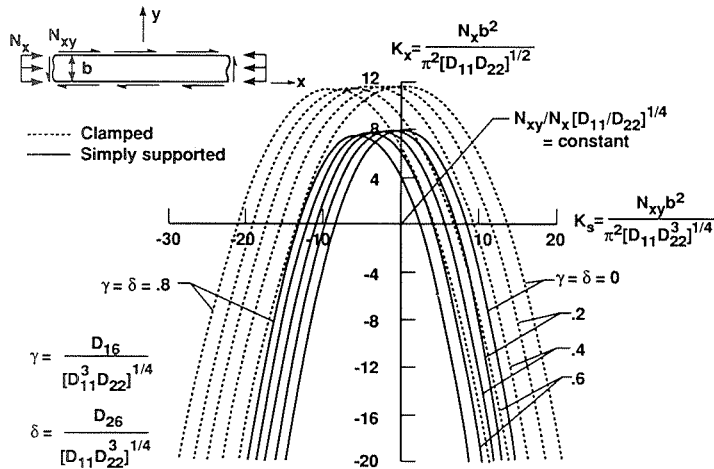


Figure 22. Effect of anisotropic parameters γ and δ on the buckling interaction curves for laminates subjected to axial tension or compression and shear ($\beta = 3$).

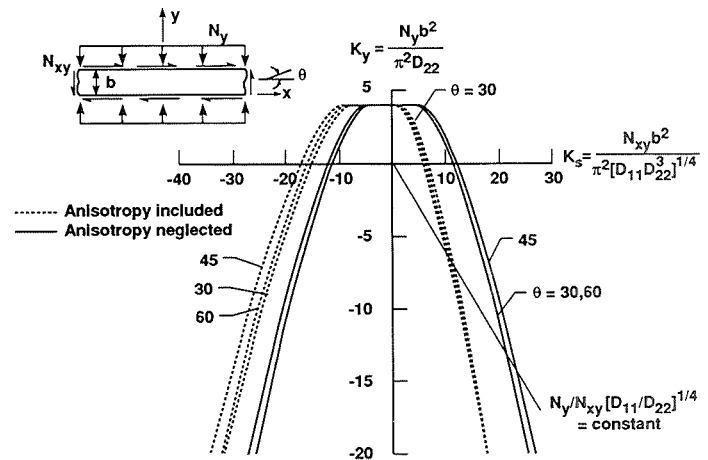


Figure 24. Buckling interaction curves for clamped $[\pm\theta]_s$ graphite-epoxy laminates subjected to transverse tension or compression and shear.

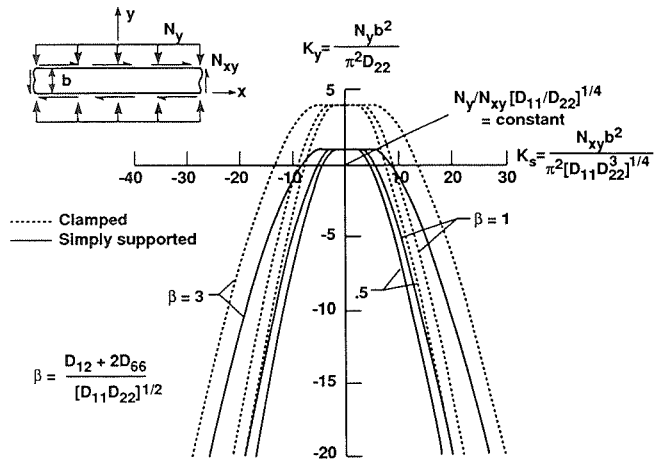


Figure 25. Effect of orthotropic parameter β on the buckling interaction curves for specially orthotropic laminates ($\gamma = \delta = 0$) subjected to transverse tension or compression and shear.

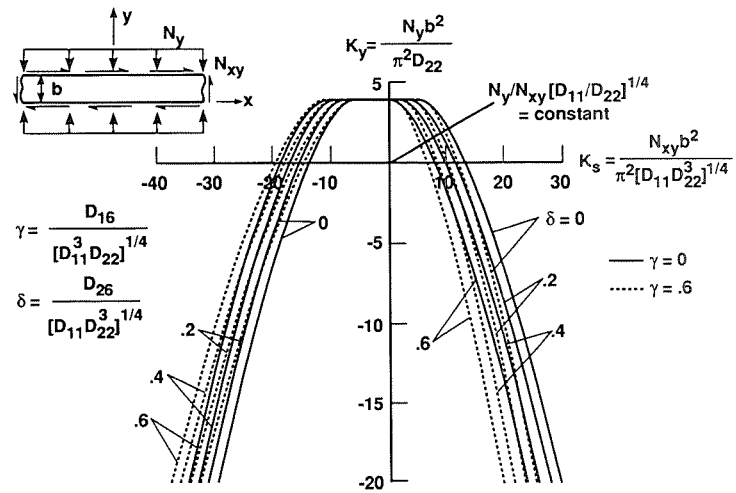


Figure 27. Effect of anisotropic parameters γ and δ on the buckling interaction curves for clamped laminates subjected to transverse tension or compression, and shear ($\beta = 3$).

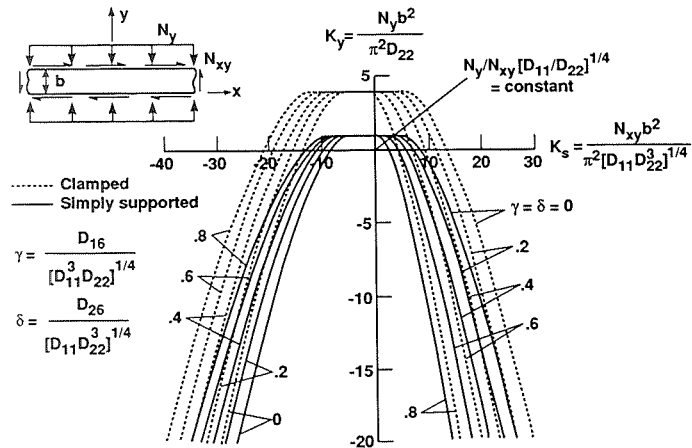


Figure 26. Effect of anisotropic parameters γ and δ on the buckling interaction curves for laminates subjected to transverse tension or compression and shear ($\beta = 3$).

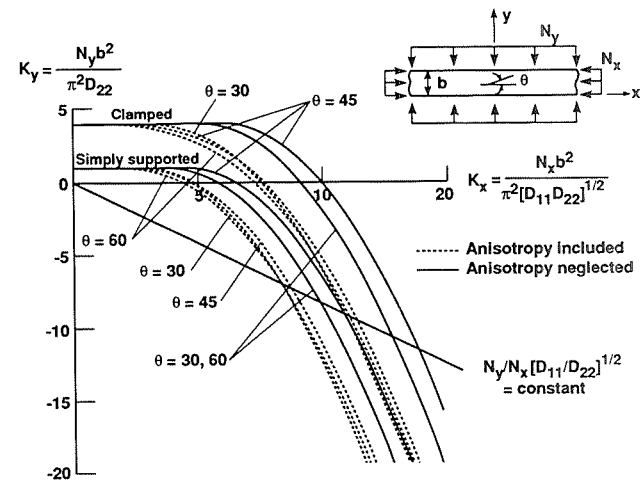


Figure 28. Buckling interaction curves for $[+\theta]_s$ graphite-epoxy laminates subjected to transverse tension or compression and axial compression.

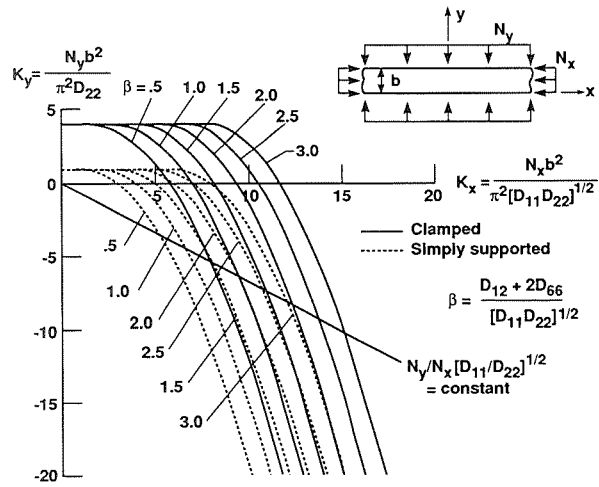


Figure 29. Effect of orthotropic parameter β on the buckling interaction curves for specially orthotropic laminates ($\gamma = \delta = 0$) subjected to transverse tension or compression and axial compression.

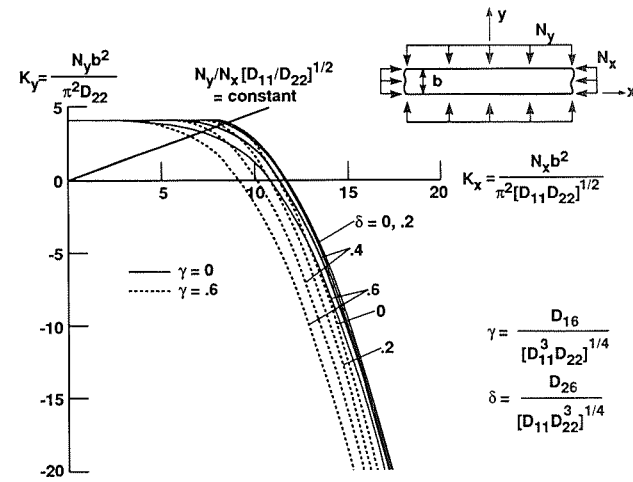


Figure 31. Effect of anisotropic parameters γ and δ on the buckling interaction curves for clamped laminates subjected to transverse tension or compression and axial compression ($\beta = 3$).

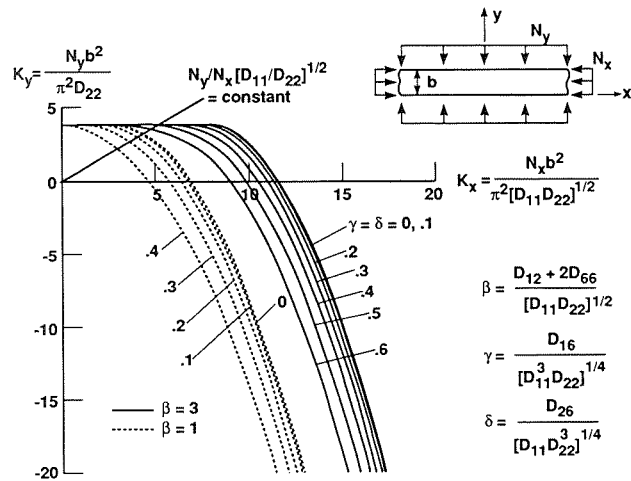


Figure 30. Effect of anisotropic parameters γ and δ on the buckling interaction curves for clamped laminates subjected to transverse tension or compression and axial compression.

COMPRESSIVE RESIDUAL STRENGTH OF GRAPHITE/EPOXY LAMINATES AFTER IMPACT

Teresa A. Guy¹ and Paul A. Lagace
Technology Laboratory for Advanced Composites
Department of Aeronautics and Astronautics
Massachusetts Institute of Technology

511-24
51379
P.22

ABSTRACT

The issue of damage tolerance after impact, in terms of the compressive residual strength, was experimentally examined in graphite/epoxy laminates using Hercules AS4/3501-6 in a $[\pm 45/0]_{2S}$ configuration. Three different impactor masses were used at various velocities and the resultant damage measured via a number of nondestructive and destructive techniques. Specimens were then tested to failure under uniaxial compression. The results clearly show that a minimum compressive residual strength exists which is below the open hole strength for a hole of the same diameter as the impactor. Increases in velocity beyond the point of minimum strength cause a difference in the damage produced and cause a resultant increase in the compressive residual strength which asymptotes to the open hole strength value. Furthermore, the results show that this minimum compressive residual strength value is independent of the impactor mass used and is only dependent upon the damage present in the impacted specimen which is the same for the three impactor mass cases. A full three-dimensional representation of the damage is obtained through the various techniques. Only this three-dimensional representation can properly characterize the damage state that causes the resultant residual strength. Assessment of the state-of-the-art in predictive analysis capabilities shows a need to further develop techniques based on the three-dimensional damage state that exists. In addition, the need for damage "metrics" is clearly indicated.

INTRODUCTION

As the use of advanced composite materials for primary structure in the aerospace and aircraft industries increases, concerns involving their damage tolerance need to be further addressed. This, in part, has led to a considerable amount of work on the subject of impact.

There are two issues involved in the subject of impact: damage resistance and damage tolerance [1]. The former deals with the actual impact event and the damage that results; the latter deals with the ability of the composite laminate to perform its desired function (e.g., carry load or retain stiffness) in the presence of damage. The latter is the main topic of the current work.

The importance of the damage size and its location increases with the complexity of the applied stress field. The most significant effects are due to damage in areas subject to high in-plane compression, shear stress, interlaminar stress, or out-of-plane bending moments [2-6]. Of the aforementioned complex stress fields, in-plane compression was

¹ currently at McDonnell Douglas Technologies Incorporated

selected as the load condition of interest for this work. Experimental evidence shows that a more severe reduction in compressive residual strength occurs from impact damage than due to the presence of an imbedded delamination with equal area (as determined by ultrasonic evaluation) [7–14]. Impact damage may also result in a more severe reduction in compressive residual strength than a hole with an equivalent diameter [6–9, 15, 16]. It is thus important to test configurations with actual impact damage rather than "simulated" damage to get an accurate evaluation of the potential loss in compressive load-carrying ability.

In the great majority of work on impact damage tolerance, researchers have attempted to correlate the post-impact strength with easily measured parameters [e.g., 9, 11, 17–21]. These parameters include planar damage area and impactor metrics (mass, velocity, energy). These results have generally shown that the compressive residual strength exhibits asymptotic behavior as damage area increases and as impactor energy increases. In at least one case [20], an apparent minimum compressive residual strength exists below an equivalent impactor diameter open hole strength value. Preliminary data [22] indicates such a minimum does exist. Furthermore, recent work by Dost, Ilcewicz, and Gosse [23] indicates the need for a full three-dimensional description of the damage state in order to properly determine the residual strength of the laminate. This indicates a need for basic understanding of the damage mechanisms which are important in controlling compressive residual strength. Thus, the main thrust of the current work is the determination of the minimum post-impact compressive residual strength and the damage state which causes it.

OBJECTIVES AND APPROACH

The specific purpose of the work was to provide answers to the following questions (in the context of the specific laminate investigated): one, what is the three-dimensional damage state that governs minimum compressive residual strength behavior; two, is this minimum compressive residual strength value dependent upon impactor mass; and, three, how does this minimum compressive residual strength value relate to impactor mass and velocity?

All laminates were made from AS4/3501-6 graphite/epoxy unidirectional tape manufactured by Hercules, Inc. in a $[\pm 45/0]_{2S}$ configuration. This laminate orientation and material system were selected because of extensive data available on damage resistance and tensile residual strength [e.g., 24]. Three different impactor masses were chosen: 1523 g, 578 g, and 8.4 g. The masses selected are representative of a range of potential impactor masses such as a dropped hand tool down to runway debris kick-up for an aircraft. The first item of the experimental program was the determination of the impactor velocity which resulted in the minimum compressive residual strength for each mass. Preliminary work [22] indicated that with a mass of 8.4 g, minimum compressive residual strength occurs due to the damage incurred at an impactor velocity of 57 m/s. This work also defined the range of velocities which causes from little or no damage to complete penetration of the specimens. (Complete penetration is defined as the tip of the impactor progressing beyond the back surface of the laminate.) Based on this, a number of impactor velocities, shown in Table 1, was chosen for each mass.

After minimum compressive residual strengths were characterized for the three impactor masses of interest, the focus shifted to defining the damage state at these

minima. The intent was to impact specimens at several velocities surrounding the minimum compressive residual strength velocity previously determined. For each impactor velocity, several specimens were destructively evaluated while others were tested for compressive residual strength for corroboration with initial test results. The need for accurate damage assessment to understand the effect of impact damage on compressive residual strength is well-documented [9, 19, 23]. Proponents of destructive evaluation methods [e. g., 25] argue that nondestructive evaluation (NDE) methods are severely limited in defining delamination at ply interfaces and only destructive methods can accurately determine the internal damage state. However, destructive methods are not an option for evaluation of composite structure in a production article nor are they useful when residual strength tests are to be subsequently conducted. Thus, nondestructive methods are being upgraded to accurately determine the through-the-thickness damage state. To that end, both destructive and nondestructive damage evaluation techniques were used in this study to characterize damage in some of the coupons subject to impact. All impact coupons were inspected by at least two NDE techniques: visual inspection, X-ray or ultrasonic scanning. Visual inspection and X-ray were methods used in all cases. Coupon sectioning and the deply technique were the destructive methods of damage evaluation. The different damage evaluation techniques were applied to compare accuracy and adequacy of information provided by the various methods. The full test matrix indicating the different types of damage evaluation techniques used for each specimen is shown in Table 1.

In addition to the impact-damaged compressive residual strength specimens, undamaged specimens and specimens with open holes were tested to provide baseline data. This test matrix is shown in Table 2. The 12.7 mm diameter hole is identical to the diameter of all impactors used in this work. Larger diameter holes were also tested to compare the compressive residual strength after impact to holes larger than the diameter of the impactor. The 25.4 mm diameter hole is the maximum size used in order to avoid finite width effects.

PROCEDURES

Coupon Preparation

All laminates were cured in an autoclave using the manufacturer's recommended cure cycle with a one-hour hold at 117°C followed by a two-hour hold at 177°C. A full vacuum and a pressure of 0.59 MPa was also maintained during the cure. All laminates also underwent an eight-hour postcure at 177°C. Laminates were subsequently cut to a specimen size of 70 mm wide by 340 mm long using a water-cooled diamond blade and were ready for impact or drilling after appropriate measurements were taken.

Impact

Two different impact test methods were used. For each, the test coupons were identical and a common holding jig, illustrated in Figure 1, was used. The holding jig includes a large aluminum plate with a rectangular opening; aluminum bars (in this case, square bars to simulate clamped boundary conditions); and threaded rods with hex nuts used to apply consistent torque (11.3 Nm) at each nut for each test.

The first impact test apparatus consists of a striker unit and an impactor unit, as shown in Figure 2. This apparatus was used with the higher impactor masses (578 g and 1523 g). A 12.7 mm diameter hemispherical steel tup was used in this work and was connected to a steel rod for the 1523 g mass case, and an aluminum rod for the 578 g mass case. A 13 mm thick plastic doughnut that acted as a timing flag was attached to the impactor rod. Impactor velocity was measured by determining the time the plastic doughnut interrupted an LED mounted between the linear bearings on the impactor unit.

The second impact device, as shown in Figure 3, was an air gun initially developed and used at NASA Langley Research Center [26]. This was used for the low mass (8.4 g) impacts. This test apparatus consists of a variable pressure source, a low pressure reservoir, a solenoid trigger, a gun barrel, and 12.7 mm diameter spherical projectiles (steel balls were used in this work). The impactor velocity is measured with an LED system. The projectile passes an infrared LED that sends a signal to the optical trigger box that triggers the timing mechanism. When the projectile passes a second infrared LED, located 200 mm further along the gun barrel, another signal is sent to the optical trigger box to stop the timing mechanism. The time to transverse the two LED's is recorded in each test.

Damage Detection

All of the impact coupons were evaluated by two nondestructive techniques. After visual inspection, X-ray photography was conducted. An enhancing agent of 1,4-Diiodobutane (DiB) was injected into the damaged area with a syringe until a small bubble appeared on the surface of the graphite/epoxy coupon. As DiB is a low viscosity liquid that penetrates into any exposed crack through capillary action, X-rays were taken after a minimum of one hour elapsed time from injection. A typical X-ray photograph of impact damage is presented in Figure 4. A schematic of the damage regions defined by X-ray evaluation is illustrated in Figure 5. The major and minor axes of damage were measured as well as the dimensions of the central region or "core" damage defined by the very dark internal region, indicative of the region of intense fiber damage.

Pulse-echo ultrasonic scanning was performed by Hercules, Inc. with a Metro Tek C403 ultrasonic scanning system. All scanning was performed at a pulse frequency of 10 MHz. A typical ultrasonic C-Scan provided a map of the damage "smeared" through-the-thickness such that the through-the-thickness location(s) of the damage(s) was not indicated. This "two-dimensional" inspection was performed on all specimens that underwent ultrasonic evaluation. In addition, three-dimensional ultrasonic C-Scan data was provided on a ply-by-ply basis for a number of specimens. In these time-of-flight C-Scans, only reflections at the ply of interest are "gated" and thus cause a signal to be received. These reflections occur at damage in the laminate. If there is no damage at the ply, no signal is received within the "gate". Because all plies were not of uniform thickness and the "time" thickness measurement of the laminate was divided by 12 to evaluate each ply, exact location within a ply is not known. The location is known to be within a ply but is unlikely to coincide exactly with a ply interface. Furthermore, if the signal is reflected before the ply, indicative of damage above that location, the area beneath the reflection will be "shadowed" in that little signal will be transmitted. Thus, even if damage at that ply exists, the reflected signal amplitude will be small and will result in no indication of damage.

After X-ray and ultrasonic scanning evaluation, several of the impact coupons were sectioned, as indicated in Table 1. At least five widthwise cuts were made per coupon with a water-cooled diamond blade, the first of which was through the center of impact. The center of impact was located by visual inspection upon placement of the coupon in the milling machine. Delaminations and fiber breaks were measured by examination of the cross-sections under a microscope at 30X magnification. A typical edge through the center of impact is shown in Figure 6. The measurements from all surfaces exhibiting damage were transcribed to schematics of damage on a ply-by-ply basis.

The deply technique [25], another destructive evaluation method, was used on a number of coupons as indicated in Table 1. The enhancing agent used in this work was a solution composed of 10 g of gold chloride in 100 ml of isopropyl alcohol. Thirty minutes after syringe injection of the enhancing agent into the damage region, the coupons were placed into an oven at 66°C for thirty minutes to drive off the excess carrier. Trimmed coupons, containing only the damaged area, were placed on a stainless steel wire mesh in a Lindbergh Furnace (Type 51442) preheated to 415–420°C. A positive pressure of nitrogen gas at approximately 0.02 MPa was fed into the furnace with a vent to an exhaust hood to remove the possibility of the harmful effects of oxygen. Partial pyrolysis of the coupons occurred after forty-five minutes (thirty minutes for eight plies [25]). The laminates were unstacked using a wide strip of transparent tape placed over the top ply (beginning with the impact surface ply). The ply was gently worked free from the specimen exposing the next interface. This was repeated until all plies were separated. However, plies 6 and 7 are both at 0° orientation and were impossible to separate.

The view of damage in the specimens evaluated by the deply technique is from the back surface towards the impact surface which is opposite of the time-of-flight ultrasonic C-Scans and cross-section schematics. Thus, the ply angles are reflected about the vertical axis. Plies were numbered sequentially beginning with the ply opposite the impact surface. Evaluation of the damage types (i.e., delamination and fiber damage) and sizes was done by visual inspection with a bright light shined on the ply to reflect the gold chloride. Photographs were then taken to provide a record of damage. A typical photograph is shown in Figure 7. There was obvious fiber damage in this ply where the tup passed through the coupon as evidenced by the white background in the photograph. The gold chloride, providing evidence of delamination where ply 1 (back surface from impact) separated from ply 2, typically appeared gray compared to the white of the background and the black of the graphite/epoxy.

After the impact coupons were evaluated by the prescribed destructive and nondestructive methods, details of the identified damage were compared. The C-Scan damage definition was directly comparable to X-ray results. The time-of-flight C-Scan damage definition was comparable to the schematics generated by cross-sectioning and the photographs from the deply evaluation. Extensive documentation and comparison of destructive and nondestructive damage evaluation methods are presented in Reference 27 and will be the topic of a future paper.

Determination of Compressive Residual Strength

After nondestructive damage evaluation, specimens were prepared for compressive residual strength tests. A honeycomb sandwich specimen, shown in Figure 8 and

The results of compressive residual strength versus impactor velocity for the cases of the three impactor masses are summarized in the left graph in Figure 9. All three data sets indicate a minimum compressive residual strength below the compressive strength for specimens with open holes. Furthermore, all three data sets exhibit asymptotic behavior approaching the strength value for the open hole of the same diameter as the impactor. (The results of the open hole and undamaged strength tests were presented in Table 2.) The right graph in Figure 9 is a plot of the same data on a scale of 0–15 m/s to better show the aforementioned trends for the 1523 g and 578 g

Residual strength data is often presented as a function of impactor velocity or energy. This presentation method complicates interpretation of results for different laminates or material systems as the issues of damage resistance and damage tolerance are not separately addressed. Thus, to address damage resistance, damage size as a function of impactor energy or velocity should also be provided. In this work, presentation of residual strength as a function of impactor velocity was used to determine the minimum compressive residual strength. Impactor velocity was the parameter then used in an attempt to repeat the damage state causing minimum compressive residual strength for insensitive destructive damage evaluation.

Minimum Compressive Residual Strength

RESULTS AND DISCUSSION

Tests were conducted using an MTS 810 Material Testing System under stroke control at a rate of 1.1 mm/min. This resulted in an approximate strain rate of 500 microstrain/min in the test section. The tests were conducted monotonically to failure. Failure stress is calculated by dividing the failure load of the damaged facesheet by the measured area (average thickness and width). The failure load of the damaged facesheet is half the total column load at failure.

The impacted coupon and an undamaged coupon were bonded to this aluminum honeycomb core after impact and nondestructive evaluation. The impacted surface was bonded to the honeycomb as it was smoother than the back surface with splinters and more likely to result in a good bond. American Cyanamid FM-123-2 film adhesive was used for bonding with a cure temperature of 107°C and pressure of 0.28 MPa for two hours. Using the same adhesive and cure cycle, fiberglass end tabs were then bonded to the graphite/epoxy to provide an efficient load transfer mechanism. Coupons with drilled holes, rather than impact damage, were also fabricated into identical compressive residual strength test specimens. Holes were drilled using diamond-coated drill bits and reamers. A strain gage was placed on the damaged facesheet, away from the damage, to provide data that was used as a specimen quality check through laminate stiffness measurement.

designed for characterization of the compressive strength of thin laminates [28], was used. Placement of the 25 mm thick honeycomb core between the two facesheets prevented global buckling of the laminate as a possible failure mode. The core was a combination of low density (72 kg/m^3) and high density (352 kg/m^3) aluminum gripping of the specimen when it is held in the hydraulic grips of the test fixture. The core located in the test section was low density to virtually eliminate load-sharing with the facesheets.

impactor mass cases. The minimum compressive residual strengths exhibited in the three data sets are: 184 MPa for the 1523 g mass at 6.3 m/s, 191 MPa for the 578 g mass at 9.2 m/s, and 187 MPa for the 8.4 g mass at 57 m/s. The three impactor masses, at their respective minimum compressive residual strength velocities, therefore caused virtually identical minimum compressive residual strengths. Thus, minimum compressive residual strength is apparently independent of impact mass.

Although it has been shown that impactor energy is not a sufficient metric [1], residual strength results are often presented as a function of impactor energies. However, in this current work, impactor energy is again found to be an inappropriate metric. The impactor energies were not equivalent at the minimum compressive residual strengths for the three impactor masses used in the test program. The impactor energies corresponding to these minima were: 30 J for the 1523 g mass, 25 J for the 578 g mass, and 13 J for the 8.4 g mass.

Since damage tolerance, and therefore residual strength, is a function of the damage present, it was hypothesized that the same damage state exists for the minimum compressive residual strength condition for all three impactor masses. One measure of the damage characteristics used for correlation to compressive residual strength was determined from the X-ray photographs of each impact coupon. The information provided by an X-ray photograph is a summary of damage integrated through-the-thickness. These measurements represent the extent of this integrated damage as seen in the plane of the photograph. As seen previously in Figure 5, these measurements include the major and minor axes of the outer fringe of delamination as well as the diameter of the "core" area. The measurement of the major axis of damage did not include the spalling of fibers off the back surface to the coupon edge as this was a surface phenomenon.

Comparison of the compressive residual strength versus major axis of damage, presented in Figure 10, shows the curve for the 8.4 g impactor mass approaching the minimum compressive residual strength at a much smaller major axis of damage size (approximately 40 mm) than the curves for the 1523 and 578 g impactor masses (approximately 70 mm). There was a significant amount of scatter among the three impactor masses. Comparison of the compressive residual strength versus minor axis of damage, presented in Figure 11, resulted in less scatter than the major axis data comparison. Though the largest scatter band of data still represented a total difference of 33%, there was no obvious separation of data between the three impactor masses as there was in the case of the major axis. Comparison of the compressive residual strength versus core damage size, presented in Figure 12, also showed the curve for the 8.4 g impactor mass approaching the minimum compressive residual strength at a smaller core damage size (13 mm) than the curves for the 1523 and 578 g impactor masses (23 and 19 mm respectively). There was again, a significant amount of scatter among the three impactor masses. From these three comparisons, it would be inadvisable to predict compressive residual strength as a function of planar damage measurements such as the major axis, minor axis, or core damage size as there is insufficient detail in these damage measurements.

This can be further seen in Figure 13 where the X-ray characterization of the damage state at the minimum compressive residual strength condition is shown for the three impactor masses. These three cases appear to have slightly different damage states as the core damage size ranges from 17 to 23 mm, the minor axis of damage ranges from

21 to 27 mm, and the major axis of damage ranges from 69 to 80 mm. The integrated damage thus does not provide sufficient detail either in the X-ray photographs shown here, or in a typical ultrasonic scan. Three-dimensional information about the damage is therefore necessary.

The three-dimensional damage state definitions at the minimum compressive residual strengths for the three impactor masses used in this work were best provided by the deply destructive damage evaluation method. The cross-section schematics also provided good definition of the three-dimensional damage state. However, this destructive evaluation method was much more time consuming and labor intensive [27]. The comparison of the three-dimensional damage state definitions by deply are similar for specimens impacted by all three masses as shown in Figures 14–16. All three summaries exhibit similar damage type, size, shape, orientation, and location. Core damage remains fairly constant through the thickness due to impact at velocities in the penetration range. Delaminations exist between every interface with the exception of interface 6 (between the two 0° plies). Delamination shape is roughly elliptical with orientation in the direction of the next ply further away from the impact surface. Delamination size increases as ply distance from the impact surface increases. And, there is consistent evidence of extensive delamination between plies 1 and 2 including indications of the back surface spalling.

The similar deply summaries of Figures 14–16 would appear to verify the hypothesis that similar minimum compressive residual strengths are due to the existence of similar three-dimensional damage states in these specimens. These summaries, however, still do not identify the controlling or key damage mechanisms.

A postmortem examination of the specimens that failed at the minimum compressive residual strengths for the three impactor mass cases was conducted to determine if the failure modes were the same. These specimens, after failure, are shown in Figure 17. The postmortem examination of these minimum compressive residual strength specimens showed sublaminar buckling of ply 1 and fiber failure in the remaining plies. (Also evident was the extensive core damage and back side spalling of ply 1 due to impactor penetration.) Although it was not possible from the postmortem examination to determine which damage mode or combination of damage modes were controlling the compressive residual strength, it was clear that the failure modes in these three cases were similar if not the same. The postmortem examination of the open hole specimens on the other hand, showed the fracture in these cases to be consistently due to in-plane mechanisms as catastrophic failure occurred completely through each facesheet with no indication of delamination as shown in Figure 18.

Comments on Damage Evaluation Methods

It is apparent that there is a key need to determine the damage state in a composite structure subjected to impact in order to determine residual performance capabilities such as strength. Several two- and three-dimensional methods were used in this work. Two-dimensional methods included X-ray enhanced via dye penetrant and pulse-echo ultrasound. Three-dimensional methods included time-of-flight pulse-echo ultrasound, deply enhanced via dye penetrant, and cross-sectioning followed by microscopy.

The two-dimensional techniques provide a characterization of the damage which is integrated through-the-thickness. These techniques were inadequate in two respects.

One, the results were somewhat inconsistent as well as difficult to evaluate, as they require interpretation of the meaning of shades of gray or color. Two, this through-the-thickness integrated picture does not provide sufficient information to characterize the damage. The location of particular types of damage, such as delamination, is generally important in determining the residual performance of the laminate. This may become more important as the thickness of the laminate increases. Plots of residual strength versus planar damage size are therefore insufficient in representing the phenomena. Such plots require an assumption as to the configuration, types, and location of the damage.

It is therefore necessary to resort to techniques which provide accurate three-dimensional characterization of the damage state. Two destructive methods, cross-sectioning and deply, were used successfully in this work. The deply technique is preferred as it provides virtually complete damage information and is less labor-intensive than the cross-sectioning technique. However, neither of these techniques is an option to characterize damage in a production part or in a specimen which will be subsequently tested.

Time-of-flight ultrasonic pulse-echo scanning was performed on specimens to provide three-dimensional damage characterization via a nondestructive technique. A summary of the results of such an inspection is shown in Figure 19 for a specimen impacted at 70 m/s with an 8.4 g mass. This is the same specimen which was depled and the damage summarized in Figure 16. The two damage summaries can therefore be directly compared. In this case, the core damage and delamination sizes seen via the time-of-flight technique are consistently larger than those seen via the deply technique. However, in general the damage sizes found via the time-of-flight technique were inconsistent with respect to the damage determined by the deply or cross-sectioning techniques.

The time-of-flight technique is limited by two other issues. One, damage "below" other damage cannot be detected. This can be somewhat mitigated by scanning from both sides of the specimen, but a complete picture may not always be possible. Two, these three-dimensional results also require interpretation of shades of gray or color as in the two-dimensional case. This latter difficulty may be overcome through continued experimentation and accumulated experience.

There is, therefore, great need to further develop nondestructive techniques to evaluate damage on a three-dimensional level in order to provide, with confidence, an accurate assessment of the damage state in the composite structure. Only this will allow proper assessment of the residual performance capability of the structure.

SUMMARY

The damage tolerance of composite laminates after impact was examined via experimentation on AS4/3501-6 graphite/epoxy laminates in a $[\pm 45/0]_{2S}$ configuration. Three different impactor masses were used. The results clearly show that a minimum compressive residual strength exists which is well below the strength of a similar specimen with a 12.7 mm diameter open hole, the same diameter as the impactors. At higher impactor velocities, the compressive residual strength asymptotes to this open hole strength value. This minimum compressive residual strength is independent of the

impactor mass used and is directly related to the three-dimensional damage state in the specimen. Nondestructive and destructive examination showed that the damage state that caused the minimum compressive residual strength was the same for all three cases of impactor mass. This damage consists of a core region, where matrix and fiber damage occurs, and a delamination at every interface except between the two 0° plies. The delamination shapes are roughly elliptical and are oriented in the direction of the next ply further away from the impact surface.

This work clearly shows the need for proper metrics to measure impact damage in order to relate damage to the residual performance capability. It is clear that a full three-dimensional characterization of the damage is necessary rather than an integrated two-dimensional measure. Correlations to various two-dimensional impact metrics, such as the major axis of damage, were unsuccessful. Therefore, methods developed to predict residual performance should be based on the actual three-dimensional damage state. Furthermore, the inadequacies of the nondestructive techniques used demonstrate the need for further development of nondestructive techniques to properly characterize damage in laminated composite structures.

ACKNOWLEDGMENTS

This work was supported by the Federal Aviation Administration. The authors wish to acknowledge the help of Dr. Douglas Cairns of Hercules, Inc. who arranged for all the ultrasonic nondestructive evaluations. His comments and cooperation were very much appreciated.

REFERENCES

1. Cairns, D. S., and P. A. Lagace, "A Consistent Engineering Methodology for the Treatment of Impact in Composite Materials," Proceedings of the American Society for Composites, Fifth Technical Conference, East Lansing, Michigan, June, 1990, pp. 589-599.
2. Wilkins, D. J., "The Engineering Significance of Defects in Composite Structures," Characterization, Analysis and Significance of Defects in Composite Materials, AGARD-CP-355, 1983, pp. 20-1 through 20-11.
3. Potter, R. T., "The Significance of Defects and Damage in Composite Structures," Characterization, Analysis and Significance of Defects in Composite Materials, AGARD-CP-355, 1983, pp. 17-1 through 17-10.
4. Garg, A. C., "Delamination—A Damage Mode in Composite Structures," Engineering Fracture Mechanics, Vol. 29, No. 5, 1988, pp. 557-584.
5. Sollars, T. A., "Shuttle/Centaur G-Prime Composite Adapters Damage Tolerance/Repair Test Program," Proceedings of the 28th AIAA/ASME/ASCE/AHS Structures, Structural Dynamics and Materials Conference, Monterey, California, April, 1987, pp. 362-375.

6. Rhodes, M. D., J. G. Williams, and J. H. Starnes Jr., "Effect of Low-Velocity Impact Damage on the Compressive Strength of Graphite-Epoxy Hat-Stiffened Panels," NASA TN D-8411, April, 1977.
7. Baker, A. A., R. Jones, and R. J. Callinan, "Damage Tolerance of Graphite/Epoxy Composites," Composite Structures, Vol. 4, No. 1, 1985, pp. 15-44.
8. Whitehead, R. S., "Certification of Primary Composite Aircraft Structures," New Materials and Fatigue Resistant Aircraft Design, Proceedings of the 14th ICAF Symposium, Ottawa, Canada, June, 1987, pp. 585-617.
9. Byers, B. A., "Behavior of Damaged Graphite/Epoxy Laminates Under Compression Loading," NASA-CR-159293, August, 1980.
10. O'Brien, T. K., "Toward a Damage Tolerance Philosophy for Composite Materials and Structures," Composite Materials: Testing and Design, Vol. 9, ASTM STP 1059, 1990, pp. 7-33.
11. Challenger, K. D., "The Damage Tolerance of Carbon Fiber Reinforced Composites—A Workshop Summary," Composite Structures, Vol. 6, No. 4, 1986, pp. 295-318.
12. Flanagan, G., "Two-Dimensional Delamination Growth in Composite Laminates Under Compression Loading," Composite Materials: Testing and Design, ASTM STP 972, 1988, pp. 180-190.
13. Pavier, M. J., and W. T. Chester, "Compression Failure of Carbon Fibre-Reinforced Coupons Containing Central Delaminations," Composites, Vol. 21, No. 1, January, 1990, pp. 23-31.
14. Demuts, E., R. S. Whitehead, and R. B. Deo, "Assessment of Damage Tolerance in Composites," Composite Structures, Vol. 4, No. 1, 1985, pp. 45-58.
15. Garrett, R. A., "Effect of Defects on Aircraft Composite Structures," McAir No. 83-010, Presented at AGARD Structures and Material Panel, London, England, April, 1983.
16. Starnes, J. H., Jr., M. D. Rhodes, and J. G. Williams, "Effect of Impact Damage and Holes on the Compressive Strength of a Graphite/Epoxy Laminate," Nondestructive Evaluation and Flaw Criticality for Composite Materials, ASTM STP 696, 1979, pp. 145-171.
17. Ilcewicz, L. B., E. F. Dost, and R. L. Coggeshall, "A Model for Compression After Impact Strength Evaluation," Advanced Materials: The Big Payoff, 21st International SAMPE Technical Conference, Atlantic City, New Jersey, September, 1989, pp. 130-147.
18. Levin, K., "Effect of Low-Velocity Impact on Compressive Strength of Quasi-Isotropic Laminate," Proceedings of the American Society of Composites, First Technical Conference, Dayton, Ohio, October, 1986, pp. 313-326.

19. Guynn, E. G., and T. K. O'Brien, "The Influence of Lay-Up and Thickness on Composite Impact Damage and Compression Strength," Proceedings of the 26th AIAA/ASME/ASCE/AHS Structures, Structural Dynamics and Materials Conference, Orlando, Florida, April, 1985, pp. 187-196.
20. Williams, J. G., "Effect of Impact Damage and Open Holes on the Compression Strength of Tough Resin/High Strain Fiber Laminates," Tough Composite Materials, NASA-CP-2334, May, 1983, pp. 61-79.
21. Clark, G., and T. J. van Blaricum, "Carbon Fibre Composite Coupons - Static and Fatigue Behavior After Impact Damage," Structures Report 422, DSTO Aeronautical Research Laboratories, Melbourne, Australia, 1986.
22. Martin, R. C., and C. Poelman, "Compressive Residual Strength of Composite Laminates After Impact," 16.622 Final Report, Department of Aeronautics and Astronautics, Massachusetts Institute of Technology, December, 1989.
23. Dost, E. F., L. B. Ilcewicz, and J. H. Gosse, "Sublaminar Stability Based Modeling of Impact-Damaged Composite Laminates," Proceedings of the American Society for Composites, Third Technical Conference, Seattle, Washington, September, 1988, pp. 354-363.
24. Cairns, D. S., "Impact and Post-Impact Response of Graphite/Epoxy and Kevlar/Epoxy Structures," TELAC Report No. 87-15, Massachusetts Institute of Technology, August, 1987.
25. Freeman, S. M., "Characterization of Lamina and Interlaminar Damage in Graphite/Epoxy Composites by the Deply Technique," Composite Materials: Testing and Design, ASTM STP 787, 1982, pp. 50-62.
26. Williams, J. G., T. K. O'Brien, and A.J. Chapman III, "Comparison of Toughened Composite Laminates Using NASA Standard Damage Tolerance Tests," ACEE Composite Structures Technology, NASA-CP-2321, Seattle, Washington, August , 1984, pp. 51-73.
27. Guy, T. A., "Compressive Residual Strength of Graphite/Epoxy Laminates After Impact," TELAC Report No. 91-9, Massachusetts Institute of Technology, June, 1991.
28. Lagace, P. A., and A. J. Vizzini, "The Sandwich Column as a Compressive Characterization Specimen for Thin Laminates," Composite Materials: Testing and Design, ASTM STP 972, Philadelphia, Pennsylvania, 1988, pp. 143-160.

Table 1. Impact Test Matrix

Mass (g)	Velocity (m/s)	Test Type ^a		
		CRS	Section	Deply
1523	4.3	1 ^b	—	—
	4.6	1	—	—
	4.8	3	—	—
	5.2	4	—	—
	5.5	3	1	—
	5.7	3	3	1
	6.0	4	2	—
	6.3	4	3	1
	6.7	3	2	—
	7.1	2	—	—
	7.5	2	1	—
	8.6	1	—	—
578	7.5	2	—	—
	8.0	2	3	—
	8.6	3	3	1
	9.2	6	3	1
	10.0	7	2	—
	10.9	3	1	—
	12.0	1	1	—
8.4	55	2	3	1
	56	1	1	—
	57	2	2	1
	58	1	3	1
	70	3	—	1

^a CRS – compressive residual strength test after impact
 Section – destructive damage evaluation by cross-sectioning
 Deply – destructive damage evaluation by deply technique

^b Indicates number of coupons tested

Table 2. Test Matrix and Results for Undamaged Specimens and Specimens with Open Holes

Diameter (mm)	Number of Specimens	Mean Compressive Strength (MPa)	Coefficient of Variation (%)
0.0	2	645	2.3
12.7	3	332	3.1
19.1	3	285	4.2
25.4	3	268	10.1

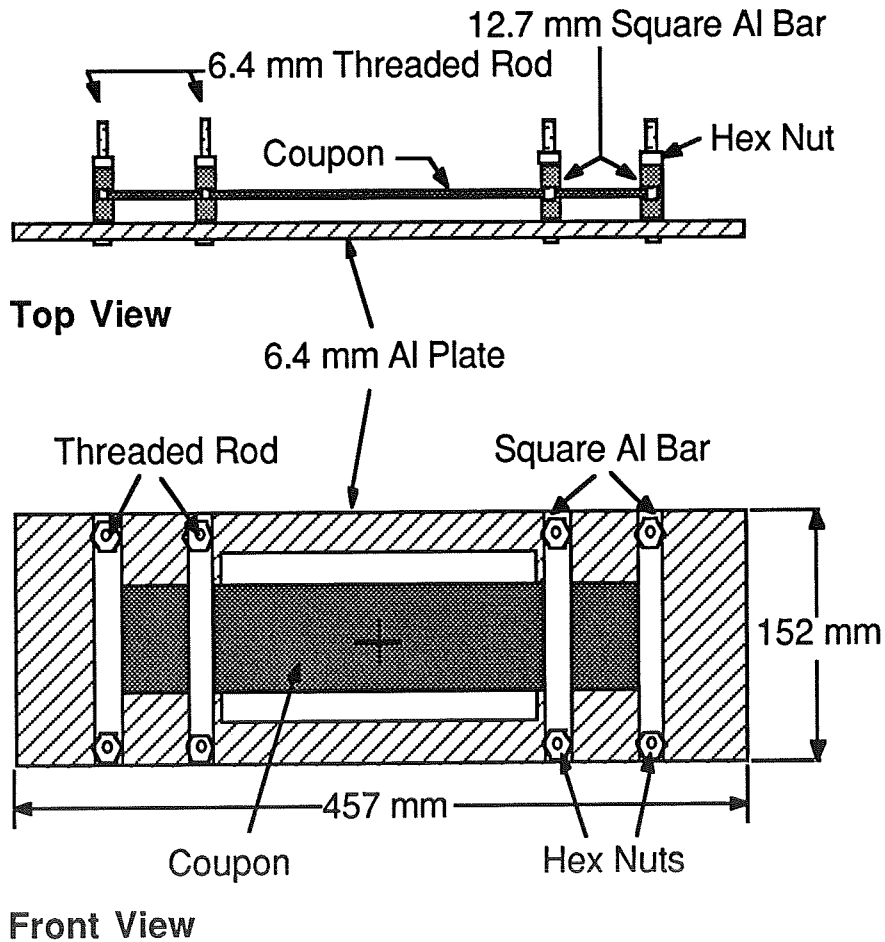


Figure 1. Illustration of Coupon Holding Jig for Impact Tests.

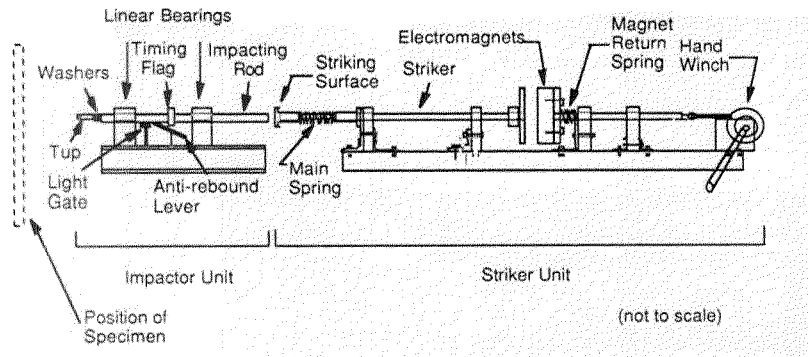
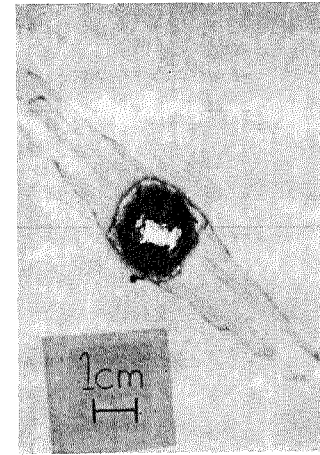


Figure 2. Illustration of Free Rolling Energy Device (FRED) Impact Test Apparatus and Setup.



(X-ray is to scale)

Figure 4. Typical X-ray Photograph of Impact Damage.

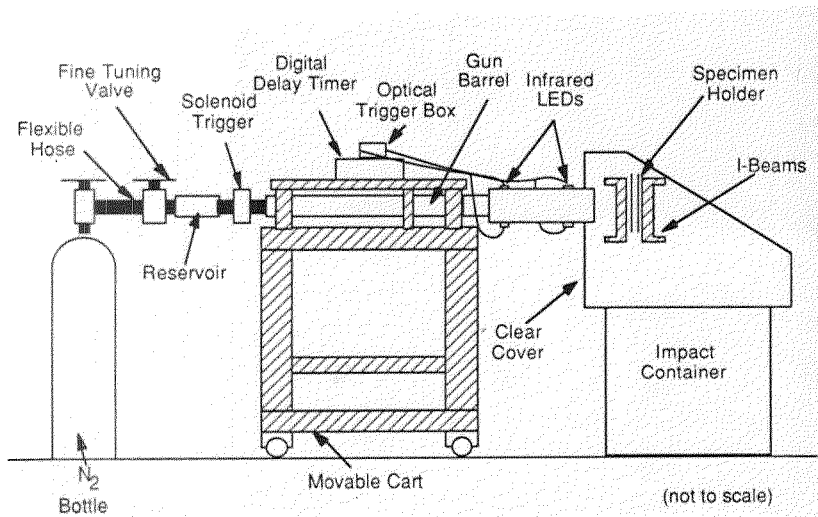


Figure 3. Illustration of Air Gun Impact Test Apparatus and Setup.

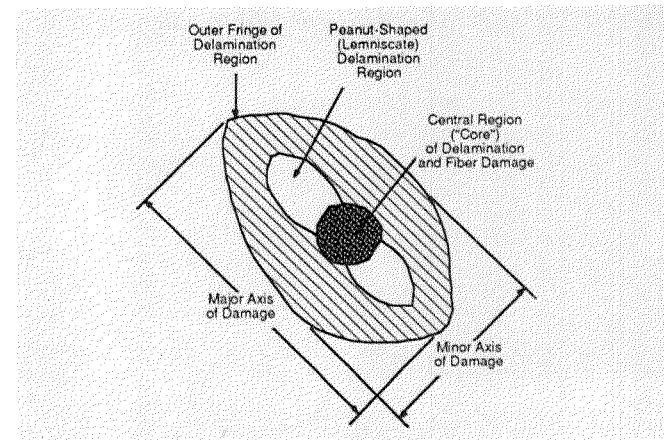
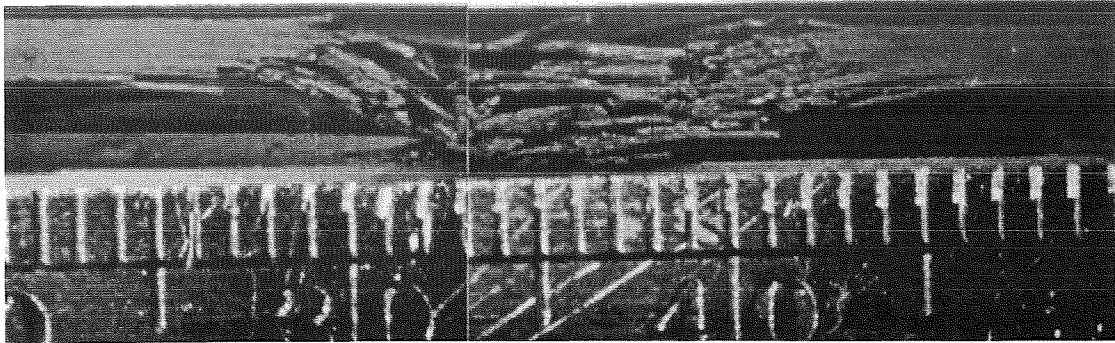
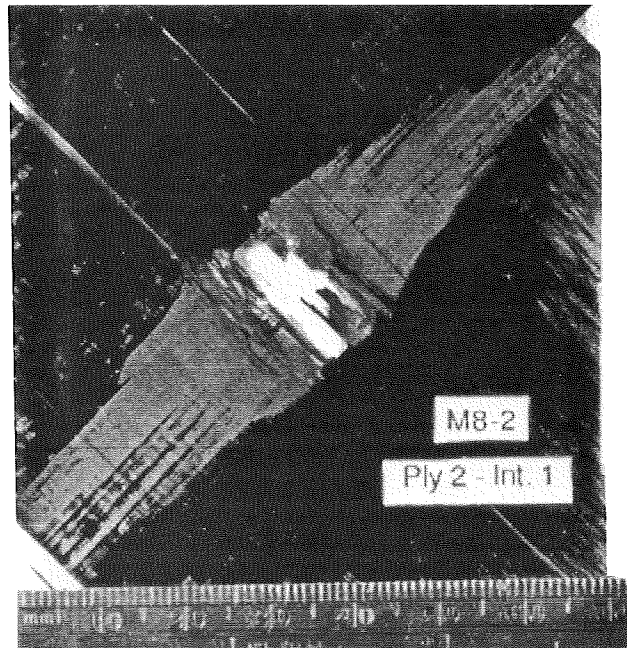


Figure 5. Schematic of Typical Damage Regions Illustrated by X-ray.



(Scale in picture is in mm)

Figure 6. Typical Photograph of Coupon Cross-Section through the Center of Impact.



[45//~~45~~/0/45/-45/0/0/-45/45/0/-45/45]—Impact Surface

(Scale in picture is in mm)

Figure 7. Typical Photograph of Ply Surface After Deply.

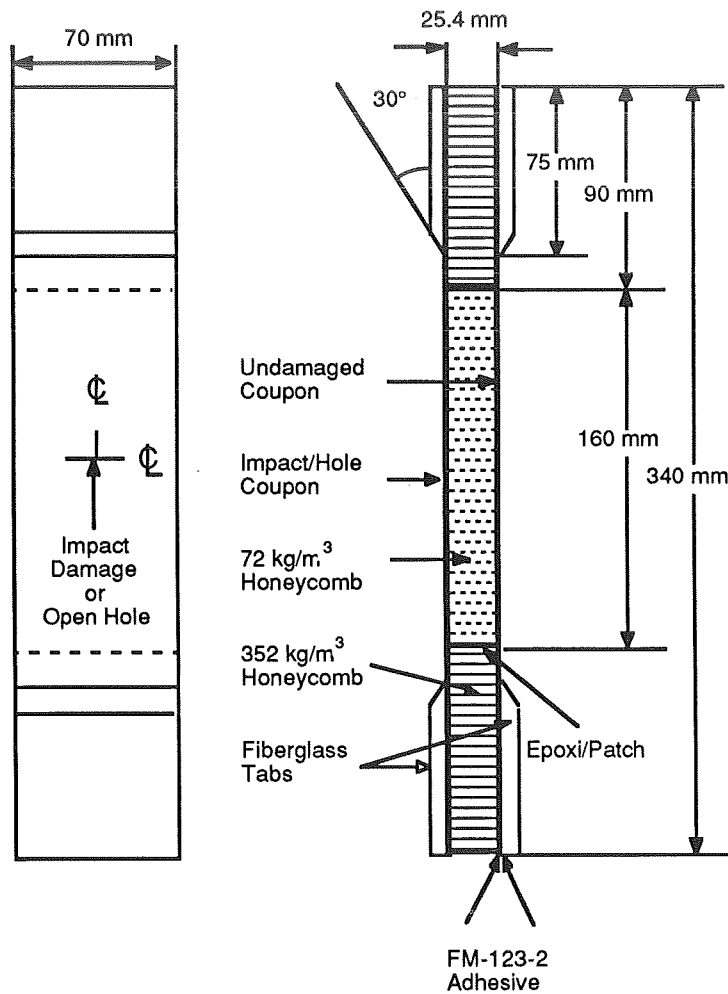


Figure 8. Compressive Residual Strength Test Specimen Geometry.

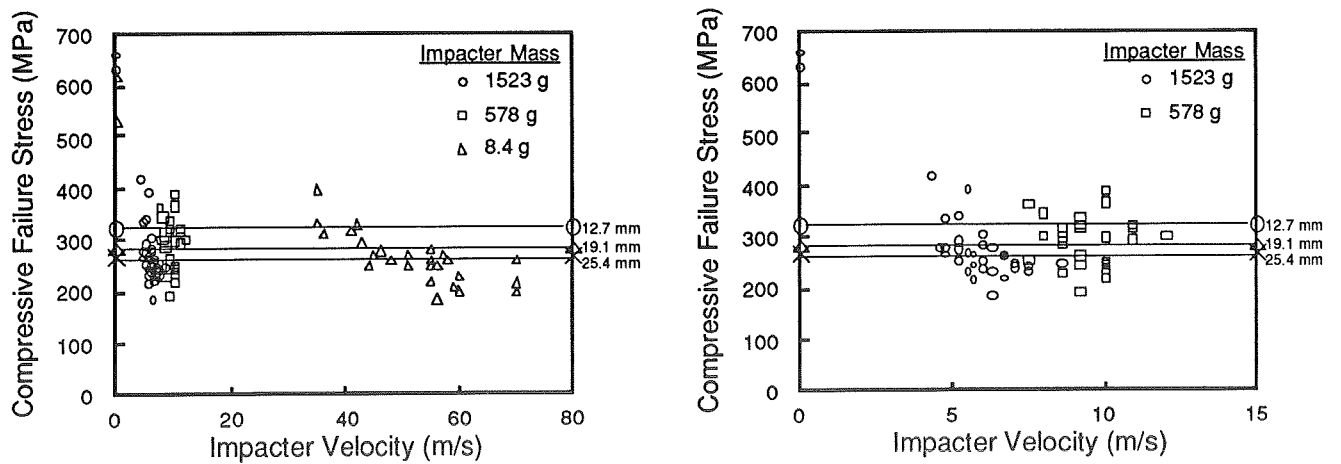


Figure 9. Compressive Residual Strength versus Impactor Velocity Data- (left) three impactor masses, (right) 1523 g, 578 g impactor masses.

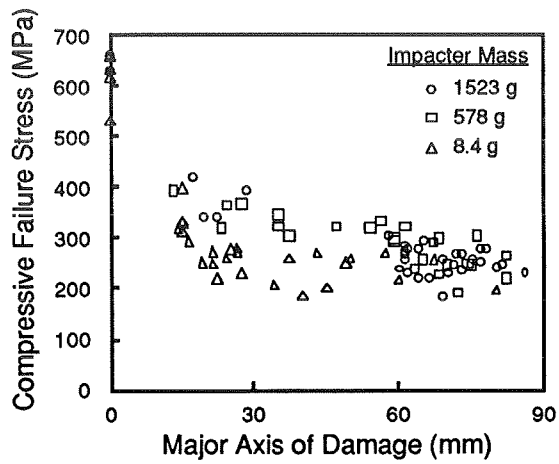


Figure 10. Compressive Residual Strength versus Major Axis of Damage Data.

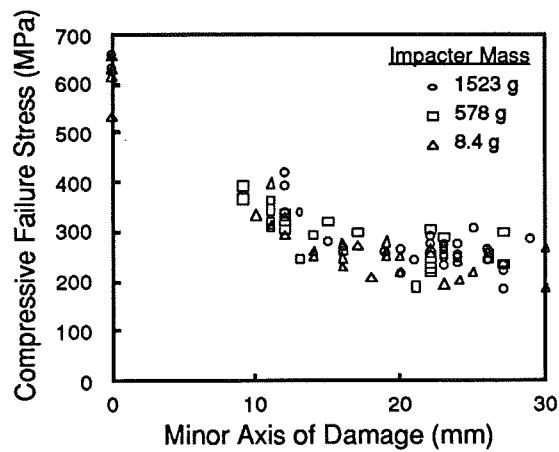


Figure 11. Compressive Residual Strength versus Minor Axis of Damage Data.

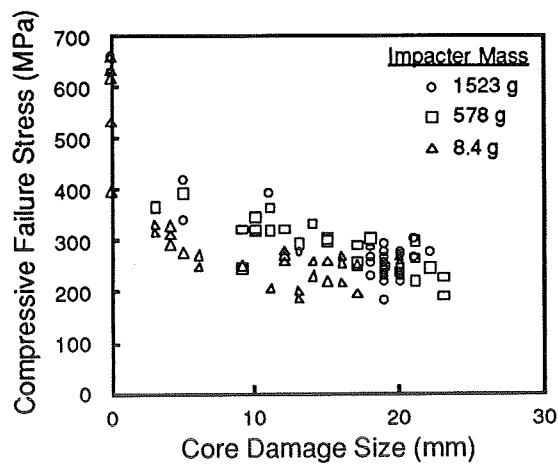
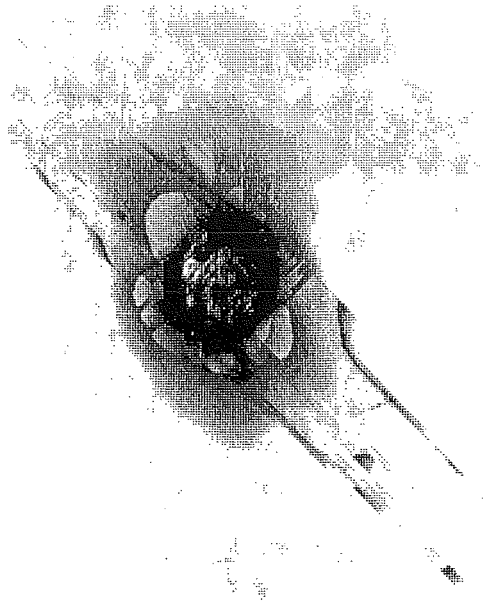
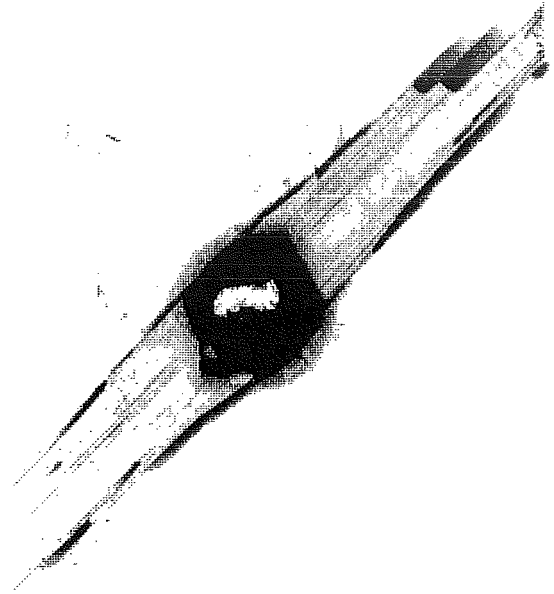


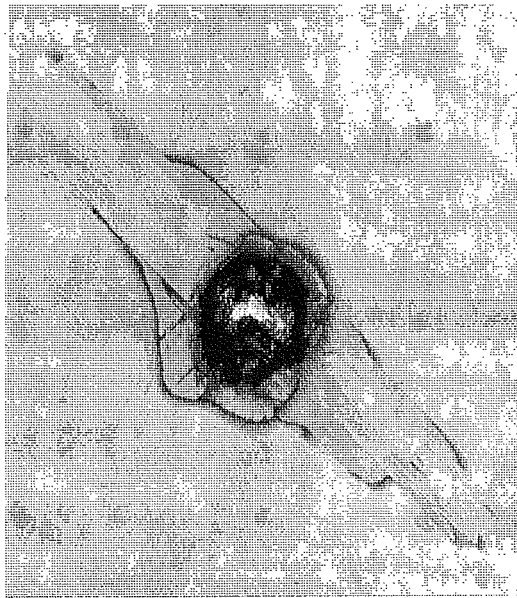
Figure 12. Compressive Residual Strength versus Core Damage Size Data.



Mass = 8.4 g



Mass = 578 g



Mass = 1523 g

(X-rays are to scale)

Figure 13. X-ray Photographs of Minimum Compressive Residual Strength Specimens for Three Impactor Masses (*top left*) 8.4 g, (*top right*) 578 g, and (*bottom*) 1523 g.

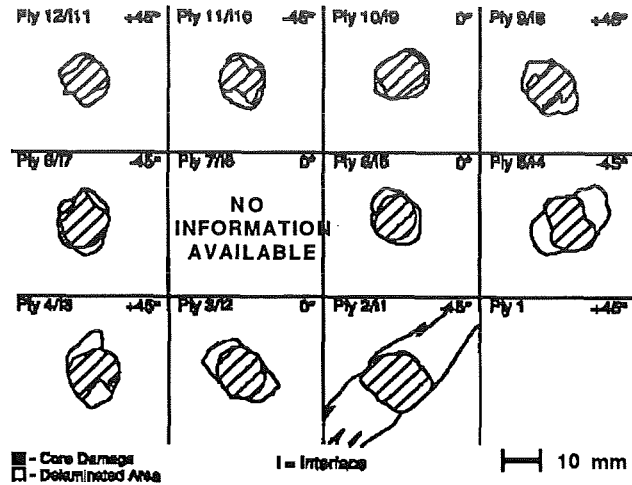


Figure 14. Summary of Damage Observed in Specimen M8-2 by Deply (Impactor Mass = 1523 g, Velocity = 6.3 m/s).

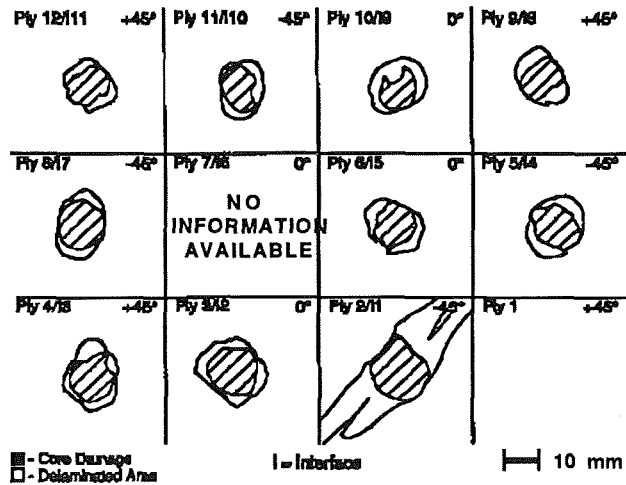


Figure 15. Summary of Damage Observed in Specimen M10-4 by Deply (Impactor Mass = 578 g, Velocity = 8.6 m/s).

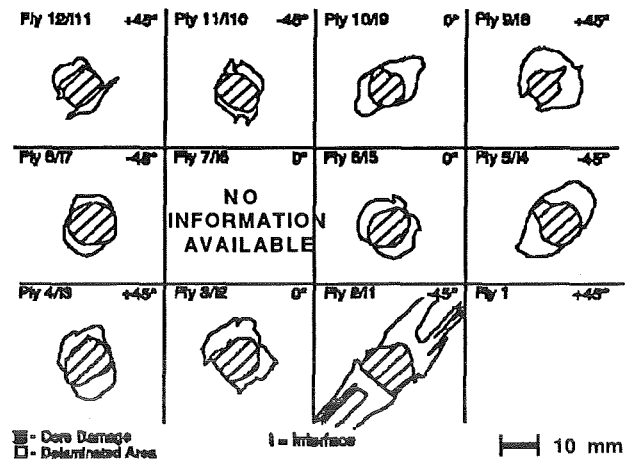
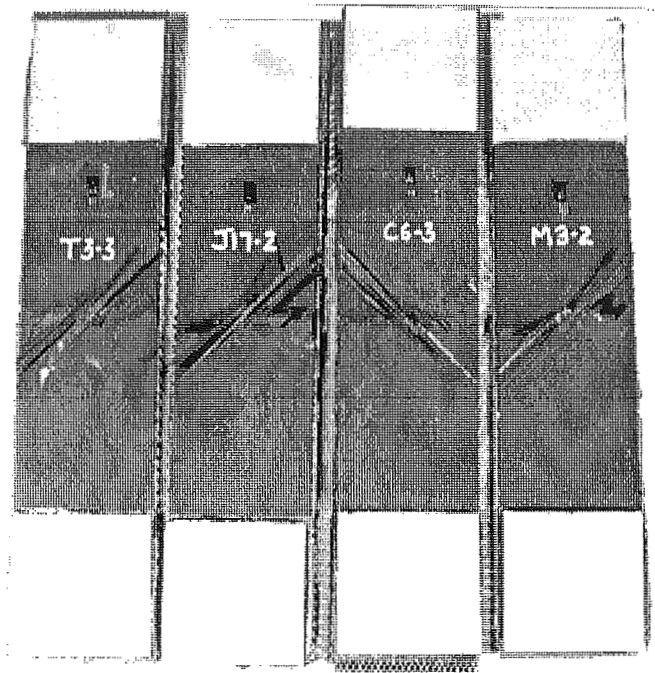
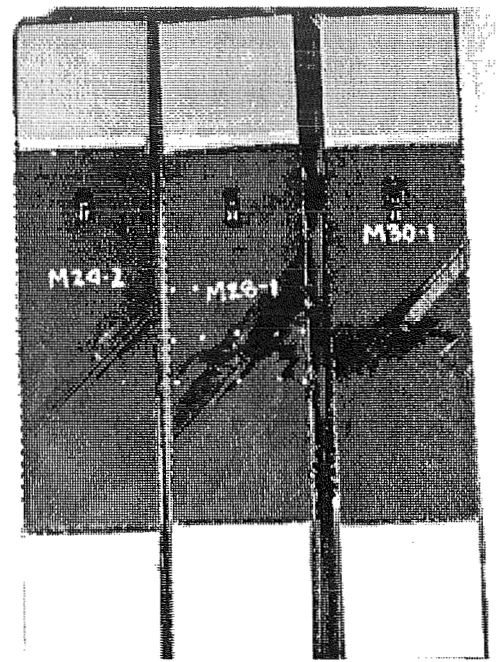


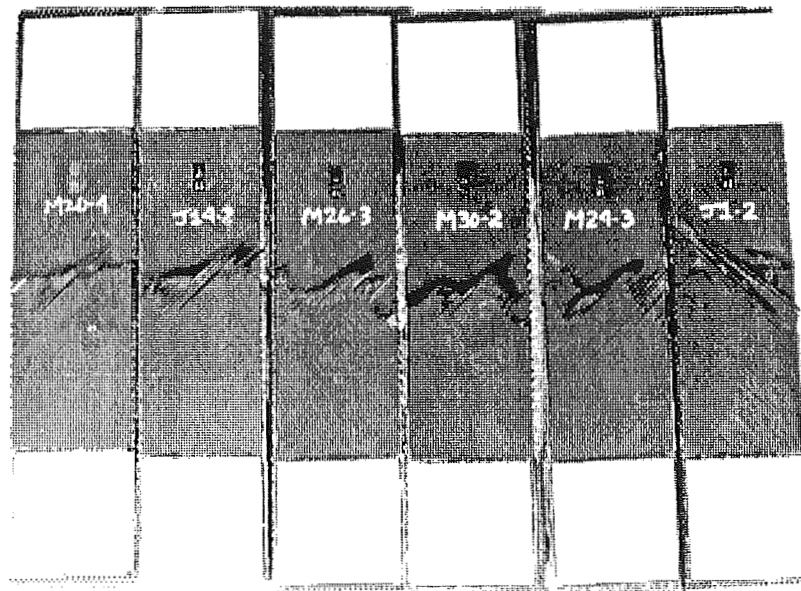
Figure 16. Summary of Damage Observed in Specimen M23-4 by Deply (Impactor Mass = 8.4 g, Velocity = 70 m/s).



(Mass of 1523 g at 6.3 m/s)



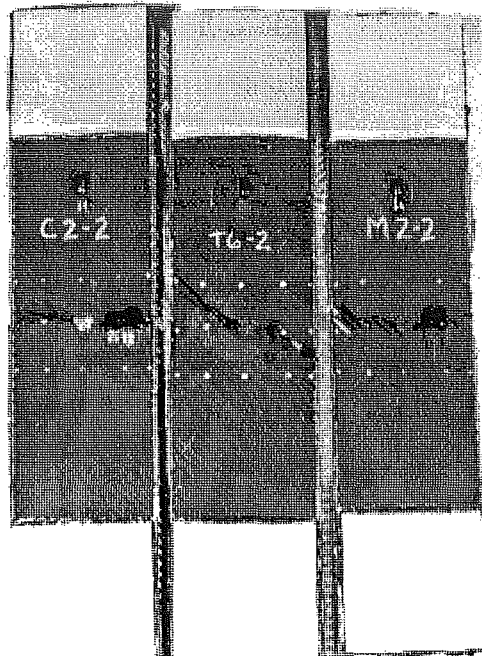
(Mass of 8.4 g at 70 m/s)



(Mass of 578 g at 9.2 m/s)

(Specimens - 70 x 340 mm)

Figure 17. Photograph of Impact-Damaged Specimens After Fracture
Masses of (top left) 1523 g, (bottom) 578 g, and (top right) 8.4 g.



(Specimens - 70 x 340 mm)

Figure 18. Photograph of 12.7 mm Open Hole Specimens After Fracture.

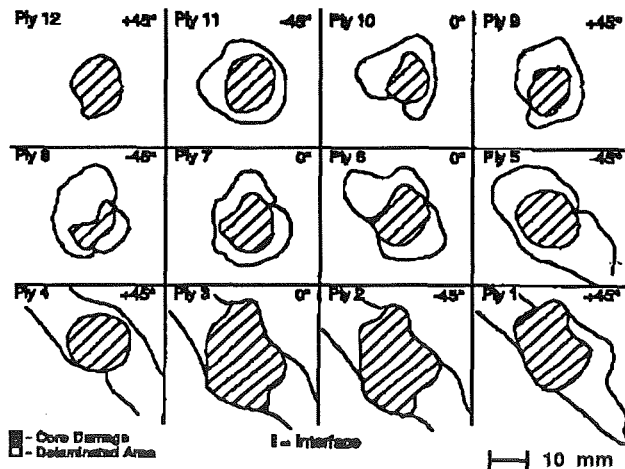


Figure 19. Summary of Damage Observed in Specimen M23-4 by Time-of-Flight Ultrasonic C-Scan (Impactor Mass = 8.4 g, Velocity = 70 m/s).

omit

SESSION III
DESIGN APPLICATIONS (A)

THIS PAGE INTENTIONALLY BLANK

APPLICATION OF ADVANCED MATERIAL SYSTEMS TO COMPOSITE FRAME
ELEMENTS

Steven Llorente, Pierre Minguet, Russell Fay
Helicopters Division, Boeing Defense & Space Group
Philadelphia, Pennsylvania

and
Steven Medwin
Composites Division
E.I. Du Pont De Nemours & Company (Inc.)
Wilmington, Delaware

512-24
57380
P-19

SUMMARY

A three phase program has been conducted to investigate DuPont's Long Discontinuous Fiber (LDF^{TM*}) composites. Additional tests were conducted to compare LDFTM composites against toughened thermosets and a baseline thermoset system. Results have shown that the LDFTM AS4/PEKK offers improved interlaminar (flange bending) strength with little reduction in mechanical properties due to the discontinuous nature of the fibers. In the third phase, a series of AS4/PEKK LDFTM C-section curved frames (representing a typical rotorcraft light frame) were designed, manufactured and tested. Specimen reconsolidation after stretch-forming and frame thickness were found to be key factors in this light frame's performance. A finite element model was constructed to correlate frame test results with expected strain levels determined from material property tests. Adequately reconsolidated frames performed well and failed at strain levels at or above baseline thermoset material test strains. Finally a cost study was conducted which has shown that the use of LDFTM for this frame would result in a significant cost savings, for moderate to large lot sizes compared with the hand lay-up of a thermoset frame.

INTRODUCTION

In weight critical applications graphite composite materials provide a highly desirable combination of structural properties since the orientation of the fibers can be selected to suit the application. In general, the hand lay-up of thermoset parts which are contoured is a difficult and time consuming process. Thermoplastic LDFTM materials offer the ability to be thermoformed while maintaining a high percentage of the continuous fiber material properties since fibers are of such a length (approximately 2 inches) that they retain properties similar to continuous fiber composites. The combination of long discontinuous fibers and a thermoplastic matrix produces a material which can be consolidated in stock shapes and then stretch-formed to a final shape. The economics are attractive since the stock shape can be produced efficiently and the final part can be contoured automatically with minimal labor. Most importantly, the fiber angles can be controlled so that they adapt to the part geometry. The general stretch forming concept is shown schematically in Figure 1.

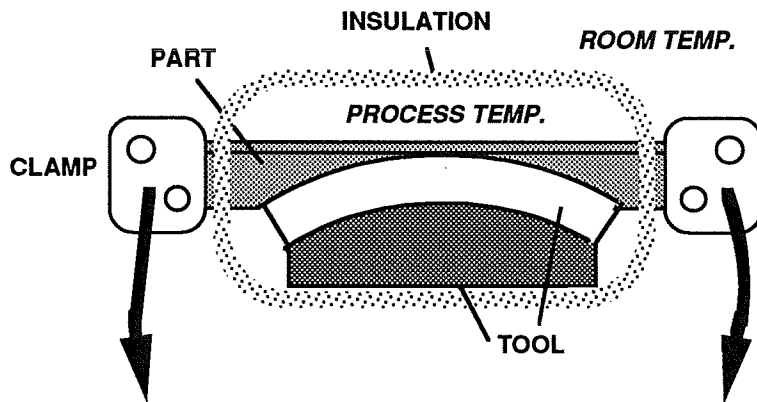
In the first phase of a three phase evaluation, laminate coupon tests were used to evaluate material stiffness and strength properties of the new material system. Emphasis was placed on evaluating the effect of the discontinuous fibers and the effect of stretching on mechanical properties. In the second phase, two types of tests were performed to

* LDF is a trademark of the DuPont Company.

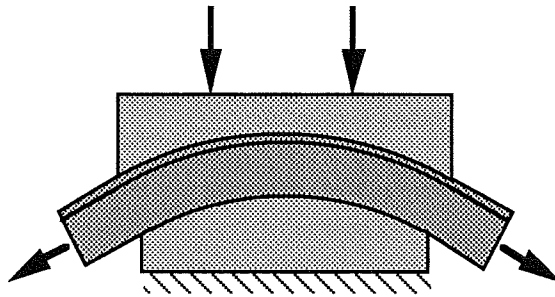
LDF STOCK PART



STRETCH FORMING



RECONSOLIDATION



COMPLETED PART

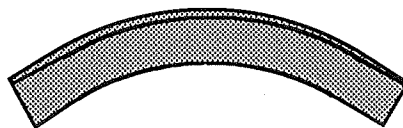


Figure 1 LDF™ Stretch-Forming Concept Definition

evaluate two critical frame failure modes: flange bending and section crippling. In addition to the LDF™ AS4/PEKK, a baseline thermoset, AS4/3501-6, and a toughened thermoset with a high strain-to-failure fiber, T800/3900, were tested for comparison purposes. In the third phase, a series of C-section curved frames manufactured with the LDF™ AS4/PEKK were manufactured and tested in combined tension and bending. To evaluate the results of this frame test, a finite element model was constructed for each frame geometry. Finally a cost study was conducted comparing the LDF™ stretch forming process to hand lay-up. This report presents the results of this investigation and details the manufacturing, testing, and supporting analysis.

PHASE 1 MATERIAL PROPERTIES

In Phase 1, the material stiffness and strength properties of LDF™ composite (AS4/PEKK) were determined through a series of (room temperature-ambient environment) coupon tests and compared with the properties of an AS4/PEKK composite made with continuous fibers. Different layups were tested in tension and compression. Several stretched (20% elongation) LDF™ coupons were also tested to evaluate the effect of stretching on mechanical properties.

The Phase 1 test matrix is shown in Figure 2. A total of 68 specimens were tested in a laboratory environment. Hot/Wet specimens were not tested due to budget restrictions. Tension tests of unidirectional [0]_g and [90]_g laminates were performed to evaluate fiber and matrix dominated properties and laminates of [± 45]_{2s} and [$\pm 45/0/90$]_{2s} layups were tested to evaluate shear and quasi-isotropic behavior. In all cases except for the [90]_g laminates, both LDF™ and continuous AS4/PEKK laminates were compared. It was not believed that fiber discontinuity would significantly affect 90° behavior. [0]_g and [$\pm 45/0/90$]_{2s} LDF™ specimens stretched by 20% in length were also evaluated.

Compression tests were conducted to determine both the modulus and ultimate strength of unidirectional [0]_g laminates. As with the tension tests, both LDF™ and continuous AS4/PEKK laminates were compared. Finally, the quasi-isotropic [$\pm 45/0/90$]_{2s} layup was evaluated in compression tests to examine the behavior of a typical laminate in the continuous, LDF™ stretched and LDF™ unstretched configuration.

RESULTS

Tension Tests

Results for tension strength and extensional stiffness are shown in Figure 3. A reduction of 5% was observed between continuous and discontinuous fibers specimens which is considered insignificant. The LDF™ stretched specimens showed higher strength, probably due to the slight tapering of these specimens after stretching. Both the LDF™ and LDF™-stretched specimens also experienced a slight reduction in modulus (7%, 5%, respectively) due to the discontinuous fibers. The 90° LDF™ specimens failed at an average stress level of 9.5 ksi. For comparison, previous results for similar tests of IM6/3501-6 tape material resulted in an average failure stress of 6.4 ksi.

Layup	Test Type	Specimen Geometry	Number of Specimens					
			LDF™ Unstretched		LDF™ Stretched		Continuous Fiber	
			RT Dry	180° Wet	RT Dry	180° Wet	RT Dry	180° Wet
[0] ₈	Tension ASTM D3039	0.5" x 9.5"	5	5	5	5	3	3
	Compression Strength ASTM D695	0.5" X 3.18"	5	5	5	5	3	3
	Compression Modulus ASTM D695	0.5" x 3.18"	3	3	3	3	3	3
[90] ₂₀	Tension ASTM D3039	1.0" x 9.5"	5	5	-	-	-	-
[±45] _{2s}	Tension	1.0" x 9.5"	5	5	-	-	5	5
[±45/0/90] _s	Tension	0.5" x 9.5"	3	3	3	3	3	3
	Compression	0.5" x 9.5"	3	3	3	3	3	3

Figure 2 Test Matrix for Phase 1 - Material Evaluation

LAYUP	AS4/PEKK Material Type	Strength (KSI)	Coeff. of Variation (%)	Modulus (MSI)	Coeff. of Variation (%)
[0] ₈	CONT. FIBER	255	6	17.7	3.1
	LDF™	242	6	16.4	6.1
	STRETCHED LDF™	274	5	16.8	21.7
[90] ₈	LDF™	9.5	19	1.52	1.0
[±45] _{2s}	CONT. FIBER	16.8	4.5	0.85	4.9
	LDF™	21.0	4.1	0.87	7.8
[±45/0/90] _s	CONT. FIBER	88	3.7	6.3	9.6
	LDF™	86	3.8	6.4	14.5
	STRETCHED LDF™	54	5.9	5.1	10.9

Figure 3 Average Tension Test Results

The ±45 tension tests showed no reduction in strength or modulus due to the discontinuous fiber. Stress based on actual thickness increased 25%. Finally, in the quasi-

isotropic layup the presence of the discontinuous fibers did not significantly reduce strength (2%), while it slightly increased the initial modulus (2%). The stretched specimens were tapered significantly lengthwise; thicknesses ranged from .035" to .042".

Compression Tests

Results for compression strength and extensional stiffness are shown in Figure 4. The LDF™ 0° strength is reduced by 15% while the modulus increased slightly (5%). A degradation of 42% in strength and 4% in stiffness was observed for stretched LDF™ specimens. These values were obtained using nominal thickness. Once again, in the stretched specimens, significant tapering occurred. Finally, in the quasi-isotropic layup the presence of the discontinuous fibers reduced strength by 19% and stretched specimens failed at an average of 38 ksi, a reduction of 65%.

LAYUP	AS4/PEKK Material Type	Strength (KSI)	Coeff. of Variation (%)	Modulus (MSI)	Coeff. of Variation (%)
[0] ₈	CONT. FIBER	257	3	19.6	9
	LDF™	218	9	20.6	13
	STRETCHED LDF™	149	13	18.9	2
[+/-45/0/90] _S	CONT. FIBER	110	5	6.3	10
	LDF™	89	6	7.7	15
	STRETCHED LDF™	38	39	5.1	11

Figure 4 Average Compression Test Results

PHASE 1 DISCUSSION

The Phase 1 stiffness and strength results were useful for determining the effect of the discontinuous fibers of the LDF™ material on basic mechanical properties. These values are in line with DuPont test results reported in the literature¹. However, the stretched LDF™ specimens suffered from a number of structural problems resulting from the unidirectional draw operation. First, the specimens were severely tapered lengthwise. Second, it is not believed that the consolidation was fully completed after drawing. This was easiest to see from the failed quasi-isotropic compression specimens. The continuous and LDF™ laminates both failed in compressive fracture. The drawn LDF™ specimen failure was due to delamination, a clear indication of poor post-stretch consolidation. These results have indicated that the process used to make flat stretched sheets from which the test specimens were made needs improvement and that this second consolidation is critical to LDF™ part performance.

PHASE 2 STRUCTURAL PROPERTIES

Phase 2 Test Matrix

In Phase 2, structural tests were performed to determine the suitability of LDF™ for curved frames. A series of compression tests on C-channel specimens to examine the

buckling and crippling behavior, and a series of flange bending tests to examine the interlaminar strength properties were conducted. For comparison, tests were also performed on specimens made with graphite/epoxy (AS4/3501-6) and a high-strain-to-failure fiber with toughened thermoset (T800/F3900), both in fabric form. The test matrix for the Phase 2 task is shown in Figure 5. For each material type, six channel specimens were tested in compression, three of them undamaged and three damaged with a 1/2 inch impactor at an energy level of five foot-pounds. Three flange bending tests were also conducted for each material type. For comparison, five specimens of each Phase 2 laminate were also tested in compression to determine their in-plane ultimate strength.

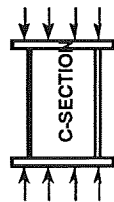
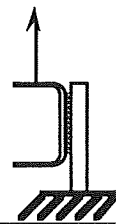

TEST TYPE				
	Channel Crippling		Flange Bending	Coupon Compression Ultimate
				
Material System	Undamaged	Damaged	Undamaged	Undamaged
AS4/PEKK LDF™ Tape [(±45) ₂ /0/90/±45/0/90] _s 20 plies (.108")	3	3	3	5
AS4/3501-6 Fabric [45 ₂ /0 ₂ /45 ₂ /0] _s 14 plies (.105")	3	3	3	5
T800/F3900 Fabric [45 ₂ /0/45/0] _s 10 plies (.110")	3	3	3	5

Figure 5 Phase 2 Test Matrix
Manufacturing and Testing

Crippling Tests

A tape layup of [(+45/-45)₂/0/90/+45/-45/0/90]_s was chosen for the LDF™ specimens to closely match the orientation of the fabric materials used for comparison. Matched metal tools were utilized. Crippling specimens were potted on each end with a room temperature curing epoxy contained in a 1/2 inch high aluminum ring (Figure 6). The channel crippling specimens were instrumented and then tested in compression after proper specimen alignment. Load was applied at a constant stroke rate until failure. Some crippling specimens were impacted by placing the potted specimen in a fixture which rigidly supported one of the flanges. The impact location is shown in Figure 6. Damage caused by the impact event was measured using ultrasonic NDI (Non Destructive Inspection) methods.

Flange Bending Tests

Flange bending specimens were obtained by cutting c-channel sections into 2.0 inch wide slices and bonding the web to a thick aluminum backing plate. The specimens were loaded through a bolt causing interlaminar tension stresses in the corner. The test was continued until multiple fractures in the radius region occurred, resulting in a significant loss of load.

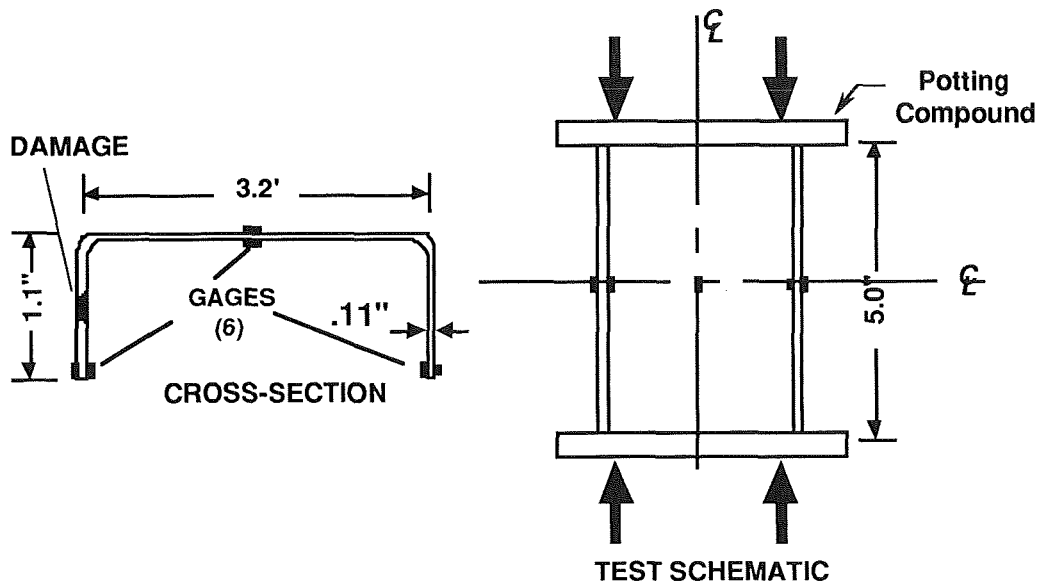


Figure 6 Crippling Test Specimen Configuration

RESULTS

Crippling Tests

During testing, all specimens buckled prior to final failure, with the web and flanges showing visible out-of-plane displacements. All specimens deformed into the shape of a one wave buckling mode, with the flanges usually opening up and the web bowing in; however, two of the undamaged LDF™ AS4/PEKK specimens experienced a change in buckling mode and switched to a two wave mode prior to failure after initially buckling in a one wave mode. In all undamaged cases, the failure sequence appears to be similar: the web starts buckling first, followed closely by the flanges. Buckling causes a rapid increase in bending strains which in turn causes an in-plane compressive failure of the flanges.

Based on NDI, impact damaged specimens showed some internal delaminations but no detectable fiber fracture. The failure mechanism for all damaged specimens appeared to be as follows: under compression loading the delaminated area under the impact site buckled locally, as indicated by the rapid increase in bending strain in the gage located next to the impact site, and delamination propagated rapidly to the specimen edge, leading to flange crippling and final failure. The appearance of the failed specimens was similar to their respective undamaged specimens, with the fracture originating at the impact site and the damaged flange showing more delamination.

As summarized in Figure 7, the undamaged LDF™ AS4/PEKK specimens failed at 42.5 ksi, while the AS4/3501-6 specimens failed in the flanges at an average stress of 41.8 ksi. The T800/F3900 specimens failed at an average stress of 58.5 ksi. After impact, failure

occurred at an average stress of 28.6 ksi for the LDF™ AS4/PEKK specimens and 28.6 KSI for the AS4/3501-6 specimens. These both correspond to reductions of approximately 32% compared to the undamaged specimens. The damaged T800/F3900 specimens failed at an average stress of 48.8 ksi, a reduction of 17% compared to the undamaged specimens. These crippling test results are compared with compression ultimate coupon test results in Figure 8. All undamaged crippling test failures occurred at average stresses significantly below laminate ultimate strength, confirming the instability type failure.

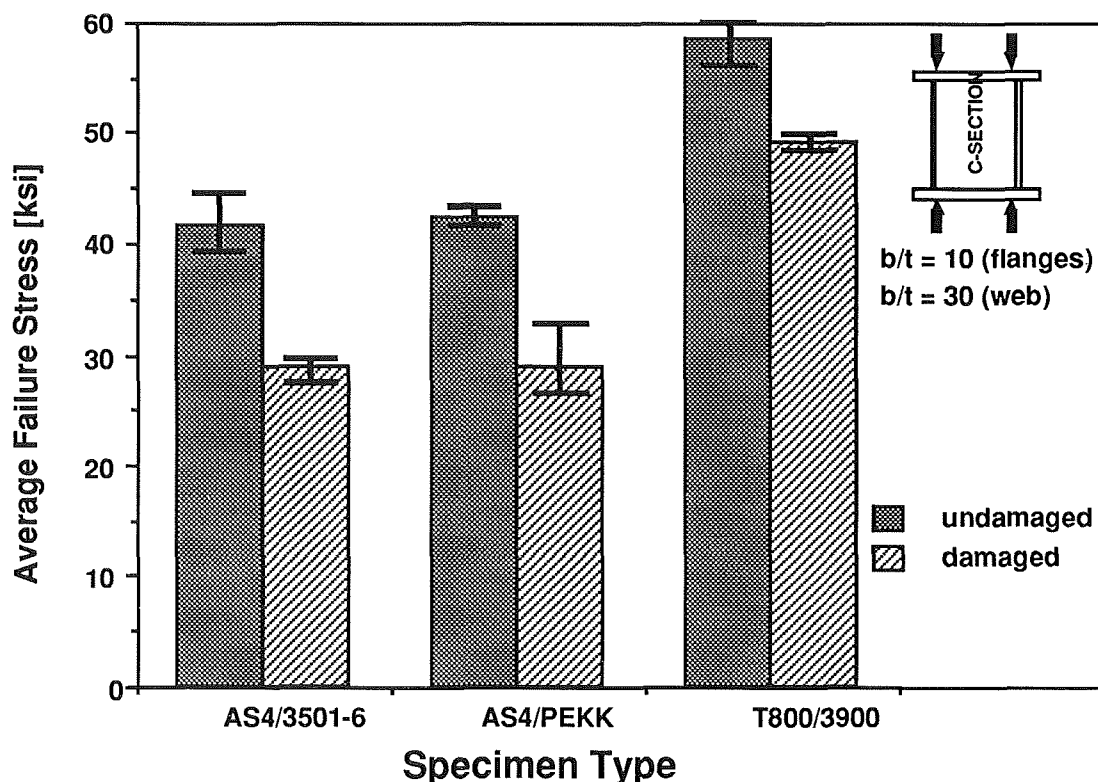


Figure 7 Average Crippling Stresses

Flange Bending Tests

Load versus displacement was recorded during testing. Indication of interlaminar failure could easily be identified by a sudden drop in load accompanied by clicking sounds. Some specimens exhibited a sudden and complete interlaminar failure of the flange, indicated by a load drop of 80% or more, while other specimens had an initial load drop of about 20%. After inspection, loading was resumed to final failure. No indication of any type of inplane damage could be seen in any specimen, thus indicating that the failure was purely interlaminar. The interlaminar tension stresses were determined for each specimen (Figure 8) and the results from these calculations for each specimen are shown graphically in Figure 9. The LDF™ AS4/PEKK material showed the highest average interlaminar tensile strength at 8200 psi, followed by the T800/F3900 at 5820 psi and the AS4/3501-6 at 4720 psi.

Material System	TEST TYPE		
	Compression Ultimate	Channel Crippling	Flange Bending
	STRESS (KSI) [CV%]	STRESS (KSI) [CV%]	STRESS(KSI) [CV%]
AS4/PEKK LDF™ Tape [(±45) ₂ /0/90/±45/0/90] _s 20 plies (.108")	106 [8.4%]	42.5 [1.1%]	8.2 [6.4%]
AS4/3501-6 Fabric [45 ₂ /0 ₂ /45 ₂ /0] _s 14 plies (.105")	97.5 [4.4%]	41.8 [6.5%]	4.7 [8.4%]
T800/F3900 Fabric [45 ₂ /0/45/0] _s 10 plies (.110")	83.5 [0.3%]	58.5 [3.7%]	5.7 [8.4%]

Figure 8 Average Strength Results

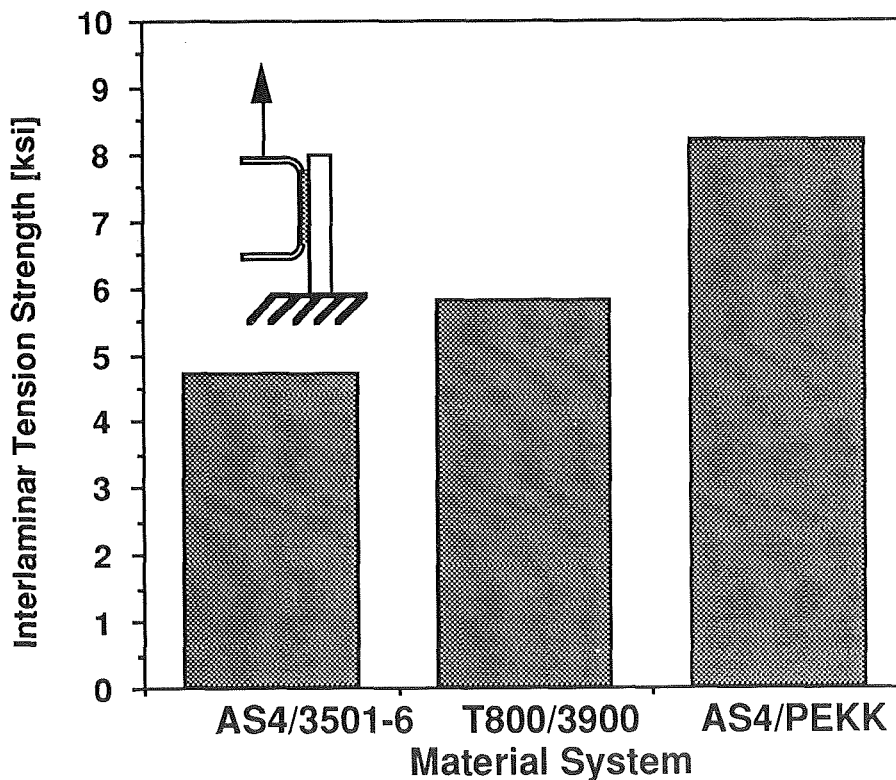


Figure 9 Summary of Average Interlaminar Tensile Strength

PHASE 3 FRAME TESTS

Frame Design

In Phase 3, a thin-gage fuselage frame section was manufactured through a stretch-forming operation. It is composed of two straight portions six inches long joined by a 45° circular bend with a 7.0 in radius; the width of the web is 1.6 in and the width of the flanges is 0.75 in. In order to evaluate the effect of layup, two layups were chosen which provide the same in-plane stiffness but different bending stiffness: $[\pm 45/0/90/0_2]_s$ and $[0_2/\pm 45/90/0]_s$. Three specimens of each kind were tested. Because of the high degree of draw in forming the curved part, additional 0° plies were added in the outer portion of the stock part. They were slightly longer than the entire curved portion of the part, insuring even stretching of the additional plies.

Frame Manufacturing

Stock Parts

Straight C channels were fabricated in matched steel tools (a fixed female and expandable 3-piece male tool). The LDF™ AS4/PEKK tape was layed-up on the male tool and then inserted in the fixed female tool. When pressure was applied to the tooling, the male tool expanded and forced the prepreg material to conform to the female tool. A 36 inch-square, 200 ton PHI hydraulic press supplied both the load and the heat required for consolidation.

Once the tooling and prepreg were loaded into the press, 5 tons were applied to insure adequate heat transfer. The pressure was increased to 45 tons (400 kN) once the process temperature of 700°F (370°C) was reached. This translates to about 750 psi (5.2 Mpa) on the part. When 700°F was reached, the platen heaters were turned off and the cooling cycle started. Pressure was maintained during cooling.

The channels were inspected by ultrasound and thickness measurements. Some variation in web and flanges thickness was observed. This was due to the design of the matched metal tools used to make the straight stock shape parts. The variation in stock shape thicknesses translated to variations in final part thicknesses.

Stretch Forming

The DuPont Research Stretch Former was designed and built to shape straight composite channels and beams into highly contoured parts. Matched metal tooling was developed to form the curved C channel. The straight C channel was inserted into the stretch forming machine and clamped in place. Electric heaters heated the part and the tooling to the process temperature of 700°F. Then the part was stretched and formed to the contour of the tool. After the stretching was complete, pressure was applied normal to the web and flanges to fully reconsolidate the part. With pressure still on the part, it was cooled to room temperature. The part was then removed from the machine and trimmed to final size using a bandsaw and wet grinder. Finally, it was ultrasonically inspected and the part checked for dimensions.

The high degree of draw (26%) required experimenting with ply buildups during the process development phase. A more detailed description of the stretch forming process can be found in US Patent No. 4,927,581 issued to the DuPont Company and titled "Method for Shaping Fiber Reinforced Resin Matrix Materials." Additional patents related to this process are pending. Both the straight and curved parts are shown in Figure 10.

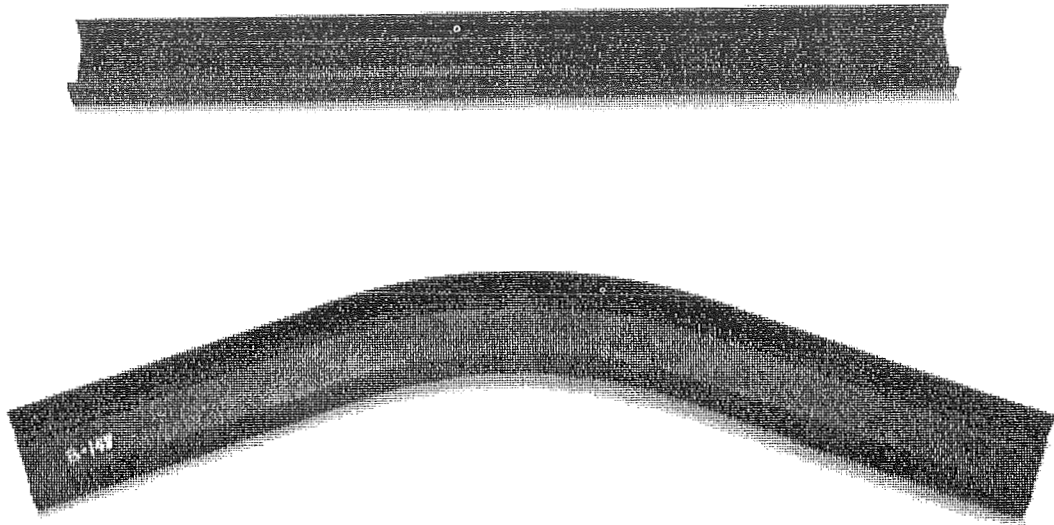


Figure 10 Stretch Forming of LDF™ Frame

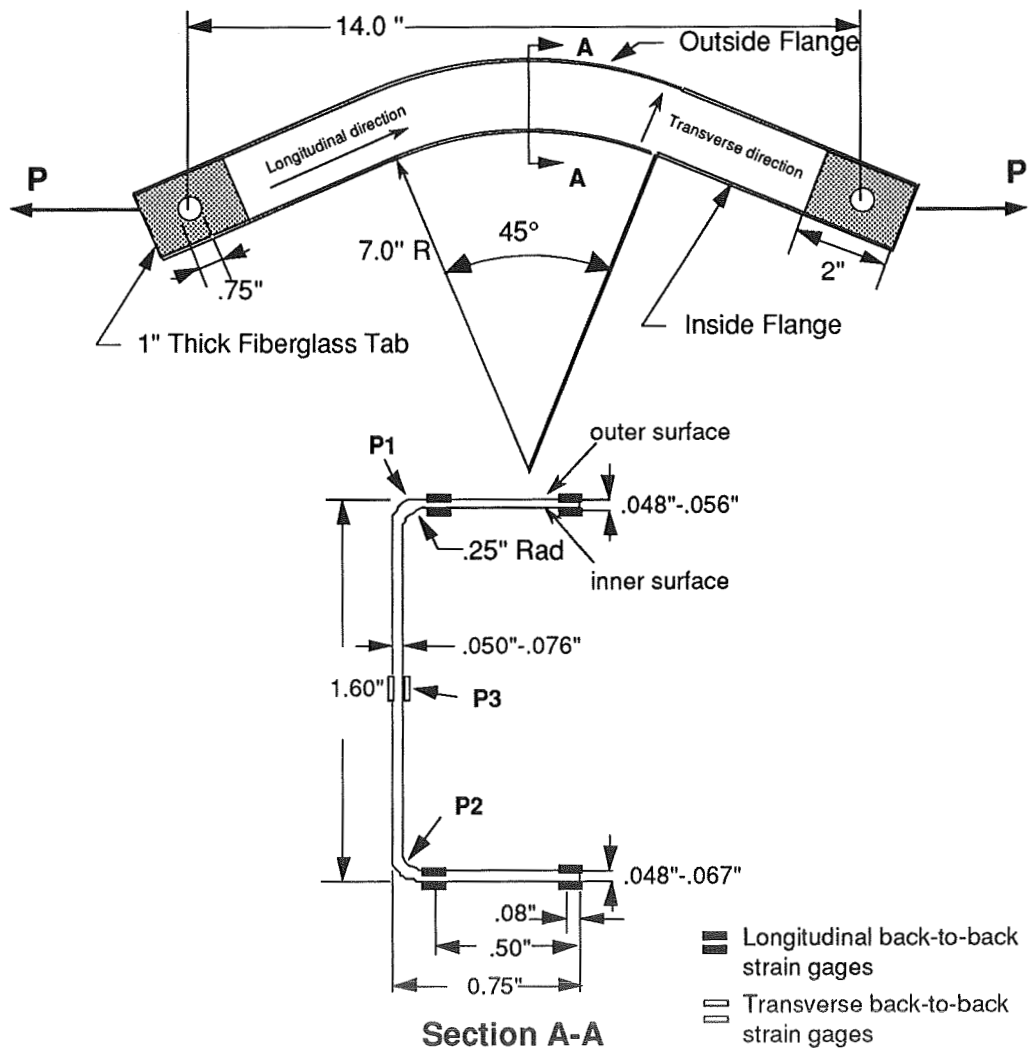


Figure 11 Curved Frame Specimen Configuration

Frame Test Method

Fiberglass/epoxy loading blocks, 1.0 inch thick by 2.5 inch long, were bonded to the inside surface at each end of the LDF™ stretched frame sections using EA9309.3 NA paste adhesive. Two holes (0.754 +/- .002) were drilled through the specimen, one in each of the two loading blocks, to provide a 14 inch separation between load application points. Final test specimen geometry is shown in Figure 11.

Several frames were tested as illustrated in Figure 12, to determine the strength of this LDF™ AS4/PEKK part after stretch-forming. The objective was to test the frame section under combined bending and axial loads while keeping the test setup fairly simple. Also, after reviewing the Phase 1 test data, a primary concern was the compressive strength of the LDF™ AS4/PEKK material after stretching. Therefore, the specimen was loaded in tension which avoided instability problems and allowed the stretched outer flange to be loaded in compression.

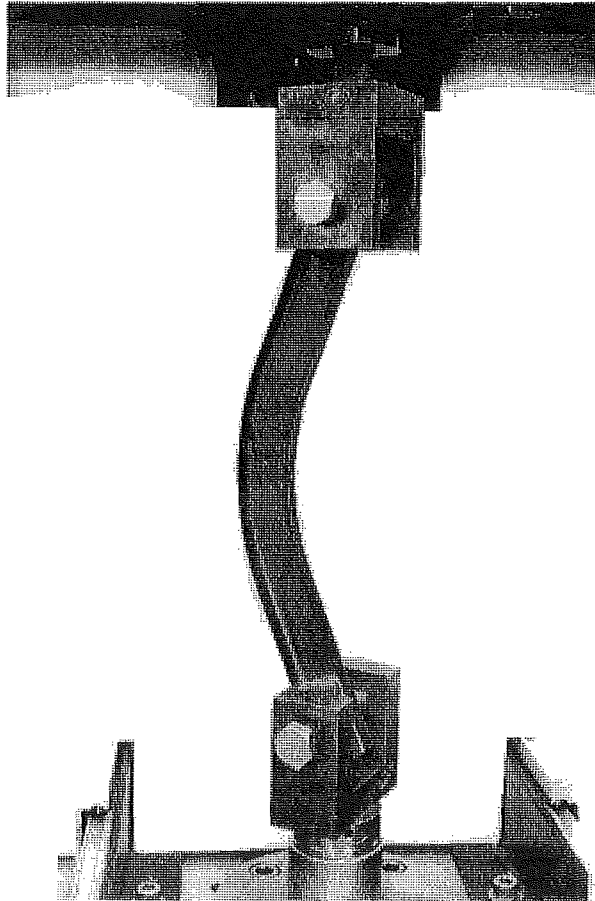


Figure 12 Frame Test Setup

Prior to testing, all specimens were instrumented with a number of strain gages. Testing was conducted in a 1127 Instron test machine with a 50,000 lb load cell. The specimens were loaded using a clevis at either end with a 0.750 inch diameter bolt. Load was applied at a constant rate until failure.

Experimental Results

During testing, large deformations of the flanges were observed in the curved section, with both flanges deforming outwards and opening up. Only a few clicking noises were heard during testing, some of which occurred at fairly low load levels and can probably be attributed to local failures in the adhesive bond of the tabs. No other significant noises were heard prior to final failure which was catastrophic in all cases. In four of the specimens, failure initiated on the tension side, in the curved section at the corner between the web and the inner flange and then propagated instantly around the cross-section with the specimen separating usually into two parts. In the remaining two specimens, failure initiated on the compression side at the corner between the web and the outer flange. A photograph of each kind of failed specimen is shown in Figure 13 and failure loads are given in Figure 14.

The following observations were made concerning the stress-strain behavior recorded during frame tests:

- The longitudinal strains at the tip of each flange are of opposite signs compared to the strains measured at the root of the same flange. This was due to the deformations of the flanges in the curved section.
- The longitudinal gages also show a slight stiffening behavior due to the fact the flanges are straightening in the curved section.
- The transverse gages on the web show a very nonlinear stiffening behavior: the reason is that the web is loaded transversely in tension, thus increasing the transverse bending stiffness of the web.

Frame Analysis

In order to better interpret the experimental results, a Finite Element (FE) model of the test specimen was generated using PDA's PATRAN modeler. PDA's FEA solver, P/FEA, was used for the analysis. A view of the analysis mesh is shown in Figure 15. The FE model consisted of 256 composite flat shell elements and was utilized to determine the ply longitudinal strain distribution at failure. Since strain gages could not be placed at the location of maximum strains, the model results were used to estimate the maximum tensile and compressive strains at failure for each specimen.

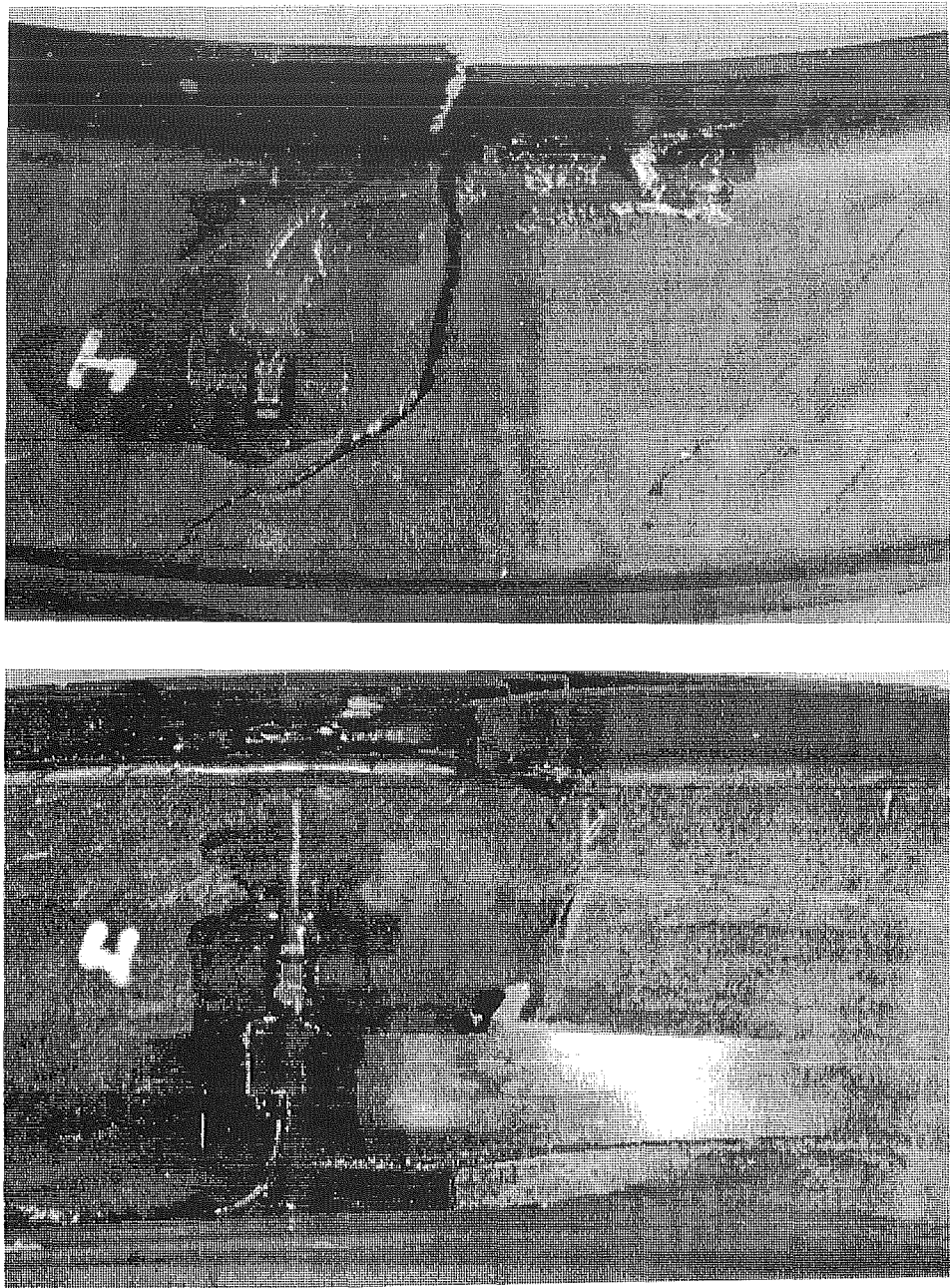


Figure 13 Frame Tensile (top) and Compressive (bottom) Failure Modes

The results of these strain calculations are shown in Figure 16. The ratios between model and experimental strains are also indicated. In Figure 17, the predicted strains around the frame cross-section are compared to strain-gage data. In general, the agreement is quite good for the membrane strain component, while there is more variation in the bending component since that measurement is more sensitive to local thickness variations. The predicted strain levels at failure in the specimens which experienced tension failures correspond well with the expected tensile strength of this material system (Phase 1 tests). Some reduction in compression strength compared to the unstretched Phase 1 test results was indicated in the specimens which failed in compression, due possibly to variations in

Specimen ID#	Layup	Outer Flange [in]	Web [in]	Inner Flange [in]	Failure Load [lb]	Failure Mode
B-130	$[\pm 45/0/90/0_2]_s$.052	.050	.048	1875	Tension
B-135	$[\pm 45/0/90/0_2]_s$.049	.076	.061	2450	Compression
B-149	$[\pm 45/0/90/0_2]_s$.051	.051	.062	1556	Tension
B-136	$[0_2/\pm 45/90/0]_s$.049	.062	.055	1870	Tension
B-143	$[0_2/\pm 45/90/0]_s$.056	.070	.065	2650	Tension
B-152	$[0_2/\pm 45/90/0]_s$.048	.071	.067	1915	Compression

Figure 14 Summary of Thicknesses and Failure Loads of Frames

the degree of reconsolidation of the material. Although some improvement in part to part consistency is needed, it is believed that this could be achieved with improved tooling. As illustrated in Figure 18, average test results show that the LDF™ AS4/PEKK structural properties after stretch-forming are not significantly different from the average failure strain levels obtained in tests of IM6/3501-6.

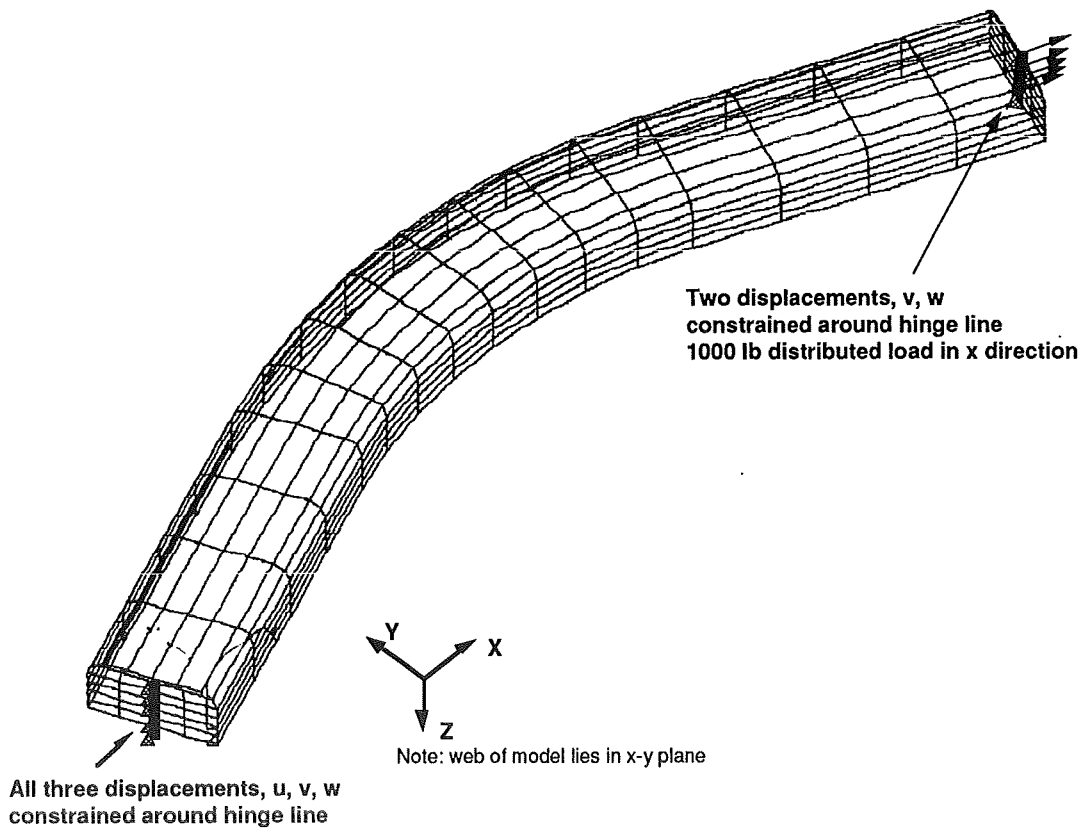


Figure 15 View of Curved Frame Finite Element Model

Specimen	Failure load [lb]	Model/Exper (membrane)	Model/Exper (bending)	Predicted Min. Strain at Failure	Predicted Max. Strain at Failure	Failure Mode (experiments)
B-135	2450	1.053	.69	-8904	12933	Compression
B-130	1875	1.06	.85	-8630	13550	Tension
B-149	1555	.80	.90	-8342	13764	Tension
B-136	1870	.99	1.12	-8672	12777	Tension
B-143	2650	1.13	.47	-9861	14840	Tension
B-152	1915	.94	.45	-8765	12650	Compression
Mean	2053	.99	.75	-8862	13419	
Std. Dev.	411 (20%)	.04 (4%)	.10 (13%)	523 (6%)	824 (6%)	

Figure 16 Curved Frame Predicted Maximum and Minimum Strains

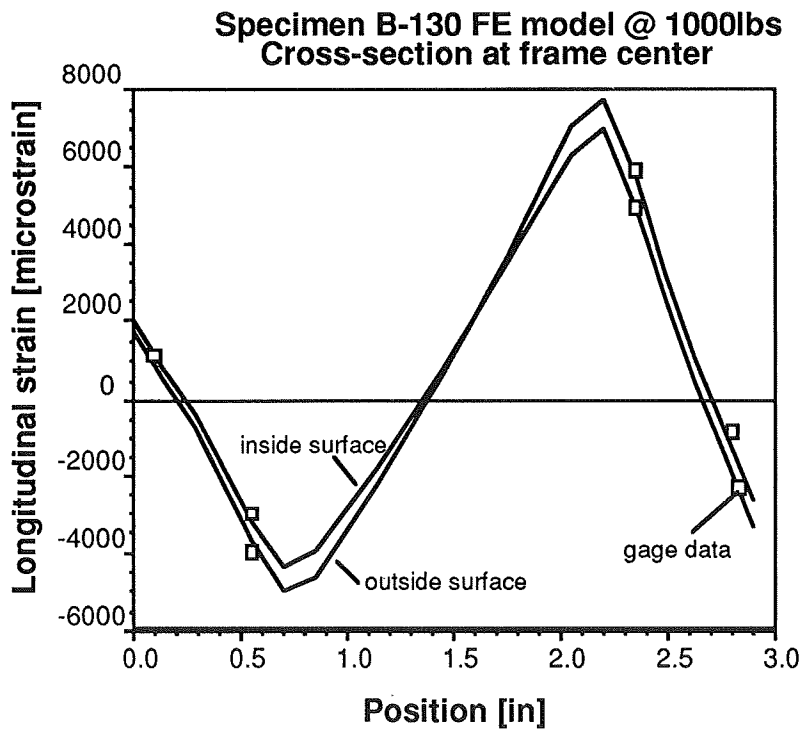


Figure 17 FEM Strains Compared to Experimental Data

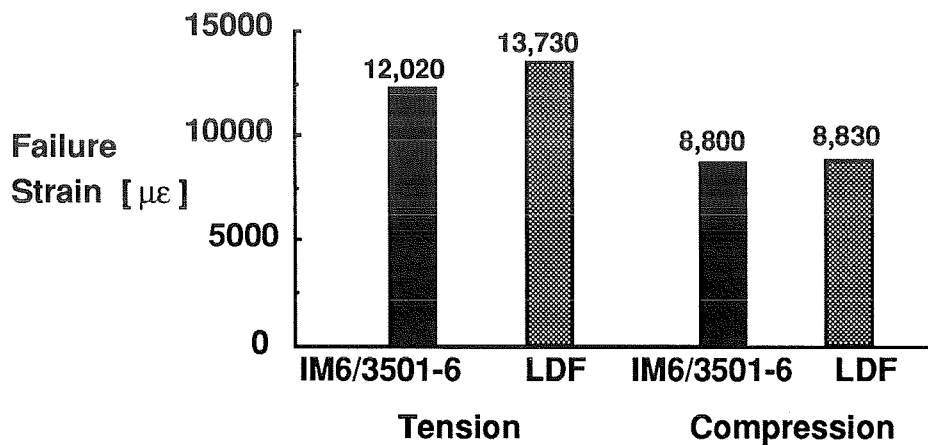


Figure 18 Comparison of LDF™ AS4/PEKK and IM6/3501-6 Average Strain Levels

FRAME COST STUDY

A cost study was conducted on the frame manufactured and tested in Phase 3. Included in the estimates of average unit cost was both recurring (labor, material) and non-recurring (tooling) costs for the manufacture of 1300 frames. Capital expenditures were omitted. The baseline, hand lay-up of a thermoset frame, requires 3 pieces to be assembled. Figure 19 is a schematic of this frame section. BH Industrial Engineering applied an 83% learning curve to these parts. Two potential material costs were used; \$50 representing current AS4/3501-6 cost and \$70 representing estimates of toughened thermoset cost. The LDF™ part, estimated by DuPont, is one-piece and uses a 90% learning curve reflecting the more automated process. Two material cost extremes were again utilized; \$110 reflecting current thermoplastic prepreg cost and \$60 reflecting large production estimates. Results are shown in Figure 20. Based on tooling costs, the unit LDF™ cost is higher for very small lot sizes. For 1300 parts the use of LDF™ for this frame results in a 43-59% savings, depending on individual material costs used.

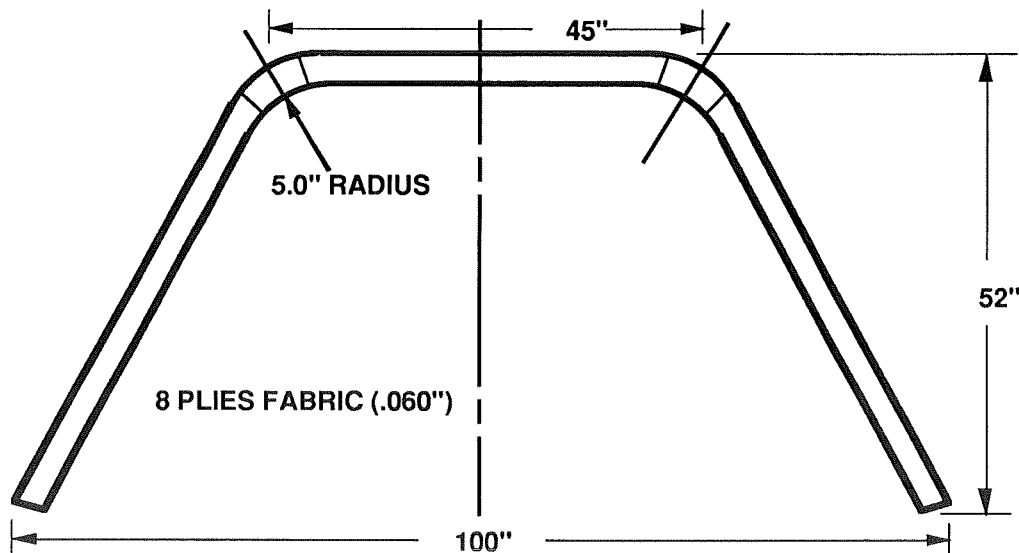


Figure 19 Frame Section in Estimate

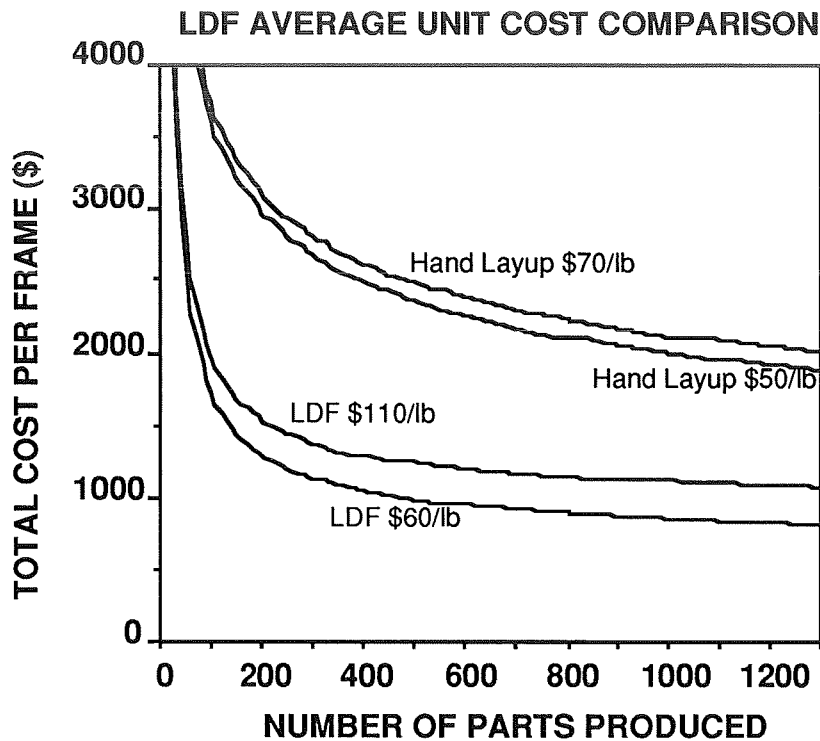


Figure 20 Cost Estimates of Frame Manufacture

CONCLUSIONS

The stretch forming of an LDF™ AS4/PEKK frame was successfully demonstrated in this investigation. It is believed that this process is feasible for thin curved rotorcraft frames and offers a significant cost advantage over the hand lay-up of thermoset frames while not compromising overall part strength. Specific conclusions are as follows:

- Material properties test results agree with values previously reported. All tensile properties for LDF™ AS4/PEKK compared favorably with those of continuous fiber AS4/PEKK composites, while compressive strength properties showed a small drop for unstretched LDF™. Low compression strength properties were obtained due to the poor quality of the stretched specimens, these results also indicating that adequate reconsolidation of the part after stretching is an important factor.
- Channel crippling tests showed similar strength results for LDF™ tape layup and continuous fiber AS4/3501-6 fabric layup. Crippling strength of high-strain graphite/toughened thermoset fabric (T800/F3900) layup was higher due to the higher modulus and strength of the fiber. Crippling tests of impact-damaged specimens showed no significant difference between the AS4/thermoset fabric and the LDF™/PEKK tape, while the toughened thermoset material showed an improvement in damage tolerance.
- Flange bending tests showed that PEKK has the highest interlaminar tensile strength, followed by the toughened thermoset F3900 and the epoxy matrix 3501-6.
- The feasibility of stretch-forming curved frame section was demonstrated. Although some improvements in part consistency are still needed (better tooling), structural testing showed only a small reduction in strength due to the manufacturing process.

- Regardless of the material cost used in the calculations, the stretch forming of LDF™ composites results in a lower cost manufacturing process compared to hand lay-up for large lot sizes.

ACKNOWLEDGMENTS

The authors would like to gratefully acknowledge the contributions of other Helicopters Division and DuPont personnel who contributed to this effort. Christian Gunther's and Jim Pratte's guidance was instrumental in the experimental investigation and final report preparation.

REFERENCES

1. Khan, S., Pratte, J.F., Chang, I.Y., and Krueger, W.H., "Composites for Aerospace Application from Kevlar Aramid Reinforced PEKK Thermoplastic", Presented at the 35th International SAMPE Symposium, Anaheim, California, April 2-5, 1990.

THIS PAGE INTENTIONALLY BLANK

DESIGN, ANALYSIS, AND TESTING OF A METAL MATRIX COMPOSITE WEB/FLANGE INTERSECTION

S. B. Biggers and N. F. Knight, Jr.
Department of Mechanical Engineering
Clemson University, Clemson, SC

S.G. Moran*
NASA Headquarters ✓
Washington, D.C.

R. Olliffe
Lockheed Aeronautical Systems Company
Marietta, GA

*Formerly employed by
Lockheed Aeronautical Systems Company

NASA
513-24
51381
P-32

SUMMARY

An experimental and analytical program to investigate the local design details of a typical T-shaped web/flange intersection made from a metal matrix composite is described. Loads creating flange bending were applied to specimens having different designs and boundary conditions. Finite element analyses were conducted on models of the test specimens to predict the structural response. The analyses correctly predict failure load, mode, and location in the fillet material in the intersection region of the web and the flange when specimen quality is good. The test program shows the importance of fabrication quality in the intersection region. The full-scale test program that led to the investigation of this local detail is also described.

INTRODUCTION

Full-scale tests conducted at Lockheed Aeronautical Systems Company (LASC) under Air Force Wright Laboratory (AFWL) sponsorship revealed an unexpected failure mode for continuous-fiber-reinforced (CFR) metal matrix composites (MMC). During fatigue testing of a full-scale vertical tail structure, the front and rear spars cracked along their fillet radius, with the beam cap flanges separating from the webs. The spars are I-section beams made of silicon carbide CFR 6061 aluminum (SiCf/Al). Failures of this type had not occurred in any of the previous structural element or subcomponent tests conducted to uncover potential problems prior to full-scale testing. Fillet shear strength and cyclic three-point bending tests conducted on intact remnants of the failed spars indicated that shear transfer from web to flange was not the cause of failure. It was, therefore, concluded that out-of-plane loading creating local bending of the spar flanges was the probable cause. This conclusion is supported by the fact that one of the failures in the full-scale test appeared to originate near a load introduction fitting. In addition, some mismatch was observed between the skin, spar, and intercostal that resulted in local bending of the flange during assembly.

Recognizing that local out-of-plane loading on the flanges is likely to occur due to a number of unavoidable sources, a study was initiated in an LASC Independent Research and Development (IRAD) program to determine the causes and possible solutions for failures in the web/flange intersection region. A test program was defined to evaluate variations in the local design detail of the web/flange intersection region. Test specimens were fabricated with eight different fillet configurations using SiCf/Al. Finite element analyses of the web/flange intersection region were conducted to evaluate the effect of the fillet configuration on the stress state. The analysis also helped to define testing conditions which would best expose the out-of-plane weakness of the specimens, thereby fully testing the ability of the fillet design variations to delay or prevent out-of-plane failures.

This paper summarizes the full-scale testing in which the problem first appeared, the development testing leading up to the full-scale test program, and the test results for the web/flange intersection specimen testing. It describes the web/flange intersection finite element model development, the analysis results obtained, and correlation of the test and analysis results.

DESIGN DEVELOPMENT AND FULL-SCALE TESTING

Since 1981, the AFWL's Advanced Metallic Structures Program Office has funded LASC to design, fabricate, and test four metal matrix composite (MMC) vertical tails representative of advanced fighter structure. One of the partially assembled vertical tail structures is shown in Figure 1 prior to installation of the near side outer skin panels. The process leading to fabrication of the full-scale test articles included extensive material characterization testing at the coupon level to develop statistically significant design allowables to support detail design and analysis; element testing of joints, stiffened panels, and large subcomponents to verify MMC analysis methods; and design verification element testing to investigate critical vertical tail design details such as the root fitting, the skin/rib/spar intersection, and hinge fitting attachment.

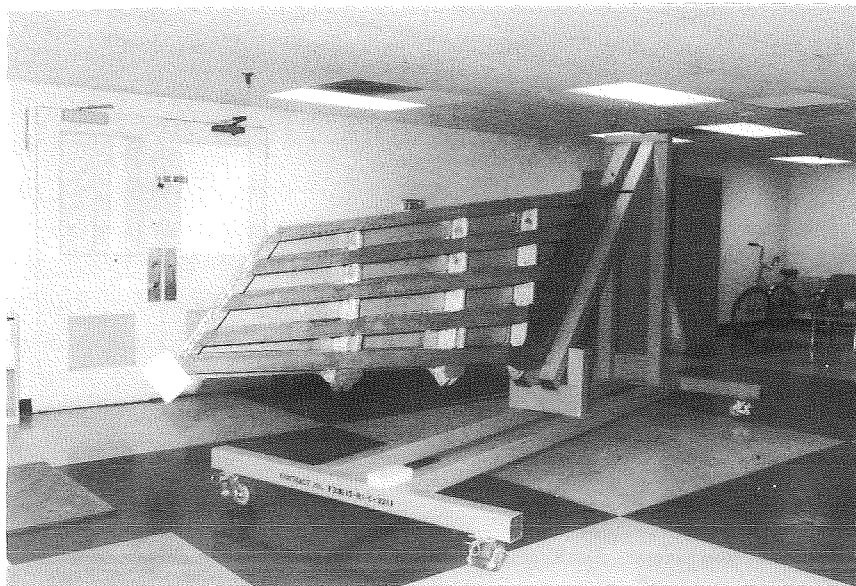


Figure 1. Partially Assembled MMC Vertical Tail Structure.

Two different multi-spar vertical tail configurations were designed, one with discontinuous silicon carbide whisker reinforced aluminum (SiCw/Al) skins (referred to in this paper as the SiCw/Al test article) and the other with continuous silicon carbide fiber reinforced aluminum (SiCf/Al) skins (referred to as the SiCf/Al test article). Both designs had the same substructure, consisting of five hot-molded SiCf/Al spars approximately ten feet long (fabricated by Textron Specialty Materials Division) joined by fourteen hot formed SiCw/Al intercostals (fabricated from large sheet supplied by Advanced Composite Materials Corporation). One static and one fatigue test article was fabricated for each configuration, for a total of four full-scale test articles.

SiCf/Al Spar Hot Molding Process Development

As shown in Figure 2, each SiCf/Al spar consists of nine individual components — two preconsolidated flange plates, a preconsolidated centerline web element, two preconsolidated channel sections which serve to tie the flanges to the webs, and four fillet radius fillers. In addition, a small gap exists between the web and flange that becomes filled with the filler material used in the fillets upon hot molding. The basic design configuration and tooling concept for these SiCf/Al spars were developed and evaluated in the SiCf/Al hot molding process development program conducted by Textron Specialty Materials Division during the initial stages of the AFWL contract.

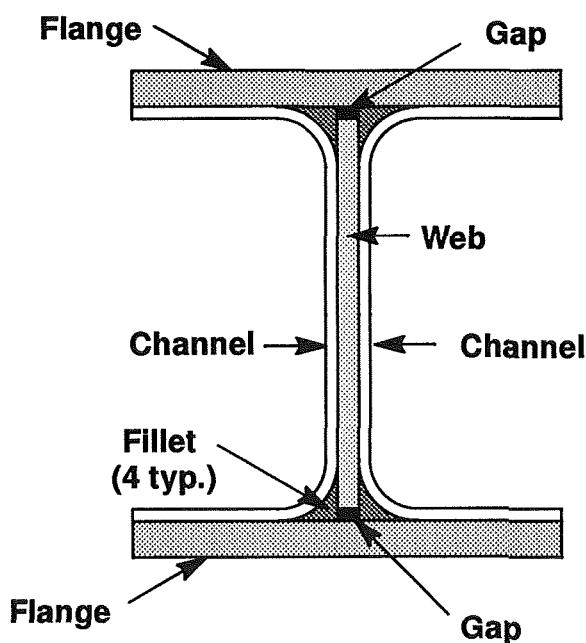


Figure 2. Individual components of a SiCf/Al spar.

The original intent in designing the SiCf/Al spars was to include 90-degree plies in the channel sections to improve pull-off strength. However, early development tests of the 5.6 mil diameter SiC fiber indicated that the minimum radius for 90-degree plies was too large to allow fabrication of practical structural shapes. The 90-degree plies were subsequently eliminated, and the spar fillet radius was dictated by the minimum radius (.25 in.) for wrapping 45-degree plies.

It was assumed in the early stages of design development that the web/flange intersection in hot molded SiCf/Al shapes would develop approximately the same shear carrying capability as unidirectional panels, i.e., 15 ksi. However, tests conducted as part of the hot molding process development efforts revealed that, even with 45-degree plies in the channel sections, the required flange pull-off strength and web/flange shear strength were not achieved due to incomplete consolidation in the fillet area of the web/flange intersection region. Through improvements in both the matrix materials and the hot molding process parameters, the fillet shear strength was improved to within acceptable limits, but never achieved a strength equivalent to that of unidirectional panels.

SiCf/Al Spar Qualification Tests

Based on lessons learned in the hot molding process development program, a qualification test was designed to measure the fillet shear strength of every SiCf/Al spar used in the full-scale test article fabrication. Samples were removed from the root and tip of each incoming spar and subjected to a special LASC-developed shear strength test. The results of these tests are shown in Figure 3 as high and low values from four tests for the root and tip segments of each spar. Also shown are finite element analysis predictions of the maximum shear loads for each spar. These maximum values usually occurred near the root.

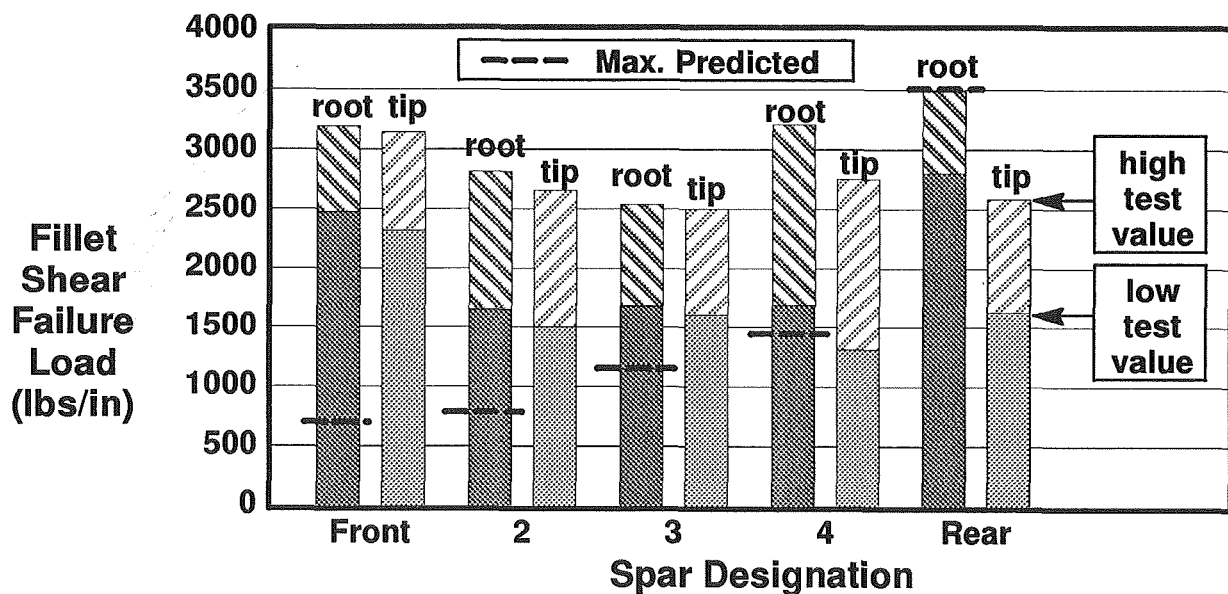


Figure 3. Measured and predicted fillet shear strength in each spar.

Although the range between the high and low strength values is significant, indicating a wide variation in fillet shear strength from spar to spar and possibly within individual spars, all of the strengths were above the predicted strength requirement except for the rear spar (minimum of 2807 lbs/in. at the root versus 3524 lbs/in. required). Based on the spar qualification test results, the full-scale test article designs were modified by bonding titanium doublers in the fillet radii of the rear spars near the root.

Design Development Element and Subcomponent Tests

Element and subcomponent tests conducted in support of preliminary design of the vertical tail structure included static and fatigue tests of chordwise joints, spanwise splices, and skin/stiffener tension and compression panels; multiple-stiffener buckling resistant and post-buckled compression and shear panels; pressure box tests of a stiffened skin panel; and a combined shear-compression-pressure test of a large stiffened fuselage shell subcomponent. In addition, several element tests were conducted to verify vertical tail design details. These verification elements included a static test of the rudder hinge fitting and fatigue tests of the skin/rib/spar intersection and the intersection of the skin and spar with the titanium root fitting. The results of these tests indicated that the analysis methods being used were quite accurate in predicting both buckling and failure loads. Although some minor damage to the SiCf/Al spars occurred during assembly of the elements and subcomponents, none of the static or fatigue tests revealed a problem with the web/flange fillet. All testing conducted prior to the full-scale vertical tail tests indicated that, although the fillet might be a weak link, its strength was adequate for the intended design once the fillet consolidation problem was solved. The spar qualification tests also supported this conclusion.

Full-Scale Test Setup

The full-scale vertical tail structural tests were conducted in a specially constructed loading frame. Five hydraulic jacks applied loads at discrete points along the front and rear spars and two jacks were used to load the tip of the tail through a loading "cradle." The discrete load points included three on the front spar at the spar/rib intersections and two on the rear spar at the upper and lower rudder hinge fittings. In the photographs shown in Figure 4, the front spar is at the top of the test article, and the rear spar hinge fitting load points can be seen at the bottom of the article. Loads were reacted through a titanium root fitting attached to the steel load frame, simulating the fuselage attachment. All loading jacks were capable of reversed loading, so that all bending and torsion load cases could be applied. The test articles were instrumented with over 220 strain gages, thermocouples, and displacement transducers.

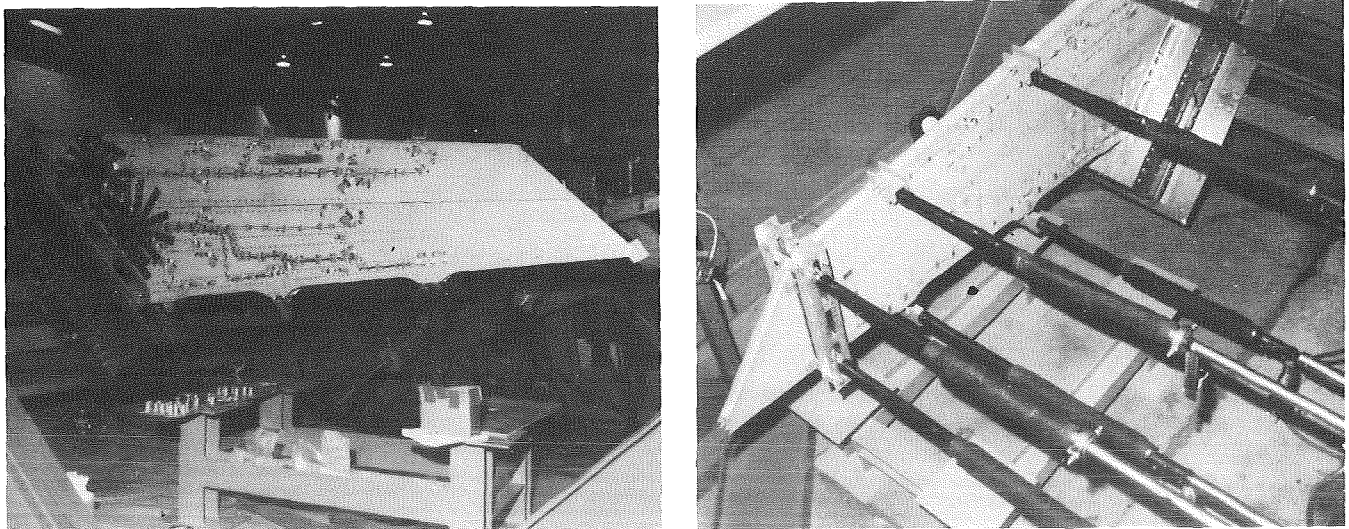


Figure 4. Full-scale structural test setup.

Full-Scale Static Tests

The first full-scale structural test was conducted on the SiCw/Al static test article. This test was conducted at temperature in a specially designed environmental chamber to simulate the actual flight environment (250°F). During design limit load (DLL) application at temperature, buckling of the two-sheet bonded SiCw/Al skins occurred well before the analytically predicted load levels were reached. Analysis of the strain gage data indicated that the adhesive bond in the two-sheet bonded skin softened enough at the elevated temperature to allow the two skin sheets to buckle independently. As a result, the subsequent ultimate load condition was applied at room temperature. Failure occurred at approximately 142% of DLL. It was difficult to determine the exact failure sequence, but post-test investigations indicated that the failure originated in Spar No. 3 (the center spar) by either flange buckling due to lack of support from the postbuckled skin or by flange bending caused by the out-of-plane loads applied by the postbuckled skin. The failure resulted in total separation of the spar flange from the web along the web/flange fillet.

Since there was no adhesive bond in the skin of the SiCf/Al test article, the full-scale SiCf/Al ultimate load test was conducted in the environmental chamber at 250°F. The limit load applications at room and elevated temperatures were accomplished without problem. Correlation of analytically predicted (finite element method) and measured strains at limit load are shown in Figure 5.

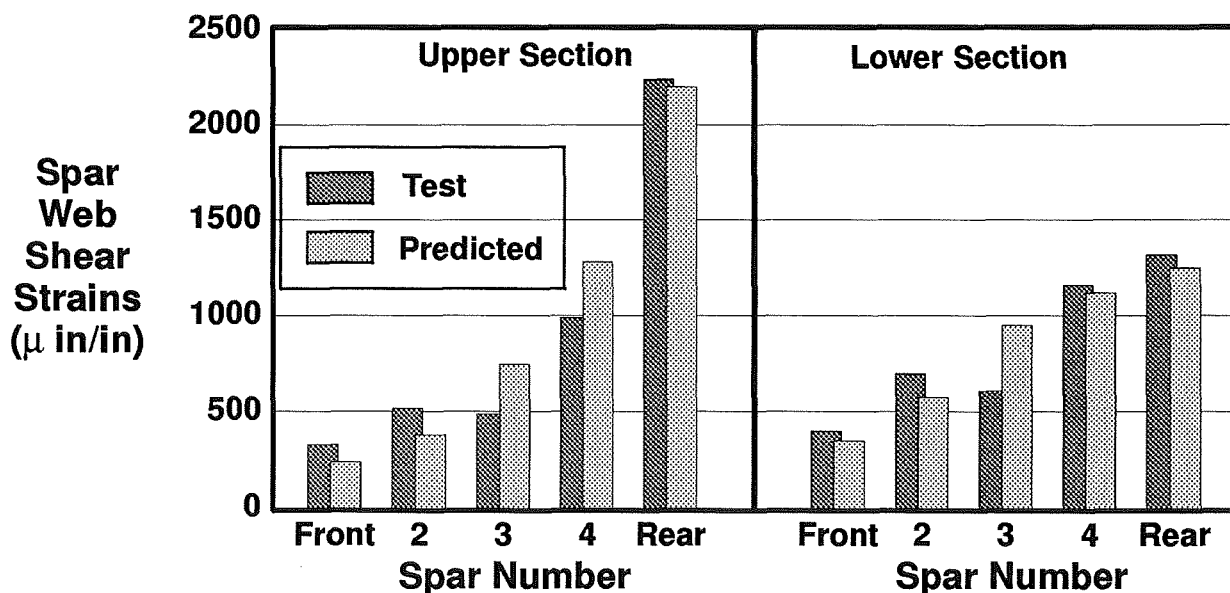


Figure 5. Predicted and measured spar web strains at limit load.

However, during application of ultimate load (150% of DLL), the load control system released all load at approximately 140% of DLL. Visual inspection from outside the environmental chamber revealed no apparent damage, so the control system was reset and load was applied again. The control system again released all load at approximately 120% of DLL, again with no apparent visible damage. The control system was reset and, on the third attempt to apply ultimate load, the test article failed at 50% of DLL. Post-test failure investigations indicated that the initial failure probably occurred at 140% of DLL by separation of the rear spar flange from the web at the flange/web fillet near the upper hinge fitting. Upon subsequent applications of load,

the flange separation progressed to the point that the spar could no longer support the skin. This change in local boundary conditions and major load redistribution caused the skin to buckle and led to total failure of the test article.

Full-Scale Fatigue Tests

The fatigue test plan of the full-scale cyclic test articles included two lifetimes of durability testing followed by one lifetime of damage tolerance testing. Each lifetime was composed of approximately 166,000 cycles of truncated spectrum loading representing the primary damaging cycles of the fatigue spectrum. These cycles were contained in 32 repeatable "passes," each composed of 124 unique "flights," for a total of 3968 "flights" per lifetime. Due to the difficulties encountered in the elevated temperature static tests, the fatigue tests were conducted at room temperature.

The SiCw/Al cyclic test article was accidentally damaged during test system checkout. A large undamaged subcomponent was subsequently tested under LASC IRAD. Problems were also encountered during fatigue testing of the SiCf/Al cyclic test article. Testing was interrupted after 308 flights, or approximately 8% of the first lifetime of durability testing, due to failure of the front spar web/flange fillet. Figure 6 shows a close up view of the failure along the compression flange of the front spar.

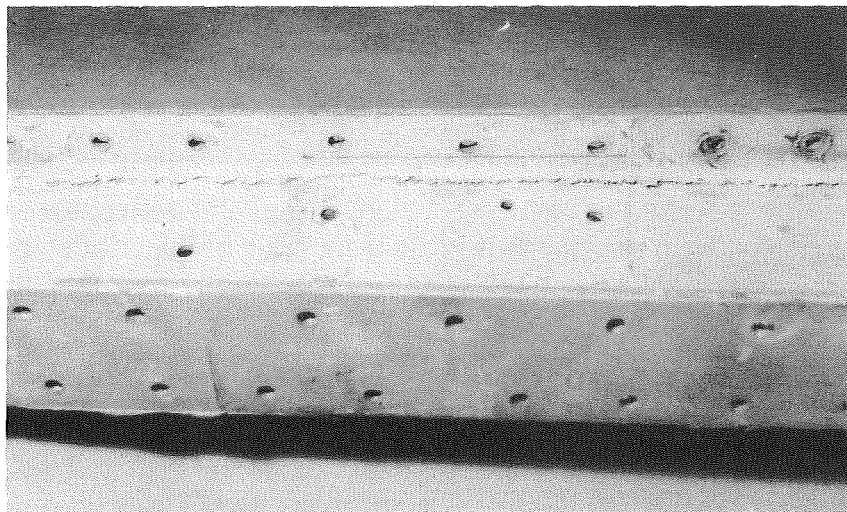


Figure 6. View of web/flange intersection fatigue failure in front spar.

Post-Test Failure Investigation

To determine whether the front spar fillets had adequate static shear strength, three fillet shear strength tests similar to the spar qualification tests were conducted on undamaged specimens removed from the upper, middle and lower sections of the failed spar. Fillet shear strengths measured 1930, 2490, and 2595 lbs/in., respectively, in the three tests. Although there was a wide variation in the strength of the front spar fillets, their strength was well above the required shear strength of 719 lbs/in.

Prior to the failure of the front spar, no cyclic tests had been conducted which included load transfer between the flange and web through bending. To determine whether cyclic shear

was causing the fatigue cracking of the spar fillets, two 3-point bending fatigue tests were conducted on undamaged segments removed from previously tested full-scale articles. Instrumentation of the test specimens included spar flange axial gages and spar web shear gages. The test setup is shown in Figure 7.

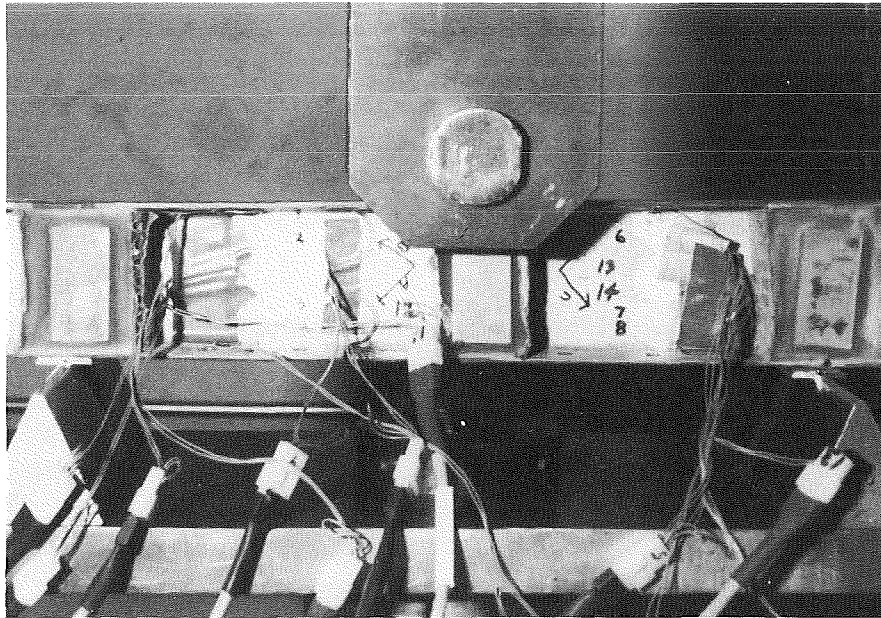


Figure 7. Three-point bending test setup.

The loads were adjusted to obtain spar flange axial and web shear strains which closely matched the strains measured during full-scale test of one of the critical load cases. For the front spar, these strains were $525 \mu\text{-in/in.}$ in the flange and $617 \mu\text{-in/in.}$ in the web; for the rear spar, they were $1000 \mu\text{-in/in.}$ in the flange and $1600 \mu\text{-in/in.}$ in the web. The specimens were cycled at constant amplitude with a minimum to maximum load ratio $R = 0.1$.

The test specimen representing the upper section of the front spar achieved 74,600 cycles at maximum strain (considerably more than the full-scale test article would experience in three lifetimes of fatigue testing) before the test was stopped. A 0.25 inch saw cut simulating a web/flange crack was then placed in the compression fillet midway between the load and reaction points and the specimen was subjected to an additional 14,000 cycles at maximum strain with no failure and no apparent crack growth. The loads were increased 50% and the specimen was cycled an additional 60,000 cycles with no failure or apparent crack growth. At this point the test was discontinued.

The test specimen representing the root of the rear spar achieved 42,500 cycles at maximum strain (again, considerably more than would be seen by the full-scale article in three lifetimes of testing) with no apparent degradation. The loads were increased 25% and the specimen was subjected to an additional 2000 cycles with no damage. A saw cut was inserted in the compression fillet and the specimen was cycled an additional 11,000 cycles at the increased load level with no failure and no apparent crack growth, at which time the test was discontinued.

The results of the static fillet shear strength tests and the 3-point bending fatigue tests indicated that the spar fillets had more than adequate static and fatigue shear strength to sustain the analytically predicted loads for the three lifetimes of fatigue testing. Based on these results, it was concluded that the spar failed due to unpredicted out-of-plane loads on the flange creating local bending in the web/flange intersection region. These loads may have been caused during assembly by pulling down gaps between the SiCf/Al skins and spar flanges or by local deformations associated with the load introduction fittings. These conclusions were reinforced by the fact that failure of the web/flange intersection did not appear in any of the extensive element, subcomponent, and design verification tests conducted prior to the full-scale tests.

Continued Full-Scale SiCf/Al Fatigue Test

To support a decision to repair and continue fatigue testing of the SiCf/Al cyclic test article, the fillet regions of the spars which had not failed were visually and ultrasonically inspected (using A scan) for additional damage. Since it was not feasible from either a schedule or cost standpoint to fabricate a new SiCf/Al front spar, an equivalent stiffness conventional aluminum spar was designed to replace the failed spar. As safety precautions, crack sensors were placed in all four fillets along the span of the four remaining undamaged spars (a total of 64 crack gages) and the number of visual inspection intervals was substantially increased to detect any possible future cracks before they could lead to further damage. The cyclic test article was reassembled, strain surveys were conducted to ensure that the new aluminum front spar did not significantly affect the strain levels or distributions in the remaining structure, and the fatigue test was resumed.

After an additional 199 flights of fatigue testing, a small crack was detected in one of the rear spar fillets near the lower hinge fitting. Video cameras were set up to record crack growth and the fatigue testing was continued until the crack grew to a significant percentage of the overall span. Testing was discontinued and the LASC IRAD-funded SiCf/Al Fillet Investigation Study reported in the remainder of this paper was initiated to determine the causes for and potential solutions to this problem in the web/flange intersection.

T-SPECIMEN ELEMENT TESTING

To examine the effects of the web/flange intersection design, T-shaped specimens were fabricated using two fillet radii (1/4 in. and 1/2 in.) and different filler materials for the fillet region. A schematic that shows the basic construction of the T-sections is presented in Figure 8. Filler materials with four fiber-volume-content percentages (0%, 17%, 33%, and 50%) were used for this purpose. It was conjectured that the more compliant low fiber-volume filler material might perform better in helping transfer flange bending stresses across the intersection. Preliminary analytical results predicted that the larger fillet radius configuration would delay failures originating in the intersection region due to high interlaminar stresses.

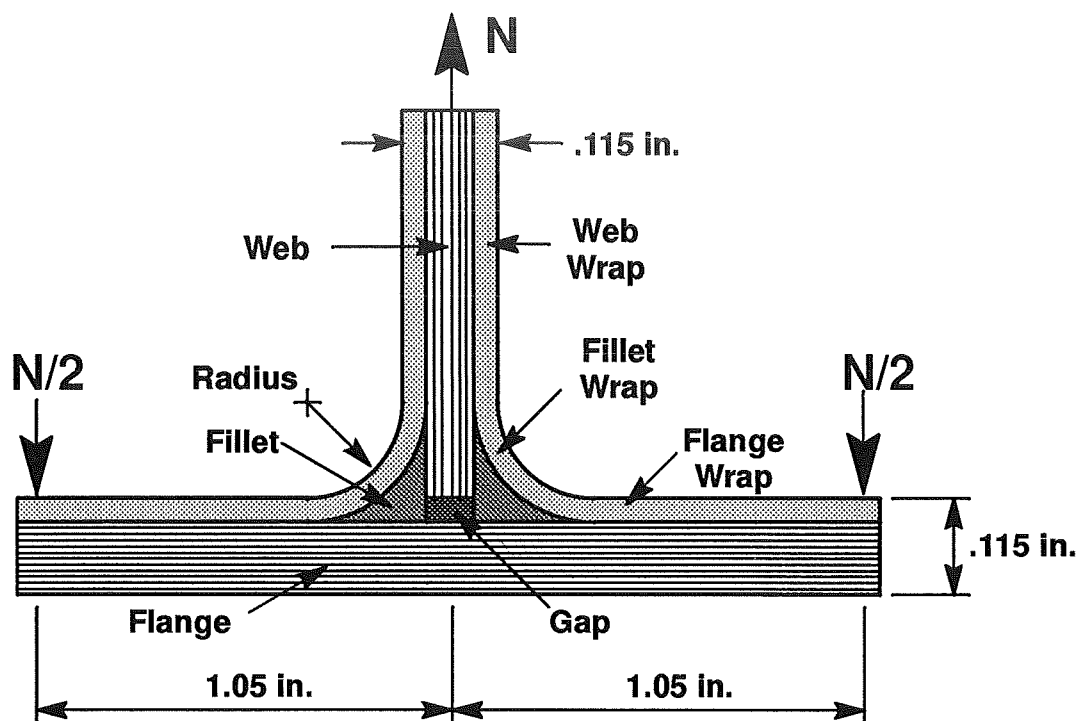


Figure 8. Schematic of T-section test geometry and nomenclature.

The basic fabrication approach is the same as that used in the spars for the full-scale test articles. The bulk of the flange laminate is formed by a preconsolidated laminate with continuous, uniform thickness, horizontal plies. A similar preconsolidated laminate comprises the central core of the web. A pair of ± 45 degree plies with continuous fiber orientations wraps around the fillet radius region and completes the flange and web laminates. Filler material is placed in the fillet regions. A variable sized "gap" exists between the preconsolidated web and flange laminates and is filled with the same material that is in the fillet radius region. This gap is on the order of two to eight ply thicknesses (nominal ply thickness is 7 mils). The inner radius of the wrap plies is either 1/4 or 1/2 inch. Including the wrap plies, the web stacking sequence is $[\pm 45/90/\mp 45/0/\pm 45]_s$ and, starting from the inside (web side) of the flange, the right flange stacking sequence is $[\pm 45/0/\pm 45/0_8/\mp 45/0]$. The corresponding left flange stacking sequence is $[\mp 45/0/\pm 45/0_8/\mp 45/0]$. The 0-degree direction referred to here is perpendicular to the plane of the model.

Specimens were cut from a single I-beam which was fabricated from SiCf/Al and incorporated three specimens of eight different design variations. A schematic of the beam and locations from which 48 T-specimens were taken is shown in Figure 9. Of this total, 46 specimens were tested to failure by symmetrically loading the web in tension and the flanges in downward bending as shown in Figure 8. In 23 of the tests the loads were applied to the flanges through rollers to simulate a simply supported condition. In the remaining tests, the flange loads were applied while clamping the flange ends to prevent rotation. Assembly conditions encountered in actual applications would fall somewhere between these two extreme boundary conditions. Each specimen was statically loaded to failure in a 60-kip Tinius Olsen Universal Test Machine used at a 2400 lb. range with an accuracy of ± 0.5 percent of the indicated load.

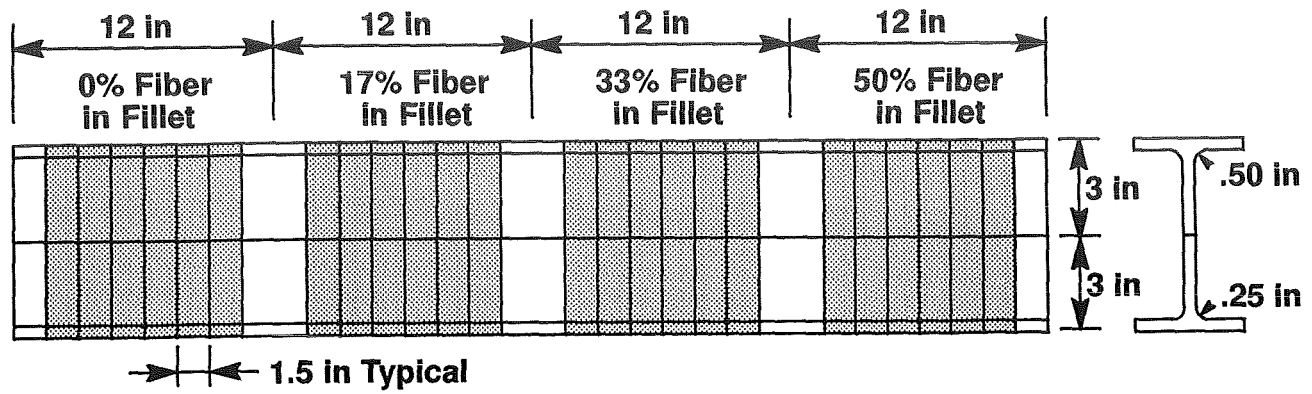


Figure 9. Fabricated I-beam from which T-specimens were taken.

Photographs of typical failed specimens are shown in Figures 10 and 11 for the 1/4-inch radius and the 1/2-inch radius specimens, respectively. In all cases, failure of the specimens initiated due to transverse cracking of the fillet material and/or delamination of the wrap plies from the fillet material. In some cases, delamination within the flange also occurred.

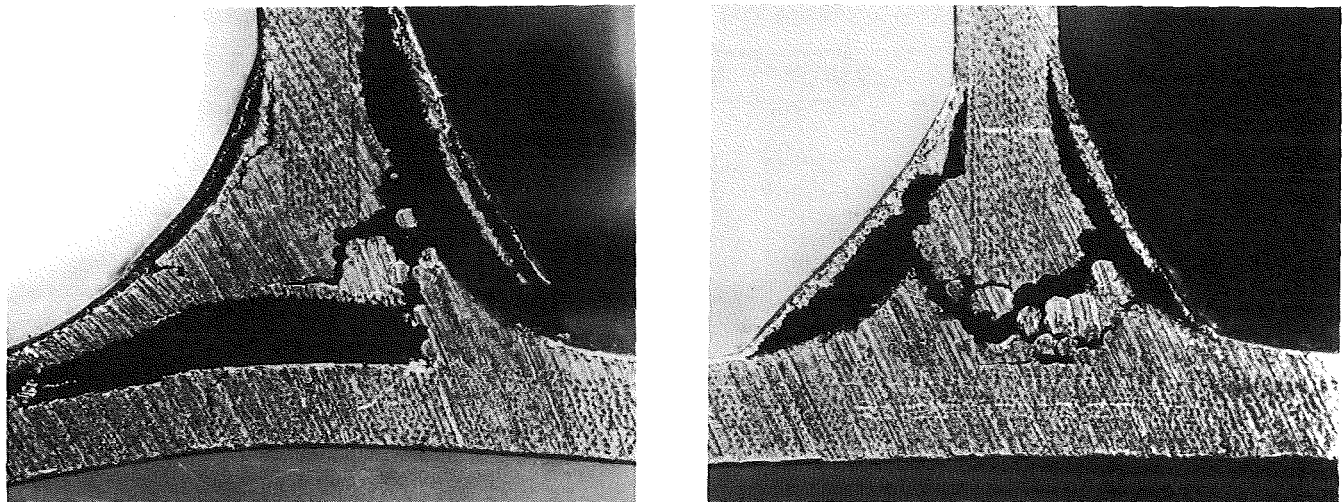


Figure 10. Intersection region of failed 1/4 inch radius specimens.

A summary of all experimentally obtained failure loads is presented in Figures 12 and 13. Consider first the results from the tests on the 1/4 inch radius specimens. Based on the average failure load of the three tests for each configuration, indicated by the dashed lines, there is some evidence that the 50 percent fiber-volume content material in the fillet produces a slightly higher failure load than the other fillet materials in both the simply supported case (Figure 12(a)) and the clamped edge case (Figure 13(a)). In addition, the test results for the 50 percent material are more consistent than with any of the others tested. It should be noted that the 50 percent, 1/4 inch radius configuration was used in the full-scale test article spars.

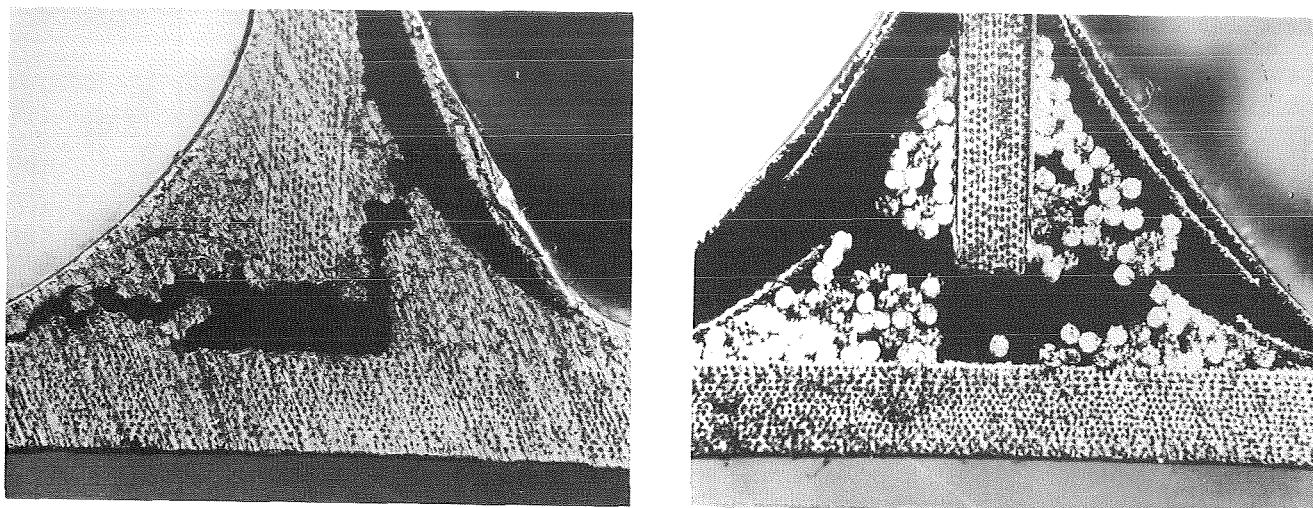


Figure 11. Intersection region of failed 1/2 inch radius specimens.

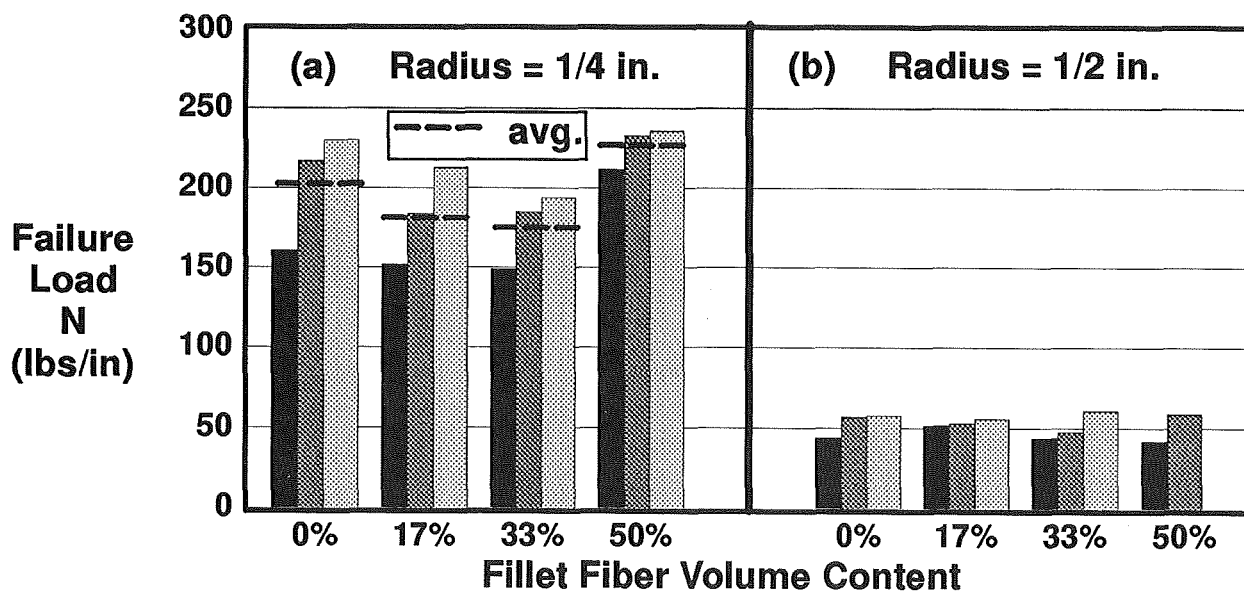


Figure 12. Test results for simply supported specimens.

Contrary to the analytical predictions to be discussed subsequently, the larger radius specimens all failed at much lower loads (see Figures 12(b) and 13(b)) than did the smaller radius specimens. Examination of the specimens prior to testing showed that the material in the critical intersection region of the 1/2 inch radius specimens was not well consolidated, making the results of these tests of questionable validity. This lack of consolidation is indicated in the post-failure photograph in Figure 11, where distinct bundles of MMC wires used to fill the fillet region can be seen. It should be noted that the hot molding process development was carried out for the 1/4 inch radius only.

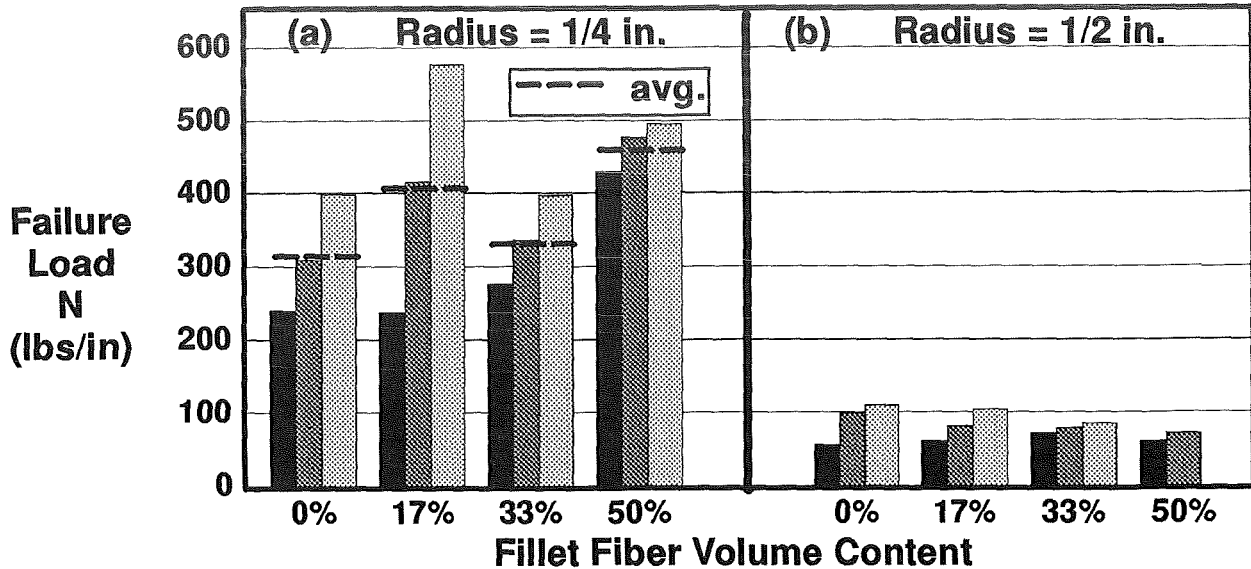


Figure 13. Test results for clamped edge specimens.

Comparison of the average failure loads in Figures 12 and 13 shows that the clamped specimens fail at loads that are 1.6 to 2.2 times higher than the failure loads of the simply supported specimens. This increase is consistent with an elementary beam analysis of the flange which shows a reduction in the maximum bending moment by a factor of 2.0 for the clamped case compared to the simply supported case.

Even though the test results for the 1/2 inch radius specimens are of little quantitative value due to the poor consolidation in the intersection region, they do point out the importance of fabrication quality in this critical region. Since the web and flange sublaminates were identically preconsolidated for the 1/4 inch and the 1/2 inch radius specimens, the low failure loads for the latter provide confirmation that the critical failure arises from the transverse tensile stresses in the 0-degree filler material in the intersection region. In these tests, no effect of fillet material fiber volume percentage is evident, as expected, since all these specimens were approximately equally flawed.

FINITE ELEMENT MODELING OF T-SPECIMENS

The purpose of the analytical investigation was to develop detailed finite element models of the T-section specimens described previously. These models allow the laminar and interlaminar stresses to be evaluated in the region of the web/flange intersection when loads creating local bending are applied. A generic model has been developed with the aim of easy variation of the geometric and material parameters so that the effects of such variations could be evaluated and an improved design developed. Specific models have been used to evaluate the local stress state in a typical test for geometries with two different fillet radii for two types of loading.

A model of a typical cross-sectional slice of the T-section is illustrated in Figure 14. Second-order, isoparametric, generalized plane-strain elements with a capability to represent fully

anisotropic material properties have been used. These elements allow most of the important laminar and interlaminar stresses to be evaluated. The wrapped plies in the critical fillet region are modeled appropriately as curved elements. The generalized plane-strain condition allows stresses perpendicular to the cross-section to be evaluated in conjunction with the laminar and interlaminar stresses in the plane of the model. Each lamina may be modeled through its thickness by one or more elements. The material properties associated with various fiber orientations of each layer in the model may be specified so that any laminate layup and stacking sequence may be considered. The number of plies in each of these laminates may be easily changed.

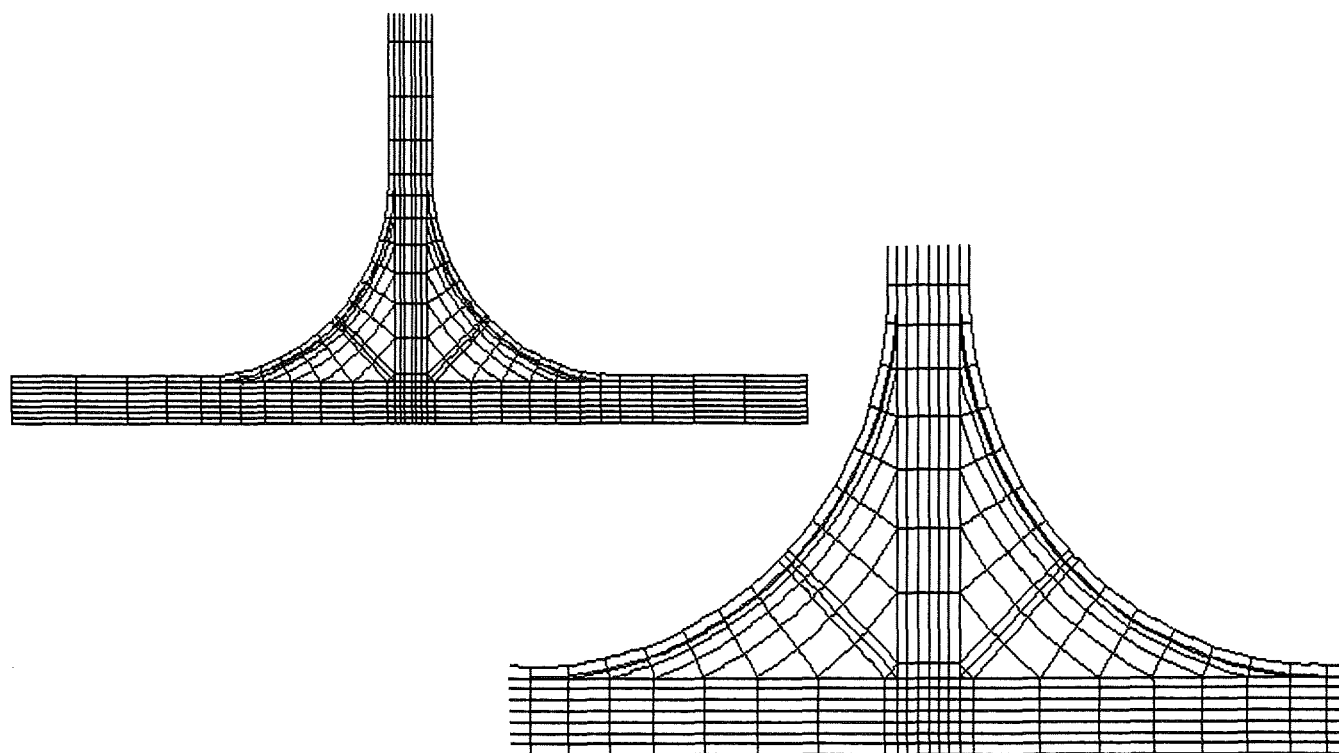


Figure 14. Finite element model mesh pattern for a typical isotropic T-specimen with a 1/2 inch fillet radius and a close-up view of the intersection region.

Boundary conditions may be defined to represent a variety of test configurations. In the results presented herein, the end of the web laminate is assumed to be fixed, and the ends of the left and right flanges are loaded by concentrated normal forces, either symmetrically or antisymmetrically about the web center-line. These conditions allow the stresses associated with flange and web bending to be developed. For these loading conditions, a half-model could be used to evaluate the response of the specimen with reduced computation time if the non-symmetry of the T-section laminates is neglected. This non-symmetry occurs in any T-shaped composite section if unidirectional materials oriented at an angle to the length of the section are used in the wrap plies. A designer may choose either to have both left and right flange laminates symmetric and the web laminate nonsymmetric, or to have the web and one flange symmetric with the remaining flange nonsymmetric. As more plies are used in the wrap and fewer in the web and flange base laminates, these effects should become more important. A full model that accounts for non-symmetry has been used to obtain the results reported herein.

It may be noted from Figure 14 that the lengths of elements in the plies may vary except in the region of the flange directly under the web. This gradation of element lengths allows smaller elements to be defined in the critical regions where the wrap plies become tangent to the web and flange. In addition, very thin and similarly short elements are used in the fillet radius region near the wrap plies. As will be shown in some sample results, these regions develop relatively large stresses both in the laminar directions and in the interlaminar directions. This result bears out the assumption that local flange bending may be a major contributor to the observed failure near the fillet radius region in the box tests and in the T-element tests.

ANALYSIS RESULTS FOR ISOTROPIC MODELS

As initial checks on the model, two models with isotropic properties were created. Analysis of the results for even these simple cases indicates to some extent the important effects of the fillet-radius region geometric parameters on the stresses in this region. For example, consider an aluminum T-section with the dimensions shown in Figure 8. These dimensions are representative of the MMC specimens tested as previously described. Concentrated loads are applied at the ends of the flanges. No restriction of rotation is imposed at the load locations. The distribution and relative magnitudes of the stresses are of primary interest. However, to put a scale on these results, vertical loads of 200 lbs/inch were applied at each flange end in the case of a symmetrically loaded model. With a 1/4 inch fillet radius, the resulting vertical deflection of the tips of the flanges is 0.036 inches and the maximum tensile principal stress found in the model is 78 ksi. The antisymmetric load case was chosen to create the same moment (based on centerline dimensions) on the web as was created on the flanges in the symmetric case. That is, equal and opposite vertical loads of 100 lbs/inch each were applied at the flange ends. The horizontal deflection of the flange is 0.091 inches, the vertical deflection of the tips of the flanges is 0.155 inches, and the maximum tensile principle stress is 104 ksi in this antisymmetric case. Typical deformed shapes, with the deformations magnified for clarity, are shown in Figure 15.

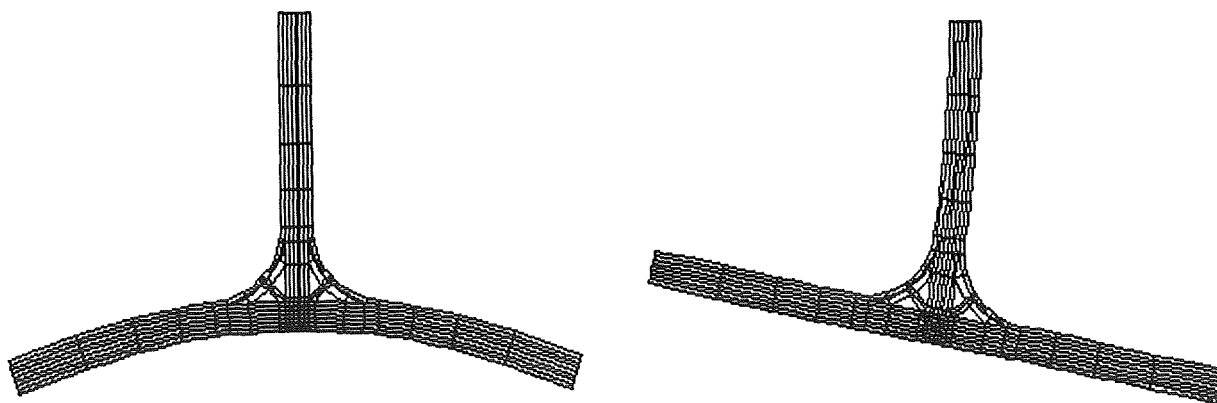


Figure 15. Symmetric and antisymmetric deformations of an isotropic T-specimen.

Symmetric Load Case

Contour plots of the normal stresses in the intersection region are shown in Figures 16 and 17 for the **global** horizontal direction (σ_{xx}) and the vertical direction (σ_{yy}), respectively. It should be noted that since the stresses shown are all in the global direction, they must be combined with the shear stresses and transformed to yield the zero surface normal and shear stresses present on the curved surface of the fillet. The tensile σ_{xx} stresses peak near the region where the fillet becomes tangent to the flange and are about 9 percent higher than the maximum compressive σ_{xx} stresses. Figure 17 indicates the presence of tensile stresses in the vertical direction that are distributed throughout the fillet region. However, rather than being reduced as they progress into the fillet, these stresses are somewhat larger than those in the web and extend into the region where the fillet becomes tangent to the flange. The presence of a sizable vertical compressive stress near the center of the fillet region is also of interest. Of course, if the direction of the bending loads is reversed, this compressive stress will become a tensile stress. The implications for a composite material are obvious even from this isotropic, homogeneous case. That is, since the vertical tensile stresses in the fillet and gap material take on values on the same order of magnitude as occur in the web laminate reinforced with fibers in the vertical direction, failure may be expected to occur in these regions that are unreinforced in the vertical direction due to the combination of vertical tensile stresses and other stresses. The normal stresses (σ_{zz}) perpendicular to the plane of the model are not shown since they are proportional to the inplane stresses for this homogeneous material in a state of generalized plane strain.

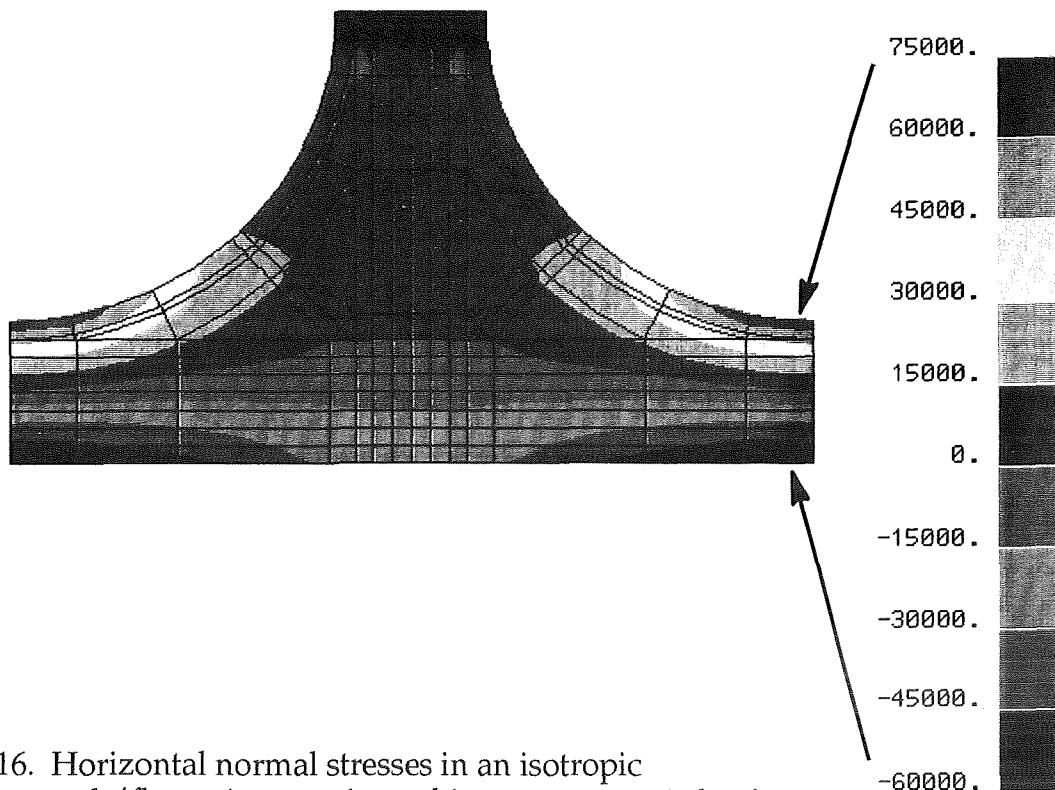


Figure 16. Horizontal normal stresses in an isotropic web/flange intersection subject to symmetric loading.

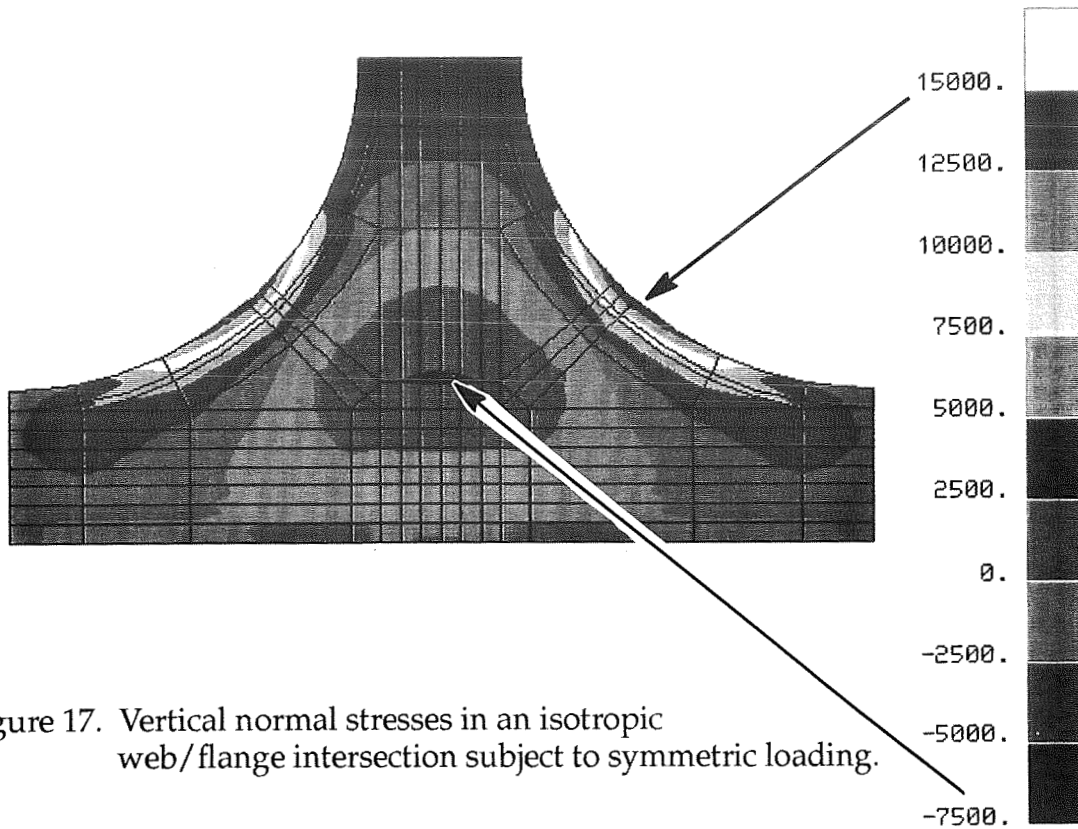


Figure 17. Vertical normal stresses in an isotropic web/flange intersection subject to symmetric loading.

Contour plots for the intersection region shear stresses (τ_{xy}) in the plane of the model are presented in Figure 18. The shear stresses show a tendency to peak near the fillet region. Again, the implication for composite materials subjected to a combination of inplane and transverse tensile stresses and transverse shear stresses is clear since this combined state of stress can lead to failure in the laminated materials.

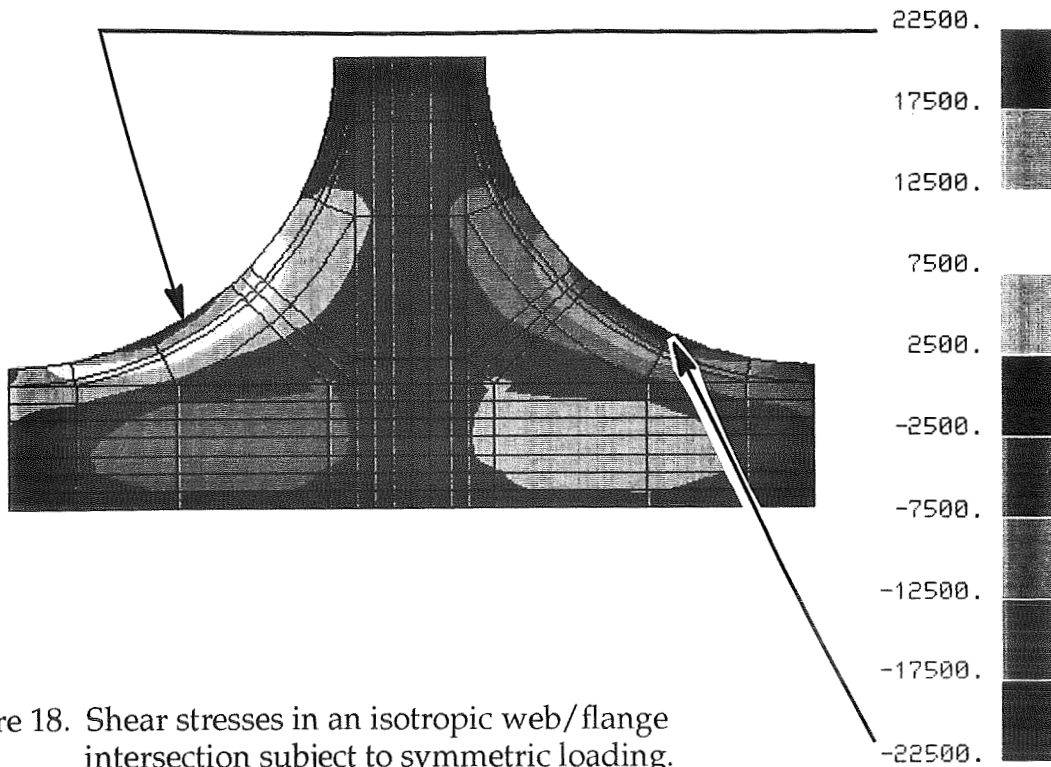


Figure 18. Shear stresses in an isotropic web/flange intersection subject to symmetric loading.

Similar results were obtained for a second model with a 1/2 inch fillet radius. A finer mesh was used in the fillet region in this case since considerably more material is now present in this region. The loads on the ends of the flanges were the same as in the first model, reducing the moment at the tangent point of the larger fillet by 33 percent. The maximum σ_{xx} (horizontal) and σ_{zz} (out-of-plane) stresses were predictably reduced by this same factor compared to the first model. The σ_{yy} (vertical) stresses and the τ_{xy} (shear) stresses were reduced by 50 and 45 percent, respectively, when compared to the smaller radius configuration. This shows the added stress reduction in the intersection region that is due to the smoother geometric transition from the flange to the web that exists with the larger fillet radius. It should be noted, however, that the deflection of the flange ends for the 1/2 inch fillet radius section model is approximately half that of the 1/4 inch fillet radius section. Therefore, if the end loads were actually generated from a given imposed deflection of the flange ends, as would be the case in an assembly of misaligned parts, the bending moment and therefore the stresses would actually be higher for the larger radius section than for its smaller radius counterpart which is considerably more flexible.

Antisymmetric Load Case

Results for this loading condition on the intersection region stresses in the model with a 1/4 inch fillet radius are shown in Figures 19 through 21 where these figures are the direct counterparts of the three figures discussed in the previous section. Most of the general trends regarding the type and distribution of stresses are the same for both types of loading conditions. However, while the results for the symmetric load case indicate that the critical location is near the fillet/flange intersection, the critical location changes to the fillet/web intersection region when the loading becomes antisymmetric about the web centerline. The other notable exceptions are that the shear stresses are only reduced by 23 percent and the vertical stresses in the web are unchanged in the antisymmetrically loaded 1/2 inch fillet radius section compared to the 1/4 inch configuration.

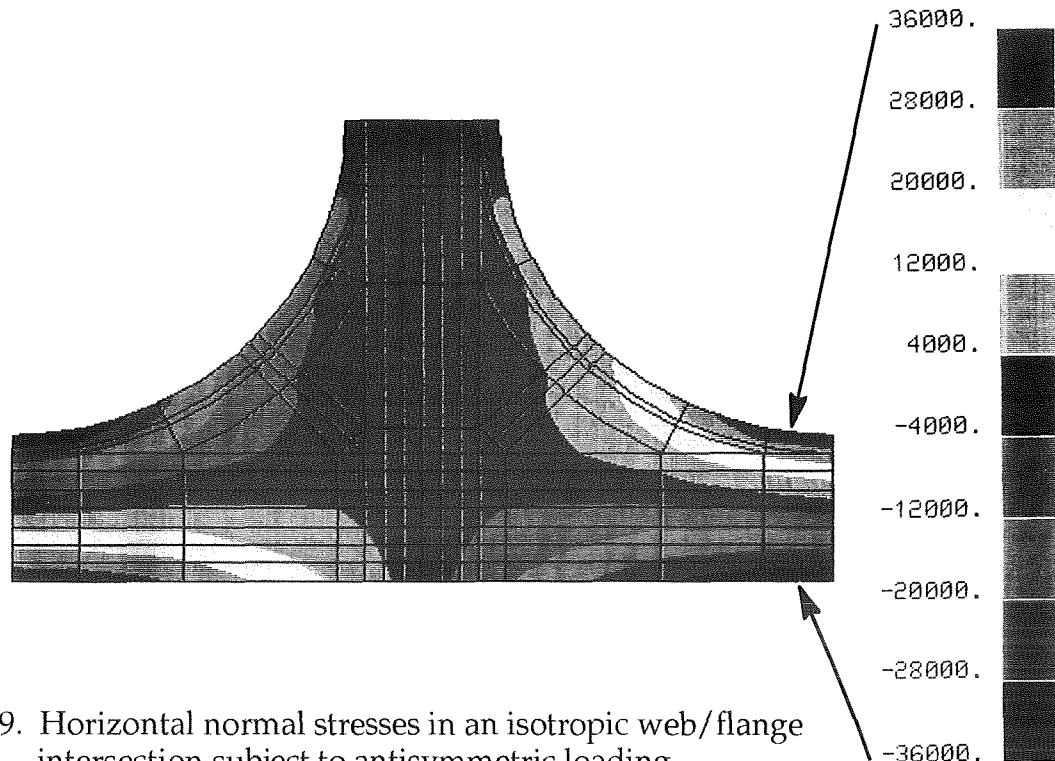


Figure 19. Horizontal normal stresses in an isotropic web/flange intersection subject to antisymmetric loading.

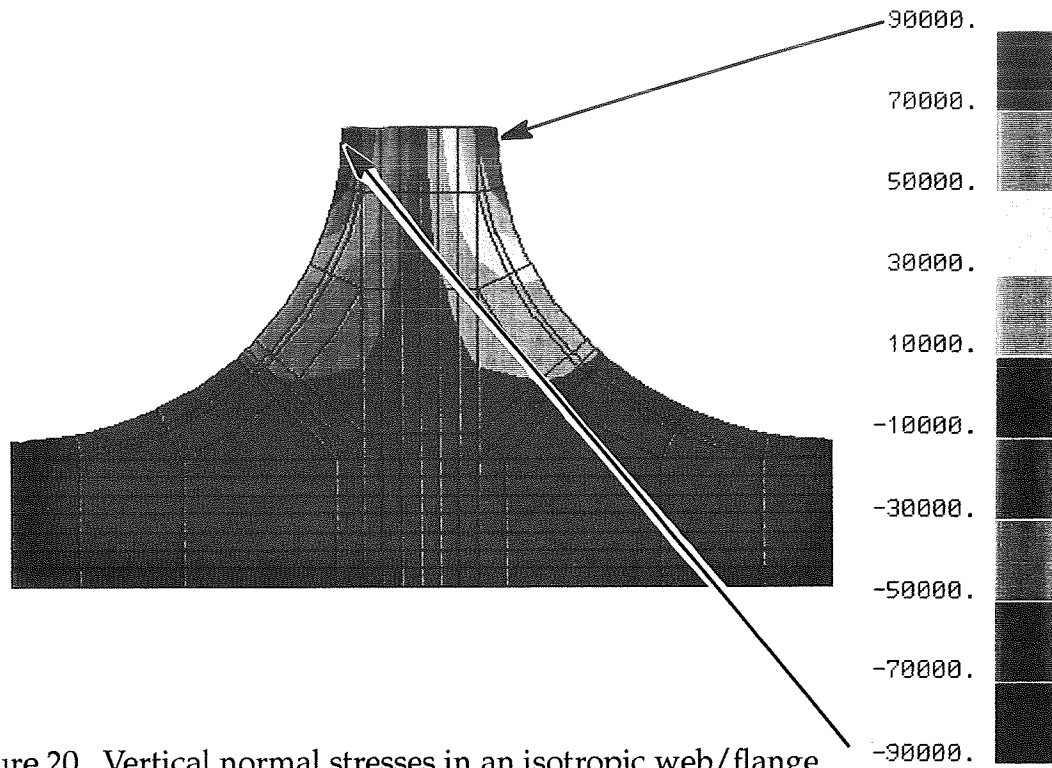


Figure 20. Vertical normal stresses in an isotropic web/flange intersection subject to antisymmetric loading.

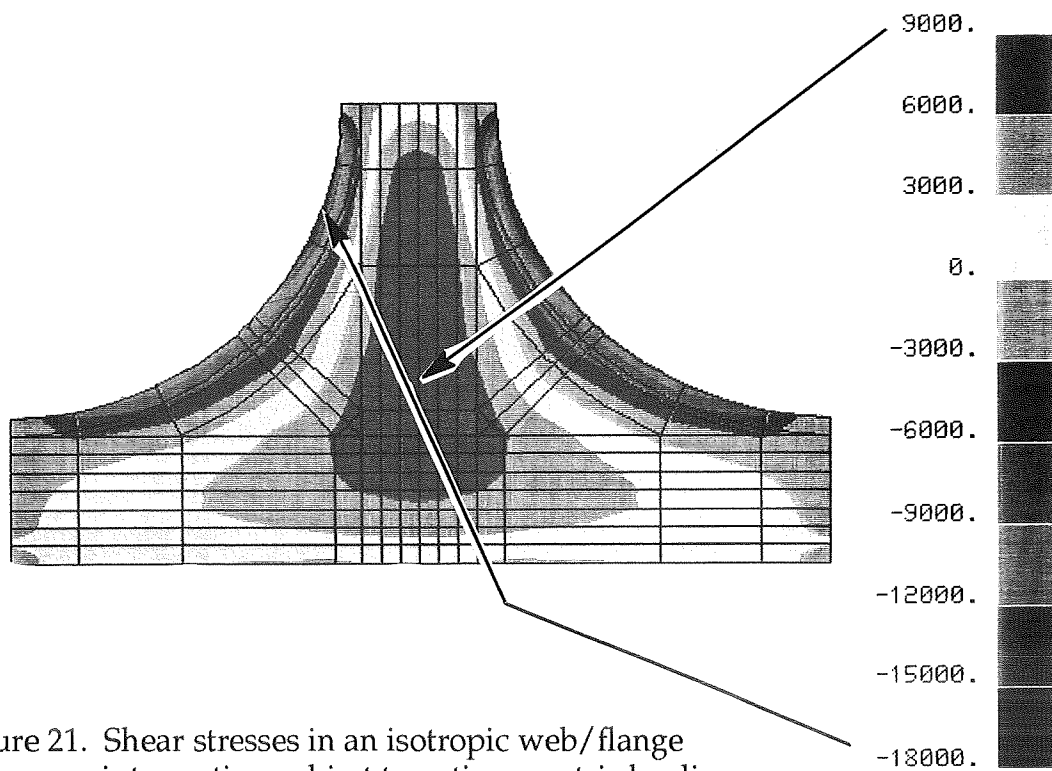


Figure 21. Shear stresses in an isotropic web/flange intersection subject to antisymmetric loading.

ANALYSIS RESULTS FOR METAL MATRIX MODELS

Models were also created for two T-shaped SiCf/Al sections representative of the specimens tested as discussed earlier. The level of detail, as shown by the 1/4 inch radius model in Figure 22, is greater than in the isotropic models. Here each ply was modeled by a separate second order element in the thickness direction. Three-dimensional anisotropic stiffness coefficients were computed for plies with 0, 90, +45, and -45 degree orientations. The following uni-directional lamina properties were used for this purpose:

$$\begin{array}{lll} E_{11}/E_{22} = 4.5 & E_{33}/E_{22} = 1.0 & E_{22} = 41.37 \text{ GPa. (6.0Msi.)} \\ G_{12}/E_{22} = 0.646 & G_{23}/E_{22} = 0.397 & G_{13}/E_{22} = 0.646 \\ \nu_{12} = 0.26 & \nu_{13} = 0.26 & \nu_{23} = 0.26 \end{array}$$

The web and flange stacking sequences are the same as used in the fabricated sections. The gap between the preconsolidated portion of the web and flange laminates is assumed to be filled with the same 0-degree material as used in the fillet and for the results to be presented the gap is assumed to be 0.02 inches in the vertical direction. The 0-degree fiber direction is perpendicular to the plane of the model.

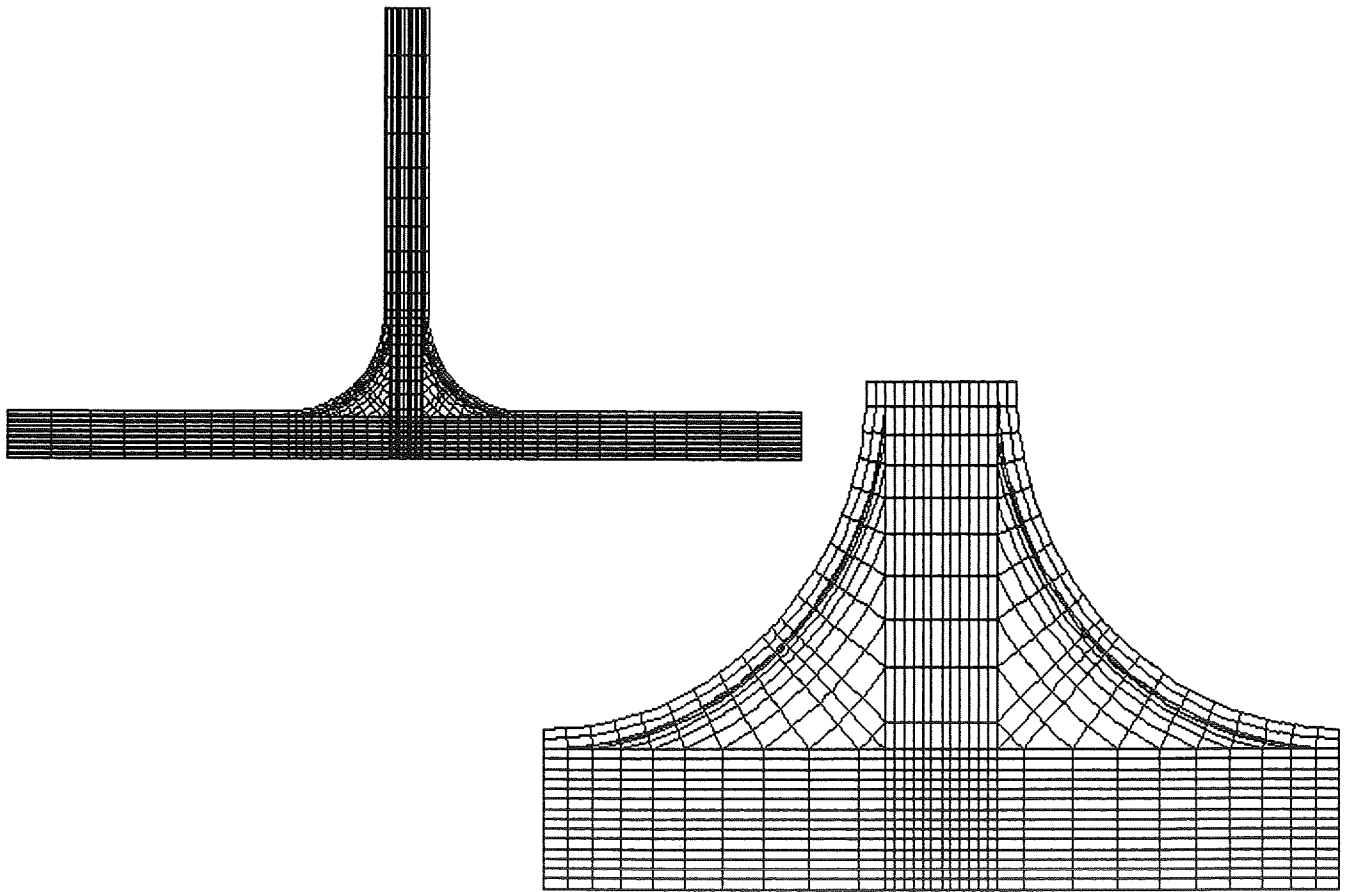


Figure 22. Finite element model mesh pattern for a typical MMC T-specimen with a 1/4 inch fillet radius and a close-up view of the intersection region.

Stresses were computed using a 1–2–3 coordinate system in which the 1–direction is along the width of the flange and the height of the web, and is circumferential in the “fillet wrap” plies and the fillet material. The 2–direction is in the ply–thickness direction for the flange, web and wrap plies and is in the radial direction for the fillet material. The 3–direction is normal to the plane of the cross–section. The material in the “gap” is assigned the same coordinate directions as the web. Therefore, the σ_{11} stresses are in the fiber direction for 90–degree plies and in the inplane transverse direction for the 0–degree plies. They are in the circumferential transverse direction for the fillet and in the vertical transverse direction for the gap material. The σ_{22} stresses are interlaminar for the web, flange, and wrap plies. They are in the radial transverse direction for the fillet material and in the horizontal transverse direction for the gap material. The τ_{12} stresses are interlaminar or transverse shear stresses in all parts of the model. The σ_{33} stresses are in the fiber direction for 0–degree plies and the material in the fillet and gap. They are in the inplane transverse direction for 90–degree plies. Fiber–direction stresses for the 45–degree plies are not reported but may be obtained by transformation of the 1–2–3 direction stresses.

Symmetric Load Case

The same load magnitudes and direction and support conditions used for the isotropic models were used in the MMC study. The maximum deflections of the loaded ends of the flanges are 0.0408 inch and 0.0221 inch for the small and large radius sections, respectively. These deflections are slightly greater than those obtained for the isotropic models since the flange bending stiffness is largely governed by the E_{22} value of the 0–degree plies that dominate the flange laminate.

Results for the 1/4 inch fillet radius configuration – Contour plots of the stresses in the full symmetrically loaded model are shown in Figures 23 (a) through 25 (a) for the 1/4 inch fillet radius configuration. Detail plots of the intersection region comprised by the fillet material and the portion of the wrap plies in this region are shown as part (b) of each figure. Recall that for these latter plots the 1–direction is circumferential and the 2–direction is radial. Some of the contour plots show small local perturbations in the stresses from element to element that are clearly a result the attempt of the contour algorithm to show detail when in reality the stresses should vary more smoothly. The primary utility of the contour plots is to show the stress gradients and locations of maximum values. A summary of the largest values of the stresses will be given later in this section.

Figure 23 (a) indicates that the largest laminar stresses occur as expected in the wrap plies where the fillet becomes tangent to the flange. It may also be noticed that the base of the web and the “gap” is in compression in the vertical direction. Most importantly, large circumferential normal stresses also occur in the fillet material adjacent to the wrap plies as can be seen in Figure 23 (b). After examination of all the stresses, it will be seen that this stress dominates the predicted failure.

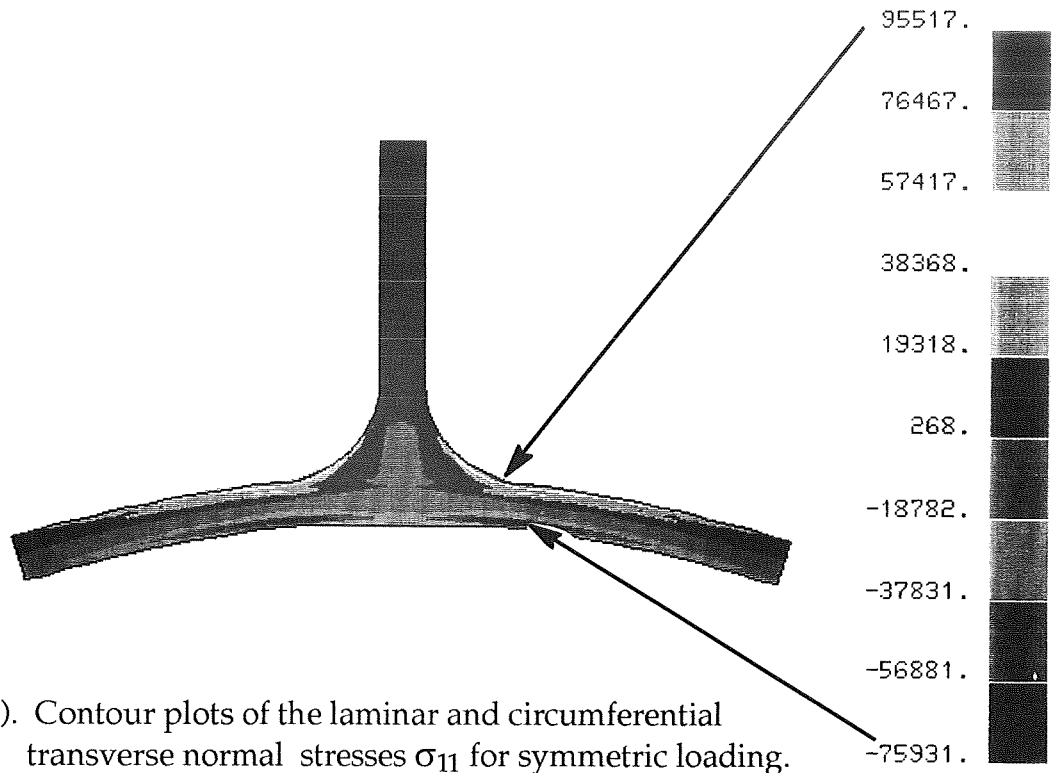


Figure 23 (a). Contour plots of the laminar and circumferential transverse normal stresses σ_{11} for symmetric loading.

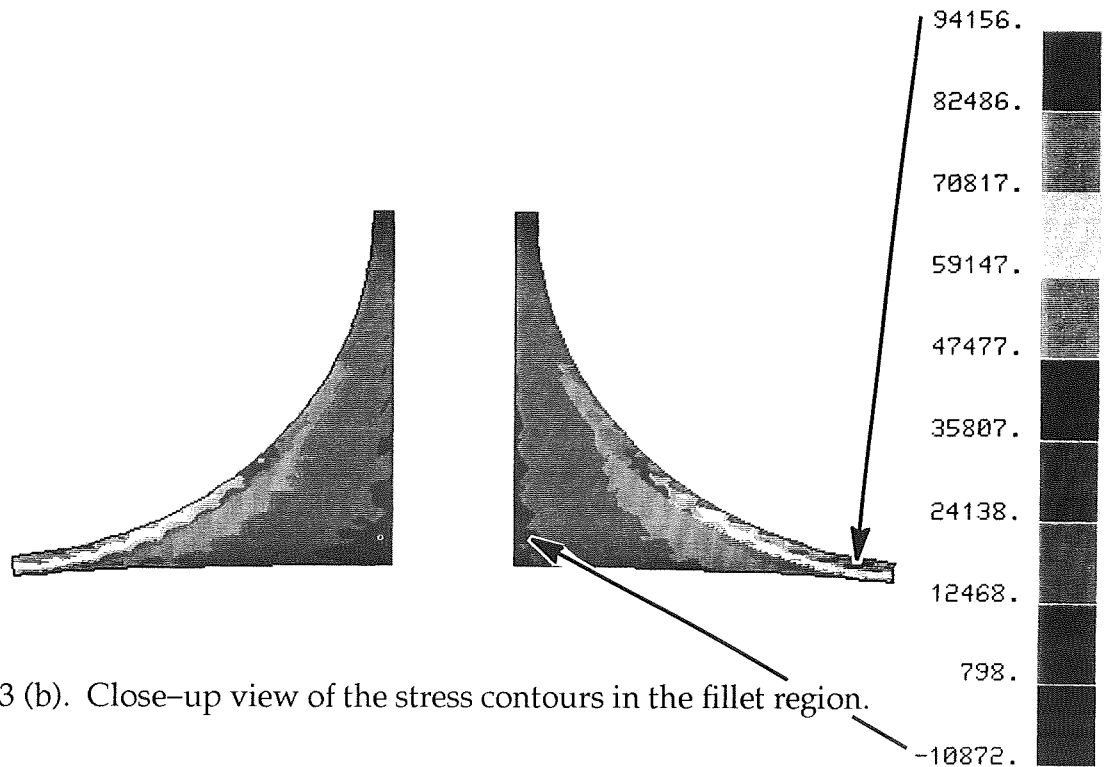


Figure 23 (b). Close-up view of the stress contours in the fillet region.

The interlaminar and radial normal stress contours are presented in Figure 24. As in the isotropic analyses, significant tensile stresses occur in the fillet and extend into the flange near the tangent point. Large tensile stresses also exist in the portion of the web that extends into the fillet. Large compressive stresses are present in the flange at the base of web near the "gap".

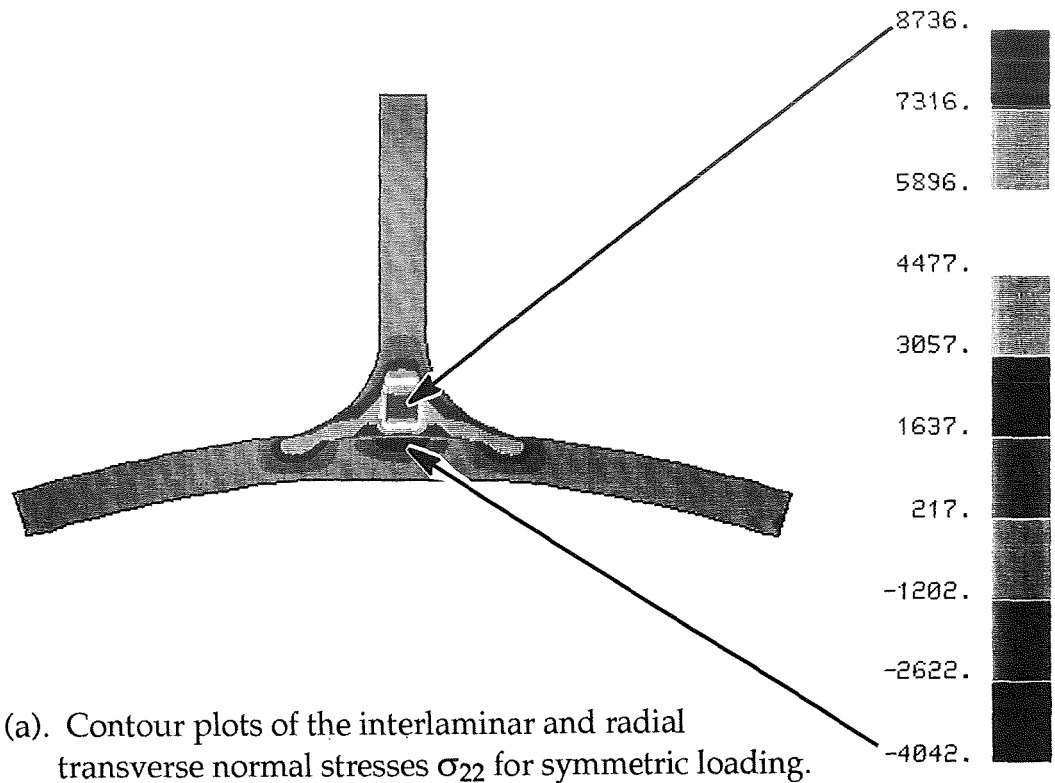


Figure 24 (a). Contour plots of the interlaminar and radial transverse normal stresses σ_{22} for symmetric loading.

The stress contours in the fillet region, shown in part (b), indicate that the radial tensile stresses are greatest where the fillet meets the web and are also large near the critical fillet-to-flange tangent point. The effect of the nonsymmetry of the part can be seen in the fillet region details of this symmetrically loaded model.

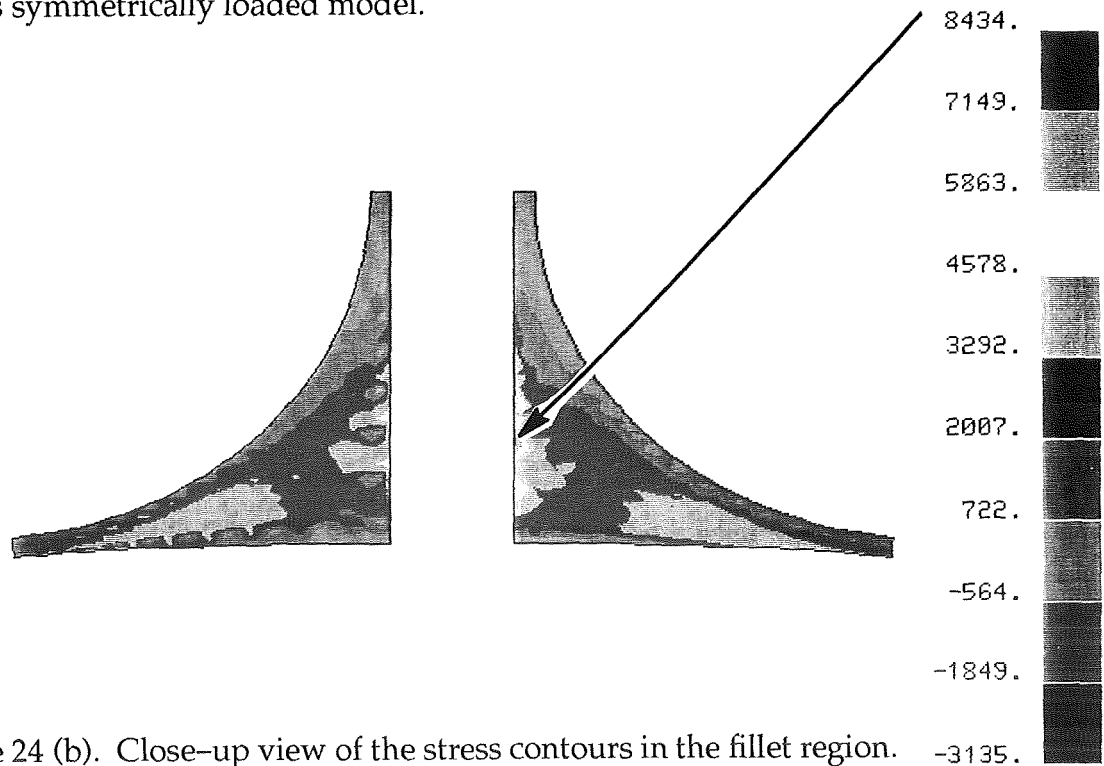


Figure 24 (b). Close-up view of the stress contours in the fillet region.

Figure 25 depicts the interlaminar and transverse shear stress distribution. Peak stresses occur in the center of the fillet and in the center of the flange directly under the fillet. Part (b) shows that sizable shear stresses extend throughout the fillet to the interface of the fillet with the wrap, web, and flange plies. However, unlike the normal stresses, the fillet/flange tangent point is not the location for the peak shear stresses.

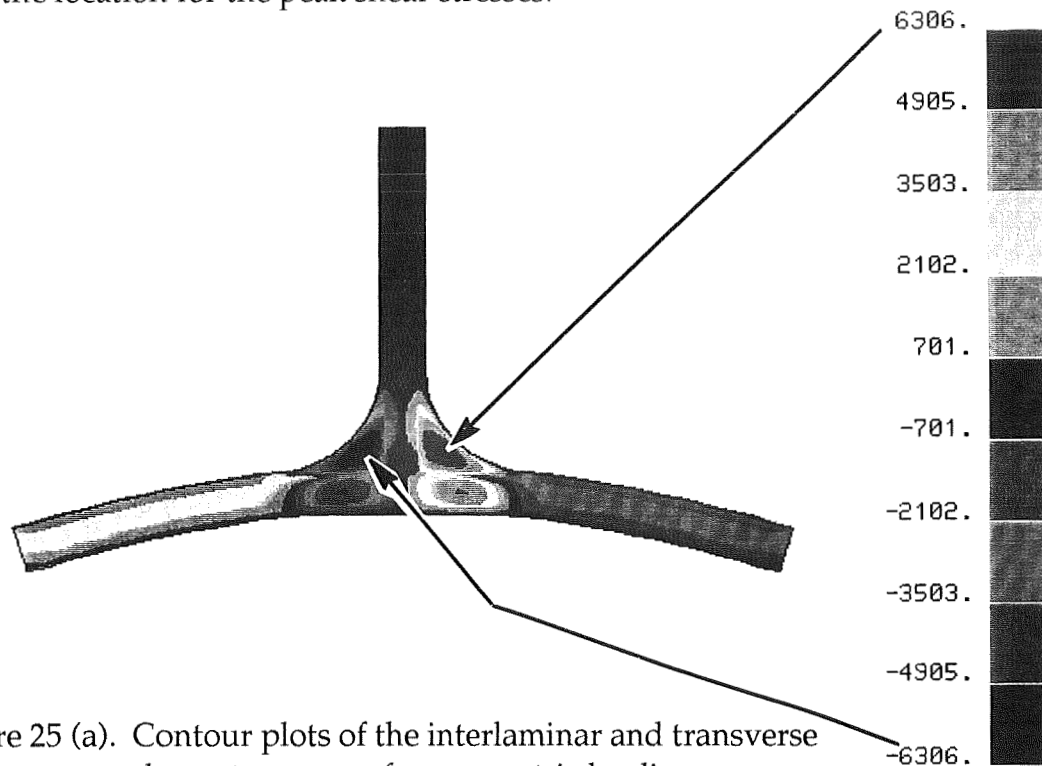


Figure 25 (a). Contour plots of the interlaminar and transverse shear stresses τ_{12} for symmetric loading.

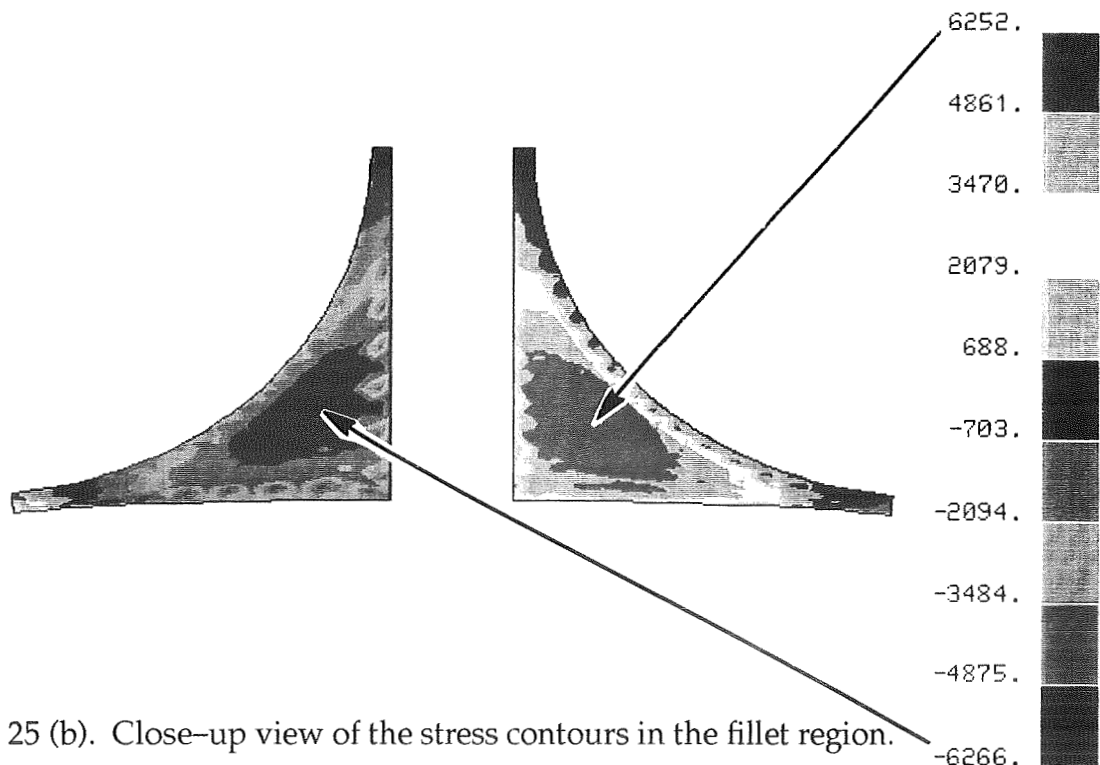


Figure 25 (b). Close-up view of the stress contours in the fillet region.

A summary of the largest positive and negative stresses σ_{11} , σ_{22} , and τ_{12} developed in various regions of the model is presented in the following figures. The abbreviations **Gp**, **Fil**, and **Wrp** stand for the gap, fillet, and fillet wrap material, respectively. **Fig.** and **Web** refer respectively to the complete flange and web laminates including the continuations of the "fillet wrap" plies. Again, the relative values of the stresses are of primary concern when evaluating these results.

The largest laminar and circumferential transverse normal stresses, shown in Figure 26, indicate that the stiff ± 45 -degree plies in the wrap and flange carry the bulk of the bending load. However the tensile stresses perpendicular to the 0-degree material in the fillet and the flange are also very high. Using a maximum stress failure criterion and ultimate stresses of 200 ksi in the fiber direction and 15 ksi transverse to the fiber direction, the fillet material would be the critical part of the specimen. If the sense of the bending were reversed, the tensile stresses in the 0-degree direction in the flange would become the critical stresses.

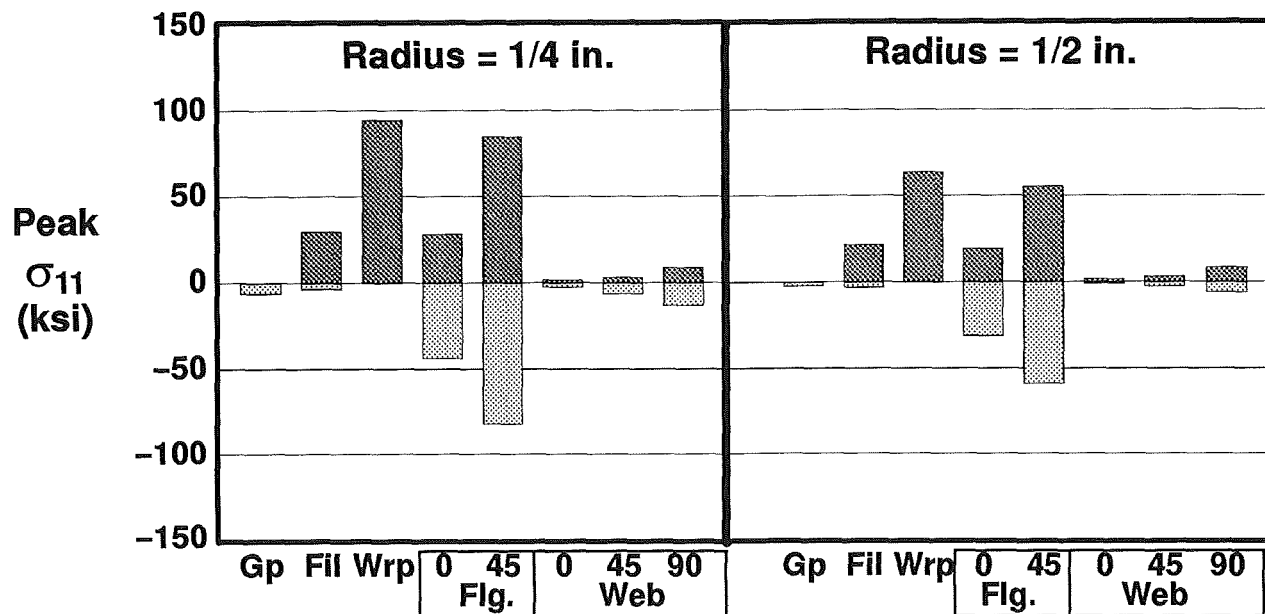


Figure 26. Peak laminar and circumferential transverse normal stresses for symmetric loading.

The largest interlaminar normal stresses are plotted in Figure 27. As seen from the contour plot, the portion of the web that extends into the fillet carries the highest interlaminar tensile stresses. However, these stresses are not nearly as severe compared to the 15 ksi ultimate transverse stress as are the circumferential transverse normal stresses in the fillet material (Figure 26) and would not govern part failure.

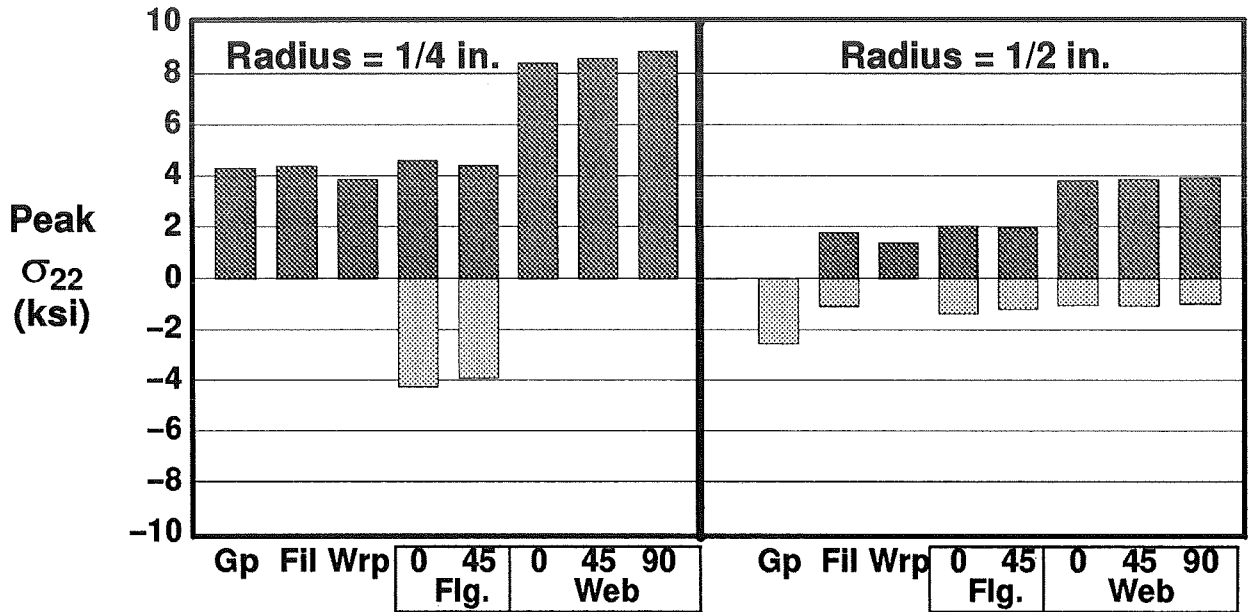


Figure 27. Peak interlaminar and radial normal stresses for symmetric loading.

The largest interlaminar and transverse shear stresses are shown in Figure 28. The largest shear stress occurs within the fillet material, but based on an ultimate stress of 15 ksi and a maximum stress criterion, it would not govern part failure.

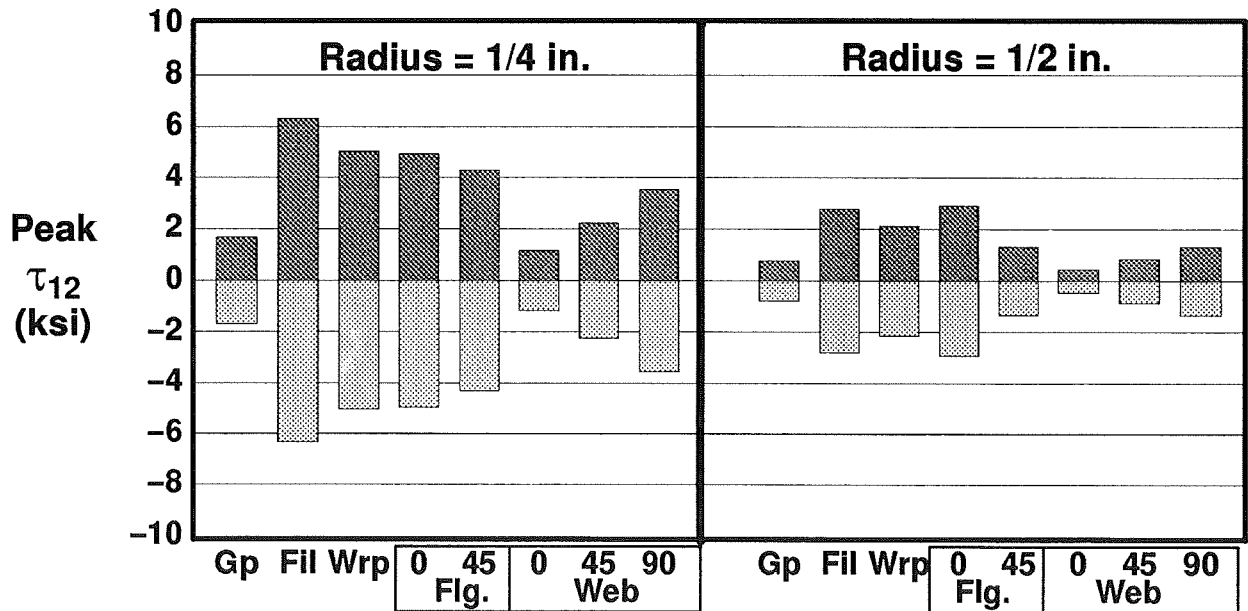


Figure 28. Peak interlaminar and transverse shear stresses for symmetric loading.

Since the total load applied to the model is 400 lbs/in, a maximum stress criterion predicts initial part failure at 200 lbs/in due to the transverse normal tensile stress in the fillet mate-

rial near the fillet/flange tangent point. A combined stress failure criterion, such as the one given in Reference 1, also predicts failure initiation near the same tangent point in the fillet material at almost the same load due to the dominance of the σ_{11} stress. The average test load for this configuration was 227 lbs/in. as shown in Figure 12. The corresponding average test load (Figure 13) for clamped edge specimens is 468 lbs/in., while the predicted load is 420 lbs/in.

Results for the 1/2 inch radius configuration – Contour plots of the stresses were also examined for the larger radius configuration. These plots are not included here since they are of the same character and since the locations of the peak stress points are unchanged from those found in the previous configuration. However, the magnitudes of these peak stresses are in most instances considerably lower than their counterparts in the smaller radius section.

A summary of stresses for the larger radius configuration is given in the second half of Figures 26–28. Comparison with their counterparts in the first half of these figures shows that the laminar stresses are reduced by approximately the same factor (33 percent) as is the applied moment (refer to the isotropic model discussion). The interlaminar normal stresses σ_{22} and the interlaminar shear stresses τ_{12} , however, are reduced by at least 41 percent, and generally by over 55 percent, for the flange, web, and wrap plies. The fillet material is exceptional in that the maximum circumferential transverse tensile stress is reduced by only 27 percent. This indicates that increasing the fillet radius is effective in reducing the interlaminar stresses in the layered material but is relatively ineffective in reducing the critical normal stresses in the fillet material. Since it is this stress and this part of the intersection region which dominates failure initiation, it would be necessary to explore other design variations, such as increasing the number of wrap plies or changing their fiber orientations in order to significantly and efficiently increase the load carrying capacity of the part. It may also be possible to improve the state of stress in the fillet by modifying the extent to which the web laminate extends into the fillet region. Changing the fillet material to one with a higher transverse strength to stiffness ratio could also be effective.

Antisymmetric Load Case

This loading condition was also chosen to be the same as used for the isotropic models, that is, 100 lbs/in vertical forces applied at the flange ends, antisymmetrically with respect to the web. The maximum horizontal deflections of the loaded ends of the flanges are 0.0668 inches and 0.0587 inches for the small and large radius sections, respectively. The maximum vertical deflections are 0.1219 inches and 0.0895 inches, respectively. These deflections are slightly lower than those obtained for the isotropic models since the web bending stiffness is largely governed by the stiff 90-degree plies near the outer surface of the web.

Results for the 1/4 inch fillet radius configuration – Contour plots of the stresses in the antisymmetrically loaded model are shown in Figures 29 through 31 for the 1/4 inch fillet radius configuration. Only the plots for the entire model are included since close-up views are not needed for clarification in these cases.

Figure 29 indicates the presence of large laminar tensile stresses in the web. The location of the 90-degree plies are clearly visible adjacent to the outermost plies (± 45 degrees) in the web. Again large circumferential transverse normal stresses exist in the fillet material, however in this case the peak stresses occur near the fillet/web tangent point rather than near the fillet/flange tangent point.

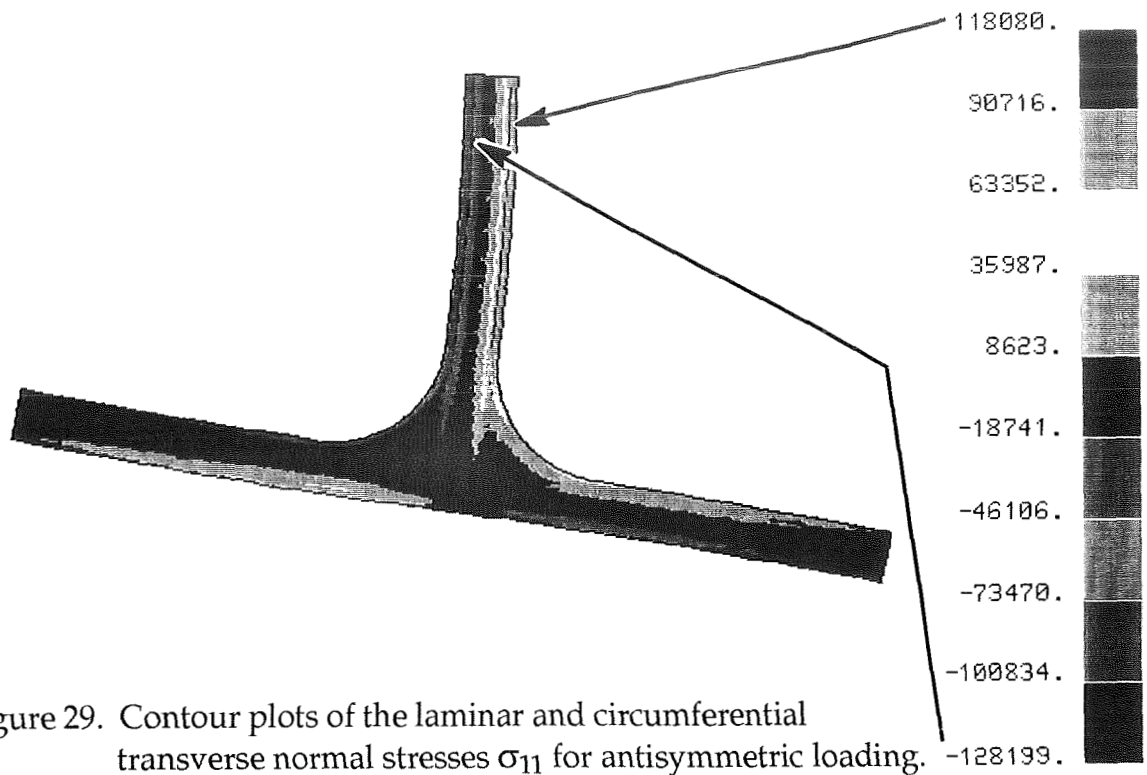


Figure 29. Contour plots of the laminar and circumferential transverse normal stresses σ_{11} for antisymmetric loading.

The interlaminar and radial transverse normal stress contours presented in Figure 30 show the largest values at the web/flange junction inside the fillet near the gap. Significant interlaminar stresses also exist near both fillet tangent points.

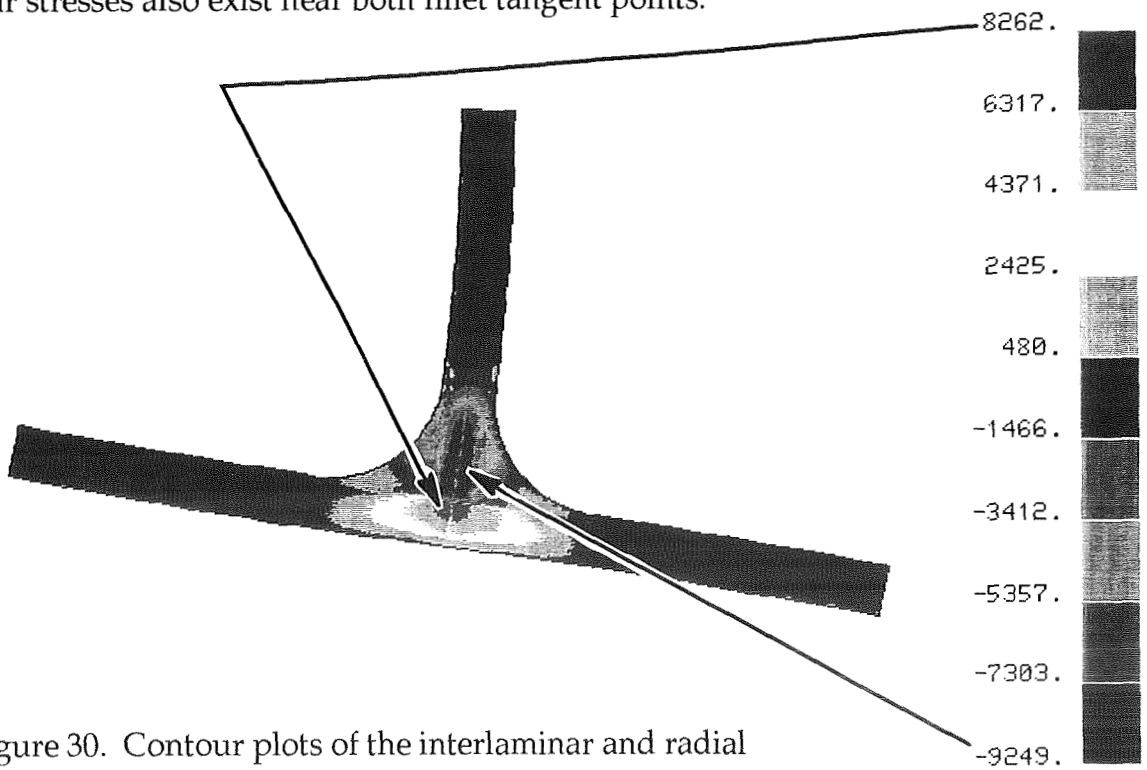


Figure 30. Contour plots of the interlaminar and radial transverse normal stresses σ_{22} for antisymmetric loading.

The largest interlaminar and transverse shear stresses occur in the portions of the web and flange inside the intersection region near the gap as shown in Figure 31. The gap material also experiences high shear stresses.

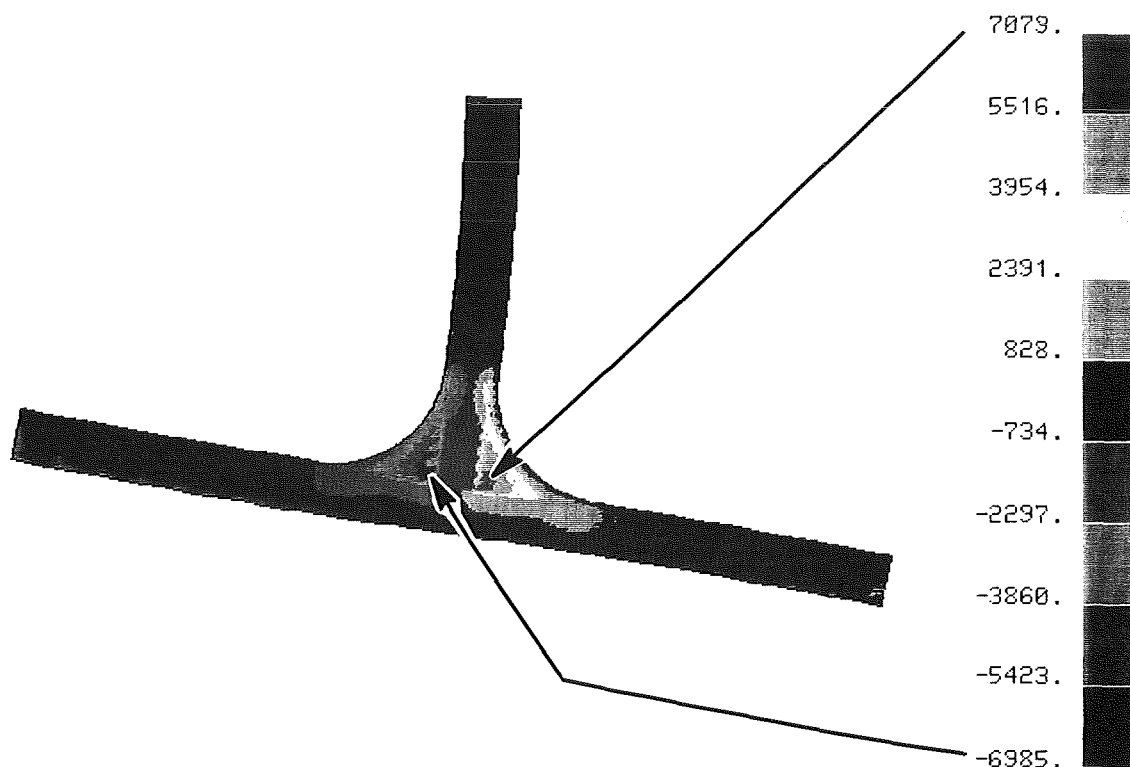


Figure 31. Contour plots of the interlaminar and transverse shear stresses τ_{12} for antisymmetric loading.

It can be seen from these figures that the conclusions drawn for the symmetric case generally apply for this case. The main exception is the location of the critical stresses. The antisymmetric loading forces this critical location to the region where the fillet becomes tangent to the web. The full-scale spar shown earlier in Figure 6 failed at this location indicating that a major anti-symmetric loading component was present. Since all actual loading conditions are a combination of symmetric and antisymmetric components, the fillet material near the tangent points to the web and/or flange is predicted to be the portion of the structure that will govern failure initiation.

A summary of the largest positive and negative stresses σ_{11} , σ_{22} , and τ_{12} developed in various regions of the model is presented in Figures 32–34. The peak circumferential normal stress in the fillet material is nearly identical to that in the symmetrically loaded case, the difference being in its location near the web/fillet tangent point. The normal stresses in the web are predictably higher than in the symmetrically loaded case.

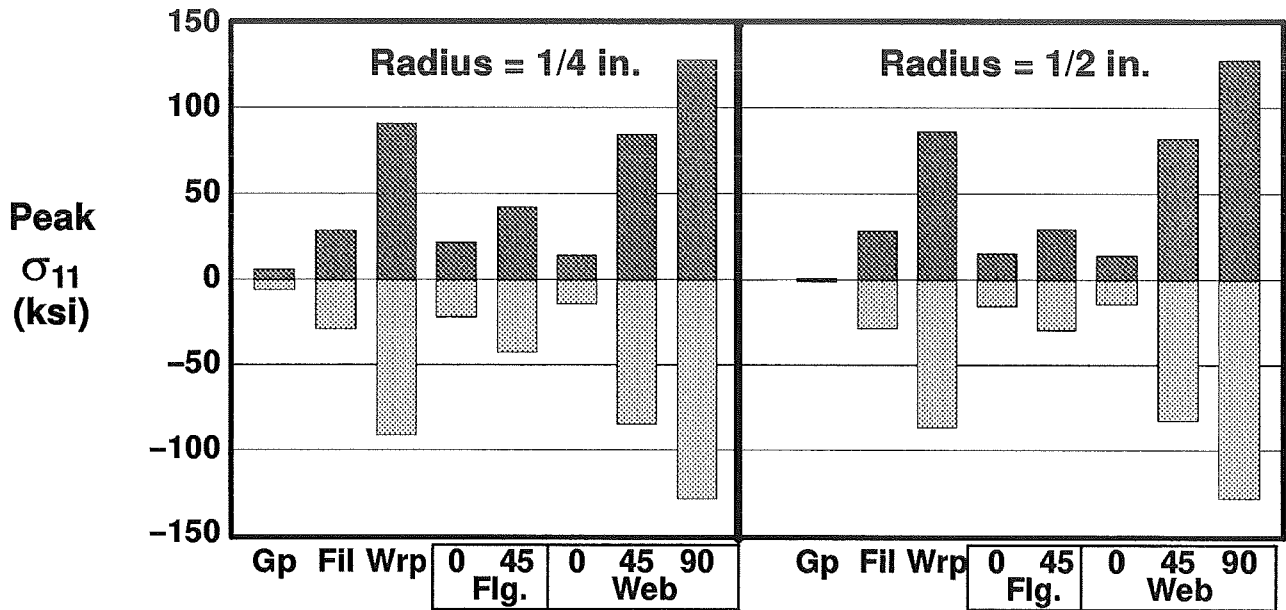


Figure 32. Peak laminar and circumferential transverse normal stresses for antisymmetric loading.

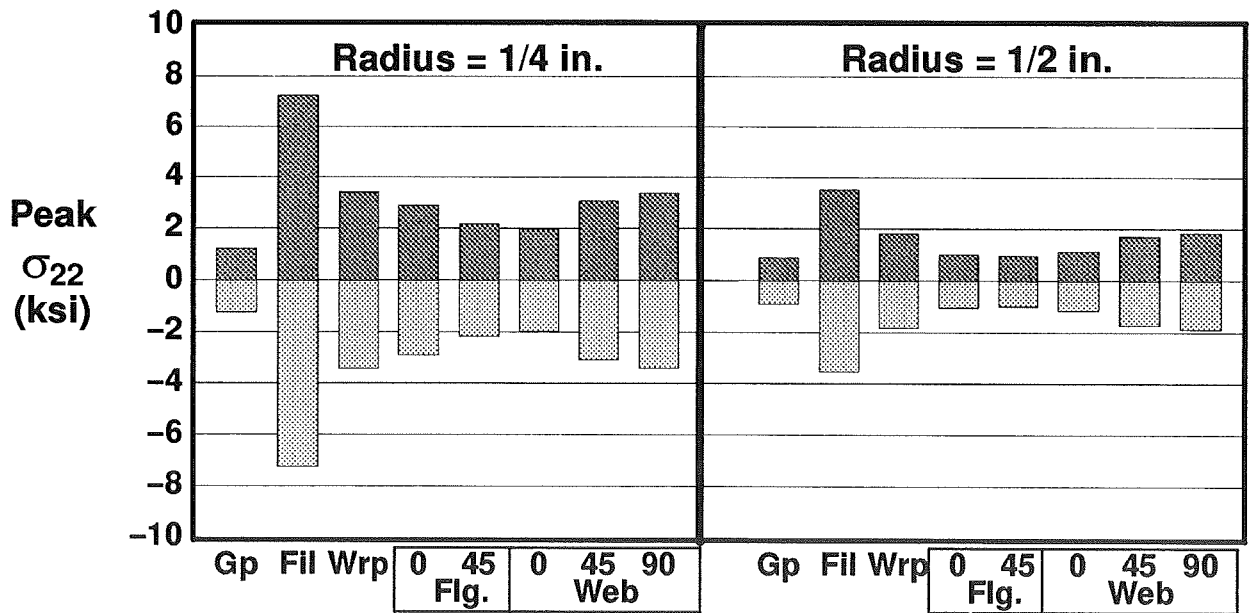


Figure 33. Peak interlaminar and radial normal stresses for antisymmetric loading.

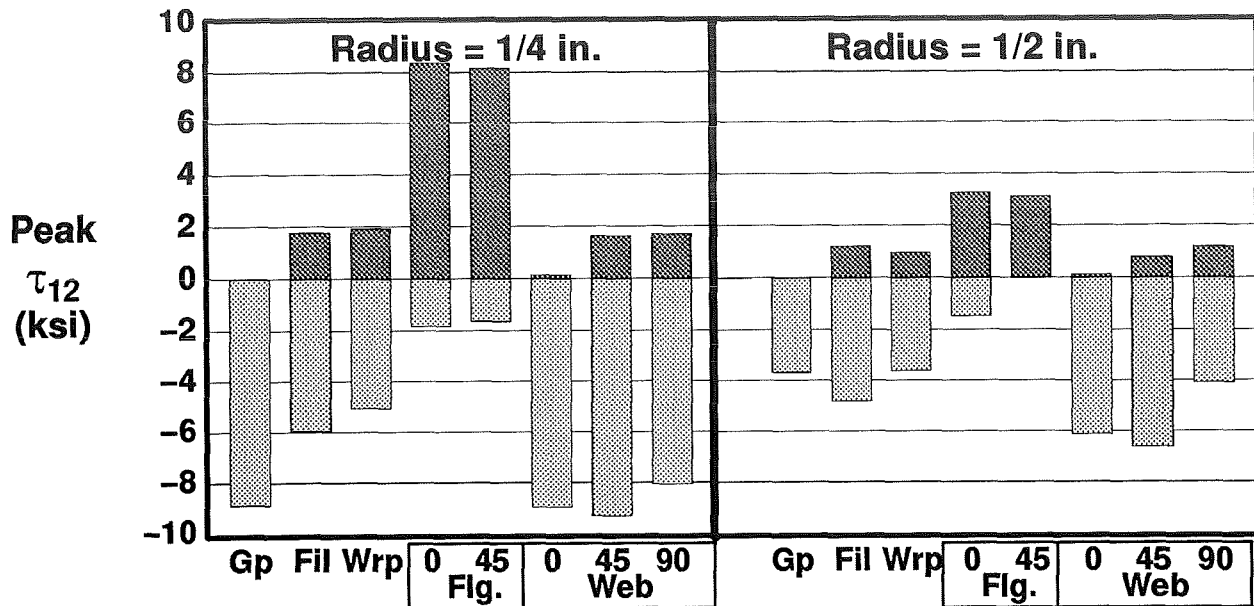


Figure 34. Peak interlaminar and radial shear stresses for antisymmetric loading.

Results for the 1/2 inch radius configuration – Contour plots of the stresses were also examined for the larger radius configuration. These plots are not shown here since they are of the same character and since the locations of the peak stress points are unchanged from those found in the smaller radius configuration. However, the effect of increasing the radius on the magnitudes of the stresses is different for the antisymmetric and symmetric loading cases.

A summary of magnitudes of the stresses for the larger fillet radius configuration is given in the second half of Figures 32–34. Comparison with their counterparts in the first half of the figure shows that the laminar stresses in the flange are reduced due to the reduced moment applied to the flange. However, the laminar stresses in the web are essentially unchanged when the fillet radius is increased. In addition, while the interlaminar normal stresses σ_{22} and the interlaminar shear stresses τ_{12} for the flange, web, and fillet wrap plies are reduced by 29 to 61 percent, the large circumferential transverse tensile stress in the fillet material is **unaffected** by the increase in fillet radius. Since this stress will dominate failure initiation, increasing the fillet radius is not effective at all in increasing the antisymmetric failure load. It is this fact that led to testing only symmetrically loaded T-specimens in the experimental program discussed earlier. Other design variations will need to be investigated if the antisymmetric load capacity is to be increased.

SUMMARY AND CONCLUSIONS

Tests on a full-scale, MMC (SiCf/Al), multi-spar box section representative of an advanced fighter vertical stabilizer revealed unexpected fatigue failures in the front and rear spars near the web/flange intersection. A separate full-scale static test on an identical multi-spar box failed just below design ultimate load with failure apparently initiating in the rear spar web/flange intersection region. An analytical and experimental investigation has been performed on an MMC T-section that is representative of this web/flange intersection and is subjected to local bending. Finite element modeling procedures have been developed which provide a rapid and

systematic way of generating detailed finite element models of various T-section configurations. The modeling and analysis approach has been applied to isotropic and MMC T-sections with 1/4 inch and 1/2 inch fillet radii. Tests have been performed on MMC specimens with several design variations in the intersection region. The analytical results obtained indicate that the peak stresses are generally lower for the larger fillet radius configuration than for the smaller fillet radius configuration, but that the degree of reduction depends on the character of the local bending.

Analysis results have been presented for loading cases that represent bending of the flange that is symmetric and anti-symmetric with respect to the web. In each case, significant interlaminar and transverse stresses occur in the fillet, in the portion of the web laminate that extends into the fillet, in the gap between the web and flange laminates, and in the flange where the fillet becomes tangent. For the symmetric loading, increasing the fillet radius is effective in reducing the interlaminar stresses in the web and flange but is not as effective in reducing the peak transverse normal stresses in the fillet material. For the anti-symmetric loading, increasing the fillet radius also reduces the interlaminar stresses in the web and flange but does not reduce the maximum transverse normal stresses in the fillet material that are the critical stresses for the material investigated. Additional simulations to investigate changes in the fiber orientations and number of wrap plies, fiber volume in the fillet material, the size of the "gap" between the web and flange laminates in the fillet region, alternate stacking sequences in the web and flange laminates, and alternate MMC systems are required to develop improved designs for the web/flange intersection.

Element tests have been conducted to experimentally evaluate eight intersection design variations. Failure was observed to initiate in the intersection region in all cases. Test failure loads within about 10 percent of the analytically predicted failure loads were obtained for the specimens that had good fabrication quality. Test failure loads much lower than predicted were obtained with specimens that had good laminate quality but poor consolidation in the filler material in the fillet and gap regions of the specimens. The critical need for reliable nondestructive quality evaluation (NDE) methods that can be applied to the fillet intersection regions of this class of commonly used structures is pointed out by these test results. In the absence of such NDE methods, designs for this region that are more defect tolerant are required.

REFERENCES

1. Brewer, J.C. and P. A. Lagace, "Quadratic Stress Criterion for Initiation of Delamination," *Journal of Composite Materials*, Vol. 22, No. 12, December 1988, pp. 1141-1155.

ACKNOWLEDGMENTS

The first two authors acknowledge support from LASC. This work was performed under the direction of the third author while he was employed by LASC, Georgia Division. All authors would like to thank Mr. Brian Cornell (LASC-GA) for his helpful review of the manuscript.

CHARACTERISTICS OF LAMINATES WITH DELAMINATION CONTROL STRIPS

C. T. Sun
School of Aeronautics & Astronautics
Purdue University
West Lafayette, IN

J. C. Goering
McDonnell Aircraft Company
McDonnell Douglas Corporation
St. Louis, MO

J. M. Alper and L. W. Gause
Naval Air Development Center
Warminster, PA

514-24
57382
p.31

SUMMARY

Tough resin is needed to resist delamination crack propagation. However, modulus often has to be compromised because it is difficult to retain both high modulus and toughness in a matrix material. A potential solution is to use a hybrid system in which tough resin strips are included within a conventional matrix composite. By adjusting the spacing of the tough resin strips, maximum delamination size can be controlled.

In this paper, experimental results for impact damage and subsequent damage propagation in laminates containing tough resin strips obtained at Purdue University, McDonnell Aircraft Company, and the Naval Air Development Center are reported. Plain adhesive strips and fiber-reinforced tough resin composite strips were used in constructing the hybrid laminates. Test results indicated that size of delamination inflicted by impact was confined between the tough resin strips. As a result, significantly increased residual compressive strength was obtained. Impacted laminates containing tough resin strips were also fatigue tested. It was found that these strips reduced the growth of the impact damage area relative to the growth seen in coupons with no tough resin strips.

Damage growth from an open hole under tension fatigue was evaluated using both tough resin strips and glass fiber-reinforced tough resin strips. Unreinforced tough resin strips retarded delamination growth from the open hole, but did not stop matrix cracks growing in the fiber direction. Fiber reinforced tough resin strips did not contain axial delamination growth from the open hole. However, they did act as crack arresters, stopping the through-the-thickness tension crack originating from the hold.

Compression tests comparing conventional graphite/epoxy laminates to hybrid graphite/epoxy laminates which included graphite fiber reinforced tough resin strips showed similar performance under room-temperature-dry conditions, but the hybrid suffered a greater reduction in compression strength during elevated-temperature-wet tests.

INTRODUCTION

The susceptibility of graphite/epoxy laminates to impact induced delamination damage is well known. Damage tolerance for Low Energy Impact Damage (LEID) is a major criterion in aircraft design, limiting composites' design allowables which results in increased weight. The primary motivation for developing new, tough resin systems is to eliminate or reduce delamination crack propagation. Unfortunately, modulus often has to be compromised in order to improve matrix toughness, which results in degraded compressive strength. Interlaminar tensile and shear strength may also be degraded. Costs of the new tough material systems are also an issue, since they are generally significantly more expensive than conventional graphite/epoxy prepregs and may require special processing.

Delamination, in and of itself, is not necessarily undesirable. Although it can lead to widespread damage within a structure, it is a mode of failure which absorbs impact energy. If we were to eliminate delamination entirely, then more impact energy would be absorbed by the fibers, increasing the likelihood of fiber breakage which is a great deal more degrading to laminate strength. Limited amounts of delamination are acceptable in a composite structure. Manufacturing inspection criteria generally allow up to one half inch diameter delaminations in a composite part. In service, composite structure must be able to tolerate impact induced delaminations up to two inches in diameter for their remaining service life without rework or repair. Known fiber breakage, on the other hand, is always repaired.

Composites containing more than two constitutive materials (that is, another material in addition to their basic fiber and matrix) are known as "hybrid composites". The purpose of hybridization is to construct a new material which retains the best features of the constitutive materials while eliminating or reducing their disadvantages. There are several classes of hybrids: *interply* - where alternate layers of different materials are stacked in a regular manner, *intraply* - where fiber tows or strips are mixed within a layer, intimately mixed *hybrids* - where different constituent fibers are mixed in random filament-by-filament basis, and *global* - where a structural element is constructed of various materials, such as glass skins on graphite ribs. Hybrid composite structures offer the potential for improved damage tolerance, damage containment, impact resistance and lower cost. Cost reductions result from the substitution of less expensive constituent materials in non-critical locations.

An example of a successful intraply hybrid composite is laminated skins incorporating crack arrester strips [1]. As applied to graphite/epoxy laminates, within the layers oriented in the primary tension loading direction, graphite fibers are periodically

replaced by glass fibers to form crack arrester strips. The glass fiber strips are softer and tougher than the adjacent graphite fiber laminate and thus form a barrier which stops a running through-the-thickness crack. By adjusting the spacing of the crack arrester strips, the size of the initial crack to be stopped can be controlled.

Another practical hybrid concept in the interply hybrid formed by including tough adhesive layers between plies in a laminate [2]. This concept has been successfully applied to reduce impact delamination in graphite/epoxy laminates. The adhesive interfere increases the impact contact area and reduces the transverse shear concentration effect. This together with the toughened interfacial properties, results in less delamination. The disadvantage of including adhesive interlayers is that the adhesive adds weight without increasing the in-plane load bearing capacity of the laminate, reduces the global stiffness and reduces the compressive strength. Moreover, suppression of delamination may result in massive fiber breakage when impact velocity exceeds a certain threshold.

Sun and Norman [3] investigated delamination and residual strength of graphite/epoxy laminates with adhesive strips subjected to transverse impact loading. The use of adhesive strips was conceived as a weight efficient means of providing delamination resistance as opposed to the use of full adhesive layers. It was also felt that the level of delamination could be controlled by the strips so that the beneficial effect of energy absorption through delamination could be gained while preventing delamination growth beyond an acceptable level. They concluded that delamination is substantially controlled by adhesive strips in laminated composites subjected to impact loading. It was shown that fabricated strength of the laminate with adhesive strips was less than the plain laminate, but residual strength after impact at higher velocities was greater for the adhesive strip hybrid. Low velocity impact studies of composite laminates with adhesive strips were also conducted in [4] with similar results.

The purpose of the research reported in this paper is to develop the concept of hybrid laminate design in which delamination is allowed to occur under impact, but its extent is limited and it is prevented from propagating under subsequent loading. A Government/Industry/University team was formed to pursue this effort cooperatively. The interests of each of the three team members were different but complementary to the overall goal of the research. Purdue University was under contract to the Office of Naval Research (ONR) to develop impact analysis and fracture methodologies for composite materials. The Naval Air Development Center (NADC), also under ONR sponsorship, was performing a program in Hybrid Composites with goals of providing a balanced hybrid laminate concept with damage growth resistance under both compression and tension loading. McDonnell Aircraft (McAir) was interested in a composite material with better damage tolerance than AS4/3501-6 but at lower cost than IM7/8551-7. McAir also required a material which could be handled and processed identically to AS4/3501-6.

DAMAGE CONTROL CONCEPT

The proposed damage control concept is to merge the adhesive delamination control strip with the crack arrester strip, Figure 1. This concept is an intraply hybrid, where the base composite material is periodically replaced by strips of fiber reinforced adhesive. The adhesive provides delamination resistance. Experience to date shows that adhesive strips must be spaced roughly 1/2 inch apart to control impact delamination. Fiberglass crack arrester strips are spaced roughly 3 inches apart to stop a running crack. Thus, we propose using two types of fibers as reinforcements in the adhesive. The base fiber is used as a reinforcement to allow the control strip to carry primary in-plane loads and improve the weight efficiency of the concept. Low modulus, high toughness fibers are periodically substituted for the base fiber as reinforcement for the adhesive to provide a through-the-thickness tension crack arrester. For example, our conceptual damage control hybrid might consist of base unidirectional graphite/epoxy plies with strips of 1/4 inch wide graphite reinforced adhesive replacing the graphite/epoxy every 3/4 inch, and S2 glass would replace the graphite fibers in every third adhesive strip.

PROGRAM PLAN

An experimental program was conducted to demonstrate the feasibility of the proposed damage control concept. The objectives were to prove impact damage reduction, crack arrester performance, damage containment under fatigue, and determine any effects of the adhesive strips on elevated-temperature-wet compression strength. Purdue University fabricated test specimens, performed air gun impact tests and post-impact compression tests. McAir performed post-impact spectrum fatigue tests on damaged specimens provided by Purdue. NADC performed tension fatigue tests to verify tension crack arrestment, compression tests to study hygrothermal effects and SACMA standard compression after impact tests.

SPECIMEN PREPARATION

Two custom batches of fiber reinforced tough adhesive prepreg were manufactured by 3M for use in this effort: AF163-2 reinforced with AS4 graphite fibers and AF163-2 reinforced with S2 glass fibers. This material was delivered to Purdue University for test specimen fabrication.

Cross-ply and quasi-isotropic AS4/3501-6 graphite/epoxy test panels were made to study impact characteristics. Some of the panels incorporated glass fiber-reinforced adhesive strips (S2/AF163-2) or graphite fiber-reinforced adhesive strips (AS4/AF163-2) to determine if they could improve the impact characteristics. Panels incorporating FM 1000 adhesive film strips were made to study tension fatigue performance.

Cross-ply Laminate

Six cross-ply 12 by 12 inch AS4/3501-6 graphite/epoxy test panels were made to study residual compressive strength characteristics. The basic layup was $[0_3/90_3/0_3/90_3/0_3]$. Four of the six cross-ply panels incorporated fiber-reinforced adhesive strips. In the test panels with fiber-reinforced adhesive strips, each group of three plies incorporated 1/4 inch wide fiber reinforced adhesive strips in the outside plies. In the following stacking sequence, "a" denotes a ply with adhesive strips, $[0_a/0/0_a/90_a/90/90_a/0_a/0/0_a/90_a/90/90_a/0_a/0/0_a]$. In these plies, the fiber-reinforced adhesive strips were spaced 1/2 inch apart.

Specimens measuring approximately 6 x 1.5 inches were cut from the test panels. The specimens were cut with the 0 degree fiber direction along the longitudinal edge of the specimen. Figure 2 depicts the fiber-reinforced adhesive strip orientation in each specimen.

Specimens were made from graphite/epoxy with adhesive strips and graphite/epoxy with glass fiber-reinforced adhesive strips to evaluate the ability of the adhesive strips to contain damage growing from an open hole during tension-tension fatigue cycling. For these specimens, graphite/epoxy strips were 1.0 inch wide and the alternating adhesive strips 0.5 inch wide. The layup geometry for these laminates was $[0_a/0/0_a/90_a/90/90_a/0_a/0/0_a/90_a/90/90_a/0_a/0/0_a]$ for specimens with FM 1000 adhesive strips and $[(0_a)_3/(90_a)_3/(90_a)_3/(0_a)_3]$ for specimens with S2/AF163-2 strips. Dimensions of the specimen were 3 inches wide, 12 inches long, with a 0.25 inch diameter hole in the center. Each specimen had 1.5 inch long fiberglass/epoxy end tabs on each end which reduced the actual test section by 3 inches. For layers containing adhesive strips, the center line of a graphite/epoxy strip coincided with the center line of the specimen. Specimens of the same dimensions and layup but without adhesive strips were made to generate baseline data.

Quasi-isotropic Laminate

Three quasi-isotropic 12 by 12 inch AS4/3501-6 graphite/epoxy test panels were prepared to study post-impact fatigue characteristics. The basic layup was $[0_2/+45_2/-45_2/90_2]_S$. Two of the three test panels incorporated fiber-reinforced adhesive strips. The following stacking sequence shows which plies contained fiber-reinforced adhesive strips, $[0/0_a/+45/+45_a/-45/-45_a/90/90_a]_S$. In these plies, 1/4 inch fiber-reinforced adhesive strips were spaced 1.25 inches apart. Specimens measuring approximately 6 x 3 inches were cut from the test panels. The specimens were cut with the 0 degree fiber direction along the longitudinal edge of the specimen.

A laminate made from graphite/epoxy with graphite-reinforced adhesive strips was used to evaluate hygrothermal effects on the compressive strength of the hybrid composite. For these specimens, graphite/epoxy strips were 1.5 inches wide, and the alternating graphite-reinforced adhesive strips 0.5 inch wide. The layup for these specimens was $[45_a/0_a/-45_a/90_a]_{3S}$. Alignment of the adhesive strips through the

thickness of the laminate was random. Specimens for static compressive strength measured 3.18 inches long and 0.5 inch wide. Coupons for residual compressive strength after impact measured 6.0 inches in length and 4.0 inches wide.

Cross-ply specimens were used to study residual compressive strength characteristics. Some of the specimens were subjected to impact by a 1/2 inch diameter steel ball, while others were impacted with a 7/8 inch diameter steel ball fired from a compressed air gun. In both cases, specimens were clamped one inch on each end in a heavy test stand so that a four-inch span resulted. The specimens were impacted at their center at various velocities. After impact, a small hole (1/16 inch diameter) was drilled through the specimens at the impact center. An X-ray blocking penetrant (1.4 diiodobutane) was injected in the specimens through this hole. X-ray radiographs of the impacted specimens were then taken.

Residual compressive strength tests were performed on the specimens after they were photographed. End tabs were epoxied to the specimens so that a 1.0 inch gage length about the impact center resulted. The specimens were loaded in compression with an MTS machine, and the failure load was recorded. Careful observation of the test and the failed specimens revealed that the specimens did not buckle before failure.

Post-impact Fatigue Tests

Quasi-isotropic specimens were used for fatigue tests. Some of the specimens were subjected to impact with a 7/8 inch diameter steel ball at a velocity of 66 feet per second as described above, and X-ray photographs of the damage were taken.

Fatigue test panels were cycled to two lifetimes of spectrum fatigue (12000 Spectrum Flight Hours (SFH)) or failure, whichever was first. The F/A-18 Wing Root Spectrum was used in fatigue testing. Before fatigue testing, the test panels were bonded with fiberglass/epoxy tabs and aluminum shims using FM 300-2K (a 250°F curing film adhesive) to allow for adequate grip area during testing. The tabbed test specimens were 2.75 inches wide by 10.00 inches long with a test section of 2.75 inches wide by 4.00 inches long. The specimens were gaged with back-to-back axial strain gages.

Tension Fatigue Test

Specimens made from graphite/epoxy with adhesive strips and graphite/epoxy with glass fiber-reinforced adhesive strips were cycled in tension-tension constant amplitude fatigue using a 100 KIP MTS servo-hydraulic test machine. Specimens were cycled at 5Hz at one of three maximum loads, Table 1, with a peak to valley ratio $R = 10$. Tests were run until failure or a maximum of 1,000,000 cycles. Damage growing from the open hole was assessed periodically using X-radiographs. Zinc-iodide penetrant was used to enhance the damaged region.

Hygrothermal Effects

Static compression testing of the graphite/epoxy coupons containing graphite reinforced adhesive strips was conducted on a 20 KIP Instron Test Machine. These tests were conducted according to the procedure detailed in [5]. Five specimens, both with and without reinforced adhesive strips, were tested at room-temperature-dry (RTD) condition. For an evaluation of hygrothermal effects (elevated-temperature-wet (ETW)), five specimens with and three specimens without reinforced adhesive strips were conditioned to one percent moisture content (by weight) and tested at 200°F.

Compression after Impact (SACMA Standard)

Four specimens both with and without reinforced adhesive strips were tested for residual compressive strength after impact. These tests were conducted according to the procedure detailed in [6]. All impact tests were conducted on a Dynatup Model 8200 drop tower. One specimen from each group was impacted at 3360 in-lbs/inch thickness to get through penetration. The remaining specimens were impacted at the specified energy level, 1500 in-lbs/inch thickness. Ultrasonic C-scan was used to determine damage size. Compression after impact tests were conducted on a Baldwin 60 KIP mechanical test machine.

TEST RESULTS

Residual Compressive Strength Tests

Figure 3 plots residual compressive strength versus impact velocity for those specimens impacted with the one-half inch diameter steel ball, while Figure 4 plots the same for those specimens impacted with the 7/8 inch diameter steel ball. Note that the residual compressive strength was obtained by dividing the ultimate load by the width of the specimen, resulting in units of pounds/inch. This was done to account for the slight differences in width of the specimens.

Figure 5 presents X-ray radiographs of specimens impacted with the one-half inch diameter steel ball at velocities of approximately 56, 69, 98, and 128 feet per second. Figure 6 presents the X-ray radiographs of specimens impacted with the 7/8 inch diameter steel ball at velocities of approximately 20, 26, 33, and 53 feet per second.

The fiber-reinforced adhesive strips are clearly effective in containing delamination. However, the matrix crack on the back face of the laminate due to excessive bending cannot be arrested. These bending cracks could induce local delamination along the crack path.

Post-impact Fatigue Tests

Table 2 lists the quasi-isotropic specimens impacted with the 7/8 inch diameter steel ball that were fatigue tested at McAir. Figure 7 presents X-ray radiographs of the impacted specimens.

The undamaged (no impact) specimens were fatigue cycled at a maximum spectrum compressive strain that corresponded to - 6000 microinches/inch as determined by an initial strain survey. These specimens were inspected ultrasonically before and after 12000 SFH of fatigue. No fatigue-induced damage was detected. The impact damaged specimens were fatigue cycled at a maximum spectrum compressive strain that corresponded to -4000 microinches/inch maximum strain as determined by an initial strain survey. These specimens were inspected ultrasonically every 1500 SFH for damage growth during fatigue cycling. A plot of damage area versus cumulative spectrum flight hours is given in Figure 8, and ultrasonic NDT A-scan data are presented in Figures 9 through 11. All fatigue testing was done at room temperature. Spectrum fatigue test data are presented in Table 2.

Tension Fatigue Tests

Results show delamination growth between the 0 and 90 degree layers in the baseline laminate, Figure 12, is retarded by adhesive strips, Figure 13. However, the strips had no effect on matrix growing in the fiber direction within a layer. These matrix cracks grew through the strip regions and then served as the site for delamination initiation between the 0 and 90 degree layers beyond the adhesive strips. Figure 14 shows the cycles to failure versus the maximum equivalent strain experienced during fatigue cycling. The use of equivalent strain aids in comparing the performance of the laminates since it compensates for the change in modulus due to the adhesive strips.

With the inclusion of the glass fiber-reinforced strips, there was no reduction in strength when compared with the baseline laminate (124 KIP with glass strips, 117 KIP without). Figure 14 again shows no difference in the overall fatigue lives of the glass-reinforced adhesive interfere and baseline specimens. Using the zinc iodide enhanced X-ray to track damage growth from the notch, it was observed that the glass fiber-reinforced strips did not contain delamination originating from the notch, Figure 15, but did act as a crack arrester for the through-the-thickness crack that originated at the notch.

Hygrothermal Effect

A summary of test results for RTD and ETW conditions is shown in Table 3. No difference is observed in the mean compressive strength at the RTD condition (- 93 KIP for the baseline, and -94 KIP for the specimens containing graphite fiber reinforced adhesive strips). However, the ETW condition has a much greater effect on specimens containing graphite adhesive strips. The mean compressive strength of the baseline

specimens was - 80.8 KIP; the mean compressive strength of specimens with graphite adhesive strips was - 51.7 KIP, which is a 36% reduction in strength.

Compression after Impact (SACMA Standard)

Specimens which were impact tested showed that the graphite-reinforced strips contained impact damage better than specimens without the strips, Table 4. The average damage area of specimens with the strips was 2.66 square inches while the average damage area for specimens without the strips was 5.6 square inches. As a result, the compressive strength of the specimens with the strips was greater than for the baseline specimens (-26.1 KIP with strips and -17.9 KIP for the baseline).

DISCUSSION

Results of the air gun impact tests show that at low impact energies there is little or no difference between baseline and fiber-reinforced adhesive strip laminates in either damage area or residual compressive strength. This is because the damage inflicted is smaller than the spacing of delamination control strips. As the impact energy becomes greater, the level of damage increases so that the control strips become active in inhibiting the delamination damage. At higher impact energies the delamination control strip specimens have less damage and higher compressive strength than the baseline. This result was true for both the post-impact compression tests performed by Purdue and the compression after impact test done at NADC. At higher energy impact levels, the back face matrix cracks were not arrested by the adhesive strips and may induce delamination. To reduce this type of delamination, the back face bending crack must be minimized. There are three possible methods for achieving this: using a single ply on the back face (instead of three plies in the present study), using an adhesive sheet beneath the surface ply, or using woven fabric on the surface of the laminate.

Post-impact compression dominated spectrum fatigue testing shows no detrimental effect of the strips on laminate life in undamaged specimens cycled to a maximum spectrum compressive strain of -6000 microinches/inch. Impact damaged specimens cycled to a maximum compressive strain of -4000 microinches/inch clearly showed retardation in delamination growth and increased life for fiber-reinforced adhesive strip specimens over unreinforced specimens.

Constant-amplitude tension fatigue tests of open hole specimens without strips, with adhesive only strips and with S2 glass reinforced strips yielded similar overall fatigue lives. Damage growth within each specimen was different. Under tension loading, the unreinforced strips stopped the delamination growing axially from the open hole, but was not effective against the matrix crack growing axially from the tangent to the hole along the fibers. These cracks grew in the 0 degree ply across the adhesive strip in the adjacent 90 degree layer. Since these cracks occur within the ply, it was not unexpected that the adhesive layer contacting the surface ply only at the ply interface would have little or no effect on this crack. The results from tension fatigue testing of

the S2 glass reinforced adhesive strips were a surprise, since in these specimens the glass fiber strips did not stop the axial delamination crack growing from the open hole. The axial glass strips were effective as crack arrester strips in containing the through-the-thickness crack originating from the hole and propagating laterally at final failure. Overall the results of fatigue testing show improvement in performance of damaged laminates under compression fatigue and no degradation in life under tension fatigue.

The undamaged RTD compression strength of plain and graphite fiber reinforced adhesive strip specimens was similar, but the adhesive strip specimens degraded more severely than the baseline in ETW tests. We feel this is because the adhesive is more sensitive to ETW conditions than the resin matrix, and that the adhesive absorbs more moisture than the matrix. Examination of the weight gain data showed that for identical environmental conditioning, the fiber-reinforced adhesive specimens gained more moisture by weight than the baseline, 1.21% versus 1.0%.

At the initiation of this effort, we had only a limited amount of fiber-reinforced adhesive available for testing. Thus, the focus of the tests was on discovering "show-stoppers" to the hybrid damage control concept. We wanted to fabricate and test panels representative of an aircraft skin which included both the graphite-fiber-reinforced delamination control strip and glass-fiber reinforced crack arrester strip. However, after providing the initial batch of AS4/AF163-2 and S2/AF163-2 fiber reinforced adhesive, we were unable to interest any material supplier in providing further quantities of reinforced adhesive for evaluation. The amount of material needed was too large to prepreg by hand but insufficient to warrant the expense and set-up of a limited production run. We were thus unable to test the "full up" damage control hybrid, but from the results of the limited testing reported here feel we have adequately demonstrated the concept.

CONCLUSIONS

Based upon the results of our experimental investigation into the behavior of fiber reinforced adhesive strips to control damage, the following conclusions were reached.

1. The inclusion of fiber reinforced adhesive strips in a laminate yields a hybrid laminate with essentially the same RTD virgin compression strength as the baseline laminate. The presence of adhesive reduces the ETW compression strength compared with the baseline since the adhesive is more sensitive to moisture pickup than the epoxy.
2. The initial degradations of strength after impact of the plain laminate and the fiber-reinforced adhesive strip laminates tested (at lower impact velocities) are similar. At lower impact velocities, the three laminates suffer a similar amount of delamination.

3. Beyond a certain impact velocity, the plain laminate continues to steadily lose its strength as the impact velocity increases. In contrast, the two laminates containing fiber-reinforced adhesive strips are able to retain their strengths at higher impact velocities. The graphite fiber-reinforced adhesive laminate offers almost 50 percent improvement in compression after impact strength versus the baseline laminate.
4. Fiber-reinforced adhesive strips significantly reduce the growth of impact damage in compression dominated spectrum fatigue loading. The strips had no apparent effect on undamaged compression fatigue performance.
5. There is no difference in the overall tension fatigue lives between the baseline laminate, the unreinforced-adhesive strip laminate or the S2-glass fiber-reinforced adhesive strip laminate.
6. Fiberglass reinforced adhesive strips can stop through-the-thickness tension cracks when oriented in the laminate as crack arrester strips, but are ineffective in stopping axially growing delamination cracks under tension fatigue.
7. The proposed damage control hybrid laminate concept offers a practical alternative to tough resins for providing damage tolerant graphite/epoxy structures.

ACKNOWLEDGMENT

The authors gratefully acknowledge the Office of Naval Research and McDonnell Aircraft Company for their support of this effort.

REFERENCES

1. Hess, T. E., Huang, S. L. and Gause, L. W., "The Development of Crack Arrester Designs for Damage Containment in Composite Structures," Report Number NADC-78063-60, Naval Air Development Center, 16 March 1978.
2. Sun, C. T. and Rechak, S., "Effect of Adhesive Layers on Impact Damage in Composite Laminates," *Composite Materials in Testing and Design, 8th Conference ASTM STP 972*, J. D. Whitcomb, Editor, American Society for Testing and Materials, 1988.
3. Sun, C. T. and Norman, T. L., "Design of Laminated Composite with Controlled-Damage Concept," *Composites Science and Technology*, **39** (1990) 327-340.

4. Eisenmann, J. R. and Ulman, D. A., "Adhesive Strip Concept for Delamination Arrestment," AFWAL-TR-85-3120, U. S. Air Force, 1985.
5. SACMA (Suppliers of Advanced Composite Materials Association) SRM1-88, Recommended test Method for Compressive Properties of Oriented Fiber-Resin Composites.
6. SACMA (Suppliers of Advanced Composite Materials Association) SRM 2-88, Recommended Test Method for Compressive Properties of Oriented Fiber-Resin Composites.

Captions

Table 1. Test Results for Notched Specimens

Table 2. Spectrum Fatigue Test Data

Table 3. Compression Strength for Specimens Containing Graphite/Adhesive Strips

Table 4. Compression after Impact Test Results

Figure 1. Damage Control Concept employing graphite-reinforced adhesive strips to contain delamination damage and glass-reinforced adhesive strips to contain running tension cracks.

Figure 2. Schematic of a cross-ply specimen. Notice that the thickness is greatly exaggerated.

Figure 3. Residual compressive strength vs. impact velocity for cross-ply laminate impacted with 1/2 inch diameter steel ball.

Figure 4. Residual compressive strength vs. impact velocity for cross-ply laminate impacted with 7/8 inch diameter steel ball.

Figure 5a. X-ray photographs of cross-ply specimens impacted with 1/2 inch diameter steel ball. From left to right the specimen types are: plain graphite/epoxy, graphite/epoxy with S2/AF163-2 strips, and graphite/epoxy with AS4/AF163-2 strips.

Figure 5b. X-ray photographs of cross-ply specimens impacted with 1/2 inch diameter steel ball. From left to right the specimen types are: plain graphite/epoxy, graphite/epoxy with S2/AF163-2 strips, and graphite/epoxy with AS4/AF163-2 strips.

Figure 6a. X-ray photographs of cross-ply specimens impacted with 7/8 inch diameter steel ball. From left to right the specimen types are: plain graphite/epoxy, graphite/epoxy with S2/AF163-2 strips, and graphite/epoxy with AS4/AF163-2 strips.

Figure 6b. X-ray photographs of cross-ply specimens impacted with 7/8 inch diameter steel ball. From left to right the specimen types are: plain graphite/epoxy, graphite/epoxy with S2/AF163-2 strips, and graphite/epoxy with AS4/AF163-2 strips.

Figure 7a. X-ray photographs of quasi-isotropic specimens impacted at 66 feet per second with a 7/8 inch diameter steel ball. The specimens are plain graphite/epoxy.

Figure 7b. X-ray photographs of quasi-isotropic specimens impacted at 66 feet per second with a 7/8 inch diameter steel ball. The specimens shown here are graphite/epoxy with S2/AF163-2 strips.

Figure 7c. X-ray photographs of quasi-isotropic specimens impacted at 66 feet per second with a 7/8 inch diameter steel ball.

Figure 8. Damage growth during spectrum fatigue cycling.

Figure 9. Panels A2 (Left) and A4 not A-scan data.

Figure 10. Panels B2 (Left) and B4 NDT A-scan data.

Figure 11. Panels C2 (Left) and C4 NDT A-scan data.

Figure 12. Baseline laminate.

Figure 13. Adhesive strip laminate.

Figure 14. Equivalent strain versus cycles for baseline, adhesive strip laminate and glass-reinforced adhesive strip laminate.

Figure 15. Laminate with fiber reinforced adhesive.

Table 1. Test Results for Notched Specimens

SPECIMEN TYPE	FATIGUE OR STATIC	<u>MAX. FATIGUE STRESS</u> <u>STATIC STRENGTH *</u>	CYCLES TO FAILURE **
BASELINE	FATIGUE	0.85	1000000
BASELINE	FATIGUE	0.85	1000000
BASELINE	FATIGUE	0.95	448954
BASELINE	FATIGUE	0.95	250241
BASELINE	FATIGUE	1	25970
BASELINE	STATIC	0.68	1
BASELINE	STATIC	1.05	1
ADHESIVE STRIP	FATIGUE	0.85	513116
ADHESIVE STRIP	FATIGUE	0.85	1000000
ADHESIVE STRIP	FATIGUE	0.95	350761
ADHESIVE STRIP	FATIGUE	0.95	1000000
ADHESIVE STRIP	FATIGUE	1	1000000
GLASS STRIP	STATIC	0.96	1
GLASS STRIP	FATIGUE	0.8	64429
GLASS STRIP	FATIGUE	0.8	225807
GLASS STRIP	FATIGUE	0.8	104699
GLASS STRIP	STATIC	1.04	1

* The static strength for baseline and adhesive strip specimens was determined by tests previously conducted at Purdue University.

Baseline static strength = 117 KSI

Specimens with adhesive strip static strength = 95 KSI

The static strength for the glass strip material was the average of the two specimens presented in this table, 124.5 KSI.

** Tests were conducted to either failure or 1,000,000 cycles, whichever came first.

Table 2. Spectrum Fatigue Test Data

SPECIMEN I.D.	THICK. (inches)	WIDTH (inches)	MATERIAL TYPE	IMPACT DAMAGED	MAXIMUM STRAIN ($\mu\text{in/in}$)	100 % TLL (lbs)	SPECTRUM FLT. HRS. COMPLETED
A2	0.085	2.850	AS-4/3501-6	YES	N/A	N/A	0
A4	0.089	2.851			-4000	-5,010	3180
A5	0.091	2.859		NO	-6000	-7,040	12000
A6	0.085	2.850				-6,550	
A7	0.085	2.853				-6,780	
B2	0.081	2.768	AS-4/3501-6	YES	-4000	-4,630	
B4	0.080	2.853		-4,730			
B5	0.088	2.864	AS-4/3501-6 WITH S-2/AF163-2 STRIPS	NO	-6000	-6,490	
B6	0.085	2.850				-7,060	
B7	0.084	2.849				-6,830	
C2	0.089	2.853	AS-4/3501-6	YES	-4000	-4,610	
C4	0.091	2.847		-4,730			
C5	0.088	2.845	AS-4/3501-6 WITH S-2/AF163-2 STRIPS	NO	-6000	-7,120	
C6	0.089	2.847				-7,060	
C7	0.089	2.848				-7,590	

TEST NOTES:

1. ALL SPECIMENS WERE LOADED IN COMPRESSION DOMINATED SPECTRUM FATIGUE USING THE F/A-18 WING ROOT SPECTRUM WRFT01.
2. ALL TESTING WAS PERFORMED AT ROOM TEMPERATURE FOR TWO LIFETIMES OF FATIGUE (12000 SFH) OR FAILURE, WHICHEVER IS FIRST. THE CYCLING RATE WAS 5 HERTZ.
3. ALL SPECIMENS WERE TESTED WITH 3/8 INCH WIDE EDGE SUPPORT BARS TO PREVENT PREMATURE BUCKLING AS SHOWN BY THE TEST SETUP IN FIGURE 1.
4. SPECIMENS CONTAINING IMPACT DAMAGE WERE INSPECTED ULTRASONICALLY EVERY 1500 SFH. SPECIMENS WITHOUT DAMAGE WERE INSPECTED BEFORE AND AFTER 12000 SFH OF FATIGUE TESTING.
5. 100% TEST LIMIT LOAD (TLL) WAS CHOSEN BASED ON AN INITIAL STRAIN SURVEY OF EACH PANEL. EACH PANEL HAD BACK-TO-BACK AXIAL GAGES LOCATED AS SHOWN IN FIGURE 2. SPECIMENS WITHOUT DAMAGE WERE FATIGUE CYCLED AT A 131% TLL THAT CORRESPONDED TO -6000 $\mu\text{in/in}$ MAXIMUM STRAIN AS DETERMINED BY AN INITIAL STRAIN SURVEY. SPECIMENS WITH IMPACT DAMAGE WERE FATIGUE CYCLED AT A 131% TLL THAT CORRESPONDED TO -4000 $\mu\text{in/in}$ MAXIMUM STRAIN AS DETERMINED BY AN INITIAL STRAIN SURVEY.
6. SPECIMEN A2 FAILED STATICALLY DURING AN INITIAL STRAIN SURVEY TO -6000 $\mu\text{in/in}$. MAXIMUM STRAIN WAS SUBSEQUENTLY CHANGED TO -4000 $\mu\text{in/in}$ FOR ALL OTHER IMPACT DAMAGED SPECIMENS.

Table 3. Compression Strength for Specimens Containing Graphite/Adhesive Strips

SPECIMEN	ENVIRONMENT (RTD OR ETW)	COMPRESSIVE STRENGTH (KSI)
BASELINE	RTD	97.2
BASELINE	RTD	94.7
BASELINE	RTD	85.9
BASELINE	RTD	88.0
BASELINE	RTD	99.0

		MEAN = 93.0
WITH GR/ADHESIVE STRIP	RTD	100.4
WITH GR/ADHESIVE STRIP	RTD	110.0
WITH GR/ADHESIVE STRIP	RTD	75.3
WITH GR/ADHESIVE STRIP	RTD	92.1
WITH GR/ADHESIVE STRIP	RTD	90.2

		MEAN = 94.0
BASELINE	ETW	78.9
BASELINE	ETW	79.8
BASELINE	ETW	83.9

		MEAN = 81.0
WITH GR/ADHESIVE STRIP	ETW	50.0
WITH GR/ADHESIVE STRIP	ETW	62.4
WITH GR/ADHESIVE STRIP	ETW	52.3
WITH GR/ADHESIVE STRIP	ETW	51.0
WITH GR/ADHESIVE STRIP	ETW	42.6

		MEAN = 52.0

Table 4. Compression after Impact Test Results

SPECIMEN	ENERGY LEVEL, IN-LB/IN (THICK.)	DAMAGE AREA, IN*IN	COMPRESSION STRENGTH AFTER IMPACT, KSI	IMPACT DEPTH, IN
BASELINE	1500	3.28	20.3	0.02
BASELINE	1500	8.22	16.1	0.021
BASELINE	1500	5.43	17.3	0.021
BASELINE	3360	5.59	16.9	THROUGH
GRAPHITE STRIP	1500	2.67	28.3	0.013
GRAPHITE STRIP	1500	2.56	24	0.01
GRAPHITE STRIP	1500	2.75	26.2	0.015
GRAPHITE STRIP	3360	3.3	18.4	THROUGH

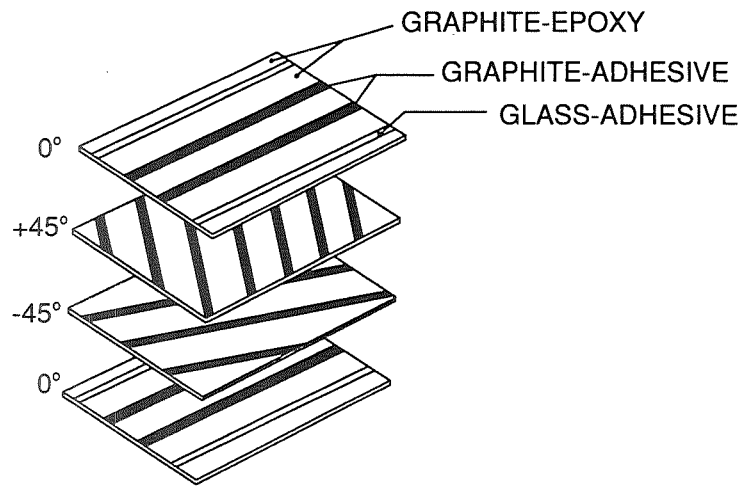


Figure 1. Damage Control Concept employing graphite-reinforced adhesive strips to contain delamination damage and glass-reinforced adhesive strips to contain running tension cracks.

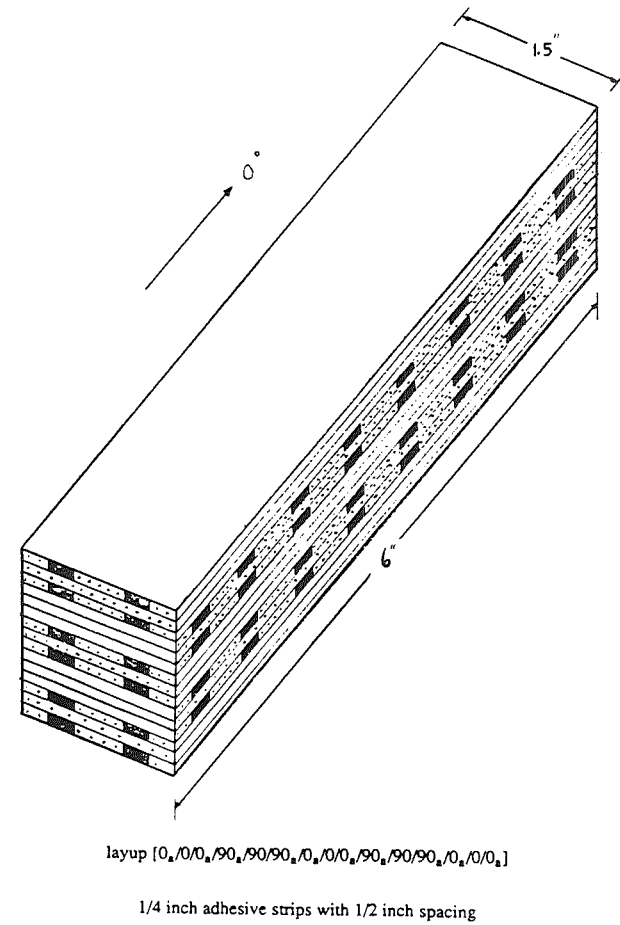


Figure 2. Schematic of a cross-ply specimen. Notice that the thickness is greatly exaggerated.

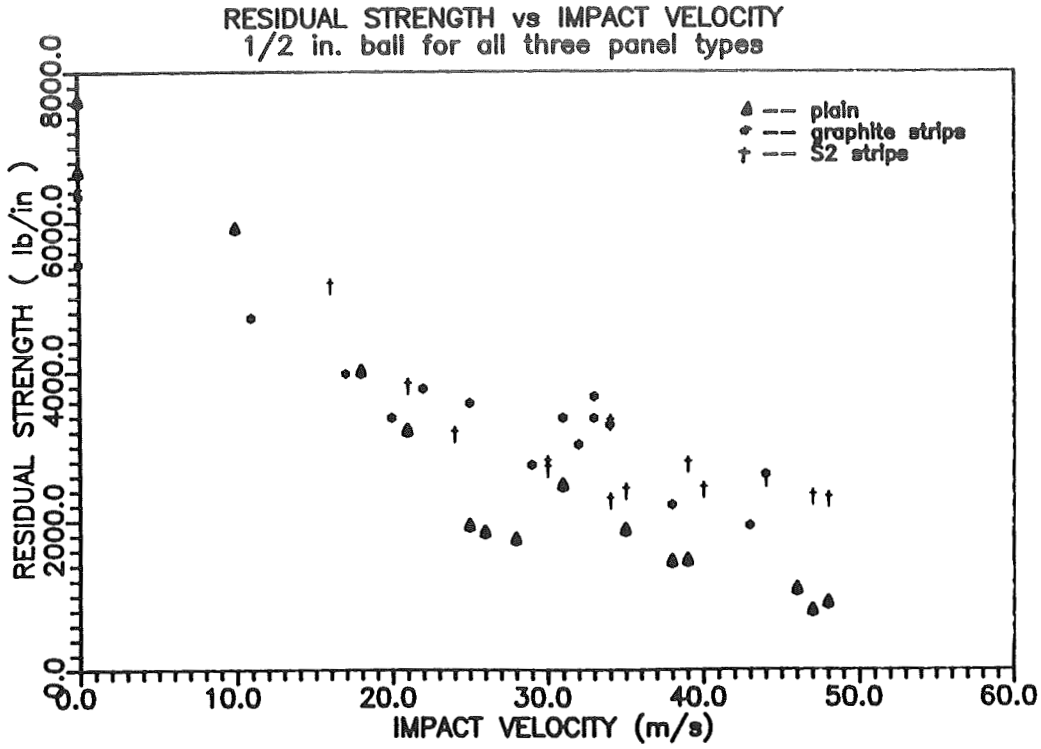


Figure 3. Residual compressive strength vs. impact velocity for cross-ply laminate impacted with 1/2 inch diameter steel ball.

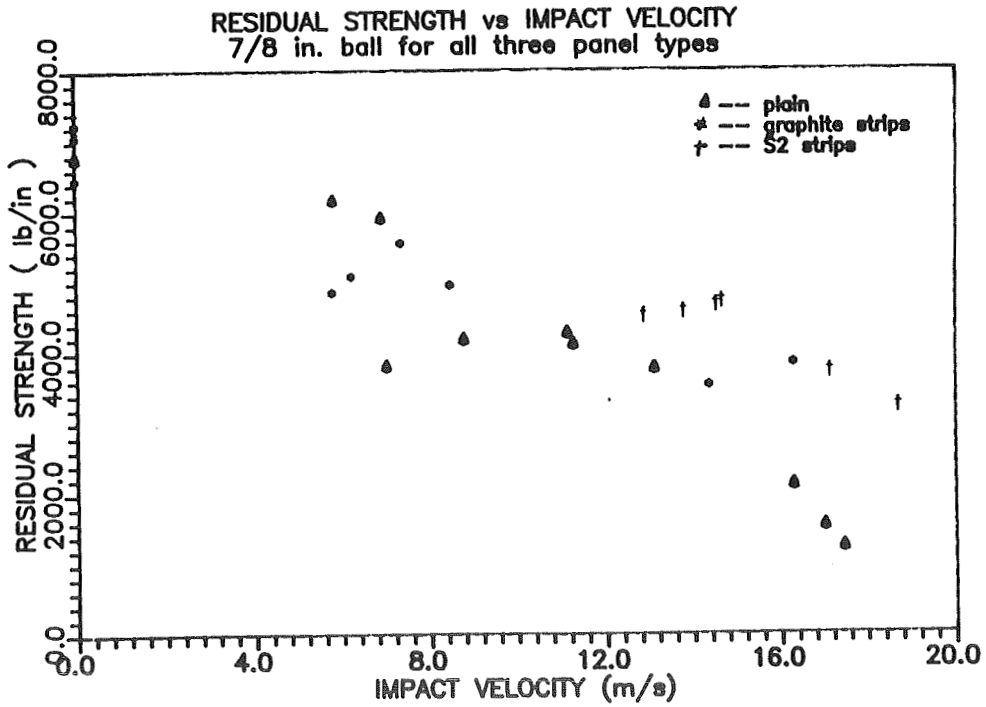
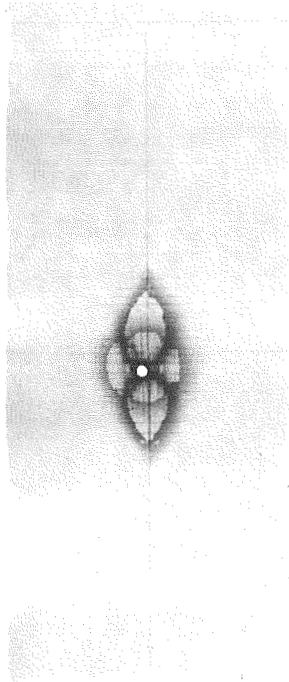
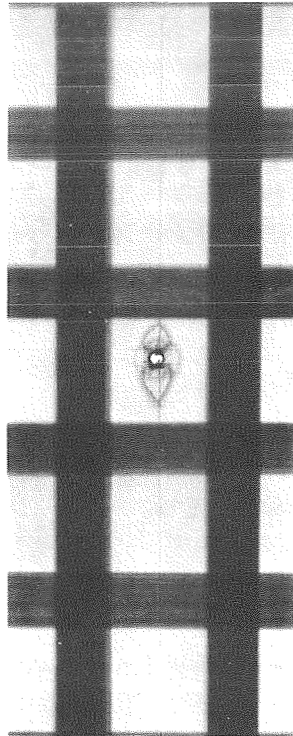


Figure 4. Residual compressive strength vs. impact velocity for cross-ply laminate impacted with 7/8 inch diameter steel ball.

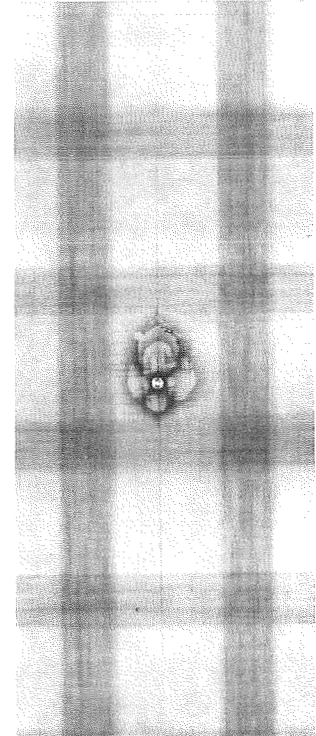
59 ft/sec



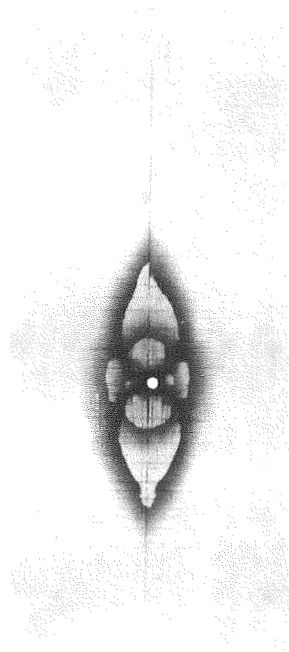
52 ft/sec



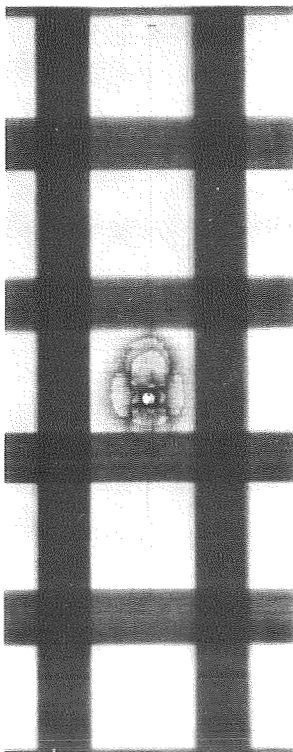
56 ft/sec



69 ft/sec



69 ft/sec



72 ft/sec

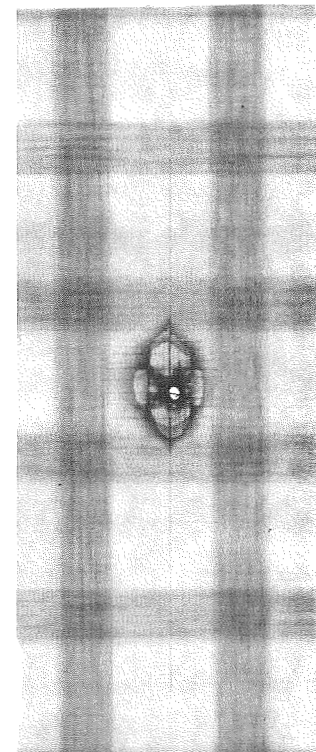
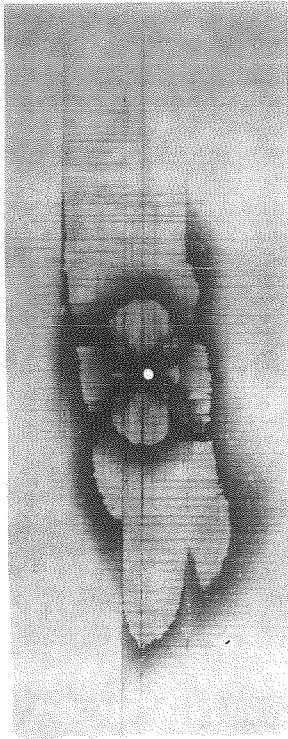
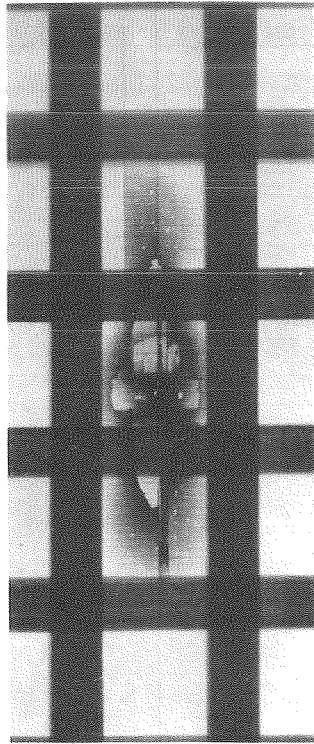


Figure 5a. X-ray photographs of cross-ply specimens impacted with 1/2 inch diameter steel ball. From left to right the specimen types are: plain graphite/epoxy, graphite/epoxy with S2/AF163-2 strips, and graphite/epoxy with AS4/AF163-2 strips.

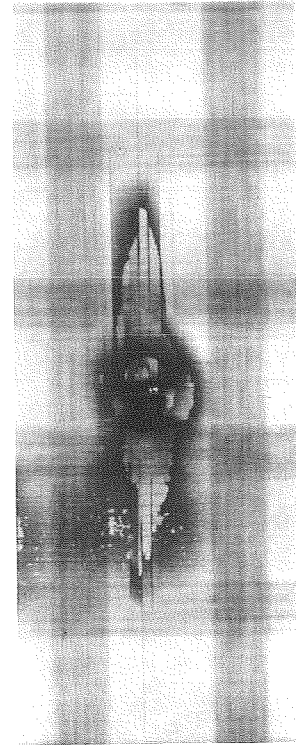
102 ft/sec



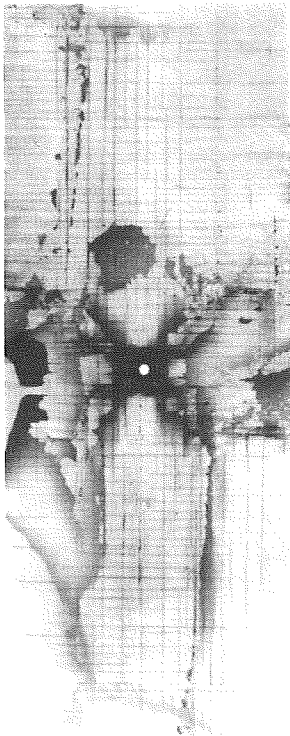
98 ft/sec



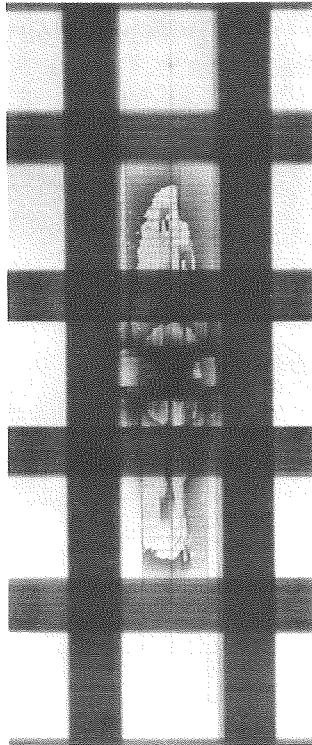
95 ft/sec



128 ft/sec



128 ft/sec



128 ft/sec

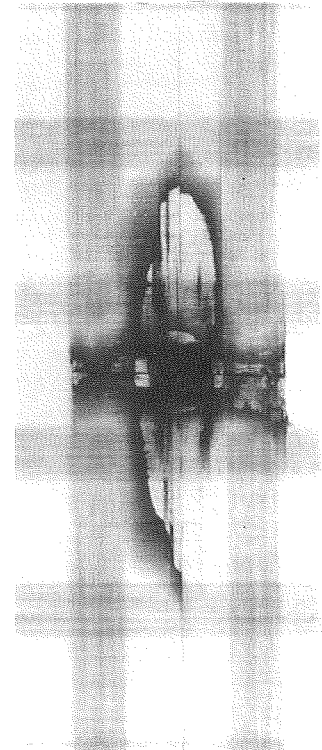
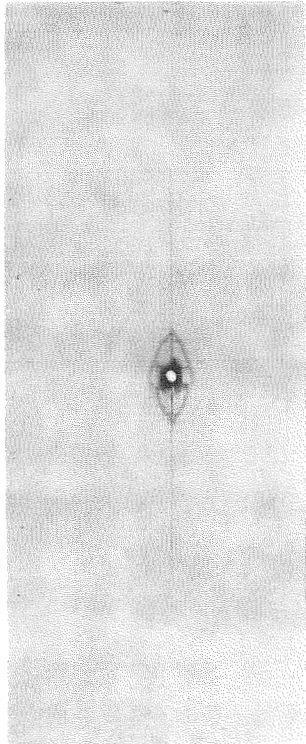
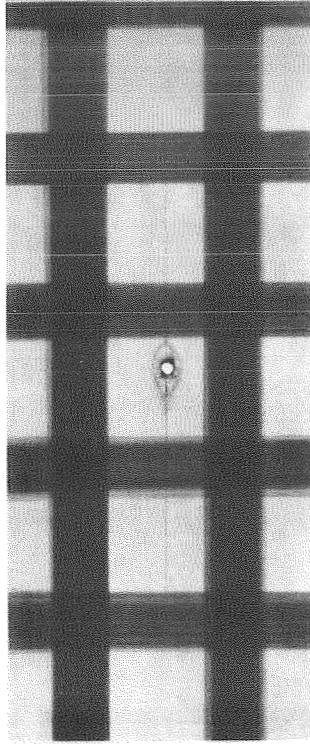


Figure 5b. X-ray photographs of cross-ply specimens impacted with 1/2 inch diameter steel ball. From left to right the specimen types are: plain graphite/epoxy, graphite/epoxy with S2/AF163-2 strips, and graphite/epoxy with AS4/AF163-2 strips.

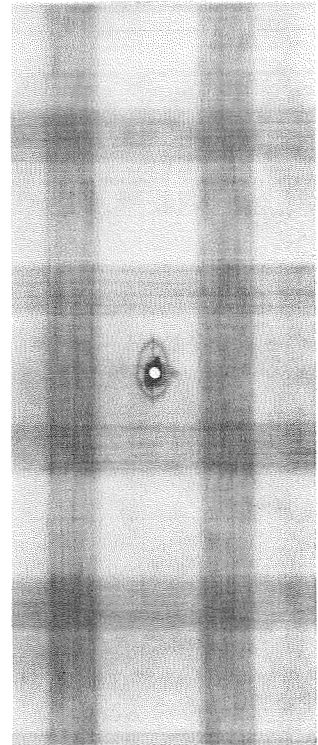
23 ft/sec



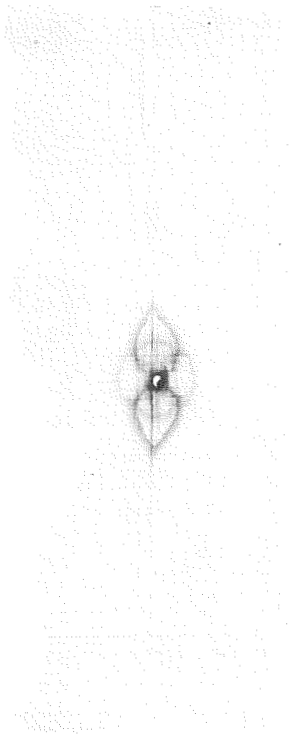
22 ft/sec



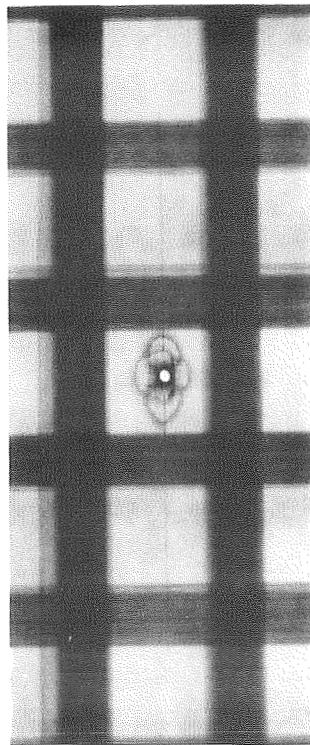
20 ft/sec



29 ft/sec



29 ft/sec



28 ft/sec

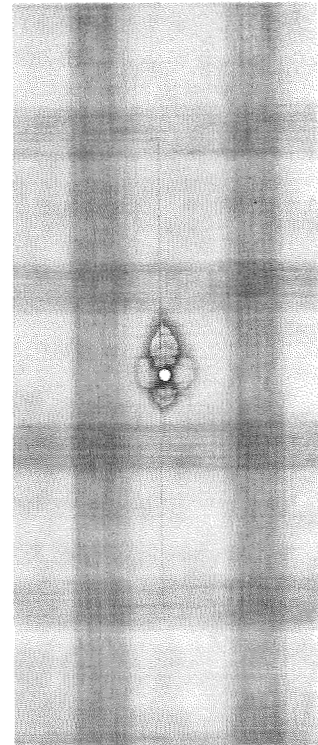
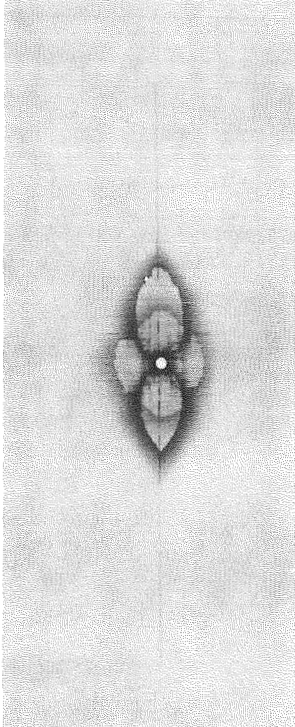
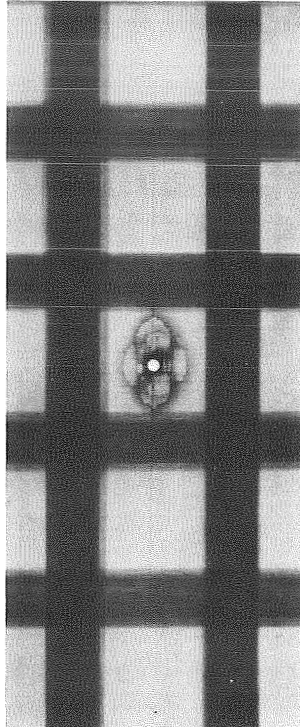


Figure 6a. X-ray photographs of cross-ply specimens impacted with 7/8 inch diameter steel ball. From left to right the specimen types are: plain graphite/epoxy, graphite/epoxy with S2/AF163-2 strips, and graphite/epoxy with AS4/AF163-2 strips.

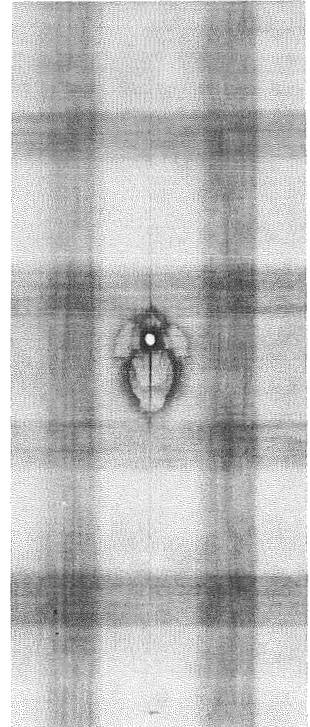
36 ft/sec



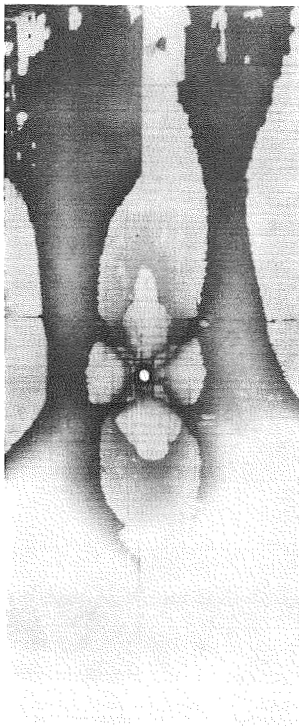
34 ft/sec



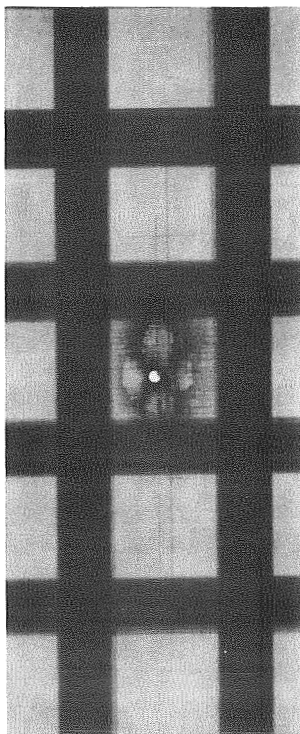
34 ft/sec



53 ft/sec



53 ft/sec



53 ft/sec

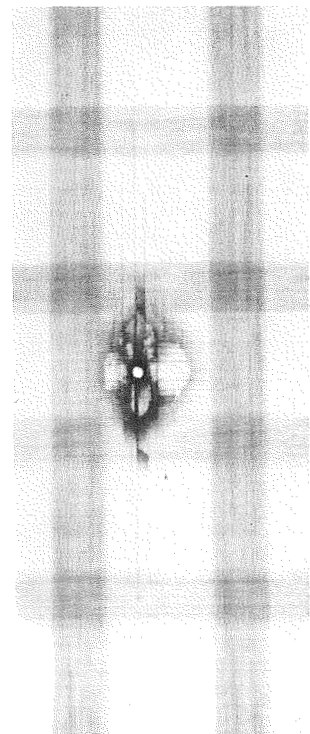
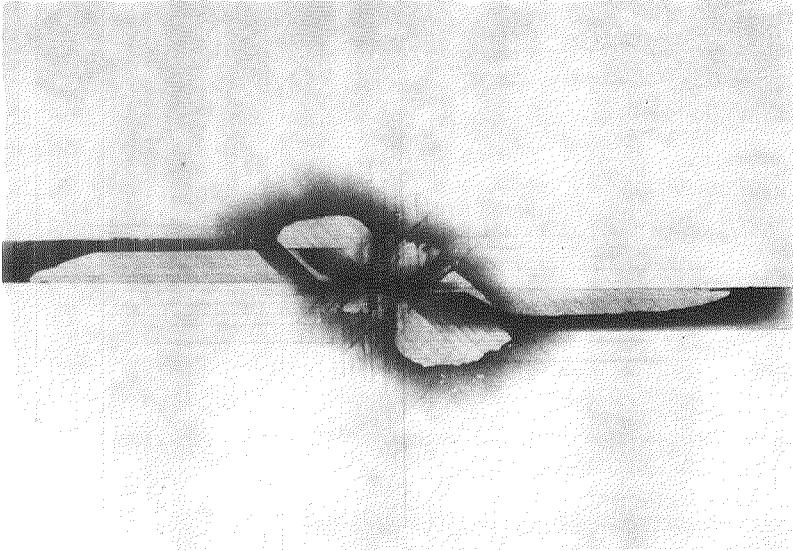
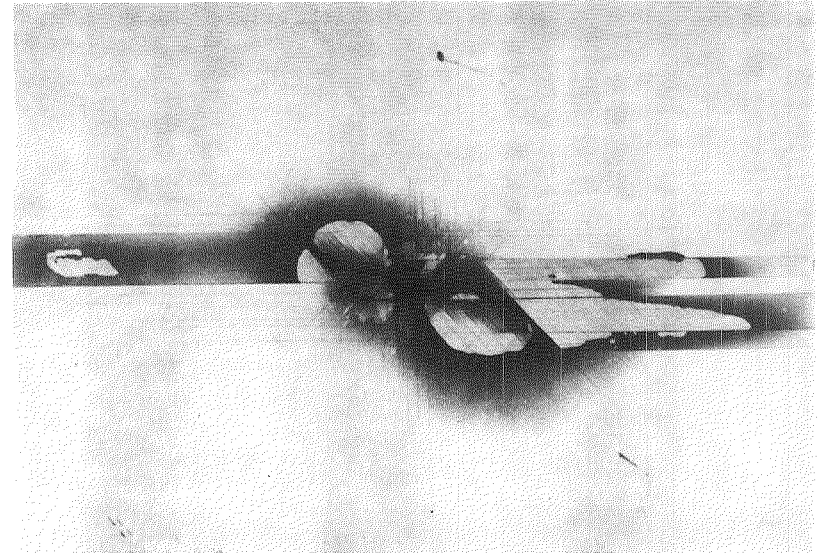


Figure 6b. X-ray photographs of cross-ply specimens impacted with 7/8 inch diameter steel ball. From left to right the specimen types are: plain graphite/epoxy, graphite/epoxy with S2/AF163-2 strips, and graphite/epoxy with AS4/AF163-2 strips.

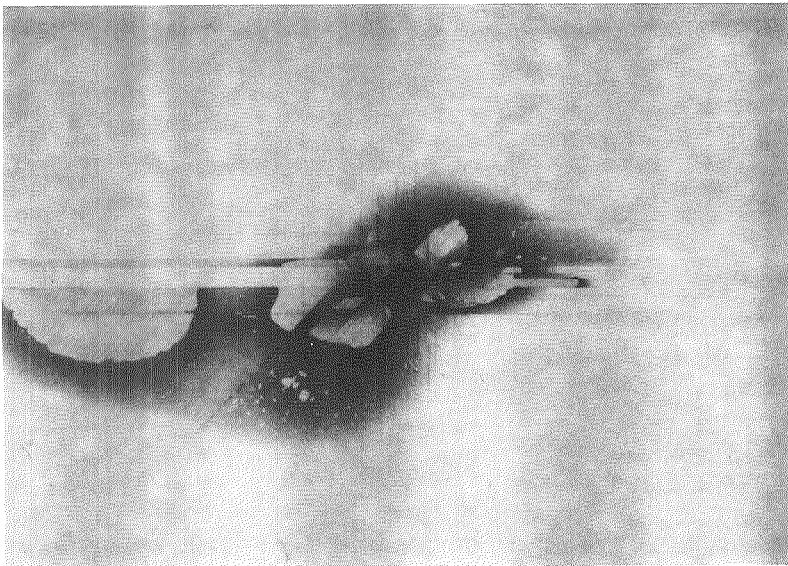
A1



A2



A3



A4

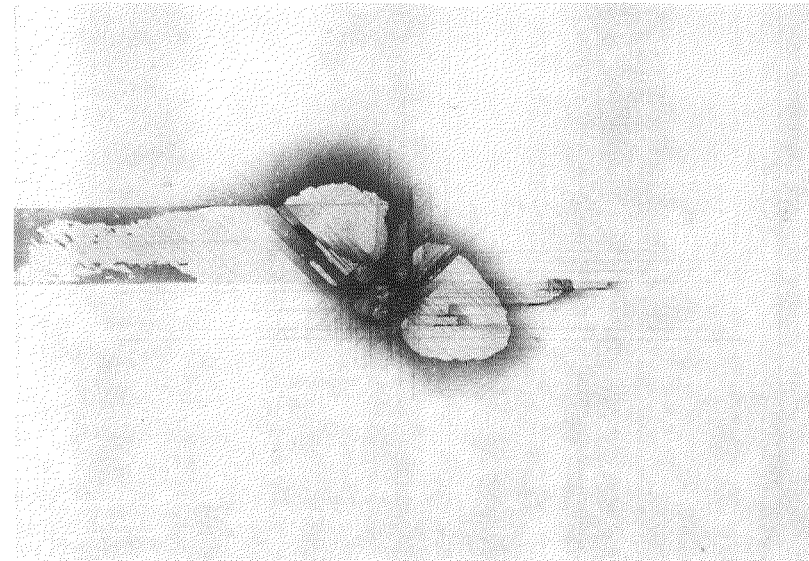
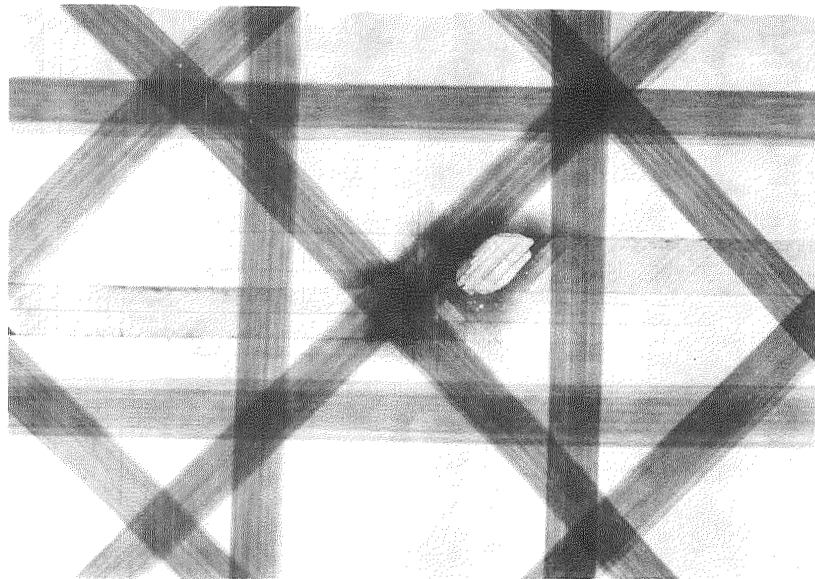
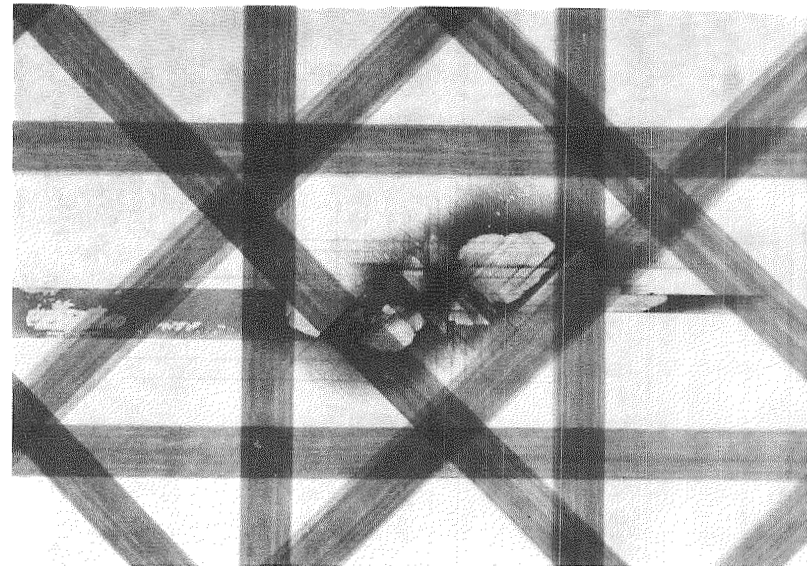


Figure 7a. X-ray photographs of quasi-isotropic specimens impacted at 66 feet per second with a 7/8 inch diameter steel ball. The specimens are plain graphite/epoxy.

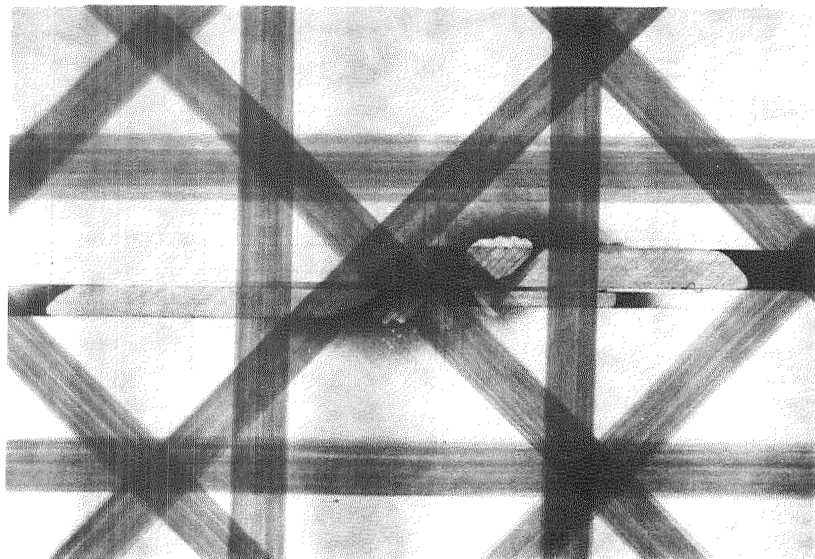
B1



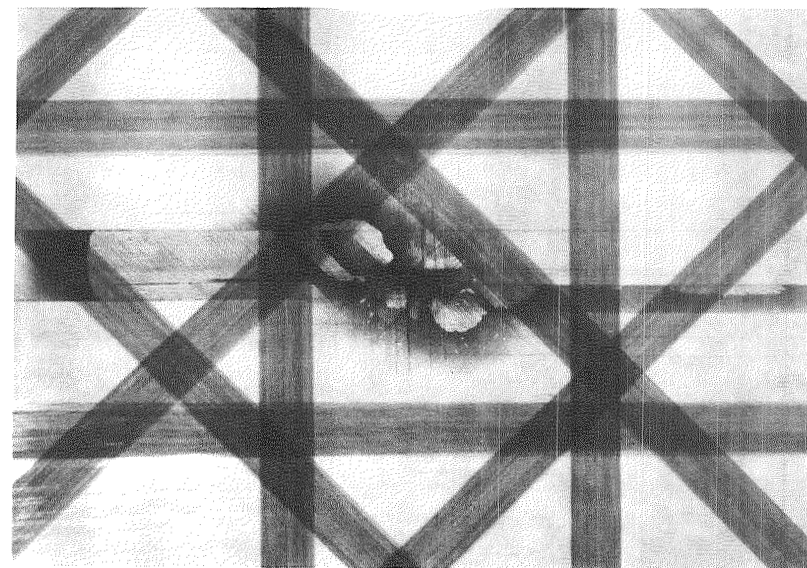
B2



B3



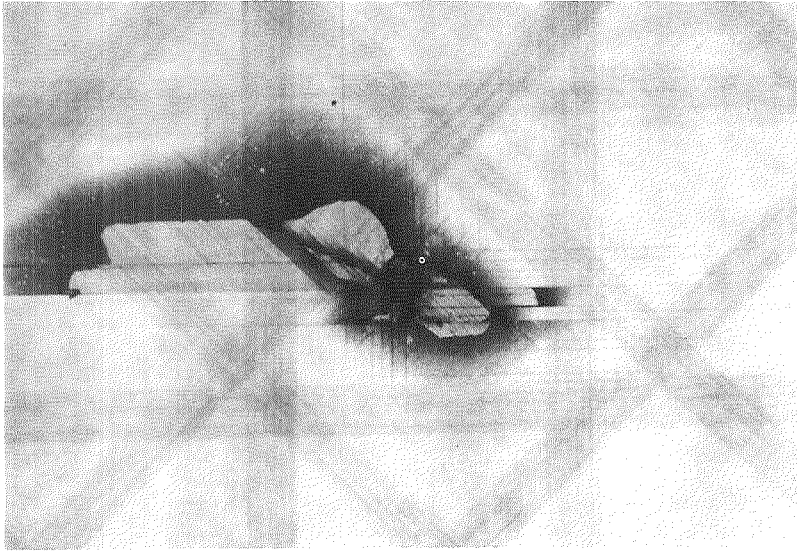
B4



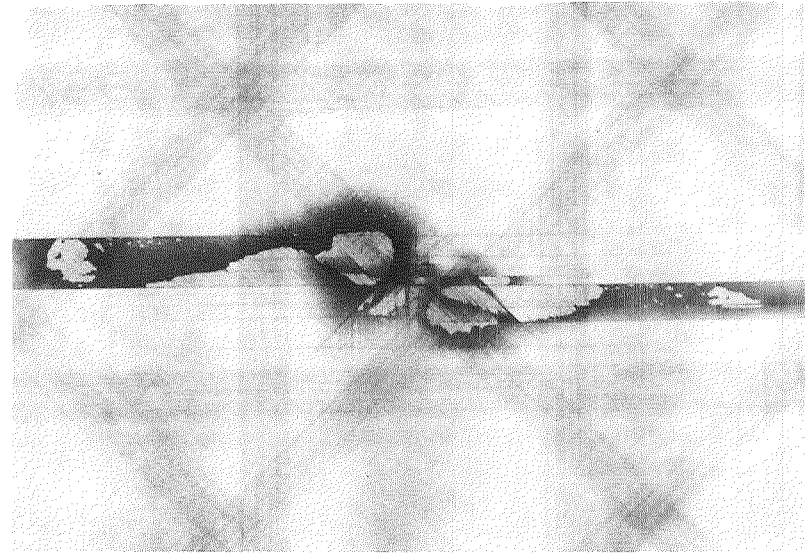
353

Figure 7b. X-ray photographs of quasi-isotropic specimens impacted at 66 feet per second with a 7/8 inch diameter steel ball. The specimens shown here are graphite/epoxy with S2/AF163-2 strips.

C1



C2



C4

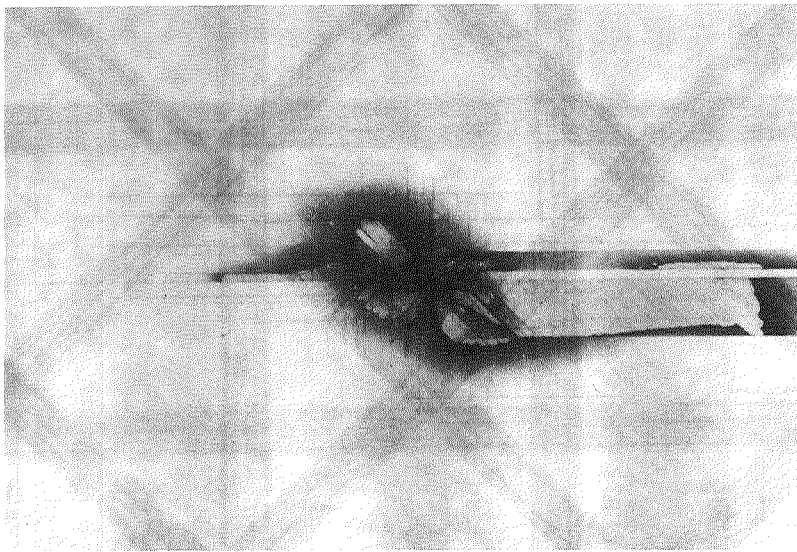
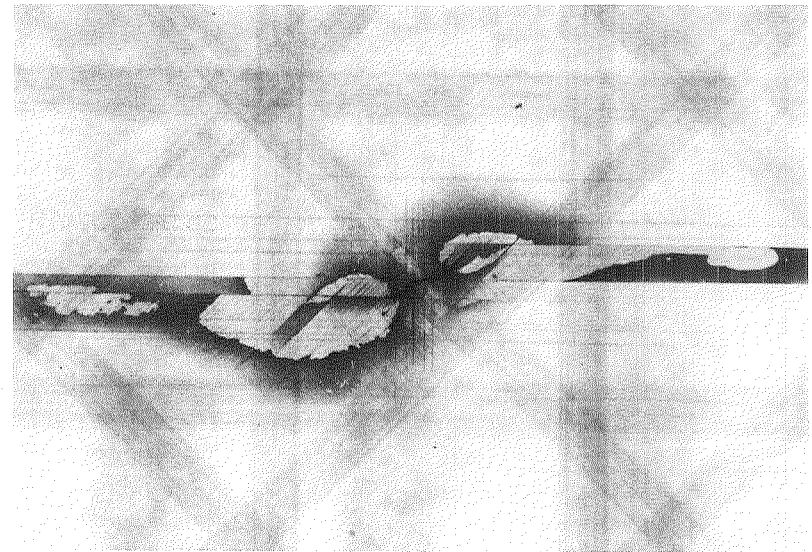
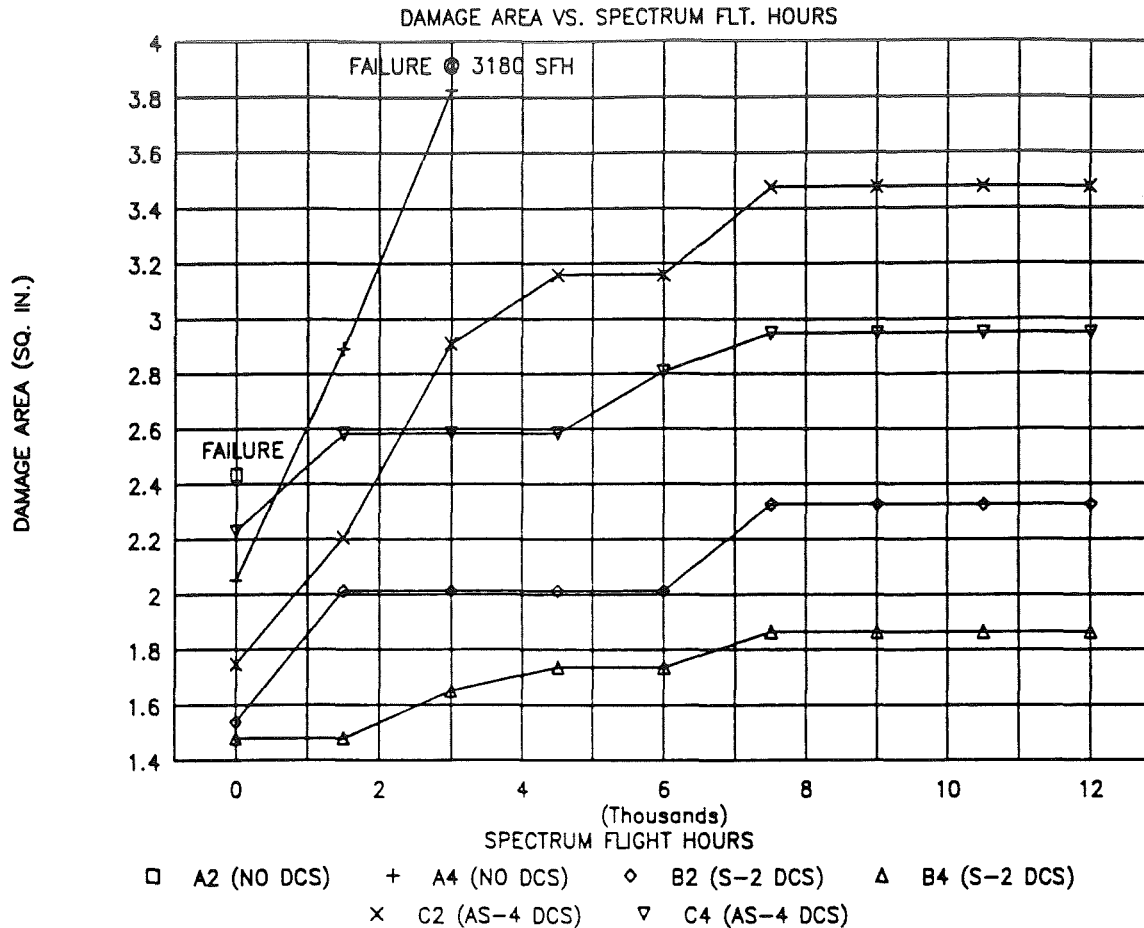


Figure 7c. X-ray photographs of quasi-isotropic specimens impacted at 66 feet per second with a 7/8 inch diameter steel ball.



SPEC. I.D.	MAXIMUM STRAIN ($\mu\text{in/in}$)	DAMAGE AREA (IN ²) @ CUMULATIVE SPECTRUM FLIGHT HOURS									
		0	1500	3000	4500	6000	7500	9000	10500	12000	
A2	N/A	2.434	Failed during initial strain survey to -6000 $\mu\text{in/in}$.								
A4	-4000	2.052	2.893	3.825	Failed at 3180 spectrum flight hours.						
B2	-4000	1.538	2.012	2.012	2.012	2.012	2.325	2.325	2.325	2.325	
B4	-4000	1.480	1.480	1.650	1.737	1.737	1.864	1.864	1.864	1.864	
C2	-4000	1.747	2.206	2.911	3.160	3.160	3.477	3.477	3.477	3.477	
C4	-4000	2.228	2.582	2.582	2.582	2.808	2.948	2.948	2.948	2.948	

NOTE:

1. AREAS WERE MEASURED FROM A-SCAN MYLAR TRACINGS USING CUTOUTS FROM A PAPER COPY TO DETERMINE AREAS BASED ON AREA/WEIGHT RATIOS.
2. FATIGUE TEST SPECTRUM USED WAS THE F/A-18 SPECTRUM WRFT01 WITH A MAX./MIN. OF 131%/-42% TLL WHERE 4735 CYCLES = 300 SFH BLOCK.

Figure 8. Damage growth during spectrum fatigue cycling.

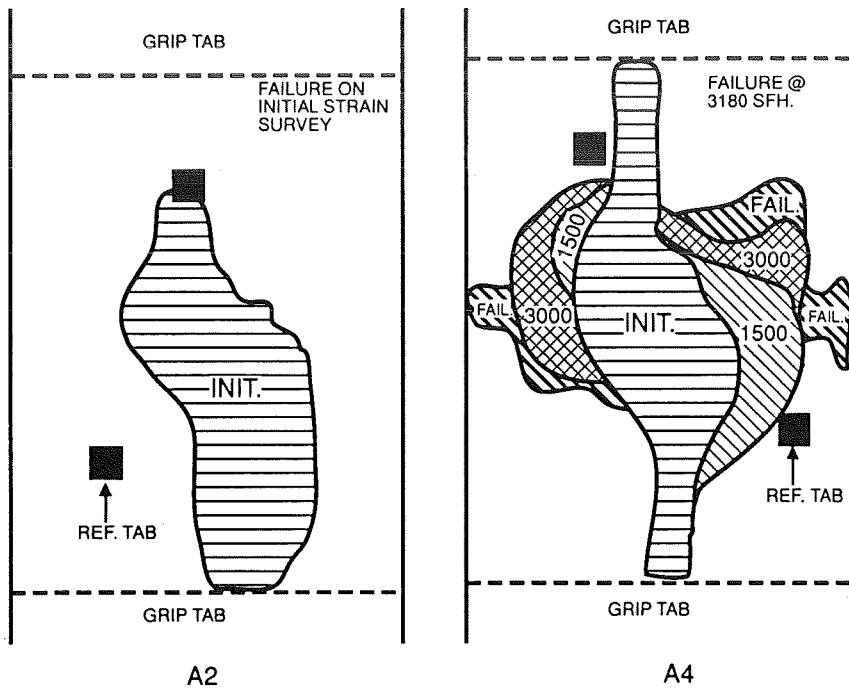


Figure 9. Panels A2 (Left) and A4 not A-scan data.

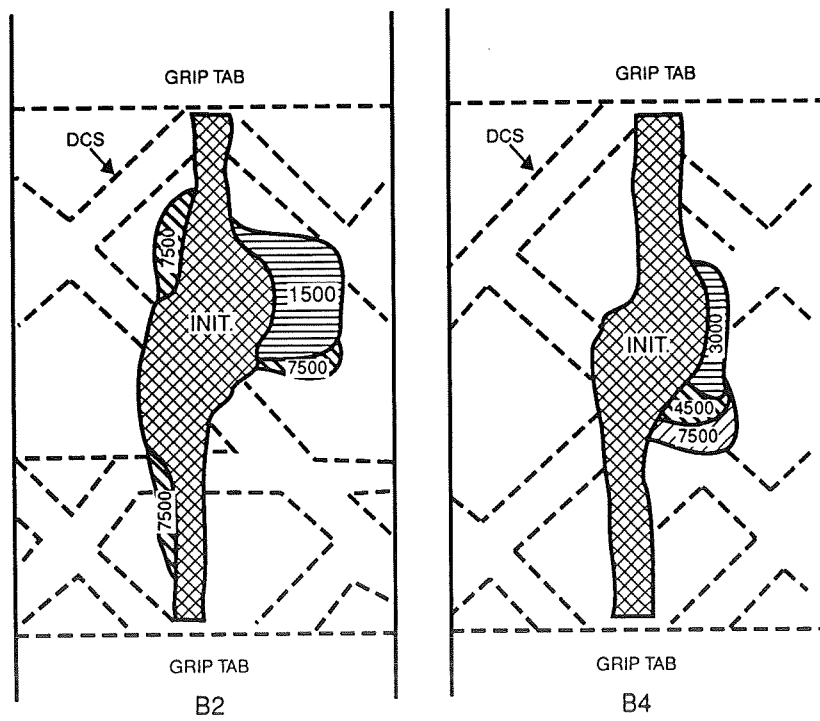


Figure 10. Panels B2 (Left) and B4 NDT A-scan data.

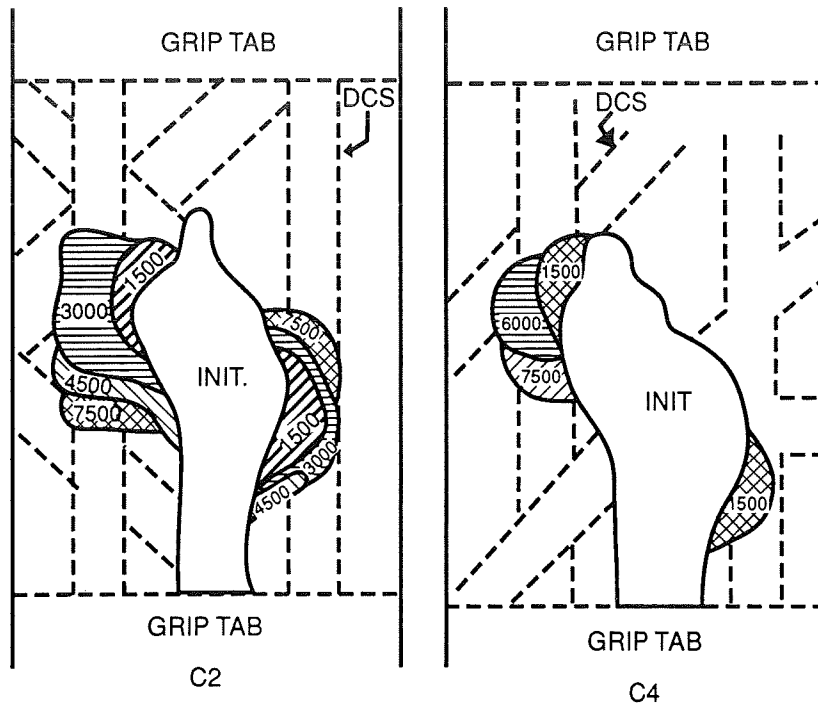


Figure 11. Panels C2 (Left) and C4 NDT A-scan data.

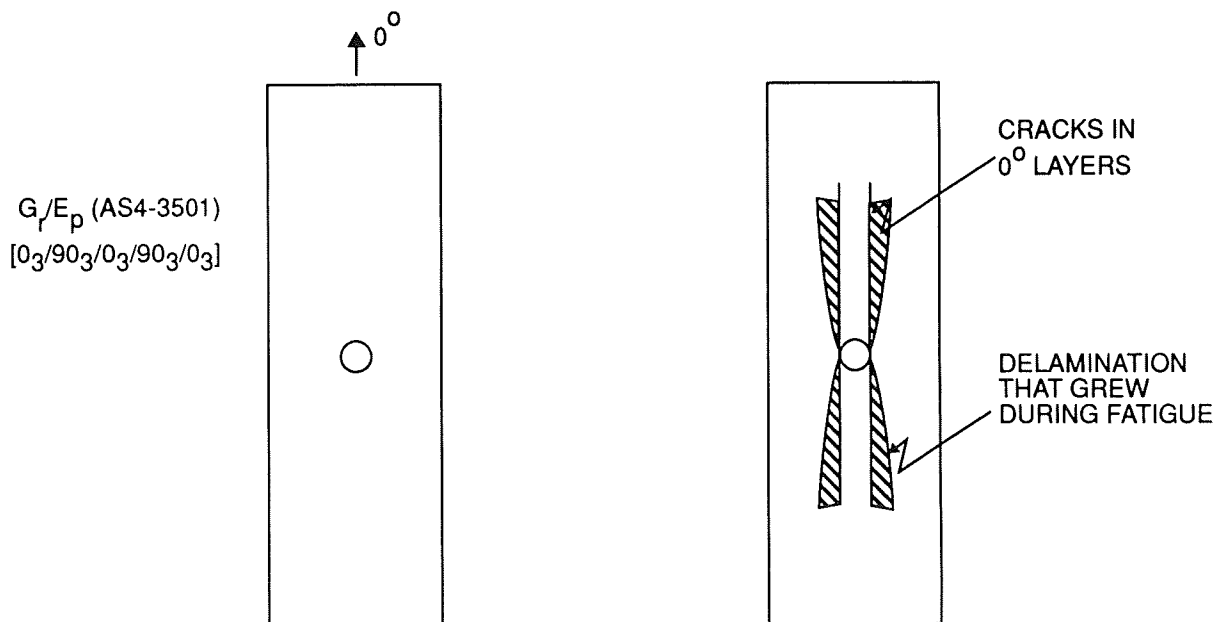


Figure 12. Baseline laminate.

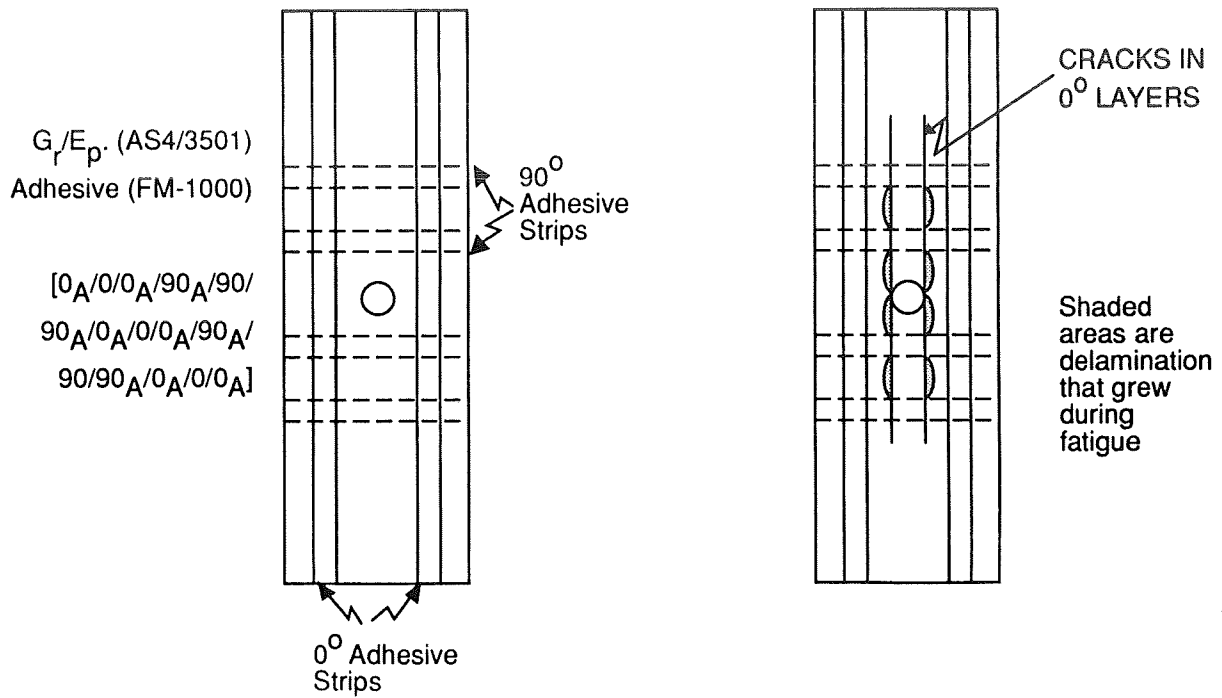


Figure 13. Adhesive strip laminate.

CONTROLLED DAMAGE CONCEPT FATIGUE LIFE

AS4/3501-6 D = 0.25 in

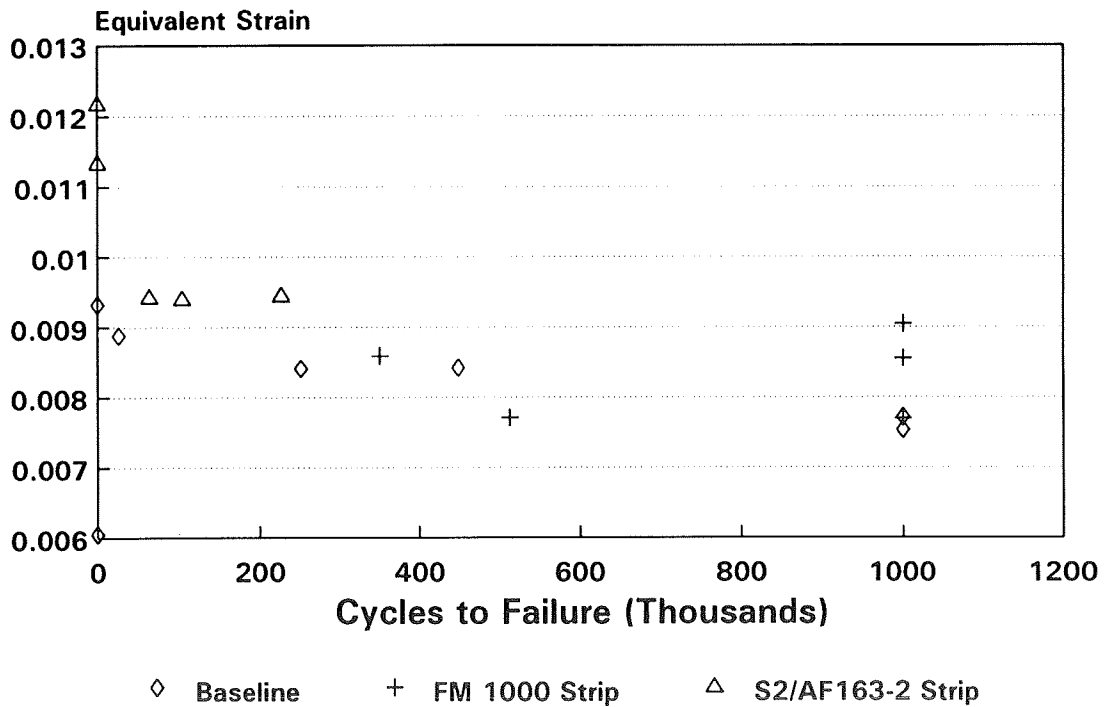


Figure 14. Equivalent strain versus cycles for baseline, adhesive strip laminate and glass-reinforced adhesive strip laminate.

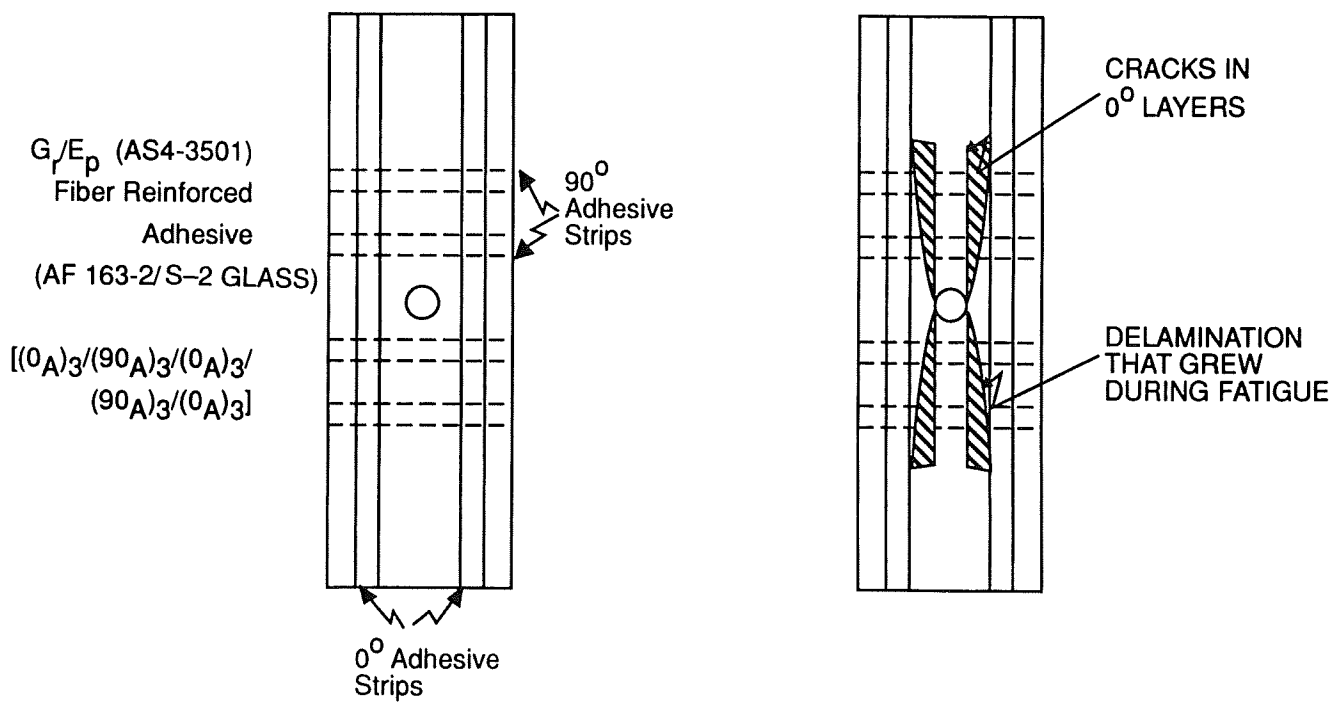


Figure 15. Laminate with fiber reinforced adhesive.

THIS PAGE INTENTIONALLY BLANK

VIBRATIONAL BEHAVIOR OF ADAPTIVE AIRCRAFT WING STRUCTURES
 MODELLED AS COMPOSITE THIN-WALLED BEAMS

O. Song, L. Librescu
 Engineering Science and Mechanics Department
 Virginia Polytechnic Institute and State University
 Blacksburg, VA

C. A. Rogers
 Center for Intelligent Material Systems and Structures
 Virginia Polytechnic Institute and State University
 Blacksburg, VA

515-24
 51384
 P-21

SUMMARY

The vibrational behavior of cantilevered aircraft wings modeled as thin-walled beams and incorporating piezoelectric effects is investigated. Based on the converse piezoelectric effect, the system of piezoelectric actuators conveniently located on the wing yield the control of its associated vertical and lateral bending eigenfrequencies. The possibility revealed by this study enabling one to increase adaptively the eigenfrequencies of thin-walled cantilevered beams could play a significant role in the control of the dynamic response and flutter of wing and rotor blade structures.

INTRODUCTION

The successful development of smart material systems technology [R1] is likely to generate new avenues and concepts toward the design of the next generation of aeronautical and aerospace vehicles. In spite of the complexity and severity of environmental conditions to which these vehicles are likely to be exposed, they must be designed as to be capable to operate safely within their flight envelope, at higher angles of attack, at superior speeds, and without weight penalties. The implementation of smart material systems could play an important role in the design of future advanced space vehicles.

As is well known, in the determination of both the dynamic response to time-dependent excitations and of resonant conditions as well as in the flutter analyses, the natural frequencies are an important physical parameter that intervenes in an explicit way [R2]. For this reason, one of the features of adaptive structural technology applied to aeronautical structures is the ability to conveniently control the eigenfrequencies of the system. In an effort to contribute to this problem, the free vibration analysis of adaptive aircraft wing structures incorporating induced strain actuation [R3,4] will be considered in this paper. The wing structure modelled as a thin-walled beam is assumed to be composed of an induced strain actuator, e.g. a piezoelectric layer superposed on the master structure.

The global constitutive equations associated with a piezoelectric material layer (the induced strain actuator), polarized in the thickness direction and exhibiting transversely isotropic properties, superposed on the thin-walled beam structure also made of a transversely-isotropic material, are derived. These equations, used in conjunction with a generalized Hamilton's variational principle [R5,6], yield the equations governing the motion of cantilevered adaptive

wing structure modelled as a thin-walled beam. Coupling the basic properties of piezoelectric materials (i.e., their actuating capabilities) with a control law, it will be shown that the natural frequencies can be controlled in a known and predictable manner.

BASIC ASSUMPTIONS

The thin-walled beam model used in the present paper is based on the following kinematic statements [R8–12]:

- 1) The original shape of the cross-sections of the beam is preserved.
- 2) The transverse shear flexibility exhibited by the advanced composite material structures is incorporated.
- 3) The non-uniform torsional model is considered. In this respect, the rate of twist assumed to vary along the beam axis constitutes a measure of the warping restraint effect. The primary warping displacement, throughout the cross-section of a beam, is assumed to have a similar distribution as the one associated with the St. Venant (uniform) torsion theory.
- 4) Incorporation of the secondary warping [R9] whose effect for composite material structures could be comparable to the primary warping.
- 5) In addition to these statements of kinematic nature, another one, of a static nature is adopted [R10]. According to this statement, the hoop stress resultant N_{ss} is considered negligibly small with respect to the remaining ones.

Based on the above assumptions, the displacement field can be expressed as [see R7–9]:

$$u(x,y,z) = u_0(z) - y\Theta(z) , \quad (1)$$

$$v(x,y,z) = v_0(z) + x\Theta(z) , \quad (2)$$

$$w(n,s,z) = w_0(z) + x(s)\theta_y(z) + y(s)\theta_x(z) - F_\omega(s)\Theta'(z) + n \left[\frac{dy}{ds} \theta_y(z) - \frac{dx}{ds} \theta_x(z) - a(s)\Theta'(z) \right] , \quad (3)$$

where

$$\theta_y(z) = \gamma_{xz}(z) - u_0'(z) , \quad (4)$$

$$\theta_x(z) = \gamma_{yz}(z) - v_0'(z) , \quad (5)$$

$$a(s) = -y(s) \frac{dy}{ds} - x(s) \frac{dx}{ds} . \quad (6)$$

The warping function is expressed as

$$F_\omega(s) = \int_0^s [\tau_n(s) - \psi] ds , \quad (7)$$

where the torsional function ψ is given by

$$\psi = \frac{\oint_C r_n(s) \frac{ds}{h(s)}}{\oint_C \frac{ds}{h(s)}} \left[\equiv \frac{2A_C}{\beta} \right], \quad (8)$$

and

$$r_n(s) = x(s) \frac{dy}{ds} - y(s) \frac{dx}{ds}. \quad (9)$$

As a result, six kinematic variables $u_0(z)$, $v_0(z)$, $w_0(z)$, $\theta_y(z)$, $\theta_x(z)$, and $\Theta(z)$ representing three translations in the x , y , z directions and three rotations about the y , x , and z axis, respectively, are used to define the displacement vector (i.e., the displacement components u , v , and w in the x , y , and z directions, respectively). Here (s, z, n) and (x, y, z) will be used to denote the surface and cross-section reference coordinate systems, respectively (see F1). The quantity $h[\equiv h(s)]$ denotes the wall thickness of the beam (allowed to vary along the periphery); A_C denotes the cross-sectional area bounded by the mid-line; β denotes the total length of the contour mid-line; $\oint_C (\cdot) ds$ denotes the integral around the entire periphery C of the mid-line cross-section of the

beam; while $\int_0^s r_n(s) ds [\equiv \Omega(s)]$ is referred to as the sectorial area.

Based on the kinematic representations, Eqs. (1)–(6), the strain measures assume the form:

Axial Strain:

$$S_{zz}(n, s, z) = \bar{S}_{zz}(s, z) + n \bar{\bar{S}}_{zz}(s, z), \quad (10)$$

where

$$\bar{S}_{zz}(s, z) = w'_0(z) + \theta'_y(z)x(s) + \theta'_x(z)y(s) - \Theta''(z)F_\omega(s), \quad (11)$$

and

$$\bar{\bar{S}}_{zz}(s, z) = \theta'_y(z) \frac{dy}{ds} - \theta'_x(z) \frac{dx}{ds} - \Theta''(z)a(s),$$

are the axial strains associated with the primary and secondary warping, respectively.

Membrane Shear Strain:

$$S_{sz}(s, z) = [\theta_y(z) + u'_0(z)] \frac{dx}{ds} + [\theta_x(z) + v'_0(z)] \frac{dy}{ds} + 2 \frac{A_C}{\beta} \Theta'(z). \quad (12)$$

Transverse Shear Strain:

$$S_{nz}(s, z) = [\theta_y(z) + u'_0(z)] \frac{dy}{ds} - [\theta_x(z) + v'_0(z)] \frac{dx}{ds}. \quad (13)$$

Within the present theory the warping measure is expressible as

$$W_M = \Theta'(z) . \quad (14)$$

Here, and in the following developments $(\cdot)' \equiv \partial(\cdot)/\partial z$.

PIEZOELECTRIC CONSTITUTIVE EQUATIONS

The linear constitutive equations for a 3-D piezoelectric continuum expressed in the contracted indicial notations are (see e.g., R13,14):

$$\begin{aligned} \sigma_i &= C_{ij}^{\mathcal{E}} S_j - e_{ki} \mathcal{E}_k , \\ D_k &= e_{kj} S_j + \epsilon_{kl}^S \mathcal{E}_l , \end{aligned} \quad (15)$$

where σ_i and S_j ($i, j = \overline{1,6}$) denote the stress and strain components, respectively, where

$$S_j = \begin{cases} S_{pr} & \text{when } p = r, j = 1, 2, 3 \\ 2S_{pr} & \text{when } p \neq r, j = 4, 5, 6 \end{cases}$$

$C_{ij}^{\mathcal{E}}$, e_{ki} , ϵ_{kl}^S are the elastic (measured for conditions of constant electric field), piezoelectric, and dielectric constants (measured under constant strain), while \mathcal{E}_k and D_k ($k = \overline{1,3}$) denote the electric field intensity and electric displacement vector, respectively. In Eqs. (15) the summation over repeated indices is implied. While Eq. (15)₁ describes the **converse** piezoelectric effect (consisting of the generation of mechanical stress or strain when an electric field is applied), Eq. (15)₂ describes the **direct** piezoelectric effect (consisting of generation of an electrical charge when a mechanical force or pressure is applied).

In a piezoelectric adaptive structure the direct effect is used for distributed sensing while the converse effect is used for the active distributed control. Equations (15) are valid for the most general anisotropic case, i.e., for triclinic crystals. In the following, we will restrict the generality to the case of a transversely isotropic continuum, the n -axis being an axis of rotary symmetry coinciding with the direction of polarization (thickness polarization).

In this case the piezoelectric continuum is characterized by 5 independent elastic constants, 3 independent piezoelectric constants and 2 independent dielectric constants. In the following developments, for the sake of simplicity, we will assume that the master structure is constructed from transversely isotropic material layers, the axis of symmetry being parallel to the n -axis.

We will also assume that the electric field vector \mathcal{E}_l is represented in terms of its component \mathcal{E}_3 only, (implying $\mathcal{E}_1 = \mathcal{E}_2 = 0$) and, as a result of the uniform voltage distribution, \mathcal{E}_3 is independent of space (but, possibly on time). In matrix form the constitutive equations are:

$$\begin{bmatrix} \sigma_1 \\ \sigma_2 \\ \sigma_3 \\ \sigma_4 \\ \sigma_5 \\ \sigma_6 \end{bmatrix}_{(k)} = \begin{bmatrix} C_{11} & C_{12} & C_{13} & & & \\ C_{12} & C_{11} & C_{13} & & & 0 \\ C_{13} & C_{13} & C_{33} & & & \\ & & & C_{44} & & \\ & & & & C_{44} & \\ & & & & & \frac{C_{11}-C_{12}}{2} \end{bmatrix}_{(k)} \begin{bmatrix} S_1 \\ S_2 \\ S_3 \\ S_4 \\ S_5 \\ S_6 \end{bmatrix}_{(k)}$$

$$- \begin{bmatrix} 0 & 0 & e_{31} \\ 0 & 0 & e_{31} \\ 0 & 0 & e_{33} \\ 0 & e_{15} & 0 \\ e_{15} & 0 & 0 \\ 0 & 0 & 0 \end{bmatrix}_{(k)} \begin{bmatrix} 0 \\ 0 \\ \xi_3 \end{bmatrix}_{(k)} \quad (16)$$

and

$$\begin{Bmatrix} D_1 \\ D_2 \\ D_3 \end{Bmatrix}_{(k)} = \begin{bmatrix} 0 & 0 & 0 & 0 & e_{15} & 0 \\ 0 & 0 & 0 & e_{15} & 0 & 0 \\ e_{31} & e_{31} & e_{33} & 0 & 0 & 0 \end{bmatrix}_{(k)} \begin{Bmatrix} S_1 \\ S_2 \\ S_3 \\ S_4 \\ S_5 \\ S_6 \end{Bmatrix}_{(k)} \quad (17)$$

$$+ \begin{bmatrix} \epsilon_{11} & 0 & 0 \\ 0 & \epsilon_{11} & 0 \\ 0 & 0 & \epsilon_{33} \end{bmatrix}_{(k)} \begin{bmatrix} 0 \\ 0 \\ \xi_3 \end{bmatrix}_{(k)}$$

where the index k in brackets affecting a quantity identifies its affiliation to the k -th layer.

In terms of the engineering constants the coefficients C_{ij} associated with a transversely-isotropic continuum are expressed as (where for the sake of simplification the

superscript \mathcal{E} was discarded):

$$\begin{aligned}
 C_{11} &= (E\nu'^2 - E')E/\Delta , \\
 C_{12} &= -(E\nu'^2 + E'\nu)E/\Delta , \\
 C_{13} &= -\nu'(1+\nu)EE'/\Delta , \\
 C_{33} &= -(1-\nu^2)E'^2/\Delta , \quad C_{44} = G' , \\
 \frac{C_{11}-C_{12}}{2} &= G(\equiv \frac{E}{2(1+\nu)}) ,
 \end{aligned} \tag{18}$$

where $\Delta = (1+\nu)(2E\nu'^2 + E'\nu - E')$ while E , ν , and E' , ν' denote Young's modulus and Poisson's ratio in the plane of isotropy and transverse to the plane of isotropy, respectively while G' denotes the transverse shear modulus. Equation (16) reveals that a piezoelectric continuum exhibiting anisotropic behavior cannot generate or detect shear stresses/strains by applying or detecting electric fields along the n -direction.

INCORPORATION OF ACTUATOR PATCHES AND ASSOCIATED CONSTITUTIVE EQUATIONS

As was stated earlier, the master structure is composed of layers of elastic materials also exhibiting transversely-isotropic behavior. Their associated constitutive equations could be established formally by discarding the electrical effects in Eq. (16) and Eq. (17).

Suppose that the master structure is composed of such layers, while the actuator (superposed on the master structure) is composed of ℓ piezoelectric layers. We also stipulate that the actuators are distributed over the entire span of the wing (i.e., along the entire spanwise coordinate z), (see F2) while along the circumferential s - and transversal n -directions they are distributed according to the law (see F3):

$$\begin{aligned}
 R_{(k)}(n) &= H(n - n_{(k^-)}) - H(n - n_{(k^+)}) , \\
 R_{(k)}(s) &= H(s - s_{(k^-)}) - H(s - s_{(k^+)}) ,
 \end{aligned} \tag{19}$$

where H denotes Heaviside's distribution and R is a spatial function [R15]. In terms of the coordinates (s, z, n) , related to the beam, the constitutive equations are expressed as

$$\begin{bmatrix} \sigma_{ss} \\ \sigma_{zz} \\ \sigma_{sz} \end{bmatrix}_{(k)} = \begin{bmatrix} C_{11} & C_{12} & 0 \\ C_{12} & C_{11} & 0 \\ 0 & 0 & \frac{C_{11}-C_{12}}{2} \end{bmatrix}_{(k)} \begin{bmatrix} S_{ss} \\ S_{zz} \\ S_{sz} \end{bmatrix}_{(k)} - \begin{bmatrix} e_{31}^{(k)} \xi_3^{(k)} R_{(k)(n)} R_{(k)(s)} \\ e_{31}^{(k)} \xi_3^{(k)} R_{(k)(n)} R_{(k)(s)} \\ 0 \end{bmatrix}$$

and

$$\sigma_{nz}^{(k)} = C_{44}^{(k)} S_{nz}^{(k)} \quad (20)$$

LOCAL BEAM CONSTITUTIVE RELATIONSHIPS

Assume that the master structure is composed of m layers while the actuator part is composed of ℓ layers. As a result, the global beam stress resultants and couples could be obtained through the integration of the 3-D stress components through the laminate thickness and afterwards through the integration of the local stress resultants along the contour of the beam. Invoking the assumption 5), the local beam stress resultants defined in terms of the associated strains are:

Stress Resultants:

$$N_{zz} = \bar{K}_{11} \bar{S}_{zz} + \bar{K}_{11} \bar{S}_{zz} - N_{zz}^a,$$

$$N_{sz} = A_{66} S_{sz},$$

$$N_{nz} = A_{44} S_{nz},$$

(21)

Stress Couples:

$$L_{zz} = \bar{K}_{11} \bar{S}_{zz} + \bar{K}_{11} \bar{S}_{zz} - L_{zz}^a,$$

$$L_{sz} = B_{66} S_{sz}.$$

In these equations K_{ij} denote the modified local stiffness coefficients while N_{zz}^a and L_{zz}^a the piezoelectrically induced stress resultant and stress couple. Their expressions are

$$\bar{K}_{11} = A_{11} - \frac{A_{12}^2}{A_{11}}; \quad \bar{K}_{11} = B_{11} - \frac{B_{12} A_{12}}{A_{11}},$$

$$\equiv K_{11} = D_{11} - \frac{B_{12}^2}{A_{11}} \quad (22)$$

$$N_{zz}^a = \left[1 - \frac{A_{12}}{A_{11}}\right] \sum_{k=1}^{\ell} \xi_3^{(k)} \left[n_{(k^+)} - n_{(k^-)} \right] e_{31}^{(k)} R_{(k)}(s,z) \quad (23)$$

$$L_{zz}^a = \sum_{k=1}^{\ell} \xi_3^{(k)} e_{31}^{(k)} R_{(k)}(s,z) \left[n_{(k^+)} - n_{(k^-)} \right] \left[\frac{1}{2} \left[n_{(k^+)} + n_{(k^-)} \right] - \frac{B_{12}}{A_{11}} \right]$$

whereas

$$A_{ij} = \sum_{k=1}^{m+\ell} C_{ij}^{(k)} \left[n_{(k)} - n_{(k-1)} \right]$$

$$B_{ij} = \frac{1}{2} \sum_{k=1}^{m+\ell} C_{ij}^{(k)} \left[n_{(k)}^2 - n_{(k-1)}^2 \right] \quad (24)$$

$$D_{ij} = \frac{1}{3} \sum_{k=1}^{m+\ell} C_{ij}^{(k)} \left[n_{(k)}^3 - n_{(k-1)}^3 \right]$$

define the stretching, bending–stretching and bending stiffness quantities, respectively. In Eqs. (23), for the sake of brevity the following notation

$$R_{(k)}(s,z) \equiv R_{(k)}(s)R_{(k)}(z) \quad (25)$$

was introduced.

It should be emphasized that the constitutive equations (21) relate the stress resultants and couples with the strain components and the electric field, ξ_3 . The analysis yielding such equations is called uncoupled because an approximate solution to the electrostatic problem is postulated, with the result that ξ_3 is constant.

THE DYNAMIC EQUATIONS OF ADAPTIVE THIN-WALLED BEAMS

In the previous sections the kinematic equations and the local constitutive equations for the considered adaptive structure were derived. In order to obtain the equation of motion of an adaptive TWB and the associated boundary conditions, we will make use of Hamilton's variational principle extended to the case of a linear 3-D piezoelectric medium [R5,6]:

$$\delta \int_{t_0}^{t_1} dt \left[\int_{\tau} \left[\frac{1}{2} \rho \dot{U}_i \dot{U}_i - \mathcal{L} + f_i U_i \right] d\tau + \int_{\Omega} (\bar{\sigma}_k \delta U_k - \bar{\sigma} \delta \phi) d\Omega \right] = 0, \quad (26)$$

where \mathcal{H} denotes the electric enthalpy density defined as:

$$\mathcal{H} = \frac{1}{2} C_{ij}^E S_i S_j - e_{ki} \xi_k S_i - \frac{1}{2} \epsilon_{k\ell}^S \xi_k \xi_\ell, \quad (27)$$

τ and Ω denote the volume and bounding surface of the continuum, respectively; $\bar{\sigma}_k$ denotes the specified surface-traction; $\bar{\sigma}$ the applied surface charge; f_i the body forces; t_0, t_1 denote two arbitrary instants of time; ρ the material density; δ the variation sign, while the overdots denote time derivatives.

Recalling that

$$\frac{\partial \mathcal{H}}{\partial S_i} = \sigma_i \quad \text{and} \quad \frac{\partial \mathcal{H}}{\partial \xi_k} = -D_k, \quad (28)$$

when $\delta f_i = 0$, defining ξ_i in terms of a potential function as

$$\xi_i = -\phi_{,i}, \quad (29)$$

taking the variations in (26) and applying Green's theorem whenever possible, we obtain, by considering the variations δU_i , $\delta \phi$ and $\delta \sigma_i$ as independent and arbitrary, a known version of the fundamental equations of the 3-D linear piezoelectricity theory, namely

$$\left. \begin{aligned} \sigma_{ij,j} + f_i &= \rho \ddot{U}_i \\ D_{i,i} &= 0 \end{aligned} \right\} \text{in } \tau, \quad (30)$$

$$\bar{\sigma}_i = \sigma_{ij} n_j \quad \phi = \bar{\phi} \text{ on } \Omega_s,$$

$$U_i = \bar{U}_i \quad \bar{\sigma} = n_i D_i \text{ on } \Omega_u,$$

are obtained, where n_i denote the components of the normal to Ω . Consideration in Eq. (26) of the displacement components U_i as $u_0, v_0, w_0, \theta_x, \theta_y$, and Θ , and of S_i as the ones defined by Eqs. (10)–(13); employment of $d\tau = dn ds dz$ and performing the integration across the s - and n -directions, the 3-D problem is reduced to an equivalent 1-D one, in which all the quantities are dependent on the z -coordinate only. To this end, the 1-D stress resultants and stress couples specific to the theory of TWBs defined in terms of the local (i.e., 2-D) beam stress-resultants are

$$\begin{aligned} T_z(z) &\equiv \oint_C N_{zz} ds; \quad Q_x(z) = \oint_C \left[N_{sz} \frac{dx}{ds} + N_{zn} \frac{dy}{ds} \right] ds, \\ Q_y(z) &= \oint_C \left[N_{sz} \frac{dy}{ds} - N_{zn} \frac{dx}{ds} \right] ds, \quad M_x(z) = \oint_C \left[y N_{zz} - L_{zz} \frac{dx}{ds} \right] ds, \end{aligned} \quad (31)$$

$$M_y(z) = \oint_C \left[x N_{zz} + L_{zz} \frac{dy}{ds} \right] ds ; M_z(z) = \oint_C N_{sz} \frac{2A_C}{\beta} ds ,$$

and

$$B_\omega(z) = \oint_C [F_\omega(s) N_{zz} + a(s) L_{zz}] ds .$$

These quantities are referred to as the axial and shear forces (in the x and y directions), and the moments (in the x, y and z directions) as well as the bimoment global quantities. In terms of the 1-D stress resultant measures, (Eq. 31), the equations of motion of adaptive TWBs become:

$$\begin{aligned} \delta u_0: \quad Q'_x - I_1 + p_x &= 0 , \\ \delta v_0: \quad Q'_y - I_2 + p_y &= 0 , \\ \delta w_0: \quad T'_z - I_3 + p_z &= 0 , \\ \delta \Theta: \quad B''_\omega + M'_z - (I_4 - I_8') + m_z + b'_\omega &= 0 , \\ \delta \theta_x: \quad M'_x - Q_y - I_5 + m_x &= 0 , \\ \delta \theta_y: \quad M'_y - Q_x - I_7 + m_y &= 0 . \end{aligned} \tag{32}$$

Here p_x , p_y , p_z and m_x , m_y and m_z are the distributed loads and moments in the x, y, and z-directions, respectively; b_ω is the bimoment of the external loads while I_i ($i = \overline{1,8}$) are the inertia terms not displayed in the paper. By virtue of Eqs. (21), (23) and (31) the stress resultant T_z , the stress couples M_x and M_y as well as the bimoment B_ω could be recast in a form in which the actuator effect appears in a separated form, namely

$$\begin{aligned} T_z &= \hat{T}_z - \tilde{T}_z ; \quad M_x = \hat{M}_x - \tilde{M}_x , \\ M_y &= \hat{M}_y - \tilde{M}_y ; \quad B_\omega = \hat{B}_\omega - \tilde{B}_\omega , \end{aligned} \tag{33}$$

where the quantities affected by an overhat ($\hat{\quad}$) and an overtilde ($\tilde{\quad}$) identify the pure mechanical and piezoelectric contributions to the indicated quantities, respectively.

Being concerned in this study with the free vibration problem only, the loading terms occurring in Eqs. (32) may be discarded. From the Hamilton's principle, in addition to the equations of motion (32), the boundary conditions (BCs) are also obtained. For the case of the beam clamped at $z = 0$ and free at $z = L$, the BCs are:

At the clamping edge ($z = 0$):

$$u_0 = \underline{u}_0; v_0 = \underline{v}_0; w_0 = \underline{w}_0; \theta_x = \underline{\theta}_x; \theta_y = \underline{\theta}_y; \Theta = \underline{\Theta}; \Theta' = \underline{\Theta}' \quad (34)$$

and at the free edge ($z = L$):

$$Q_x = \underline{Q}_x; Q_y = \underline{Q}_y; T_z = \underline{T}_z; M_y = \underline{M}_y; M_x = \underline{M}_x, \\ M_z + B'_\omega = \underline{M}_z; B_\omega = \underline{B}_\omega, \quad (35)$$

where the undertilde sign affects the prescribed quantities and where L denotes the length of the beam. It could be verified that consistent with seven boundary conditions at each edge, a fourteenth order governing equation system is obtained.

In the case of the general anisotropy of the layer materials (i.e., of the master structure, of the actuator patches or of both of them), the system of governing equations results in a complete coupled form. However, in the present case of anisotropy, the governing equations obtainable from Eqs. (32)_{1,6} appear decoupled from the ones obtainable from (32)_{2,5} and (32)_{3,4}. In other words, in the present case of anisotropy, the governing system of equations and the associated BCs are splitting exactly into three uncoupled sub-systems. While the first mentioned sub-system of equations governs the lateral bending motion (or in helicopter terminology, the flap-lag motion), the second and the third ones govern the vertical bending and twist motions, respectively.

In this study only the undamped free bending vibration case is studied. The pertinent governing equations for free vibration of thin-walled beams are:

For transverse bending vibrations:

$$a_{55}(v_0'' + \theta_x') + b_1\omega^2 v_0 = 0 \\ a_{33}\theta_x'' - a_{55}(v_0' + \theta_x) + \omega^2(b_4 + b_{14})\theta_x = 0. \quad (36)$$

with the BCs at $z = 0$:

$$v_0 = \theta_x = 0 \quad (37)$$

and at $z = L$:

$$v_0' + \theta_x = 0 \quad \text{and} \quad a_{33}\theta_x' = \tilde{M}_x \quad (38)$$

For lateral bending vibrations:

$$a_{44}(u_0'' + \theta_y') + b_1\omega^2 u_0 = 0 \quad (39)$$

$$a_{22}\theta_y'' - a_{44}(u_o' + \theta_y) + \omega^2(b_5 + b_{15})\theta_y = 0$$

with the BCs at $z = 0$:

$$u_o = \theta_y = 0 \quad (40)$$

and at $z = L$:

$$u_o' + \theta_y = 0 \quad \text{and} \quad a_{22}\theta_y' = \tilde{M}_y. \quad (41)$$

These equations were obtained by considering the following harmonic time-dependence

$$\mathcal{F}(z,t) = \bar{\mathcal{F}}(z)\exp(i\omega t), \quad i = \sqrt{-1} \quad (42)$$

where \mathcal{F} stands for a generic field variable.

Both the governing equations and the associated BCs are expressed in terms of the quantities involving the dependence on the z -coordinate only, i.e., according to Eq. (42) in terms of the barred counterparts of the field variables. However, for the sake of simplicity these overbars have been dropped. The expressions of elastic constants a_{ij} and mass terms b_i

intervening in Eqs. (36) and (39) are not displayed here. In the same equations \tilde{M}_x and \tilde{M}_y denote the piezoelectrically induced moments expressed as:

$$\begin{aligned} \tilde{M}_x = & \oint_C \sum_{k=1}^{\ell} \tilde{\alpha}_3^{(k)} \left[n_{(k^+)} - n_{(k^-)} \right] e_{31}^{(k)} R_{(k)}(s,z) \left[y \left[1 - \frac{A_{12}}{A_{11}} \right] \right. \\ & \left. + \frac{dx}{ds} \frac{B_{12}}{A_{11}} \right] ds - \frac{1}{2} \oint_C \left[\frac{dx}{ds} \sum_{k=1}^{\ell} \tilde{\alpha}_3^{(k)} \left[n_{(k^+)}^2 - n_{(k^-)}^2 \right] e_{31}^{(k)} R_{(k)}(s,z) \right] ds, \end{aligned} \quad (43)$$

$$\begin{aligned} \tilde{M}_y = & \oint_C \sum_{k=1}^{\ell} \tilde{\alpha}_3^{(k)} \left[n_{(k^+)} - n_{(k^-)} \right] e_{31}^{(k)} R_{(k)}(s,z) \left[x \left[1 - \frac{A_{12}}{A_{11}} \right] \frac{dy}{ds} \frac{B_{12}}{A_{11}} \right] ds \\ & + \frac{1}{2} \oint_C \left[\frac{dy}{ds} \sum_{k=1}^{\ell} \tilde{\alpha}_3^{(k)} \left[n_{(k^+)}^2 - n_{(k^-)}^2 \right] e_{31}^{(k)} R_{(k)}(s,t) \right] ds \end{aligned}$$

For the case of the symmetrically located actuators across the thickness of the beam structure, the terms affected by a solid line in Eqs. (43) vanish. In light of the actuator configuration, it may be inferred that the expressions (43) are independent on the z -coordinate. This explains why their contribution in the governing equations is immaterial and why in the BCs they intervene as nonhomogeneous terms.

THE CONTROL LAW

The adaptive nature of the wing (or rotor blade) structure is introduced by requiring the applied electric field \mathcal{E}_3 to be dependent to one of the mechanical quantities of the structure in motion. With this in mind, a number of control laws could be implemented. Their efficiency may be measured by their ability to modify as much as possible the natural frequencies of the structure with respect to the energy input. In the present considerations, two control laws were considered.

The two independent control laws require that: i) the applied electric field \mathcal{E}_3 is proportional to the vertical or lateral bending moments at the wing root, $\hat{M}_x(o)$ or $\hat{M}_y(o)$, depending on whether the control of the natural frequencies is associated with the vertical or lateral motion, respectively and ii) the applied electric field \mathcal{E}_3 is proportional to the vertical ($v_o(L)$) or lateral ($u_o(L)$) deflections of the beam tip, depending on the two directions of vibrations whose frequencies are to be controlled. In light of these control approaches, we may formulate the following control laws (labelled as CL1 and CL2) by involving also the boundary conditions given in expression (38) and (41).

CL1)

a) Associated with the vertical bending

$$\theta'_x(L) = K_p \theta'_x(o) \quad (44)$$

b) Associated with the lateral bending

$$\theta'_y(L) = K_p \theta'_y(o) \quad (45)$$

CL2)

a) Associated with the vertical bending

$$\theta'_x(L) = \bar{K}_p v_o(L) \quad (46)$$

b) Associated with the lateral bending

$$\theta'_y(L) = \bar{K}_p u_o(L) \quad (47)$$

As can be seen from Eqs. (44)–(47), the feedback gains \bar{K}_p and K_p are dimensional and nondimensional, respectively. The nondimensional counterpart of \bar{K}_p is \check{K}_p defined as $\check{K}_p = \bar{K}_p L^2$.

These control laws express the fact that the control bending moments at the wing tip (induced by the piezoelectric strain) should be proportional as per the CL1 to the mechanical bending moments at the wing root, and within the CL2 to the transversal or lateral deflections at the wing tip.

NUMERICAL ILLUSTRATIONS AND DISCUSSION

The adaptive wing is modelled as a symmetric composite box-beam. In order to control the vertical bending frequencies, the piezoceramic actuator layers (selected to be of PZT-4 ceramic) are located on the upper and bottom surfaces of the master structure only, while in order to control the lateral bending frequencies the piezoceramic layers are located on the lateral walls of the master structure. The geometrical characteristics (restricted to the former situation, only) are displayed in F2 while the constants characterizing the PZT-4 piezoceramic (see [R16]) are:

$$\begin{aligned}
 C_{11} &= 2.016 \times 10^7 \text{ psi}; & C_{12} &= 1.128 \times 10^7 \text{ psi} \\
 C_{13} &= 1.0776 \times 10^7 \text{ psi}; & C_{33} &= 1.6679 \times 10^7 \text{ psi} \\
 C_{44} &= 3.7128 \times 10^6 \text{ psi}; \\
 e_{31} &= -0.0297 \text{ lb/inV}; & e_{33} &= 0.08623 \text{ lb/inV} \\
 e_{15} &= 0.07252 \text{ lb/inV}.
 \end{aligned}$$

For the sake of simplicity assume that the master structure is composed of a transversely-isotropic material whose elastic characteristics are identical to the piezoceramic actuator layers.

By using the exact approach devised in [R17-19] and extended afterwards in [R7-9], the eigenvalue problems associated with the vertical and lateral vibrations of TWBs yield the variation of the nondimensional eigenfrequencies $\tilde{\omega}$ vs. the feedback gains K_p and \check{K}_p .

In F4-7, by using the control law CL1, the variation of the first four eigenfrequencies associated with the vertical bending vs. the feedback gain was diagrammatically represented, while in F8 and 9, by using the control law CL2, the variation of the vertical (plunging) and lateral bending fundamental frequencies $\tilde{\omega}$ vs. the feedback gain \check{K}_p was obtained. F4-7 reveal that within control law CL1 the increase of the odd eigenfrequencies occurs for negative feedback gains while the increase of the even eigenfrequencies requires implementation of positive feedback gains. F8 and 9 (as well as the results obtained, but not displayed in the paper) reveal that within control law CL2 the increase of the eigenfrequencies occurs generally for positive feedback gains. Within a CL2 type control a similar trend was also obtained in R20.

It should be pointed out that in all diagrams, F4-9, the frequencies were normalized with respect to the ones corresponding to the non-adaptive structure (for which case $K_p = 0$).

Having in view that, roughly speaking, $\omega \sim D^{1/2} \sim h^{3/2}$, where D and h are the associated bending rigidity and thickness of the beam, we could infer that the linear increase of eigenfrequencies would have been accomplished without the help of this adaptive technology through an unaffordable weight penalty. The obtained results reveal, once again, the great importance of the implementation of adaptive technology applied to the control of the material frequencies of the structure. In short, the obtained results reveal that by using the adaptive properties of the structure it is possible to increase the eigenfrequencies of the system and consequently to modify in a beneficial way the dynamic response characteristics of the structure, whose role in the present case could be played by an aircraft wing or a rotor blade structure.

ACKNOWLEDGEMENT

The partial support of this work by the Office of Naval Research (ONR/DARPA Grant N00014-88-0721) is gratefully acknowledged.

REFERENCES

1. Rogers, C. A., "An Introduction to Intelligent Material Systems and Structures," in Intelligent Structures, pp. 3-41, (Eds. Chong, K. P., Liu, S. C. and Li, J. C.), Elsevier Applied Science, London and New York, 1990.
2. Librescu, L., Elastostatics and Kinetics of Anisotropic and Heterogeneous Shell-Type Structures, Noordhoff International Publ., The Netherlands, 1975.
3. Wang, B.-T. and Rogers, C. A., "Laminate Plate Theory for Spatially Distributed Induced Strain Actuators," Journal of Composite Materials, Vol. 25, No. 4, April 1991, pp. 433-452.
4. Wang, B.-T. and Rogers, C. A., "Modeling of Finite-Length Spatially-Distributed Induced Strain Actuators for Laminate Beams and Plates," Journal of Intelligent Material Systems and Structures, Vol. 2, No. 1, January 1991, pp. 38-58.
5. Tiersten, H. F., Linear Piezoelectric Plate Vibrations, Plenum Press, New York, 1969.
6. Lee, P. C. Y. and Haynes, D. W., "Piezoelectric Crystals and Electro-Elasticity," R. D. Mindlin and Applied Mechanics, (Ed. G. Hermann), Pergamon Press, 1977, pp. 227-253.
7. Librescu, L. and Song, O., "Static Aeroelastic Tailoring of Composite Aircraft Swept Wings Modelled as Thin-Walled Beam Structures," in "Achievements in Composites in Japan and the United States," Ed. A. Kobayashi, Fifth Japan-U.S. Conference on Composite Materials, Tokyo, Japan, June 24-27, 1990, pp. 141-149.
8. Librescu, L. and Song, O., "Behavior of Thin-Walled Beams Made of Advanced Composite Materials and Incorporating Non-Classical Effects," in "Mechanics Pan-America", 1991, Applied Mechanics Review, Eds. R.A. Kitte and D.T. Mook, Vol. 44, No. 11, Part 2, Nov. 1991, pp. 174-180.
9. Song, O. and Librescu, L., "Free Vibration and Aeroelastic Divergence of Aircraft Wings Modelled as Composite Thin-Walled Beams," The 32nd SDM Conference, Paper AIAA 91-1187, 1991.

10. Rehfield, L. W., Atilgan, A. R. and Hodges, D. H., "Nonclassical Behavior of Thin-Walled Composite Beams," Journal of the American Helicopter Society, Vol. 35, No. 2, April, 1990, pp. 42-50.
11. Gjelsvik, A., The Theory of Thin-Walled Bars, John Wiley & Sons, New York, 1981.
12. Rehfield, L. W., "Design Analysis Methodology for Composite Rotor Blades," Proceedings of the Seventh DoD/NASA Conference on Fibrous Composites in Structural Design, AFWAL-TR-85-3094, June, 1985, pp. v(a)-1) - v(a)-15).
13. Mason, W. P., Crystal Physics of Interaction Processes, Academic Press, New York and London, 1966.
14. IEEE Standard on Piezoelectricity, IEEE Std. 176-1978, The Institute of Electrical and Electronics Engineers, Inc., 1978.
15. Wang, B.-T. and Rogers, C. A., "Laminate Plate Theory for Spatially Distributed Induced Strain Actuators," in "Achievements in Composites in Japan and the United States," A. Kobayashi, Ed., Fifth Japan-U.S. Conference on Composite Materials, Tokyo, Japan, June 24-27, 1990, pp. 595-607.
16. Berlincourt, D. A., Curran, D. R., and Jaffe, H., "Piezoelectric and Piezomagnetic Materials and Their Function in Transducers," Physical Acoustics - Principles and Methods, (Ed. W. P. Mason), Vol. 1, Part A, Academic Press, New York and London, 1964, pp. 169-270.
17. Librescu, L. and Thangjitham, S., "The Static Aeroelastic Behavior of Sweptforward Composite Wing Structures Taking Into Account Their Warping Restraint Effect," Proceedings of the Fourth Japan-U.S. Conference on Composite Materials, Washington, D.C., June 24-27, 1988, pp. 914-922.
18. Librescu, L. and Thangjitham, S., "The Warping Restraint Effect in the Critical and Subcritical Static Aeroelastic Behavior of Swept-Forward Composite Wing Structures," 1989 SAE, General Aviation Aircraft Meeting and Exposition, Century II, Wichita, Kansas, April 11-13, 1989, Paper 891056.
19. Librescu, L. and Thangjitham, S., "Analytical Studies on Static Aeroelastic Behavior of Forward-Swept Composite Wing Structures," Journal of Aircraft, Vol. 28, 2, pp. 151-157, 1991.
20. Tzou, H.S. and Zhong, J.R., "Adaptive Piezoelectric Shell Structures: Theory and Experiments," AIAA Paper 91-1238-CP, 32nd AIAA SDM Conference, Baltimore, Maryland, April 8-12, 1991.

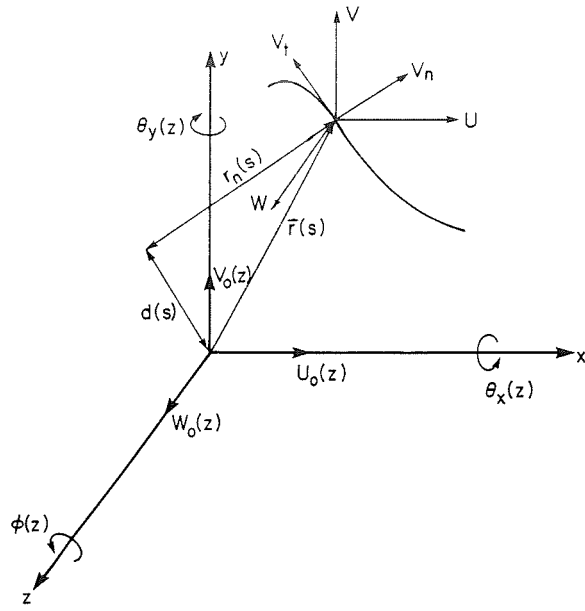


Fig. 1 Coordinate systems and Kinematic variables.

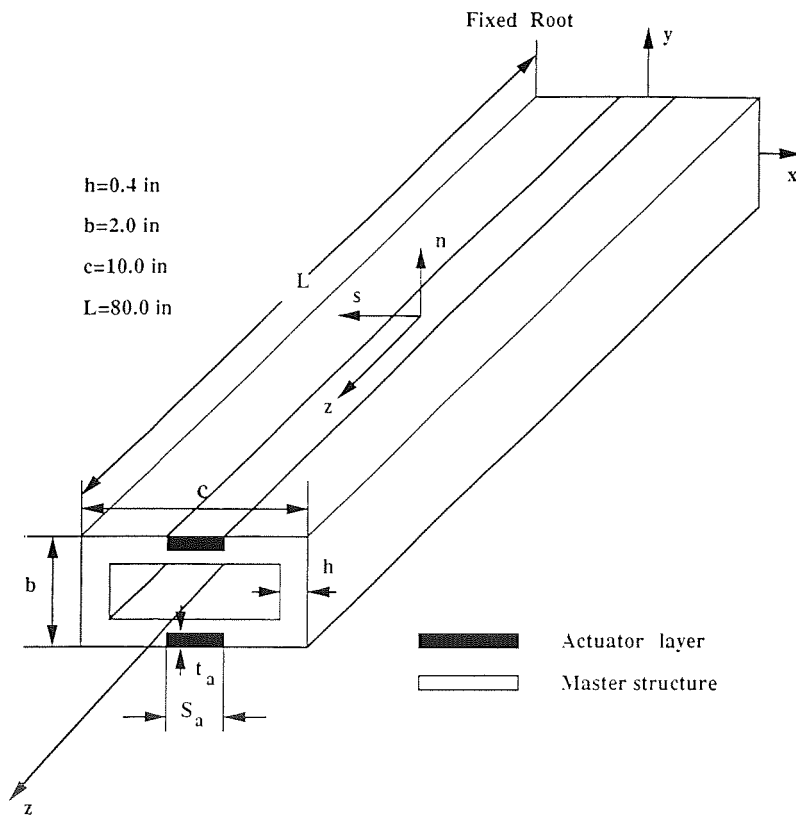


Fig. 2 Geometry of box beam (not scaled).

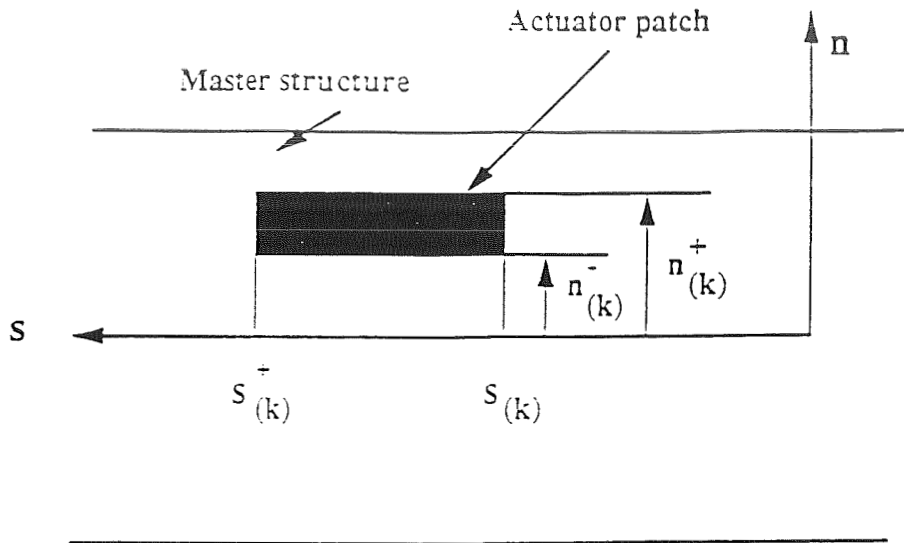


Fig. 3 Actuator patch.

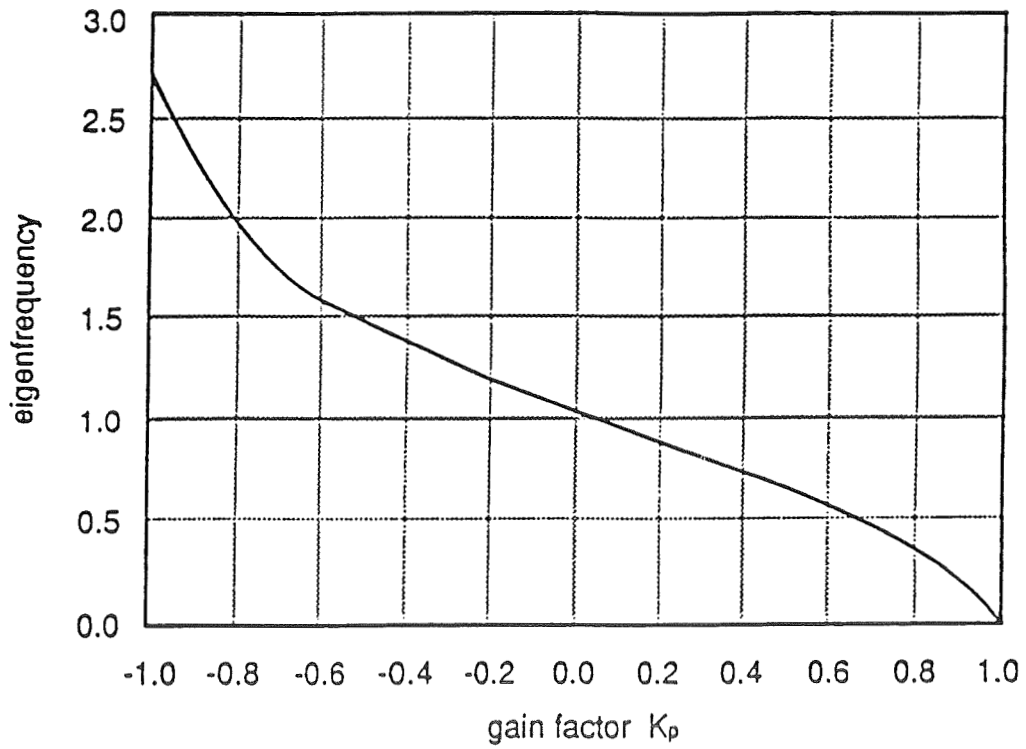


Fig. 4 Variation of the normalized plunging eigenfrequency vs. the control gain (first mode and first control law).

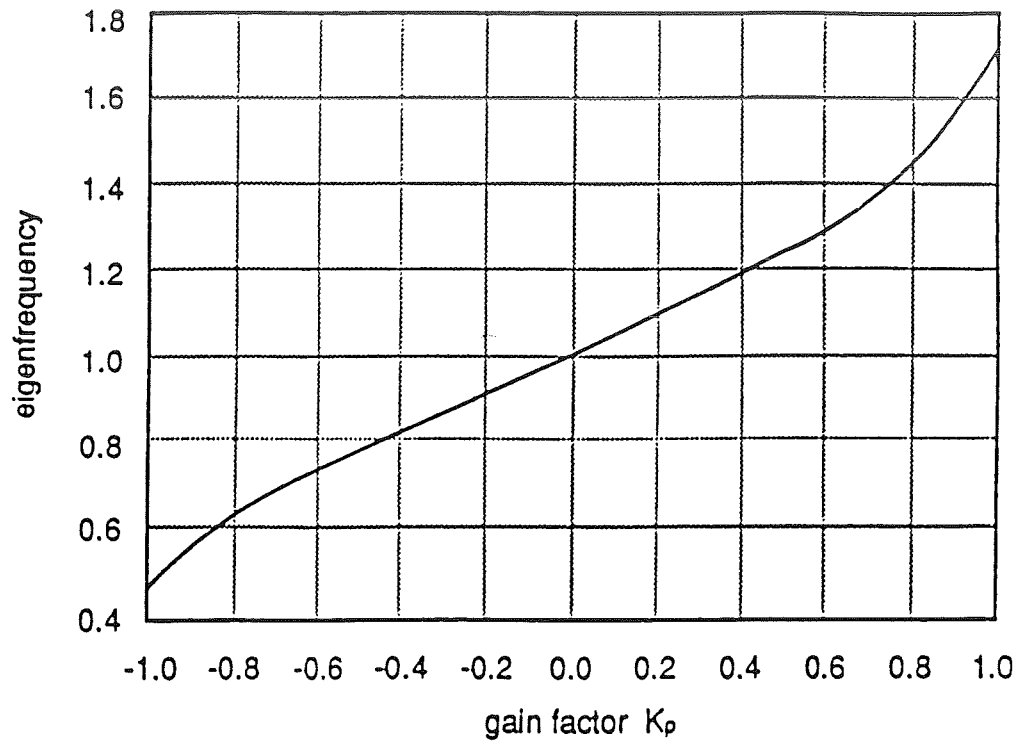


Fig. 5 Variation of the normalized plunging eigenfrequency vs. the control gain (second mode and first control law).

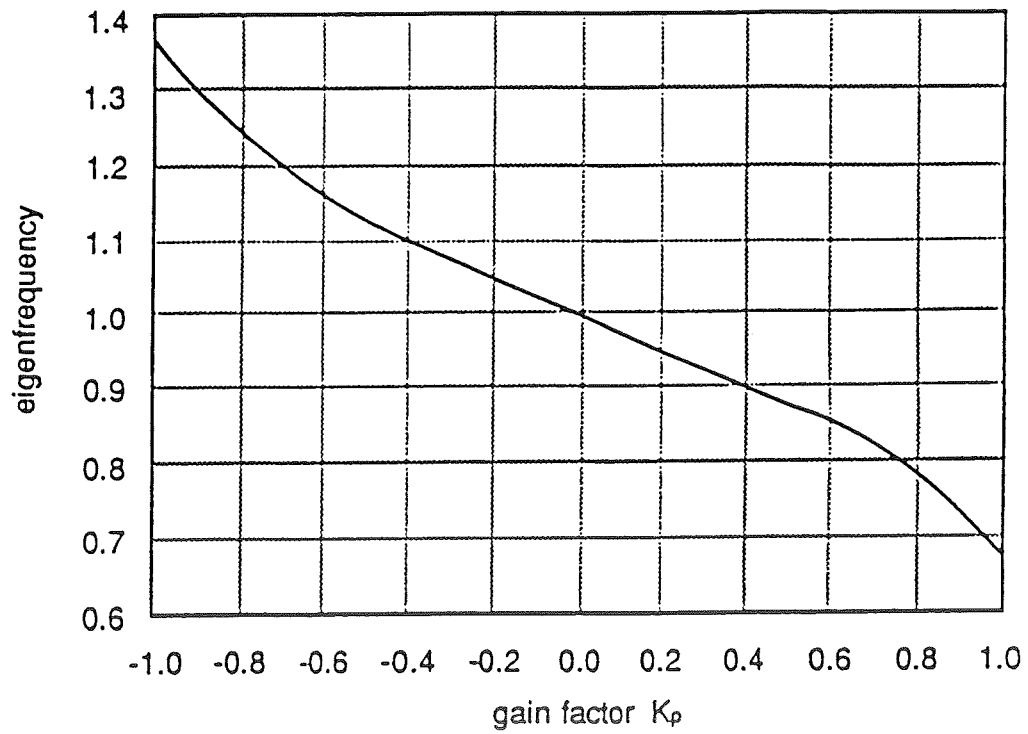


Fig. 6 Variation of the normalized plunging eigenfrequency vs. the control gain (third mode and first control law).

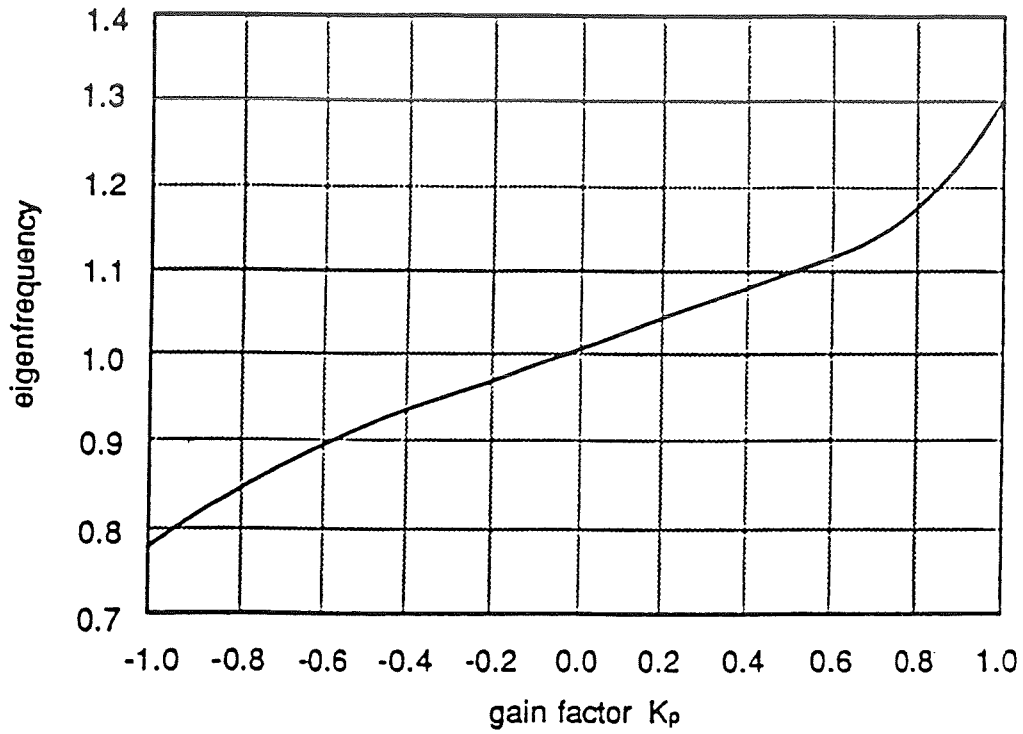


Fig. 7 Variation of the normalized plunging eigenfrequency vs. the control gain (fourth mode and first control law).

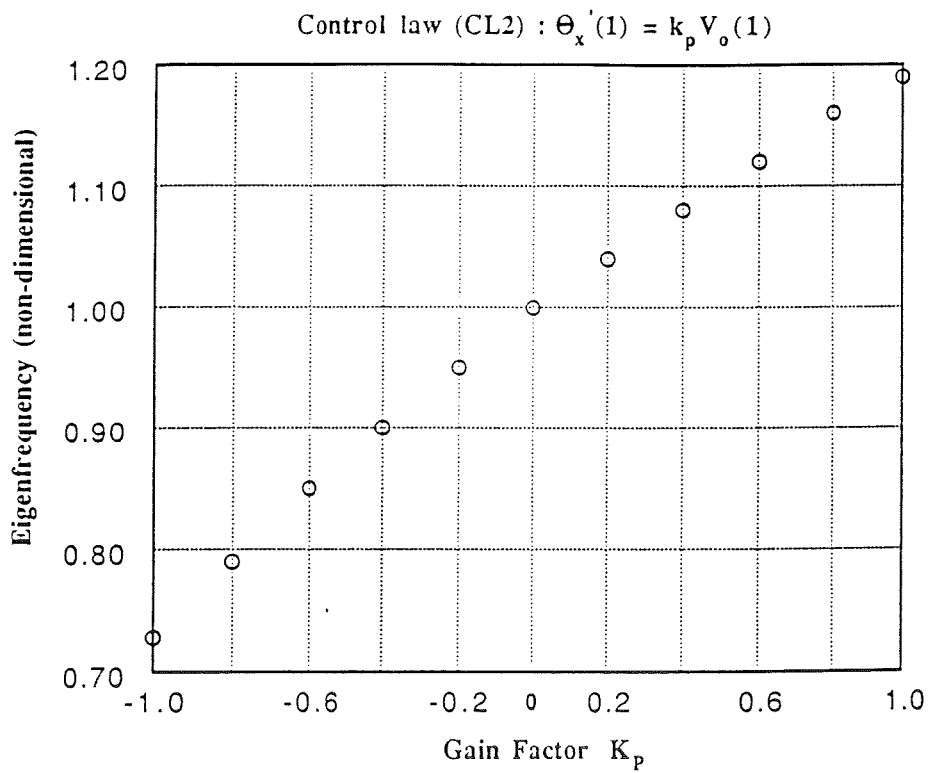


Fig. 8 Variation of the normalized plunging eigenfrequency vs. the control gain (first mode and second control law).

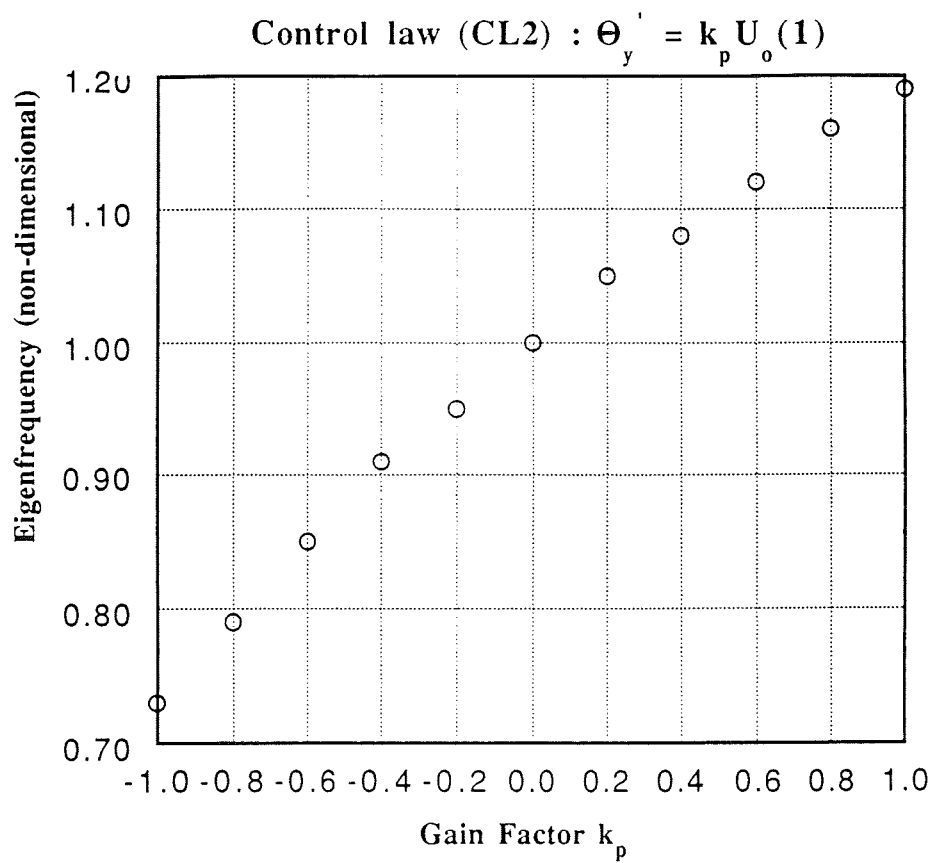


Fig. 9 Variation of the normalized lateral bending eigenfrequency vs. the control gain (first mode and second control law)

THIS PAGE INTENTIONALLY BLANK

**UNIQUE CONSIDERATIONS IN THE
DESIGN AND EXPERIMENTAL
EVALUATION OF TAILORED WINGS WITH
ELASTICALLY PRODUCED CHORDWISE CAMBER**

Lawrence W. Rehfield, Peter J. Zischka,
Michael L. Fentress and Stephen Chang

University of California, Davis

516-24
51384
p18

SUMMARY

In this paper, some of the unique considerations that are associated with the design and experimental evaluation of chordwise deformable wing structures are addressed. Since chordwise elastic camber deformations are desired and must be free to develop, traditional rib concepts and experimental methodology cannot be used. New rib design concepts are presented and discussed. An experimental methodology based upon the use of a flexible sling support and load application system has been created and utilized to evaluate a model box beam experimentally.

Experimental data correlate extremely well with design analysis predictions based upon a beam model for the global properties of camber compliance and spanwise bending compliance. Local strain measurements exhibit trends in agreement with intuition and theory but depart slightly from theoretical perfection based upon beam-like behavior alone. It is conjectured that some additional refinement of experimental technique is needed to explain or eliminate these (minor) departures from asymmetric behavior of upper and lower box cover strains. Overall, a solid basis for the design of box structures based upon the bending method of elastic camber production has been confirmed by the experiments.

INTRODUCTION

Elastic tailoring refers to the utilization of the design flexibility of composites to achieve performance goals. The goals are usually accomplished by selecting an appropriate structural concept, fiber orientation, ply stacking sequence and a blend of materials. In aeronautical applications, emphasis has been given to tailoring deformations which influence the aerodynamics of the system (ref. 1). This is called "aeroelastic tailoring." Aeroelastic instabilities may be avoided in this manner (ref. 1), as in the X-29, or performance enhancements, such as increased lift (refs. 2, 3) or maximizing lift-to-drag ratio (ref. 1), can be achieved.

Early work in aeroelastic tailoring focused on simple laminated construction of plate-like, rather low aspect ratio lifting surfaces. The design procedures are described in ref. 4 in the following manner:

"The design for a desired static aeroelastic response was initially an iterative process performed by a structural engineer trying to satisfy a requirement for twist and camber established by an aerodynamicist."

Since that time, considerable progress has been made, including the effective use of optimization algorithms (refs. 1,4). Emphasis, however, seems to have been given always to tailoring specific configurations to specific missions, a practice that did not foster scientific understanding or permit a firm grasp of the cause-effect relationship between configuration and response. In contrast to this approach, our research breaks with the past and focuses upon understanding, modeling, tailoring mechanisms and creating design concepts that accentuate individual behavioral characteristics.

Interest in swept forward wings, which resulted in the X-29, focused attention on wing bending and twisting deformations. As these deformation modes are understood rather well now, our research has emphasized elastically produced chordwise camber. While camber deformations have been tailored by ad hoc methods for specific configurations (ref. 4), it remained to create the basis for scientific understanding of behavior and design concepts which accentuate this deformation mode.

Structural tailoring concepts have been developed to create wings with elastically produced camber for the purpose of increasing the lift generated by the wing. Currently, the usual means of accomplishing this is with controls, the most common of which are flaps. If natural, intrinsic means are used to enhance lift, then flap requirements and their associated systems may be reduced. This will yield weight savings, acquisition cost savings and maintenance cost savings. The desired effects are presented in figure 1.

The fundamental mechanisms that are utilized produce camber deformations in response to the usual loading of the wing such as bending moments and torque. The camber enhances the production of lift and further modifies the loads. Significant lift increases may be produced by tailoring using modern composite material systems (refs. 2,3). An overview of this research is given in ref. 2.

There are several general concepts that have been used in our tailoring work. They are illustrated in figures 2 and 3. The continuous filament grid stiffened structures (figure 3) are particularly useful for tailoring response.

In this paper, we address two issues that are unique to chordwise deformable wings. Since chordwise elastic camber deformations are desired and must be free to develop, traditional rib concepts and experimental methodology cannot be used. We present and discuss new rib design concepts and an experimental methodology based upon the use of a flexible sling support and load application system. Experimental data are shown to be in excellent agreement with design analysis predictions for the bending method of producing elastic chordwise camber.

The cornerstone of elastic tailoring with composites is modeling. We selected the well established thin-walled beam theory (refs. 5-7) to serve as a basis for our models of high aspect ratio wings, appropriately modified to predict chordwise camber deformations (refs. 2,3). An established body of knowledge appears in refs. (2,3,8-12). Of particular importance is the correlation shown between the beam model and extensive finite element simulations for the bending case (refs. 8,12).

RIB CONCEPTS FOR CHORDWISE DEFORMABLE WINGS

Along with the development of elastically tailored chordwise deformable wings, it is necessary to design a compatible rib structure that allows the chordwise deformation to occur while still performing some of the traditional functions of a rib. A traditional rib is designed to: 1) preserve the cross section geometry, 2) distribute pressure loads to the spars and stiffeners, 3) support the wing covers, and 4) serve as attachment locations for system equipment. The new chordwise deformable rib still transfers pressure loads and provides cover support, but it must allow the cross section geometry to camber. Five new rib design concepts appear in figures 4-8.

Figure 4 shows the Vertical Column Support type of rib structure. This style of rib is attractive because it is easily joined to the proposed grid stiffening structure of the wing box (refs. 2,3,8-10). Due to the method of constructing the grid structure, convenient points of attachment for the columns are created. To minimize the restraint of the rib on chordwise deformation, it is proposed to use universal joints to attach the columns to the grid. The grid structure needs to be sized such that the columns can be placed at the proper spanwise intervals so that they support the covers against general instability buckling modes.

The Accordion Rib, unlike the column supports, provides continuous chordwise support to the covers while still allowing differential expansion of the upper and lower structural wing box covers. The Accordion Rib looks much like the pleated portion of an accordion. The pleats will conform to the grid structure as shown in figure 5.

The Diagonal Rib Structures, figures 6 and 7, consist of diagonal columns fastened to the grid structure like the Vertical Columns via universal joints. Figure 6 shows the Segmented Diagonal Columns jointed at their intersection while figure 7, Crossed Diagonal Columns, shows no midsection joint.

The Floating Rib Structure, figure 8, is constructed of crossed diagonal ribs with one end fastened with a universal joint and the other free to float. The floating end rests on an abrasion pad that attaches to the upper and lower wing covers.

A detailed design analysis is required for sizing the individual elements in these configurations. These suggestions should prove useful as technology for chordwise deformable wings advances.

EXPERIMENTAL METHODOLOGY

Attention is restricted to the bending method (refs. 2,3,8-10,12) of creating elastically produced chordwise camber deformation. This method produces an intentionally exaggerated form of anticlastic chordwise curvature, which is a natural tendency in response to spanwise bending. The key to successfully using this approach is to create large effective Poisson's ratios in the wing box covers while preserving the essential integrity of the box cross section.

The "best" test to perform in order to evaluate and validate camber production experimentally is a four-point bending test. This test method creates a gage section in the specimen that is exposed to a pure spanwise bending moment only, a simple state of loading that isolates the desired effect of anticlastic curvature. The challenge, of course, is to create a way of performing the test that utilizes methods of load application and support that permit chordwise camber deformations to freely occur.

Test Specimen Design

The box beam test specimen (figure 9) has been designed with three factors in mind. First, due to the dimensions of our PHI laminating press, the box covers are limited to a maximum length of twenty inches. The cover layup is taken to be $[\pm 26]$ in keeping with our optimized design without stiffeners (refs. 2,3,12). Second, to prevent the covers from buckling under the four point bending loading, a cover width of four inches and a thickness of twelve plies has been selected. This also is in concert with the third factor, which is to produce easily measurable strain levels.

To prevent the covers from buckling, it is necessary to predict the buckling load of the box beam covers. The bending stiffness of the beam was determined using the cross sectional geometry of the box and material properties of the laminate and aluminum channel. Two methods have been used to calculate the buckling load of the box covers and the results compare well with each other. The properties of AS4/3501-6 graphite-epoxy have been used in the design analysis (refs. 2,3,12) for the covers.

The first method used was to derive the buckling equations for an orthotropic plate with two fixed opposing ends and two simply supported opposing ends. A closed form solution for a buckling problem with these boundary conditions does not exist, so the commercially available numerical solution program "Theorist" was used to solve for the determinant of the buckling equation. This solution yields a buckling load of 1,016 lbs, which in turn relates to a strain level of $1,565\mu\epsilon$. The second method used was to

determine the ratio of buckling loads for a simply supported isotropic plate to that of a fixed-fixed, simply supported isotropic plate with the same aspect ratio. This factor was then used to determine the buckling load of the orthotropic fixed-fixed simply supported plate from that of a simply supported on all sides orthotropic plate. The resulting buckling load and strain level were determined to be 1,102 lbs. and 1,701 $\mu\epsilon$, respectively. Thus, in view of the approximate nature of the second method, the results compare rather well.

Experimental Methodology

A number of possible approaches for performing the four-point bending tests were devised and thoroughly evaluated. With the help of Dr. Damodar Ambur of the NASA Langley Research Center, the "Sling Supported Method" was selected for implementation. Figure 10 illustrates this approach in schematic form. An attractive feature of this method is the fact that the entire assembly is placed in the hydraulic grips of our 75 kip MTS universal testing machine and pulled in tension. The flexible slings of nylon strap material are used to both support the test specimen and apply the four-point loading. This concept would seem to provide minimal resistance to the elastically produced camber deformations.

In addition to testing the wing box, a series of component and coupon tests and a detailed finite element analysis of the fixtures were performed. Measured property data on coupon tests were used for correlating the test results with theory in the second method of camber correlation, which is discussed subsequently.

All specimen response measurements were made with resistance strain gages. While displacement measurements would have been useful, the floating nature of the test setup makes them extremely inconvenient and potentially unreliable. A diagram showing the strain gage nomenclature and locations appears in figure 11.

RESULTS AND DISCUSSION

Basic Strain Gage Data

Strain gage data appear in figures 12-14 as functions of applied bending moment. Figure 12 shows data from the chordwise strain gages. The zero reference line is provided because, in a theoretically perfect test, the top and bottom gage readings should be symmetrically located about this reference line.

Data from the two spanwise centrally located gages appear in figure 13. Again the zero reference line is provided. Ideally, the two gages should read the opposite of each other.

Data from the two outer or remote spanwise gages mounted on the bottom surface are presented in figure 14. These data were used, together with turnbuckle adjustments, to balance out the load application system with a small amount of preload applied. Theoretically, if the test conditions were ideal, the data from these two gages would be identical. This would correspond to perfect four-point bending conditions.

The above test results suggest that the objectives of the experiment were met, and the behavior reflected is as anticipated. They must be regarded as preliminary, however, as we believe that a further developed testing technique may produce results in closer agreement with "theoretical perfection."

Of particular interest is the ability of the structure to produce global chordwise camber curvature. This capability was optimized for the box covers with the $[\pm 26]$ ply layup for AS4/3501-6 graphite-epoxy (refs. 2,3,12). Several basic relations are needed to interpret the measured data.

Elementary Mechanics Model

The first relationship involves the spanwise curvature and membrane strains in the box. Let "1" denote the spanwise direction and "2" the normal chordwise direction. If the usual Bernoulli-Euler assumption, which is valid under pure bending, is adopted, we can write

$$\kappa_{11} = \text{Spanwise Curvature} = (\epsilon_{11}^{\ell} - \epsilon_{11}^u) / (H+h) \quad (1)$$

where κ_{11} is the spanwise curvature, ϵ_{11} is the spanwise membrane extensional strain, H is the thickness or depth of the box, h is the cover thickness and the subscripts " ℓ " and " u " refer to the lower and upper covers of the box, respectively.

The second relation provides the elastic law relating spanwise curvature and bending moment. It is, in the notation of ref. 5,

$$\kappa_{11} = S_{55} M_y \quad (2)$$

The spanwise bending moment is M_y , and S_{55} is the spanwise bending compliance. It is related to the stiffness, C_{55} , as follows (ref. 5):

$$S_{55} = (C_{55})^{-1} \quad (3)$$

and

$$\begin{aligned} C_{55} &= \text{Spanwise Bending Stiffness} \\ &= 2c_s K_{11} \left(\frac{H}{2}\right)^2 + 2(EI)_c \end{aligned} \quad (4)$$

In equation (4), c_s denotes the structural chord or width of the box. $(EI)_c$ is the bending stiffness of the aluminum closure channel (figure 9) about a chordwise parallel axis, and K_{11} is the spanwise extensional stiffness of the box covers. It is shown in ref. 5 that

$$K_{11} = A_{11} - (A_{12})^2 / A_{22} \quad (5)$$

where the A_{ij} ($i, j = 1, 2, 6$) are membrane stiffnesses from lamination theory.

For balanced cover configurations and uniaxial stress conditions (ref. 5)

$$\epsilon_{22} = - (A_{12} / A_{22}) \epsilon_{11} \quad (6)$$

The ratio (A_{12} / A_{22}) is an effective Poisson ratio for the laminated covers.

From classical Bernoulli-Euler bending theory

$$\begin{aligned} \kappa_{22} &\equiv \kappa_c, \text{ the Camber Curvature} \\ &= (A_{12} / A_{22}) \kappa_{11} \end{aligned} \quad (7a)$$

$$= (A_{12} / A_{22}) S_{55} M_y \quad (7b)$$

$$= (\epsilon_{22}^u - \epsilon_{22}^{\ell}) / (H+h) \quad (7c)$$

Eq. (7c) is analogous to eq. (1), and ϵ_{22} is the chordwise extensional membrane strain. Consequently, we define the camber bending compliance such that

$$\kappa_c = S_{c5} M_y \quad (8)$$

and the camber compliance is

$$S_{c5} = (A_{12}/A_{22}) S_{55} \quad (9)$$

Camber Correlation

The most desirable way to correlate theory and experiment is to use measured properties on the actual test specimen itself in the theoretical calculations. This is because there is batch-to-batch variation in composite materials themselves and some amount of variation from part-to-part due to processing. This is normal for composite structures and is accounted for in design by the allowable properties that are used in the design analysis. Our purposes here, however, are to evaluate (1) actual versus theoretical elastic camber production, (2) the suitability of the test methodology and (3) the validity of the model that has been created for use in design analysis. With these objectives in mind, our correlation study proceeded in a direct manner along two paths.

The first path or method is based upon using the experimentally determined spanwise bending compliance as the primary cover load-bearing elastic characteristic. This compliance is readily determined from the plot of experimental data shown in figure 15. This figure is based upon the use of eqs. (1) and (2). The measured spanwise bending compliance, S_{55} , together with the theoretical value of the effective Poisson ratio of 1.26 (refs. 2,3) and eq. (9), permits an estimate of the camber compliance to be calculated. This value is compared with the experimentally determined one obtained from figure 16 in table 1. The "experimental" value is based upon eqs. (7c) and (8).

While the agreement reflected in table 1 is excellent, another way of interpreting this information is that (A_{12}/A_{22}) can be found experimentally from measured compliances (figures 15,16) and eq. (9). This yields an effective Poisson ratio of 1.27, which is in good agreement with the value assumed in the design analysis (1.26). If the cover spanwise membrane stiffness K_{11} is back calculated from the experimentally determined spanwise bending compliance, known dimensions and properties of the closure channels, a value of 0.41×10^6 lb/in is obtained.

The second path or method utilizes a completely theoretical calculation with a value of K_{11} of 0.52×10^6 lb/in obtained from the test of a coupon specimen from another $[\pm 26]_{3S}$ laminate. The correlation of spanwise bending compliance appears in table 2. Camber compliance correlation is presented in table 3. Agreement is considered quite good by this method, so this data, together with that of table 1, confirms that the box beam behaves in a global manner consistent with the beam-like model of ref. 5.

CONCLUDING REMARKS

In this paper, we have addressed the unique considerations that are associated with the design and experimental evaluation of chordwise deformable wing structures. Since chordwise elastic camber deformations are desired and must be free to develop, traditional rib concepts and experimental methodology cannot be used. New rib design concepts are presented and discussed. An experimental methodology based upon the use of a flexible sling support and load application system has been created and utilized to evaluate a model box beam experimentally.

Experimental data correlates extremely well with design analysis predictions based upon a beam-like model for the global properties of camber compliance and spanwise bending compliance. Local strain measurements exhibit trends in agreement with intuition but which depart slightly from theoretical perfection in terms of upper and lower cover asymmetry. Additional work on the experiment technique is needed to help establish the cause for this (minor) departure from beam-like local behavior. Overall, a solid basis for the design of box structures based upon the bending method of elastic camber production has been confirmed by the experiments.

We wish to record our frustration at a drawback to experimental composite structures research in a university environment. Needed materials are required only in small quantities and are, therefore, difficult to obtain if prudent resource management is exercised. For example, our original test specimen design was based upon the use of standard aluminum channels that are 0.75 inches high and composite covers made of AS4/3501-6 graphite-epoxy unidirectional tape. Unfortunately, because AS4/3501-6 material is used in current aircraft production programs (which is the reason that we selected it), we were unable to obtain it in a timely manner and in a suitable quantity. Also, the desired aluminum channel stock was not available in Northern California. As a consequence, substitutions were made. The unfortunate result is that the extensive finite element correlation study results reported in refs. 3 and 12 cannot be compared directly to our experimental findings.

Since the agreement between finite element simulations and the beam-like predictions was excellent (refs. 3,12) in the earlier studies and the correlation with experiments is very good here, we consider that the design of high aspect chordwise deformable wings by utilizing the bending method of producing camber is on firm ground. Nevertheless, we are somewhat frustrated by the circumstances.

ACKNOWLEDGMENTS

This research was sponsored by the NASA Langley Research Center under Advanced Composites Technology Program Contract NAS1-18754. This support is gratefully acknowledged. A particular debt is owed to Dr. Damodar R. Ambur, the NASA Project Engineer, for his help with the development of the experimental methodology and his wise counsel. In addition, we thank Dr. T. J. Petersen of the Boeing Commercial Airplane Group for supplying us with the composite material, which was Fortafil 3(c)/8601 graphite-epoxy unidirectional tape.

REFERENCES

1. Shirk, M.H., Hertz, T.J. and Weisshaar, T.A., "A Survey of Aeroelastic Tailoring-Theory, Practice, Promise," Journal of Aircraft, Vol. 23, No. 1, January 1986, pp. 6-18.
2. Rehfield, L.W., Chang, S., Pickings, R.D., Zischka, P.J. and Holl, M.W., "Tailored Composite Wings With Elastically Produced Chordwise Camber," NASA Conference Publication 3104, Part 2, 1991, pp. 1037-1047.
3. Rehfield, L.W., Chang, S., Zischka, P.J., Pickings, R.D. and Holl, M.W., "Tailoring of Composite Wing Structures for Elastically Produced Camber Deformations," AIAA Paper No. 91-1186, Proceedings of the 32nd AIAA Structures, Structural Dynamics and Materials Conference, April 8-10, 1991, Baltimore, MD, Part 3, pp. 2123-2127.
4. Rogers, W.A., Braymen, W.W. and Shirk, M.H., "Design, Analysis, and Model Tests of an Aeroelastically Tailored Lifting Surface," AIAA Paper No. 81-1673, AIAA Aircraft Systems and Technology Conference, August 11-13, 1981, Dayton, OH.
5. Rehfield, L.W., "Design Analysis Methodology for Composite Rotor Blades," Proceedings of the Seventh DoD/NASA Conference on Fibrous Composites in Structural Design, AFWAL-TR-85-3094, June 1985, pp. (V(a)-1)-(V(a)-15).
6. Rehfield, L.W., Hodges, D.H., and Atilgan, A.R., "Nonclassical Behavior of Thin-Walled Beams with Closed Cross Sections," Journal of the American Helicopter Society, Vol. 35, No. 2, April 1990, pp. 42-50.
7. Rehfield, L.W. and Atilgan, A.R., "Toward Understanding the Tailoring Mechanisms for Thin-Walled Composites Tubular Beams," Proceedings of the First USSR-US Symposium on Mechanics of Composite Materials, 23-25 May 1989, Riga, Latvia, USSR, ASME, pp. 187-196.
8. Rehfield, L.W., Pickings, R.D., Chang, S. and Holl, M.W., "A Comparison of Classical Mechanics Models and Finite Element Simulation of Elastically Tailored Wing Boxes," NASA Conference Publication 3104, Part 2, pp. 809-816.
9. Ambur, D.R. and Rehfield, L.W., "Effect of Stiffness Characteristics on the Response of Composite Grid-Stiffened Structures," AIAA Paper No. 91-1087, Proceedings of the 32nd AIAA Structures, Structural Dynamics and Materials Conference, April 8-10, 1991, Baltimore, MD, Part 2, pp. 1349-1356.
10. Rehfield, L.W., Chang, S. and Atilgan, A.R., "New, Unusual and Nonclassical Behavior of Thin-Walled Composite Structures," Eighth International Conference on Composite Materials, Honolulu, HI, July 15-19, 1991, Composites: Design, Manufacture and Application, S.W. Tsai and G.S. Springer, editors, SAMPE, 1991, (26-A-1)-(26-A-9).
11. Zischka, P.J., "Aerodynamics of Wings with Elastically Produced Camber," MS Thesis, University of California, Davis, CA, Spring 1991.
12. Pickings, R.D., "Comparison of Theoretical Results with a Finite Element Model for Predicting Camber Induced by Bending of a Wing Box," MS Thesis, University of California, Davis, CA, Fall 1991.

TABLE 1.- CAMBER CORRELATION-METHOD 1

	<u>ANALYSIS</u>	<u>EXPERIMENT</u>
CAMBER COMPLIANCE (LB-IN ²) ⁻¹ × 10 ⁶	1.08	1.08
PERCENT DIFFERENCE	----	0.5

TABLE 2.- SPANWISE BENDING COMPLIANCE CORRELATION-METHOD 2

	ANALYSIS	EXPERIMENT
SPANWISE BENDING COMPLIANCE (LB-IN ²) ⁻¹ × 10 ⁶	0.78	0.85
PERCENT DIFFERENCE	----	9.0

TABLE 3.- CAMBER CORRELATION-METHOD 2

	<u>ANALYSIS</u>	<u>EXPERIMENT</u>
CAMBER COMPLIANCE (LB-IN ²) ⁻¹ × 10 ⁶	0.99	1.08
PERCENT DIFFERENCE	----	9.1

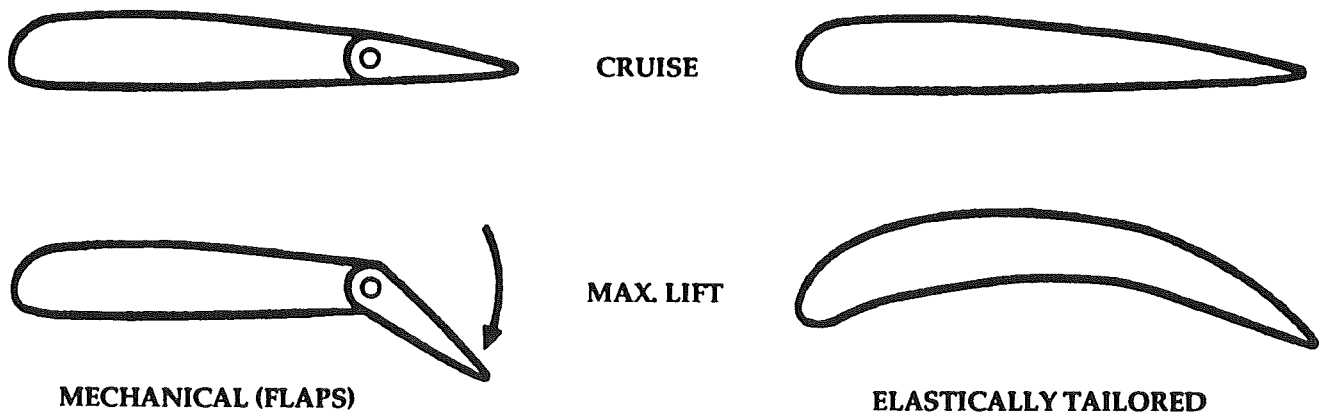


FIGURE 1. - METHODS OF INCREASING AIRFOIL LIFT

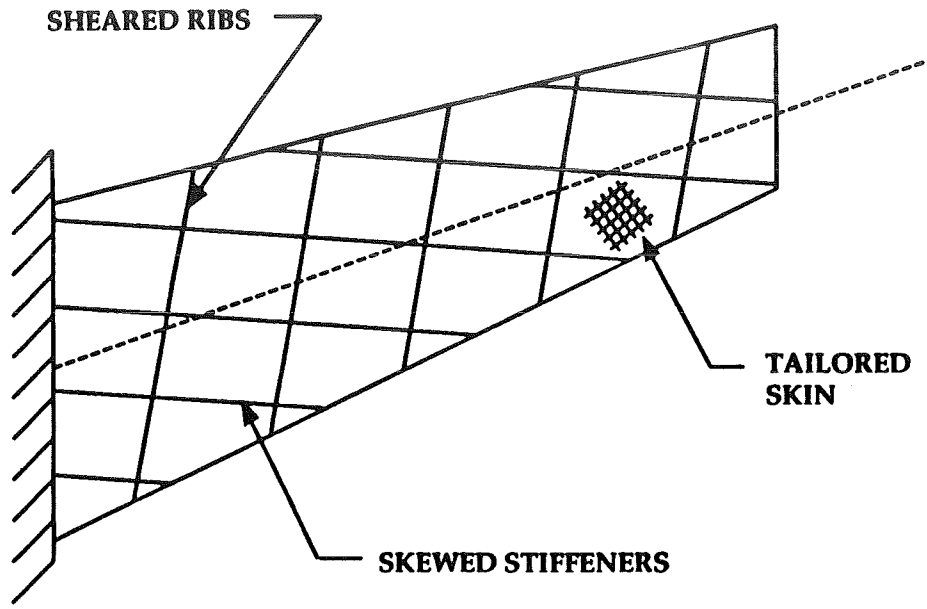


FIGURE 2. - METHODS FOR PRODUCING ELASTIC COUPLING IN HIGH ASPECT RATIO WINGS

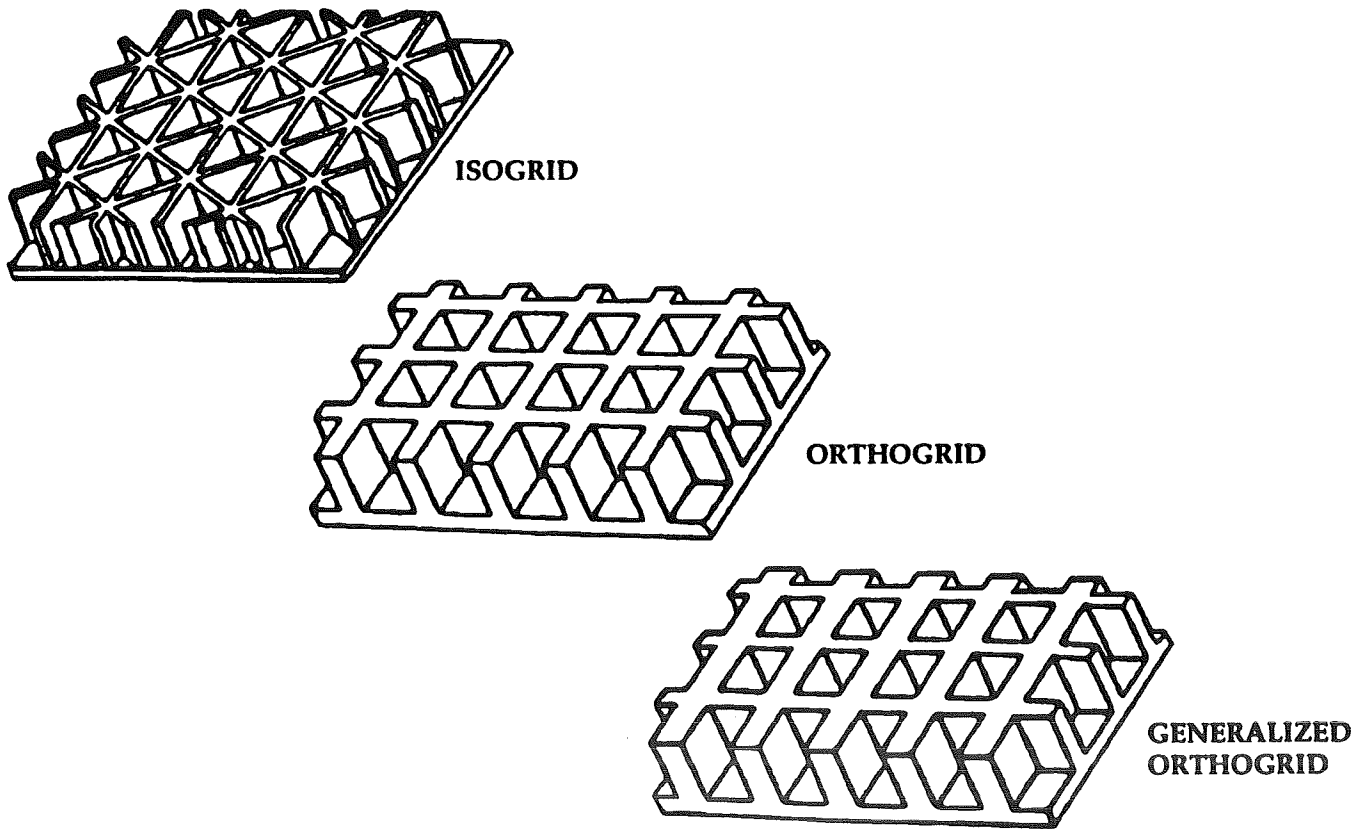


FIGURE 3. - GRID CONFIGURATIONS

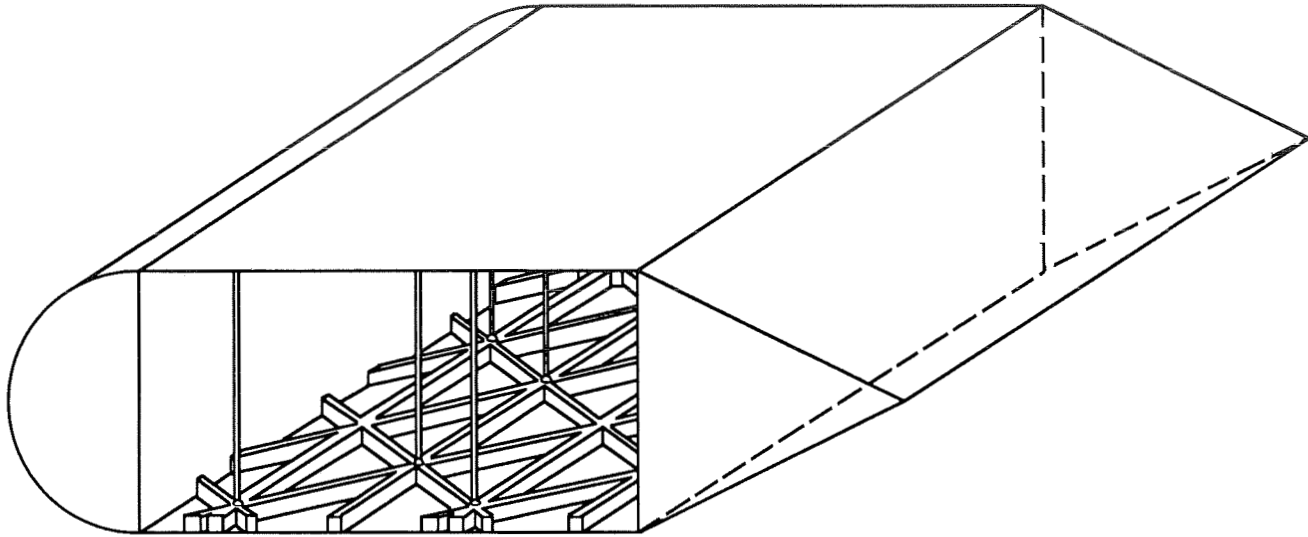


FIGURE 4. - VERTICAL COLUMN SUPPORT

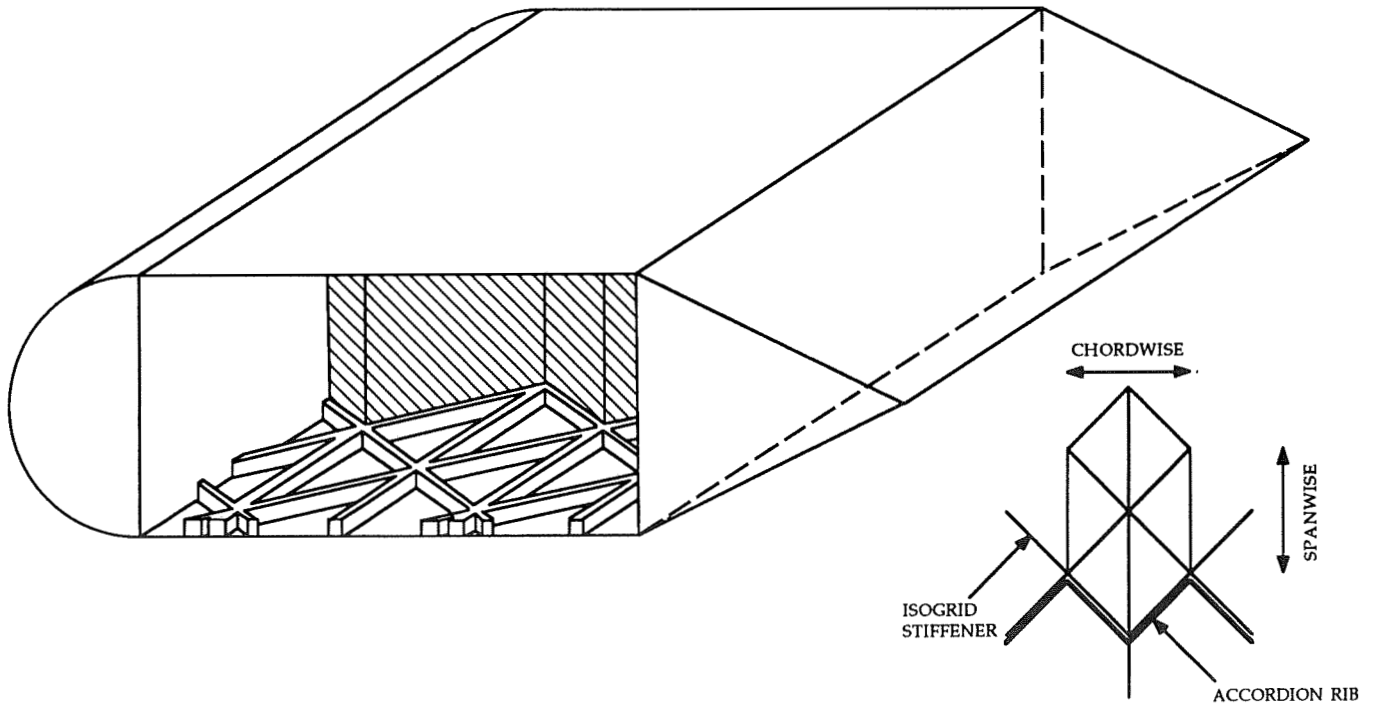
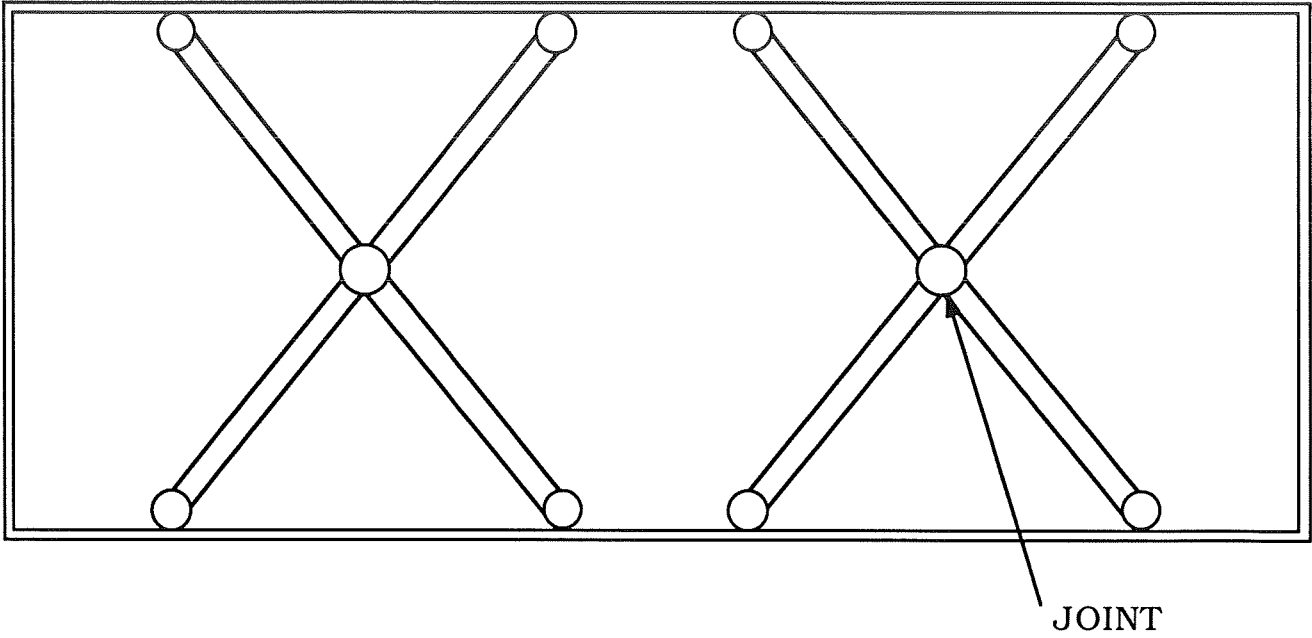
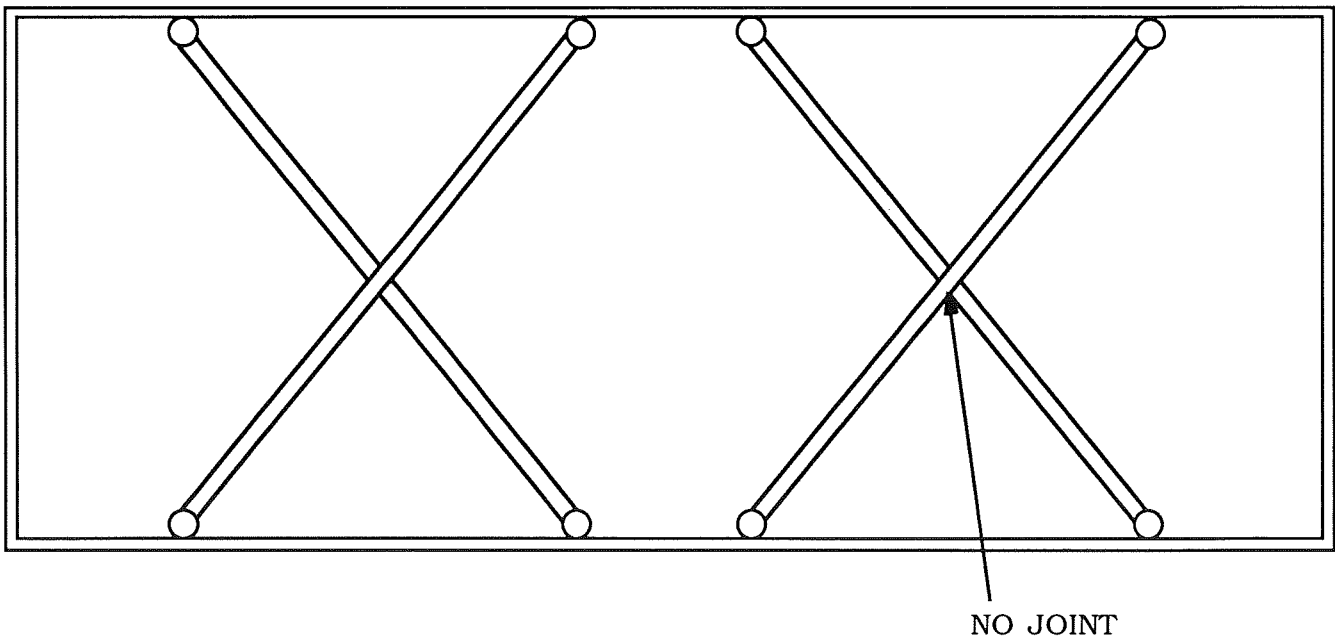


FIGURE 5. - ACCORDION RIB SUPPORT



**FIGURE 6. - SEGMENTED DIAGONAL COLUMNS
WITH MIDSECTION JOINTS**



**FIGURE 7. - SEGMENTED DIAGONAL SUPPORTS
WITHOUT MIDSECTION JOINTS**

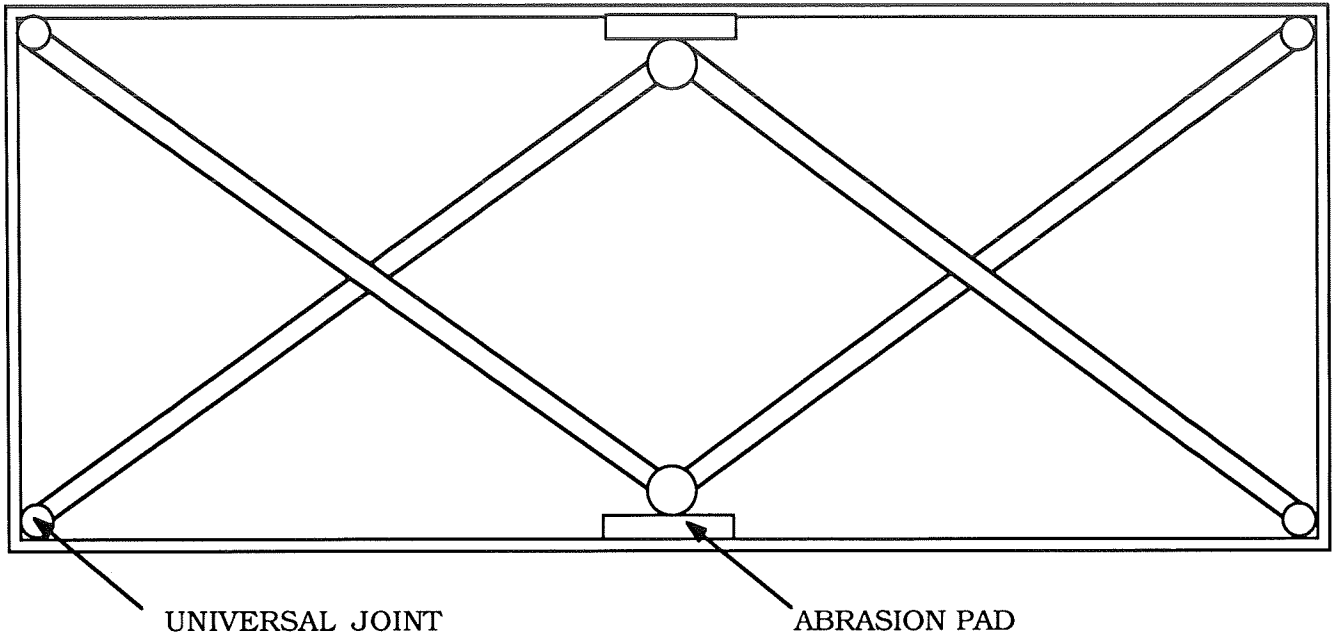


FIGURE 8. - FLOATING RIB STRUCTURE

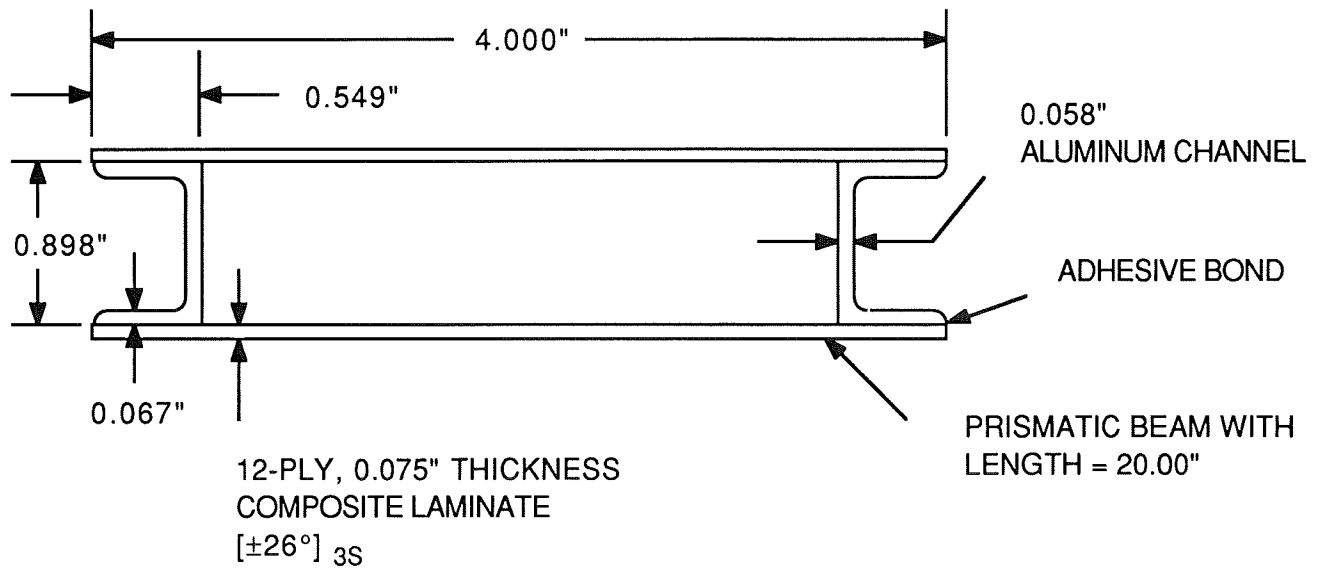


FIGURE 9. - BOX BEAM TEST SPECIMEN

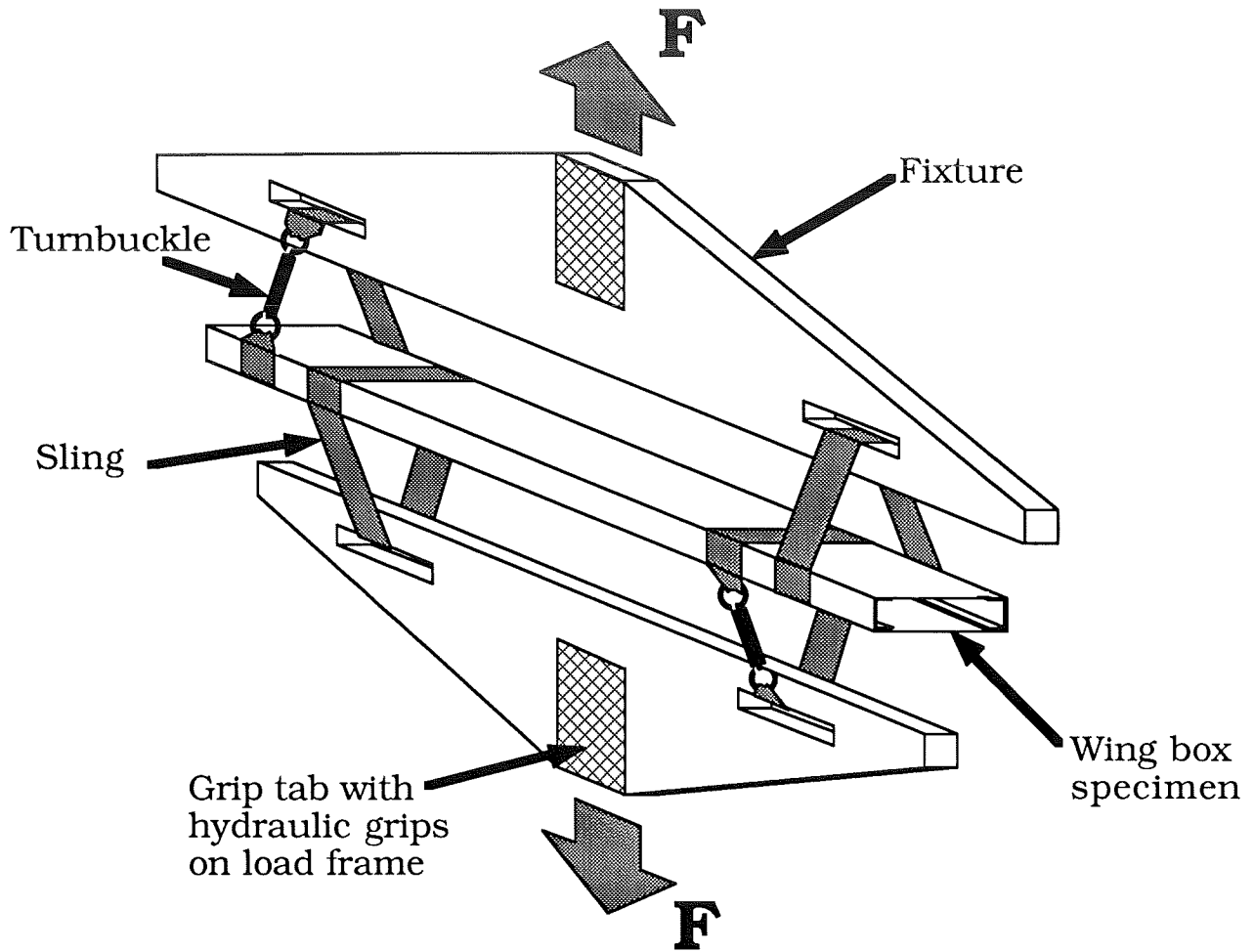


FIGURE 10. - OVERALL TEST CONFIGURATION

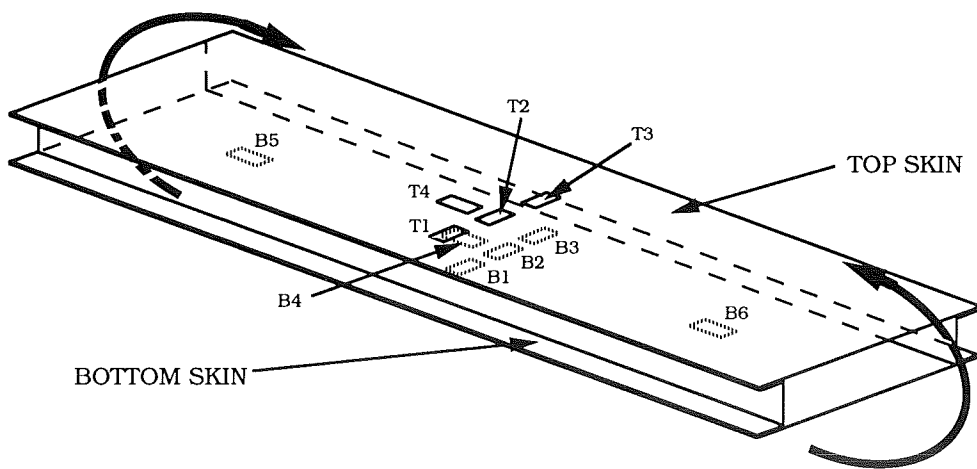


FIGURE 11. - STRAIN GAGE NOMENCLATURE AND LOCATIONS ON BOX BEAM

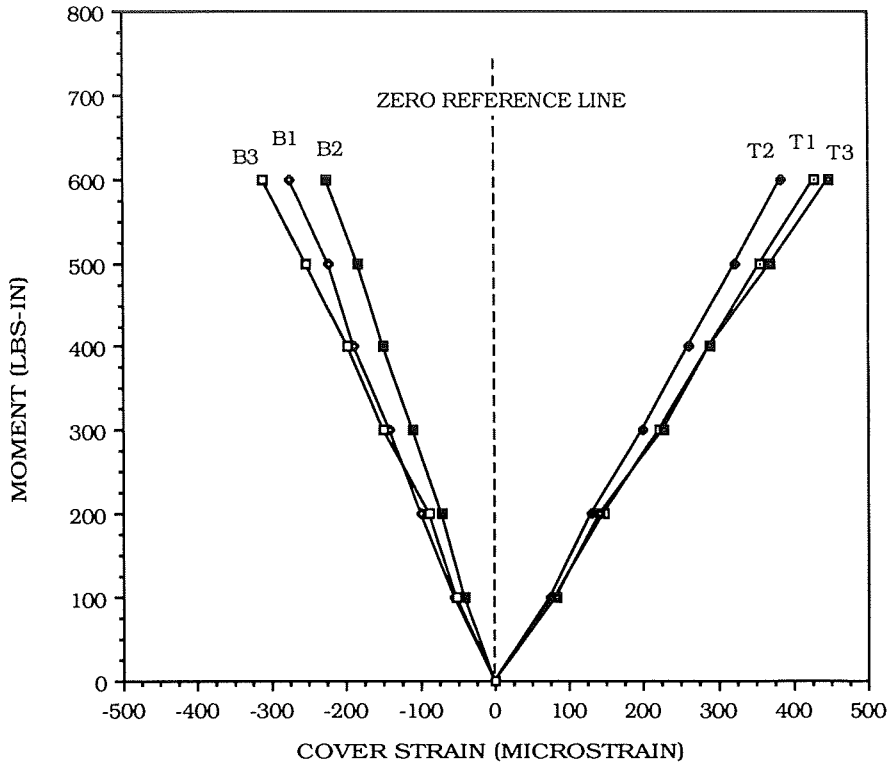


FIGURE 12. - BENDING MOMENT VS CHORDWISE GAGE STRAIN

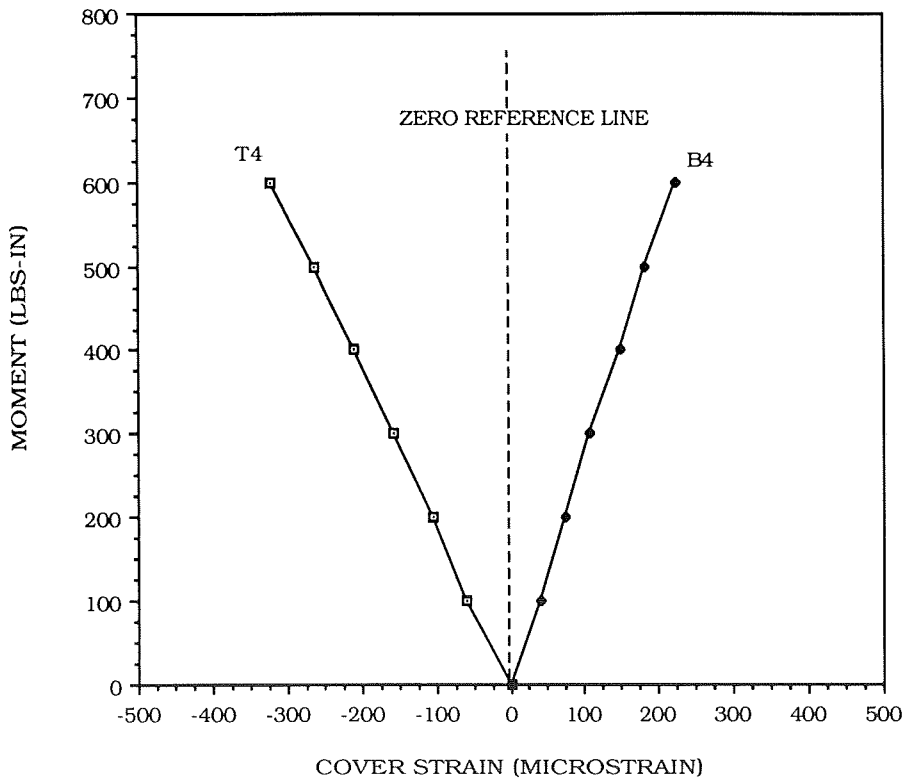


FIGURE 13. - BENDING MOMENT VS SPANWISE GAGE STRAIN

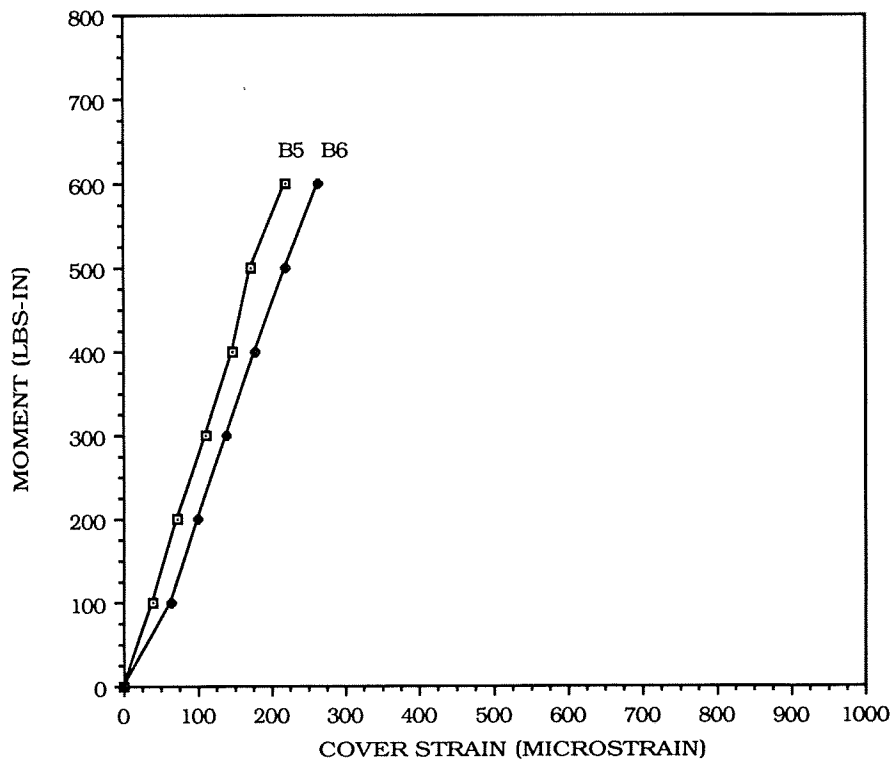


FIGURE 14. - BENDING MOMENT VS OUTER SPANWISE GAGE STRAIN

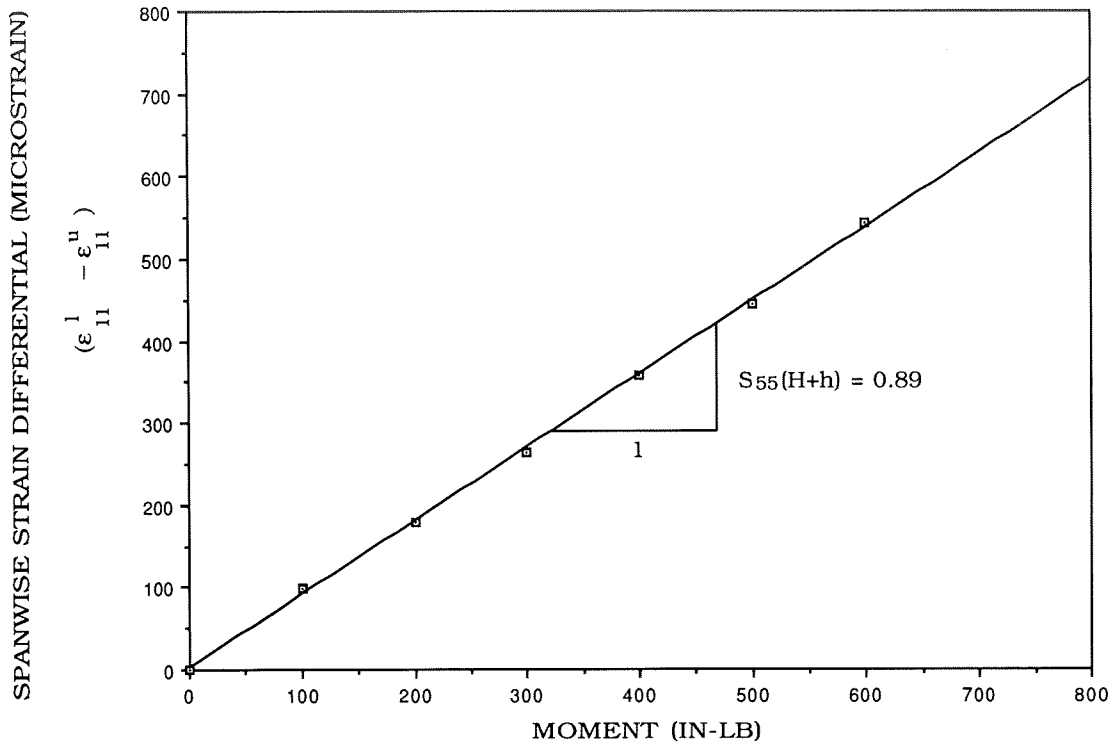


FIGURE 15. - SPANWISE STRAIN DIFFERENTIAL VS. APPLIED MOMENT

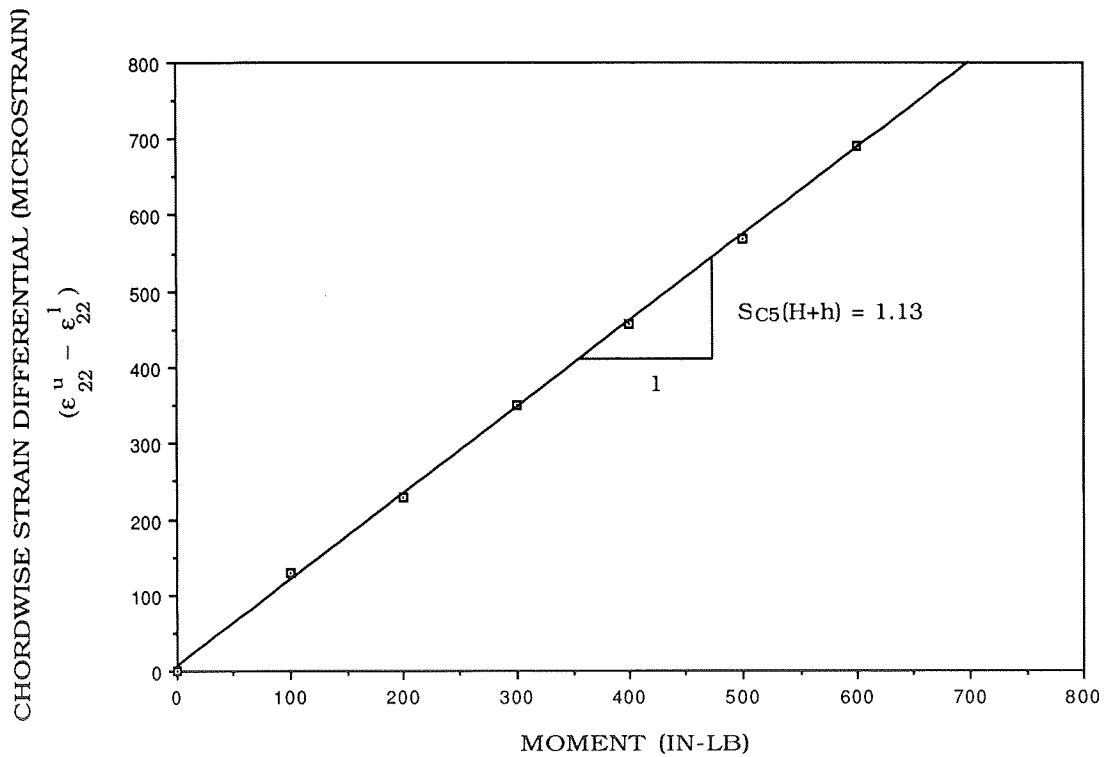


FIGURE 16. - CHORDWISE STRAIN DIFFERENTIAL VS. APPLIED MOMENT

**C-130 ADVANCED TECHNOLOGY CENTER WING
BOX CONCEPTUAL DESIGN/COST STUDY***

R.S. Whitehead
Northrop Corporation
Hawthorne, California

C.R. Foreman
LTV Advanced Products Group
Dallas, Texas

Capt. K. Silva
Wright Laboratories/FIBAC
Dayton, Ohio

517-24
51385

7-19

ABSTRACT

A conceptual design was developed by Northrop/LTV for an advanced C-130 Center Wing Box (CWB) which could meet the severe mission requirements of the SOF C-130 aircraft. The goals for the advanced technology CWB relative to the current C-130H CWB were: (1) the same acquisition cost; (2) lower operating support costs; (3) equal or lower weight; (4) a 30,000 hour service life for the SOF mission; and (5) minimum impact on the current maintenance concept. Initially, the structural arrangement, weight, external and internal loads, fatigue spectrum, flutter envelope and design criteria for the SOF C-130 aircraft CWB were developed. An advanced materials assessment was then conducted to determine the suitability of advanced materials for a 1994 production availability and detailed trade studies were performed on candidate CWB conceptual designs. Finally, a life-cycle cost analysis was performed on the advanced CWB. The study results demonstrated that a hybrid composite/metallic CWB could meet the severe SOF design requirements, reduce the CWB weight by 14 percent, and was cost effective relative to an all metal beefed up C-130H CWB.

* This work was performed under USAF Contract No. F33657-90-D-0027 Task Order 0005, September 1990 to April 1991.

INTRODUCTION

The airframes of SOF C -130 aircraft have approximately one-third the service life of a C-130H airframe. In addition, the center wing box (CWB) structure, which is common to both the C-130H and SOF C -130, is the life limiting portion of the airframe. The reduced service life of the SOF C -130 airframe can be attributed to two primary factors, these are: a severe tactical flight mission profile and high operational weight. As a consequence, the SOF C -130 CWB structure has a fierce time compliance technical order (TCTO) maintenance burden, which generates high operating and support costs. Several life extension alternatives exist for these airframes: (1) revised mission scenarios; (2) increased inspection frequency; (3) a beefed-up metal CWB; or (4) application of advanced structures and materials technologies to a redesigned CWB. The purpose of this study (Reference 1) was to explore the latter alternative. Specific objectives were to develop an advanced technology SOF C -130 CWB conceptual design and to determine its acquisition and operation and support costs. The goals for the advanced technology CWB relative to the current C-130H CWB were: (1) the same acquisition cost; (2) lower operating and support costs; (3) equal or lower weight; (4) a 30,000 hour service life for the SOF mission; and (5) minimum impact on the current maintenance concept.

C-130H CWB STRUCTURAL ARRANGEMENT

An isometric view of the C-130H CWB structure is shown in **Figure 1**. The CWB structure spans WS 220 left to WS 220 right, minus the leading edge structure forward of the front beam and trailing edge structure aft of the rear beam. The box consists of upper and lower multi-piece hat stiffened skins, front and rear beams (spars) and ten ribs. Bladder type fuel tanks are contained between WS 61 and 178 left and right. The current design is all metal, mainly 7075-T73 aluminum alloy.

The advanced design CWB has to maintain several structural interfaces. These are (1) fuselage attachments at WS 20 ribs left and right to BL20 fuselage upper longerons, (2) fuselage attachments at WS 61 left and right - lower skin to drag angle, front beam to fuselage post, and aft beam to fuselage post, (3) the inboard engine truss mount left and right, (4) the outer wing attachment through upper and lower rainbow fittings, corner fittings, and spar web splices at WS 220 left and right, and (5) the leading edge assembly attachment to the front beam and trailing edge attachment at the rear beam. System interfaces are: (1) fuel systems that penetrate the front beam and ribs at WS 178, (2) electrical controls (engine and flight) and ECS along the front beam outside of the box, and (3) multiple penetrations in the center dry bay area.

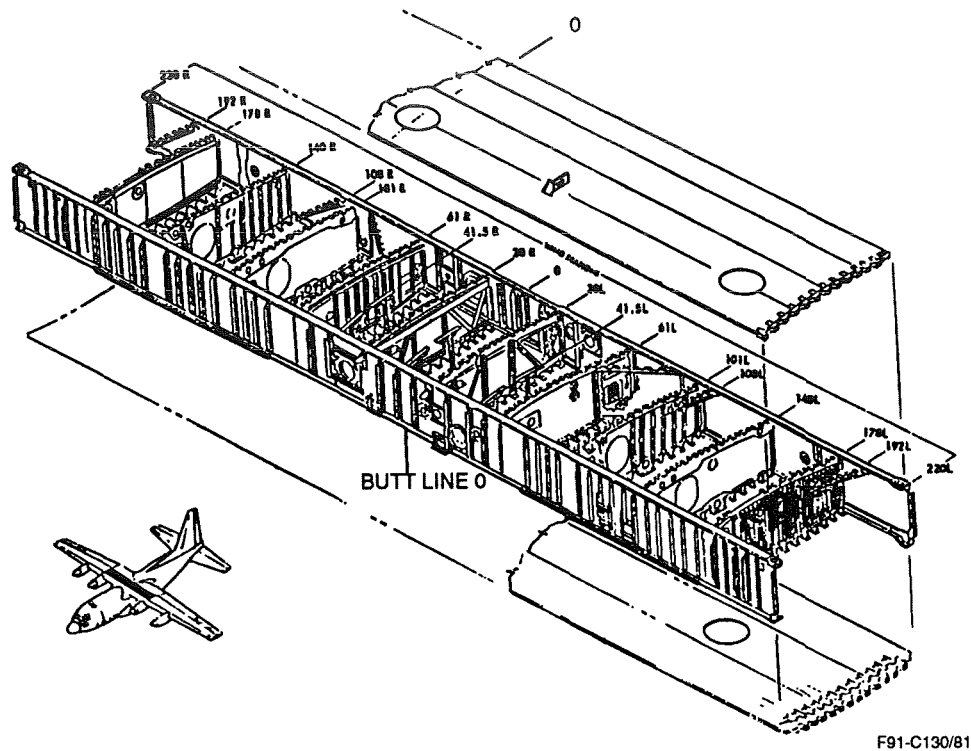


Figure 1. C-130 CWB Structural Arrangement.

A weight breakdown of the C-130H CWB is presented in **Figure 2**. Total weight is 4811 lb, where the upper and lower wing skins represent approximately two-thirds of this weight. Previous studies have shown that a metal “beef-up” of approximately 1000 lb is required to provide a durable CWB for the SOF C -130 mission profile.

The primary external loads on the C-130H CWB were derived from flight maneuver, gust loads, and ground conditions. Six critical conditions constitute the corner points of the load envelope for the middle of the CWB at WS 95. These load envelopes are shown in **Figure 3**. These six load conditions were selected for internal loads development for the baseline C-130H CWB and included maximum and minimum bending moments, shears and torsions, and combinations thereof. The loads in **Figure 3** were increased by 20% to account for the more severe SOF C mission. The advanced CWB was designed to these increased loads.

The SOF C -130 CWB fatigue load spectrum was not available for this conceptual design study program. An approximate SOF C -130 CWB fatigue spectrum was developed with Air Force approval. The mission mix was specified as 20 percent proficiency training, 30 percent short range logistics, and 50 percent combat training. Exceedance data for tactical training, ferry and Red Flag

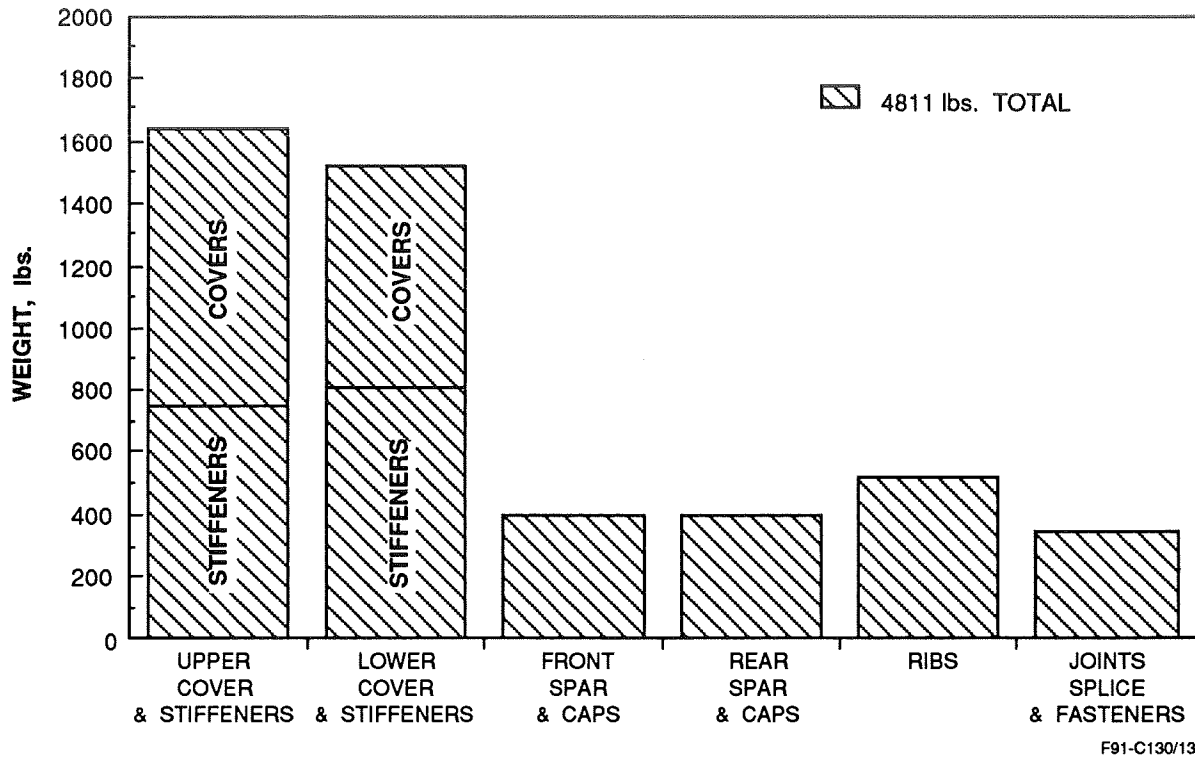
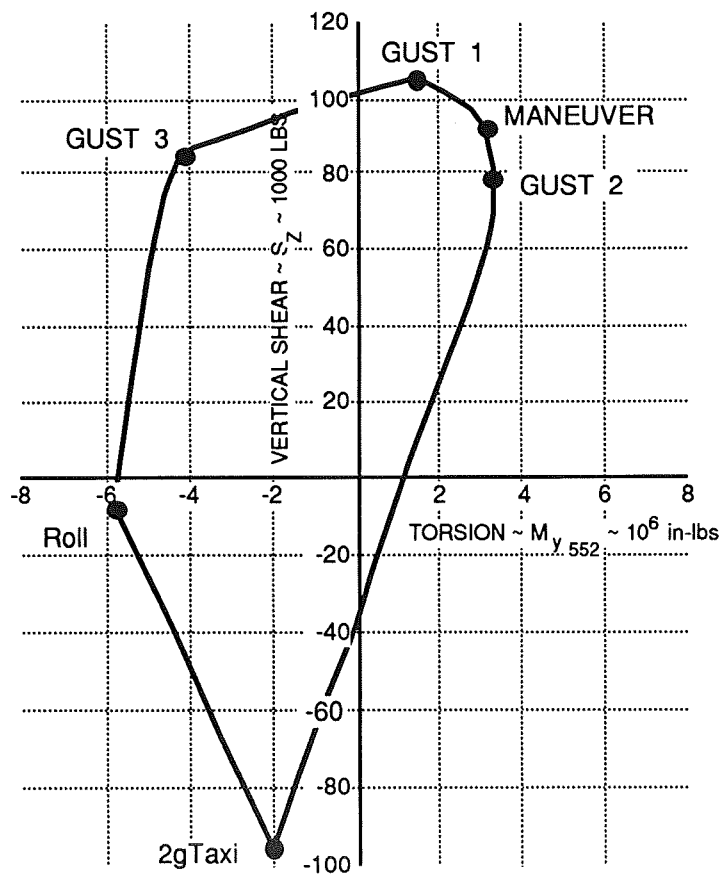
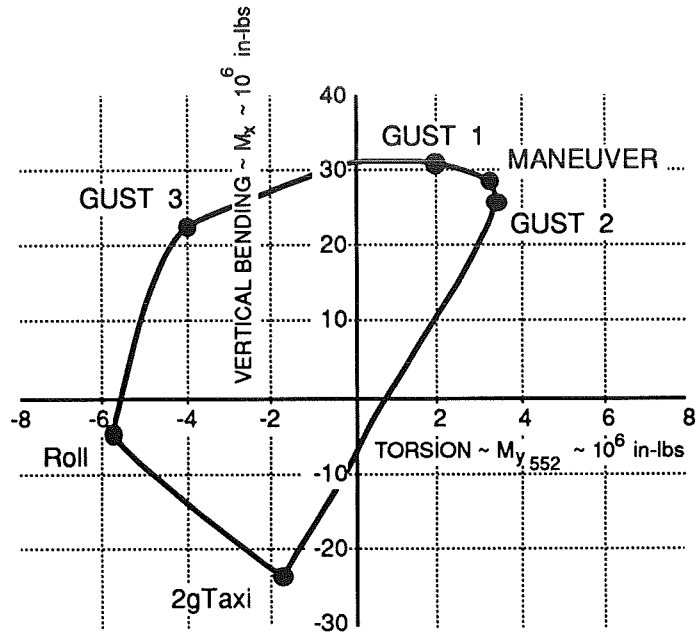


Figure 2. C-130H CWB Weight Breakdown.

were used respectively for the three specified missions. The delta load factor versus cumulative exceedances curve developed for the Red Flag mission is presented in **Figure 4**. These delta load factor exceedance data were subsequently used for fatigue analysis.

DESIGN CRITERIA

General structural design criteria were based on AFGS-87221A. For the purposes of this study, durability/damage tolerance design criteria were as follows: metallic structure was designed to a fatigue life of four times service life (120,000 hours). Fatigue life was defined as crack initiation to 0.01 inch. Composite structure was designed to damage tolerance requirements because of their insensitivity to undamaged fatigue loading. Composite upper skins were required to sustain 100 ft-lb impact or visible damage, whichever occurred first. The 100 ft-lb impact represents a 25 lb tool box drop from four feet with an impactor diameter of 1 inch. The lower skin threat was a 25 ft-lb impact or fuel leakage caused by foreign object damage such as runway debris. The residual static strength (P_{xx}) load requirement was specified as 1.2 x DLL after two design life times (60,000 hours) of fatigue loading.



F91-C130/23/A

Figure 3. C-130H External Loads Envelope – Wing Station Limit Loads.

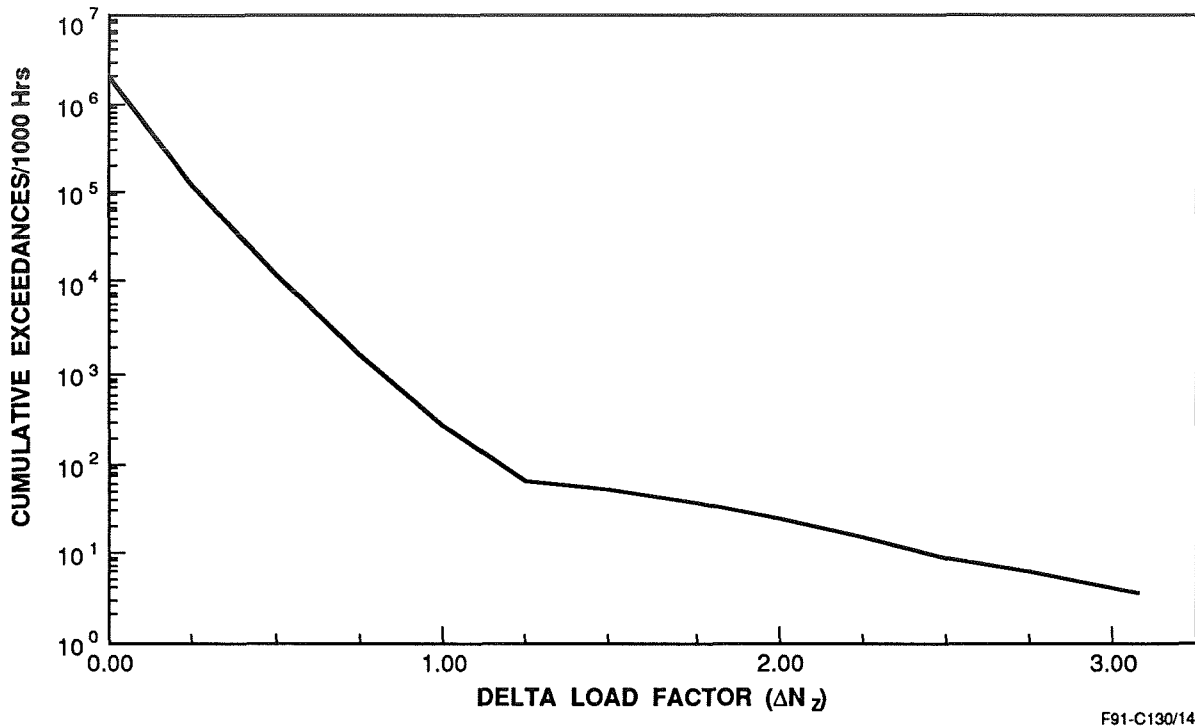


Figure 4. C-130 Red Flag Delta Load Factor Exceedances.

Design allowables for mature metallic alloys were taken from MIL-HDBK-5. Advanced metallic alloy allowables were derived from in-house data. Two classes of composite materials were utilized in the study: two first generation epoxies, AS4/3501-6 and AS4/3502, and two second generation toughened thermosets with an intermediate modulus fiber; they were IM7/8552 and IM7/5250-4. These materials were selected after a comprehensive advanced materials assessment which is documented in Reference 1. Lamina and laminate strength design allowables for unidirectional tape are given below:

Lamina Allowables

AS4/3501-6 or 3502	{	Tension Modulus E_1	= 18.7 Msi
		Compression Modulus E_2	= 17.6 Msi
IM7/8552 or 5250-4	{	Tension Modulus E_1	= 22.6 Msi
		Compression Modulus E_2	= 20.2 Msi

Laminate Allowables

$$\epsilon_{\text{ALLOW}}^{\text{TENSION}} = \epsilon_{\text{ALLOW}}^{\text{COMPRESSION}} = 5,000 \mu\text{in/in}$$

Interlaminar Tension Strength

$$\sigma_{\text{ALLOW}}^{\text{TENSION}} = 2400 \text{ psi}$$

The laminate strength allowables (for all materials) of 5000 $\mu\text{in/in}$ are based on a 0.25 inch fastener hole and account for an operating environment of -67°F to 180°F with end-of-lifetime moisture content. Test data indicate a potential for laminate strain allowables in excess of 5000 $\mu\text{in/in}$. However, the laminate strain allowable was limited to 5000 $\mu\text{in/in}$ for three reasons: (1) bolted repair capability; (2) minimization of bolt bearing by-pass effects; and (3) ballistic damage tolerance. The interlaminar tension strength allowable is derived from test data on low-to-medium toughness thermoset systems such as AS/3501-6 and AS4/5250-3.

The durability design allowable is driven by control of hole wear in highly loaded holes. This is achieved by limiting bearing stresses such that

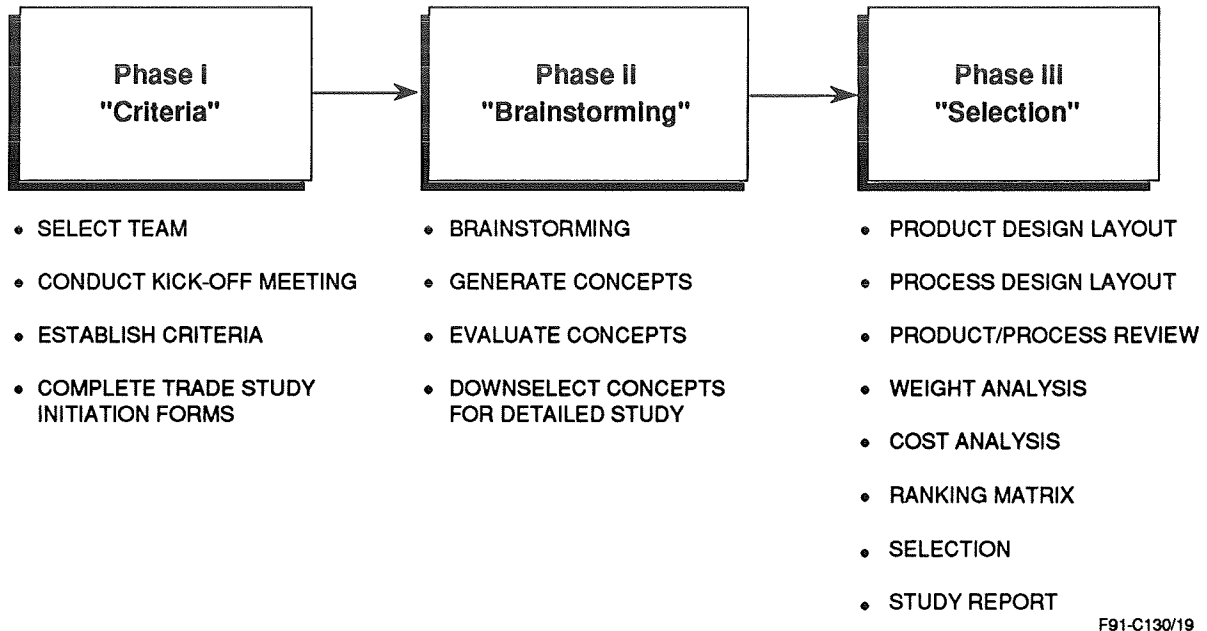
$$\sigma_{\text{ALLOW}}^{\text{BEARING YIELD}} = \text{DESIGN LIMIT LOAD} = 70 \text{ ksi}$$

Damage tolerance allowables at design ultimate load ranged from 3125 $\mu\text{in/in}$ to 5000 $\mu\text{in/in}$ because of their dependency on impact threat severity, material toughness, and laminate thickness.

TRADE STUDIES

Figure 5 summarizes the overall trade study approach, which was conducted in three phases. In Phase I, the team is selected, a kick-off meeting is convened, and the study criteria are established based on customer needs which are translated into product and process design requirements. At the end of Phase I, trade study initiation forms are completed for each task.

In Phase II, team brainstorming sessions generate design concepts from which candidate concepts are downselected for further evaluation. The brainstorming sessions develop as many viable concepts as possible in order to increase the chances of identifying and selecting the best approach. Preliminary downselection of the candidate concepts is based on the Pugh method of concept evaluation.



F91-C130/19

Figure 5. Overall Trade Study Approach.

The Pugh method results in a manageable number of relevant design concepts that can be evaluated in greater detail. The Phase III approach developed to accomplish this evaluation is a tailored approach which uses traditional trade study measures of merit and weighting factors. Also, elements and techniques common to the application of Quality Function Deployment and “Forced Decision Making” have been incorporated into the methodology. Included among these elements is a strong emphasis on team effort, the physical format, and the “What-How” approach to evaluating the relationships between the concepts and the selection criteria. Forced Decision Making requires each concept to be evaluated not only with respect to how well it satisfies the design requirements, but also how well it satisfies these requirements with respect to the other concepts. To adequately assess the concepts in Phase III, a thorough understanding of each of the downselected concepts is required. It is essential for the Pugh preliminary downselection process to eliminate as many concepts as possible to reduce the effort required in Phase III.

Trade studies were conducted on the CWB wing skins, spars, ribs, and rainbow fitting. The wing skin trade study is discussed because it had the most impact on the final conceptual design.

Wing Skin Trade Studies

The objective of this trade study was to compare design configurations and manufacturing methods for fabricating the stiffened upper and lower wing skins for the center wing box of the

C-130. Skin stiffener configurations and potential tooling and fabrication approaches were analyzed and evaluated to select the preferred concept for full-scale development.

Five candidate skin concepts emerged from the Phase II brainstorming for preliminary concept evaluation using the Pugh method. The first concept was an advanced metallic skin. The other four were composite wing skin design concepts which featured different stiffener configurations for integrally stiffened, monolithic one-piece composite skins. The stiffener cross-sections included blades, hats, "I-beams," and "J"s. Figure 6 shows the results of the Pugh analysis of these five concepts. The advanced metal concept was rated unsatisfactory for weight because it could not meet the weight target and satisfy the durability requirements. It was concluded that the excellent

TRADE STUDY CONCEPT COMPARISON		PAGE 1 OF 1				
TITLE: C-130 CWB - Wing Skins		STUDY LEADER: J. LUZAR A. HIKEN			DATE: 11/15/90	
CRITERIA	CONCEPTS	1 ADVANCED METALLIC	2 COMPOSITE BLADE	3 COMPOSITE HAT	4 COMPOSITE I-BEAM	5 COMPOSITE "J"
STRUCTURES						
DAMAGE TOLERANCE/FATIGUE	↑ BASELINE ↓	+	+	+	+	+
BALLISTIC		S	S	S	S	S
LIGHTNING		S	-	-	-	-
INTERFACE		S	S	S	S	S
FUEL PRESSURE		S	-	-	-	-
WEIGHT		U	+	+	+	+
MAT'L'S & PROC						
FUEL SEALING		S	S	S	-	-
CORROSION CONTROL		S	+	+	+	+
MANUFACTURING						
ACQUISITION COST		S	S	S	-	-
RISK		S	S	S	-	-
R & M						
INSPECTABILITY		S	S	S	S	S
MAINTAINABILITY		+	+	+	+	+
REPAIRABILITY	S	S	S	-	-	
TOTAL	+	U	4	4	4	4
	-		2	2	6	6
SCALE + CLEARLY BETTER - CLEARLY WORSE S ABOUT THE SAME U UNACCEPTABLE						

F91-C130/52

Figure 6. Phase II Pugh Preliminary Concept Evaluation for Wing Skin Trade Studies.

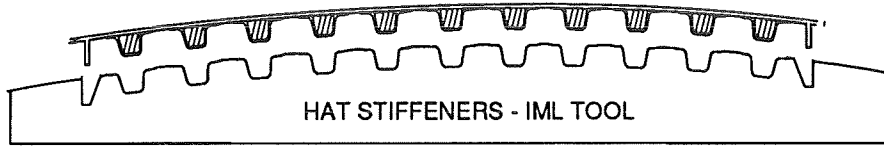
durability characteristics of composite wing skins were necessary to achieve the CWB structural weight goal. Preliminary downselection eliminated the “I-beam” and “J” configurations (Concepts 4 and 5), primarily based on the greater manufacturing risk and higher cost of these configurations compared to the blades and hats (Concepts 2 and 3). Fuel sealing requirements were also considered in this preliminary evaluation. The assessment of manufacturing risk and cost was based on the complexity of the stiffener shape, the number of details comprising the stiffener, the tooling requirements, and the manufacturing experience of Northrop and LTV. The Pugh evaluation in Figure 6 shows that blade and hat stiffeners were preferred to “I-beam” and “J” stiffeners, because they had major advantages in the areas of fuel sealing, cost, risk and repairability. Therefore, the hat and blade stiffened composite wing skin concepts were selected as the candidates for the more detailed Phase III evaluation prior to downselecting to a preferred approach. OML and IML tooling concepts were considered for both stiffening configurations; **Figure 7** shows the four candidate concepts. The detailed downselection focused on manufacturing risk issues - tooling, fabrication, and assembly - and on achieving an integral fuel tank.

A key issue in the selection of the wing skin stiffening concept was continuous versus discontinuous stiffening elements. Fuel sealing at the fuel closeout rib/wing skin-stiffener intersection was a critical requirement in the integral fuel tank design. Successful, reliable fuel sealing at this intersection is dependent on many factors, including the rib and stiffener configurations.

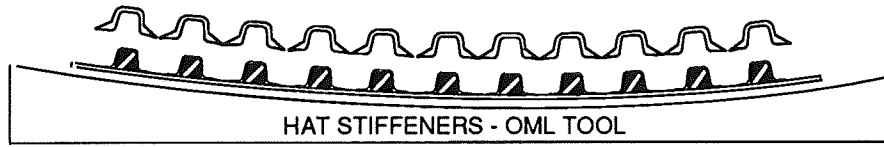
The continuous stiffening approach uses wing skin stiffeners uninterrupted at the fuel closeout rib intersections. The rib caps are joggled around the stiffeners or are relieved at the stiffener intersections and separate fittings are used to achieve the fuel seal. In the discontinuous stiffener approach, the stiffeners are interrupted at the rib intersections and a flat rib cap assembles to a flat land area on the wing skin, creating the fuel seal. It is clear from a structural load carrying perspective, that the continuous stiffener approach is preferred. The severe loading conditions and the proximity of the outboard fuel closeout ribs to the wing attach fitting do not favor the discontinuous stiffener concept. The ability to transition loads from the wing skin stiffeners around (into the skin) or through (using a separate fitting) the fuel closeout rib was a critical factor in the wing skin stiffening concept decision making process. A discontinuous wing skin stiffening approach is preferred when considering the fuel sealing requirements at the rib cap/wing skin stiffener intersections. In this approach, the fuel seal can be accomplished without the need for a complex rib cap configuration or subsequent assembly operations.

Continuous stiffening was determined to be the preferred approach for satisfying the wing skin and the integral fuel tank requirements. Using concurrent engineering in the development

HATS

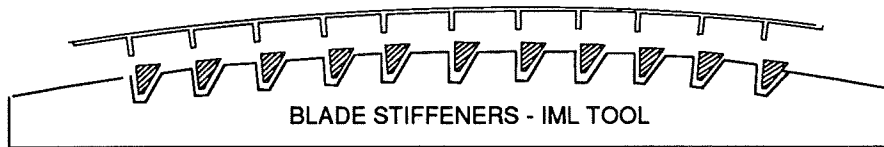


Concept A1

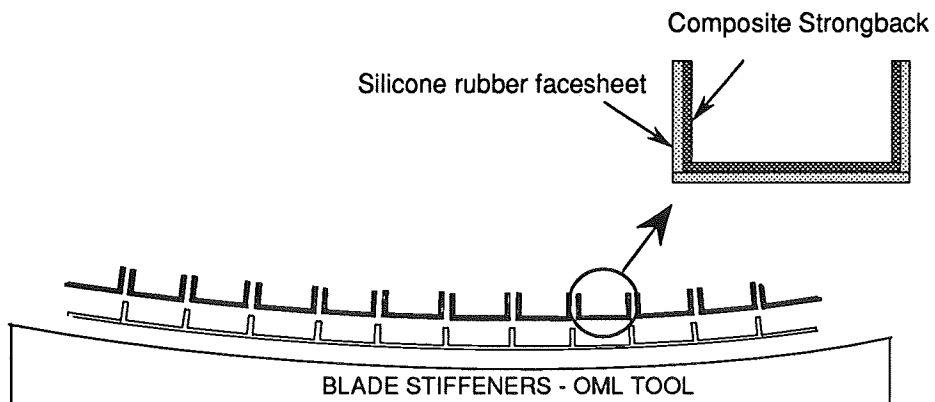


Concept A2

BLADES



Concept B1



Concept B2

F91-C130/53/A

Figure 7. Phase III Candidate Wing Skin Concepts.

process, and applying the trade study methodology, it was determined that the design and manufacturing complexity resulting from stiffener discontinuity would outweigh the potential fuel sealing benefits. As a result, the wing skin stiffener configuration candidates shown in **Figure 7** assumed continuous stiffeners in the design.

Recent successful IR&D activities for developing integral fuel tank designs using cocured hat stiffened skins and the IML tooling approach (Concept A1 in **Figure 7**) have identified and addressed many of the manufacturing risk issues. As a result of the IR&D development, Northrop/LTV have a high degree of confidence in this approach. IML tooling is preferred as a means of controlling the assembly surfaces to support the incorporation of an integral fuel tank into the wing box design. Concept A2 which has OML tooled hat stiffened skins (while extensively used, and highly successful on the YF-23) does not support the incorporation of an integral fuel tank into the center wing box design.

The blade stiffened skins concepts (B1 and B2) reflect the approaches currently used on bomber wing skins. Northrop uses the IML tooling concept, while LTV uses the OML tooling approach. The fabrication and tooling risks associated with an IML tooled, blade stiffened wing skin are high (relative to the other concepts) due to the size requirements for a C-130 CWB. The IML tooled blade stiffened wing skin concept (B1) is comparable to the IML tooled hat stiffened skin (Concept A1) with respect to manufacturing risk and cost, but is less preferable for the incorporation of the integral fuel tank into the CWB design. The evaluation of the candidate concepts using the downselection methodology indicated that the IML tooled, hat stiffened approach (Concept A1) was the preferred concept. The downselection matrix is shown in **Figure 8**.

Structural trade studies were conducted to determine the relative weights of hat and blade stiffened composite wing skins. The results are presented in **Figure 9**. Substantial weight savings (22%-45%) were achieved for both hat and blade stiffener configurations. For the same skin lay-up, the intermediate modulus toughened thermoset (IM7/8552 or 5250-4) provided approximately 10% additional weight savings over the first generation (AS4/3501-6 or 3502) systems. Composite wing skins are, therefore, extremely attractive from the product design viewpoint.

ADVANCED CWB CONCEPTUAL DESIGN

The selected advanced CWB design is shown in **Figures 10 and 11**. The CWB is a hybrid composite/metal structure. The upper and lower skins, front and rear spars and rib webs are composite. The rainbow fittings are titanium, and the remaining structure, except fasteners, are aluminum. The upper and lower skins are one piece with cocured hat stiffeners. All stiffeners are

		PRIMARY	SECONDARY	TERTIARY	TARGET VALUE	A1	A2	B1	B2	
PROCESS DESIGN REQUIREMENTS	LOW RISK	TOOLING	CONFIGURATION	FEMALE CORNERS	↓ MINIMIZE	5				
				TOOLING DETAILS	EASY REMOVAL					
			MATERIAL	COST (RAW MAT'L)	↓ MINIMIZE					
				COST (FABRICATION)	↓ MINIMIZE					
				DURABILITY	↑ MAXIMIZE					
	ACCURACY	↑ MAXIMIZE								
	FABRICATION	LAYUP COMPLEXITY (STIFFENER)	↓ MINIMIZE							
		PROCESS MATURITY	CURRENT IN-HOUSE PRODUCTION							
		STIFFENERS	↓ COST							
	ASSEMBLY	ACCESSIBILITY	MINIMIZE BLIND FASTENERS							
TOLERANCE BUILDUP ALLOWANCE		NO HARD SHIMS								
LOW COST	FABRICATION OPERATIONS (DETAILS PER PART, DEBULKING, PREFORMING, TRIM, INSPECTION, etc.)	↓ MINIMIZE	2	9	3	1	3			
PROCESS DESIGN SUBTOTAL SCORE						123	101	67	111	
PRODUCT DESIGN REQUIREMENTS	INTEGRAL FUEL TANK	FUEL SEALING SURFACES		TOOLED/NO MARKOFF	5	9	1	9	3	
		FUEL SEALING ASSEMBLY JOINTS		↓ MINIMIZE						
		FUEL SEALING FASTENERS (QTY)		↓ MINIMIZE						
	PERFORMANCE	STRUCTURES	DAMAGE TOLERANCE/FATIGUE		↑ MAXIMIZE					
			BALLISTIC		MEETS EXISTING					
			LIGHTNING		MEETS EXISTING					
			INTERFACE		MEETS EXISTING					
			FUEL PRESSURE		13 PSI					
			WEIGHT		≤ BASELINE (LBS)					
	M & P	CORROSION	↓ MINIMIZE							
	R & M	INSPECTABILITY		CONVENTIONAL						
		MAINTAINABILITY		↓ COST						
		REPAIRABILITY		EASY ACCESS						
PRODUCT DESIGN SUBTOTAL SCORE						45	5	45	15	
TOTAL SCORE						168	106	112	126	
RANK						1	4	3	2	

IMPORTANCE WEIGHTING FACTOR
5 → 1
STRONG WEAK

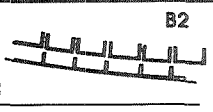
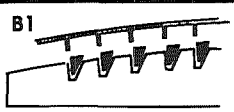
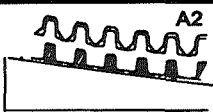
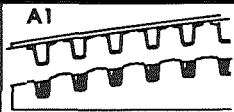


Figure 8. Phase III Wing Skin Concepts Downselection Methodology.

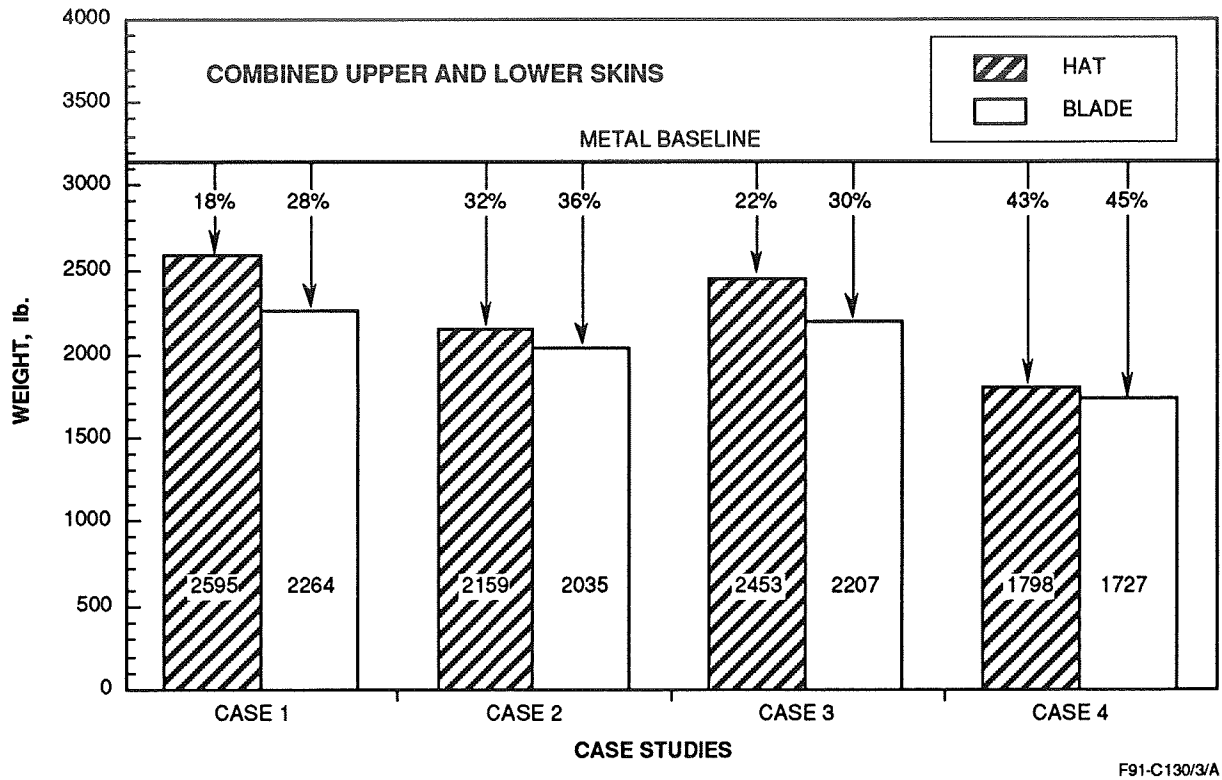


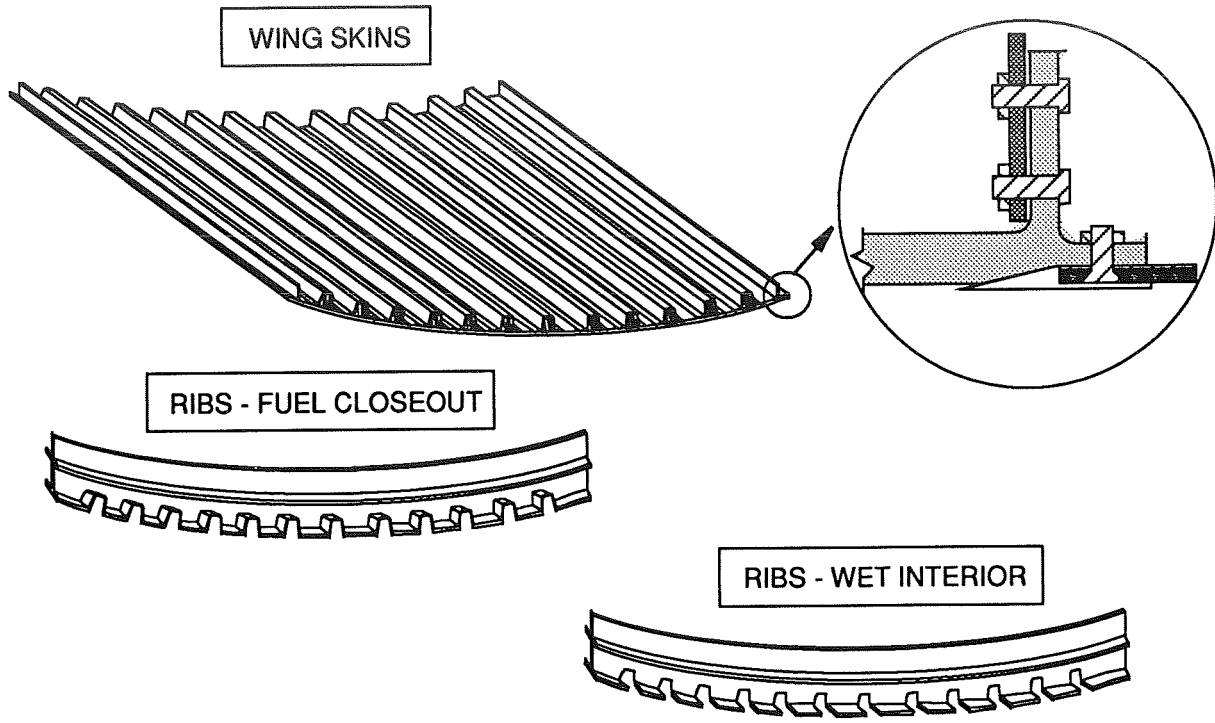
Figure 9. Combined Upper and Lower Wing Skin Weight Results.

continuous from tip to tip except at access holes. Integral front and rear spar caps are also built into the upper and lower skins. Spar webs are flat with cocured stiffeners. The ribs are discontinuous multi-piece structure with full-depth webs and caps. Key features of the design are: assembly simplicity, 60 percent fewer fasteners than the C-130H metal CWB, two integral fuel tanks and product design robustness.

Figure 12 presents a summary of the advanced CWB weight breakdown and material distribution. The CWB weight using first generation epoxies (such as AS4/3501-6 or 3502) is 4150 lb, which represents a 14 percent weight savings over the baseline C-130H CWB. If an intermediate modulus fiber and tough resin are used for the advanced CWB composite parts (e.g., IM7/8552 or IM7/5250-4) a 24 percent weight savings can be achieved in the advanced CWB. Figure 12 also shows the advanced CWB material distribution, which is 72 percent composite, 19 percent aluminum, and 9 percent titanium.

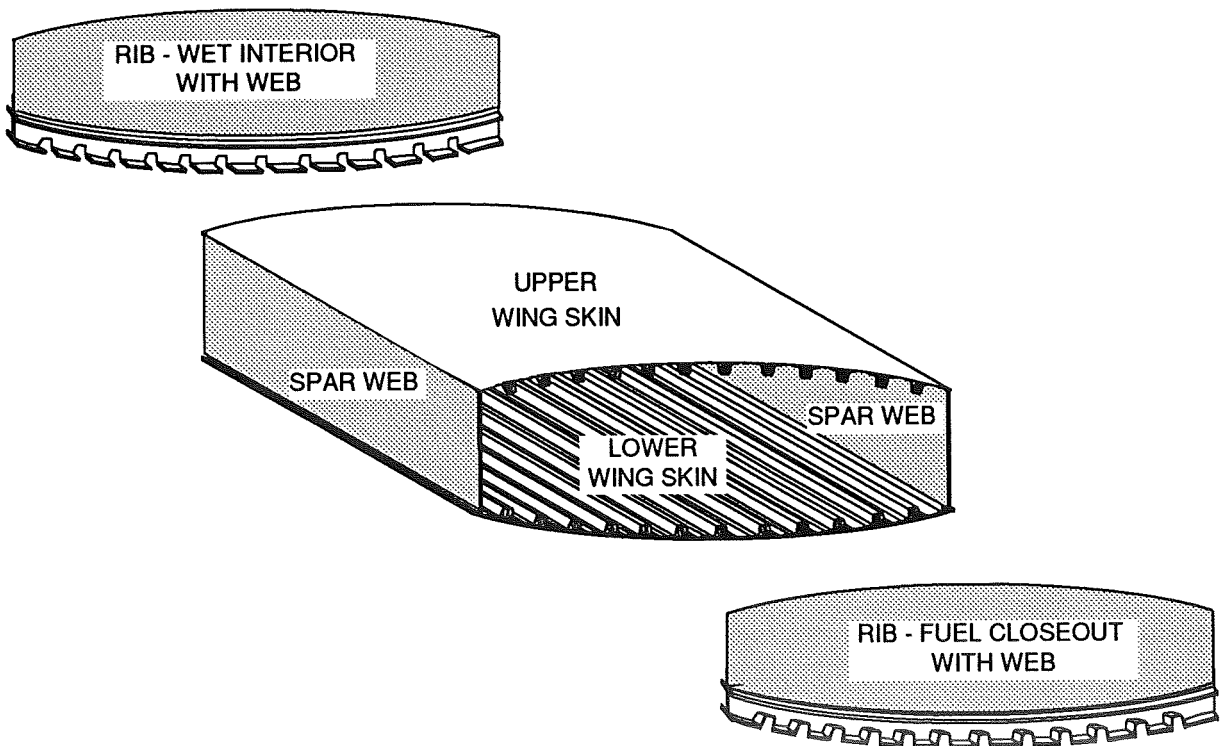
COST ANALYSIS

A summary of the advanced CWB costs are presented in Figure 13. The costs assume



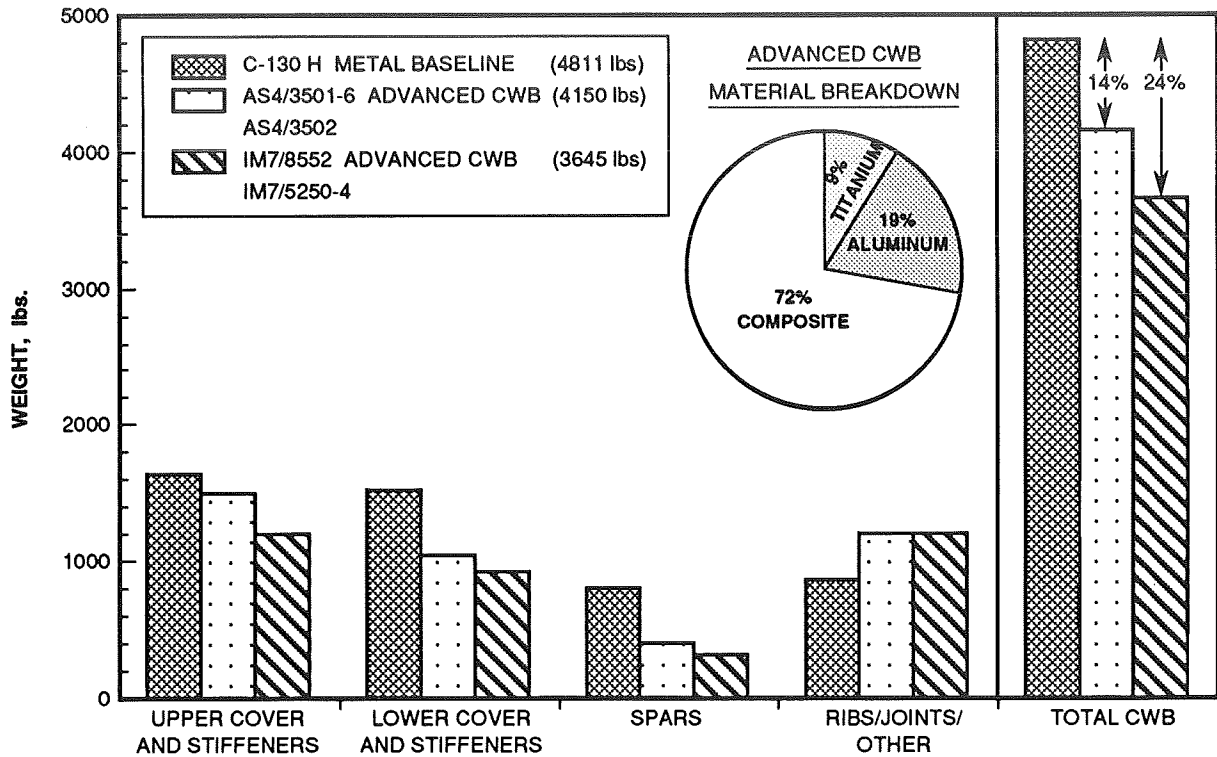
F91-C130/87

Figure 10. Selected Concepts for the Advanced CWB.



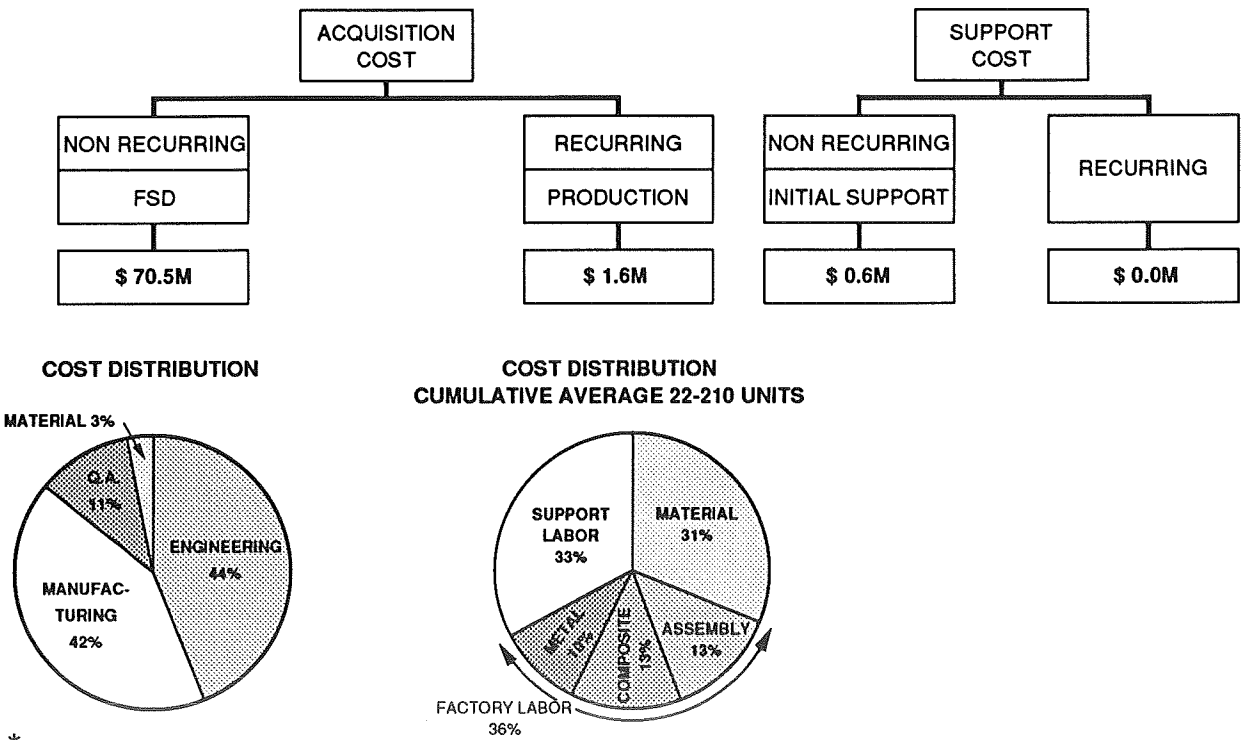
F91-C130/88

Figure 11. Selected Assembly Concepts for the Advanced CWB.



F91-C130/89

Figure 12. CWB Weight Breakdown.



* \$100/hour Assumed Wrap Rate

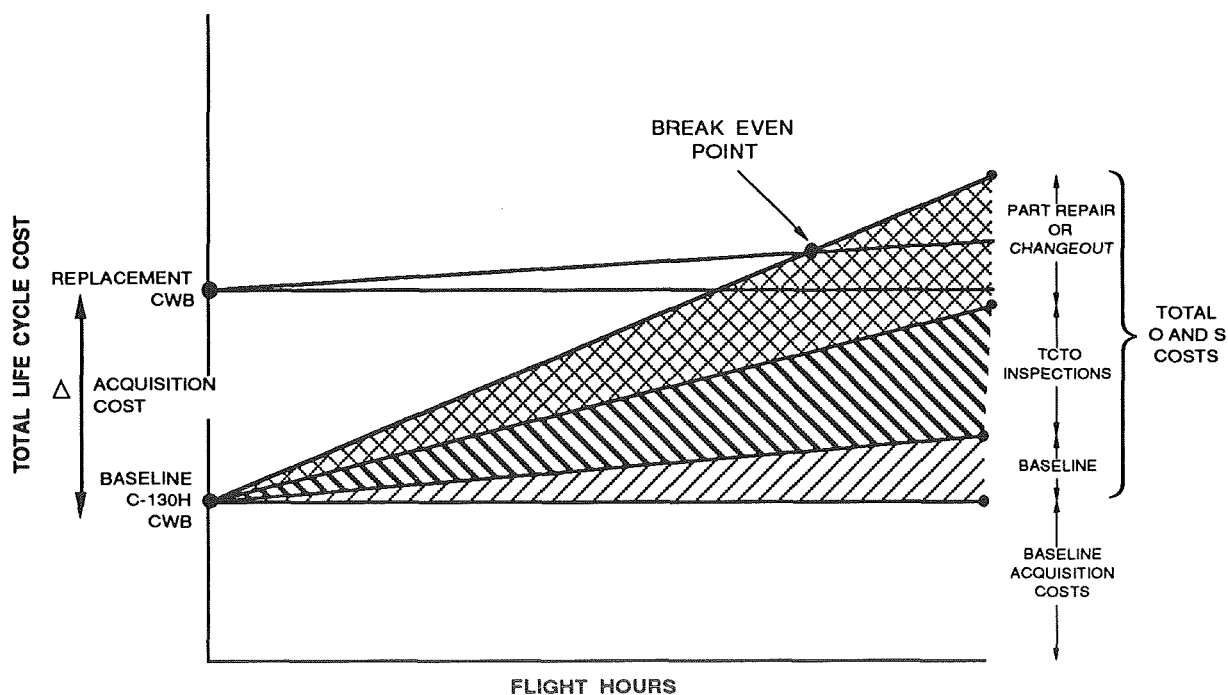
F91-C130/90

Figure 13. Advanced CWB Cost Summary.*

a \$100/hour wrap rate. Nonrecurring FSD costs are approximately \$70 million. The cumulative average recurring cost for a 22-210 unit buy is \$1.6 million.

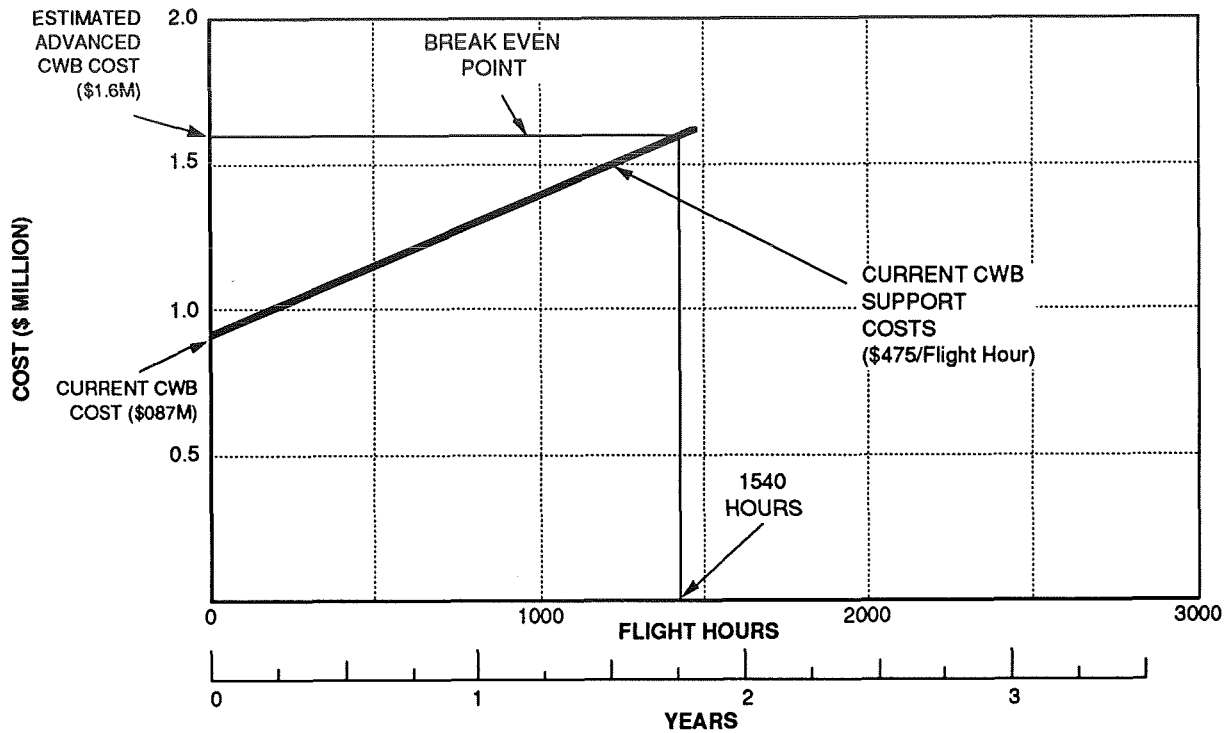
Figure 14 summarizes the life-cycle cost comparison approach for the advanced CWB and the C-130H CWB flown to an SOF mission profile. Baseline operation and support (O&S) costs are common costs for all CWBs. TCTO inspection and part repair or changeout are incurred on aircraft. Thus, in the break-even life-cycle cost scenario, it is the latter two which determine the break-even point, if the advanced CWB has a higher acquisition cost than the C-130H CWB.

Figure 15 applies this methodology directly to the advanced CWB and a C-130H CWB operating under durability limits. The advanced CWB cost of \$1.6 million is approximately 84 percent higher than a standard C-130H CWB at \$871,000. However, since the current C-130H CWB costs \$475/hour in maintenance costs, it consumes the price of its acquisition cost in 1833 flight hours. In addition, after 1540 flight hours, the current wing box has a life-cycle cost of \$1.6 million, equal to the advanced CWB acquisition cost, which requires no TCTO action. Therefore, the breakeven point of the advanced CWB in total life-cycle costs is 1540 flight hours or less than two calendar years. It should be noted that if nonrecurring FSD costs are amortized over 210 units, the break-even point will be reached in the third year.



F91-C130/44

Figure 14. Life Cycle Cost Comparison Approach for the Advanced CWB versus C-130H CWB.



F91-C130/45

Figure 15. Break Even Life Cost for Advanced CWB versus Current C-130H CWB.

SUMMARY

The selected hybrid composite/metallic advanced C-130 CWB concept met the severe SOF design requirements, reduced CWB weight by 14%-24%, and was cost effective relative to the current metal C-130H CWB. A significant composite weight fraction was needed to meet the severe SOF mission profile and the 4811 lb target. Lessons learned from prior Northrop/LTV programs were significant drivers in design concept selection, FSD approach and cost analysis.

ACKNOWLEDGMENTS

More than fifty Northrop personnel contributed to this program; their many and varied contributions are gratefully acknowledged. Special thanks are due to Govind Chanani, J.A. Hangen, John Luzar, Mike Jankowski, Daniel Acevedo, Tod Palm, Edmund Unterreiner III, Monica Rommel, Rick Kane, Alan Hiken, Scott Harris, and Douglas Sylvers, each of whom made invaluable contributions to the program. The team members from LTV played a crucial role in the program. Their participation and experience significantly influenced and improved the end product of this effort. Special thanks are due to Charles Foreman, Digger O'Dell, John Pimm, and Steven Rice.

Special acknowledgment and thanks go to Captain Kevin Silva and Lt. David Marcontell (WR/ALC) for their tireless efforts in supplying supporting information for the program. Without their interest and dedication, the execution of this program would have been extremely difficult.

REFERENCES

1. Whitehead, R.S., et al, "C-130 Advanced Technology Center Wing Box Conceptual Design/ Cost Study", Report No. WL-TR-91-3059, August 1991.
2. Jacobson, M.J., et al., "Battle Damage Tolerant Composite Wing Structure," Northrop Subcontract P.O. 600037 to Boeing Military Airplanes, NADC Contract Number N62269-89-C-0251.
3. Horton, R.E., et al., "Damage Tolerance of Composites," Volume II - Investigation of Thermoplastics (AS4/APC-2), Configuration Effects and Battle Damage Tolerance, AFWAL-TR-87-3030, July 1988.

THIS PAGE INTENTIONALLY BLANK

DEVELOPMENT OF COMPOSITE CARRYTHROUGH BULKHEAD*

R. J. Ehlen
 McDonnell Aircraft Company, St. Louis, MO
 and
 M. Libeskind
 Naval Air Development Center, Warminster, PA

518-24

51386

7-81

SUMMARY

A structural development program was recently completed in which the weight and fatigue advantages of an all composite major load carrying bulkhead was successfully demonstrated. Fabrication of a full scale article, including static and fatigue testing of the carry-through beam portion verified the producibility, strength and durability of this design, thereby presenting the opportunity for use on aircraft upgrades and new aircraft. A 15% weight saving is achievable and, more importantly, the fatigue problems that normally plague metal bulkheads are virtually eliminated.

INTRODUCTION

Current use of composite materials for primary structure in Navy production aircraft has been limited mainly to wing structure, tail structure, and fuselage panels. The weight and cost savings which were achieved through the use of carbon/epoxy were largely the basis for which these structures were selected for production application. The use of advanced composite materials in other applications which are subjected to high concentrated loads have been investigated to a limited extent, but full scale development work leading to concept verification has not as yet been performed.

An application which shows considerable promise in eliminating recurrent structural problems is the use of composites in highly loaded fuselage bulkheads. Advantages such as corrosion resistance and fatigue insensitivity of composite materials could be exploited to reduce high life cycle costs associated with structures in these limited access areas.

This program addressed the development and test of a highly loaded bulkhead for use on an emerging Navy tactical aircraft. The F-18 F.S. 453, Figure 1, is the baseline bulkhead for this program. It was selected because it is highly loaded and can provide direct comparisons between aluminum and composite bulkheads to determine the benefits and risks of composite application.

This was a six phase program. Phase one was an industry-wide review to identify design approaches used in recent composite bulkhead development programs. Phase two consisted of identifying design requirements and preliminary designs, and conducting structural trade studies. In phase three coupon and element tests were conducted and design refinement took place. Phase four

* This Contracted Research and Development (CRAD) program has been funded by the Naval Air Development Center through contract NO. N62269-87-C-0216, Development of Composite Carry-through Bulkhead. The work was performed by McDonnell Aircraft Company (MCAIR) in St. Louis.

consisted of the fabrication of the first full size composite bulkhead. Phase five involved a payoff evaluation and risk assessment comparing the baseline and composite designs. Phase six included the fabrication of a quarter bulkhead subcomponent as a further manufacturing risk reduction and then the fabrication and testing of a second full-scale bulkhead.

Goals for the composite bulkhead relative to the aluminum bulkhead were: a 20% weight reduction, a 10% cost reduction, and improved durability relative to fatigue and corrosion. The cost reduction goal included acquisition costs as well as operations and support costs.

The end-product of this program was the demonstrated availability of composite carrythrough bulkhead technology for use on emerging Navy aircraft.

BULKHEAD DESIGN AND FABRICATION

TECHNOLOGY REVIEW

A comprehensive literature review of recent and ongoing composite bulkhead development work was conducted to assess the design approaches used and problems encountered. Composite fuselage subcomponents of several existing and future aircraft have been fabricated and tested and composite bulkheads of varying degrees of complexity were addressed. The results of this review are documented in Reference 1 and 2.

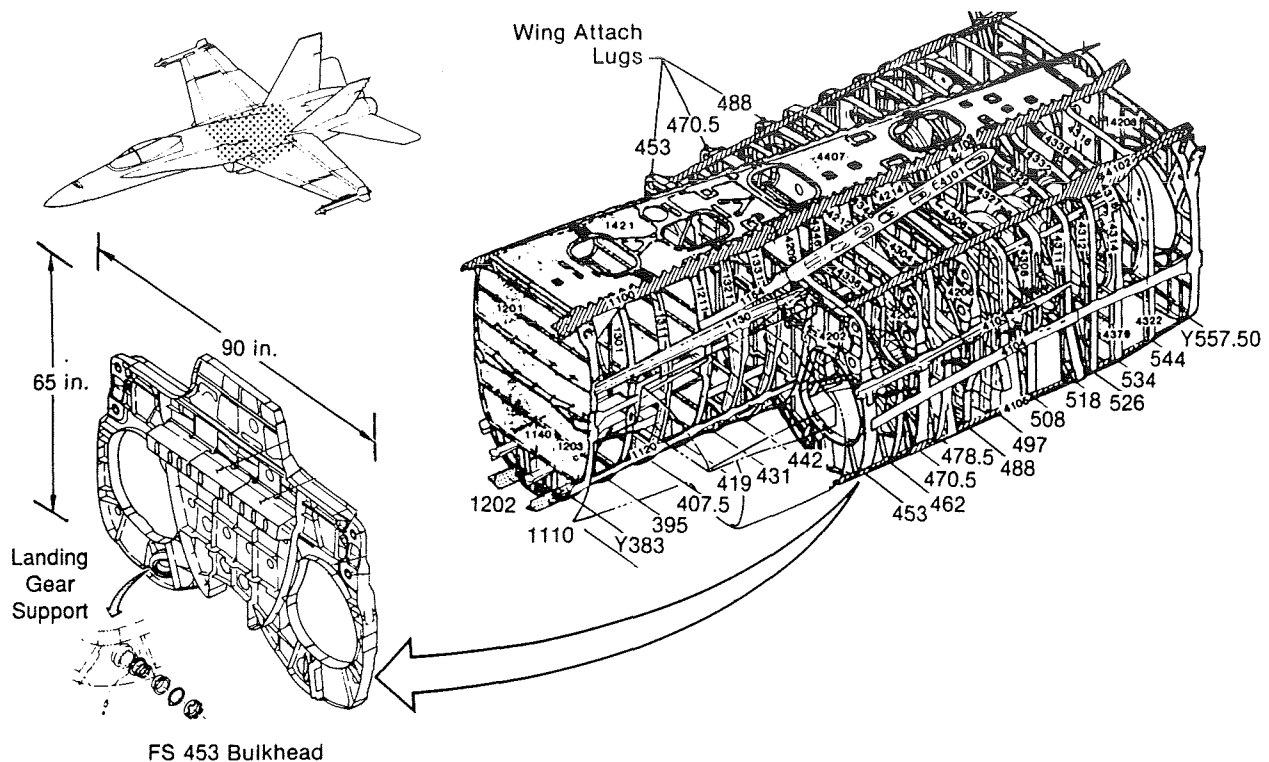
It was evident from this literature survey that the fabrication of a composite bulkhead with the complexity of the F-18 F.S. 453 had not yet been attempted.

A. BASELINE DESIGN

The baseline for this program was an aluminum bulkhead from the F-18. It was selected because it will permit a direct comparison of the benefits and risks for the same bulkhead made from composites. A large amount of manufacturing, service, and test data is available for the metal bulkhead.

The selected baseline, Figure 1, is the F-18 F.S. 453 bulkhead to which the wing is attached and from which the main landing gear forward trunnion is supported. The baseline is machined from 6 in. 7050-T73651 aluminum plate and weighs 264 lbs. Stiffeners, flanges, and wing attachment lugs are integral with the bulkhead. The upper dorsal section is made separately and is mechanically fastened to the bulkhead lower section. Cutouts in the center web area permit fuel system plumbing to pass through. The plumbing is joined at the web by fittings.

The maximum fuel pressures on the bulkhead are 13.2 psi ultimate forward-acting uniform pressure, occurring during arrested landing, and 8.2 psi aft-acting uniform pressure, occurring during a maximum acceleration catapult. Fuel constraints limit the temperature to 200°F; therefore, the bulkhead temperature does not exceed 200°F.



GP14-0175-4

Figure 1. F-18 Aluminum Production Bulkhead

The wing support lugs are integral parts of the bulkhead. Lug thicknesses and pin diameters are different for the upper and lower lugs, reflecting the magnitude and direction of the primary loads carried by each lug. The upper lug load acts primarily inboard; therefore the lug is sized for compression bearing stress. The lug is 1.56 in. thick and the pin diameter is 2.42 in. The lower lug load acts primarily outboard and is sized to prevent failure due to cleavage and tearout. This lug is 3.20 in. thick and pin diameter is 2.67 in.

Load paths in bulkhead structures are not nearly as direct as sometimes presumed in the generic bulkheads studied during aircraft design development. Bulkheads include structural details like abrupt thickness changes, intersecting stiffener radii, cutouts for fuel and control systems, flange joggles, secondary bending caused by shifts in load paths, and infringement of inlet ducts on the ideal load path. Such situations are addressed on the F-18 F.S. 453 baseline.

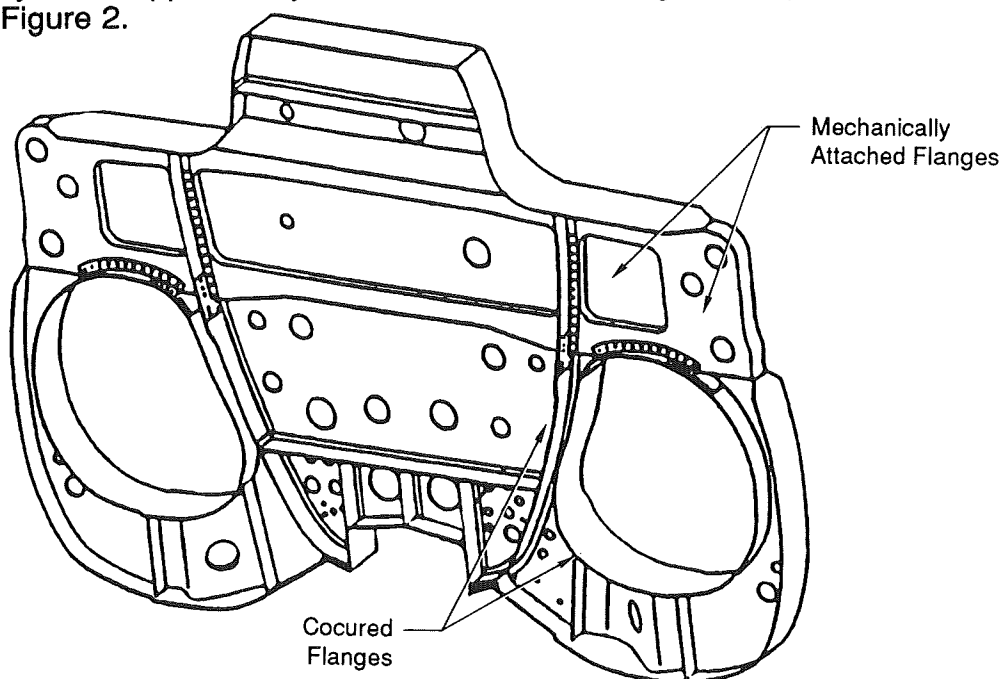
B. DESIGN REQUIREMENTS

The primary design requirement for the composite bulkhead was that it would have the form and function of this baseline bulkhead and would be capable of carrying all loads currently applied to the metal baseline. Specific requirements were that it must be able to withstand static ultimate loads (1.5 times limit load) without failure for critical design conditions, and that it must be capable of

withstanding two lifetimes (12000 spectrum flight hours) of enhanced (to account for composite scatter) fatigue loading. Low energy damage tolerance requirements were also imposed on the structure. In addition, the bulkhead was designed for -65°F to +200°F service temperature with moisture equivalent to 10 years on Guam.

C. TRADE STUDIES

Ten preliminary design concepts were defined and evaluated with respect to weight, cost, supportability, and fabricability. Selection of the best overall concept was made based on the results of this evaluation. Weight was the most important consideration in the selection of the preferred concept followed by cost, producibility, and supportability, in that order. The design concept selected is shown in Figure 2.



GP14-0175-3

Figure 2. Selected Composite Bulkhead Concept

A number of thermoset, both epoxy and bismaleimide, and thermoplastic matrices was considered. Critical properties for the selection of a matrix were the elevated temperature wet compressive strength, the residual strength after low velocity impact, and its resistance to microcracking. Based on these parameters, 8551-7 toughened epoxy, produced by Hercules Aerospace Co., was selected as the most appropriate matrix. AS4 and IM7 carbon fibers, also produced by Hercules Aerospace Co., were selected to reinforce this matrix. The high modulus IM7 fibers were used in unidirectional tape, wherever practical, to satisfy stiffness requirements with minimum weight, and AS4 cloth was used for web plies that wrapped around corners to form flanges. (AS4/8551-7 cloth was not available at this time.) Subsequent to this survey, Hercules modified the 8551-7 resin to improve tack and increase use temperature. The modified resin was labeled 8551-7E. This resin was further modified to improve out time and was designated as 8551-7A.

PRELIMINARY DESIGN AND TESTING

Coupons and critical structural elements were fabricated and tested to demonstrate fabrication methods, determine static strength and fatigue life and to validate critical design details. The structural elements represented specific areas of the bulkhead, as shown in Figure 3. Various elements were static and fatigue tested in room temperature dry and elevated temperature wet environments. In addition, some specimens were tested after low velocity impact damage had been introduced. Test conditions and results are summarized in Figure 4.

FIRST BULKHEAD FABRICATION

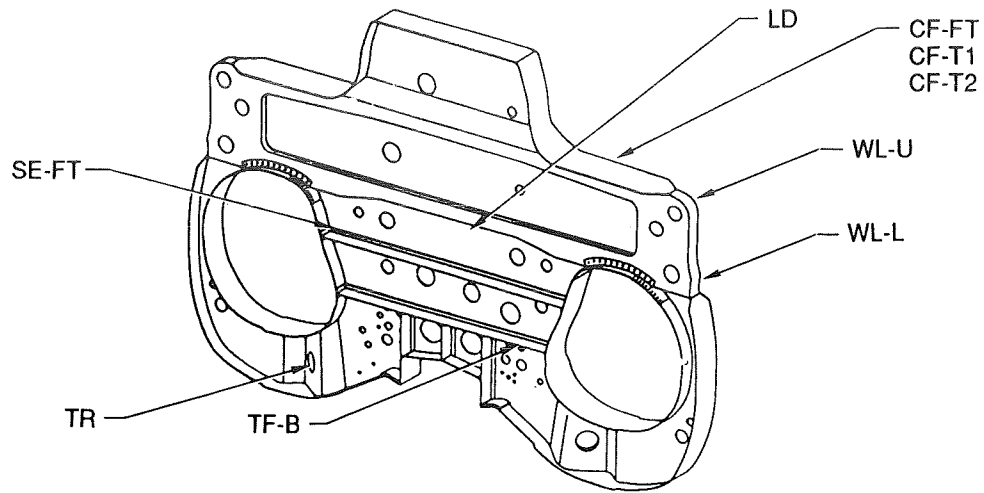
Tooling used to fabricate the bulkhead consisted of aluminum, graphite, steel, carbon/epoxy and conformal pieces. The most important feature of the tooling is the conformal tool. The conformal tool is flexible and is pressurized during the autoclave cycle. This tool is capable of providing uniform pressure, simultaneously, against the web and adjacent flanges of the bulkhead. This tooling concept produces excellent corner details on the bulkhead and leaves no tool mark off. Figure 5 shows two conformal tools being used against the two sides of a bulkhead.

The design of the bulkhead was such that it could be fabricated as an assembly of subcomponents. These subcomponents consisted of 1) the carrythrough beam, 2) trunnion webs, 3) stiffeners, 4) the forward web plies, and 5) the aft web plies. The carrythrough beam, trunnion webs, and stiffeners were all made up of unidirectional tape plies. The carrythrough beam and trunnion webs were similar, in that each consisted of two complementary ply packs that sandwiched the main web of the bulkhead. The plies for each pack were cut, collated, room temperature debulked, and held under vacuum until ready for final assembly.

The fore and aft web subcomponents were made of cloth plies that formed the main web of the bulkhead as well as the centermost plies of the carrythrough beam and trunnion webs. In addition, these plies were folded perpendicular to the plane of the bulkhead to form the innermost plies of the duct and moldline flanges. As with the other subcomponents, the web plies were room temperature debulked before final assembly.

The fabrication of a large and complex component such as the F-18, FS453 carrythrough bulkhead was an industry achievement in 1989. Figure 6 shows the full scale bulkhead. In this figure, the mechanical fittings as shown in Figure 2 are not yet attached. Non-destructive Inspection (NDI) indicated the bulkhead contained porosity and delaminations. Load testing was not performed on this bulkhead.

The material system of this first bulkhead was AS4/8551-7A cloth and IM7/8551-7A. IM7/8551-7A cloth was not available at the time of the fabrication effort. The previously fabricated test elements contained AS4/8551-7E cloth and IM7/8551-7E tape. The change from the 8551-7E to the 8551-7A resin allowed longer out-time and the subsequent retention of mechanical properties.



View Looking Forward

Specimen	Region Represented	Loading	Test Load (kips)	No. of Tests	Environment	Remarks
LD	Web Area Between Inlet Ducts	Spectrum Fatigue	14.0	2	RTD	Tested for 1 Lifetime at DLL Following LVID
TF-B	Tank Floor Support, Bending	Static Shear	0.8	1	ETW1	Bending of Tank Floor Support Flange After LVID
		Spectrum Fatigue	0.5	1	ETW2	
		Spectrum Fatigue	0.5	1	RTD	
SE-FT	Stiffener End Tie-In, Flatwise Tension	Static Tension	2.1	1	ETW1	After LVID
		Static Tension	2.1	1	RTD	
		Spectrum Fatigue	1.3	2	ETW2	
		Spectrum Fatigue	1.3	1	RTD	
		Spectrum Fatigue	1.3	1	RTD	
WL-U	Wing Attach Lug-Upper	Static	307	1	ETW1	Full Scale
WL-L	Wing Attach Lug-Lower	Static	308	1	ETW1	Full Scale
CF-FT	Carrythrough Beam Flange Flatwise Tension	Static	2.2	1	ETW1	
		Spectrum Fatigue	1.5	1	ETW2	
CF-T1	Carrythrough Beam Flange Inboard/Outboard Tension	Static	-12.0	1	ETW1	
		Spectrum Fatigue	-8.0	1	ETW2	
CF-T2	Carrythrough Beam Flange Fore/Aft Tension	Static	12.4	1	ETW1	
		Spectrum Fatigue	8.3	1	ETW2	
TR	Trunnion Attach Lug	Static	140 Inbd 160 Vert	1	ETW1	

Notes:

1. ETW1: 200°F, saturation after 75 days. Used for static tests.
ETW2: 160°F, saturation after 75 days. Used for fatigue tests.
2. All static tests will be to failure except specimen TR, which will be tested to ultimate load at the two most critical design conditions.
3. All fatigue tests will utilize the F-18 wing root spectrum.
4. All fatigue tests except those for LVID specimens will be tested to failure.
5. LVID specimens will be impacted, and then spectrum fatigue tested at DLL for one lifetime, while monitoring damage growth.

GP14-0175-2

Figure 3. Element Test Matrix

Specimen ID	Test Requirement		Design Requirement		Test		Comments
	Type	Temperature	Load (lb)	Life (SFH)	Load (lb)	Life (SFH)	
LD-1	SF After LVID	RTD	4,700	6,000	4,700	6,000	No Growth in Delamination Area
LD-2	SF After LVID	RTD	5,577	6,000	5,577	6,000	No Growth in Delamination Area
LD-3	SF After LVID	RTD	6,455	6,000	6,455	6,000	No Growth in Delamination Area
TF-B-1	Static	200°F Wet	284	Static Ultimate	525	Static	First Load Drop – Failure at 1,286 lb
TF-B-2	SF	160°F Wet	217	12,000	217, 260, 290, 320, 370	12,000 at Each Load Level	No Failure
TF-B-3	SF After LVID	RTD	217	6,000	217	6,000	No Growth in Delamination Area
SE-FT-1	Static	RTD	2,550	Static Ultimate	5,387	Static	Separation of Stiffener End From Flange
SE-FT-2	Static	200°F Wet	2,100	Static Ultimate	4,948	Static	Separation of Stiffener End From Flange
SE-FT-3	SF	RTD	1,584	12,000	1,584, 3,700, 4,000, 4,200, 4,700, 5,000	12,000 SFH Each Load	Failure at 5,000 lb, 7,661 SFH
SE-FT-4	SF After LVID	RTD	1,584	6,000	1,584, 1,800, 1,985, 2,620	6,000 SFH Each Load	Failure at 2,620 lb, 897 SFH
SE-FT-5	SF	160°F Wet	1,266 (80% DLL)	12,000	1,266, 2,200, 2,500, 2,800	12,000 SFH Each Load Except Failure	Failure at 2,800 lb, 2,784 SFH
SE-FT-6	SF	160°F Wet	1,740 (110% DLL)	12,000	1,740, 2,200, 2,500, 2,650	12,000 SFH Each Load Except Failure	Failure at 2,650 lb, 10,300 SFH
WL-U	Static	200°F Wet	307,000	Static Ultimate	310,800	Static	Shear Failure, No Bearing Failure
WL-L	Static	200°F Wet	308,000	Static Ultimate	400,000	Static	Reached Test Machine Capability With No Failure
CF-FT-1	Static	200°F Wet	2,960	Static Ultimate	6,718	Static	Flange Peeled From Cap
CF-FT-2	SF	160°F Wet	1,960	12,000	1,960, 2,160	12,000, 1,535	Failure at 2,160 lb, 1,535 SFH, Start of Flange Peel
CF-T2-1	Static	200°F Wet	12,400	Static Ultimate	13,425	Static	Fasteners Failed. No Specimen Failure
CF-T2-2	SF	160°F Wet	9,360	12,000	9,360, 13,325	12,000 SFH Each Load Level	No Failure
TR-1	Static	200°F Wet	160,000 Vertical	Static Ultimate	126,000	Static	Interlaminar Shear Failure (Web Delamination). Crippling Failure of Upper Cap

SF denotes Spectrum Fatigue
LVID denotes Low Velocity Impact Damage

RTD denotes Room Temperature Dry
SFH denotes Spectrum Flight Hours

GP14-0175-1-D/jam

Figure 4. Summary of Element Test Results

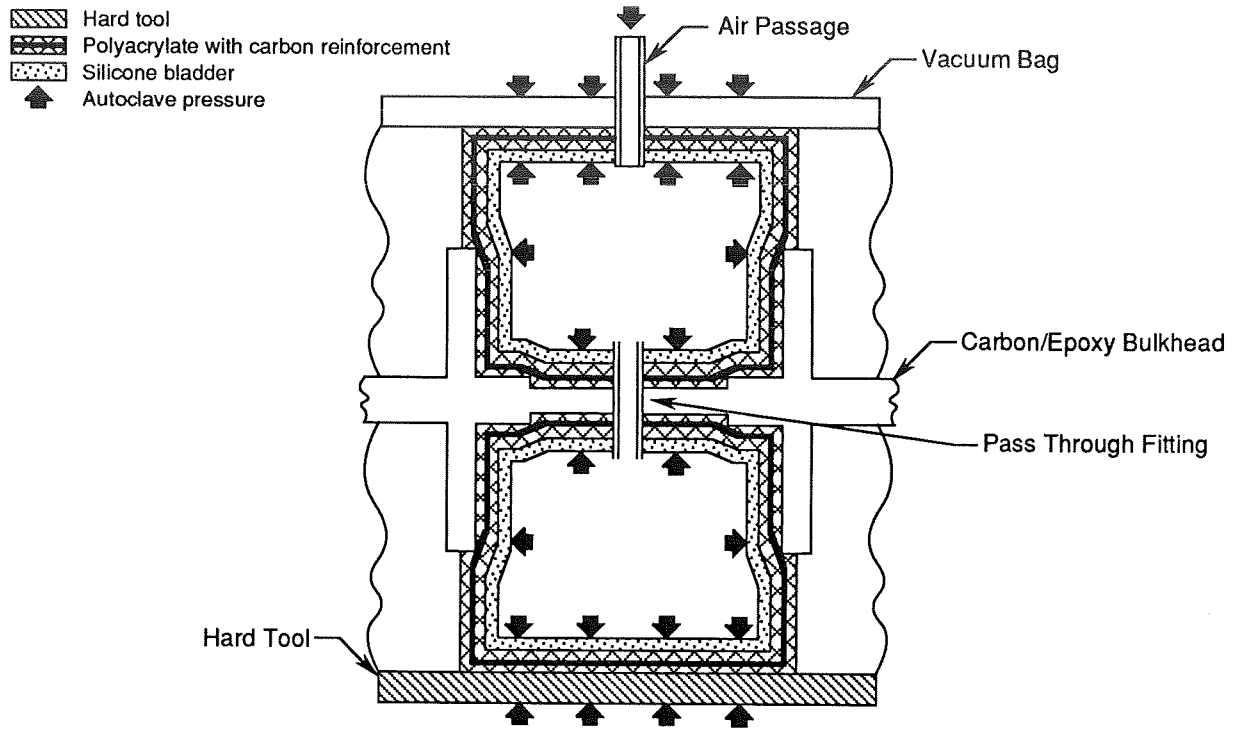


Figure 5. Conformal Tooling for First Bulkhead

GP14-0175-5-D/cjg

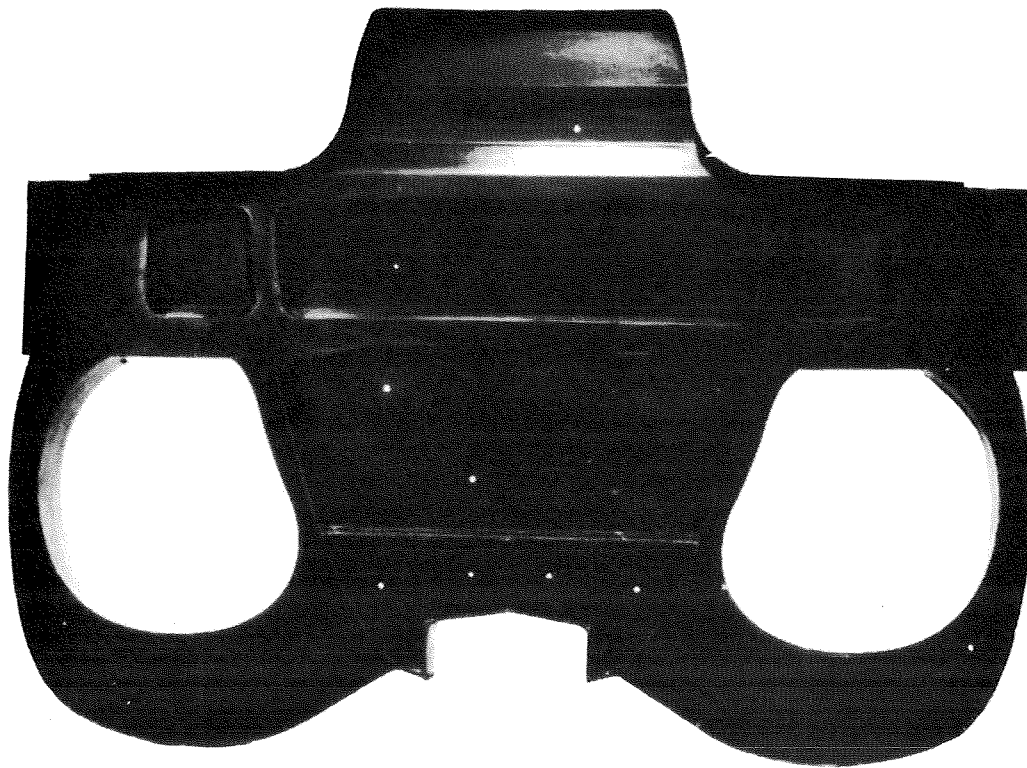


Figure 6. First Bulkhead
Forward Side

GP14-0175-6

MANUFACTURING RISK REDUCTION FOR THE SECOND BULKHEAD

The first bulkhead played a significant role in this program in terms of manufacturing lessons learned. An example is air leakage detected from the conformal tools during the autoclave cycle. The lack of the appropriate pressure in the conformal tools during the autoclave cycle caused the porosity and delaminations of the bulkhead. Conformal tooling improvements were identified.

Lessons learned from the first bulkhead fabrication now went into planning the second bulkhead. As part of this risk reduction effort, design modifications, tooling changes, and processing changes were first demonstrated on a quarter bulkhead subcomponent. This subcomponent was fabricated prior to the second bulkhead to verify the manufacturing, cure cycle, and detail changes.

The summary of the risk reduction effort is:

- Reduced the number of conformal tools.
- Built new conformal tools, with improvements, to reduce leakage
- Refined the processing cycle.
- Implemented a bulkhead design improvement.
- Fabrication of the subcomponent.

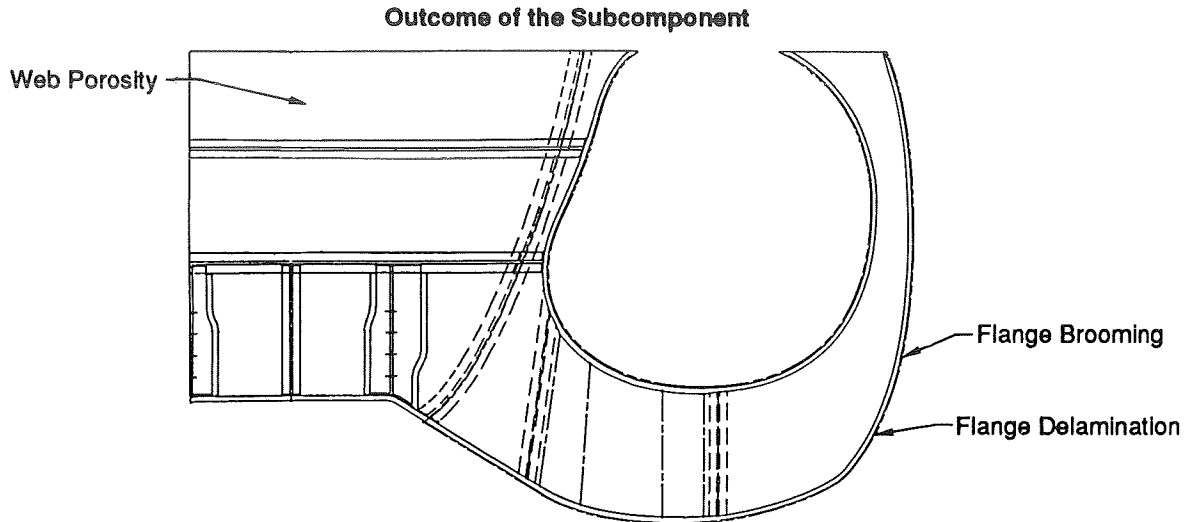
The material system which was used on the subcomponent as well as what was used on the second bulkhead is IM7/8551-7A tape and cloth.

The risk reduction subcomponent had significantly improved quality from the first bulkhead but still contained some abnormalities. Figure 7 shows the few abnormalities of the subcomponent and the further corrective action to be applied to the second bulkhead.

To prevent the flanges from brooming, the flange width was reduced. Narrower flange width avoids flange contact with the bond tool. This approach has no detrimental impact to the bulkhead; the flanges are oversized during the cure cycle and then later trimmed to blueprint width.

The flange delamination occurred where the tape ply pack and cloth ply pack interface. FM300 adhesive was inserted at this interface on the second bulkhead.

The corrective action for the web porosity was to lay porous teflon cloth between the bulkhead web and the conformal tool. The porous teflon cloth helps to prevent the entrapment of air between the bulkhead web and the bond tools.



Corrective Action to Be Applied to the 2nd Bulkhead

- Flange Brooming: Pre-Machined Flange Width Reduced to Avoid Tool Contact
- Flange Delamination: FM300 Inserted Between the Tape Ply Pack and Cloth Ply Pack
- Web Porosity: Porous Teflon Inserted Between the Bulkhead and the Conformal Tool

GP14-0175-7

Figure 7. Lessons Learned From Subcomponent Fabrication

SECOND BULKHEAD FABRICATION

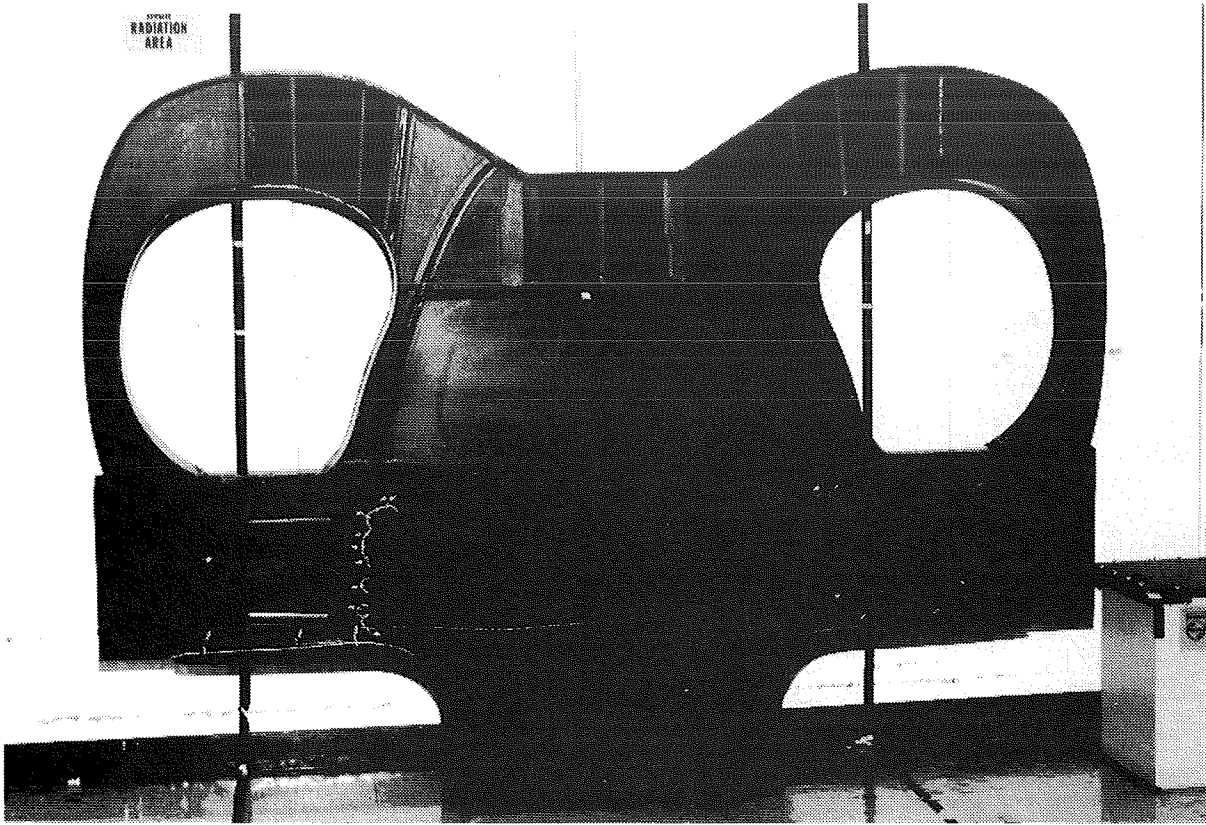
The second bulkhead fabrication procedure benefited from the lessons learned from the first bulkhead and the quarter-bulkhead subcomponent. Figure 8 shows this bulkhead after curing. The mechanical fittings shown in Figure 2 are not yet installed.

Automated through transmission C-scan and pulse-echo A-scan ultrasonic inspections were performed on the bulkhead webs and flanges. Abnormalities detected were further investigated by radiography.

The second bulkhead was of significantly better quality than the first bulkhead. Some porosity, delaminations, and foreign material were detected. Figure 9 shows the NDI results.

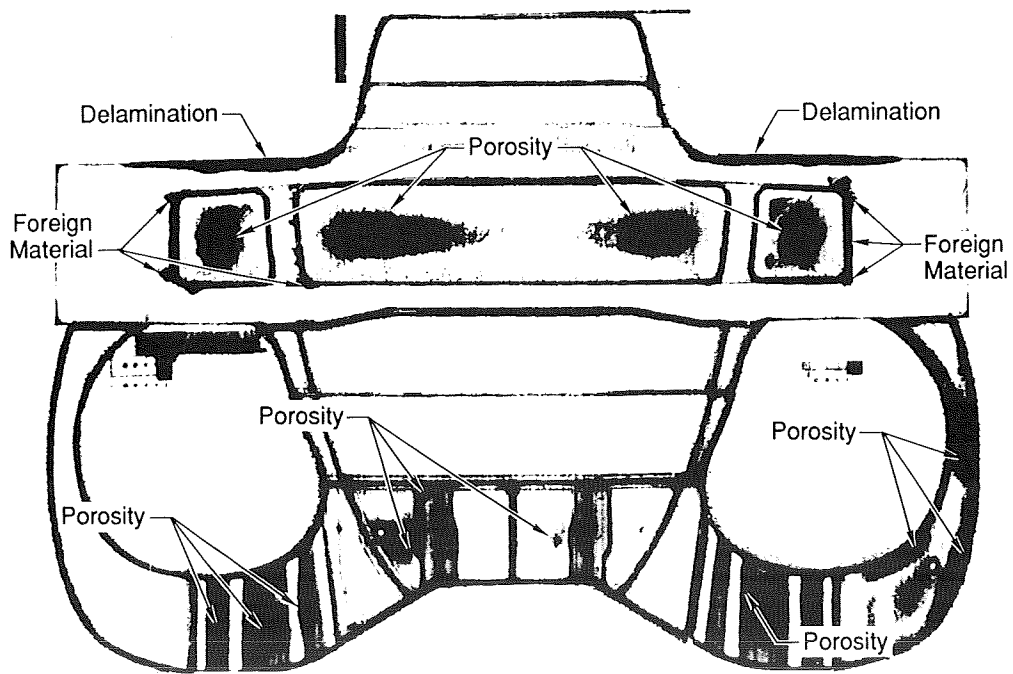
The porosity, delaminations, and foreign material damage were all reviewed for possible repair to blueprint equivalent strength.

Resin injection and mechanical fastening were considered for repair methods of the delaminations. While limited resin injected repair data are available for the 3501 resin system, little data exist for the 8551-7A system. Hence, mechanical fastening was chosen for the delamination repair. Figure 10 shows this repair.



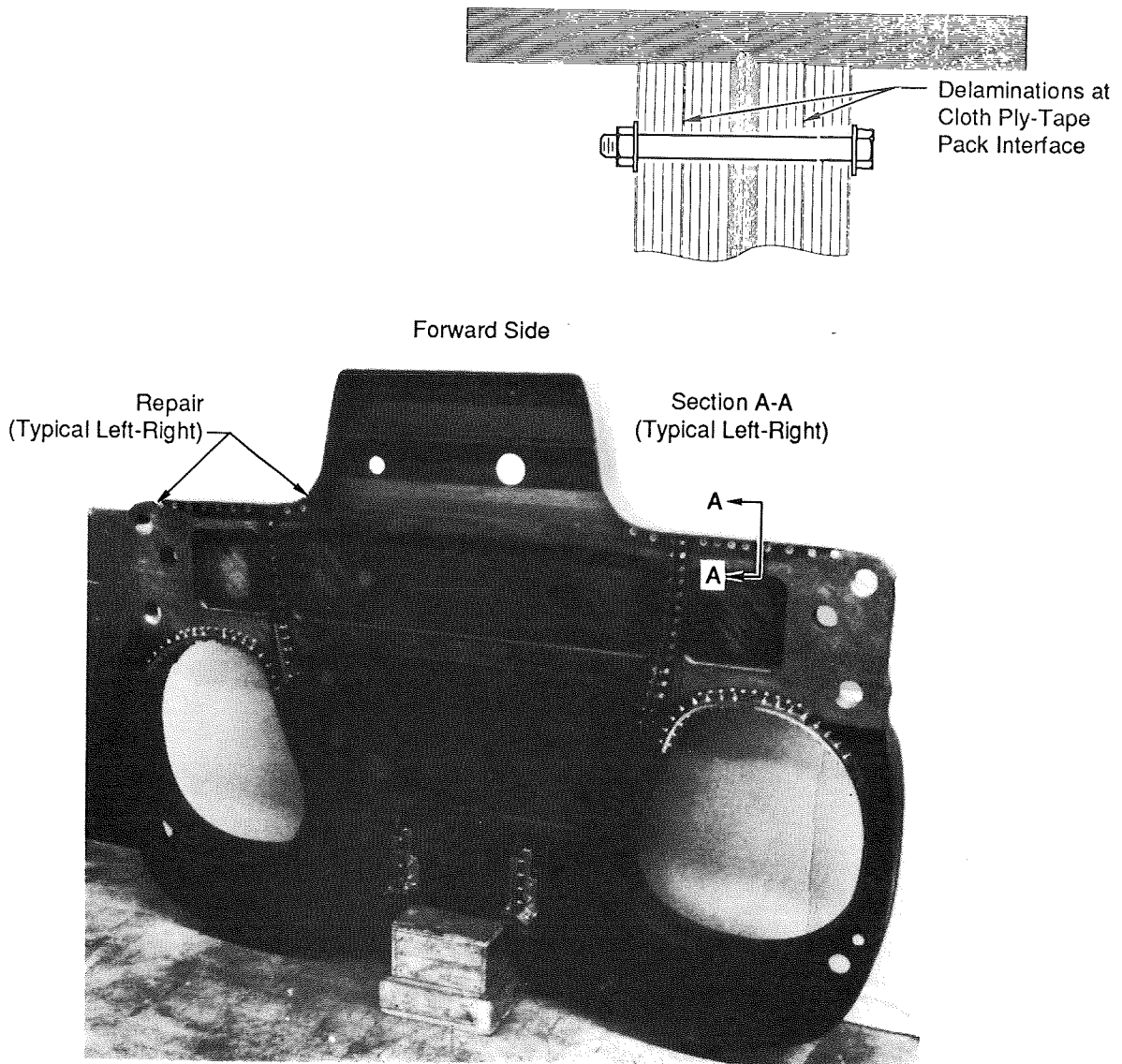
GP14-0175-8

**Figure 8. Second Bulkhead
Forward Side**



GP14-0175-9

Figure 9. Ultrasonic Inspection Summary of Second Bulkhead



GP14-0175-10

Figure 10. Delamination Repair

As with all thermosets, porosity is not repairable. The approach to evaluating the strength impact of porosity was to create "delta dB (decibel) vs. strength retention" data for the material system in use. Delta dB is the difference of ultrasonic attenuation between a "flaw free" laminate and a "flawed" laminate. By having the delta dB of a family of flawed laminates, and through mechanical testing to obtain the drop in strength properties for these laminates, curves of this nature can be created. This program took advantage of "delta dB vs. strength retention" curves for IM7/8551-7A that were created by MCAIR during a previous program.

The foreign material contamination is of little strength consequence to the bulkhead due to its location.

The final assembled bulkhead has mechanically attached fittings. One set of these fittings is used to complete the upper portion of the inlet flange, another set to splice the fuselage interface flange, and the other set is used to carry high-magnitude "kick" loads along the lower-inboard moldline flange.

LOAD TESTING THE SECOND BULKHEAD

Load testing of the bulkhead focused on the wing attach lugs. Wing bending moment was applied to the wing attach lugs but no wing vertical shear loads were applied. The wing vertical shear was not applied due to extreme complexities of simulating the "as installed in the aircraft" bulkhead boundaries in the test fixture.

The load test events for the wing attach lugs were:

- Proof load to the highest load in the enhanced fatigue spectrum (142% design limit load)*
- F-18 wing root enhanced spectrum fatigue test - 2 Lifetimes (12000 Spectrum Flight Hours)
- Static test to ultimate load - 150% design limit load
- Static test to failure

During the initial proof load testing, a load noise was heard at 113% design limit load. Upon inspection, a fracture along the carrythrough beam and the basic bulkhead web interface was found. This fracture existed on both the left and right side of the part. Since there were no strain gages in this immediate vicinity, no unusual strain indications were observed during loading. Testing was stopped and an investigation into the cause of this fracture was initiated. During this investigation, it was determined that a problem existed with the finite element model.

In the finite element model, an axial load path in the moldline flange was modeled where it did not exist. This modeling error caused a misrepresentation of the adjacent web strains; hence the web strains in the model were lower than actual since the moldline flange was carrying the load in the model when in reality it could not. It is important to recognize this fracture was due to a finite element modelling oversight and should not reflect upon the potential of composite structure of the type being addressed in this program. The finite element model was remodeled to properly represent the moldline flange and to account for the lost load path of the fractured web.

Further analysis indicated that this discontinuity should not present a problem with continuing the test of the carrythrough beam portion of the bulkhead, but would require repair if the trunnion area were to be tested as planned. Strain gages were installed in the vicinity of the fracture to monitor any growth during subsequent testing. Proof loading and subsequent fatigue testing were completed without any additional incidents.

* The fatigue testing included an enhancement factor to account for composite scatter. Reference 3 is the source of this enhancement factor.

Fatigue testing consisted of the application of two lifetimes of enhanced, to account for composite fatigue scatter, spectrum loads to the bulkhead carrythrough beam in order to demonstrate the durability of the design. The maximum fatigue load of this enhanced spectrum was equivalent to 142% design limit load.

Following the fatigue testing, the bulkhead was loaded to failure which occurred at 186% design limit load. Failure was a tension failure in the lug area. This failure load exceeds 150% DLL by a sufficient margin to account for environmental degradation and statistical scatter of the composite material.

The planned testing of the trunnion area was deleted from the program due to lack of funding required to perform the test and to repair the carrythrough beam and web interface.

PAYOFF EVALUATION AND RISK ASSESSMENT

Weight - The second composite bulkhead, including the mechanical fittings weighs 233 lbs. after trim. This weight also includes the fasteners used to repair the delamination. The F-18 aluminum bulkhead weighs 265 lbs. Thus, a weight savings of 12% was achieved, however, a larger weight savings (approximately 15%) would result if the repair was not necessary. This scenario demonstrates the need for follow-on programs to develop composite materials or forms which will not have penalties for the lack of out-of-plane strength. This comment is made in light of the fact that some of the mechanical fittings on the second bulkhead were installed to carry out-of-plane loads.

Cost and Supportability - Figure 11 shows the relative cost of the composite bulkhead to the comparable aluminum bulkhead. This figure also shows the relative supportability efforts.

Damage Tolerance - Damage tolerance was demonstrated during the bulkhead load testing. Porosity, which did occur in the second bulkhead, simulated the planned inducement of low velocity impact damage. No load testing results were degraded due to the presence of porosity.

Repairability - The second bulkhead did contain some delaminations and porosity. Repairability of the delaminations was achieved as described earlier.

Concept	Relative Weight (Actual)	Relative Cost (Estimated)	Relative Supportability (Estimated)
Composite	0.89	2.37	0.94
Aluminum	1.0	1.00	1.00

Note: Low value is better

GP14-0175-11-D/cjg

Figure 11. Payoff Evaluation

RESULTS AND DISCUSSION

The bulkhead developed in this program is one of the more complex one-piece composite structures ever attempted. The geometry of this bulkhead, coupled with the use of a new material system and an advanced tooling concept, have provided a substantial technical challenge. While not perfect, the prototype component has met this challenge and represents a significant step forward in the development of composite bulkhead technology.

The use of composite materials for large, complex, and highly loaded components has been advanced as a result of this program. Further research is recommended in design and fabrication so that flight worthiness of components of this type can be demonstrated. This is an essential step for the transition of this technology into emerging aircraft programs.

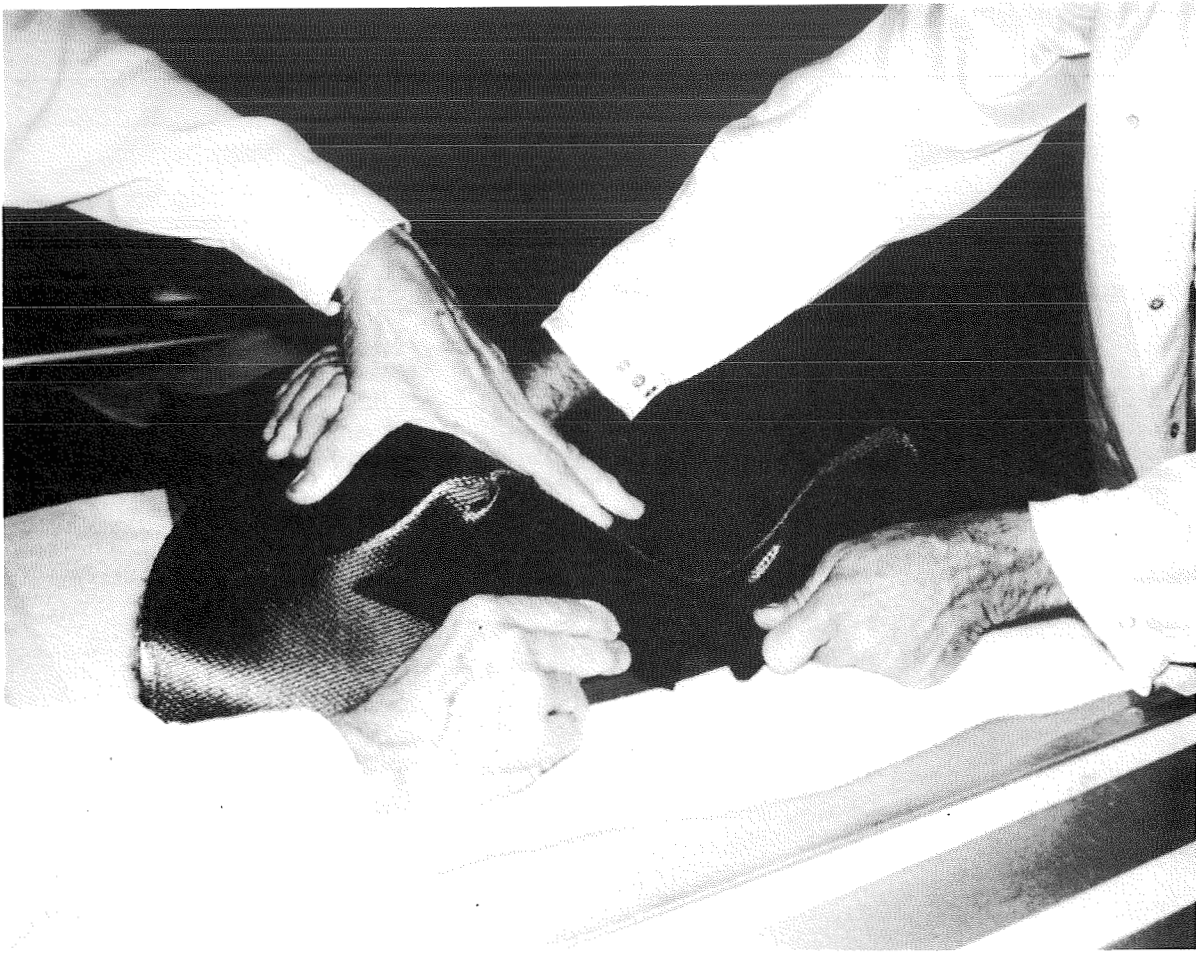
Engineering design guidelines and manufacturing guidelines are listed to aid future composite bulkhead work.

ENGINEERING DESIGN GUIDELINES

- Avoid ply darting. When laying broadgoods into complex surfaces, the fabric may not be formable to all surfaces. If ply darting cannot be avoided, verify dart details through analysis and structural testing. An example of ply darting is shown in Figure 12.
- Avoid abrupt ply termination. An example of abrupt ply termination is shown in Figure 13.
- Design for secondary loads induced onto the mating structure of the part. Figure 14 shows an example of secondary loads. Another consideration is the secondary loads that develop from the curved flange phenomenon.

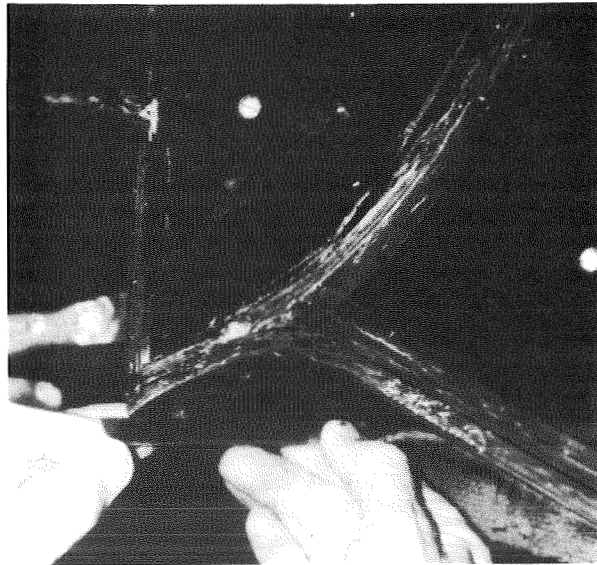
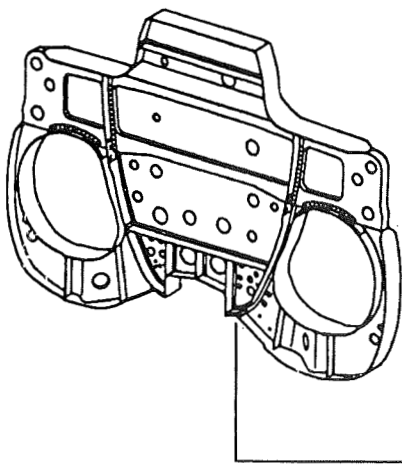
MANUFACTURING GUIDELINES

- Use conformal tools for fabrication of parts with multiple integral flanges. The conformal tools could be of the nature shown in Figure 15. If a remain-in-place mandrel is used for bladder lay-up and fabrication, it should be a material that will not puncture the bladder.
- It is advised to use film adhesive during the component lay-up to fill voids. A commonly occurring void is shown in Figure 16.
- To avoid porosity in thick laminates the use of multiple debulk cycles should be considered as shown in Figure 17.
- Use computer codes such as "Computer Aided Curing of Composites" (Reference 4) for the development of the autoclave cycle.
- Verify the manufacturing and design details by fabrication of a subcomponent.



GP14-0175-12

Figure 12. Ply Dart for the Trunnion Support Web



GP14-0175-13

Figure 13. Ply Termination Conjunction on First Bulkhead

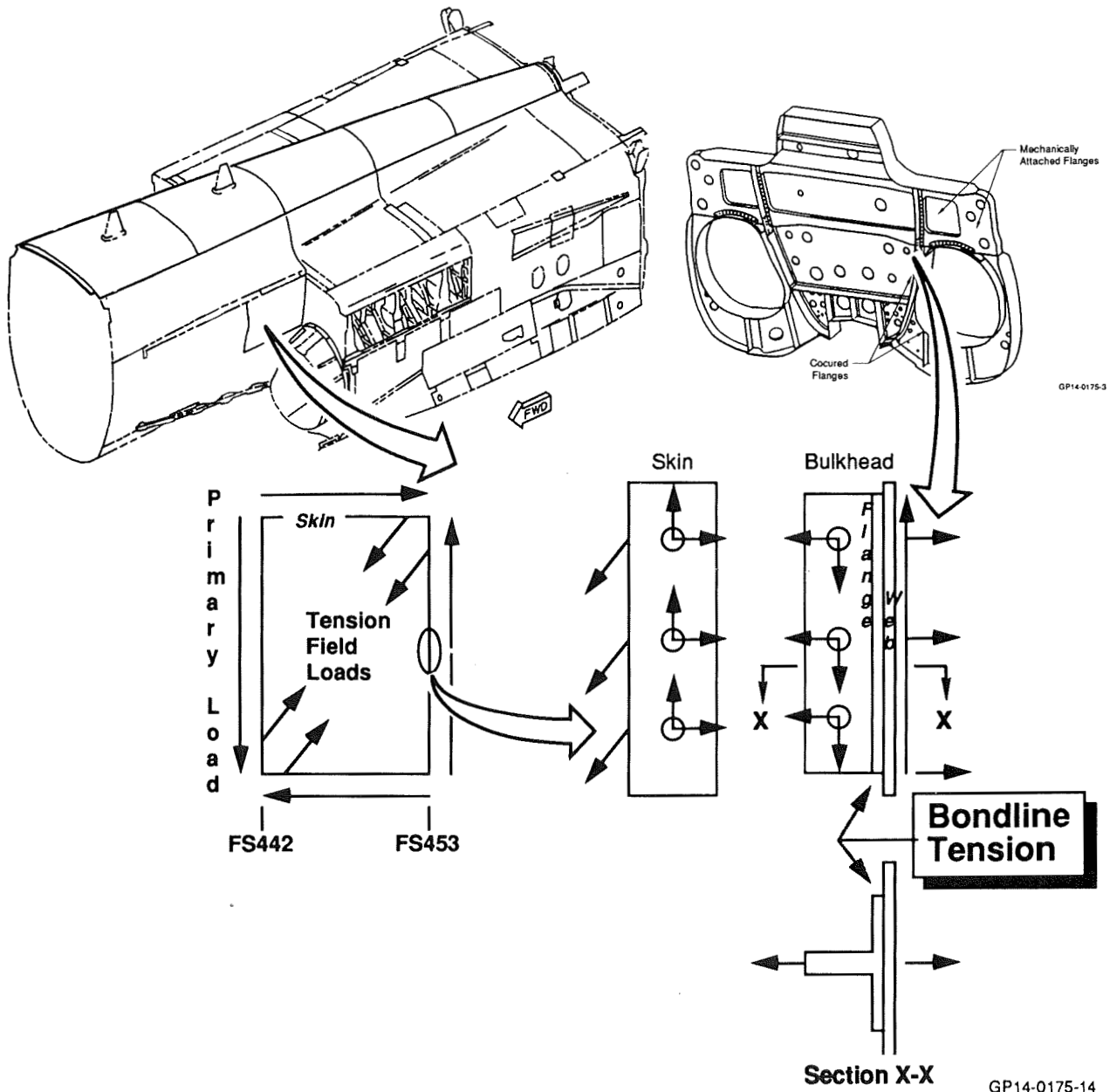


Figure 14. Bondline Tension From Secondary Loads

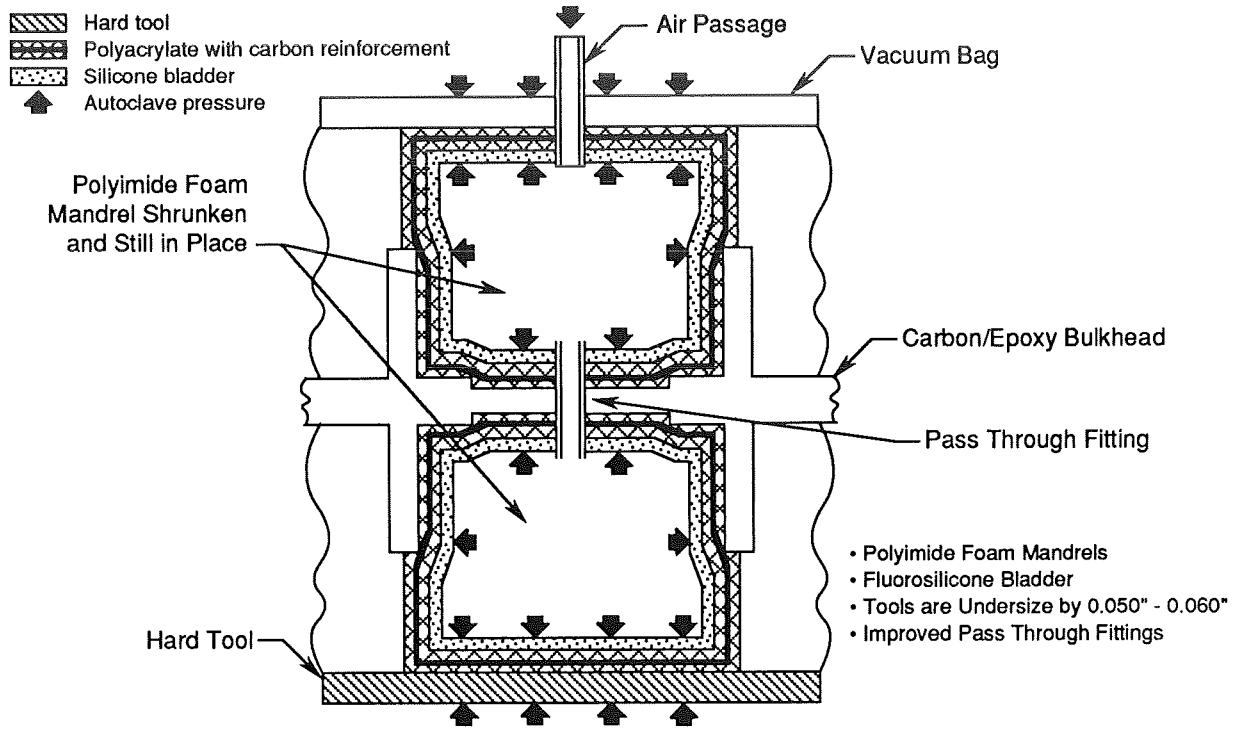


Figure 15. Conformal Tooling for Second Bulkhead

GP14-0175-15-D/cjg

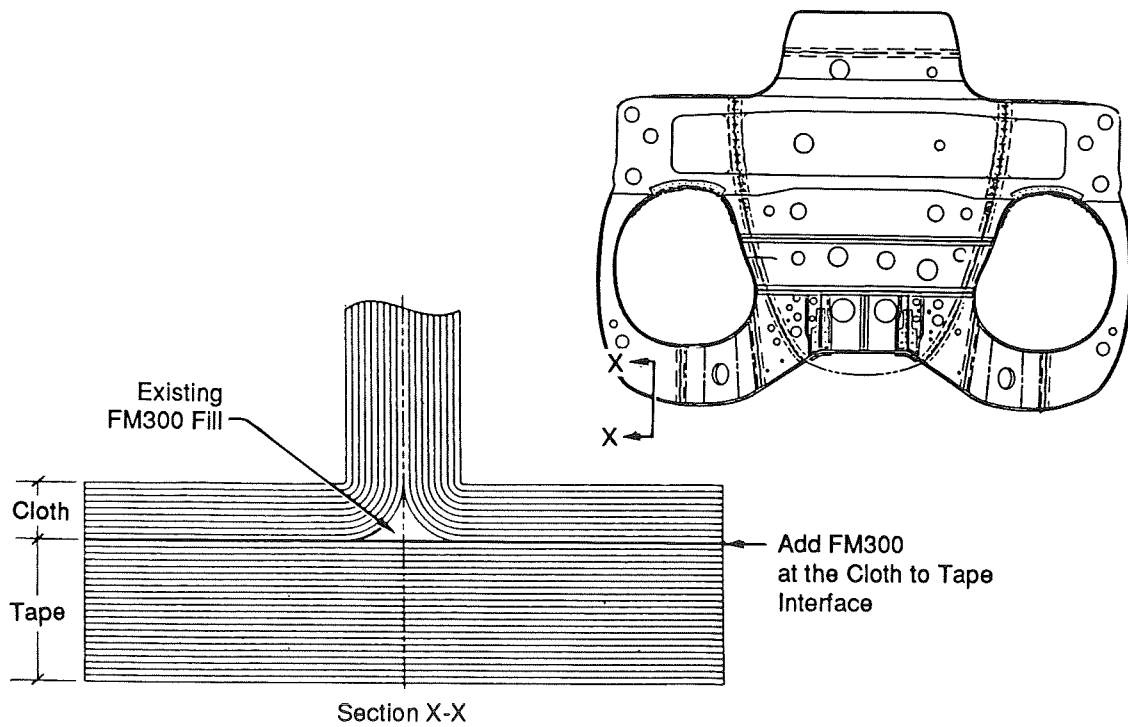
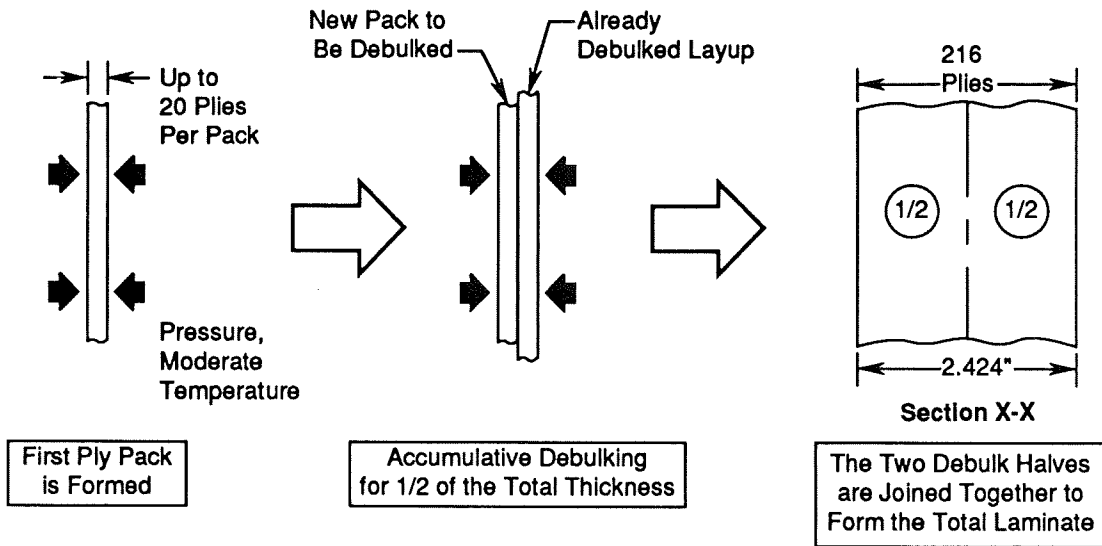
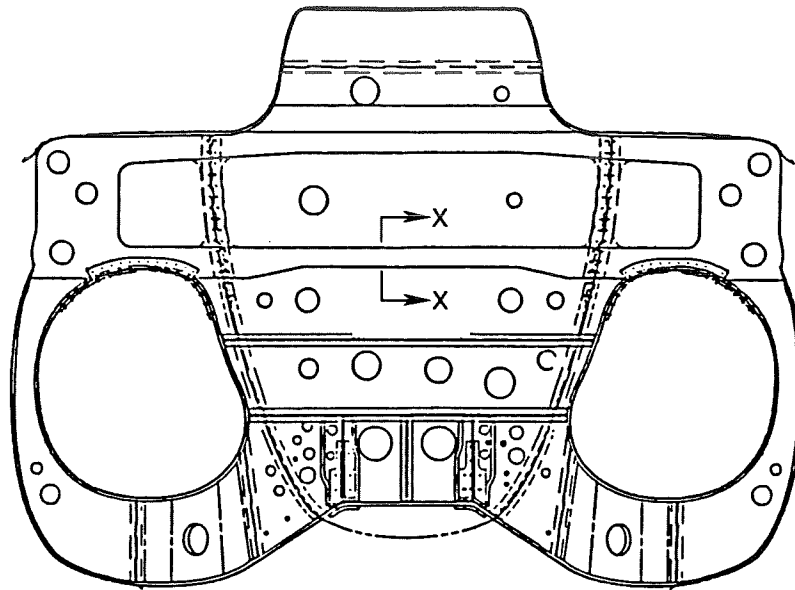


Figure 16. Adhesive Usage During Layup

GP14-0175-16



GP14-0175-17

Figure 17. Multiple Hot Debulking Cycles

CONCLUDING REMARKS

In 1992, the Final Technical Report should be available through the Defense Technical Information Center (DTIC). Details of this program can be found in this report.

REFERENCES

1. Behrens, R.S., Goering, J.C., "Development of Composite Carrythrough Bulkhead: Interim Technical Report", Naval Air Development Center Report No. NADC-90032-60, June, 1989.
2. Goering, J.C., Libeskind, M., "Development of Composite Wing Carrythrough Bulkheads for Fighter Aircraft", Eighth DoD/NASA/FAA Conference on Fibrous Composites in Structural Design", November, 1989.
3. Whitehead, R.S., et al., "Certification Methodology for Composite Structure", Naval Air Development Center Report No. NADC-87042-60, October, 1986.
4. Thomas, J.A., et al., "Computer-Aided Curing of Composites", Wright Research and Development Center Report No. WRDC-TR-89-4084, October 1989.

CONCLUDING REMARKS

In 1992, the Final Technical Report should be available through the Defense Technical Information Center (DTIC). Details of this program can be found in this report.

REFERENCES

1. Behrens, R.S., Goering, J.C., "Development of Composite Carrythrough Bulkhead: Interim Technical Report", Naval Air Development Center Report No. NADC-90032-60, June, 1989.
2. Goering, J.C., Libeskind, M., "Development of Composite Wing Carrythrough Bulkheads for Fighter Aircraft", Eighth DoD/NASA/FAA Conference on Fibrous Composites in Structural Design", November, 1989.
3. Whitehead, R.S., et al., "Certification Methodology for Composite Structure", Naval Air Development Center Report No. NADC-87042-60, October, 1986.
4. Thomas, J.A., et al., "Computer-Aided Curing of Composites", Wright Research and Development Center Report No. WRDC-TR-89-4084, October 1989.

THIS PAGE INTENTIONALLY BLANK

EFFECTS OF FLOOR LOCATION ON RESPONSE OF COMPOSITE FUSELAGE FRAMES

Huey D. Carden and Lisa E. Jones
 NASA Langley Research Center
 Hampton, VA

Edwin L. Fasanella
 Lockheed Engineering and Sciences Company
 Hampton, VA

NASA
 319-24
 51387
 p. 15

SUMMARY

Experimental and analytical results are presented which show the effect of floor placement on the structural response and strength of circular fuselage frames constructed of graphite-epoxy composite material. The research was conducted to study the behavior of conventionally designed advanced composite aircraft components. To achieve desired new designs which incorporate improved energy absorption capabilities requires an understanding of how these conventional designs behave under crash type loadings. Data are presented on the static behavior of the composite structure through photographs of the frame specimen, experimental strain distributions, and through analytical data from composite structural models. An understanding of this behavior can aid the dynamist in predicting the crash behavior of these structures and may assist the designer in achieving improved designs for energy absorption and crash behavior of future structures.

INTRODUCTION

The Landing and Impact Dynamics Branch of NASA Langley Research Center has been involved in crash dynamics research since the early 1970's. For the first 10 years, the emphasis of the research was on metal aircraft structures for both the General Aviation Crash Dynamics Program (R1-13) and the Controlled Impact Demonstration (CID) Program, a transport aircraft program which culminated in the controlled crash test of a Boeing 720 aircraft in 1984 (R14-16). Subsequent to the transport work, the emphasis has been on composite structures. Currently, efforts in crash dynamics research are being directed in three areas: (1) developing a data base for understanding the behavior, responses, failure mechanisms, and general loads associated with the composite material systems under crash type loadings; (2) analytical studies/development relative to composite structures; and (3) full-scale tests of metal and composite structures to verify performance of structural concepts.

Considerable research has been conducted into determining the energy absorption characteristics of composites (R17-20) which indicated that composite structures, if properly designed, can absorb more energy than comparable aluminum structures. Because of the brittle nature of the composites, however, attention must be given to designs which will take advantage of their powerful energy absorbing material properties while providing desired structural integrity when the composites are fabricated into aircraft structural elements and substructures. To achieve the desired new designs requires an understanding of how the more conventional designs behave under crash loadings.

The purpose of this paper is to present experimental and analytical data from a study of the effect of floor placement on the structural response and strength of conventionally designed circular fuselage frames constructed of graphite-epoxy composite material. Response of the composite fuselage frame structures for different floor locations is illustrated through photographs, experimental results, and through analytical data from finite element structural models. The determination of the effect of the floor location on the structural response of fuselage frames will aid in the understanding and prediction of full-scale subfloor or fuselage response to crash loading. Consequently, data from the present study are also compared to experimental

dynamic strain measurements on two previously tested composite subfloor structures (R21-22). Utilizing such data to gain an understanding of the fundamental behavior of subfloor structures may lead to improved designs for better energy absorption under crash loading conditions.

TEST SPECIMENS

I-, J-, C- and Z-cross sections are often used for fuselage frames in metal aircraft and have also been proposed for composite aircraft structures because of their structural efficiency. Several circular frames with these cross-sections (F1) were fabricated for testing. Earlier research with a Z cross-section circular frame (R23) indicated that failure of the anti-symmetric Z-frame without skin was initiated by a torsional instability. These out-of-plane rotations created complex boundary conditions and increased the difficulty of testing and analyzing the section. Consequently, a 3.5 inch wide skin material was added to the I-, J-, and C- frame concepts which increased the torsional stiffness of the cross-sections and limited out-of-plane rotations and deformations, as does the actual skin material in a fuselage structure. The skin, a $[\pm 45/0/90]_{2s}$ lay-up sixteen ply (.08 inches) thick, was cocured with the 6 foot diameter frames. Lay-up of the frame was $[\pm 45/\mp 45/90/0]_{3s}$. Both the skin and the frame were fabricated with AS4/5208 graphite-epoxy material. Only the I-frame is used in the study reported in this paper.

TEST APPARATUS AND PROCEDURE

F2 shows a typical set-up of a composite fuselage I-frame in a 120 000-lbf loading machine prior to a quasi-static test. A steel I-beam was attached horizontally across the composite frame at the diameter position to simulate the floor. The horizontal floor positions were designated by the included angle measured between the ends of the floor attachments about the center of curvature of the frame. For example, the frame with the floor at the diameter is designated the 180° floor since the arc is 180° between the attachment points. A vertical compressive load was applied to the composite fuselage frame through the simulated floor beam and the lower platen of the load machine. Special clamps (See F2(d)) were used to bolt the I-beam to the composite frame and a 170° F melting point metal was poured into the small gap between the clamp and the frame to eliminate possible motion in the joint. As shown in F2(b) and 2(c), additional tests were conducted wherein the floor location was moved to produce 120°, and 90° arcs. In each test the specimen was loaded at a rate of 500 lbf/minute up to a maximum of 1000 lbf. Up to 64 channels of strain (for the 180° floor) as well as vertical load and vertical displacement were recorded at a rate of 8 sample/sec (initial test was 16 samples/sec) using a PC-based data acquisition system. Details of strain gage lay outs on the composite I-frame are shown in F3 and T1. A commercial software program was utilized to condition, convert data to engineering units, filter, and process the data for display.

ANALYSIS TOOLS

To gain an understanding of the physics of behavior, the experimental research of structures under crash loadings is generally accompanied by analytical prediction or correlation studies whenever feasible. Thus, various finite element codes which have capabilities for handling dynamic, large displacement, non-linear response problems of metal and composite structures were used as tools in the research efforts.

DYCAST Computer Code

The analytical results presented in this paper were generated with a nonlinear finite element computer code called DYCAST (DYnamic Crash Analysis of STructures (R24) developed by Grumman Aerospace Corporation with principal support from NASA and the FAA. The basic element library consists of (1) stringers or rod elements with axial stiffness only; (2) three-dimensional beam elements with 12 fixed cross-sectional shapes typical of aircraft structures with axial, two shear, torsional, and two bending stiffnesses; (3) isotropic and orthotropic membrane skin triangles with membrane stiffnesses; (4) isotropic plate bending triangles with membrane and out-of-plane bending stiffnesses; and (5) nonlinear translational or rotational spring elements that provide stiffness with user-specified force-displacement or moment-rotation tables (piece-wise linear). The spring element can be either elastic or dissipating. The

springs are useful to model crush behavior of components for which data are available and/or whose behavior may be too complex or time consuming to model otherwise. Curved composite beams, composite plate and curved shell elements were not available in the DYCAST element library at the time of this study.

In the present study two different analytical models, both with straight beam elements, were used for predicting response of the composite fuselage I-frame. One model designated as the compound beam was somewhat more detailed than the second simpler I-beam element model. F4 illustrates cross-sectional details of each of the two analytical model formulations.

Compound Beam Model.- Since the skin portion of the fuselage frame had a different lay-up and hence had a different stiffness from the I-frame, a compound beam approach was used to represent the frame in modeling the composite fuselage structure. In the compound beam model (See F4(a)), the I portion of the frame was modeled using a straight I-beam (ISEC) with appropriate material properties; whereas, the 0.08 inch thick skin was modeled with the solid rectangular beam (SREC) with appropriate but different material properties. The program allows these two different sections to be combined to act as a unit where specified geometry locates grid points, shear centers and centroid points at the appropriate location in the cross-section of the combination. A total of 78 elements (39 I-beam and 39 rectangular beam elements) were used in the model of the 180° fuselage frame. Symmetry about the ground contact point was used, thus only half of the 180° frame segment had to be discretized in the model. For the other floor positions, the model was reduced by the appropriate number of elements to represent the shorter frame segments.

I-Beam Model.- In the case of the I-beam model (See F4(b)), the combination of skin and I-frame were modeled with only I-beam elements. Since the skin lay-up provided less stiffness than the lay-up of the I-frame, the skin width was reduced by the ratio of the computed stiffnesses of the skin to the I-frame. As a result, the 3.5 inch skin width was reduced to approximately the same 2.5 inch width as the bottom flange of the I-frame itself. Thus, the resulting model consisted of straight ISEC elements wherein the bottom flange and skin were combined to be 0.16 inches in thickness with only the material properties of the I-frame being used in the model. Only half as many I-beam elements were needed as for a comparable compound beam model. The analytical results of the two different models are compared to each other and to the experimental data in the following section.

RESULTS AND DISCUSSION

F5-9 present results from studies with composite fuselage frames under static loadings for different floor locations. Analytical results are compared to the experimental behavior of the composite frame structure. The behavior of these standard frames with different floor locations under the same loading condition is considered as a first step in the design process of new frame structures for improving energy absorption and crash behavior.

Static experiments.- F5(a) presents a typical static strain distribution from tests of the composite I-frame used in the present study with a simulated floor fabricated from a steel I-beam located at the 180° floor position. Strain as a function of the circumferential position in degrees is plotted for the outer skin, the center of the web, and the inner flange of the I-frame under a load of 1000 lbf. It should be noted that the outer skin exhibits a distribution which resembles a "sea gull" shape. This shape occurs because of the maximum compressive strain is at the contact region of the bottom of the frame with the platen (0° position), and two tensile strain maximums occur at $\pm 60^\circ$ from the contact region. Strain in the web and inner flange is reversed relative to the skin. Near the contact region the strain is tensile and is higher in magnitude than the compressive strain in the skin.

A comparison of the strain distributions in the outer skin of the composite I-frame for the 180°, the 120° and 90° floors are presented in F5(b). The strain distributions for the 120° and 90° floor positions are similar to the 180° floor results. The constraint of the floor for the 90° and 120° has compressed the "sea

gull" strain distribution shape into the shorter arc length, otherwise the general shape still has the maximum strain at the 0° contact region and the two maximums at symmetric \pm positions. Additionally, for the given 1000 lbf load the magnitude of the strain in the flanges and skin (not shown) for each of the lower floor positions was less than the 180° floor. The strains are lower because the bending moments are decreased and the effective global structural stiffness is increased as the structural frame arc length is decreased for the lower floor positions.

Static analytical studies.- To analytically demonstrate the behavior of the frames under load, two DYCAST finite element models were constructed to analyze the frame behavior. The frame model was loaded at the top node and a simulated ground plane modeled by ground contact springs resisted the vertical movement of the frame during load application. Boundary conditions were imposed at the bottom node of the model to account for the symmetrical situation, thus only half the frame had to be modeled. The top node was initially constrained to allow only vertical displacement simulating the effect of a very stiff floor across the frame diameter. The static analytical load was increased linearly to 1000 lbf in 50 pound increments.

Evaluation of the analytical strain distribution on the frame for the 180° floor position shown in F6(a) indicates a number of important points which include: (a) maximum strains for the 1000 lbf load were at the 0° or ground contact location with two secondary maximums occurring at symmetric locations between 45° - 55° from the bottom contact area; (b) the predicted outer skin strain distribution exhibits the same "sea gull" shape as measured in the experiment; and (c) similar inverted circumferential strain distributions were noted for the center of the web and for the inner flange of the frame as occurred in the experiment.

F6(b) presents a comparison of the experimental outer skin strain with the predicted distribution with the original clamped boundary and vertical force loading on the analytical model. As may be noted, initial model results are similar to the experimental distribution; however, the position of the maximum strain at approximately $\pm 45^\circ$ is lower than the experimental maximum which occurs at approximately $\pm 60^\circ$. As a consequence, the agreement between the experimental and analytical strain magnitudes is substantially different. Careful comparison of the experimental set-up and the analytical simulation was made. It was noted that experimental boundary attachments do not physically permit the load to be applied through the shear center of the composite I-frame. In the analytical models, however, the load was being applied through the shear center. Consequently, the model was altered to allow in-plane rotation at the loading point and a load with an off-set (load and moment) was applied at the top node point. The off-set distance was varied from 1 to 3 inches.

The effects of the boundary (pinned and clamped) and load application changes on the predicted strain distribution with the I-beam model are shown in F6(c). A comparison of the analytical cases indicates a substantial effect of the new load introduction and boundary change on the behavior patterns of the strain distribution. The major effect on the distribution is the shift of the upper maximum strain locations from $\pm 45^\circ$ to approximately $\pm 60^\circ$, and to increase the magnitude of the strain throughout all circumferential locations. An analytical case was also conducted with the load applied through the shear center where there was no off-set and in-plane rotation was allowed at the load point. As shown in F6(c), allowing the rotational degree-of-freedom at the pinned end load point produced the largest effect in the analytical results. As previously noted, two analytical models were formulated in the study, the compound beam and the I-beam models. F6(d) presents a typical comparison of the predicted strain distributions with the two models (off-set = 3 inches) with the experimental outer skin distribution. Results of the two analytical models are essentially the same with some small differences in the magnitude of the strain at the maximum compressive and tensile strain locations. The I-beam model appears to agree better with the experimental results. Therefore, for ease of computations, the remainder of the analytical results presented in the paper are from the simpler I-beam analytical model.

Once the effect of the loading and boundary application was established, more comprehensive comparisons of the experimental and analytical results were made. For example, F7(a) to 7(c) present typical comparisons of the analytical distributions of strain with the experimental distributions for the 180° , the 120° , and the 90° floor positions, respectively. The agreement in the magnitudes of the analytical and

experimental strains and the shape of the distributions are excellent.

In addition to the circumferential strain distributions, comparisons were also made, as shown in F8, between the predicted radial strain which is measured through-the-section and the experimental data for the 180° floor. Strains on the inner flange, the center of the web, and the outer skin at three circumferential locations of 7.5°, 17.5°, and 37.5° are presented. It may be noted that the analytical and experimental radial distributions are in excellent agreement for all three circumferential positions.

Comparison of Frame Behavior with Subfloors

The determination of the effect of the floor location on the structural response of fuselage frames has aided in the understanding and predicting of full-scale subfloor or fuselage response to crash loading. For example, F9(a) shows two composite subfloor specimens, skeleton and skinned, (See R21-22) which were statically and dynamically tested. F9(b) shows a comparison of the normalized experimental dynamic strain distribution on the flange of the skeleton subfloor and the skin location corresponding to the flange position of the skinned composite subfloor specimens with the analytical I-frame strain of the present study. The results from the simple frame show a strong similarity to the response of the more complex subfloors structures. The structures share in common the generally circular or cylindrical shape, the vertical loading situations, and under vertical loads have strain (moment) distributions which have maximums at the point of loading and at approximately $\pm 45^\circ$ to $\pm 60^\circ$, depending on boundary conditions, around the circumference from the ground contact point. Analytical results show the same distribution with maximums corresponding to the experimental locations. Failures of the subfloor structures were noted between these same 45° to 60° circumferential locations in the dynamic tests (See R21).

Lessons Relearned

Often efforts can be diverted to the wrong area when poor correlation is obtained in an initial comparison of experimental data with analytical predictions. Several important lessons, both experimentally and analytically, were relearned in the current studies which should be emphasized when analyzing and testing both composite and metal structures. The lessons are: (1) simple boundary conditions, such as fully clamped, are difficult or impossible to achieve in real structures, (2) systematic variations of the analytical boundary and load application should be examined carefully to assess the influence and effects on the correlation prior to any large scale changes of the analytical model or experiment; and (3) experimental and analytical personnel should collaborate closely in their efforts. Being reminded of such lessons can help dynamists gain a better understanding of what to expect from such structures in crash-loading situations, and can guide analysts to formulate adequate analytical models for predicting structural response under crash loadings. The latter task is a difficult one for composite structures as well as for metal structures.

CONCLUDING REMARKS AND OBSERVATIONS

Some unique structural behavior results from the research with composite aircraft fuselage frames have been presented and discussed and analytical results have been included to help explain the behavior noted. From the observations made in the present study, the following conclusions are made:

(1) The effects on the response of the composite frame from changing the floor position in the composite frame were: (a) to alter the magnitude of the strain (moment) but not the common, general "sea gull" shape of the distribution under vertical loading; (b) to constrain the general "sea gull" shaped strain distribution to occur in the frame segment below the floor attachment locations; and (c) to increase the effective global structural stiffness of the frame as arc length of the frame was decreased.

(2) Correct simulation of the experimental boundary/load application to the frame was critical in obtaining good correlation between the analytical and experimental results.

(3) Analytical finite element models of the frame predicted the circumferential and radial strain magnitudes and distribution.

(4) Correlation of normalized experimental strain distributions for floor structures and the composite I-frame indicated that the behavior of the simpler structures embodied the behavior of the more complex structural components.

(5) Knowledge of unique and predictable strain responses of composite fuselage frames will be used to achieve better future designs for energy management in a crash situation.

(6) Important lessons relearned in the present study were that (a) simple boundary conditions, such as fully clamped, are difficult or impossible to achieve in real structures, (b) systematic variations of the analytical boundary and load application should be examined carefully to assess the influence and effects on the correlation prior to any large scale changes of the analytical model; and (c) experimental and analytical personnel should collaborate closely in their efforts.

REFERENCES

1. Alfaro-Bou, Emilio; and Vaughan, Victor L., Jr.: Light Airplane Crash Tests at Impact Velocities of 13 and 27 m/sec. NASA TP 1042, November 1977.
2. Castle, Claude B.; and Alfaro-Bou, Emilio: Light Airplane Crash Tests at Three Flight-Path Angles. NASA TP 1210, June 1978.
3. Hayduk, Robert J.: Comparative Analysis of PA-31-350 Chieftain (N44LV) Accident and NASA Crash Test Data. NASA TM 80102, October 1979.
4. Castle, Claude B.; and Alfaro-Bou, Emilio: Light Airplane Crash Tests at Three Roll Angles. NASA TP 1477, October 1979.
5. Vaughan, Victor L., Jr.; and Alfaro-Bou, Emilio: Light Airplane Crash Tests at Three Pitch Angles. NASA TP 1481, November 1979.
6. Vaughan, Victor L., Jr.; and Hayduk, Robert J.: Crash Tests of Four Identical High-Wing Single-Engine Airplanes. NASA TP 1699, August 1980.
7. Carden, Huey D.; and Hayduk, Robert J.: Aircraft Subfloor Response to Crash Loadings. SAE Paper 810614, April 1981.
8. Williams, M. Susan; and Fasanella, Edwin L.: Crash Tests of Four Low-Wing Twin-Engine Airplanes with Truss-Reinforced Fuselage Structure. NASA TP 2070, September 1982.
9. Carden, Huey D.: Correlation and Assessment of Structural Airplane Crash Data with Flight Parameters at Impact. NASA TP 2083, November 1982.
10. Carden, Huey D.: Impulse Analysis of Airplane Crash Data with Consideration Given to Human Tolerance. SAE Paper 830748, April 1983.
11. Castle, Claude B.; and Alfaro-Bou, Emilio: Crash Tests of Three Identical Low-Wing Single-Engine Airplanes. NASA TP 2190, September 1983.
12. Thomson, Robert G.; Carden, Huey D.; and Hayduk, Robert J.: Survey of NASA Research on Crash Dynamics. NASA TP 2298, April 1984.
13. Carden, Huey D.: Full-Scale Crash Test Evaluation of Two Load-Limiting Subfloors for General Aviation Airframes. NASA TP 2380, December 1984.

14. Hayduk, Robert J.(Editor): Full-Scale Transport Controlled Impact Demonstration. NASA CP 2395, April 1985.
15. Fasanella, Edwin L.; Widmayer, E.; and Robinson, M. P.: Structural Analysis of the Controlled Impact Demonstration of a Jet Transport Airplane. AIAA Paper 86-0939-CP, May 1986.
16. Fasanella, Edwin L.; Alfaro-Bou, Emilio; and Hayduk, Robert J.: Impact Data from a Transport Aircraft During a Controlled Impact Demonstration. NASA TP 2589, September 1986.
17. Farley, Gary L.: Energy Absorption of Composite Materials. NASA TM 84638, AVRADCOM TR-83-B-2, 1983.
18. Bannerman, D.C.; and Kindervater, C.M.: Crashworthiness Investigation of Composite Aircraft Subfloor Beam Sections. IB 435-84/3(1984), Deutsche Forschungs-und Versuchsanstalt fur Luft-und Raumfahrt, February 1984.
19. Cronkhite, J.D.; Chung, Y.T.; and Bark, L.W.: Crashworthy Composite Structures. ASAAVSCOM TR-87-D10, U.S. Army, December 1987. (Available from DTIC as AD B121 522.)
20. Jones, Lisa E.; and Carden, Huey D.: Evaluation of Energy Absorption of New Concepts of Aircraft Composite Subfloor Intersections. NASA TP 2951, November 1989.
21. Carden, Huey D.; and Robinson, Martha P.: Failure Behavior of Generic Metallic and Composite Aircraft Structural Components Under Crash Loads. NASA RP 1239, November 1990.
22. Boitnott, Richard L.; and Fasanella, Edwin L.: Impact Evaluation of Composite Floor Sections. SAE Paper 891018, General Aviation Aircraft Meeting and Exposition, Wichita, Kansas, April 1989.
23. Boitnott, Richard L.; Fasanella, Edwin L.; Calton, Lisa E.; and Carden, Huey D.: Impact Response of Composite Fuselage Frames. SAE Paper 871009, April 1987.
24. Pifko, A.B.; Winter, R.; and Ogilvie, P.L.: DYCAST - A Finite Element Program for the Crash Analysis of Structures. NASA CR 4040, January 1987.

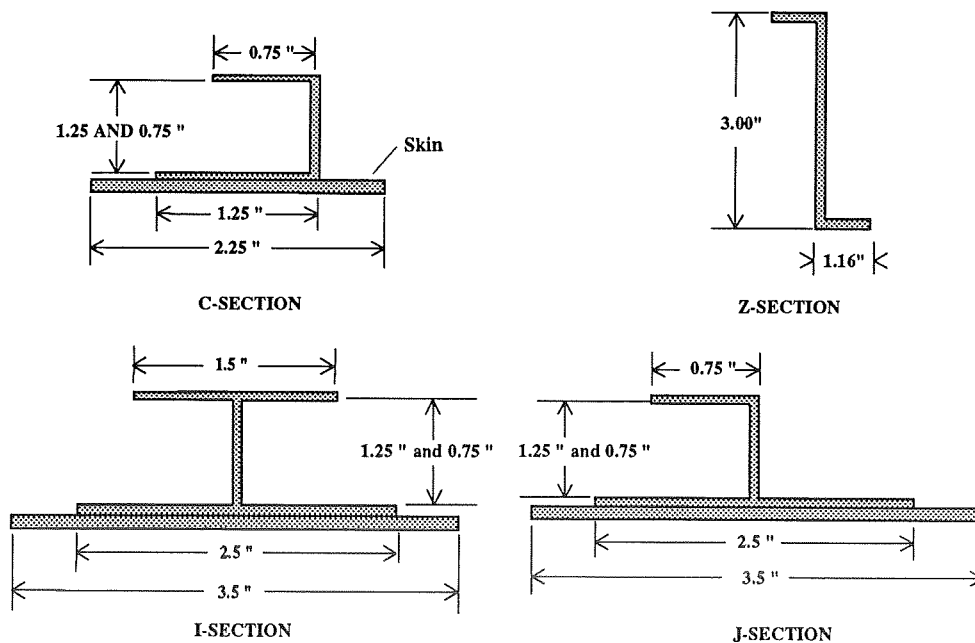
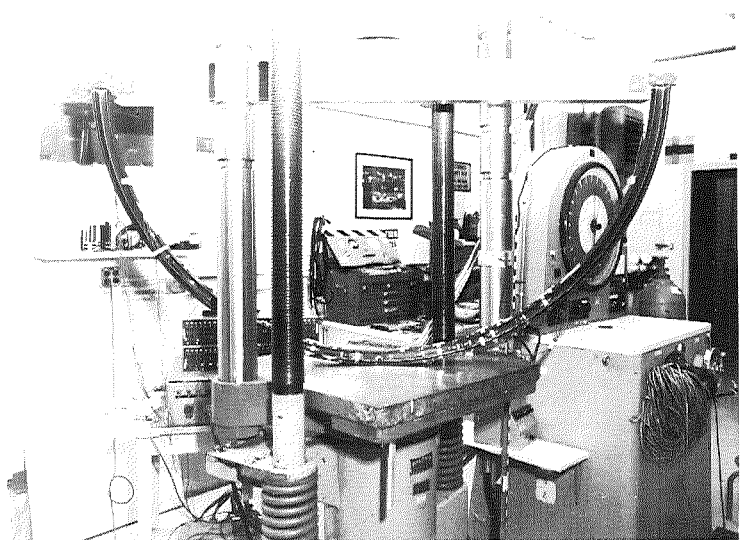
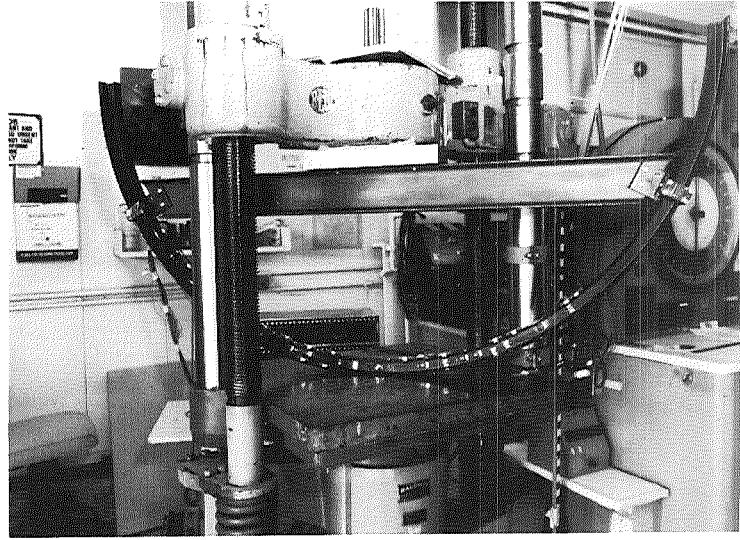


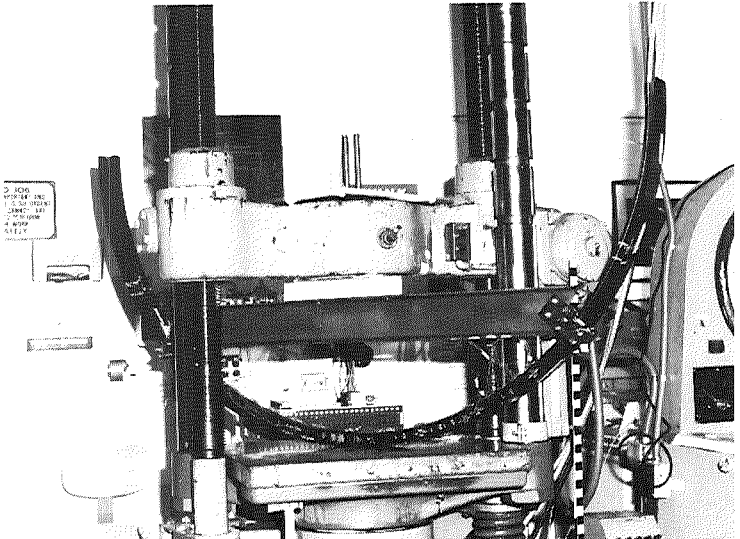
Figure 1.- Typical cross-sections of composite fuselage frame concepts.



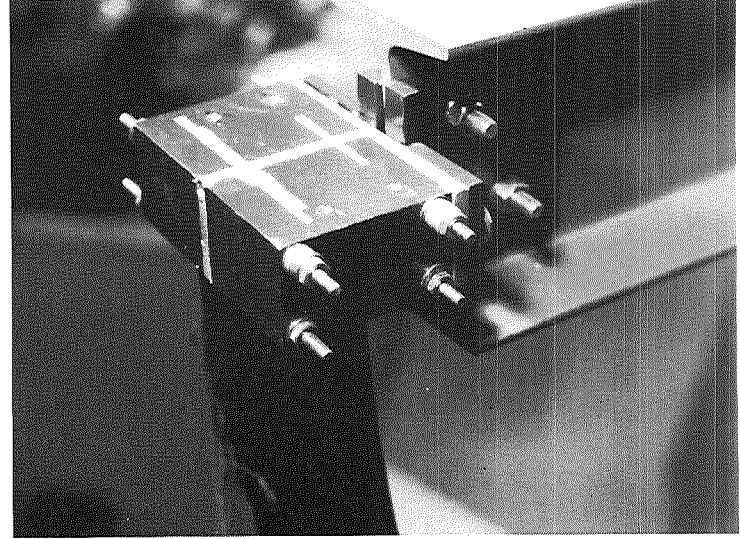
(a) 180° floor.



(b) 120° floor.



(c) 90° floor.



(d) Floor attachment.

Figure 2.- Typical experimental set-up of composite I-frame in static testing machine.

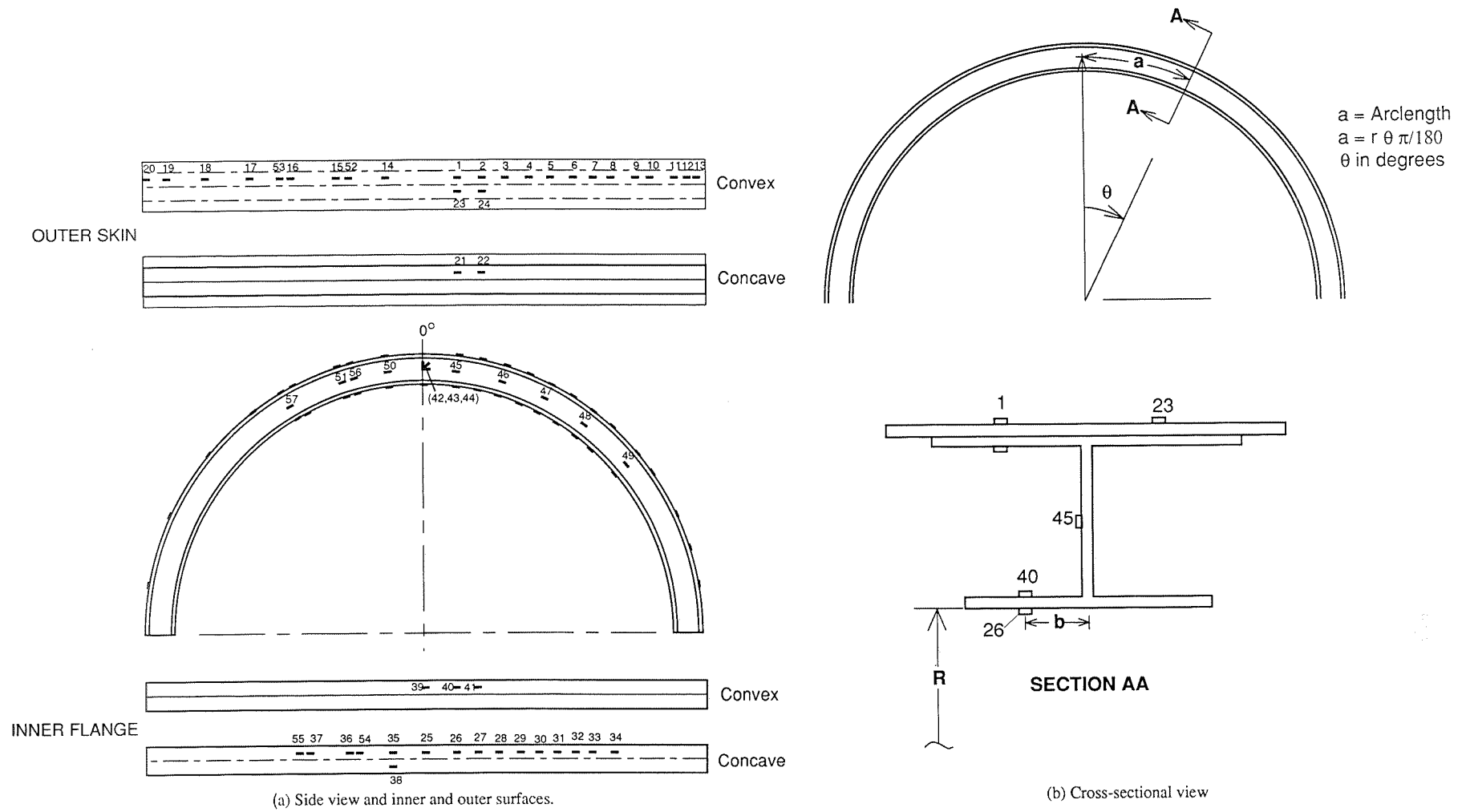


Figure 3.- Strain gage placement on I-frame.

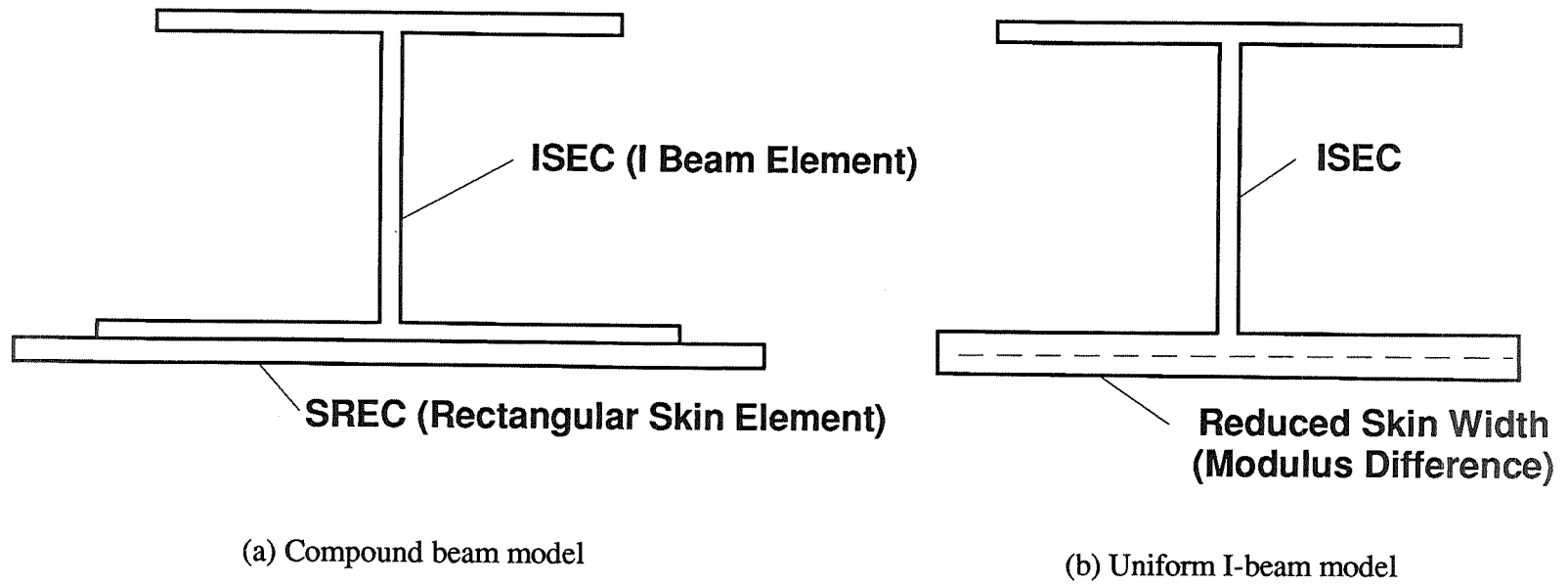
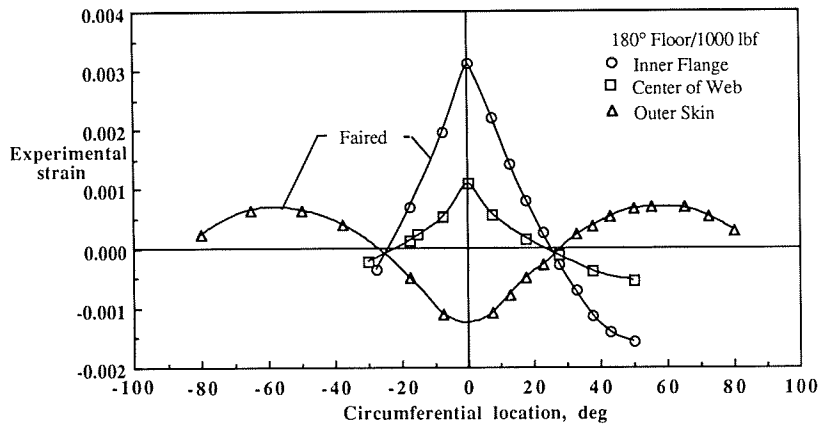
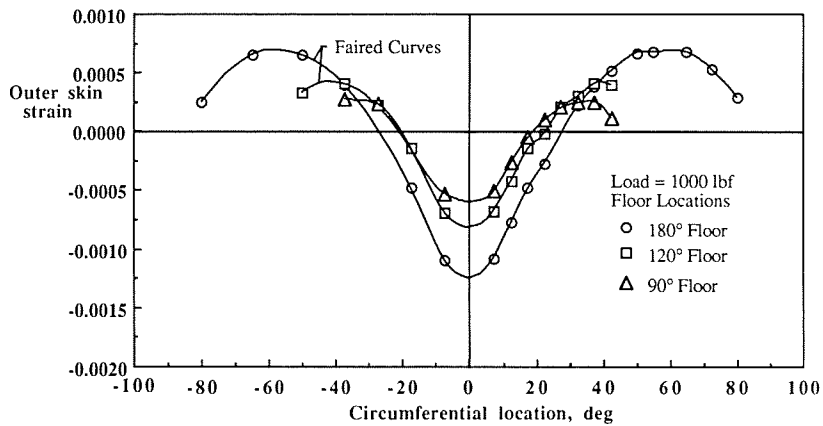


Figure 4.- Cross-section of analytical models of composite I-frame.

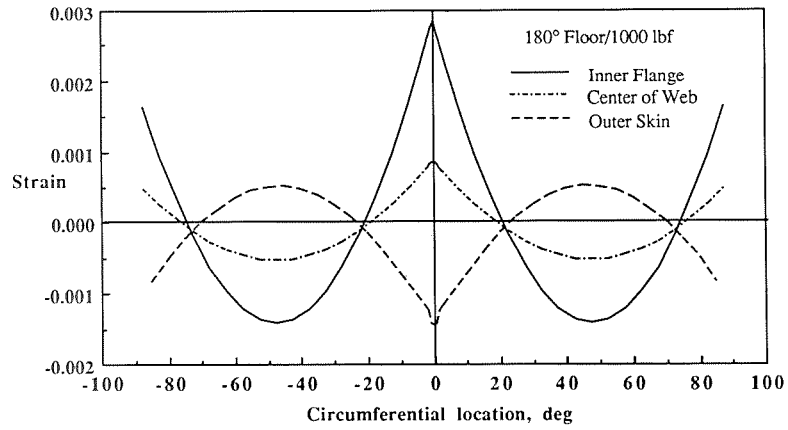


(a) 180° floor position.

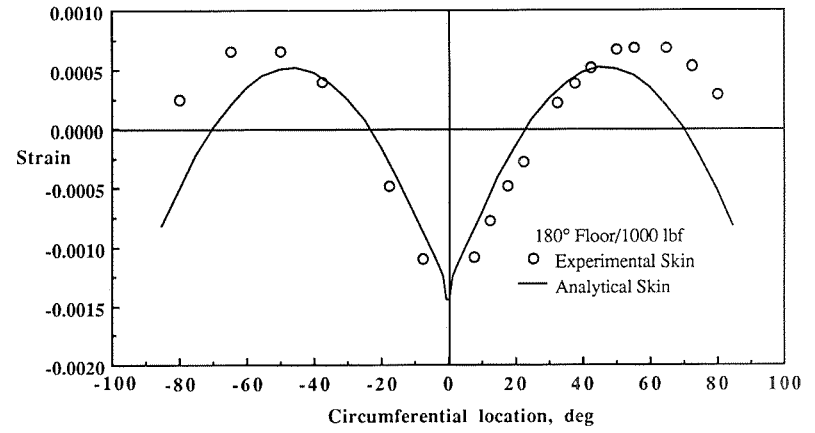


(b) 180°, 120°, and 90° floor positions.

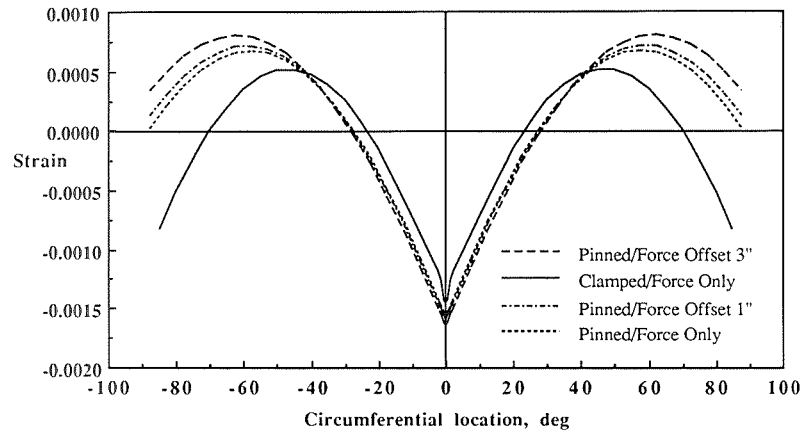
Figure 5.- Typical experimental strain distributions on composite I-frame.



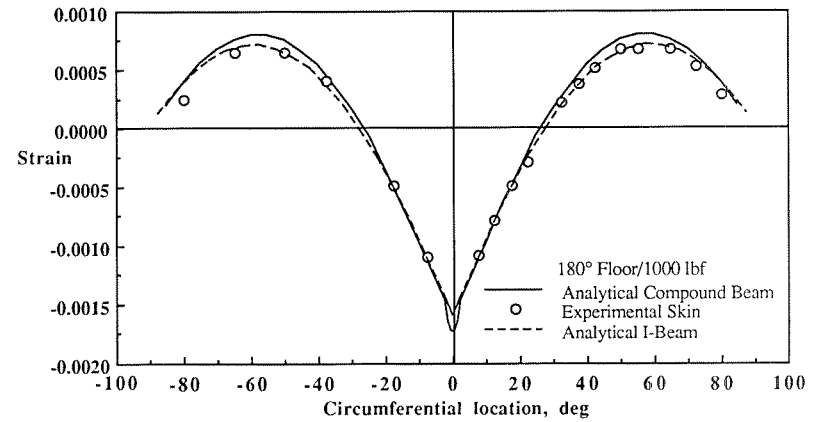
(a) Analytical 180° floor position.



(b) Experimental and analytical comparison with original boundary condition.

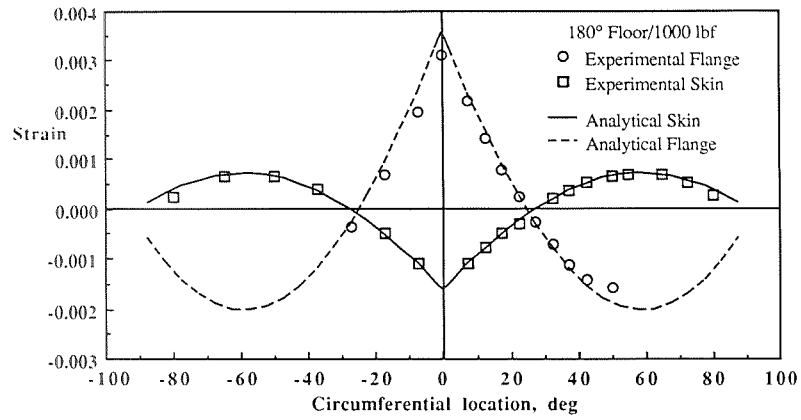


(c) Analytical boundary/loading results.

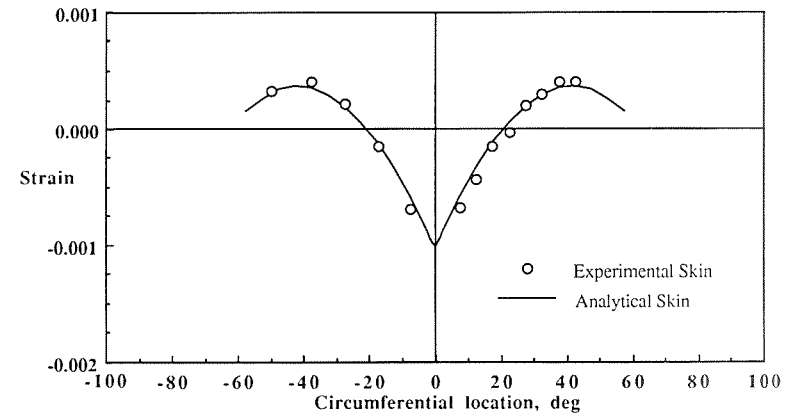


(d) Comparison of analytical models and experiment.

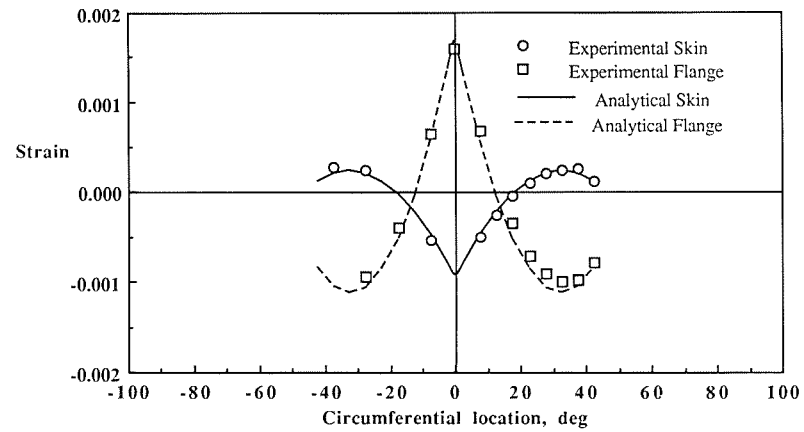
Figure 6.- Typical strain distribution on composite I-frame.



(a) Modified boundary and loading on 180° floor.



(b) Modified boundary and loading on 120° floor.



(c) Modified boundary and loading on 90° floor.

Figure 7.- Comparison of experimental and analytical strain distributions.

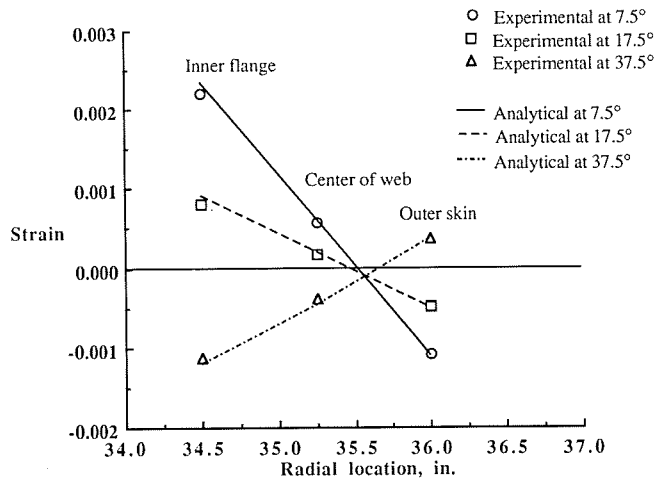
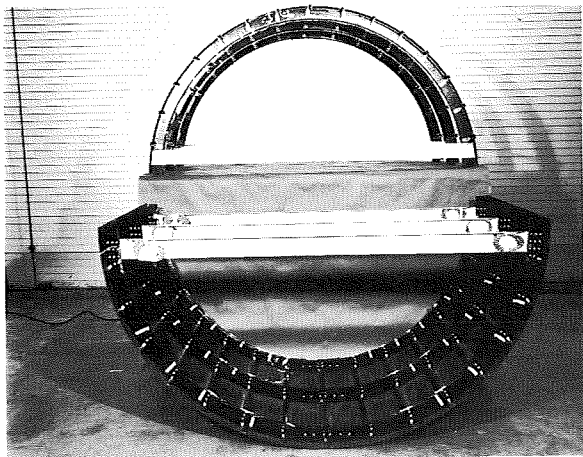
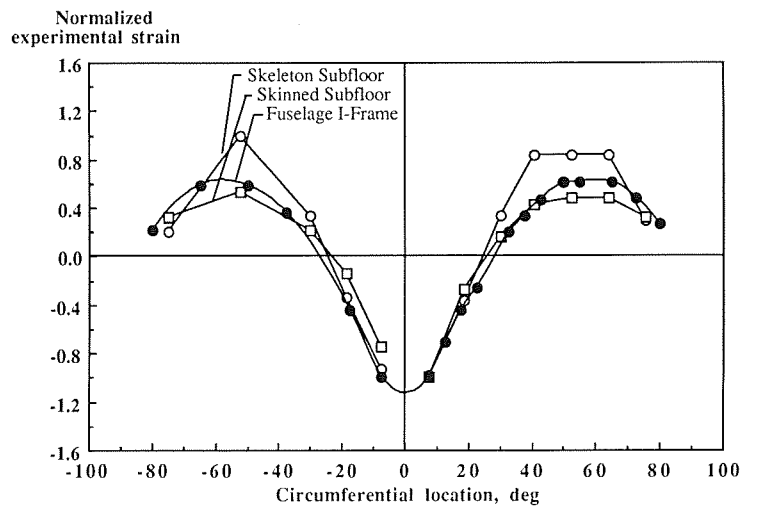


Figure 8.- Typical experimental and analytical radial strain distributions on I-frame with floor location at 180°.



(a) Skinned and skeleton composite subfloors.



(b) Experimental normalized strain distributions.

Figure 9.- Typical composite structural specimens.

TABLE 1.-STRAIN GAGE LOCATIONS FOR COMPOSITE FRAME					
SG#	R, INCHES	THETA, DEG.	a, INCHES	b, INCHES	COMMENT
1	36	7.5	4.71	(5/8)	
2	36	12.5	7.85	(5/8)	
3	36	17.5	11	(5/8)	
4	36	22.5	14.1	(5/8)	
5	36	27.5	17.3	(5/8)	
6	36	32.5	20.4	(5/8)	
7	36	37.5	23.6	(5/8)	
8	36	42.5	26.7	(5/8)	
9	36	50	31.4	(5/8)	
10	36	55	34.6	(5/8)	
11	36	65	40.8	(5/8)	
12	36	72.5	45.5	(5/8)	
13	36	80	50.3	(5/8)	
14	36	-7.5	-4.71	(5/8)	
15	36	-17.5	-11	(5/8)	
16	36	-27.5	-17.3	(5/8)	
17	36	-37.5	-23.6	(5/8)	
18	36	-50	-31.4	(5/8)	
19	36	-65	-40.8	(5/8)	
20	36	-80	-50.3	(5/8)	
21					BTB W/#1
22					BTB W/#2
23	36	7.5	4.71	-(5/8)	
24	36	12.5	7.85	-(5/8)	
25	36	0	0	(3/8)	
26	36	7.5	4.5	(3/8)	
27	34.5	12.5	7.5	(3/8)	
28	34.5	17.5	10.5	(3/8)	
29	34.5	22.5	13.5	(3/8)	
30	34.5	27.5	16.6	(3/8)	
31	34.5	32.5	19.6	(3/8)	
32	34.5	37.5	22.6	(3/8)	
33	34.5	42.5	25.6	(3/8)	
34	34.5	50	30.1	(3/8)	
35	34.5	-7.5	-4.5	(3/8)	
36	34.5	-17.5	-10.5	(3/8)	
37	34.5	-27.5	-16.6	(3/8)	
38	34.5	-7.5	-4.5	-(3/8)	
39					BTB W/#25
40					BTB W/#26
41					BTB W/#27
42,43,44	35.25	0	0	0	ROSET/CLWEB
45	35.25	7.5	4.6	0	
46	35.25	17.5	10.8	0	
47	35.25	27.5	16.9	0	
48	35.25	37.5	23.1	0	
49	35.25	50	30.8	0	
50	35.25	-7.5	-4.6	0	
51	35.25	-17.5	-10.8	0	
52	36	-15	-9.42	(5/8)	
53	36	-30	-18.85	(5/8)	
54	34.5	-15	-9.03	(3/8)	
55	34.5	-30	-18.06	(3/8)	
56	35.25	-15	-9.23	0	
57	35.25	-30	-18.46	0	

THIS PAGE INTENTIONALLY BLANK

omit

SESSION IV
DESIGN CRITERIA, RELIABILITY, SUPPORTABILITY

PRECEDING PAGE BLANK, NOT FILLED

PAGE 458 INTENTIONALLY BLANK

THIS PAGE INTENTIONALLY BLANK

omit

**A Critical Review of Evolving Qualification Approaches
for Contemporary Composite Airframes**

**Keith R. Kedward
University of California**

**John C. Halpin
Wright Aeronautical Systems Division**

**John E. McCarty
Consultant**

PRECEDING PAGE BLANK NOT FILMED

THIS PAGE INTENTIONALLY BLANK

Page intentionally left blank

Page intentionally left blank

Structural Design Optimization with Survivability Dependent Constraints
Application: Primary Wing Box of a Multi-role Fighter †

Douglas J. Dolvin

Flight Dynamics Directorate
Wright Laboratory, Wright Patterson Air Force Base, Ohio

S20-05

51388

P. J. D.

INTRODUCTION

The superior survivability of a multi-role fighter is dependent upon balanced integration of technologies for reduced vulnerability and susceptibility. Current methods for preliminary design of these vehicles do not employ analytical methods nor empirical procedures for simultaneous assessment of structural survivability as a function of structural efficiency. The Air Force, NASA, and many airframe contractors have invested significant resources in the development of multidisciplinary optimization methods which integrate aeroelastic tailoring into the conventional strength dependent design (references 1-5). These computationally intensive procedures form the foundation of preliminary design, yet they do not have the capability to assess effects of survivability dependent constraints on structural weight. A comprehensive survey of current capabilities and future requirements for automated methods of multidisciplinary design is presented in reference 6.

The dependent relationship between survivability and structural weight will dominate preliminary design trade studies for future Air Force aircraft (reference 7). Therefore, significant benefits exist for expanding current design codes to include a structural design methodology for optimization with survivability dependent constraints. The multidisciplinary optimization program ASTROS (Automated STRuctural Optimization System) is ideally structured to enable users to add analysis for other disciplines and therefore this code will function as the basis for methodology development of this project (reference 8). The proposed enhancement will support development of a preliminary design of greater balance through parallel optimization for requirements of survivability and maneuverability, rather than performing separate analysis for each discipline. Further, this effort will provide methodology for comprehensive studies of survivability performance on derivative configurations of a conceptual aircraft, thus identifying design deficiencies early in development when corrections can have the greatest impact on vehicle performance and life cycle cost.

† this work was performed by the Air Force Project Engineer with Air Force Facilities

OBJECTIVE

The objective of this project is to develop a methodology for structural design optimization with survivability dependent constraints. The principal design criteria for optimization will be survivability in a tactical laser environment. The author will investigate the following analyses to establish a dependent design relationship between structural weight and survivability:

- 1) develop a physically linked global design model of survivability variables
- 2) apply conventional constraints to quantify survivability dependent design

BENEFITS

This research will provide design methodology for structural optimization with non-optimal design constraints and will advance the in-house capabilities for preliminary design by integrating requirements for laser survivable structures into multidisciplinary methods for design optimization. The Air Force Flight Dynamics Directorate has identified this technology area as providing high payoff for future aircraft including a multi-role fighter (reference 9). Further, strategic plans of the HQ-AFSC have determined that technology for increasing aircraft survivability 'have vital importance to future Air Force capability needs' (reference 10).

APPROACH

The context of this paper will present a summary of in-house work being performed under Task 1 of a cooperative program between Air Force and Georgia Tech Research Institute (GTRI) entitled: Design Development for Survivability.

Under Task 1, the project engineer will develop design methodology and perform survivability analysis of a primary wing box for multi-role fighter which employs technology for increased survivability including structural arrangement, substructure configurations, cocured lower wing skins, composite fastened upper wing skins, and damage tolerant composite face sheets with syntactic foam cores. The principal design criterion will be vulnerability against High Energy Laser (HEL) threat. The multidisciplinary optimization code ASTROS will be employed in development of a design methodology for optimization with survivability dependent constraints. ASTROS is derived from NASTRAN finite element procedures and performs analysis of structural, static aeroelastic, unsteady flutter, dynamic and blast conditions. In addition, this code incorporates significant algorithms of aeroelastic tailoring and mathematical programming from two procedures developed under Air Force contract (references 2 and 3). Current preliminary design methods require successive evaluation of the Finite Element Model (FEM) under flight loads followed by the Survivability Model (SUM) under threat loads. During this process, the designer would iteratively modify the models until all performance criteria are satisfied within a defined tolerance. A preferred approach would be to develop an overall design model which includes both structural and survivability dependent elements and to optimize the design model for survivability in the same manner as would be pursued for conventional constraints of strength or strain. To establish a dependent design relationship between structural weight and laser survivability, trade studies will be

conducted on a design model with new constraint types which are survivability specific and existing constraint types in a manner which is survivability dependent. The laser vulnerability code VAASEL (Vulnerability Analysis of Aircraft Structures Exposed to Lasers) will be used to assess the survivability improvement attained from integration of advanced technologies versus associated weight penalty (reference 11).

Under Task 2 of this program, researchers of the Signature Technology Laboratory at GTRI will perform the optical design and survivability analysis of a leading edge for multi-role fighter which employs advanced technology for decreased susceptibility including; geometric shaping, low reflectivity coatings, holographic filters, submicron periodic arrays, and inorganic absorbers (reference 12). The principal design criteria will be multispectral surface reflectivity at wavelengths corresponding to airborne targeting and LIDAR threats. The infrared/visual analysis code GTSIG (Georgia Tech Signatures) will be used to analyze laser signature of the baseline edge design and to conduct trade studies on advanced configurations.

Under Task 3, the project engineer will fabricate two full scale components and perform tests against high energy laser and low energy LIDAR threats. The components will be fabricated at the Composites R & D Facility of the Flight Dynamics Directorate; the baseline structural concepts have been selected and survivability evaluation of representative test panels is scheduled for March 1992 (see figure 1). Upon completion of the susceptibility testing, the undamaged component will be attached to a full scale composite wing box to be developed under an in-house effort entitled Bolted Advanced Survivable Structures (reference 13). The component will be designed to provide redundant paths for load redistribution after ballistic impact. The box is constructed of three bays; a load introduction cell, a load reaction cell, and a multi-spar / multi-rib airfoil section which employs many structural concepts and damage resistant materials incorporated in this design study including the structural arrangement, substructure configurations, and laminate constructions. Current plans include laser vulnerability testing at the WL/ML LHMEF facility, susceptibility testing at the GTRI Signature facility, and ballistic survivability testing at the WL/FIV range.

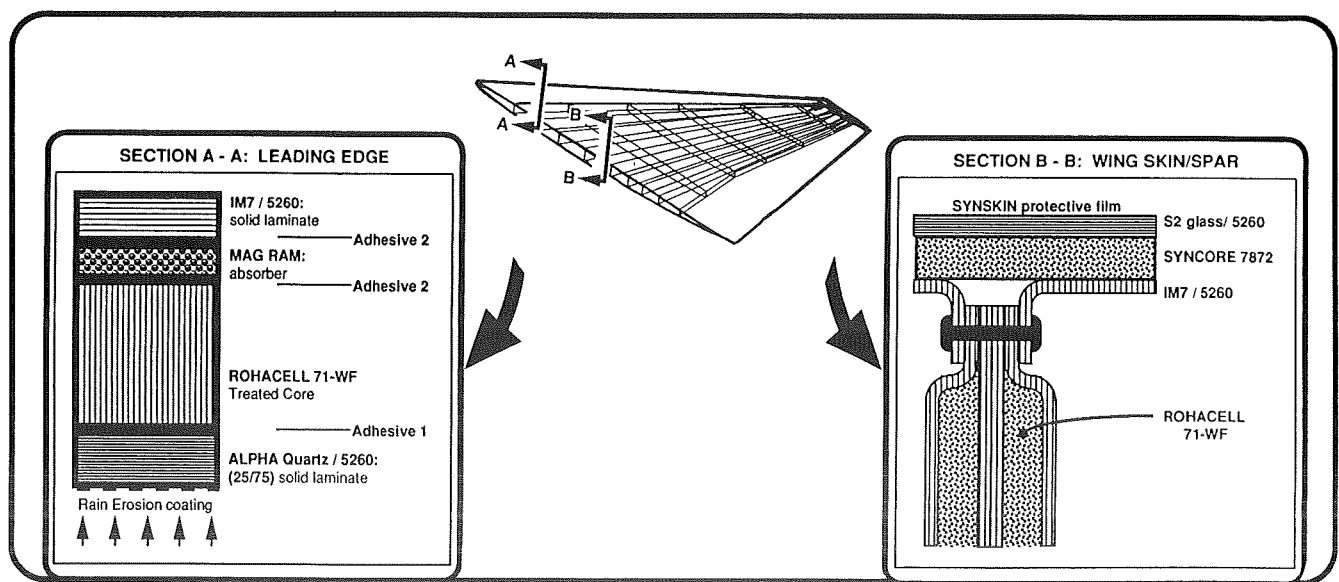


FIGURE 1 - structural concepts for the design baseline

DESIGN CRITERIA

The aircraft performance criteria were adopted from Air Force conceptual design studies on Tail-less Fighter performed by WL/TXA and from the best available performance data on Multi-Role Fighter developed under ASD/XR Multi-Role Fighter Concept Assessment Studies. The mission and general aircraft performance criteria are presented in figure 2 (reference 14). The critical maneuver point selected for this design study is as follows: symmetric pull-up under instantaneous load of 9 g, at a speed of MACH 0.78, applying maximum A/B power, and flying at an altitude of 10,000 feet. The wing loading applied during this maneuver shall include pressure of steady aerodynamics, structural weight, 50 % fuel weight of 2900 lbs/wing, and two AIM-9L missiles. Aircraft pitch stability is attained from integrated control of two aerodynamic surfaces per wing, two canted tails, and 2-D thrust vectoring nozzles.

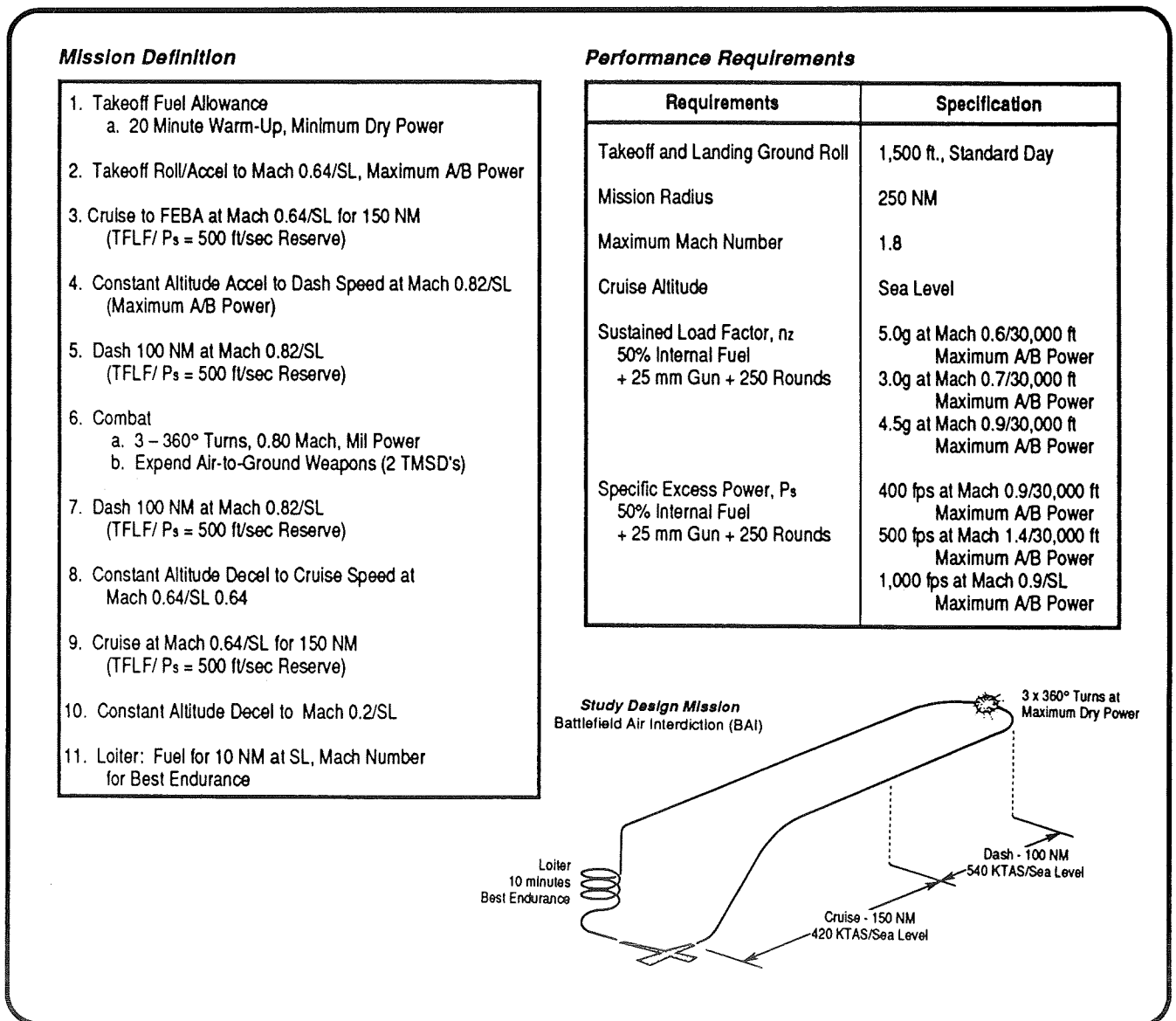


FIGURE 2 - general aircraft performance criteria

The following structural design criteria were developed from consolidation of requirements for current aircraft including F-16 and Air Force sponsored studies on future aircraft including multi-role Fighter and a non-conventional ASTOVL fighter.

Strength Requirements (application limited to design of the wing):

- limit load for rolling pull out to include abrupt displacements of control surfaces
- quasi-static loads for nose and main landing gear (sink rate of 10 feet/second)
- primary structure reacts aerodynamic loads and maneuver loads with inertia relief
- secondary structure reacts local air loads and distributes loads to primary structure
- no buckling of skins at 2G and/or 115% limit load
- no buckling of ribs and spars at ultimate load
- no buckling of substructure at 115% limit load if it restricts mechanical operability
- structural deformation shall not affect aerodynamics or survivability
- waviness and smoothness tolerances of OML determined by structural assembly

Operational Requirements:

- peacetime service life of 6K hours and total operational life of 24K hours
- equivalent design temperature of 180°F, stagnation 248°F, and adiabatic wall 217°F
- maximum acoustic pressure of 165db occurs on deck of fuselage aft body

Durability Requirements:

- composite parts apply reduced strength allowables where applicable
- metallic parts apply reduced allowables in design of joints and lugs

Damage Tolerance Requirements (based on AFGS MIL-STD-87221A):

- no visible dent resulting from low velocity impact of 100 ft/lb on upper skin, 25 ft/lb on lower skin, and 6 ft/lb leading edges
- composite parts have visible damage detection limit of 0.1 inch
- zones of high probability for damage designed with reduced allowables
- skin panels of minimum gage designed with reduced allowables

Material Strength Requirements:

- composite structure: MIL-HANDBOOK 17; when data of this confidence level is not available, use material properties generated under DoD sponsored research programs
- metal structure: MIL-HANDBOOK 5
- structural sandwich core: MIL-HANDBOOK 23

Survivability Requirements: The principal design criterion is survivability in a tactical laser environment. Therefore, the analysis will focus on thermal loads resulting from laser threats. Upon laser engagement, the primary load carrying wing box structure must retain sufficient strength to enable the aircraft to return to safe basing operating with only moderate limitations to the maneuver envelope. A representative mission has been adopted from work performed under the Air Force sponsored Structural Assessment and Vulnerability Evaluation (SAVE) program (reference 15). The mission depicts a multi-role fighter which is configured as a Wild Weasel for suppression of enemy air defenses. The aircraft encounters ground based High Energy Laser (HEL) systems during an attack on surface to air missile batteries.

DESIGN TRADE STUDIES

Analyses were performed on a finite element model of the baseline wing to establish reference levels of structural weight and survivability performance. Detail models were developed for two advanced configurations which incorporated structural concepts and composite materials for increased survivability. Optimization studies were performed on the three models to assess functional dependence between structural weight and survivability performance. Design differences are as follows.

Structural Configurations: The baseline wing, designated WING.BL, has four spars, seven ribs, and integrally stiffened skins. The wing attaches to the fuselage carry-through bulkheads with clevis lugs and bolts. The spars are oriented perpendicular to the fuselage, which provides efficient load transfer and eliminates the structural weight penalties resulting from kick loads. The forward most spar attachment reacts only the vertical shear loads while the remaining spar attachments react the wing bending moments as well as vertical shear. The ribs provide buckling stability and react loads from wing torque, fuel pressure, and air pressure. The torque box employs solid laminate skins with hat-section stringers of non-linear distribution in the spanwise direction. This design provides a smaller effective panel width and minimizes weight in a postbuckled structure. The advanced wing designs have seven spars, twenty-seven ribs, and sandwich stiffened skins. The first configuration, designated WING.11, has spars which are oriented perpendicular to the fuselage carry through structure; and the second advanced configuration, designated WING.21, has spars which are oriented along constant percent chord sections of the wing .

Structural Concepts: The baseline wing is designed with conventional solid laminate skins of current composite materials and mechanically fastened metallic substructure. The advanced configurations employ the following high survivability concepts :

- multi-spar/multi-rib wing box with redundant load paths
- sandwich composite skins with syntactic foam near inner surface
- damage arresting strips at cut-outs and through thickness stitching of spar caps
- spar caps use two rows of fasteners at boundaries of the fuel tank
- spar flanges are oriented towards outside of fuel tank to minimize leak paths
- outer plies $\pm 45^\circ$ of principal load axis for improved compression after impact
- outer surface of skin treated for laser attenuation
- inner surface of skin treated with elastomer for fuel containment after impact
- comingled outer surface ply of nickel-coated Gr/BMI for lightning strike protection and fiberglass/BMI inner-most ply for corrosion protection

In addition, the following structural concepts were identified for improved supportability and were applied to the advanced configurations in locations where supportability features would not compromise survivability (reference 17).

- sandwich composite skins of toughened thermoset composites
- mechanically fastened upper skins and cocured lower skins
- minimum laminate thickness of 0.033 and compression strain allowable of 3500 μ in/in for increased damage tolerance and durability
- close out assemblies over wrapped with fiberglass/BMI for damage resistance

Structural Materials: The baseline wing is designed with AS4/3501-6 composite skins, 7075-T6 Aluminum spars, 7075-T6 Aluminum ribs, and 2024-0 close out edges. The advanced configurations employ the following materials for increased survivability:

- IM7/5260 BMI outer skins * having laminate construction: $[0/\pm 45_n/90]_s$
- syntactic foam core of 0.1875 thickness
- IM7/5260 BMI inner skins having laminate construction: $[\pm 45]_n$
- S2glass/BMI inner-most ply having laminate construction: $[0]$
- IM7/8551-7A spars and ribs having laminate construction: $[\pm 45]_n$
- 7075-T6 Aluminum connecting rods
- S2 glass/8551-7A close out edges

* the susceptibility analysis will be performed on a modified configuration having S2 glass/5260 or HVR Nicalon/5260 BMI outer skins of laminate design $[0/\pm 45_n/90]_s$.

FINITE ELEMENT MODEL (FEM)

Model Construction: The basic finite element model represents a preliminary level design of typical monocoque construction with 392 nodes and 1573 structural elements having 2358 Degrees of Freedom. The model was constructed with the aid of a pre-processor developed at the University of Notre Dame entitled XPUT (reference 18). XPUT is capable of generating the nodal coordinates and element assignments but it is limited in that spars must be located at constant percent of chord and ribs must be parallel to the global X-Y plane. The wing must have a constant airfoil section with no twist. The resultant FEM employs conventional NASTRAN elements with associated constraints, physical properties and material cards (reference 19). Access doors and antenna panels which do not carry load are modelled as normal membranes of negligible stiffness. Notched allowable material properties at 180°F were used for composite skins. In addition, the material densities were multiplied by a factor to account for ply build-ups at joints and hard points. The finite element model of shells is presented in figure 4 and the rod model is presented figure 5.

Composite wing skins are modelled with 324 QUAD4 elements which react inplane tension/compression. The membrane option was selected because ASTROS does not support optimization of bending stiffness for shell elements and the superior shear modelling of the QUAD4 element is not required for loads typical of deltoid wings.

Composite spar/rib webs are modelled with 351 SHEAR elements which react inplane shear. The shear flow distribution is constrained to satisfy equilibrium conditions and stress constraints are calculated from average shear stresses at the nodes.

Isotropic spar/rib caps are modelled with 702 ROD elements which react uniaxial tension/compression. The ROD element was selected because ASTROS can efficiently optimize for uniaxial loads and the out of plane bending capability of BAR elements was not required because this function is performed by connecting rods.

The upper and lower wing skins are connected by 196 ROD elements which react uniaxial tension/compression. The connecting posts are required to transmit wing bending moments around shear panels used to model spar and rib webs.

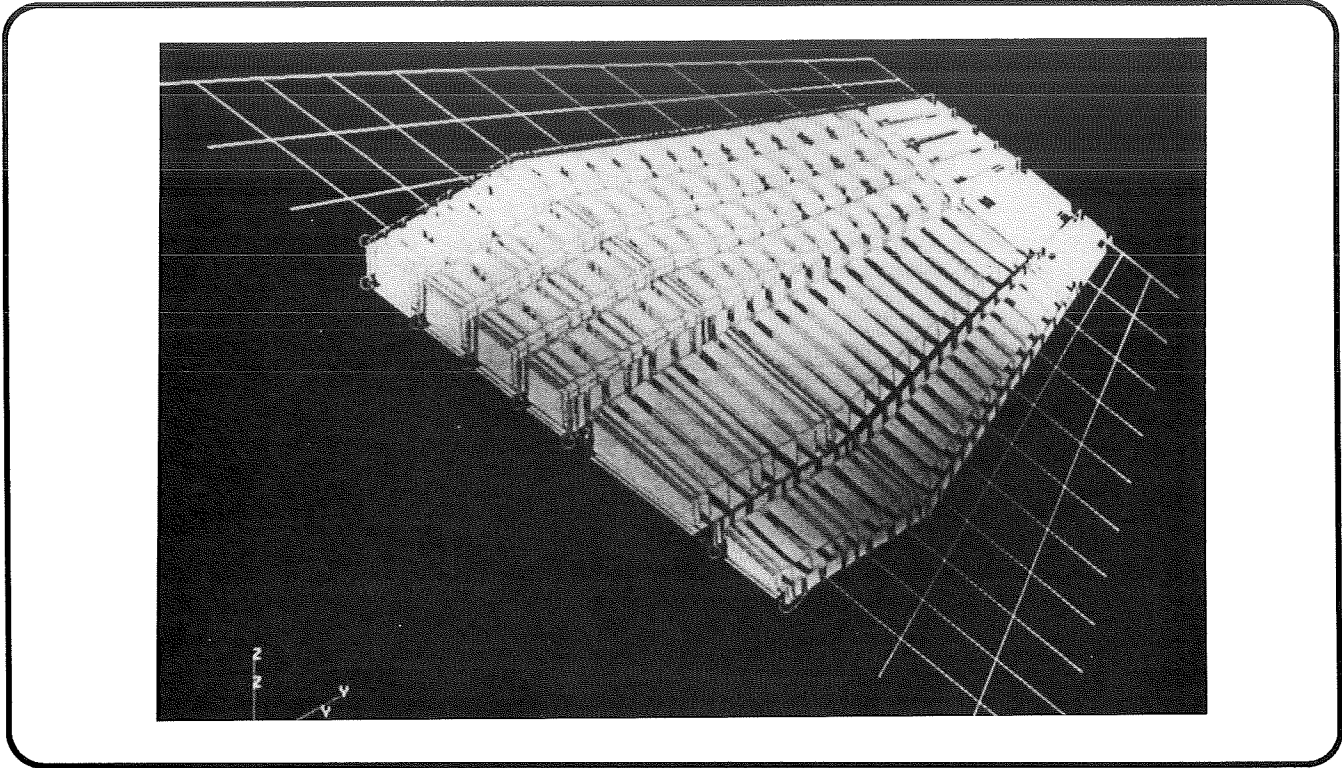


FIGURE 4a - Finite Element Model of shells for configuration MRFWING.11

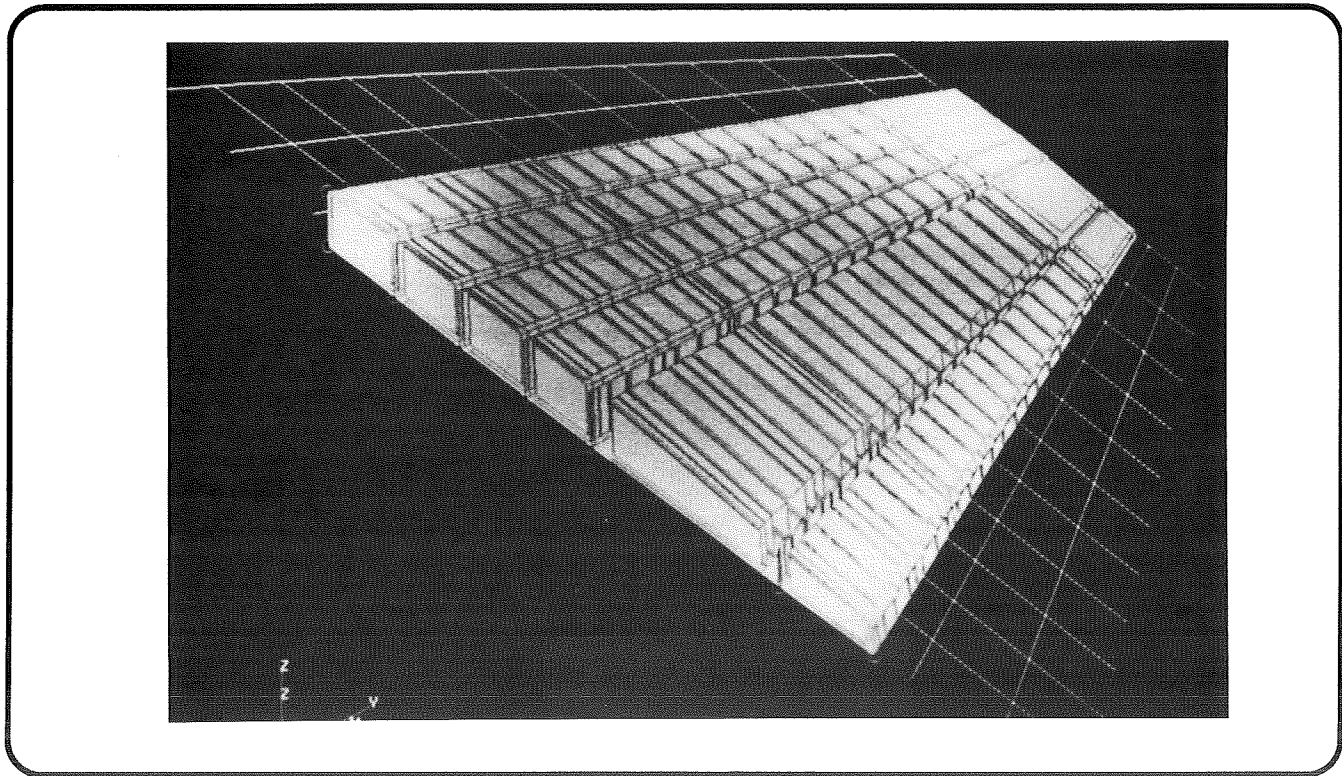


FIGURE 4b - Finite Element Model of shells for configuration MRFWING.21

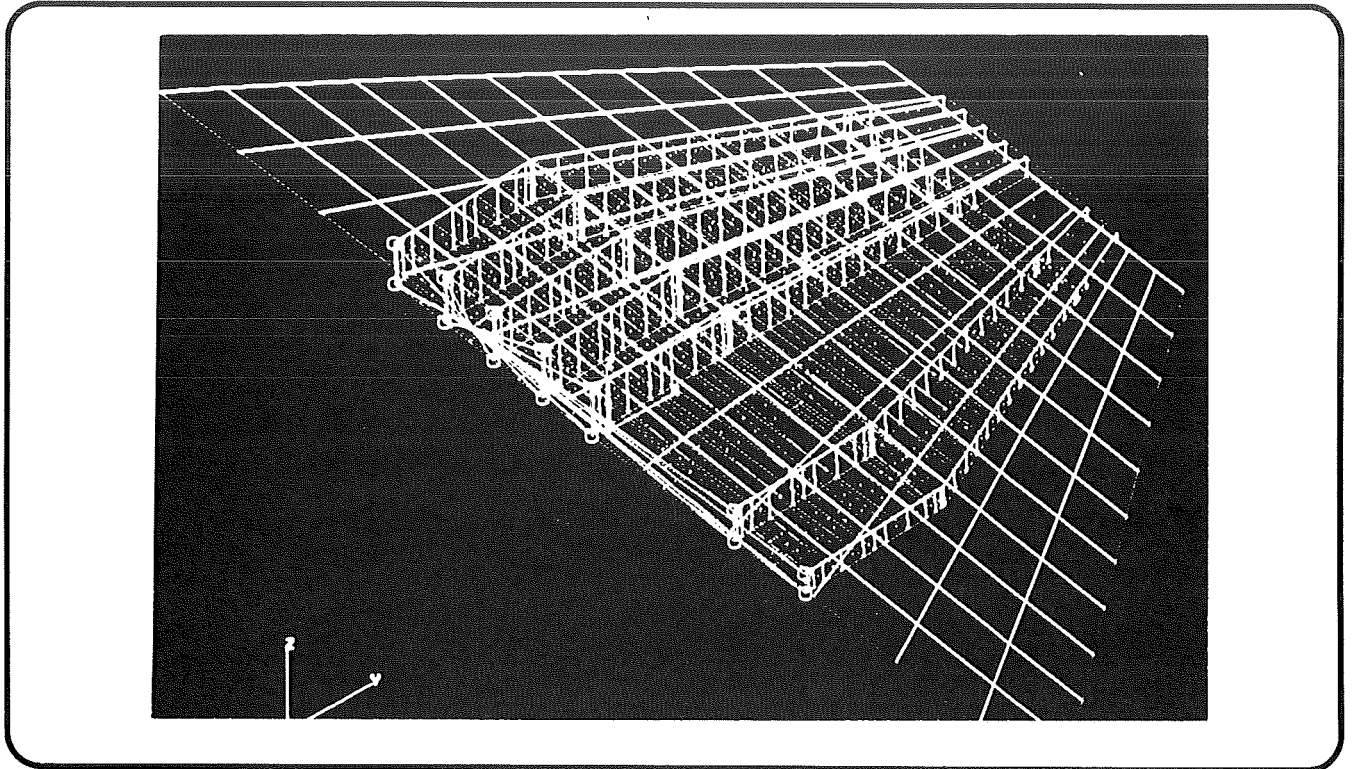


FIGURE 5a - Finite Element Model of rods for configuration MRFWING.11

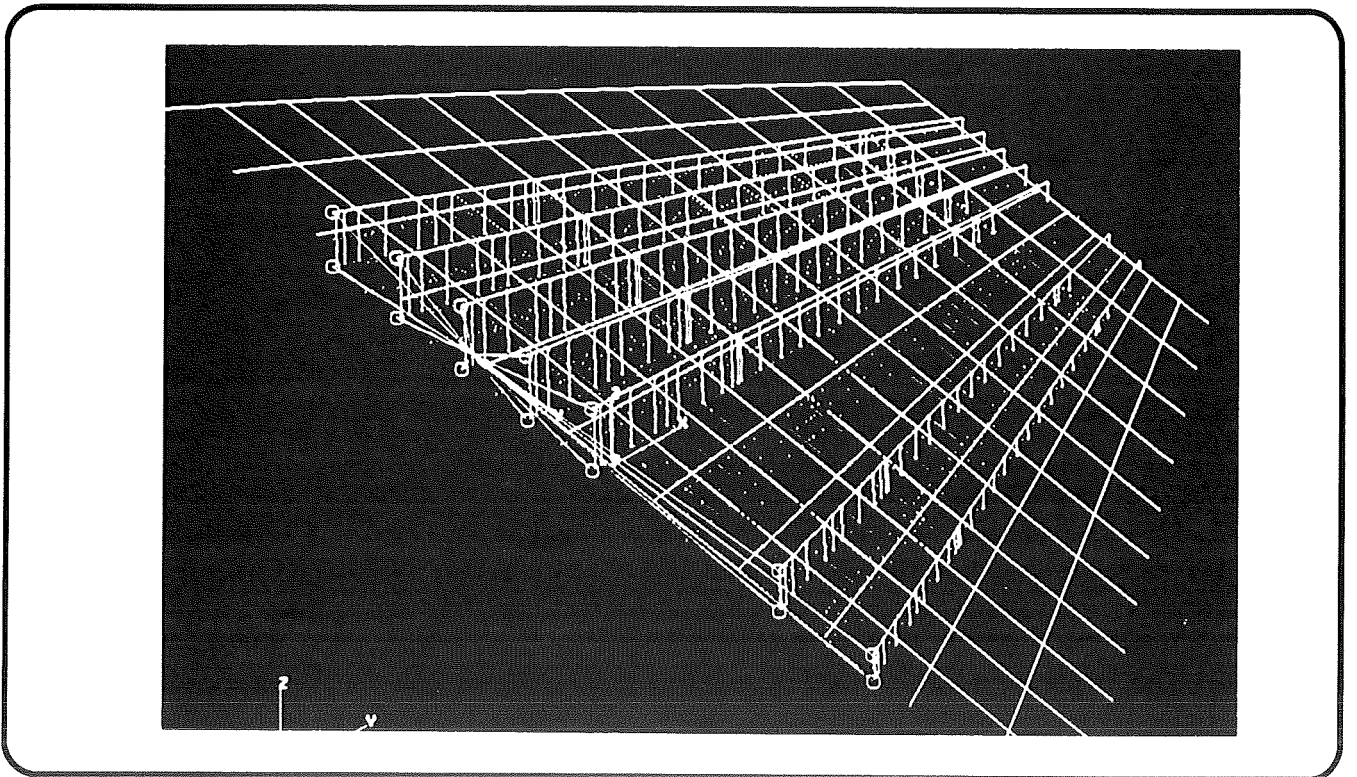


FIGURE 5b - Finite Element Model of rods for configuration MRFWING.21

AERODYNAMIC MODEL

The air loads for steady aerodynamic analysis were calculated with the Unified Subsonic and Supersonic AEROdynamics (USSAERO) which is a numerical procedure embedded in ASTROS (reference 20). USSAERO computes steady pressure loading on a wing-body-tail configuration during a trimmed maneuver. The structural model and aero model are coupled through splining matrices; the aerodynamic loads are splined to structural nodes on the upper surface of the wing.

Wing Geometry: A single aerodynamic panel model was used for all three wing configurations because the planform dimensions remained constant. USSAERO differentiates between the structural configuration and the panels used to discretize the aerodynamic surfaces. This capability allows for detail description of the wing in terms of planform geometry, airfoil thickness and camber. The model is constructed of seven chordwise divisions and nineteen spanwise divisions for a total of 133 panels. The aero model employs a thin supersonic airfoil (NACA 64-206) with a sharp leading edge which is representative of current high survivability fighters like the Northrop proposed configuration for ATF YF-23. Basic guidelines for construction of the USSAERO panel model were obtained from reference 21.

Trim Condition: The wing is trimmed for lift during a symmetric pull-up where load factor $n_z = 9.0$, MACH = 0.78, altitude = 10k ft, and angle of attack is the free variable.

DESIGN MODEL (DEM)

The design model refers to the collection of information found in bulk data which defines the design task in a format compatible with ASTROS operations. The design model defines the form of the objective function and the assignment of design variables which represent global properties of the finite element model. In most cases, the design model is optimized for structural weight, thus the objective function is weight. The design model also includes physical constraints and element lists which define the functional relationship between elements connected by a single design variable. The variables must satisfy the following mathematical equation;

$$\{t\} = [P] \{v\}$$

where $\{t\}$ is a vector of local variables and $\{v\}$ is a vector of global relationships. The mathematical procedure operates directly on the $\{v\}$ vector; where the vector $\{t\}$ is determined indirectly and the $[P]$ matrix is invariant. The designer must generate the operational relationships of the $[P]$ matrix and the initial values of the $\{v\}$ vector. An inherent understanding of this equation is required to manage interaction between variables and ensure the best possible design is developed. The final objective function may vary considerably depending on sophistication of the initial design model and accuracy of the applied loads.

The comprehensive assignment of design constraints is critical for rapid convergence of the optimization process. The design constraints must satisfy one of the following mathematical equations:

$$g_j(v) \leq 0 \text{ where } j=1, n_{con}$$

$$h_k(v) = 0 \text{ where } k=1, n_e$$

$$v_i(\text{lower}) < v_i < v_i(\text{upper})$$

where $i=1$ thru number of design variables

where g specifies the function of inequality constraints and h specifies the function of equality constraints. The equation for v specifies side constraints on global design variables (reference 10). The design model for advanced configurations of the multi-role fighter wing employs the following constraints:

- side constraints: establish minimum gage for survivability and damage tolerance
- principal strain constraints: compression after impact for composite skins
- Tsai-Wu stress constraints: notched hole allowables at 180°F for composite skins
- Von Mises stress constraints: B allowables for isotropic materials of rods and shears
- survivability constraints: the development of special constraints for panel buckling and signature effectiveness is ongoing at WL/FIB

DESIGN OPTIMIZATION

The design optimization is performed by mathematical algorithms which resize the design and force the objective function towards the minimum value which satisfies all performance criteria. The local design variables are linked together and operated on as a tractable number of global variables. The assignment of global design variables and design constraints governs the path the optimizer follows to develop the final design, thus the design model must be constructed efficiently to guide the optimization process towards the best solution.

Boundary Conditions; assigned in solution control

- MPC: 42 dependent multi-point constraints at wing root (1,2&3 degrees of freedom)
- SPC: 1181 independent single point constraints on rotational degrees of freedom
- SUPPORT: 1 reference node at aircraft cg to support the z direction for inertia relief

Optimization parameters; assigned in the engineering module ACTCON

- NRFAC set to 0.5 to limit retained constraints to below 200
- EPS set to -0.100 to limit cutoff constraint value
- DELOBJ set at 2.0 to limit relative change in objective function between successive iterations. This parameter was increased during initial runs to accelerate verification of design methodology; yet generate sufficient information to evaluate dependency of the constraints.

MAXITR set at 3 to accelerate verification of design methodology

The mathematical optimization process establishes a practical limit on the number of discrete design variables (approximately 200), thus variables should be limited to the minimum required to evaluate a desired relationship in the design model. The design variables are separated into two types by optimization function. This acts to minimize the total number of variables operated on during a single mathematical procedure and ensure most efficient optimization.

Local Design Variables: The local design variables $\{t\}$ are those used to represent physical properties of the individual finite elements including thickness, cross sectional area, and laminate construction, mass, and stiffness. The mass and stiffness matrices of physical properties are a linear function of the design variable value. At the completion of each design iteration, the total weight of designed elements is determined by summation of the variables multiplied by element size and material densities. Note that this calculation will not include the weight of non-optimal structure, non-structural hardware, fuel, or subsystems. The design model for the multi-role fighter wing is comprised of 5461 local design variables which are allocated as follows; 4212 variables for thicknesses of each lamina of the composite membranes, 351 variables for thicknesses of the composite webs, and 898 variables for cross sectional areas of the isotropic rods.

Global Design Variables: The global design variables $\{v\}$ are those used to control relationships between elements of a set. Actual element thicknesses are obtained by multiplying global design variables and the thicknesses defined on the property cards. The design model developed in this project for a multi-role fighter wing is comprised of 202 global design variables. To maximize the benefits of aeroelastic tailoring, more than fifty percent of these variables are used to describe design relationships between elements of the composite wing skins (reference 22).

Physical Linking of Design Variables: Physical linking requires that one global design variable uniquely define a collection of local design variables. This option provides for simultaneous variation of all elements forming a structural region, which implies that there is no preconceived reason why each element must be designed independently. Further, physical linking requires that a single column of the $[P]$ matrix be derived from thicknesses specified on the element property entries; all other columns specify rows controlled by the element lists (PLIST) which are zero. The design model for the multi-role fighter wing employs 118 groups which are physically linked according to substructure type (example: inboard wing skins on the upper side and all webs for a specific spar). This assignment was selected because it resulted in a significant variation in structural weight and this translates into the largest variation in structural resilience to laser damage.

DESIGN CONSTRAINTS

The strength of finite elements are bound by physical constraints on material properties which represent allowables established by mechanical loading and environmental exposure. The size of finite elements are bound by side constraints on global design variables which represent limits established by survivability, damage tolerance, and manufacturing.

SURVIVABILITY MODEL (SUM)

The structure of the multi-role fighter wing box will be designed against catastrophic failure such that the aircraft can continue flying without severe limitations to the maneuver envelope. The finite element based code Vulnerability Analysis of Aircraft Structures Exposed to Lasers (VAASEL) will be used to model structural response during the laser encounter (reference 11). VAASEL is capable of modelling ablation, systematic failure and load redistribution as the laser beam slews across composite materials. The development of a 3D thermal model for vulnerability evaluation of the advanced configuration is under current study. Detailed characteristics of the proposed threat are classified SECRET, therefore, a generic ground based laser threat was selected from reference 11 to verify the modelling approach. The normal incident laser intensity is 6.1 kW/cm² during a laser encounter of 5 seconds. The wing is exposed to the laser beam for 1.5 seconds as it slews over the upper skin. The pursuit of this task has been significantly hindered by difficulty in collection of the thermal data required to model particular structural concepts and composite materials employed in the advanced configurations. Due to a high level of confidence in data for the baseline material (AS4/3501-6), the design of the wing skins may be modified for all VAASEL analysis to use a solid laminate of this material and eliminate sandwich construction.

DESIGN RESULTS

Of foremost interest is whether or not the work performed under this study will produce significant improvements in laser survivability. At this time, the only definitive result is that the application of physical variable linking has affected distribution of structural weight and this usually translates into variation in structural resilience to laser damage. The total structural weight of the advanced configurations varied by approximately 30 percent. Note these values include only the weight of optimized elements and do not account for joints, subsystems, fuel, and other nonstructural elements. The design weight of the advanced configuration with spars at constant cord is approximately 20 percent lighter than the baseline design. The weight penalty is attributed to the high kick loads which are found in the region of transition from perpendicular inboard spars to constant cord outboard spars. Another significant result is that the advanced designs with far more spanwise stiffeners resulted in a lighter weight design, thus an optimal stiffener spacing versus sectional area could be determined. An analysis segment was performed after the design optimization task to obtain print of final strain distributions and to evaluate the final model under additional boundary conditions. The results of this analysis are presented in figures 6 thru 8. The stress-strain distributions correlate very closely with the displacement plots. Further, note the effect of the AIM-9 missile at span Y=34 inches. Figure 9 presents a convergence summary of the optimization parameters and figure 10 presents a summary of the design constraints applied in the optimization. The evaluation of HEL vulnerability is under current study and mechanical influence testing of composite panels will be conducted in September 92.

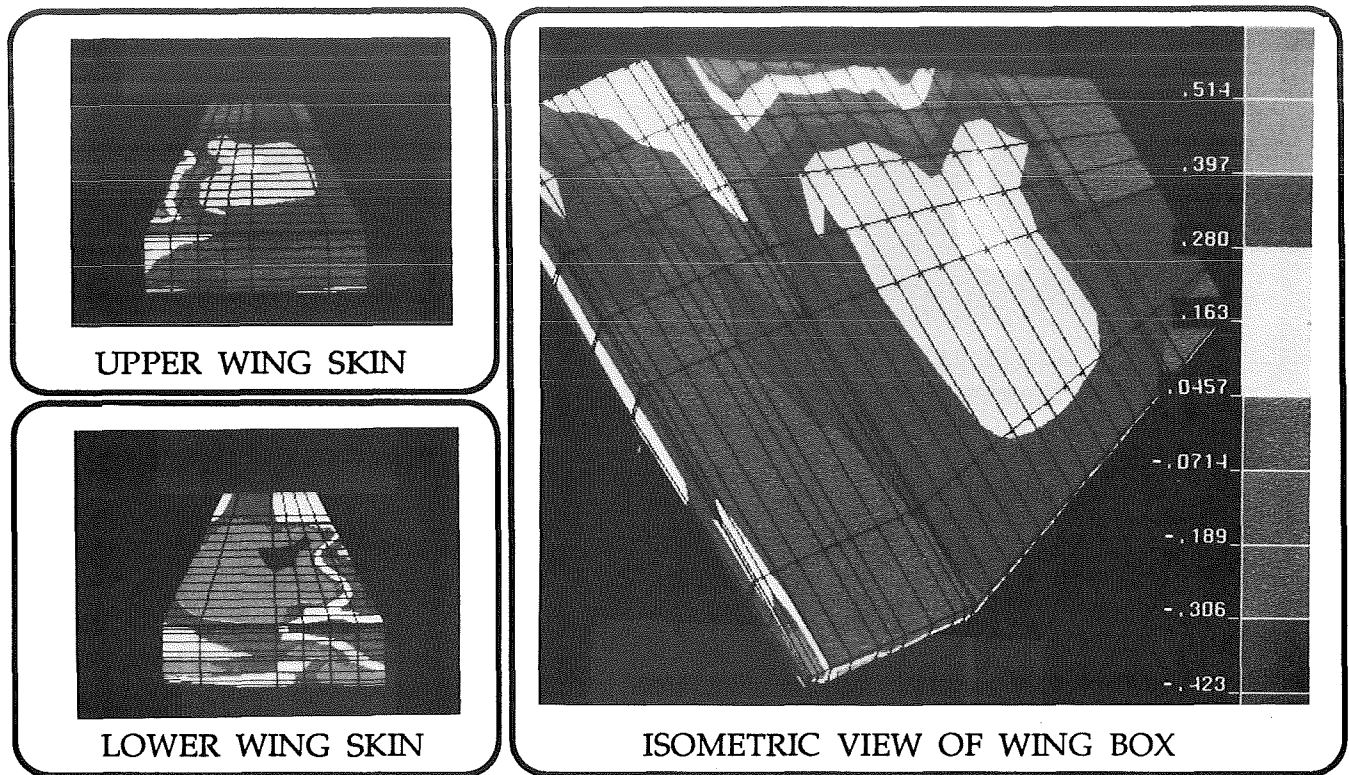


FIGURE 6a - Spanwise Maximum Stress Distribution for configuration MRFWING.11

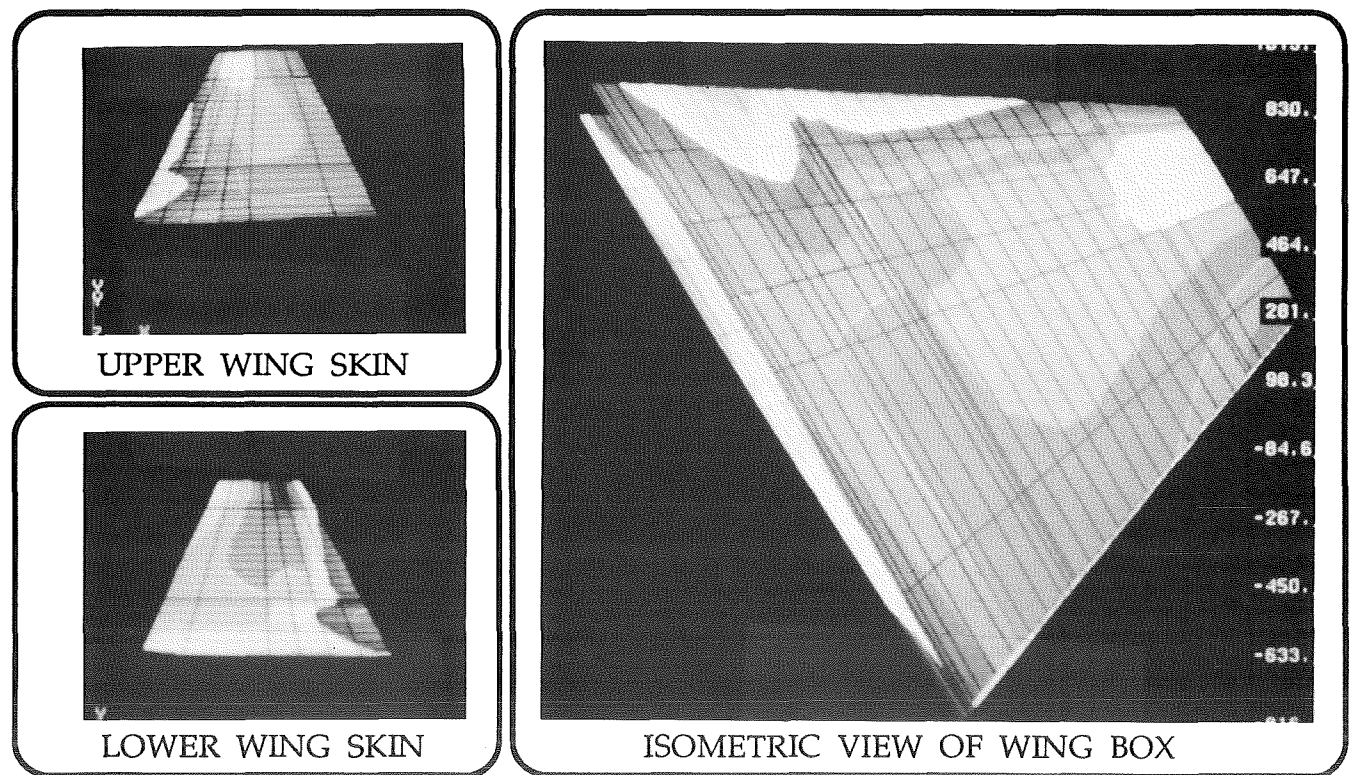


FIGURE 6b - Spanwise Maximum Stress Distribution for configuration MRFWING.21

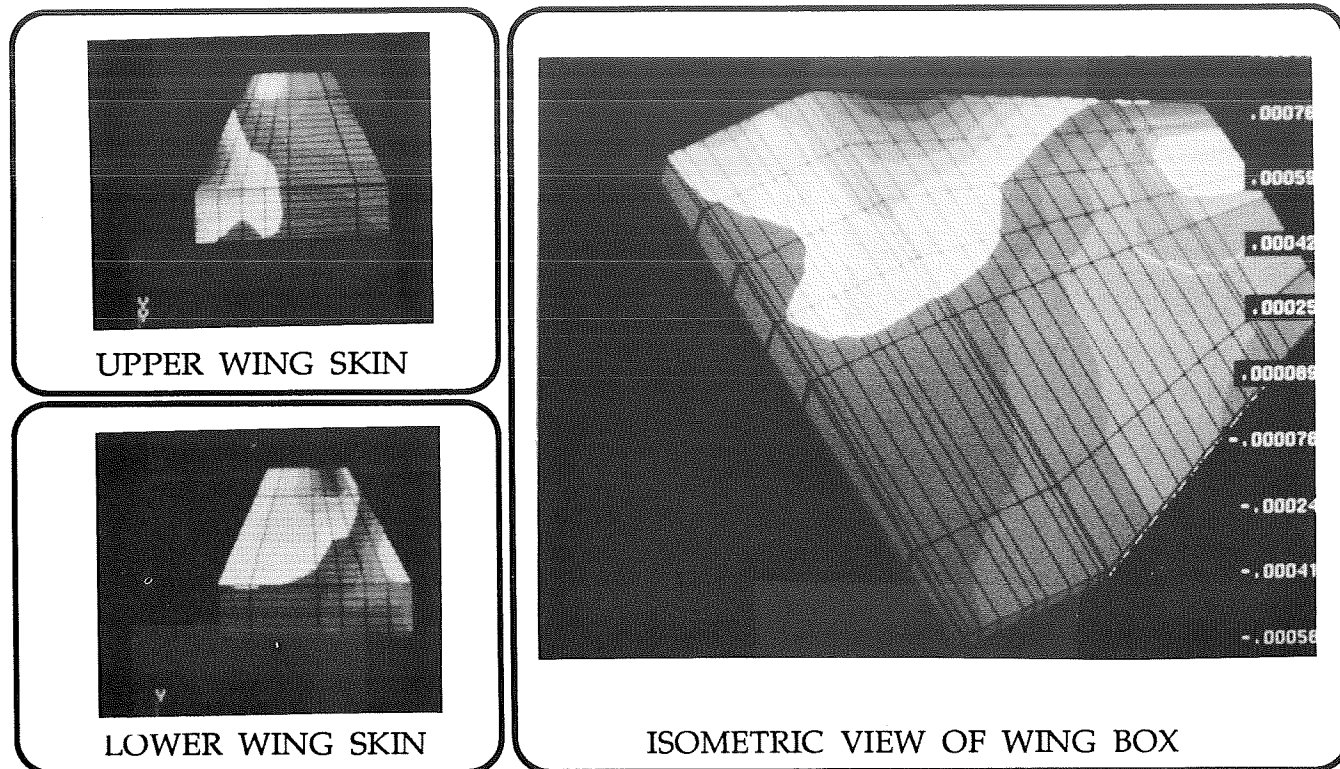


FIGURE 7a - Spanwise Strain Distribution for configuration MRFWING.11

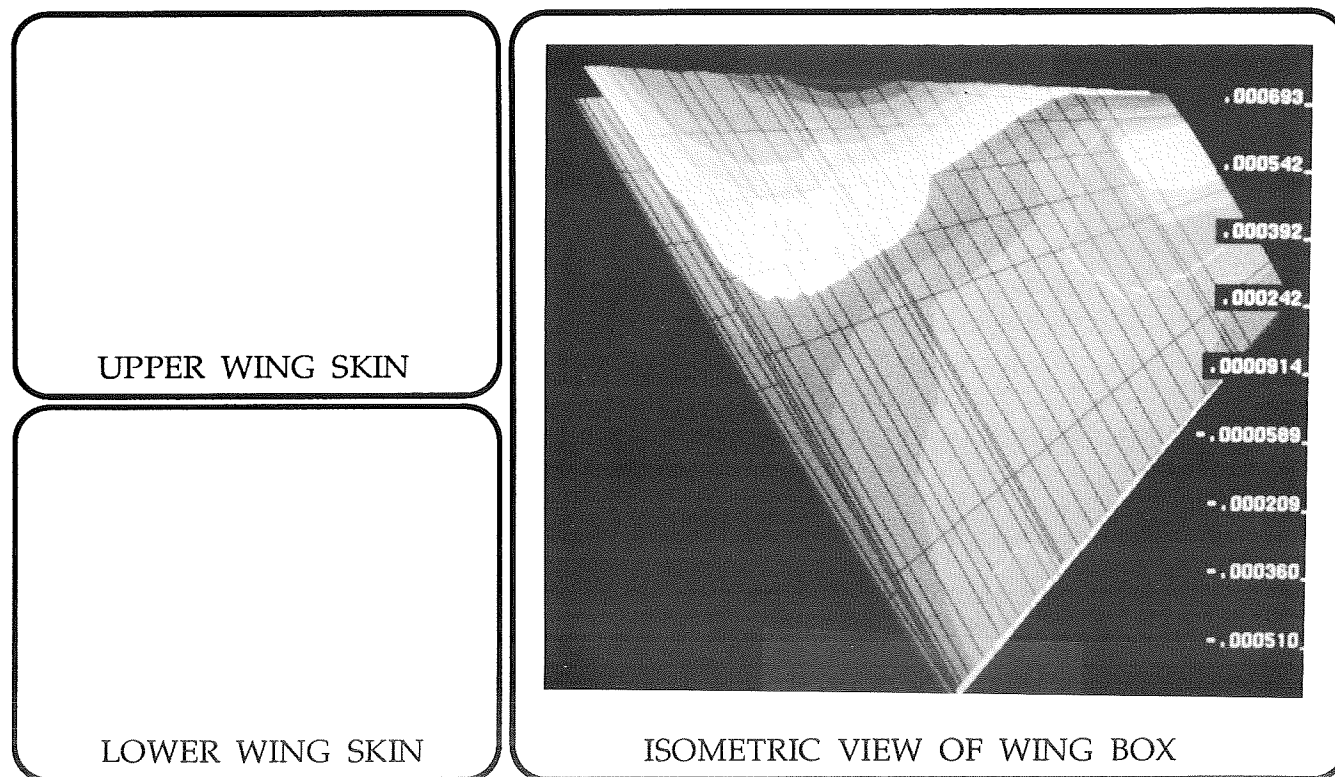


FIGURE 7b - Spanwise Strain Distribution for configuration MRFWING.21

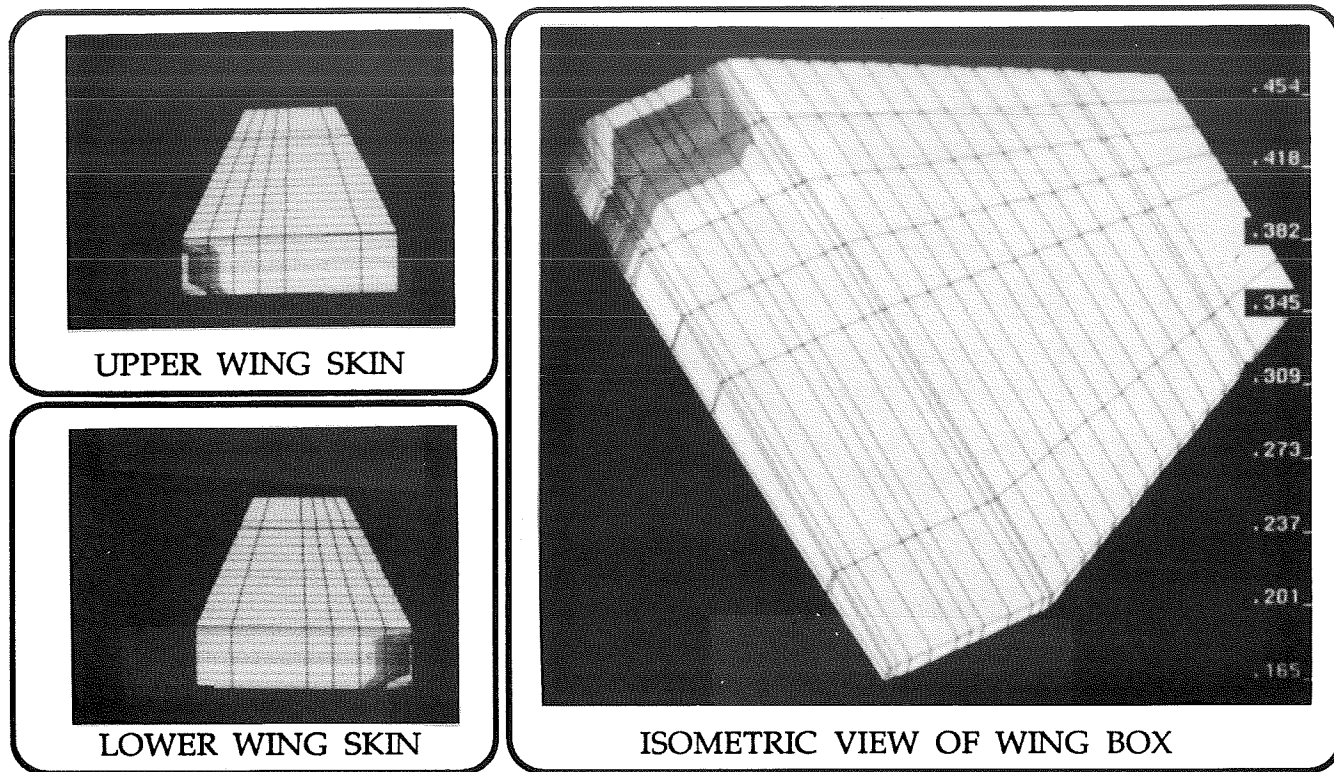


FIGURE 8a - Element Thickness Distribution of configuration MRFWING.11

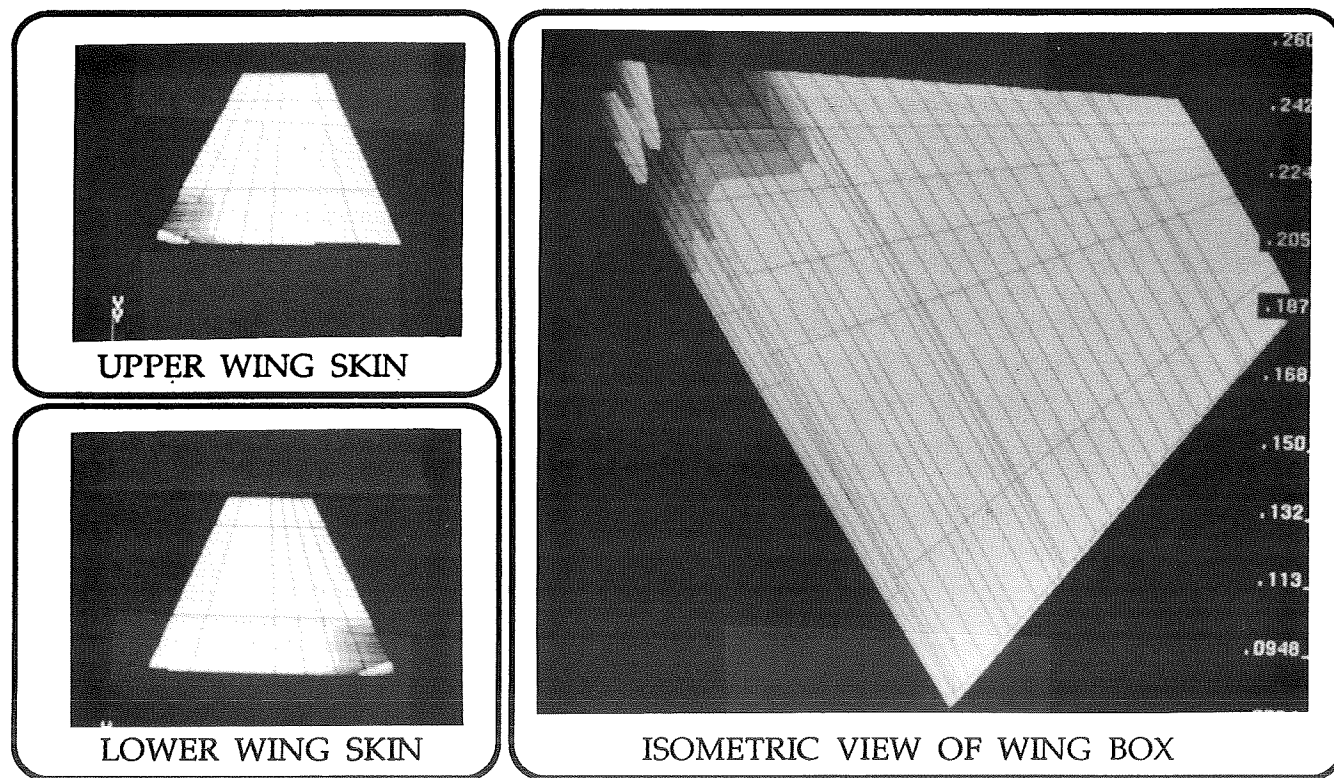


FIGURE 8b - Element Thickness Distribution of configuration MRFWING.21

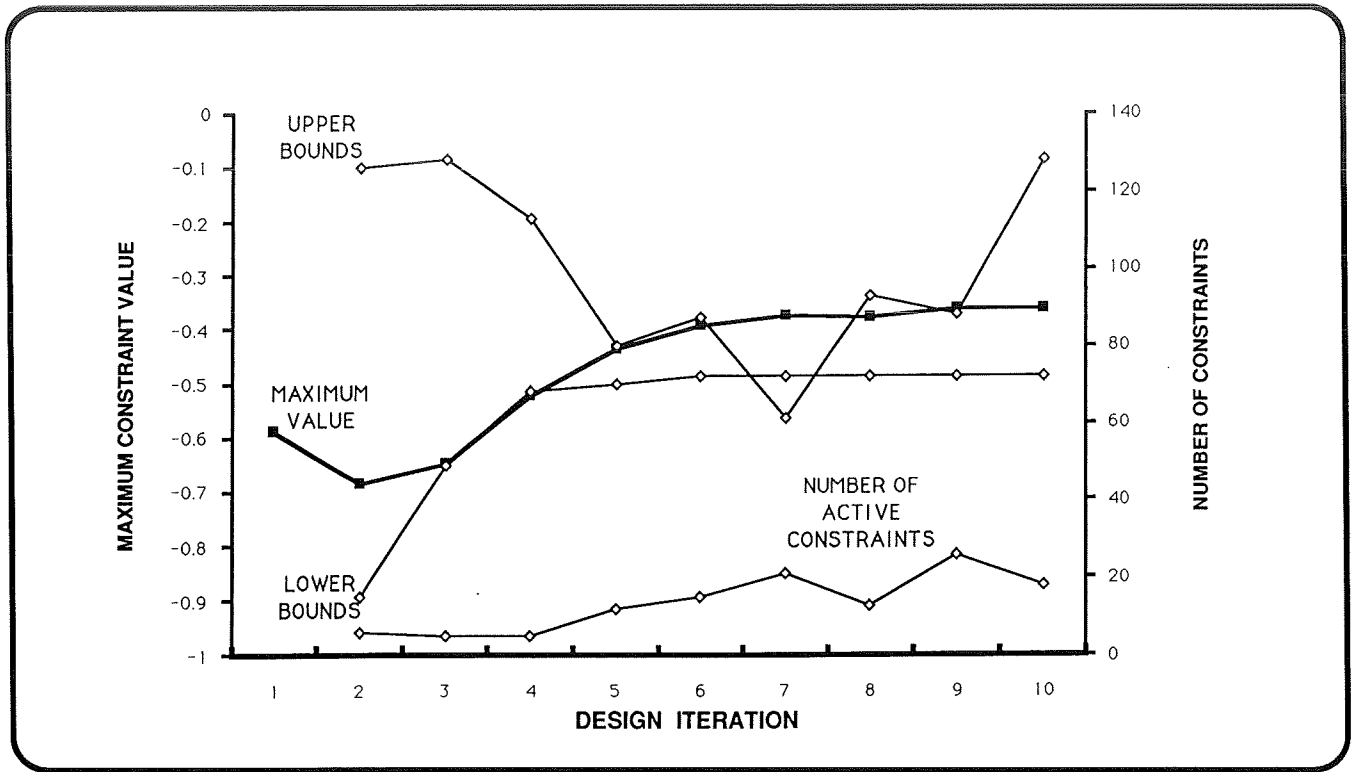


FIGURE 9a - Design convergence summary for configuration MRFWING.11

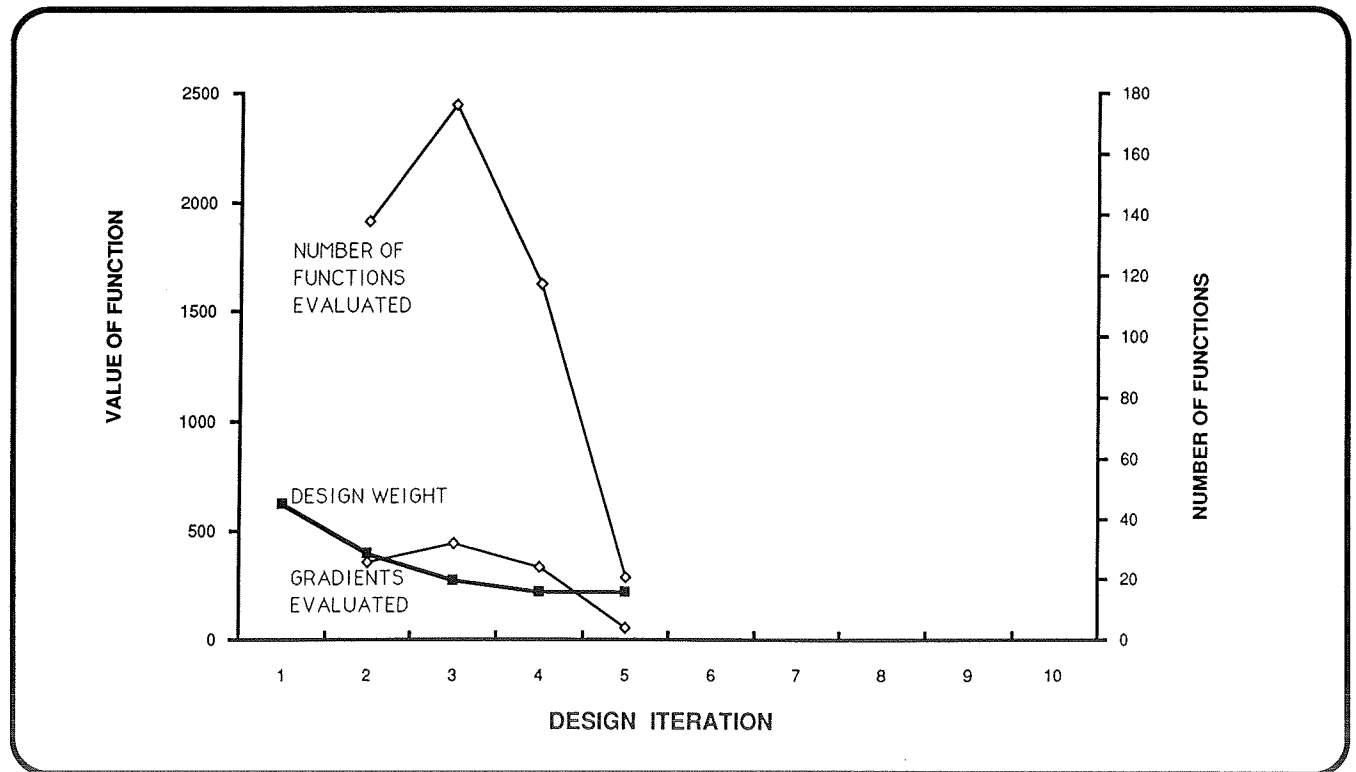


FIGURE 9b - Design convergence summary for configuration MRFWING.21

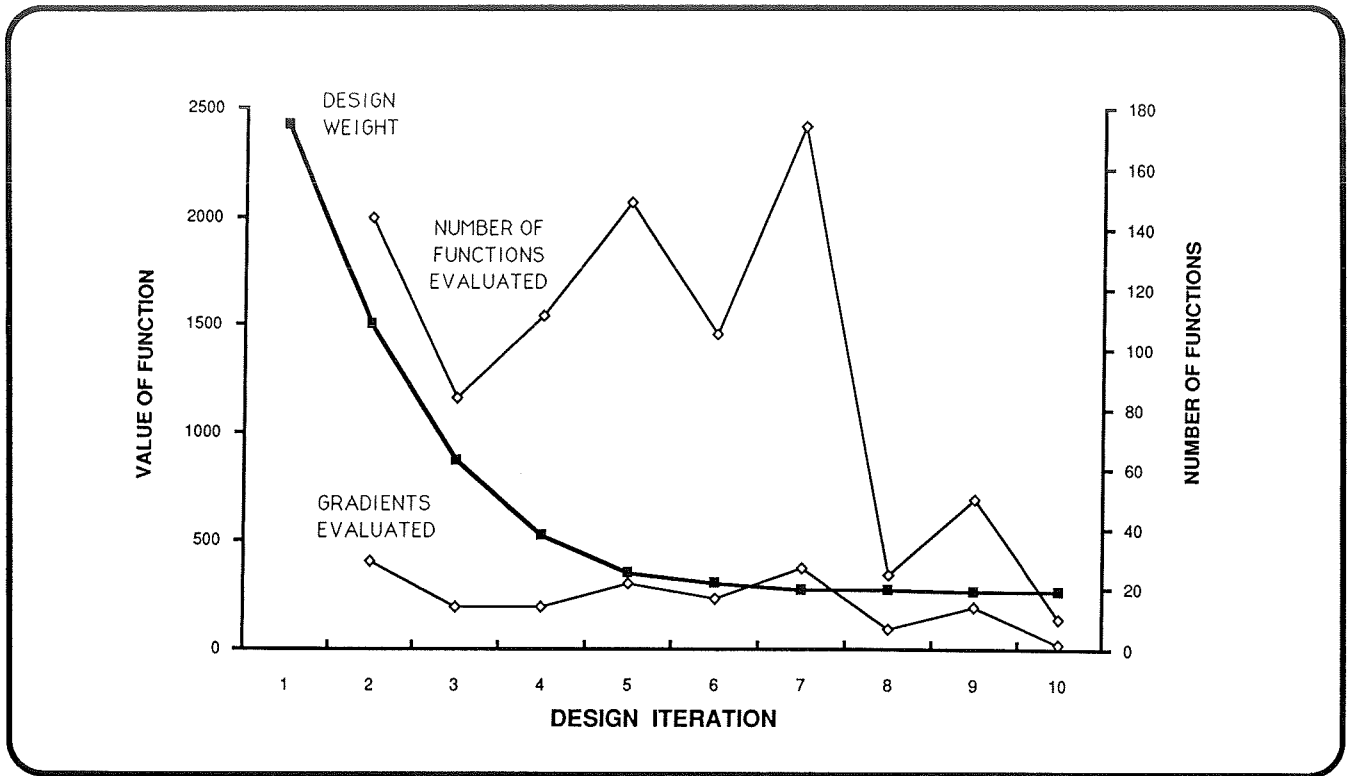


FIGURE 10a - summary of optimization constraints for configuration MRFWING.11

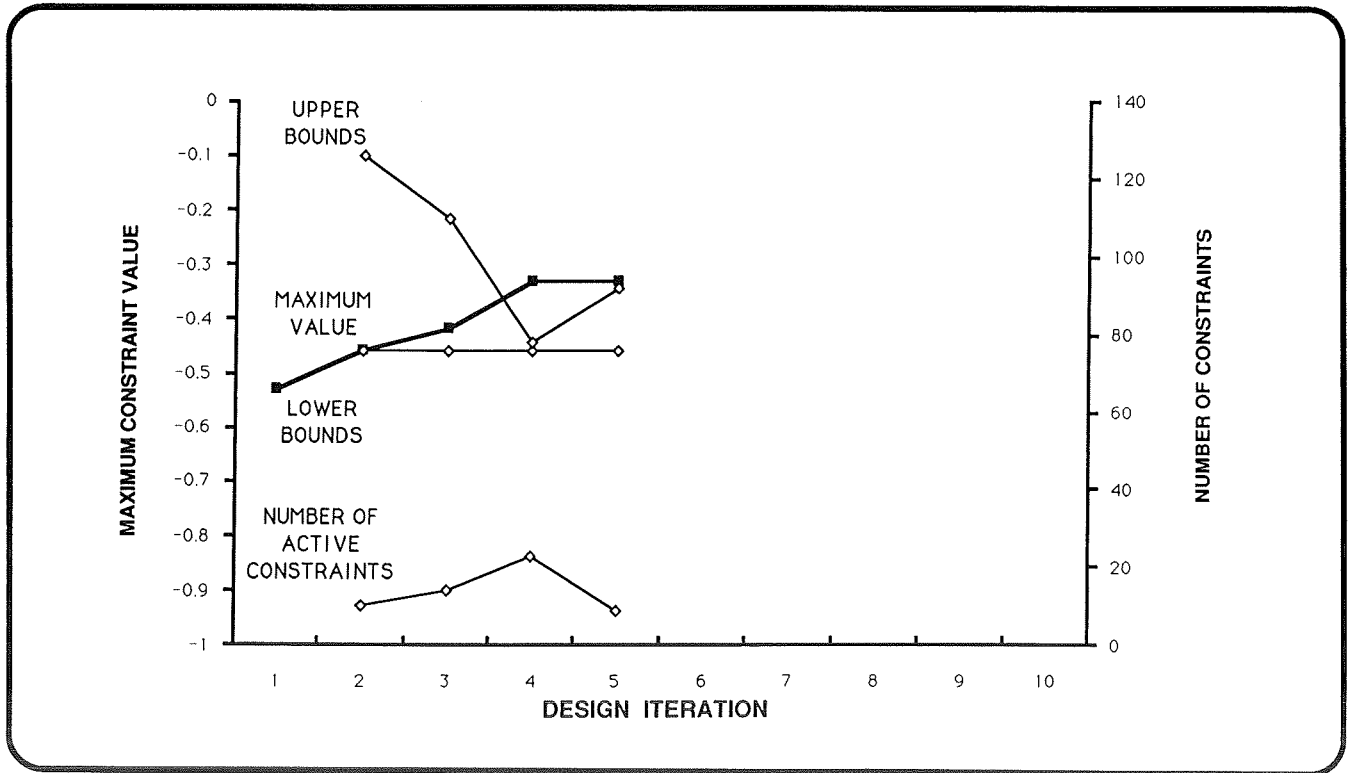


FIGURE 10b - summary of optimization constraints for configuration MRFWING.21

CONCLUSIONS

Under the scope of this effort, it was not possible to develop an exact approach which would include all aspects of survivability dependent design, therefore the author offers analysis guidelines for solving similar problems. The following recommendations are presented for researchers who wish to pursue development of a specialized constraint type or the non-conventional application of constraints.

Methodology: When developing new methodology for non-conventional constraints, it is critical that the researcher select a baseline finite element model which has been well characterized. The preferred approach would be to use an established benchmark model which has a very robust dependence on conventional variables and is not optimized within a tight bandwidth. The model should possess all of the characteristics required to assess the relationship between cause and effect, but should not be so complex that the effect of the new methodology is normalized by interaction between many dependent variables. In the case of this research, the author unwisely elected to develop new models for three configurations of the wing box for a conceptual aircraft having insufficient maturity. This resulted in excessive time being spent on evaluating the correctness of the model, thus limiting the resources available for verification of results attained from new methodology.

Optimization: The selection of design variables and linking type is critical to success of the optimization process. It is important to isolate a relationship between design variables early in methodology development and then focus on only those variables which are dependent on this relationship. The linking type applied in this research was physical linking of element thicknesses because this assumes no predefined dependency between elements and applies fewer inherent constraints in optimization. Further, physical linking offers flexibility to modify linked sets of elements without changing coefficients of the design model. The negative attribute of physical linking is the lack of the capability to apply multiple links per element; thus the model requires an excessive number of design variables. An alternative approach is to apply shape function linking or a combination of the two. In general, the designer should select an approach to optimization which provides the greatest control of specific elements under study without effecting optimization of the rest of the model.

Visual Data Analysis (VDA): The visualization of design models and analysis results with graphical processing software will greatly enhance the researcher's ability to identify functional dependencies and dedicate resources to the development of methodology. These codes prove invaluable for interactive evaluation of large multidimensional datasets, thus preventing the expenditure of considerable time in pursuit of an incorrect relationship. In the case of this research, the author used the commercially available code PATRAN coupled with an FEM pre-processor code developed at the University of Notre Dame (reference 18). An Air Force developed translator was used for conversion from ASTROS output to PATRAN neutral format.

Structural Test: A structural test is worth a million bits of data. The significance of analytical studies must be verified through hardware demonstration. Under Task 3 of this program, the WL/FIBC Composites Facility will fabricate and test two full scale components against both high energy laser and low energy LIDAR threats.

In addition, the leading edge component will be attached to a full scale composite wing box which will be developed under the in-house effort intitled Bolted Advanced Survivable Structures (reference 13). Thus, the fabrication and test of a representative structural component will substantiate the analytically predicted improvement in survivability. We are currently developing a subscale leading edge having similar structural design and materials. This effort is being pursued to develop expertise in fabrication of thermoset composite tooling and to gain experience in processing parts of the unique core materials (see figure 11).

ACKNOWLEDGMENT

The author would like to thank Mr Ray Kolonay for continued support in the application of ASTROS and the development of an approach for design optimization.

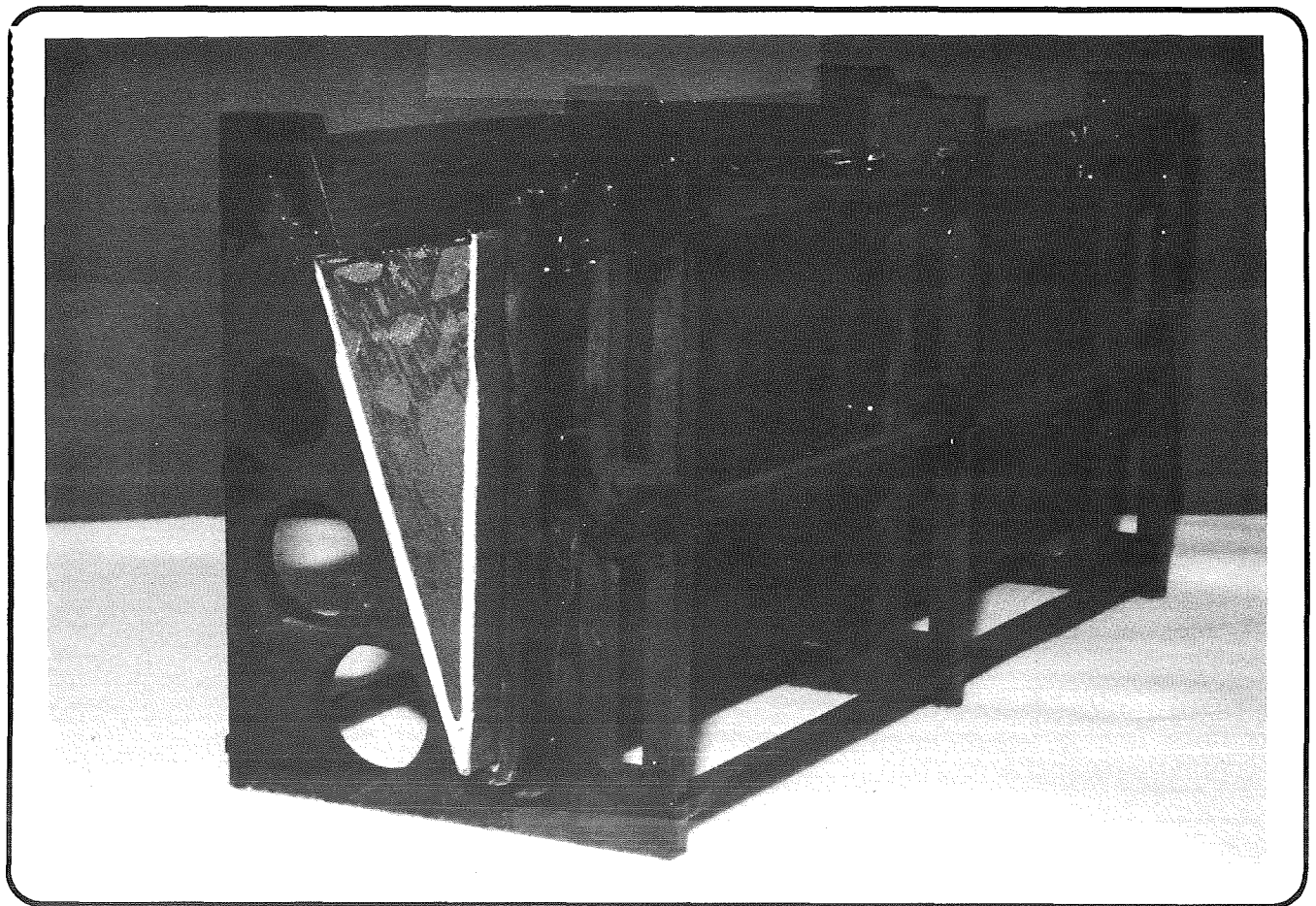


FIGURE 11 - leading edge composite tooling for producibility assessment

REFERENCES

1. Canfield, R.A. Capt, et al., "Automated Strength - Aeroelastic Design of Aerospace Structures, Statement of Work," Air Force contract F33615-83-C-3232, Flight Dynamics Laboratory, Air Force Wright Aeronautical Laboratories, July, 1983.
2. Lynch, R.W., et al., "Aeroelastic Tailoring of Advanced Composite Structures for Military Aircraft; Volume III - Modifications and User's Guide for Procedure TSO," AFFDL-TR-76-100, Volume III, February, 1978.
3. Markowitz, J. and Isakson, G., "FASTOP-3: A Strength Deflection and Flutter Optimization Program for Metallic and Composite Structures," AFFDL-TR-78-50, Volumes I and II, May, 1978.
4. Schmit, L.A., Jr. and Miura, H., "Approximation Concepts for Efficient Structural Synthesis," NASA CR-2552, March, 1976.
5. Sobieszczanski, S.J., James, B.B., and Dovi, A.R., "Structural Optimization by Multilevel Decomposition," AIAA Journal, Volume 23, No. 11, November, 1985.
6. Venkayya, V.B., "Structural Optimization: Review and Some Recommendations," International Journal for Numerical Methods in Engineering, Volume 13, 1978.
7. Jones, W.F., et al., "Development of a Strategic Plan for Nonmetallic Structures Through The Year 2010," ORNL-CC-SP-90/1, December, 1990.
8. Herendeen, D.L., Johnson, E.H., and Neill, D.J., "Automated Structural Optimization System (ASTROS)," AFWAL-TR-88-3028, Volume I and II, July, 1988.
9. Peterson, R.L., Lizza, A.S., et al., "FY91 Air Vehicles Technology Area Plan," Headquarters Air Force Systems Command, DCS/Technology, Andrews AFB, MD, August, 1990.
10. Rankine, R.R. Jr., Maj Gen, "Vision for Air Force Laboratories," Headquarters Air Force Systems Command, DCS/Technology, Andrews AFB, MD, 28 November, 1990.
11. Blauvelt, R.E., Kudva, J.N., Megginson, B.J., Saether, E.S., Hinds, M., Legner, H.H., "Vulnerability Analysis of Aerospace Structures Exposed to Lasers (VAASEL); Volume I - Modelling Guide," WRDC-TR-90-3070, Volume I, September, 1990.
12. Meadors, J.E., "Technology for Reduced Susceptability to Lidar and Vulnerability to High Energy Lasers in an Advanced Concept Leading Edge, Task X-7," Project Proposal, Air Force contract F33615-88-C-1728, Flight Dynamics Laboratory, Air Force Wright Aeronautical Laboratories, July, 1983.
13. Baron, W.G., and Oetting, J.D., "Baseline Evaluation of the Airflow Test Fixture," WRDC-TM-90-336-FIBCA, October, 1990.

14. Mace, J., Bingaman, D., et al., "Propulsion Integration for Aero Control Nozzles," WL-TR-91-3009, March, 1991.
15. Speers, J., "Structural Assessment and Vulnerability Evaluation (SAVE)," Air Force Contract F33615-88-C-3207, First Interim Report for Period March 89 - August 89: Volume I - Threat Assessment, December, 1989.
16. Fields, D. et al., "Aero Configuration and Weapons Fighter Technology; Statement of Work," Air Force contract F33615-83-R-3004, Flight Dynamics Laboratory, Air Force Wright Aeronautical Laboratories, June, 1989.
17. Suarez, J.A., "Advanced Composites Supportable Structures," AFWAL-TR-88-3112. Final Report for Period November 1983 - September 1988, August 1989.
18. Swift, R., "Application of Finite Element Methods to the Preliminary Design of Lifting Surfaces," M.S.A.E. Thesis , University of Notre Dame, 1989.
19. Rodden, W.P., Editor, MSC/NASTRAN Handbook for Aeroelastic Analysis, The MacNeal - Schwendler Corporation, Pasadena, California, 1987.
20. Woodward, F.A., "An Improved Method for the Aerodynamic Analysis of Wing-body-Tail Configurations in Subsonic and Supersonic Flow," Part I - Theory and Applications, NASA CR-2228, May, 1973.
21. Hinrichsen, R., "A Comparison of Aerodynamic Paneling Methods Applied to Structural Optimization," Third Air Force / NASA Symposium on Recent Advances In Multidisciplinary Analysis and Optimization, September, 1990.
22. Kane, D.M., Palm, T.E., "Ultralightweight Structures," WL-TR-91-3034, Interim Report for Period September 1988 - February 1991, October, 1991.

THIS PAGE INTENTIONALLY BLANK

RELIABILITY ANALYSIS OF COMPOSITE STRUCTURES

Han-Pin Kan

Northrop Corporation, Aircraft Division, 3853/MF
Hawthorne, California321-24
51389
P-13

ABSTRACT

A probabilistic static stress analysis methodology has been developed to estimate the reliability of a composite structure. Closed form stress analysis methods are the primary analytical tools used in this methodology. These structural mechanics methods are used to identify independent variables whose variations significantly affect the performance of the structure. Once these variables are identified, scatter in their values is evaluated and statistically characterized. The scatter in applied loads and the structural parameters are then fitted to appropriate probabilistic distribution functions. Numerical integration techniques are applied to compute the structural reliability. The predicted reliability accounts for scatter due to variability in material strength, applied load, fabrication and assembly processes. The influence of structural geometry and mode of failure are also considerations in the evaluation. Example problems are given to illustrate various levels of analytical complexity.

INTRODUCTION

Application of composite materials to primary aircraft structures requires proven certification procedures to demonstrate their reliability. The development of certification procedures for primary composite structures must recognize the inherent characteristics of composites. One of these characteristics is the scatter in static strength and fatigue life data. Because of the higher static strength and fatigue life data scatter in composites (as compared to metals), the structural reliability provided by the conventional deterministic certification approach would be different for composite and metallic structures. The variation of static strength reliability with the material data scatter can be seen in Figure 1. In this figure, the material strength distribution is characterized by a two-parameter Weibull distribution. The reliability at design limit load is computed based on a static design with a factor of safety of 1.5 and a margin of safety of 0.0. Reliabilities based on both A-basis and B-basis designs are shown in the figure. As shown in the figure, for a Weibull shape parameter α of 20 (typical for composites) the B-basis reliability is 0.99996832, and at $\alpha = 25$ (typical for aluminum alloys) it is 0.99999583. Although these reliabilities appear to be equally high, significant difference exists in the risk of the

1 This work was performed under Northrop IRAD project R-1056, entitled "Strength and Life Assurance Technology for Aircraft Structures."

design or the probability of failure. The risk for composite structures is 3.2×10^{-5} as compared to 4.2×10^{-6} for metals. This example indicates that in order for composite structure to achieve the same level of reliability as metallic structures a probabilistic based reliability analysis methodology is needed. The importance of the probabilistic approach is more obvious when fatigue life of composites is considered, because of the even higher data scatter observed in composite fatigue tests.

In addition to the scatter in strength and life data, another factor that affects the reliability of a structure is the uncertainty in the applied load. These uncertainties are conventionally covered by a factor of safety. A 1.5 factor of safety, traditionally used in aircraft structural design, generally provides a very high level of reliability. However, this deterministic approach cannot be used to assess the risk involved in a structural design. Thus, trade studies cannot be conducted to optimize the risk of failure. A more desirable approach is the probabilistic approach that utilizes the statistical distribution of the applied loads and the material strength. The probability of failure can be computed by integrating the overlapping region of these two distributions. Using this technique, the risk of failure of a structure can be estimated and the risk can be minimized within the limits of cost and performance needs. The conventional factor of safety approach and the probabilistic approach are illustrated in Figure 2.

There have been several efforts to develop reliability analysis methods for composite structures (References 1 through 7). The work in Reference 1 concentrated on the evaluation of certification approaches relating to structural reliability. An integrated impact damage tolerance reliability analysis method was proposed in Reference 2. Attempts were made in Reference 3, 4 and 5 to statistically characterize the applied load distribution. References 6 and 7 proposed a micromechanics approach to characterize the scatter in the mechanical properties.

In this paper, a comprehensive probabilistic static stress analysis methodology is proposed. The methodology integrates structural mechanics methods, scatter in material properties, uncertainties in applied loads and the variability in fabrication and assembly processes into a single analysis package to estimate the reliability of a composite structure. The various levels of analytical complexity are illustrated by example problems.

ANALYSIS APPROACH

Structural reliability analysis methods depend on the structural configuration and the anticipated mode of failure and, therefore, are problem specific. In this section, a general approach is first outlined. Example problems are then used to illustrate various levels of analytical complexities.

General Approach

The general approach for reliability analysis of composite structures can be summarized below.

1. Select static analysis method
2. Identify scatter parameters
3. Characterize applied load distribution statistics
4. Compute structural reliability

Closed form stress analysis methods are the primary analytical tools used in the present methodology. Static stress analysis provides results that describe the general response of a structure in response to applied loads. In addition, for reliability analysis, static analysis methods can also be used to identify independent variables and failure modes. Only those variables whose scatter significantly affects the performance of the structure are selected for reliability analysis. These variables are then statistically characterized based on experimental data. The probabilistic distributions of the structural parameters are finally incorporated into the static stress analysis method for reliability computations.

The macromechanics approach recommended in Reference 1 is used here for scatter parameter characterization. This approach is selected over the micromechanics approach proposed in References 6 and 7 because it significantly reduces the number of primitive variables. Furthermore, extensive database at the macromechanics level exists in the literature to verify the analysis.

A second data item that requires statistical characterization is the applied loads. In the case of existing aircraft types, the basic source of loads data is the flight loads recorder data generated from the aircraft type. The loads data are generally available in form of exceedance function. The exceedance functions must be transformed into a probabilistic function for reliability analysis. Attempts were made in References 3, 4 and 5 to fit the exceedance function into a probabilistic function.

The exceedance data are fitted into a two-parameter Weibull distribution in References 3 and 5. The Weibull shape parameter for air combat maneuvers missions for the F-16 wing structures is found to be between 8 and 10 in Reference 5. In Reference 3, the cumulative probability of exceeding a given load in one lifetime was defined by a Weibull function with a shape parameter of 6 and a 0.001 probability of exceeding design ultimate load (DUL). This distribution of applied load is shown in Figure 3. Both the cumulative probability of exceedance and the probability density are shown in the figure. As shown in the figure, the probability that an applied load exceeds the design limit load (DLL) in the lifetime of an aircraft is approximately 0.55. The figure also indicates that during the lifetime of the aircraft, the most frequently occurred (modal) load is approximately 1.05DLL. Such a load distribution may be reasonable for a military aircraft but rather severe for a civil airplane. A less severe distribution has a Weibull shape

parameter of two and retains the assumption that there is a 0.001 chance of an applied load exceeding DUL. This distribution gives approximately 0.05 probability that the flight load exceeds DLL and the modal load is approximately 0.4DLL. This approach is used here for applied load distribution characterization.

Once the key structural variables and the applied load are statistically characterized and the probabilistic distributions are incorporated into the selected stress analysis method, the structural reliability can be evaluated numerically. The principle of reliability analysis was shown in Figure 2. The risk or probability of failure is assessed by integrating the area of the shaded region of the joint probability distribution shown in the figure. However, in reality, more than two random variables are encountered in the analysis, and these variables may or may not be totally independent. Special numerical techniques are required for these analyses. Several reliability algorithms are available (References 1, 3-5 and 8-11). In References 3-5 the reliability or the probability of failure is obtained by direct integration of the joint probability function as shown in Figure 2. This approach is used in the present paper.

Structures With Single Variable and Single Failure Mode

As a first example, consider a simple tensile composite element with cross-sectional area A and axial Young's modulus E subjected to axial load P. The element is designed based on B-basis allowable strain (ϵ_{ALL}) with zero margin of safety at design ultimate load (DUL) and the factor of safety is 1.5. That is $\epsilon_{DUL} = \epsilon_{ALL}$ and $\epsilon_{DLL} = \epsilon_{ALL}/1.5$. Assuming that the design allowable is derived from a two-parameter Weibull distribution of strength data, from the definition of the B-basis allowables the Weibull scale parameter (with a 95% confidence) is given by

$$\beta = \frac{1.5}{[-\ln(0.9)]^{1/\alpha}} \quad (1)$$

Notice that the strains are normalized with respect to the design limit load (DLL). The value of α is determined from statistical analysis of the material strength data. For the commonly used graphite/epoxy composite $\alpha = 20$ is a reasonable estimate (Reference 1). The reliability of the structure subjected to a discrete applied load P is then given by

$$R = \text{Exp} \left[- \left(\frac{x}{\beta} \right)^\alpha \right] \quad (2)$$

where $x = (P/AE)/\epsilon_{DLL}$ is the normalized strain. The reliability of the structure subjected to a distributed load over the lifetime of the structure is

$$R = 1 - \int_0^\infty f(\epsilon) F(P) dP \quad (3)$$

where

$F(P)$ is the probability of occurrence of the applied load at level P .

It should be noted that the integral on the right-hand side of equation (3) is the risk or the probability of failure. The integral is evaluated by numerical integration. The reliability of the structure thus evaluated is shown in Figure 4. The load distribution used in this evaluation is based on the assumptions used in Reference 3, i.e. the load distribution is described by a two-parameter Weibull distribution and the probability for applied load exceeding DUL is 0.001. The figure shows the reliability of the tensile element with a 95% confidence. As shown in the figure the reliability is generally higher than 0.99. The figure also indicates that the reliability increases with material strength shape parameter (α_S). However, based on the load distributions assumed, the reliability decreases as the load shape parameter (α_L) increases.

The influence of the factor of safety (FS) on the reliability of the structure was examined for this simple structure. The results are shown in Figure 5. These results were obtained for $\alpha_S = 20$ and $\alpha_L = 6$. The figure shows that the reliability increases rapidly with FS for FS less than 1.4. The risk or the probability of failure (P_f) is plotted in terms of FS in the insert of Figure 5. The figure shows that the FS increases linearly with the negative order of magnitude of the risk. This trend indicates that the weight increases at an exponential rate with reducing risk. Also shown in Figure 5 is the reliability of the structure operated under the discrete applied DLL. It can be seen that this reliability is significantly higher than that predicted by distributed load.

Structures With Multiple Variables and Single Failure Mode

The reliability evaluation of an open hole element is a second example for illustration purposes. The reliability computation in this example is more complicated because of the increased complexity of the stress analysis procedure and, therefore, more scatter variables involved. The strength prediction of an open hole under uniaxial tension loading has been investigated by many authors. For illustrative purposes, the average stress criteria suggested in Reference 12 is selected here.

In Reference 12 the static strength of an orthotropic plate with a circular hole under uniaxial tensile loading can be approximated by

$$\epsilon_f = \epsilon_0 \cdot 2(1 - \xi) / [2 - \xi^2 - \xi^4 + (K - 3)(\xi^6 - \xi^8)] \quad (4)$$

where

ϵ_f is the static failure strain of the plate with a hole

ϵ_0 is the unnotched failure strain of the laminate

K is the stress concentration factor

$\xi = R/(R+a_0)$ with R is the radius of the hole and a_{0p} is a characteristic length

Equation (4) states that the plate failure occurs when average strain (stress) within the region characterized by a_0 reaches the unnotched strength of the laminate. Equation (4) suggests that the reliability of the hole strength can be evaluated in two separate parts: the unnotched strength and the hole quality. The unnotched strength (ϵ_0), as can be seen from equation (4), is independent of the hole geometry and quality. The reliability contributed by this part can be treated in the same manner as in the previous example. The second part or the hole quality is more complex because of the number of variables involved. These variables are: hole size (R), elastic properties (K is a function of the elastic moduli in an orthotropic plate) and the characteristic length (a_0). For the purpose of this illustration, the hole size and the elastic properties are assumed to be within the design tolerance limits. Thus, the influence of these variables on the reliability is negligible. This is a reasonable assumption because small variations in hole size and moduli have a negligible effect on the strength scatter. The major contributing parameter for the strength scatter is the hole quality characterized by a_0 .

By considering only the scatter of the unnotched strength and the characteristic length in the reliability evaluation, the probability that a hole strength exceeds a certain strain ϵ_f is then given by

$$p(\epsilon_f) = \text{Exp} \left[-\left(\frac{\epsilon}{\beta_s}\right)^{\alpha_s} \right] \cdot \text{Exp} \left[-\left(\frac{a}{\beta_a}\right)^{\alpha_a} \right] \quad (5)$$

In equation (5), both the unnotched strength and the characteristic length distributions are assumed to be Weibull. Equation (5) was used, together with the loads distribution and numerical integration technique described previously, to evaluate the reliability of a structure with an open hole. The results are shown in Figure 6. The figure shows the results for a plate with a 1/4 inch diameter hole with a stress concentration factor of 4.75. Three values of average characteristic length (a_0) are shown; they are 0.10, 0.12 and 0.15 inch. The value of a_0 used in the design analysis was 0.10 inch, which gave a design notch strength of $0.545\epsilon_{ALL}$ at DUL. The lifetime reliability of an unnotched structure based on the same load distribution is 0.99848. Figure 6 shows that the hole quality scatter may significantly affect the reliability of the structure when the scatter in hole quality is large (small α_a).

Structures With Competing Failure Modes

A third example here illustrates the effects of competing failure modes on the reliability of a structure. In general, the probability of failure for a structure with N failure modes is given by

$$P_f = P_{f1} + P_{f2} + \dots + P_{fN} = \sum_1^N P_{fi} \leq 1.0 \quad (6)$$

where p_{fi} is the probability of failure due to i th failure mode.

The reliability is then

$$R = 1 - p_f \geq 0.0 \quad (7)$$

Consider a beam-column with compression and buckling as two competing failure modes. The beam-column is designed to buckle at DUL and the prebuckling strain at DUL equals the compression design allowable ϵ_{ALL} , which is derived from a Weibull distribution. Then the probability of failure at applied strain ϵ due to compression is

$$P_{fc} = 1 - \text{Exp} \left[- \left(\frac{\epsilon}{\beta_s} \right)^{\alpha_s} \right] \quad (8)$$

The buckling strain is

$$\epsilon_{cr} = k \frac{(2\Pi)^2}{L} \frac{t^2}{12(1-\nu_{xy}\nu_{yx})} \quad (9)$$

where

L is the length of the beam

t is the thickness of the beam

ν_{xy} and ν_{yx} are the Poisson's ratios

k is a coefficient depending upon the boundary condition

The scatter variables in equation (9) are k , L , t , ν_{xy} and ν_{yx} . In the present example, only the thickness variation is considered. Then the probability of failure, at applied strain ϵ , due to buckling is given by

$$P_{fb} = 1 - \text{Exp} \left\{ - \left[\frac{1}{\beta_t} \frac{\sqrt{12}}{k} (1-\nu_{xy}\nu_{yx}) \epsilon \left(\frac{L}{2\Pi} \right)^{\alpha_t} \right] \right\} \quad (10)$$

where α_t and β_t are the Weibull shape and scale parameter for the thickness distribution.

The results of a clamped beam-column are shown in Figure 7. The beam-column is designed for $\epsilon_{DUL} = 0.009$ ($= \epsilon_{ALL}$) with a factor of safety of 1.5. The coefficient $k = 1.030629$ for clamped ends. Figure 7 shows the results for a fixed strength scatter ($\alpha_s = 20$) and variable load and thickness scatters. The nominal thickness of the beam is 0.132 inch. The reliability of the beam without taking buckling into consideration is also shown in the figure. The

results indicate that the reliability may be significantly influenced by the buckling failure at higher α_L and lower α_T . In the practical range (α_L between 2 to 6 and α_T approximately 40) the reliability for compression failure only ranges from 0.99848 to 0.99951. These values reduced to 0.98942 to 0.99812 when buckling is considered as a competing failure mode.

SUMMARY

A probabilistic static stress analysis and structural reliability prediction approach have been outlined. This approach uses conventional structural mechanics methods and associates probabilistic distributions with the most significant variables. In addition, the uncertainties in the applied loads is also considered in the structural reliability evaluation. The level of complexity in the reliability analysis depends on the complexity of the structure and the number of competing failure modes. Therefore, the actual analysis method is structure specific. However, the overall approach outlined in this paper is generic and can be applied to composite structures.

REFERENCES

1. Whitehead, R. S., Kan, H. P., Cordero, R., and Saether, E. S., "Certification Testing Methodology for Composite Structures," Report No. NADC-87042-60, October 1986, Volumes I and II.
2. Kan, H. P., Cordero, R., and Whitehead, R. S., "Advanced Certification Methodology for Composite Structure," Draft Final Report, NADC Contract No. N62269-87-C-0259, September 1989.
3. Lincoln, J. W., "Certification of Composites for Aircraft," Proceedings of the USAF Aircraft Structural Integrity Program Conference, Sacramento, CA., December 1986.
4. Lincoln, J. W., "Risk Assessment of an Aging Military Aircraft," Journal of Aircraft, Volume 22, November 8, August 1985.
5. Cornog, D. O. and Lincoln, J. N., "Risk Assessment of the F-16 Wing," Proceedings of the 1988 Structural Integrity Program Conference, San Antonio, TX, November 1988, WRDC-TR-89-4071, May 1989.
6. Stock, T. A., Bellini, P. X., Murthy, P. L. N. and Chamis, C. C., "A Probabilistic Approach to Composite Micromechanics," Presented at the 29th AIAA/ASME/ASCE/AHS/ACS SDM Conference, Williamsburg, VA., April 1988.
7. Chamis, C. C. and Stock, T. A., "Probabilistic Simulation of Uncertainties in Composites Uniaxial Strengths," Presented at the 45th Annual Conference of the Society of Plastics Industry Reinforced Plastics/Composites Institute, Washington, D. C. February 1990.
8. Chamis, C. C., "Probabilistic Structural Analysis Methods for Space Propulsion System Components," NASA TM 88861, June 1986.
9. Shiao, M. C. and Chamis, C. C., "Probability of Failure and Risk Assessment of Propulsion Structural Components," NASA TM 102323, May 1989.
10. Shiao, M. C., Nagpal, V. K. and Chamis, C. C., "Probabilistic Structural Analysis of Aerospace Components Using NESSUS," NASA TM 102324, April 1988.
11. Wu, Y. T., "Demonstration of a New, Fast Probability Integration Method for Reliability Analysis," Journal of Engineering for Industry, Transaction of the ASME, Volume 109, February 1987.
12. Whitney, J. M. and Nuismer, R. J., "Stress Fracture Criteria for Laminated Composites Containing Stress Concentrations," Journal of Composites Materials, Volume 8, 1974.

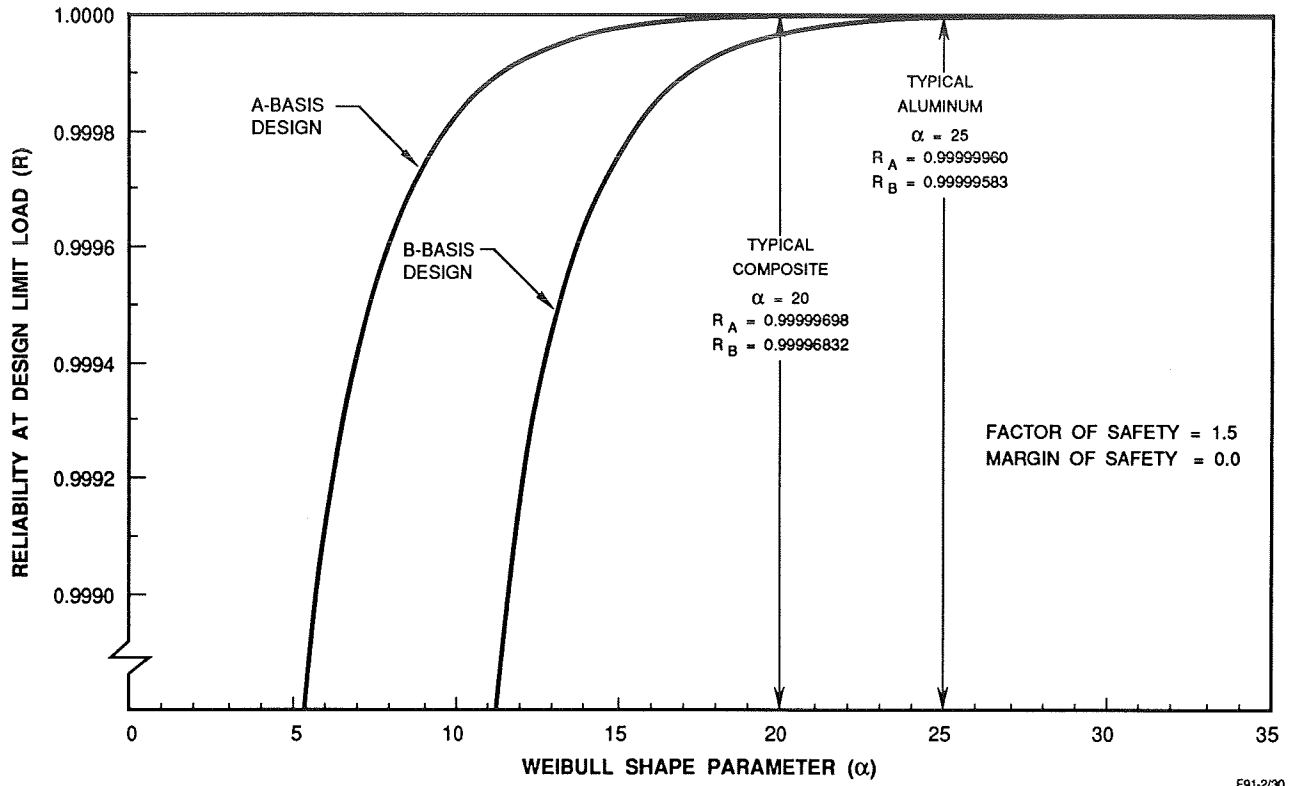


Figure 1. Variation of Structural Reliability With Strength Scatter.

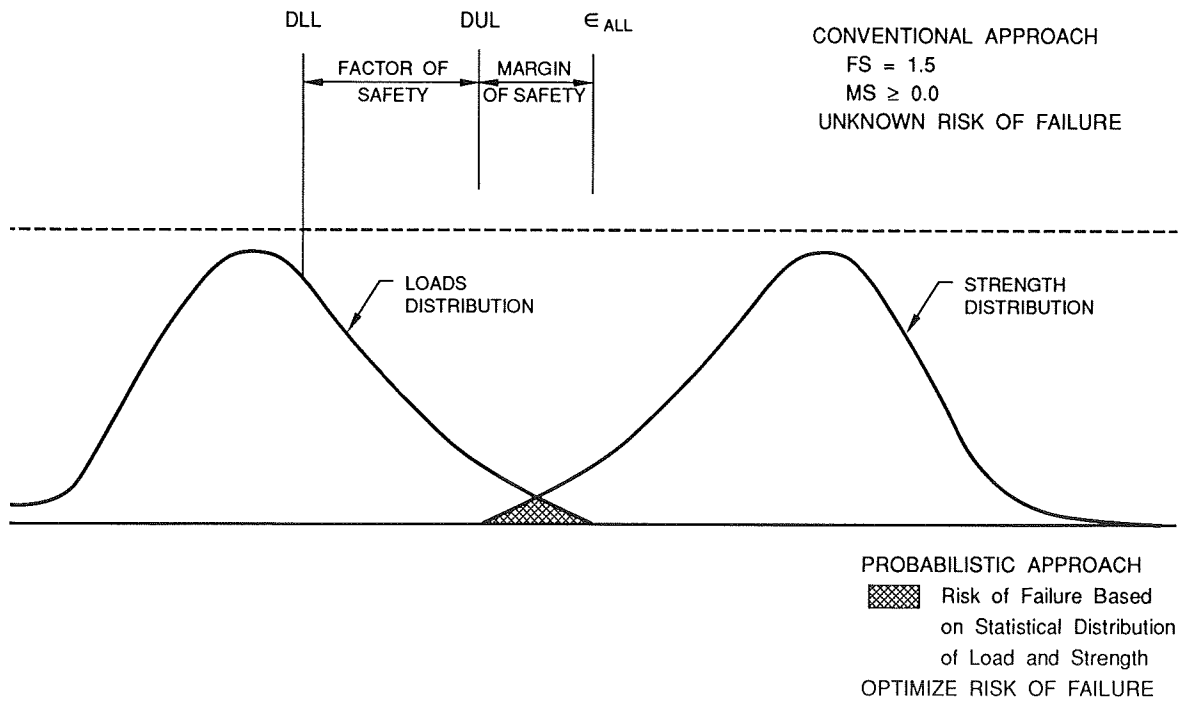
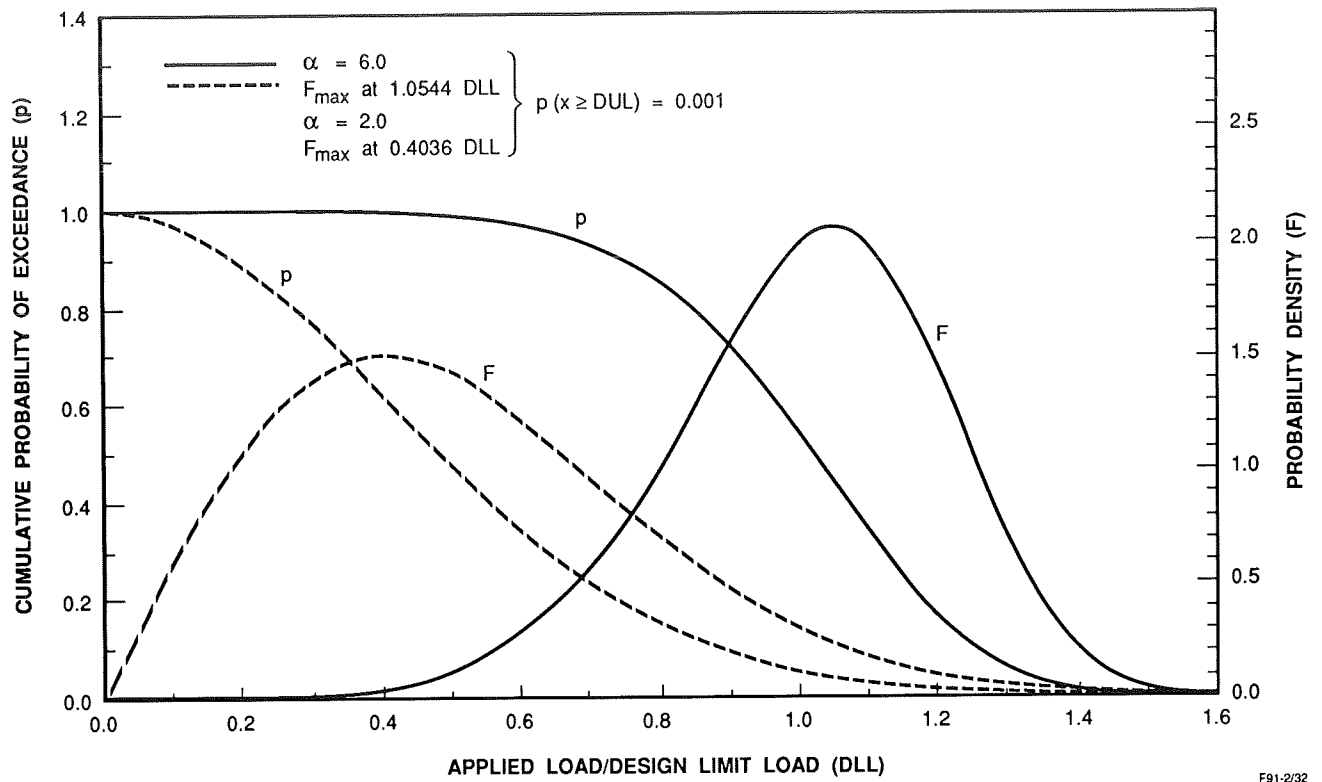
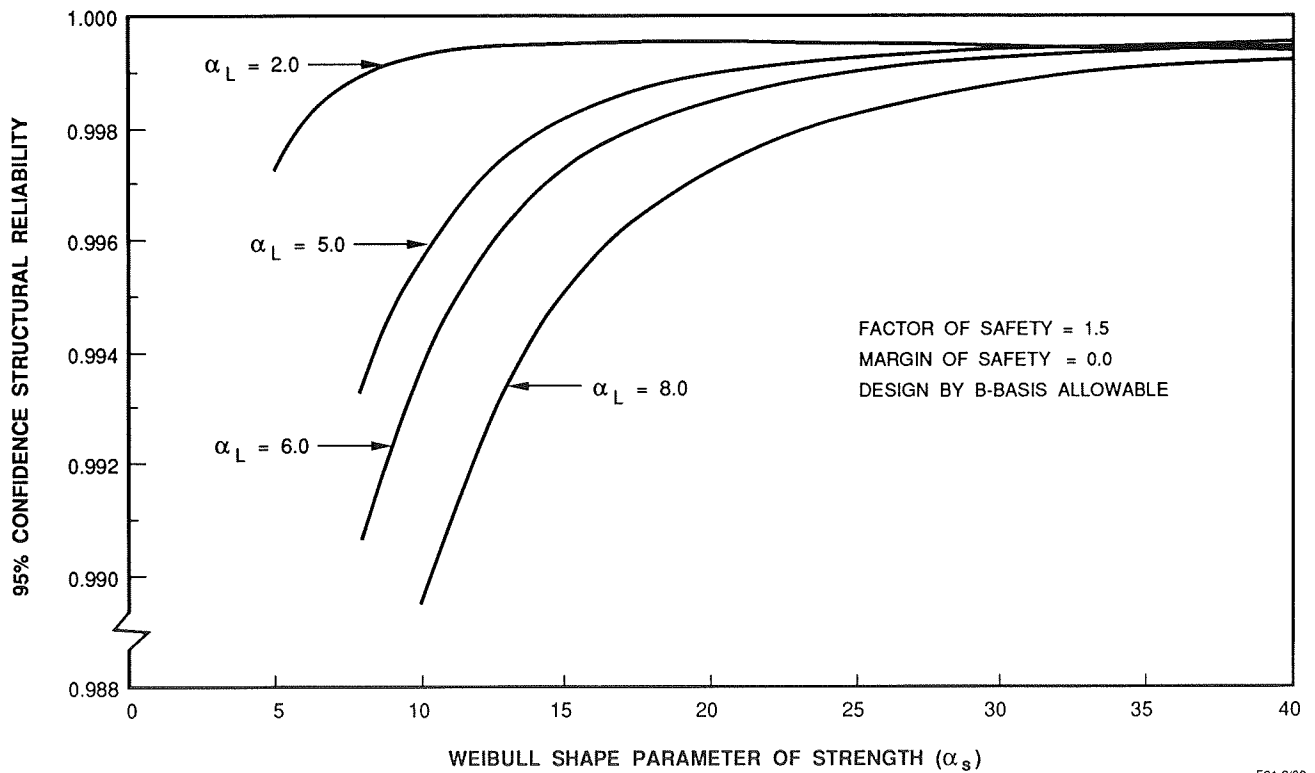


Figure 2. Static Strength Certification Approaches.



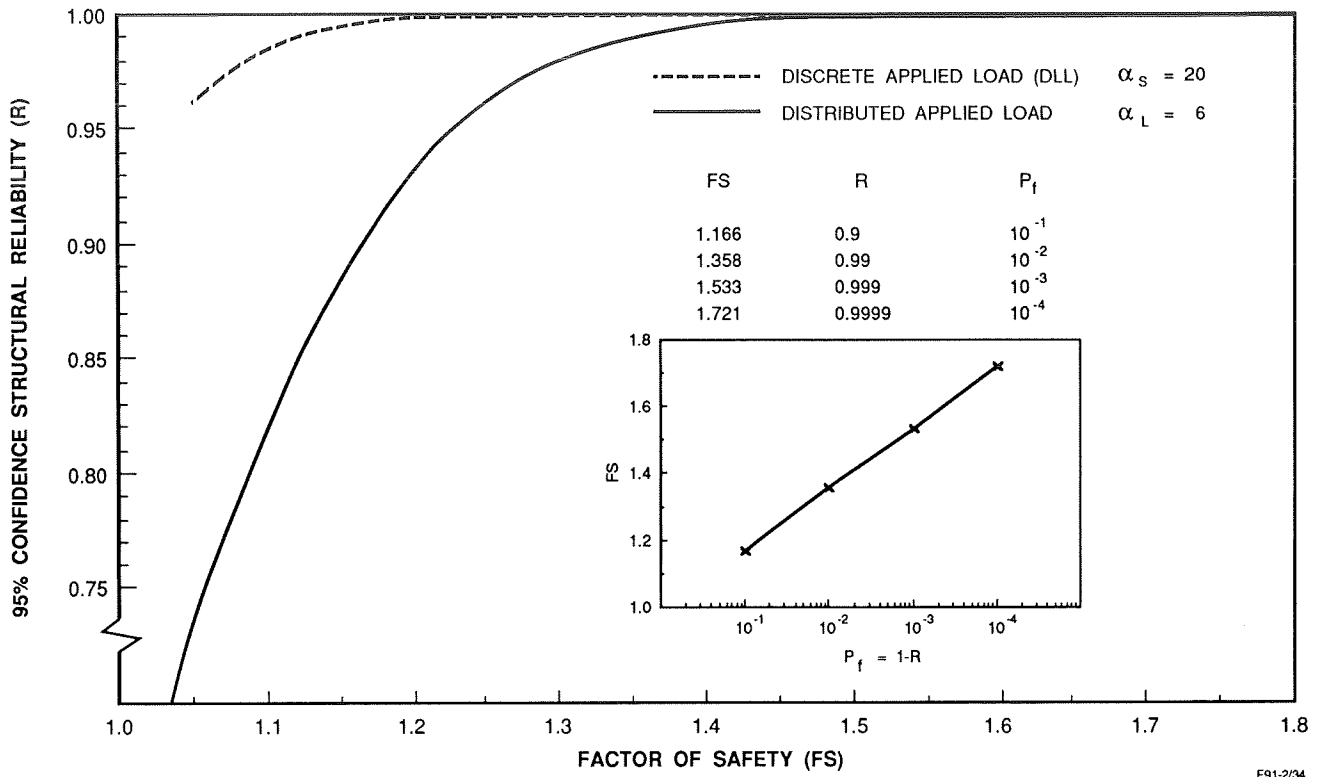
F91-2/32

Figure 3. Probabilistic Distribution of Applied Loads.



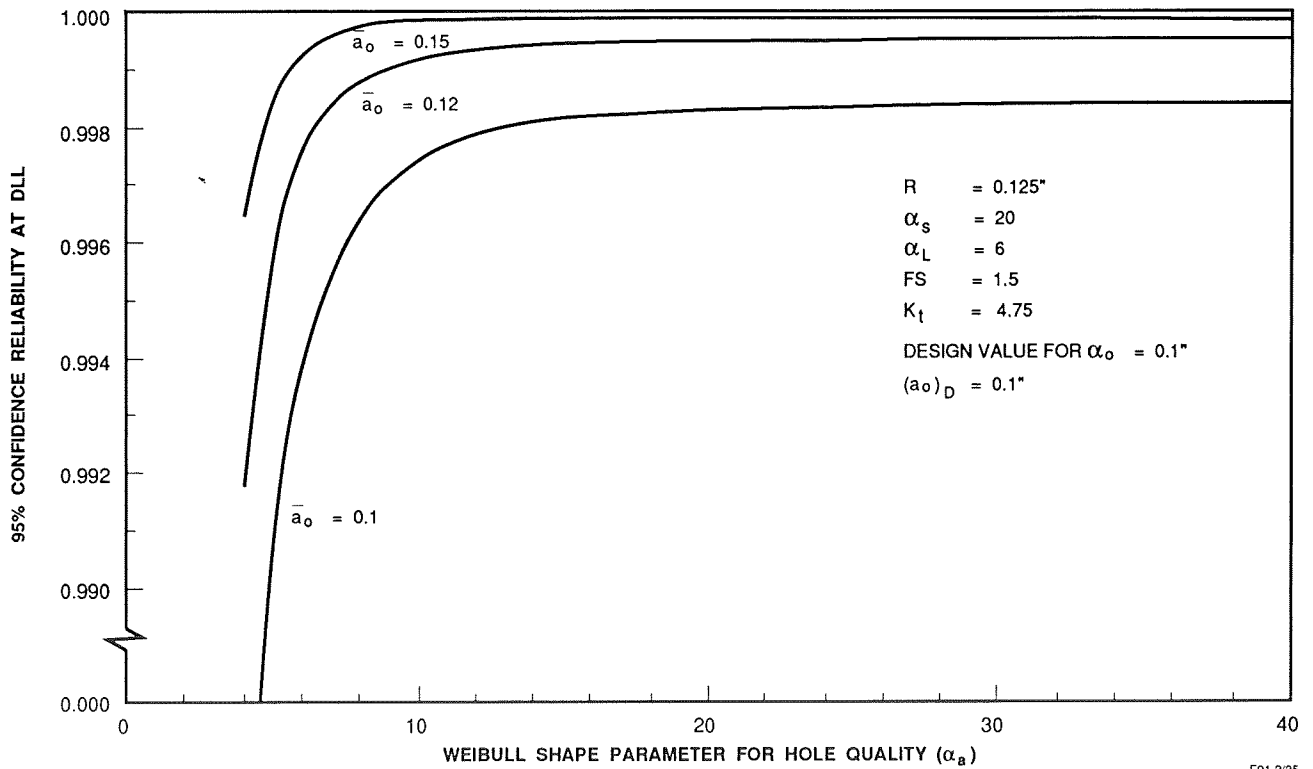
F91-2/33

Figure 4. Influence of Weibull Shape Parameter on the Reliability of a Tensile Element.



F91-2/34

Figure 5. Influence of Factor of Safety on the Reliability of a Tensile Element.



F91-2/35

Figure 6. Influence of Hole Quality Scatter on the Reliability of a Structure With an Open Hole.

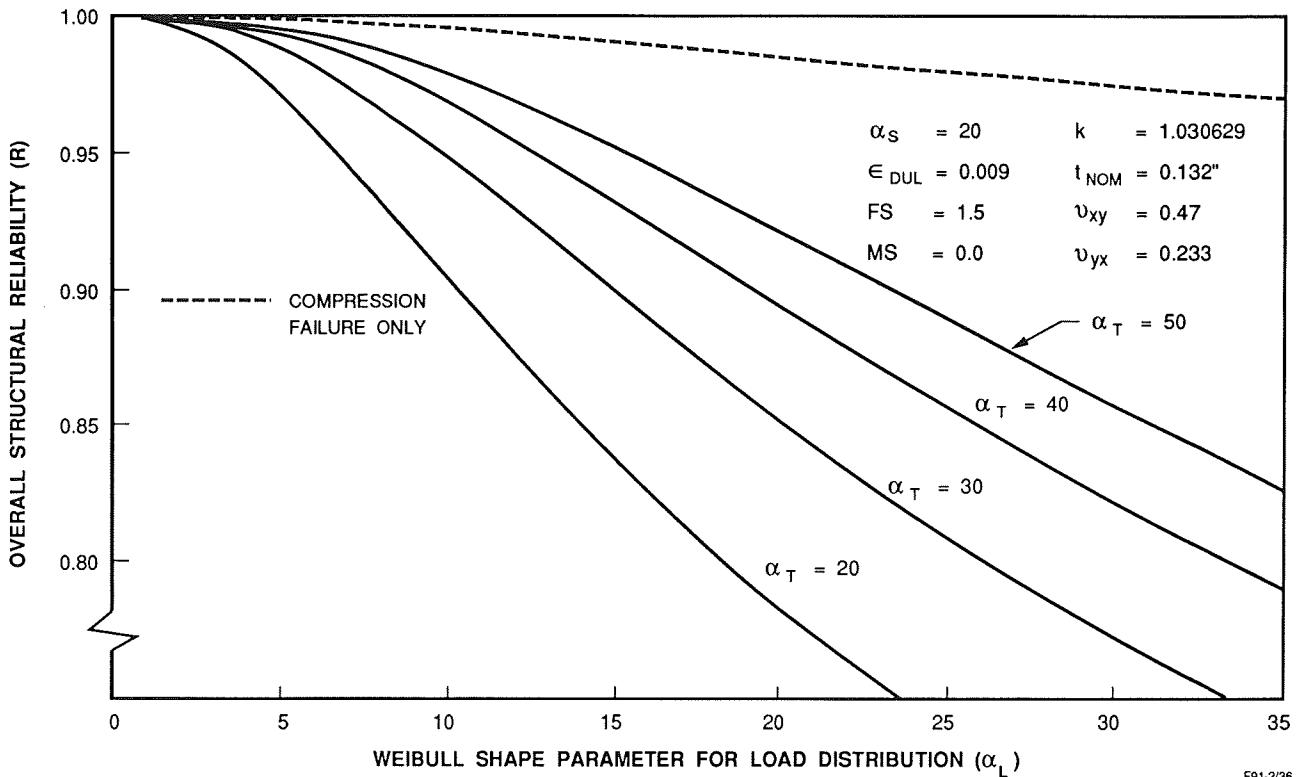


Figure 7. Structural Reliability of a Beam-Column With Compression and Buckling as Competing Failure Modes.

THIS PAGE INTENTIONALLY BLANK

UNCERTAINTIES IN OBTAINING HIGH RELIABILITY
FROM STRESS-STRENGTH MODELS

522-38

51390

p. 19

Donald M. Neal, William T. Matthews, and Mark G. Vangel

U.S. Army Materials Technology Laboratory
Watertown, Massachusetts

ABSTRACT

There has been a recent interest in determining high statistical reliability in risk assessment of aircraft components. This report identifies the potential consequences of incorrectly assuming a particular statistical distribution for stress or strength data used in obtaining the high reliability values. The computation of the reliability is defined as the probability of the strength being greater than the stress over the range of stress values. This method is often referred to as the stress-strength model.

A sensitivity analysis was performed involving a comparison of reliability results in order to evaluate the effects of assuming specific statistical distributions. Both known population distributions, and those that differed slightly from the known, were considered. Results showed substantial differences in reliability estimates even for almost nondetectable differences in the assumed distributions. These differences represent a potential problem in using the stress-strength model for high reliability computations, since in practice it is impossible to ever know the exact (population) distribution.

An alternative reliability computation procedure is examined involving determination of a lower bound on the reliability values using extreme value distributions. This procedure reduces the possibility of obtaining nonconservative reliability estimates. Results indicated the method can provide conservative bounds when computing high reliability.

INTRODUCTION

There has been an interest in quantitative reliability-based structural design for many years. An early example is the structural reliability development by Freudenthal.¹ Stress-strength reliability computations are a principal consideration in structural reliability design. Reliability methods have been considered for many structural applications including: civil engineering,² nuclear reactors,³ fixed wing aircraft,⁴ rotorcraft,⁵ and space vehicle propulsion systems.⁶ Very high structural reliability is expected to be achieved for most applications. A reliability goal of 0.9₍₉₎ per flight hour was suggested in 1955 by Lundberg⁴ for fixed wing civil aircraft. Recently, Lincoln,^{7,8} using reasoning similar to that of Lundberg, cited a reliability goal of 0.9₍₇₎ per flight for fixed wing military aircraft. The U.S. Army has instituted a new structural fatigue integrity criterion for rotorcraft which has been interpreted⁵ as a requirement for a lifetime reliability of 0.9₍₆₎.

The use of advanced materials whose structural properties are best characterized on a statistical basis appears to be a stimulant for increased interest in statistical-based structural design for airborne structures.

A significant feature associated with predictions of structural reliability is that the consequence of a failure event may be more than reduced system performance or the inconvenience of a system being out of service; structural failure can be catastrophic in terms of loss of life and property. In this context it is imperative to evaluate the sensitivity of structural reliability predictions to uncertainties. It appears that this issue has received little attention except for a brief note by Harris and Soms⁹ and a recent presentation by Berens.¹⁰

There are many issues to be faced in obtaining quantitative structural reliability predictions. Such issues include system complexity (many components, multiple failure modes in each component, and interdependence of component behavior), sample or data set size associated with structural loading spectrum conditions and with mechanical properties, and the basis for characterizing structural qualification tests (the number of duplicate specimens and methods for compensation for untested effects such as the effect of environment).

In addition, when predictions of structural behavior are required in the high reliability range, since sufficiently large data sets are usually not available, it is necessary to use parametric modeling methods. Assumed parametric functions permit extrapolation from available data to determine the probability of failure. Since the probability of failure is extremely small, this will always involve substantial extrapolation from what can be observed experimentally. The estimated reliability will therefore depend strongly on the assumed parametric probability density function (PDF). Slight deviation from the assumed model in tail regions can have a dramatic effect on high reliability estimates.

In fact, one might argue, as does Freudenthal,¹¹ that because of the extrapolation involved, statistically-based high reliability calculations for complex systems must always be suspect:

"When dealing with probabilities a clear distinction should be made between conditions arising in design of inexpensive mass products in which the probability figures are derived by statistical interpretation of actual observations or measurements (since a sufficiently large number of observations are actually obtainable), and conditions arising in design of

structures or complex systems. In the latter, probability figures are used simply as a scale or measure of reliability that permits the comparison of alternative designs. The figures can never be checked by observations or measurement since they are obtained by extrapolations so far beyond any possible range of observation that such extrapolation can no longer be based on statistical arguments but could only be justified by relevant physical reasoning. Under these conditions the absolute probability figures have no real significance"

Nonparametric stress-strength procedures do not require specific parametric assumptions, and so it might be hoped that such procedures could circumvent this difficulty. However, Johnson¹² has noted that "The nonparametric approach has one serious drawback. In return for its distribution free property, it is not possible to establish high reliability even with moderate sample sizes." With respect to the use of parametric models, Box¹³ has observed "all models are wrong, but some are useful," meaning that no parametric statistical model should be accepted uncritically. Whenever a model is used, it is the obligation of the analyst to investigate the consequences of departures from an assumed model which, though small, are consistent with available data. Harris and Soms⁹ has illustrated a "serious problem in the use of stress-strength relationships in estimating reliability." In particular, "stress-strength models in reliability theory are highly sensitive to small perturbations in extreme tails." The perturbations considered may arise from an alternative mode of failure such as the presence of a flaw in a structure. Further, they note that the problem cannot be eliminated unless "astronomically large sample sizes are employed."

In the following, the examination of the sensitivity of structural reliability estimates focuses attention on one of the previously cited issues: the selection of a parametric PDF. The examination of the sensitivity of stress-strength reliability estimates is extended to additional perturbation effects. The sensitivity of reliability estimates to the selection of parametric models is considered with emphasis on graphical representations. The results are evaluated with regard to the usefulness of parametric stress-strength models for application to the high reliability regime of 0.9₍₆₎ to 0.9₍₇₎ when the consequence of failure may be catastrophic. An alternative reliability computation procedure is examined involving determination of a lower bound on reliability which can be obtained independently of the assumed PDFs.

STRESS-STRENGTH MODEL

The statistical reliability as referred to in this report is determined in the following manner. Shown in Figure 1 is the stress-strength model where $f_2(s)$ and $f_1(S)$ represent the PDFs for the applied stress s and material strength S .

Since the joint probability dR for the strength being greater than s_1 can be written as,

$$dR = f_2(s_1) ds \int_{s_1}^{\infty} f_1(S) dS \quad (1)$$

then the reliability for all s values is

$$R = \int_{-\infty}^{\infty} f_2(s) \left[\int_s^{\infty} f_1(S) dS \right] ds. \quad (2)$$

Normal stress-strength model

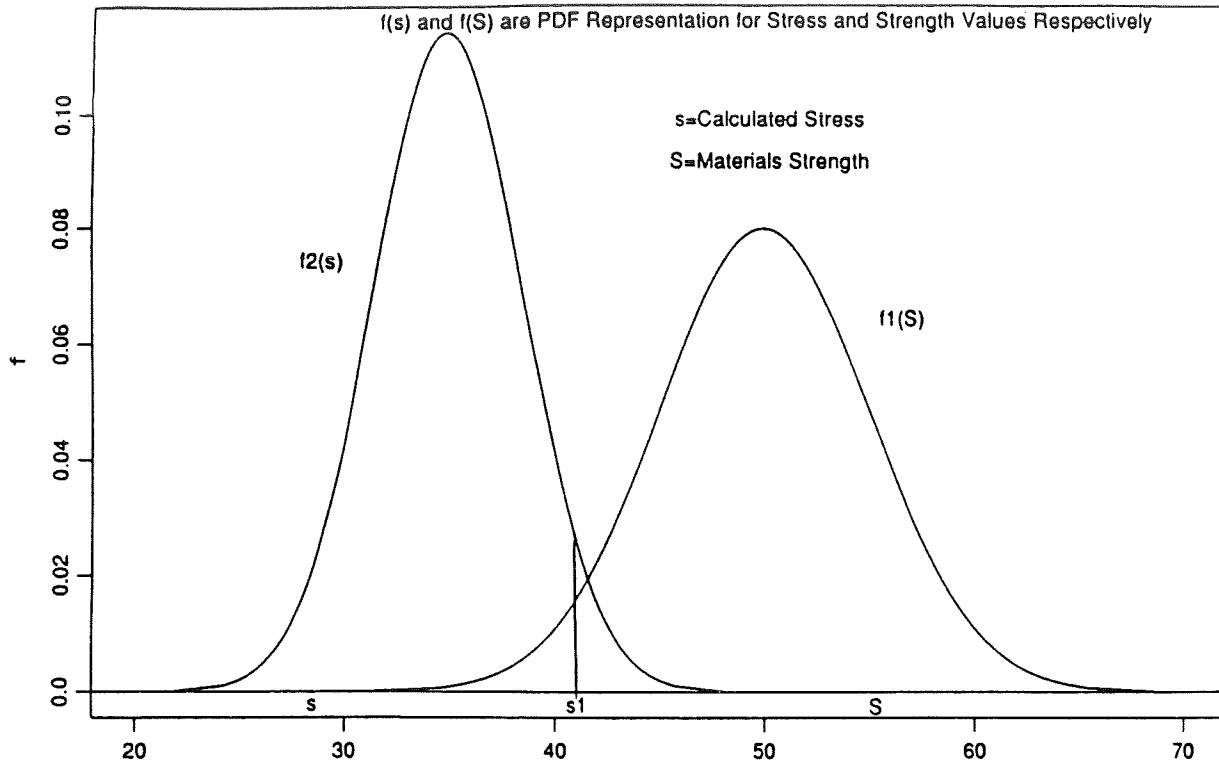


Figure 1. Normal-normal stress-strength model.

PROBABILITY DENSITY FUNCTIONS

A wide variety of PDFs may be applied in obtaining R values. Some examples of PDFs are as follows:

The PDF most often used in stress-strength models is the normal distribution (see Figure 1),

$$f_N(S) = N(S, \sigma^2) = \frac{1}{\sigma \sqrt{2\pi}} \exp \left\{ -\frac{1}{2} \left(\frac{S - \mu}{\sigma} \right)^2 \right\}, \quad (3)$$

where $-\infty < S < \infty$, $\mu > 0$, and $\sigma > 0$. The mean of the population is μ , and the standard deviation σ for this model.

A model which is more easily justified on physical grounds is the Weibull PDF,

$$f_w(S) = \frac{\beta}{\alpha} \left(\frac{S}{\alpha} \right)^{\beta-1} \exp \left[-\left(\frac{S}{\alpha} \right)^\beta \right], \quad (4)$$

where $S > 0$, $\alpha > 0$, and $\beta > 0$. Despite the relevance of the Weibull distribution¹⁴ to the strength of brittle materials, it is not often used, possibly because it is more difficult computationally to obtain reliability values than with the normal model.

If S follows the Weibull PDF, then $\ln(S)$ will have an extreme value distribution with PDF

$$f_{\min}(S) = \frac{1}{b_1} \exp \left[\frac{S-u_1}{b_1} - \exp \left(\frac{S-u_1}{b_1} \right) \right]. \quad (5)$$

The distribution of $-\ln(s)$ is

$$f_{\max}(s) = \frac{1}{b_2} \exp \left[- \left(\frac{s-u_2}{b_2} \right) - \exp \left(- \left(\frac{s-u_2}{b_2} \right) \right) \right]. \quad (6)$$

Both of the above formulas are referred to as extreme value distributions. The use of extreme value distributions in a stress-strength model is illustrated in Figure 2. The extreme value distribution parameters are related to the Weibull parameters as follows:

$$b = \frac{1}{\beta} \quad \text{and} \quad u = -\log \alpha.$$

In order to obtain the population Weibull shape and scale parameters β and α from the known population mean μ and standard deviation σ , the following approximations are suggested:

$$\beta = 1.27 \mu / \sigma - 0.56 \quad (7)$$

and

$$\alpha = \mu / \Gamma \left(\frac{1}{\beta} + 1 \right).$$

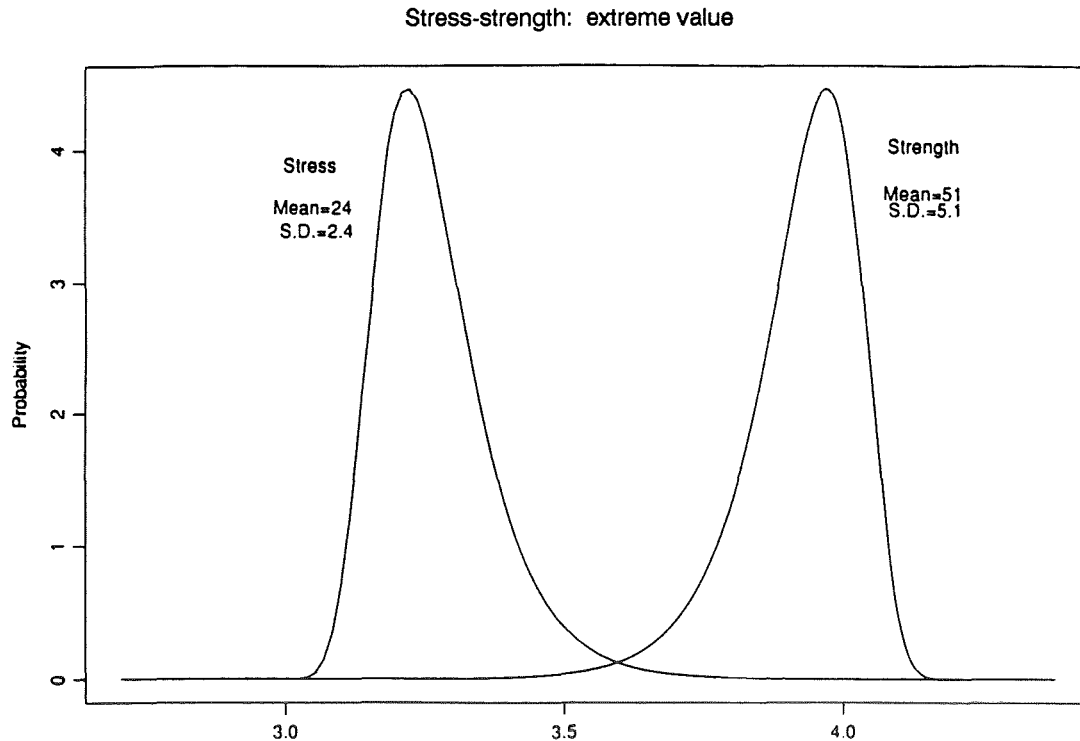


Figure 2. Stress-strength extreme value functions.

The functions defined in Equations 3, 4, 5, and 6 clearly have different shapes and they exhibit dramatically different tail behavior. Since reliability estimates depend strongly on the extreme upper tail of the stress PDF and the extreme lower tail of the strength PDF, the choice of model will typically have a substantial effect on the reliability estimate. For example, R is usually higher when calculated from the normal distribution than when the extreme value model is assumed.

Applying PDFs that are capable of obtaining accurate high reliability estimates (e.g., 0.9₍₆₎) requires prior knowledge of the functional form of the population PDF in addition to the availability of large data sets (e.g., 1,000 replicate specimens). For lower reliability values (e.g., 0.9), a goodness-of-fit test for PDF identification with a moderate amount of data is generally adequate. The consequence of incorrect PDF selection and limited sample sizes are discussed later in this report.

METHODS FOR COMPUTING RELIABILITY R

In determining R from Equation 2 it should be noted that the integration process does not determine an area. The area A described by the intersecting functions in Figure 3 does not represent a 1 - R failure probability. The area A is the probability (P) that either S < T or s > T, that is,

$$A = P(S < T) + P(s > T) , \tag{8}$$

where T is the point of intersection of the two functions. The area A is obviously not the same as the 1 - R from Equation 2 which determines P(S > s) jointly with P(s).

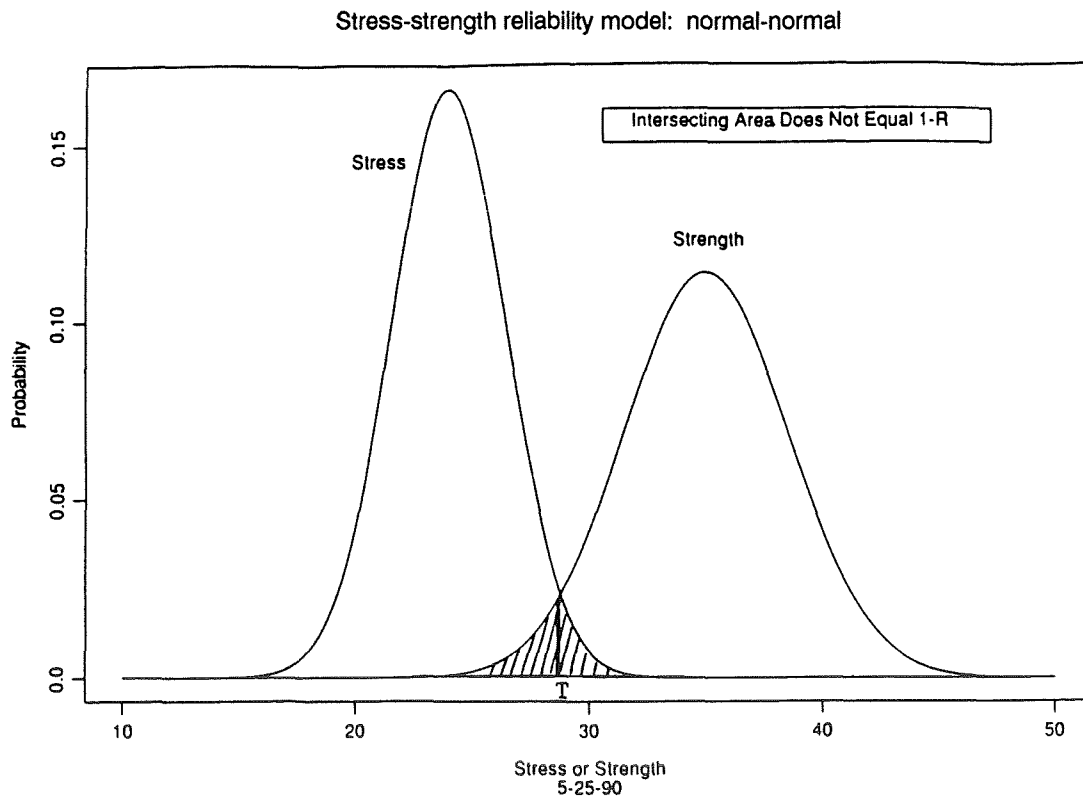


Figure 3. Stress-strength incorrect unreliability region.

Numerical Integration

Numerical integration procedures are usually suggested if a closed form solution of Equation 2 is not available. The numerical integration process involves repeated application of a method such as Simpson's Rule. The inner integral in Equation 2 is evaluated numerically for each ordered s_i value $i = 1, \dots, n$ resulting in an $I_1(i)$ array of values. Each of $I_1(i)$ is then multiplied by the corresponding $f_2(s_i)$ forming another array $I_2(i) = f_2(s_i)I_1(i)$. R is obtained from the I_2 array by reapplying the numerical integration method. This process will usually provide accurate results for $51 \leq n \leq 101$, where n is the number of mesh points in the integration process. Simulation results showed that the limits of integration can be obtained from \pm six standard deviations from the mean.

Closed form solutions are available when the assumed stress and strength PDFs are both normal or both Weibull.

R Computation from Closed Form Solution

If both stress and strength data can be represented by normal PDFs $N(\mu_s, \sigma_s^2)$ and $N(\mu_S, \sigma_S^2)$, respectively, then,

$$R = P(S > s) = \Phi \left(\frac{\mu_S - \mu_s}{\sqrt{\sigma_S^2 + \sigma_s^2}} \right), \quad (9)$$

where (Φ) is the standard $N(0, 1)$ normal cumulative distribution function, μ_s and μ_S are means, and σ_s^2 and σ_S^2 are variances of the stress and strength, respectively.

If both f_1 and f_2 in Equation 2 are Weibull with different scale parameters α_1 and α_2 , but with a common shape parameter β , then the integration indicated in Equation 2 gives the following closed form expression¹²

$$R = \frac{1}{1 + \left(\frac{\alpha_1}{\alpha_2}\right)^\beta} \quad (10)$$

The common shape parameter means that both the stress and strength are skewed in the same way, which is a serious limitation. It is much more reasonable to have a stress distribution with a heavy upper tail and a strength distribution with a heavy lower tail, but this is not possible unless the shape parameters can be varied separately.

Nonparametric Method

This method does not assume a PDF for either stress or strength data. It determines reliability from the ordered array of m stress (s) and n strength (S) values, where each of the S values are compared with all s values. R is the proportion of times $S > s$ for the total number of comparisons, that is

$$R = \frac{1}{m n} \sum_{j=1}^m \sum_{i=1}^n \alpha_i, \text{ where } \alpha_i = \begin{cases} 1, & S_i > s_j \\ 0, & s_j \geq S_i \end{cases} \quad (11)$$

This method is not useful for obtaining high reliability even for relatively large data sets. It is obvious from Equation 11 that for high reliability calculations, mn must be very large; for example, 10^6 would be required in order to obtain R of 0.9(6).

The Weibull, normal, or other parametric PDFs can provide estimates of high R values because of their ability to extrapolate beyond the available empirical data. Unfortunately, the amount of extrapolation dependency determines the magnitude of relative error in R .

CONTAMINATED PROBABILITY DENSITY FUNCTIONS

In order to illustrate the sensitivity of high reliability calculations to small deviations from assumed models, we will take the following approach. Consider the situation where with a high probability of $1 - \epsilon$, specimens are obtained from a primary PDF, while with probability ϵ , specimens come from a secondary PDF. This probability model is referred to as a contaminated model. The secondary component is called the contamination, and the probability ϵ is the amount of contamination.

An example may help clarify this idea. Consider the situation where 97% of the time a specimen is obtained from a population of "good" specimens while the remaining 3% of the time consistently lower strength measurements are obtained, either due to manufacturing defects or to faulty testing. The primary PDF would correspond to the "good" specimens, the contamination would represent the distribution of flawed specimens, and the amount of contamination would be $\epsilon = 0.03$.

The following procedure is introduced in order to examine the effects of computing high reliability values when uncertainties exist in selecting the functions for the stress-strength model. Initially, high reliability values are obtained from the normal stress-strength model (see Equation 9) using known PDFs with different mean values but equal coefficients of variation. The difference in mean values was determined from the required level of high reliability. Another R value is then obtained by applying this known distribution with a small amount of contamination (ϵ) in order to show an almost undetectable difference graphically between the true and contaminated PDFs. The effects of this difference in the reliability computation are discussed in the following sections in order to examine the sensitivity of the stress-strength model to the assumed PDFs. This procedure provides an effective way of demonstrating the effects of assuming a specific PDF in determining high reliability.

The normal PDF with variance contamination for the strength data is,

$$N_{S_v}(\mu_S, \sigma_v^2) = (1 - \epsilon) N(\mu_S, \sigma_S^2) + \epsilon N(\mu_S, K_1 \sigma_S^2), \quad (12)$$

where μ_S and σ_S^2 are the mean and variance for the uncontaminated normal strength distribution, K_1 is a scaling factor, and 100ϵ is the percent contamination.

The strength distribution with location contamination is

$$N_{S_L}(\mu_L, \sigma_S^2) = (1 - \epsilon) N(\mu_S, \sigma_S^2) + \epsilon N(\mu_S \pm K_2 \sigma_S, \sigma_S^2), \quad (13)$$

where K_2 is a scaling factor for the mean μ_S , and the sign determines which tail of the distribution is to be contaminated and σ_S^2 is the variance on $\mu_S \pm K_2\sigma_S$. The location contaminated PDF (see Equation 13) can provide reliability estimates to represent the potential of a secondary failure mode. Contamination of the stress distribution would be similar to that in Equations 12 and 13. It was not necessary to include contaminated distributions for both stress and strength in order to show substantial reduction in the high reliability estimates. The strength PDF contamination was sufficient.

A linear relationship to obtain R for the reliability models when a combination of both contaminated and uncontaminated stress and strength normal PDFs can be written as,

$$R = (1 - \varepsilon_1) (1 - \varepsilon_2) R_{00} + \varepsilon_1 (1 - \varepsilon_2) R_{10} + \varepsilon_2 (1 - \varepsilon_1) R_{01} + \varepsilon_1 \varepsilon_2 R_{11} \quad (14)$$

where $100 \varepsilon_1$ and $100 \varepsilon_2$ are percent contamination for the stress and strength distribution, and the R_{ij} values are obtained for the case of variance contamination only; that is,

$$R_{ij} = \Phi \left(\frac{\mu_S - \mu_s}{\sqrt{\sigma_{S_j}^2 + \sigma_{s_i}^2}} \right). \quad (15)$$

and for location contamination, R_{KL} would be

$$R_{KL} = \Phi \left(\frac{\mu_{S_L} - \mu_{s_K}}{\sqrt{\sigma_S^2 + \sigma_s^2}} \right). \quad (16)$$

Equation 14 can be extended to include all combinations of variance and location contamination simultaneously, but it was not necessary for this sensitivity analysis. In Equation 16, if $i, j = 0$, then there is no contamination; for $i, j = 1$, then both stress and strength are contaminated. For example, if there is contamination of variance of strength only, then

$$R = (1 - \varepsilon_2) R_{00} + \varepsilon_2 R_{01} \quad (17)$$

where

$$R_{00} = \Phi \left(\frac{\mu_{S_0} - \mu_{s_0}}{\sqrt{\sigma_{S_0}^2 + \sigma_{s_0}^2}} \right)$$

and

$$R_{01} = \Phi \left(\frac{\mu_{S_0} - \mu_{s_0}}{\sqrt{\sigma_{S_1}^2 + \sigma_{s_0}^2}} \right)$$

LOWER RELIABILITY BOUND

A conservative lower bound on the reliability is introduced in order to protect against incorrectly identifying statistical functions in determining high R. The bound is obtained from a method proposed by Bolotin,¹⁵ and modified to employ the extreme value PDFs

(see Equations 5 and 6). The method provides more conservative bounds than would be obtained from standard methods which are dependent on the assumed PDFs. The selection of the extreme value functions provides additional conservatism because of their heavier tails. The method is simple to use and is not restricted to any specified PDF. The reliability bounds are (see Figure 4),

$$1 - W_1 W_2 > R > (1 - W_1)(1 - W_2) \quad (18)$$

where $[(1 - W_1)(1 - W_2)]$ represents the probability $s < s_1$ and $S > S_1$, which can be a somewhat conservative estimate.

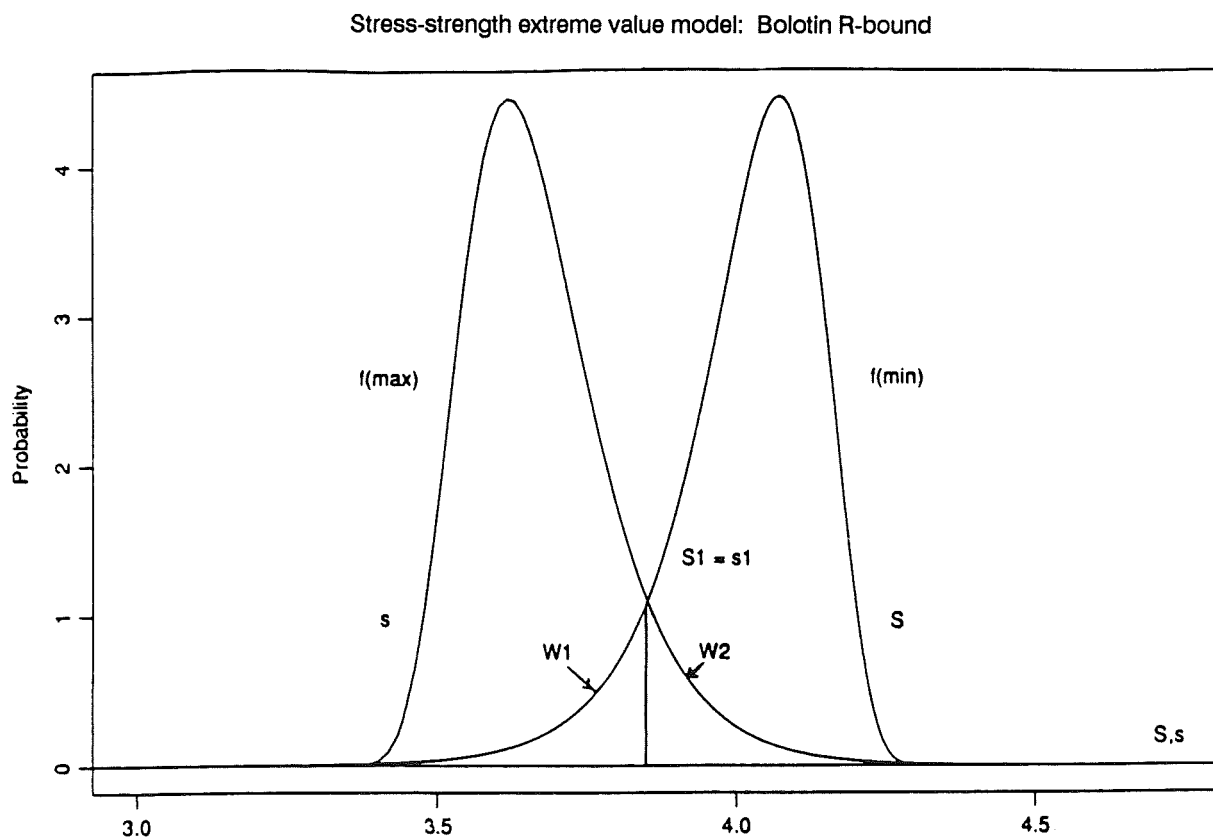


Figure 4. Bolotin reliability bounds using extreme value functions.

The lower bound is then,

$$R_L > (1 - W_1)(1 - W_2) , \quad (19)$$

where

$$W_2 = \int_{s_1}^{\infty} f_2(s) ds \quad \text{and} \quad W_1 = \int_{\infty}^{S_1} f_1(S) dS$$

for any choice of $s_1 = S_1$.

GOODNESS-OF-FIT TEST

The capability of determining desired PDFs from empirical data was investigated. The choice of PDF will be shown in the following sections to have a substantial effect on high reliability computations, so it is important to examine model selection procedures. A statistical test¹⁶ of goodness-of-fit was introduced in addition to graphical displays in order to select the desired PDFs. Empirical data used in the investigation was obtained by randomly selecting a relatively large number of values from a known normal PDF. A comparison of known contaminated PDFs and the uncontaminated PDF is made with respect to the empirical values.

RESULTS AND DISCUSSIONS

Variance Contamination

Shown in Figure 5a are reliability computation results and a graphical display of a normal/normal stress-strength reliability model, where a 1% ($\epsilon = 0.01$) variance contamination was introduced and scaled by $K_1 = 4$. The graphical display was obtained from application of Equations 12 and 13, where $N(\mu_S, \sigma_S^2)$ is defined in Equation 3. The graph shows an almost undetectable difference between the contaminated and uncontaminated PDFs. This indicates that the choice of ϵ and K are reasonable with respect to the potential differences between assumed and actual PDFs. However, the reliability values differ substantially (0.9₍₆₎ versus 0.998989). This implies that either one failure in a million or 1011 failures in a million is predicted depending on the selection of PDFs which can differ in probability values by less than 0.0005 in the extreme tail regions (see Figure 5b). Using "good" representative PDFs in the stress-strength model in predicting only a single failure will occur in one million operations (e.g., number of flight hours) for $R = 0.9_{(6)}$ can result in a severe anticonservative estimate since for almost identical PDFs, 1011 failures per million could also be predicted.

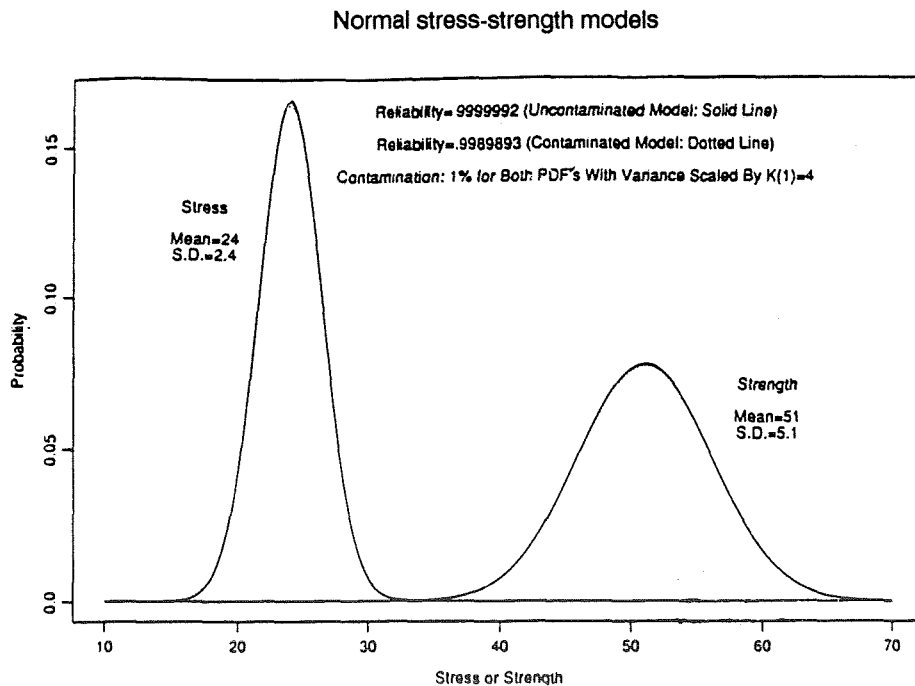


Figure 5a. Stress-strength normal functions with and without variance contamination.

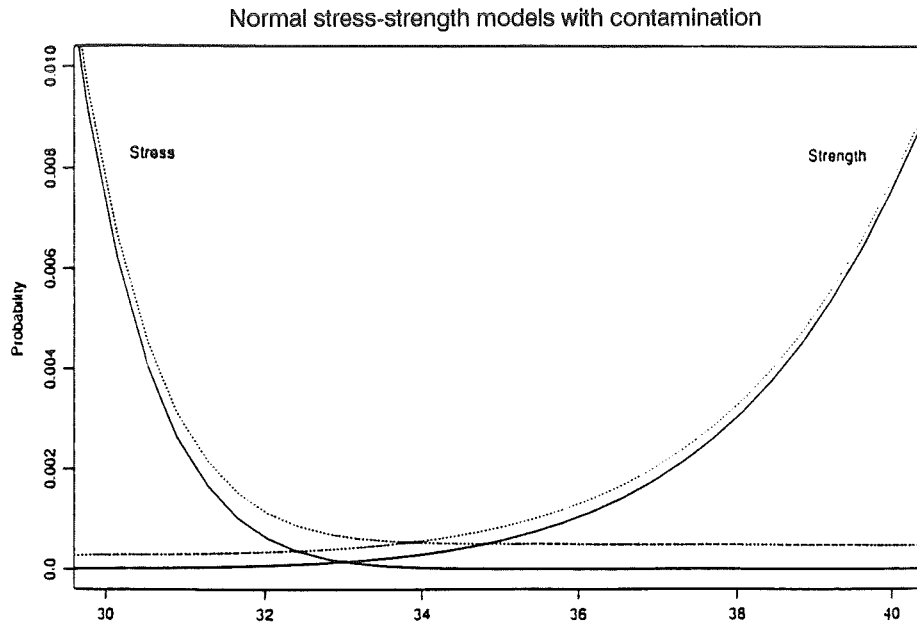


Figure 5b. Detailed region of intersecting functions (see Figure 5a).

The accuracy of the high R estimates depends on the level of precision in defining the extreme tail of PDFs. This requires selecting a PDF from a data set that accurately represents the known population function in the extreme tail regions with a probability difference of much less than 0.0005. Unfortunately, this would require an unrealistically large data set. In current practice, if a very large data set is not available, then PDFs are selected from smaller sets with reliance on the functional representation in regions less than first ordered or greater than the largest value.

The stress-strength procedure is quite effective for the range of R values between 0.5 and 0.95 since usually in the extrapolation process, a small difference in the extreme tail probabilities values will not effect the required accuracy in R . Reliability results from uncontaminated and variance contaminated ($\epsilon = 0.05$ and $K_1 = 5$) PDFs showed no differences for a known $R = 0.95$. Unfortunately, in order to obtain high reliability, extrapolation into the extreme tail of the PDFs is required, thereby increasing the required level of precision necessary to distinguish between, for example, 0.998 and 0.9₍₆₎.

In order to demonstrate the uncertainties in selecting specific PDFs from empirical data when computing high reliability values, the following displays are shown in Figure 6. In Figure 6a, a plot is shown of the empirical normal cumulative density function (CDF) and the corresponding contaminated and uncontaminated normal distribution functions where the mean is 50 and standard deviation (SD) is 5, with sample size $\mu = 100$. Reliability values are also tabulated from the stress-strength model results using all six candidate functions. For example, $R(3, 5)$ is the reliability obtained from variance contamination of 3% and a scale of 5 for variance. A statistical goodness-of-fit test¹⁶ that measures the relative differences in the tail region of the distributions was applied in addition to visual inspection in order to establish if each function could represent the CDF of the ranked data. Results showed this to be true; see Figure 6b for the tabulated observed significance level (OSL) which shows in all cases $OSL > 0.05$, a requirement for the assumed function to be considered from the same population as the empirical data.

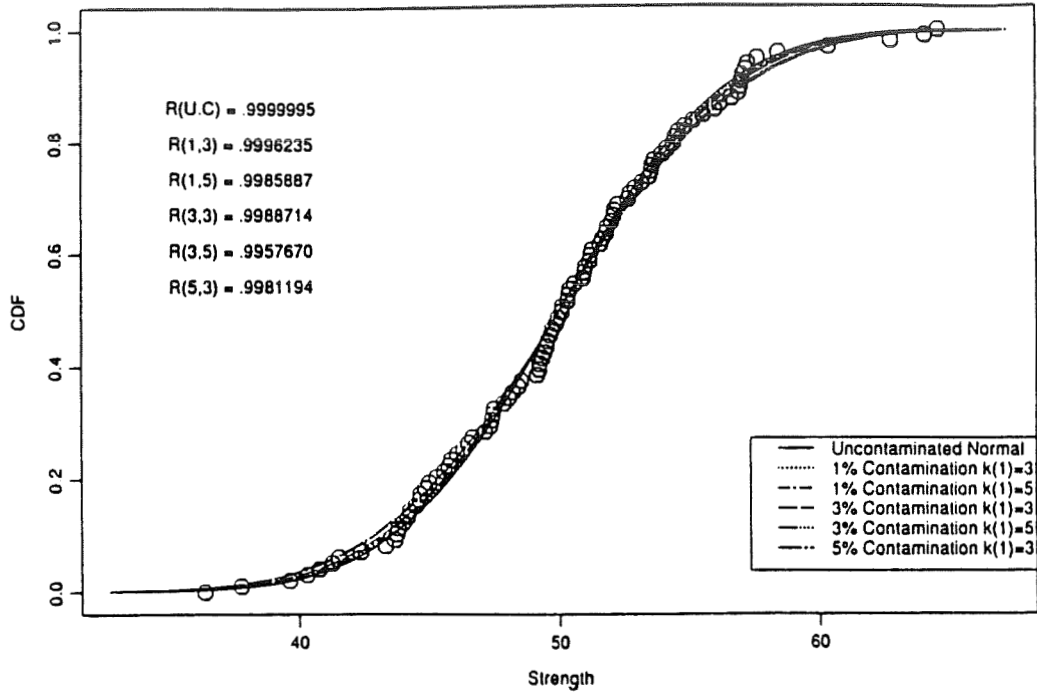


Figure 6a. Goodness-of-fit: empirical versus functional normal CDFs.

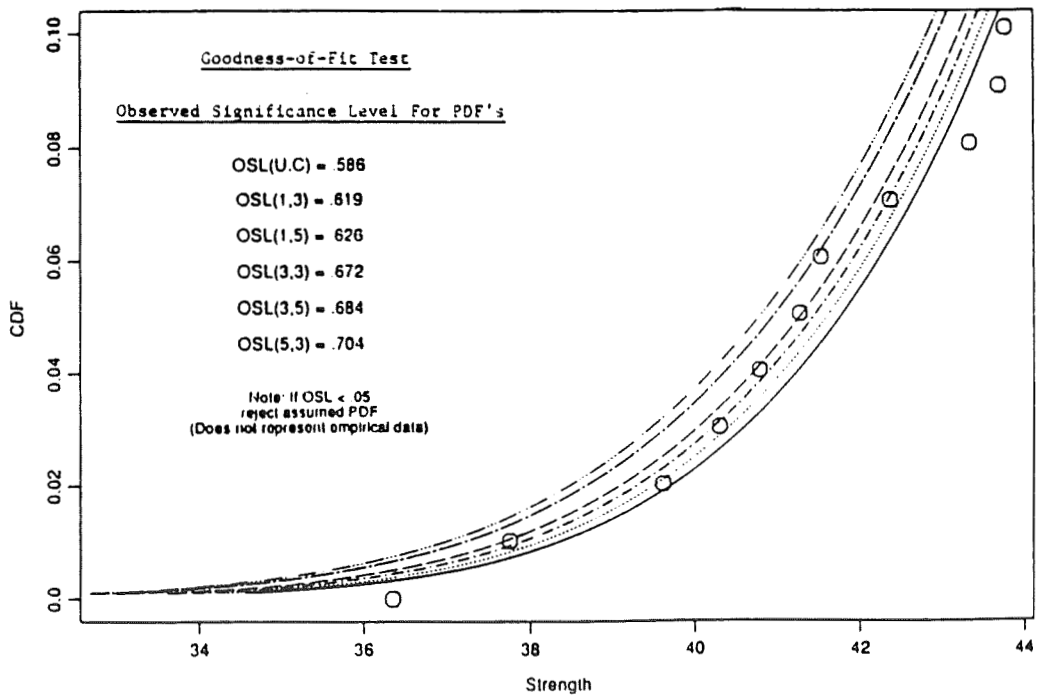


Figure 6b. Lower tail of empirical/normal distributions (see Figure 6a).

The results show that although each distribution fits the data quite well (see Figure 6b), there is a large relative difference in R values: $0.9_{(6)}$ for R(U.C) and 0.9957 for R(3, 5). In Figure 7, the results are similar to those in Figure 5. The variance contamination was 1% with a scale factor of 6 for both σ_S and σ_s . Again, although the functions are similar, the relative reliabilities differ substantially ($0.9_{(6)}$ versus 0.9977197). As was the case in Figure 5, severe consequences could exist if $R = 0.9_{(6)}$ is assumed and the actual reliability was 0.9977197. This could result in a number of premature failures, 2280 in one million, compared to the assumed one failure in a million. The results showed a low level of sensitivity to the selection of the factor K_1 .

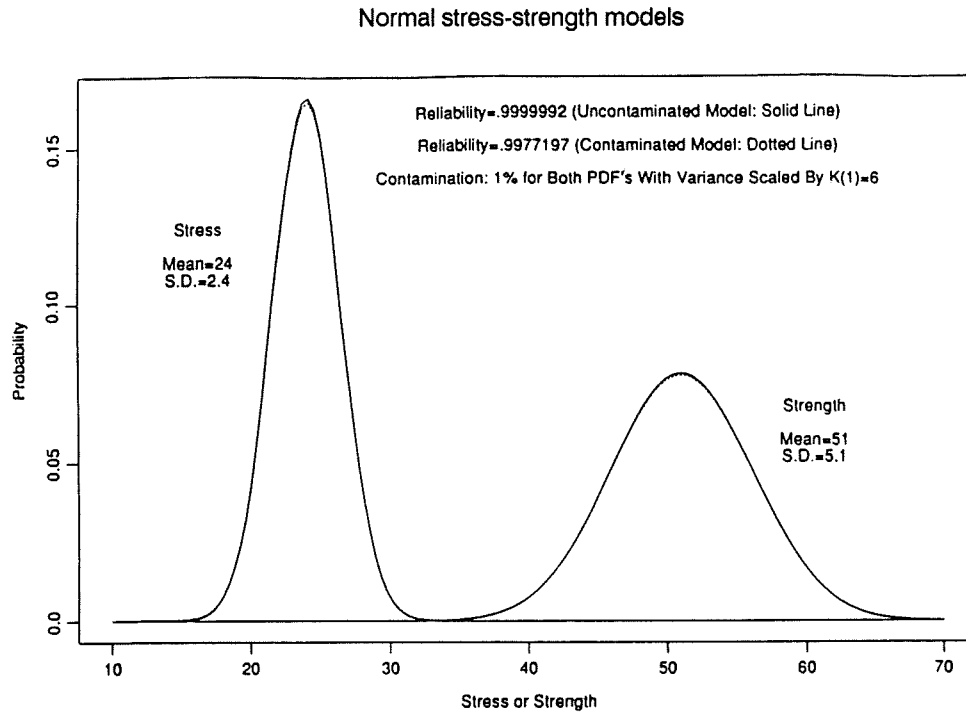


Figure 7. Reliability/normal functions with and without variance contamination.

Location Contamination

In Figure 8, reliability computation results and a graphical display of the stress-strength models are shown. The contaminated functions were obtained from 1% ($\epsilon = 0.01$) location contamination as defined in Equation 13 where $K_2 = 4$ and the (-) value is used for strength and (+) value for stress. The contamination in this case represents a secondary failure mode not considered when assuming a specified function from the test results. For example, ignoring the possibility that one in every 100 parts may have a lower strength level, say 4 standard deviations from the mean, can result in the reliabilities tabulated in the figure. That is, for the assumed correct model, $R = 0.9_{(6)}$, and the actual case where there was a lower strength level having one chance in 100 of occurring resulted in $R = 0.999459$. Figure 9 provides similar results to those in Figure 8 except there is a greater difference in reliability values $0.9_{(6)}$ versus 0.991012 due to a greater shift ($K_2 = 6$) in the mean value for the contaminated PDF. With a 1% contamination this result is predictable since one in a hundred times a failure should occur because $\mu_S - K_2\sigma$ is less than the mean of stress value. The above figure shows the consequences of not being able to identify the correct function because of the inability to always detect a flawed component. The result is the determination of an overly optimistic reliability value when the true reliability could actually be orders of magnitude less.

Normal stress-strength models

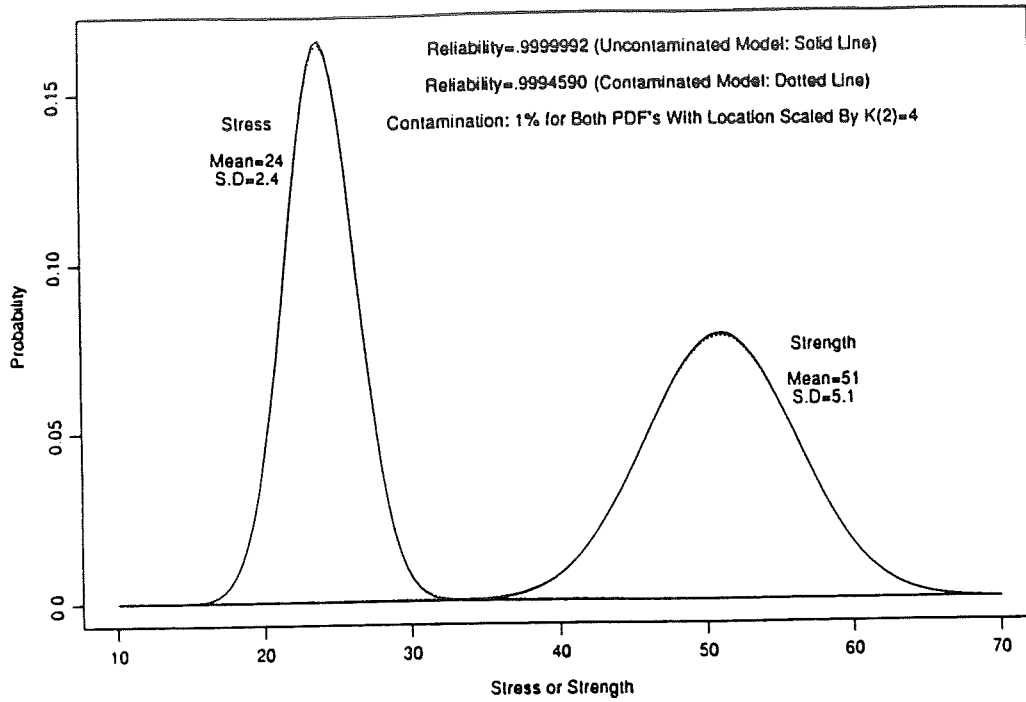


Figure 8. Reliability/normal functions with and without location contamination.

Normal stress-strength models

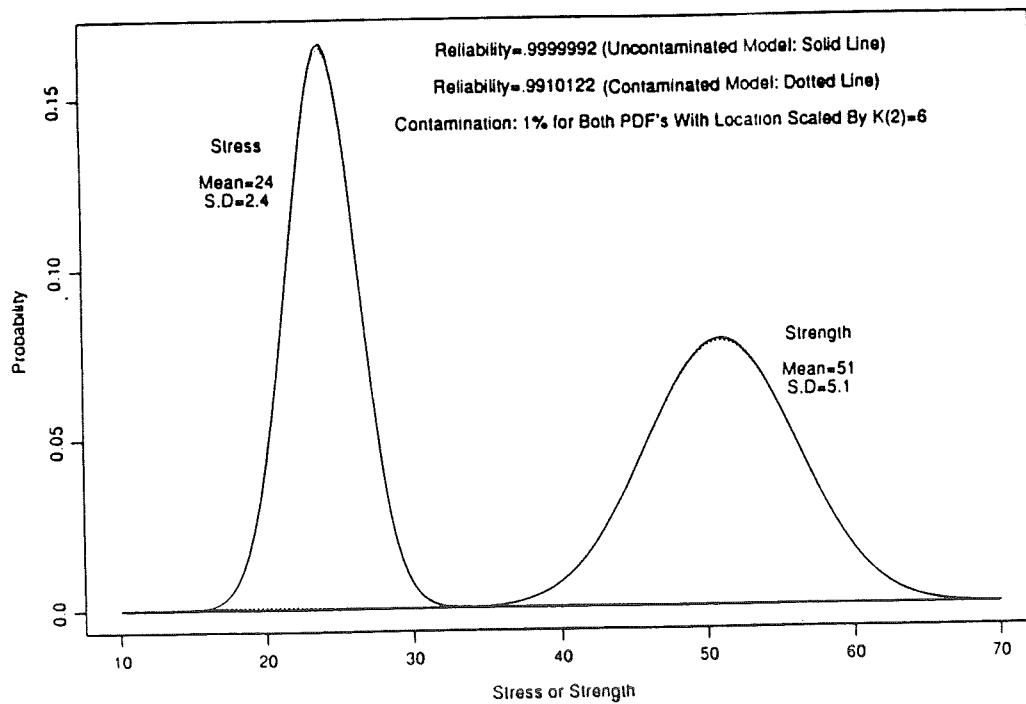


Figure 9. Reliability/normal functions with and without location contamination.

The results in Figure 10 are similar to those in Figure 5 except these were obtained from $\epsilon = 0.03$ and $K_1 = 3$. If the estimated $R = 0.9987350$ is obtained from the empirical data and a higher R value is required ($R = 0.9_{(6)}$), then a material with either greater strength or less contamination would be required. In order to obtain the required $0.9_{(6)}$ from the original contaminated model, a mean strength of 87 is required (see Figure 11). The mean of 87 requirement may not be acceptable to the designer, but this situation can occur if there is a substantial amount of dispersion in the strength data resulting in a long-tailed PDF. The above situation shows when a potentially over-design situation could occur because of the inability to identify the correct PDF in the stress-strength model due to inherent sensitivity and lack of information in the tail regions. This could prevent a good design from being accepted if it is required that the assessment of the design be based upon reliability only.

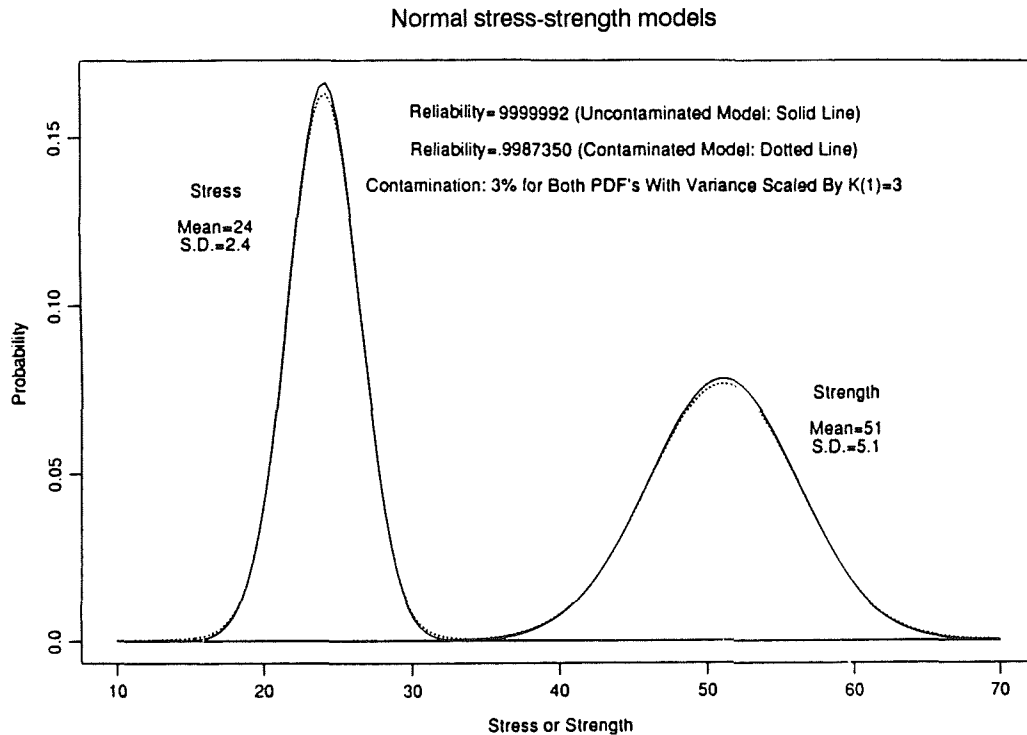


Figure 10. Reliability/stress-strength with and without contamination.

The display in Figure 12 presents four possible reliability values for the case where the means and standard deviation are: stress (24, 2.4) and strength (51, 5.1). The result from the uncontaminated normal is $0.9_{(6)}$. $R = 0.995043$ was obtained from the contaminated PDF application. Since, as was shown previously, the stress-strength model will often provide either relatively very high or low R values depending upon the chance selection of the PDFs. In order to compensate for the uncertainty in selecting the PDFs for stress and strength data, extreme value distributions are introduced (see Figure 2) in the reliability computation. This resulted in $R = 0.999045$. Unfortunately, this did not provide a value lower than the contaminated model result of 0.9950428. In order to obtain additional conservatism in the R estimate, a modification of a method by Bolotin is examined involving the determination of lower bound on R (see Figure 4 and Equation 19) in conjunction with the extreme value PDFs. The resultant lower bound estimate of 0.9796063 provides a significantly lower value than that of the contaminated model. This was also true for all contaminated models in this study.

Normal stress-strength models

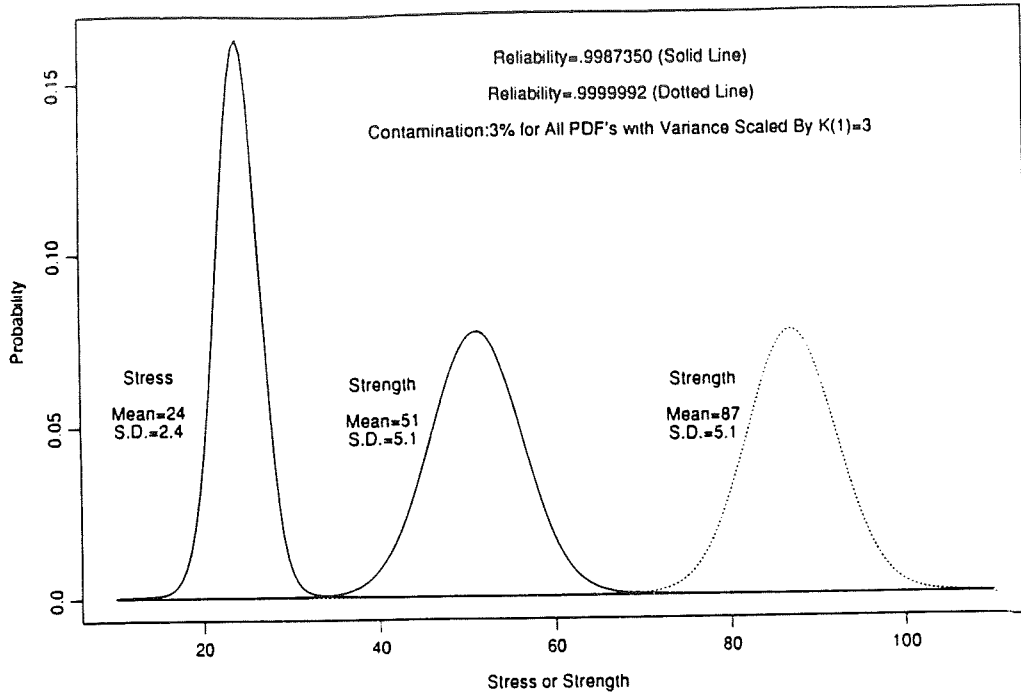


Figure 11. Increased strength requirements for high reliability.

Extreme value stress-strength model

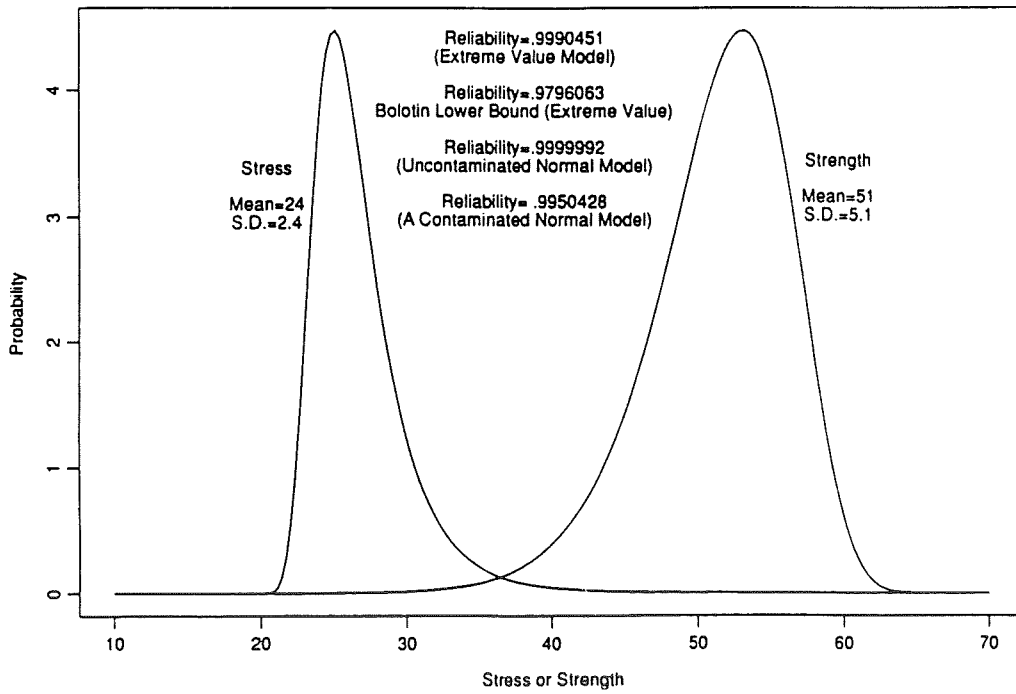


Figure 12. Reliability comparison: PDFs and lower bound.

This lower bound estimate could provide some security in estimating R, although results may be excessively conservative for some practical applications. In Table 1, the distribution of R values as a function of the sample size is presented. R values were obtained from repeated application of the uncontaminated stress-strength model of Figure 5 using randomly selected, normally distributed samples. For a sample size of 10, R ranges from 0.9₍₆₎ to 0.998417 indicating the instability associated with small samples. Higher order quantiles (e.g., 60%) were not included since they were all greater than 0.9₍₆₎.

Table 1. DISTRIBUTION OF R VERSUS SAMPLE SIZE

Distribution (%)	Reliability R			
	Sample Size			
	10	50	100	1000
0.1	0.998417 (1583)	0.999932 (68)	0.999980 (20)	0.999998 (2)
1	0.999160 (840)	0.999968 (32)	0.999991 (9)	0.999998 (2)
10	0.999943 (57)	0.999994 (6)	0.999998 (2)	0.999999 (1)
25	0.999994 (6)	0.999998 (2)	0.999999 (1)	0.999999 (1)
50	0.999999 (1)	0.999999 (1)	0.999999 (1)	0.999999 (1)

() Corresponding Number of Failures Per Million

A sample size of 50 or 100 provides reasonable stability, and a sample of 1000 shows essentially no variability. The results from Table 1 show that for a sample of 1000, an estimate of $R = 0.9_{(6)}$ would be acceptable. This is not necessarily correct since results from the table only address the sample size issue which is independent of the uncertainties in the PDF selection process. There are two requirements for obtaining accurate high reliability values from the strength model: large samples ($n > 1000$) and knowledge of the population PDF. Reliability estimates of 0.95 are much less sensitive to the PDF assumption. If there is a secondary failure mode due to occasional undetected poor manufacturing of the material or an unusually large load occurs that is not accounted for in the design process, then unknown lower reliability values ($R < 0.95$) can exist.

CONCLUSIONS

High reliability estimates from application of the statistical stress-strength model can vary substantially even for almost undetectable differences in the assumed stress and strength PDFs. Specifying high R values (e.g., 0.9₍₆₎) for acceptable structural design can result in higher failure rates than anticipated if the assumed PDFs contain shorter tails than actually exist. Over-design situations can also occur when excessively long-tailed PDFs are applied to the stress-strength model. An effective method for identifying this nonrobust behavior involved application of contaminated and uncontaminated PDFs in the determination of reliability values.

A suggested method for obtaining a lower bound on the reliability estimate provided potentially overly conservative results but was effective in determining values that were lower than any of the R values computed for the contaminated models.

The authors' position regarding the computation of high reliability of $0.9_{(6)}$ agrees with Breiman¹⁷ who says "The probability of failure $P_f = 1 \times 10^{-6}$ has an Alice in Wonderland flavor and should be banned from nonfiction literature." It is therefore recommended that if high reliability calculations are absolutely essential, then the results should be subjected to a sensitivity analysis using contaminated distributions. High reliability values are meaningful only when these values are not substantially affected by an amount of contamination (ϵ) consistent with the sample sizes, and a severity of contamination which is identified by engineering judgement.

ACKNOWLEDGMENT

The authors wish to thank Lucy Ohannesian and the IMA-V group of U.S. Army Materials Technology Laboratory for preparing this manuscript for publication.

REFERENCES

1. FREUDENTHAL, A. M. *The Safety of Structures*. Trans. ASCE, v. 112, 1947.
2. CORNELL, C. A. *A Probability-Based Structural Code*. J. Am. Conc. Inst., v. 66, 1969, p. 974-985.
3. U.S. Nuclear Regulatory Commission. *Reactor Safety Study: An Assessment of Accident Risks in U.S. Nuclear Power Plants*. NRC Report WASH-1400, 1975.
4. LUNDBERG, B. *Fatigue Life of Airplane Structures*. J. of the Aeronautical Sciences, v. 22, no. 6, June 1955, p. 349.
5. ARDEN, R. W., and IMMEN, F. H. *U.S. Army Requirements for Fatigue Integrity*. Proceedings of American Helicopter Society National Technical Specialists Meeting on Advanced Rotorcraft Structures, Williamsburg, VA, October 1988.
6. SHIAO, M. C., and CHAMIS, C. C. *Probability of Failure and Risk Assessment of Propulsion Structural Components*. NASA Technical Memorandum 102323, 1989.
7. LINCOLN, J. W. *Risk Assessment for an Aging Military Aircraft*. J. of Aircraft, v. 22, no. 8, August 1985, p. 687.
8. CORNOG, D. O., and LINCOLN, J. W. *Risk Assessment of the F-16 Wing*. Proceedings of the 1988 Structural Integrity Conference, San Antonio, TX, WRDC-TR-89-8071, Wright-Patterson AFB, Ohio, 1989.
9. HARRIS, B., and SOMS, A. P. *A Note on the Difficulty Inherent in Estimating Reliability from Stress-Strength Relationships*. MRC-2123, Mathematics Research Center, U. of Wisconsin, AD-A073637, October 1980.
10. BERENS, A. *Structural Risk Analysis in Aging Aircraft Fleets*. Proceedings of the 1988 Structural Integrity Conference, San Antonio, TX, WRDC-TR-89-8071, Wright-Patterson AFB, Ohio, 1989.
11. FREUDENTHAL, A. M. *Fatigue Sensitivity and Reliability of Mechanical Systems, Especially Aircraft Structures*. WADD Technical Report 61-53, Wright-Patterson AFB, Ohio, 1961.
12. JOHNSON, R. A. *Stress-Strength Models for Reliability*. Handbook for Statistics, Elsevier Science Publishers, New York, v. 7, 1988, p. 27.
13. BOX, G. E. P. *Robustness in the Strategy of Scientific Model Building*. Robustness in Statistics, R. L. Launer, and G. N. Wilkinson, eds., Academic Press, Inc., New York, 1979.
14. BURY, K. V. *Statistical Models in Applied Science*. John Wiley and Sons, Inc. (New York, London, Sydney, Toronto), 1975.
15. BOLOTIN, V. V. *Statistical Methods in Structural Mechanics*. Holden-Day, Inc., San Francisco, CA, J. J. Brandstatter, ed., 1969.
16. ANDERSON, T. W., and DARLING, D. A. *A Test of Goodness-of-fit*. J. Am. Statis. Assoc., v. 49, 1954, p. 765-769.
17. BREIMAN, L., and STONE, C. *Broad Spectrum Estimates and Confidence Intervals for Tail Quantiles*. Technical Report No. 46, Stat. Dept., University of California, Berkeley, CA, 1985. Also to be published in Journal of Statistical Computation and Simulation.

THIS PAGE INTENTIONALLY BLANK

PROBABILISTIC DESIGN
OF
ADVANCED COMPOSITE STRUCTURE

P. M. GRAY

M. G. RISKALLA

LTV AEROSPACE AND DEFENSE

AIRCRAFT DIVISION

DALLAS, TEXAS

ABSTRACT

Advanced composite technology offers potentials for sizable improvements in many areas: weight savings, maintainability, durability, and reliability. However, there are a number of inhibitors to these improvements. One of the biggest inhibitors is the imposition of traditional metallic approaches to design of composite structure. This is especially detrimental in composites because new materials technology demands new design approaches. Of particular importance are the decisions made regarding structural criteria. Significant changes cannot be implemented without careful consideration and exploration. This new approach is to implement changes on a controlled, verifiable basis. Probabilistic design is the methodology and the process to accomplish this. Its foundation is to base design criteria and objectives on reliability targets instead of arbitrary factors carried over from metallic structural history.⁽¹⁾

This paper discusses the background of probabilistic design and presents the results of a side-by-side comparison to generic aircraft structure designed the "old" way and the "new". Activities are also defined that need to be undertaken to evolve available approaches to probabilistic design followed by summary and recommendations.

INTRODUCTION

Current aerospace design procedure disregards the fact that component dimensions, environment (temperature and aging), manufacturing quality, and even the externally applied loads pertaining to aircraft structure are statistical in nature as opposed to deterministic, or single-valued variables. That is, these variables fall within a spectrum of possible values, and no specific value should be singled out as representing a reliable solution for a mechanical equation. Conventional solutions to design equations generally result in an uncertainty between prediction versus performance; this uncertainty is hidden under a blanket of safety factors. A more rational

solution to this reality is to strive for a predetermined reliability goal. This will require more knowledge about the nature of design inputs. The ultimate goal is to change the design path from: "...if it can happen at all, design to it," to "...design to an acceptable probability of failure, accounting for the likelihood and consequences of occurrence."

Composite materials are known to be susceptible to two environmental factors: elevated temperature and moisture. They are also sensitive to flaws that can originate during the manufacturing process or in operational usage. The conventional design approach adopted by government and industry does not recognize the variable nature of design manufacturing and operational input data. Current procedures force the engineer to design aircraft structure for worst-case scenarios adhering to contractually defined margins of safety with no knowledge of reliability performance. This is the traditional deterministic approach. In effect, it forces a weight increase with an unknown reliability that must be tolerated for every part regardless of the probability of encountering adverse conditions.

Composite part design is governed by compounded conservatism illustrated by the following criteria:

- o Worst case loading X safety factor (1.5) ⁽²⁾
- o Worst case temperature
- o Worst case moisture
- o Worst case damage, undetected

The effect of combining these conservative structural criteria is to continually drive down the allowable stresses. This has reduced weight savings to the extent that composites are not realizing the payoffs originally forecast. This current approach is illustrated in Figure 1. Significant changes must occur in the design approach to future military and space programs to take full advantage of composite material performance and to be able to more accurately manage risk.

DETERMINISTIC VS. PROBABILISTIC DESIGN

Figure 2 presents a comparison of the two (2) different approaches. The deterministic philosophy utilizes worst case design parameters to produce structural components which are overly conservative and heavy. The deterministic approaches possess positive margins to withstand given maximum load, but there also are inherent, unknown reliabilities at the given load levels.

An intermediate approach is to apply a portion of probabilistic design but still retain the limit to ultimate factor. This type of risk analysis augments the structural design engineer's current capabilities and allows him to quantify the structural reliability of the aircraft structure. Previous risk analyses have shown that by accounting for the stochastic nature of design parameters and identifying the risk drivers, one can produce reliability based structures which meet the operational requirements.

The probabilistic approach is to utilize the design data characterized by statistical distributions to identify/optimize the risk drivers to produce minimum weight structures for which the reliability has been specified.

PROBABILISTIC DESIGN

Probabilistic design is a finely integrated process as shown schematically in Figure 3. The approach is to define/develop the functional relationships of the operations within the boxes, then build the relationships between them, thus integrating the entire process. In this way, when a factor in one operation changes, its effect can be determined on the others. The most important evaluation is the effect on failure probability.

A flowchart of the LTV-AD Probabilistic Design model is shown in Figure 4. This model consists of four major activities, namely the design process, material production, manufacturing, and operations. Output from the design process is the expected operating stress distribution resulting from the flight spectra. The remaining three activities provide the material strength distribution, determined through Monte Carlo simulation of random variables representing random variation of incoming material strength, manufacturing defects, and operational factors. Probability of failure occurs when the stress exceeds the strength. This is calculated by a double integral of the stress and the strength probability density functions to determine the probability that "stress exceeds strength."

The basic probabilistic design concept, as shown below, looks into the probability distributions of both material strength and operating stress. Because failure is a local phenomenon, division of a component into nodes can be done to represent all the locations at which failure is possible to occur. In general, the distributions are assumed to be identical at all the nodes. Step 7 assumes that material strengths at the nodes are independent from each other. As in step 8, if the calculated probability of failure does not agree with the pre-defined and acceptable level, sensitivity analysis resulting from changes in distribution(s) will provide invaluable information on needed changes in the design.

Step No.

1. Establish allowable failure rate.
2. Establish the number of nodes where failure is possible.
3. Determine probability distribution for loads.

$$P(X_S < x_S) = F(x_S)$$

4. Determine the operating stress probability density function $f_S(x)$.
5. Determine probability distribution for strength.

$$P(Y_M < y_M) = F(y_M)$$

6. Determine the material strength probability density function $f_M(y)$.

7. Calculate failure probability P.

$$P_f = \int_x f_S(x) [1 - (\int_{y>x} f_M(y) dy)^N] dx$$

8. If P_f is not in agreement with the established failure rate, then modify 2 or 3.

Probabilistic analysis requires that the random variables be statistically characterized. Statistical design databases, in general, do not exist.

In order to conduct a probabilistic design exercise one must characterize many parameters, including the following:

- (1) Incoming material mechanical properties
- (2) External loads anticipated during the life of the article.
- (3) Manufacturing processes and their effect on material strength.
- (4) Environmental effect on strength.
- (5) Environmental history during operational usage.
- (6) Flaw locations, severity, probability of occurrence and effect on strength.

Quality of incoming composite material is crucial to final product quality. To assure incoming material meets specifications, testing procedures and measured value limits must be established to sufficiently discriminate between inferior and specified material. These criteria must be agreed upon by producer and consumer. Each wants to minimize their risk. The producer's risk is the probability of rejecting good material and the consumer's risk is the probability of accepting inferior material.

PROBABILISTIC DESIGN APPLICATION AND EVALUATION

In order to calculate potential weight savings from a probabilistic design, a simplified two-cell box beam was selected to represent aircraft wing and tail structure. Most of the usual design concerns and requirements inherent in military aircraft programs can be simulated in multicell, pressure-loaded box beams. Two independent design approaches were implemented: the traditional deterministic method and probabilistic design.

The generic composite, two-cell, three-spar wingbox used in this exercise is presented in Figure 5. The wingbox is fixed (i.e., cantilevered) at the root ($Y=0.0$). Design ultimate pressures of 10.0 and 5.0 psi are applied to the forward and aft cell lower skins, respectively, in the upward (+z) direction. The ultimate pressures were used only for the deterministic analysis. Geometric details of the wingbox are presented in Figure 6, and the wingbox section thicknesses are presented in Figure 7. Two categories of

aircraft were evaluated in this program, a Class A (attack) aircraft and a Class B_{II} (bomber) aircraft. Both spectra were derived from Mil-A-08866B⁽³⁾ and are shown in Figure 8.

The composite wingbox was optimized for minimum weight using both the deterministic and probabilistic design approaches. Buckling and damage tolerance criteria were major factors in the sizing. The wing weight reduction as a function of probability of failure is presented in Figure 9. The reliability target determines the amount of weight savings. Two criteria were applied:

- (1) The probability of failure for an aircraft's single flight should be 1×10^{-7} or less.
- (2) The expected number of aircraft lost by structural failure in the lifetime of the fleet should be less than one.

Probabilistic design showed a possible weight savings of 13% when using a fighter load spectrum, and a weight savings of 20% when using a bomber load spectrum.

Deterministic/Probabilistic Equivalence

Incorporated in the methodology is the ability to relate probabilistic design to the factor-of-safety used in deterministic design. The issue is to determine the benefits to the aircraft if probabilistic advantages were converted to increased performance rather than weight savings. Figure 10 shows how much gain is available in maneuver load factor using probabilistic design assuming the weight of the two design approaches is the same. The fighter aircraft can sustain a 62 percent increase in "g" level (i.e., 16.2 vs. 10.0 g's) indicating the significant increase in maneuverability.

SUMMARY/RECOMMENDATIONS

Probabilistic Design is a powerful alternative to today's approach for composite design. It will require the development of sophisticated techniques in probability and statistics and characterization of statistical data for engineering variables just now becoming available. However, it is gaining momentum as more people become aware of its presence and benefits.

"One Time Only" designs that cannot be tested to failure (such as missiles and flight vehicle systems) are best designed by probabilistic methods where the additional analysis complexity is justified from a safety or economic standpoint. Likewise, in situations where a design is put into production before it can be tested, probabilistic design would be the best way to predict service life. In addition, probabilistic design is the best way to minimize the weight of a component, and so should be used to design critical parts for lightweight applications such as aerospace vehicles.⁽⁴⁾

As the demand grows for more accurate, sophisticated designs, the requirement for probabilistic design methodology will become more and more a necessity. The incorporation of Probabilistic Design, while quite challenging technically, will net significant payoffs in the form of improvement in vehicle performance accompanied by a reduction in operating costs. To be in a position

to approach a new design/program from a probabilistic standpoint, additional studies need to be performed including:

- Probabilistic Design Philosophy/Methodology
- Risk analysis of current aircraft structure
- Fighter/bomber probabilistic design study
- Development of statistical data bases required for probabilistic design
- Total quality management relating to material performance (i.e., Reliability-based material acceptance criteria)
- Probabilistic Design of Advanced Primary/Secondary Aircraft Structure
- Qualification/certification methodology.

The application of Probabilistic Design to new and emerging aerospace systems will result in minimum weight structures which have reliability as the heart of the design and not just a "fall-out" from a designed-in capability to withstand a given load.

REFERENCES

1. AFP 800-7, "USAF R&M 2000 Process", 1 January 1989.
2. Muller, G. E. and Schmid, C. J., "Factor of Safety - USAF Design Practice", Technical Report AFFDL-TR-78-8, April 1978.
3. MIL-A-008866B, "Military Specification: Airplane Strength and Rigidity Reliability Requirements, Repeated Loads, and Fatigue", 22 August 1975.
4. Lincoln, J. W. and Snead, J. M., " the X-30 Structural Integrity Program: The Challenge Ahead".

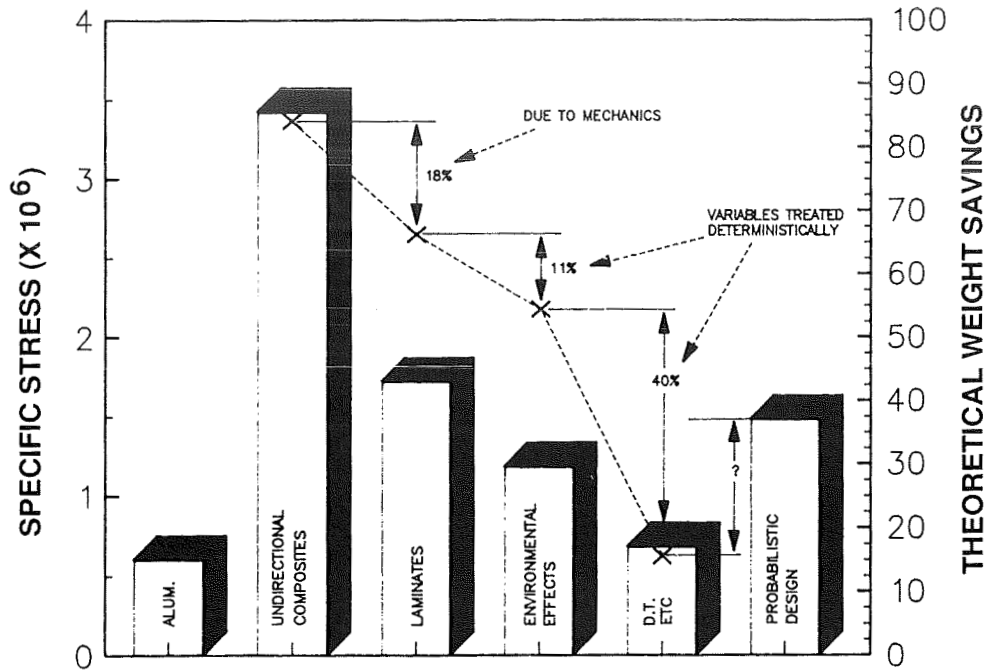


FIGURE 1. DETERMINISTIC REDUCTION FACTORS VS. PROBABILISTIC WEIGHT SAVINGS

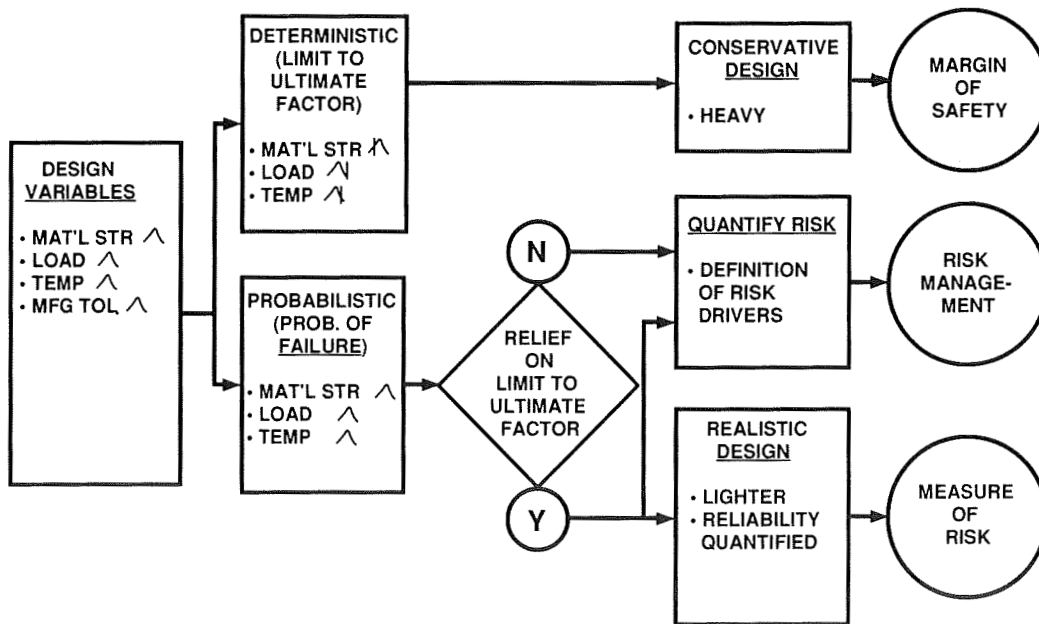


FIGURE 2. PROBABILISTIC VS. DETERMINISTIC DESIGN

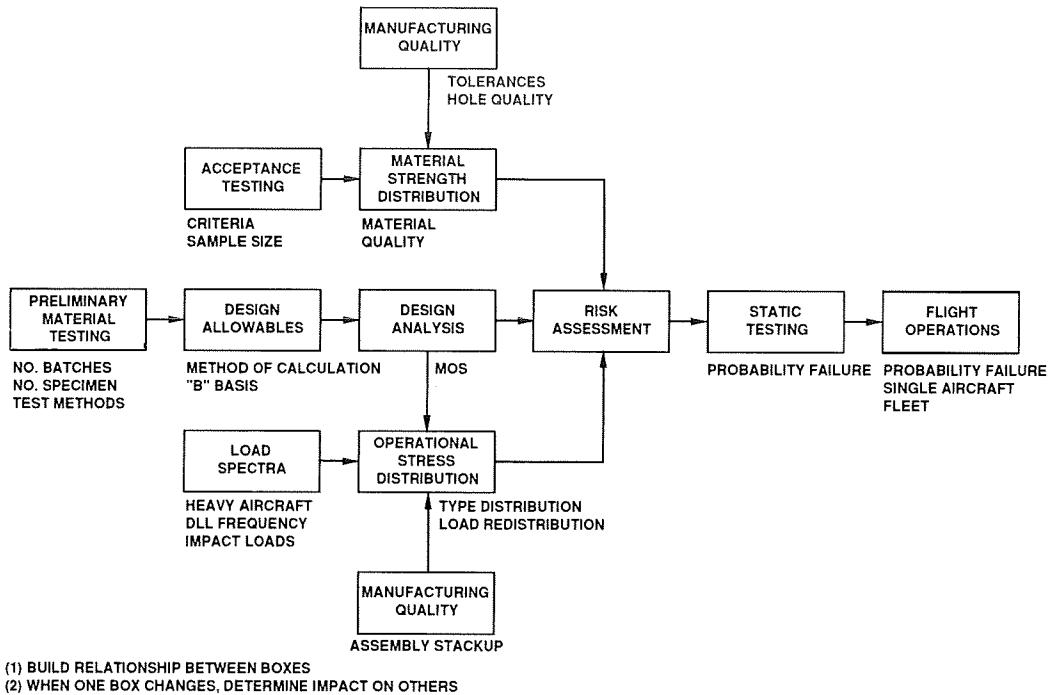


FIGURE 3. FULL PROBABILISTIC ANALYSIS

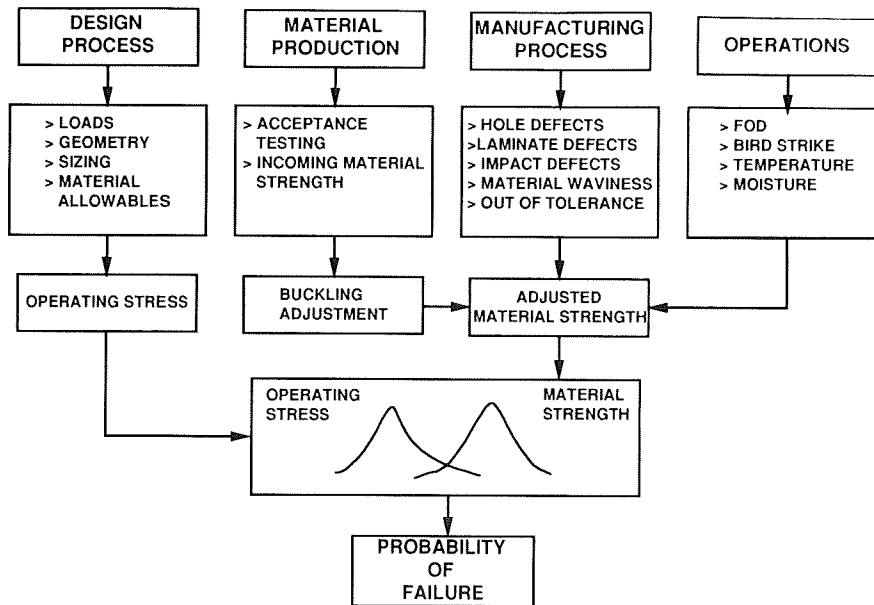


FIGURE 4. PROBABILISTIC DESIGN

STRUCTURAL FEATURES

- TENSION SKIN
- COMPRESSION SKIN
- SPARS
- RIBS
- FASTENERS (JOINTS)
- TAPERED THICKNESSES
- BUCKLING
- DAMAGE CRITERIA
- COMBINED LOADS
- VARIABLE PLY ORIENTATION

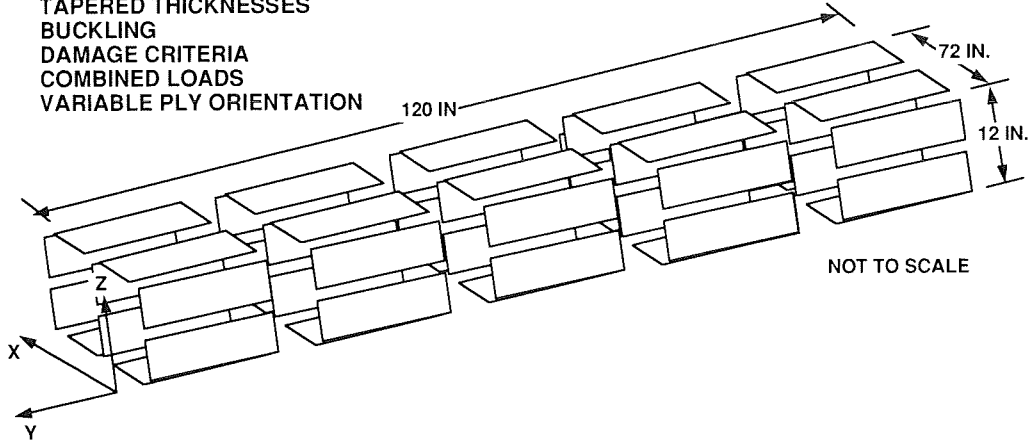


FIGURE 5. GENERIC COMPOSITE WINGBOX

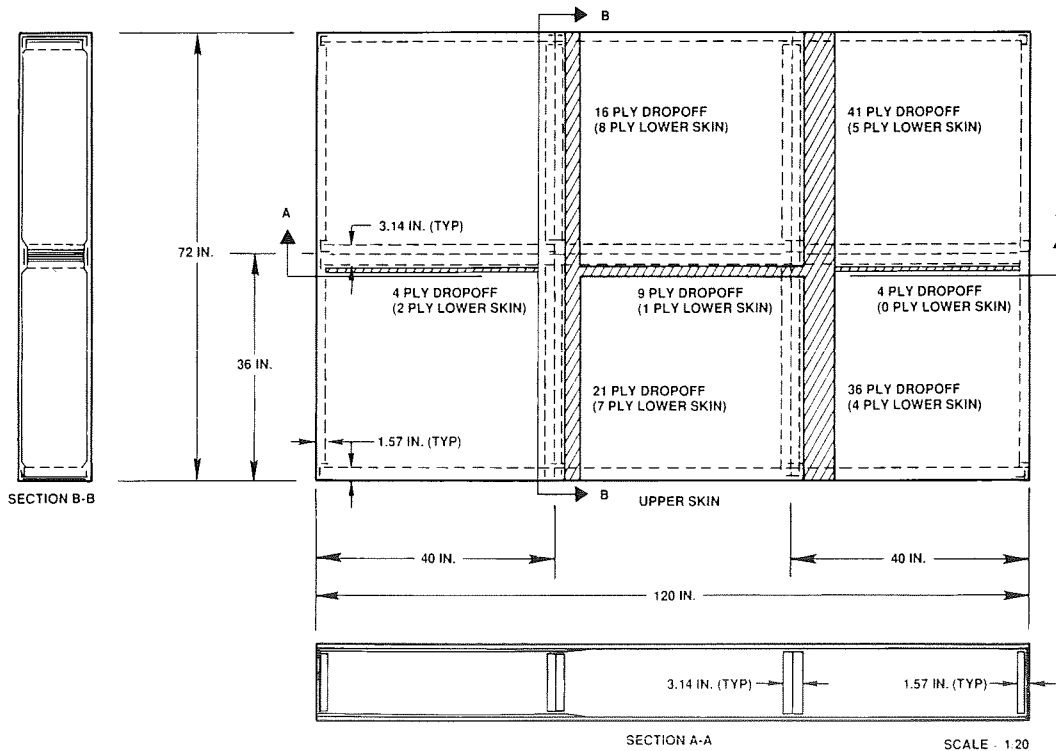


FIGURE 6. WING BOX CONSTRUCTION

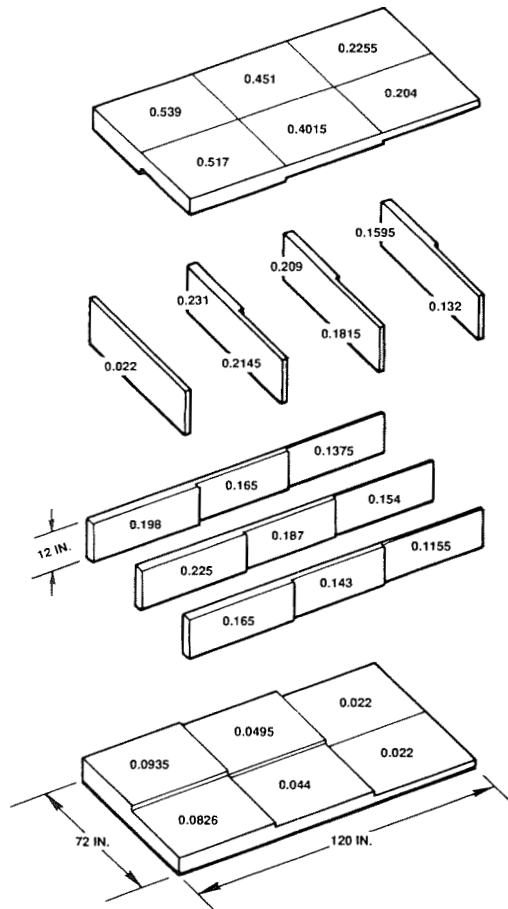


FIGURE 7. WINGBOX SECTION THICKNESSES

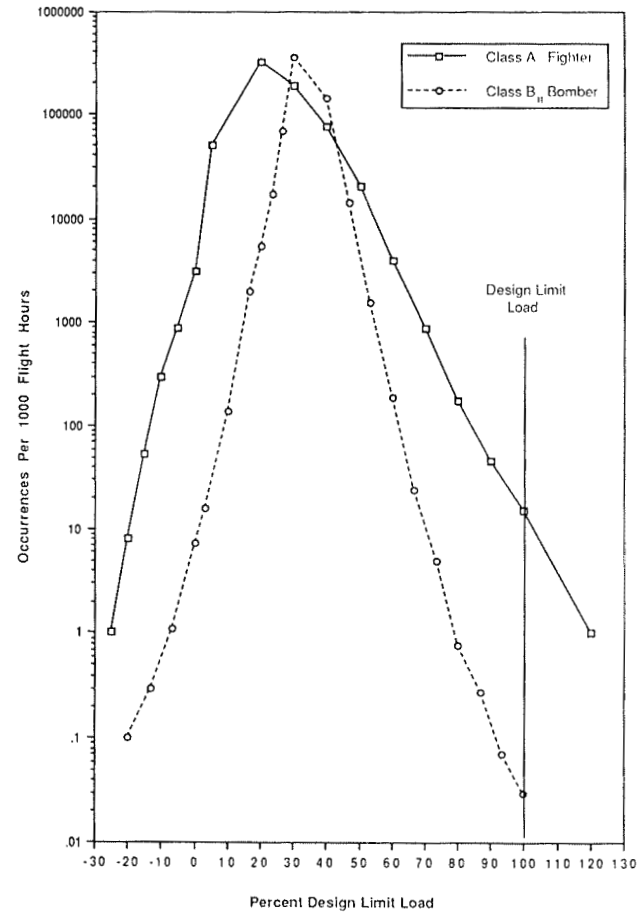


FIGURE 8. AIRCRAFT LOAD SPECTRA

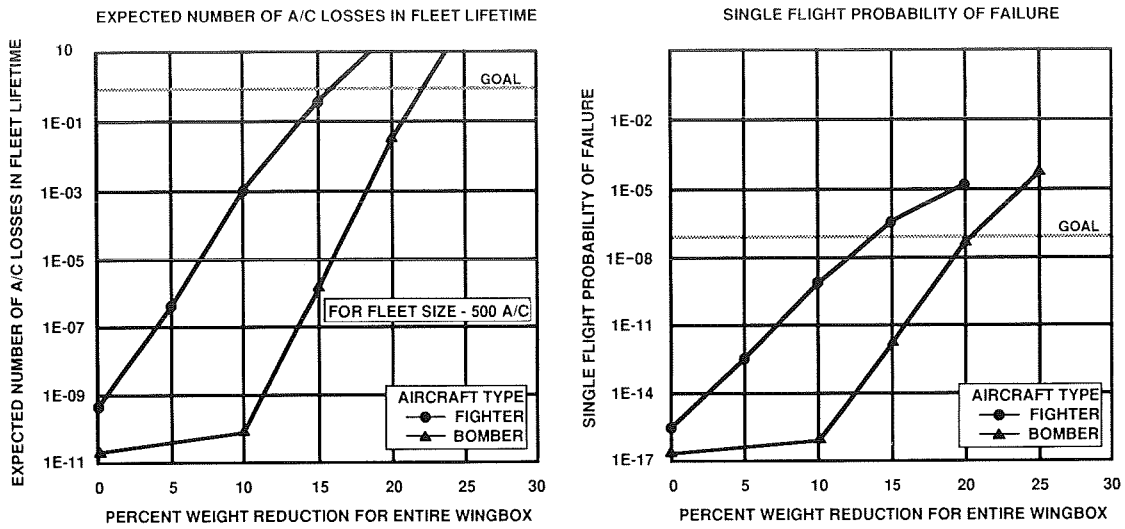


FIGURE 9. COMPOSITE WINGBOX WEIGHT REDUCTION BENEFITS

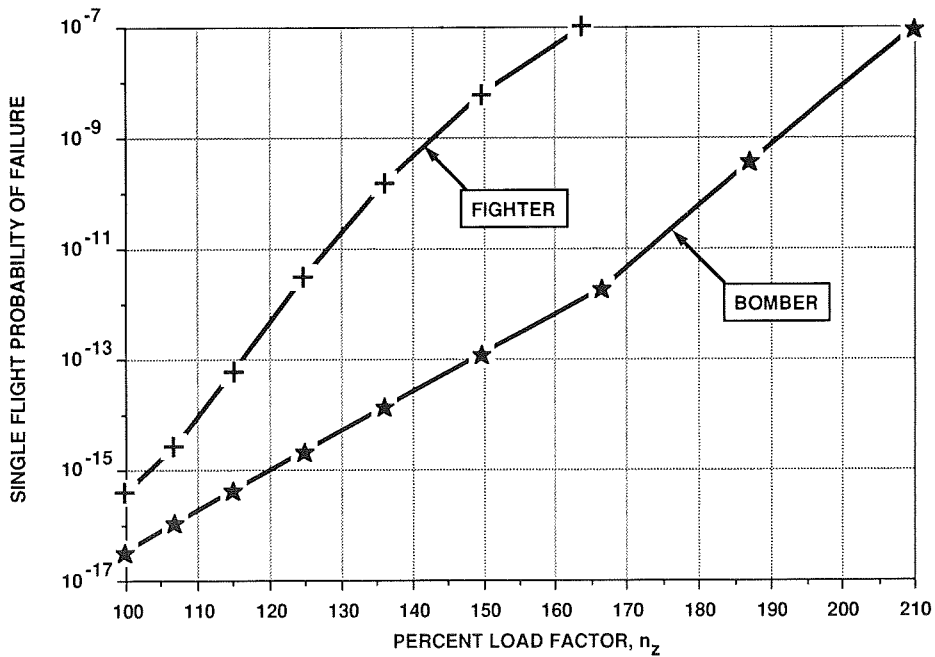


FIGURE 10. DETERMINISTIC/PROBABILISTIC EQUIVALENCE

THIS PAGE INTENTIONALLY BLANK

PROBABILISTIC EVALUATION OF FUSELAGE-TYPE COMPOSITE STRUCTURES

Michael C. Shiao
Sverdrup Technology, Inc.
Lewis Research Center Group
Brookpark, Ohio

Christos C. Chamis
NASA Lewis Research Center
Cleveland, Ohio

NASA
524-05
51392
P-13

SUMMARY

A methodology is developed to computationally simulate the uncertain behavior of composite structures. The uncertain behavior includes buckling loads, natural frequencies, displacements, stress/strain etc., which are the consequences of the random variation (scatter) of the primitive (independent random) variables in the constituent, ply, laminate and structural levels. This methodology is implemented in the IPACS (Integrated Probabilistic Assessment of Composite Structures) computer code. A fuselage-type composite structure is analyzed to demonstrate the code's capability. The probability distribution functions of the buckling loads, natural frequency, displacement, strain and stress are computed. The sensitivity of each primitive (independent random) variable to a given structural response is also identified from the analyses.

INTRODUCTION

Composites are becoming an important class of engineering material in aerospace design. Their outstanding mechanical properties are very attractive to the aerospace industry especially the high strength to low density ratio. They also possess excellent fatigue strength and the ability to resist corrosion and impact. The mechanical properties of composites are derived from a wide variety of variables. The variables are, for example, fiber and matrix material properties at the constituent level and fabrication variables at the ply level such as fiber volume ratio, void volume ratio, ply orientation, ply thickness etc. These primitive variables are statistical in nature, therefore, the mechanical properties of a composite material can not be quantified deterministically. As a consequence, the behavior of composite structures shows a scatter from its average value. Traditionally, a "safety factor" is used to account for those unpredictable behavior. However, this concept results in either an overconservative design or a design of a structure with a high probability of failure. Because of the void in design for a

PRECEDING PAGE BLANK, NOT FILED

535

PAGE 534 INTENTIONALLY BLANK

probabilistic assessment of composite structures, a methodology was developed at NASA Lewis Research Center. The methodology is based upon the identification of uncertain variables at every structural level such as at the constituent, ply, or laminate level. The uncertain variables are then filtered through an analyzer which combines the composite mechanics, structural mechanics and probability theory. The output of the analyzer is the desired structural response such as displacement, stress/strain, buckling load, natural frequency, etc. These types of problems can normally be solved by the Monte Carlo simulation method. But, it is computationally expensive. In order to save computational time, the newly developed methodology integrates composite mechanics, finite element methods and probability algorithms to provide an efficient and affordable way for the probabilistic assessment of uncertain composite structures. The methodology is implemented in the computer code IPACS (Integrated Probabilistic Assessment of Composite Structures) and is described in the following sections. A fuselage-type composite structure is analyzed to demonstrate the code's capability. Buckling, natural frequency and static analyses are performed. The probability distributions for buckling load, natural frequency, nodal displacement, nodal strain and stress are computed. The sensitivity of each primitive (independent random) variable to a given structural response is also identified.

SYMBOLS

E_{f11}	: fiber modulus in longitudinal direction
E_{f22}	: fiber modulus in transverse direction
G_{f12}	: in-plane fiber shear modulus
G_{f23}	: out-of-plane fiber shear modulus
ν_{f12}	: in-plane fiber Poisson's ratio
ν_{f23}	: out-of-plane fiber Poisson's ratio
α_{f11}	: fiber thermal expansion coefficient in longitudinal direction
α_{f22}	: fiber thermal expansion coefficient in transverse direction
ρ_f	: fiber mass density
N_f	: number of fiber per end
d_f	: filament equivalent diameter
C_f	: fiber heat capacity
K_{f11}	: fiber heat conductivity in longitudinal direction
K_{f22}	: fiber heat conductivity in in-plane transverse direction
K_{f33}	: fiber heat conductivity in out-of-plane transverse direction
S_{fT}	: fiber tensile strength
S_{fC}	: fiber compressive strength
E_m	: matrix elastic modulus
G_m	: matrix shear modulus
ν_m	: matrix Poisson's ratio
α_m	: matrix thermal expansion coefficient
ρ_m	: matrix mass density

C_m : matrix heat capacity
 K_m : matrix heat conductivity
 S_{mT} : matrix tensile strength
 S_{mC} : matrix compressive strength
 S_{mS} : matrix shear strength
 β_m : matrix moisture coefficient
 D_m : matrix diffusivity
 fvr : fiber volume ratio
 vvr : void volume ratio
 θ_p : ply misalignment
 t_{psk} : ply thickness of skin
 t_{pst} : ply thickness of stringer
 K_{cTR} : translational spring constant
 K_{cTO} : torsional spring constant
 C_z : out-of-plane nodal uncertainties on stringers at free edges
 $stdv$: standard deviation
 M_p : material properties
 R : structural response
 V_i : independent random variable
 ϵ : strains
 κ : curvatures
 N : resultant in-plane forces
 M : resultant moments

CONCEPT OF PROBABILISTIC ASSESSMENT OF COMPOSITE STRUCTURES

To start a probabilistic assessment of a composite structure, the uncertainties within the model should be identified at micro and macro levels. For example, at constituent level, the uncertain constituent primitive variables are the fiber and matrix material properties. At the ply level, they are fiber volume ratio, void volume ratio, ply orientation and ply thickness, etc. At the structural level, uncertain loads, temperatures, geometry or the boundary condition may also be included. All the uncertain sources are characterized by their own probability distribution functions. The uncertain sources are then fed into an analyzer of composite mechanics, structural mechanics and probability theory. From the analysis, structural responses and degraded material properties are obtained which can only be properly represented by a probability distribution function. The detail is illustrated in figure 1. PICAN and NESSUS in figure 1 are probabilistic analyzers for both composite and structural mechanics which will be described next.

PROBABILISTIC COMPUTER CODE IPACS

IPACS is a computer code for probabilistic analysis of composite structures. It integrates several NASA in-house computer programs developed in recent years such as COBSTRAN, PICAN and NESSUS. COBSTRAN is a model generator for composite structures which generates finite element models for structural analyses. PICAN (Probabilistic Integrated Composite Analyzer) used to determine the perturbed and probabilistic composite material properties at the ply and laminate level. NESSUS (Numerical Evaluation of Stochastic Structures Under Stress) is used to determine the perturbed and probabilistic structural response at structural, laminate and ply levels. PICAN and NESSUS share the same sub-module, FPI (Fast Probability Integrator), for the probabilistic method. The architecture of IPACS software system is depicted in figure 2. The details of PICAN, NESSUS and FPI are explained in the following.

PICAN has evolved from the deterministic composite mechanics code ICAN (Integrated Composite Analyzer) (ref. 1). This module performs a comprehensive multi-level perturbation and probabilistic analysis of composite material properties based on the primitive (independent random) variables occurring at the constituent (fiber and matrix material properties) and at ply level (fiber volume ratio, void volume ratio, ply orientation and ply thickness). Perturbed material properties at every level corresponding to all the perturbed primitive variables are computed. With this information, mathematical functions to represent the relationships between the material properties and the primitive variables can be determined numerically. The functions can be expressed by equation 1 for a linear relationship or equation 2 for a nonlinear relationship.

$$M_p = a_0 + \sum a_i V_i \quad (1)$$

$$M_p = a_0 + \sum a_i V_i + \sum b_i V_i^2 \quad (2)$$

where M_p is any material property; V_i are primitive variables; and a_0 , a_i , b_i are constants. Using equation 1 or 2 and the probability distributions of the primitive variables, probabilistic methods can then be applied to find the probability distribution function of any material property.

NESSUS is a finite element module for the perturbation and probabilistic structural analysis, which is developed by South West Research Institute under NASA contract. This module is being modified to include the capability for structural analysis with uncertain composite material properties. For a given perturbation on any coefficient in the matrices A , C and D as defined in equation (3), the corresponding structural responses will be computed by this module. The A , C and D matrices are the relationship between resultant force/moment and strain/curvature from laminate theory.

$$\begin{Bmatrix} N \\ M \end{Bmatrix} = \begin{bmatrix} A & C \\ C & D \end{bmatrix} \begin{Bmatrix} \epsilon \\ \kappa \end{Bmatrix} \quad (3)$$

where N are the resultant forces and M are the resultant moments; ϵ are the in-plane strains and κ are the curvatures. Because the perturbed coefficients in matrices A , C and D are computed using composite mechanics with a perturbed primitive variable, and the perturbed structural response is computed using the perturbed coefficients in matrices A , C and D , structural responses can be related to the primitive variables and the relationship between the structural response and the primitive (independent random) variables can be developed numerically. This relationship can also be expressed by equation 1 or 2 but replacing the material properties M_p with the structural response R as shown in equations 4 and 5.

$$R = a_0 + \sum a_i V_i \quad (4)$$

$$R = a_0 + \sum a_i V_i + \sum b_i V_i^2 \quad (5)$$

Similarly, the probability distribution functions of structural responses will be determined by probabilistic methods.

The FPI module evolved from the probability algorithm FORM (First Order Second Moment Reliability Method) with Wu's version (refs. 2,3). After the perturbation study, a database is created. The relationship between the structural responses and the primitive variables can be determined numerically by FPI. If the perturbed variables are independent of each other with known probability distribution functions, FPI can be used to compute the discrete cumulative distribution function (cdf). An analytical probability distribution function of a structural response is then determined using this discrete cdf value.

Using IPACS for probabilistic assessment of composite structures, the uncertain primitive variables at constituent and ply levels are identified. These variables are then selectively perturbed several times in order to create a database for the determination of the relationship between the desired structural response (or the desired material property) and the primitive variables. For every given perturbed primitive variable, micro mechanics are applied to determine the corresponding perturbed mechanical properties at the ply and laminate level. Laminate theory is then used to determine the perturbed resultant force/moment-strain/curvature relationship. With this relationship at the laminate level, a finite element perturbation analysis is performed to determine the perturbed structural responses corresponding to the selectively perturbed primitive variables. This process is repeated until enough data is generated and the proper relationship

between structural responses and primitive variables can be determined through a numerical procedure. With the known probabilistic distributions of the primitive variables and a numerically determined relationship between the structural response and the primitive variables, fast probability integration is applied. For every discrete response value, a corresponding cumulative probability can be computed quickly by FPI. This process is repeated until the cumulative distribution function can be appropriately represented. The probabilistic material properties at ply and laminate levels are also computed in the same way as for the structural responses. The output information from FPI for a given structural response includes its discrete cdf values, the coefficients for a special type of probability distribution function, and the sensitivity factors of the primitive variables to the structural response.

NUMERICAL EXAMPLES AND DISCUSSIONS

A cylindrical shell with 10 ft. in diameter and 50 ft. in length is analyzed by IPACS. Four vertical stringers and three ring stringers shown in figure 3(a) are used to strengthen the shell-skin structure shown in figure 3(b). Three hundred and twelve nodes including ninety six duplicate nodes are used to model the structure for the finite element analysis. The structure is fixed at one end by translational and torsional springs and is free at the other end as shown in figure 4(a) and 4(b). The composite structure is made of graphite fiber and epoxy matrix. The average ply thickness for the shell skin is 0.005 inches with a $[0,-45,45,90]_s$ ply lamination. The average ply thickness for the stringers are 0.05 inches with 10 zero degree plies. The primitive variables identified at constituent level are: (1) 17 material properties for fiber, (2) 12 material properties for matrix. The identification and statistics of these twenty nine primitive variables are listed in Table 1. At ply level, the fabrication variables are: (1) fiber volume ratio, (2) void volume ratio, (3) ply orientation and (4) ply thickness. Their statistical data are listed in Table 2. At structural level, translational and torsional spring constants for boundary rigidity are modeled as uncertain parameters. Uncertainties are also assigned to those nodes on the free edge of the vertical stringers in their out of plane directions. Their statistics are shown in Table 3. Three analyses are performed: (1) buckling analysis, (2) static analysis and (3) natural frequency analysis. Ninety three uncertain primitive variables are considered including sixty six variables from stringer and skin in the constituent and ply levels, three variables for the uncertain boundary conditions and twenty four out-of-plane nodal uncertainties in the vertical stringers.

From the buckling analysis, the probabilistic buckling load of the first buckling mode is computed. The cumulative distribution function (cdf) of the buckling load is plotted in figure 5. The sensitivity factors of six most important primitive variables are plotted in figure 6. It shows that the probabilistic buckling load is highly sensitive to the ply thickness, fiber volume ratio and fiber modulus of

the skin and the stringer ply thickness. The uncertain torsional springs also show some effect on the scatter of the probabilistic buckling load. In this analysis, the distance between the ring stringers is assumed to be constant. However, the distance should be included in the probabilistic analysis even if the distance shows a small scatter, because the first buckling mode shape is very sensitive to the distance between the rings.

Modal analysis is also conducted. The deterministic first vibration frequency is 1.1 rad/sec. The cdf of this frequency is plotted in figure 7. The sensitivity factor of each primitive variable to the scatter of the vibration frequency is shown in figure 8. Again, it is found that skin ply thickness is the most important variable with a sensitivity factor equal to 0.88.

Static analysis is performed using an equivalent load to the first buckling load. The displacement at the free end in the longitudinal direction is analyzed. Its cdf is plotted in figure 9. The sensitivity analysis shows that the fiber modulus, fiber volume ratio and ply thickness of both skin and stringer have approximately the same contribution to the scatter of the displacement. The sensitivity factors are plotted in figure 10. Also studied are the strain and stress of the node at the fixed end in the vertical stringer. The cdf of the strain and its sensitivity factors are plotted in figures 11 and 12 respectively. The cdf of stress and its sensitivity factors are plotted in figures 13 and 14 respectively. The sensitivity analysis again shows that the scatter of the strain and stress all are strongly dominated by the ply thickness, fiber volume ratio and fiber normal modulus of both skin and stringers. The sensitivity results for strain and stress are similar to those for displacement because of the fact that stress/strain analyses are highly dependent on displacement analysis.

Once the probability distribution functions are determined, reliability assessments of the entire structures can be assessed as proposed by Shiao and Chamis (refs. 4, 5, 6, 7).

CONCLUDING REMARKS

A methodology is developed to computationally simulate the uncertainties in the composite structural analysis. The methodology is implemented into the computer code IPACS which can efficiently and effectively simulate the uncertain structural responses. The code is capable of handling the uncertainties in the constituent, ply and laminate levels of composite structures. A large amount of useful information such as the probability distributions of desired structural responses and the sensitivity of each independent primitive variable to the probabilistic structural response can be obtained through the analysis. A reliability assessment can be performed once this information is available.

REFERENCES

1. Murthy, P.L.N., Chamis, C.C., "Integrated Composite Analyzer (ICAN), Users and Programmer's Manual", NASA TP 2515, March, 1986
2. Lind, N.C., Krenk, D., and Madsen, H.O., Methods of Structural Safety, Prentice-Hall, New York, 1985
3. Wu, Y.T. "Demonstration of a New, Fast Probability Integration Method for Reliability Analysis", Advances in Aerospace Structural Analysis, O.H. Burnside and C.H. Parr, eds., ASME, New York, 1985, pp. 63-73
4. Shiao, M.C., Nagpal, V.K., Chamis, C.C., "Probabilistic Structural Analysis of Aerospace Component Using NESSUS", NASA TM 102324
5. Shiao, M.C., Chamis, C.C., "Probability of Failure and Risk Assessment of Propulsion Structural Components", NASA TM 102323
6. Shiao, M.C., Chamis, C.C., "A Methodology for Evaluating the Reliability and Risk of Structures Under Complex Service Environments", NASA TM 103244
7. Shiao, M.C., Chamis, C.C., "First-Passage Problems: A Probabilistic Dynamic Analysis for Degraded Structures", NASA TM 103755

Table 1. Material Properties at Constituent Level for both Skin and Stringers

	unit	Distribution type	Mean	coefficient of variation
E_{f11}	Msi	Normal	31.0	0.05
E_{f22}	Msi	Normal	2.0	0.05
G_{f12}	Msi	Normal	2.0	0.05
G_{f23}	Msi	Normal	1.0	0.05
ν_{f12}	---	Normal	0.2	0.05
ν_{f23}	---	Normal	0.25	0.05
α_{f11}	ppm/°F	Normal	-0.55	0.05
α_{f22}	ppm/°F	Normal	5.6	0.05
ρ_f	lb/in ³	Normal	0.063	0.05
N_f	---	constant	10,000	0.00
d_f	in	Normal	0.0003	0.05
C_f	BTU/in/°F	Normal	0.17	0.05
K_{f11}	BTU.in/hr/in ² /°F	Normal	580	0.05
K_{f22}	BTU.in/hr/in ² /°F	Normal	58	0.05
K_{f33}	BTU.in/hr/in ² /°F	Normal	58	0.05
S_{fT}	Ksi	Weibull	400	0.05
S_{fC}	Ksi	Weibull	400	0.05
E_m	Msi	Normal	0.5	0.05
G_m	Msi	Normal	0.185	0.05
ν_m	---	Normal	0.35	0.05
α_m	ppm/°F	Normal	42.8	0.05
ρ_m	lb/in ³	Normal	0.0443	0.05
C_m	BTU/in/°F	Normal	0.25	0.05
K_m	BTU.in/hr/in ² /°F	Normal	1.25	0.05
S_{mT}	Ksi	Weibull	15	0.05
S_{mC}	Ksi	Weibull	35	0.05
S_{mS}	Ksi	Weibull	13	0.05
β_m	in/in/1%moist	Normal	0.004	0.05
D_m	in ³ /sec	Normal	0.002	0.05

Table 2. Fabrication variables at ply level

	unit	Distribution type	mean	Coefficient of variation
fvr	---	Normal	0.60	0.05
vvr	---	Normal	0.02	0.05
θ_p	degree	Normal	0.00	0.9 (stdv)
t_{psk}	in	Normal	0.005	0.05
t_{pst}	in	Normal	0.02	0.05

Table 3. Uncertainties in the structural level

	unit	Distribution type	mean	coefficient of variation
K_{eTR}	lb/in	Normal	30E+06	0.30
K_{eTO}	lb-in/rad.	Normal	12E+02	0.30
C_z	in	Normal	0.0	0.01 (stdv)

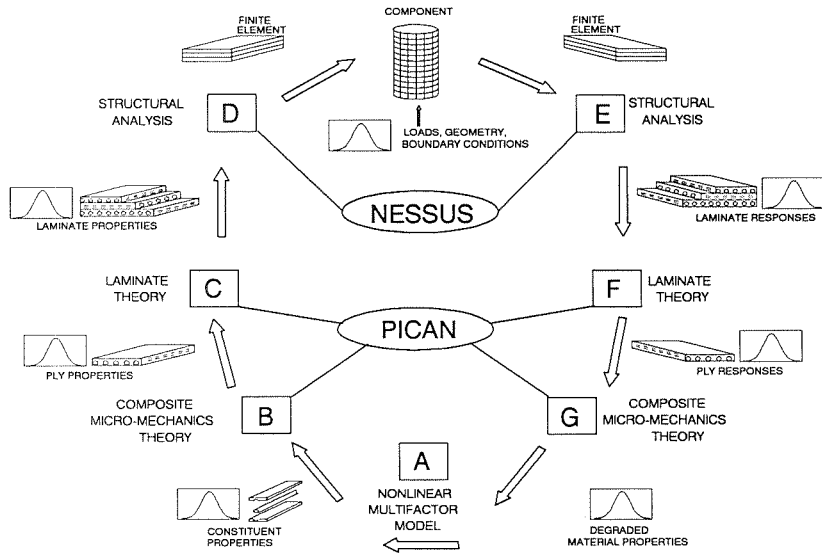


Figure 1. Concept of Probabilistic Assessment of Composite Structures

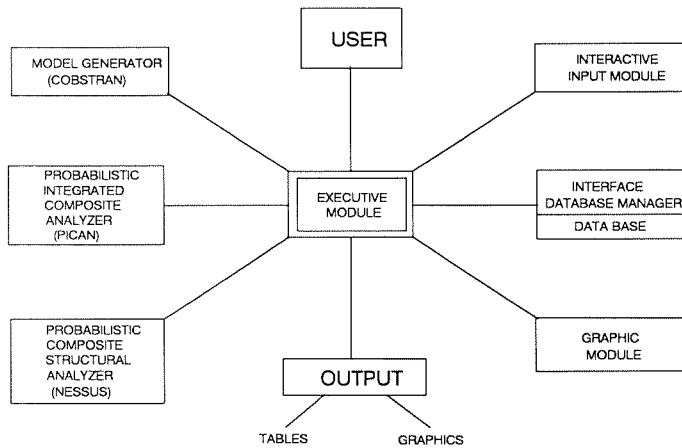
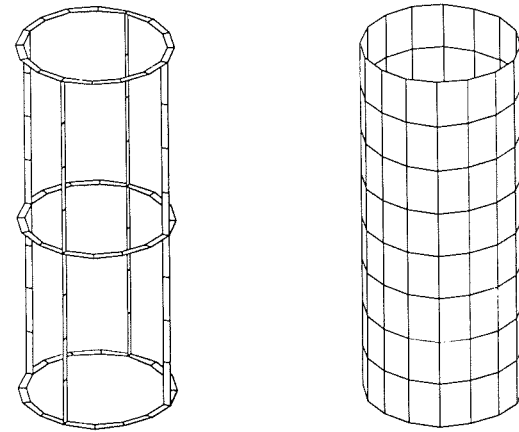


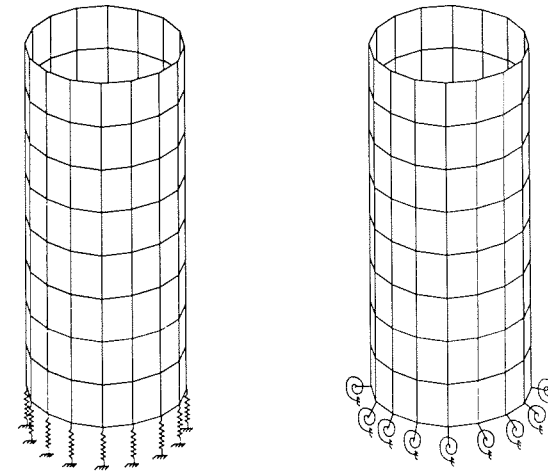
Figure 2. Architecture of IPACS Software System
(IPACS: Intergrated Probabilistic Assessment of Composite Structures)



(a) frames/stringers

(b) skin

Figure 3. Finite Element Model of a Composite Cylindrical Shell



(a) translational springs

(b) torsional springs

Figure 4. Boundary Conditions of a Composite Cylindrical Shell

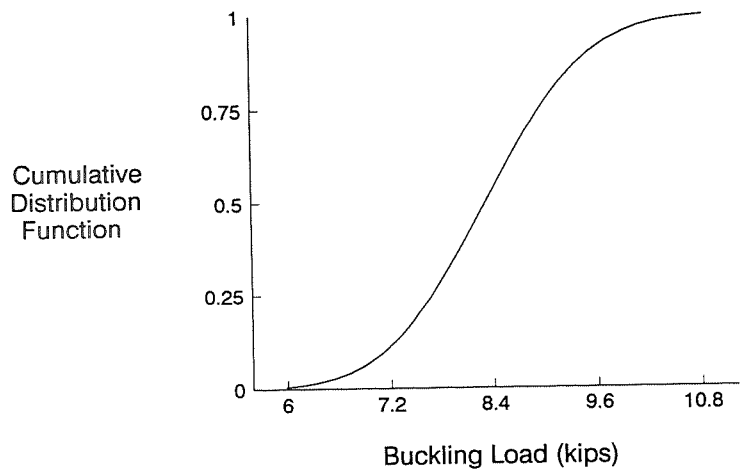


Figure 5. Cumulative Distribution function of first buckling load

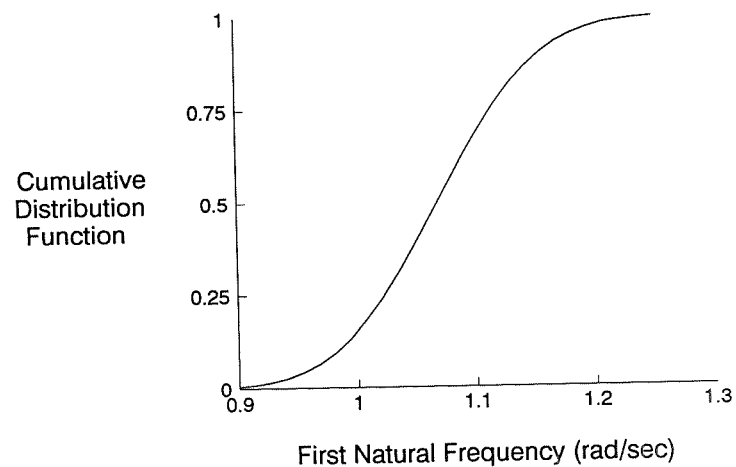


Figure 7. Cumulative Distribution function of first natural frequency

545

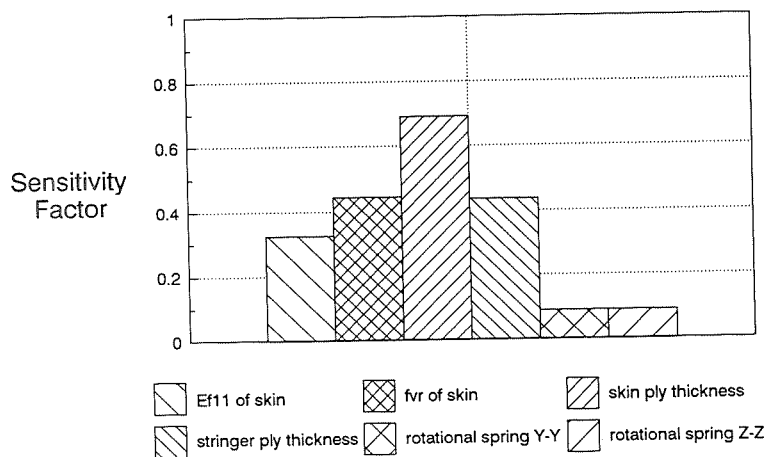


Figure 6. Sensitivity factors of six most important primitive variables to the first buckling load at probability level 0.005

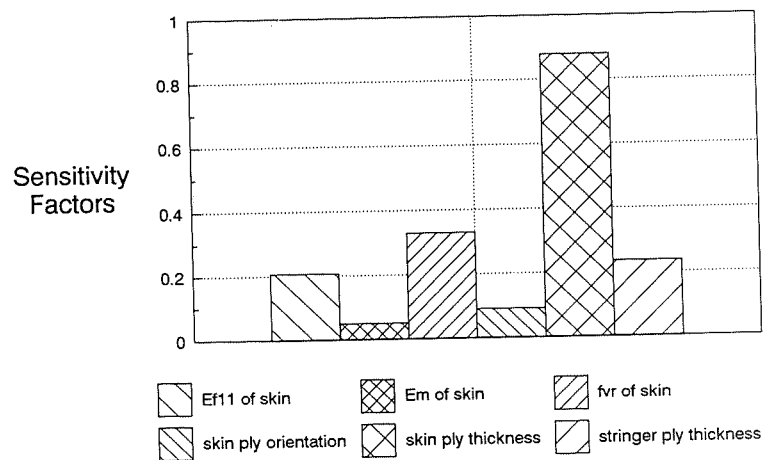


Figure 8. Sensitivity factors of six most important primitive variables to the first natural frequency at probability level 0.005

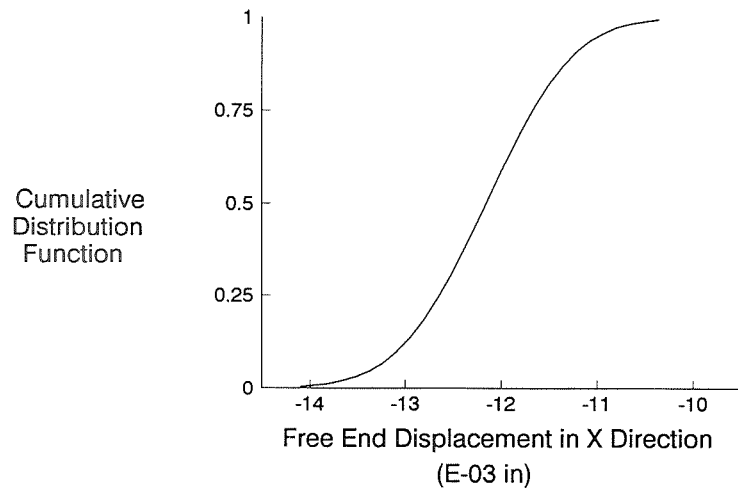


Figure 9. Cumulative Distribution function of free end displacement in X direction

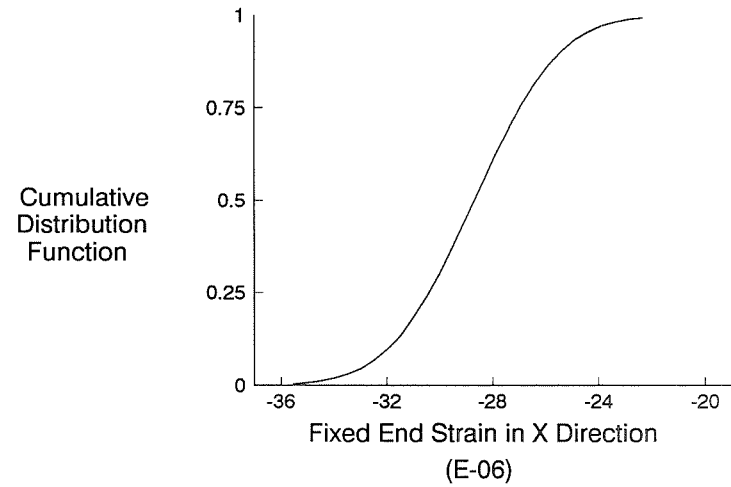


Figure 11. Cumulative Distribution function of fixed end strain in X direction

546

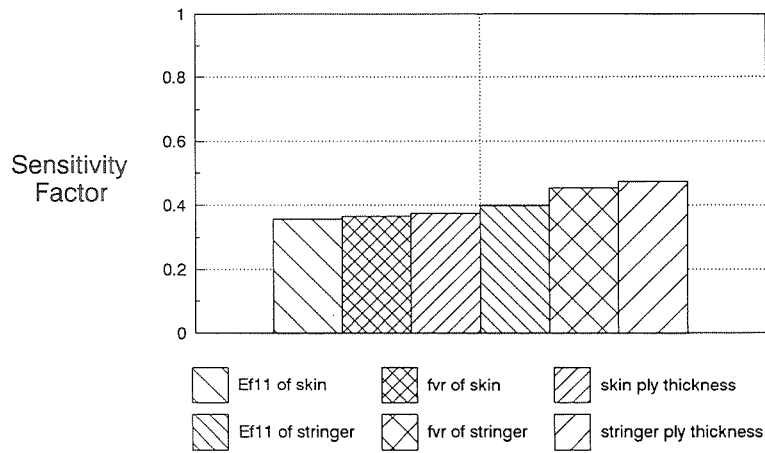


Figure 10. Sensitivity factors of six most important primitive variables to free end displacement in x direction at probability level 0.005

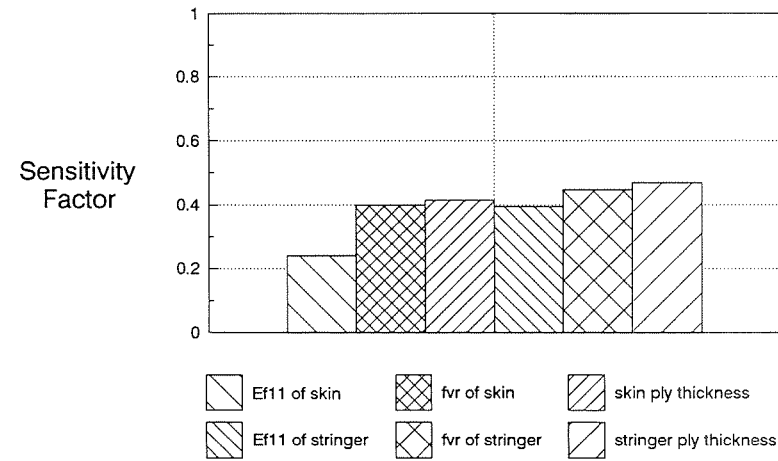


Figure 12. Sensitivity factors of six most important primitive variables to fixed end strain in x direction at probability level 0.005

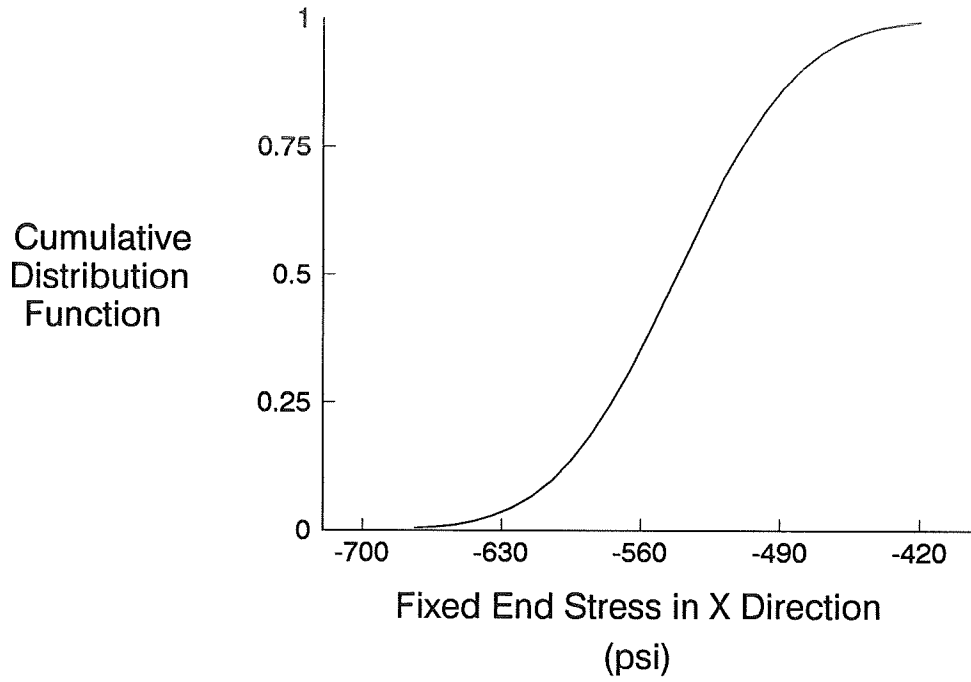


Figure 13. Cumulative Distribution function of fixed end stress in X direction

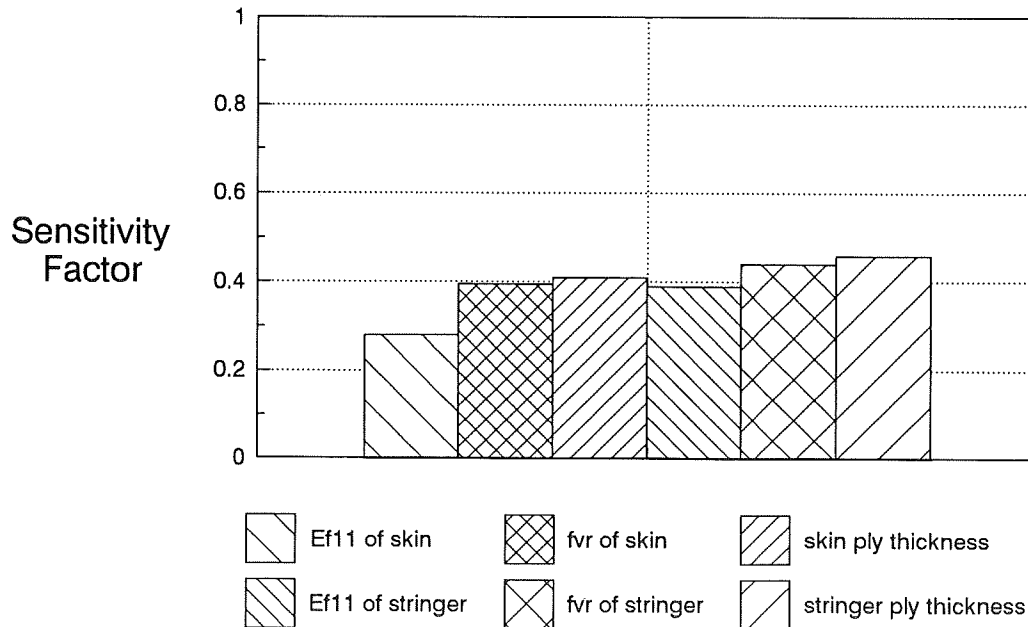


Figure 14. Sensitivity factors of six most important primitive variables to fixed end stress in x direction at probability level 0.005

THIS PAGE INTENTIONALLY BLANK

Proof Test Methodology for Composites¹

by

Edward M. Wu² and David K. Bell³

Naval Postgraduate School

Monterey, California 93943

20 7
[REDACTED]
p-12
57393**Summary**

The special requirements for proof test of composites are identified based on the underlying failure process of composites. Two proof test methods are developed to eliminate the inevitable weak fiber sites without also causing flaw clustering which weakens the post-proof-test composite. Significant reliability enhancement by these proof test methods has been experimentally demonstrated for composite strength and composite life in tension. This basic proof test methodology is relevant to the certification and acceptance of critical composite structures. It can also be applied to the manufacturing process development to achieve zero-reject for very large composite structures.

Introduction

High performance composites are being specified for load bearing structures in increasing number for land, sea, air and space applications. These applications include man-safe vehicles and hazard containers which demand high safety; inaccessible-after-launch space applications which require high functionality; and very large structures such as ship and submarine hulls which must be manufactured meeting zero reject criterion if they are to be economically feasible. The structural reliability in all these applications requires quantitative reliability estimation and reliability assurance.

For conventional materials such as aluminum or steel, the reliability methodology is frequently experience based. Factors of safety are determined from an extensive data base that have been refined from up to 100 years of structural application experiences. Conversely, for high performance composites, significant improvements in reinforcing fibers and matrix binders are continually being developed. The number of permutations and combinations of fibers and matrixes for different composites is approaching intractable. The very attribute of specifically tailored composite for specific applications also reduces the common reliability data base. Without an

¹This investigation was supported partially by the Defense Advanced Research Projects Agency (Materials, Submarine Technology Program - James J. Kelly, Program Area Manager).

²Professor of Aeronautics

³Lieutenant, United State Navy

adequate engineering application data base, reliability of composite must be based on the analytical modeling of its intrinsic failure processes and the experimental confirmation of the model and measurement of the model parameters.

This investigation explores one aspect of composite reliability: the composite reliability which is dominated by the fiber filament tensile failures. Current understanding of the composite failure process in tension is first reviewed and the salient parameters which affect the composite reliability are identified. By combining this physical understanding with the mathematical failure model, two proof test methods are developed to enhance composite reliability. The first proof test method deals with subjecting manufactured articles to preload prior to putting it into service, this is relevant to certification and acceptance methods. The second method deals with pre-loading during processing, this is relevant to manufacturing. The benefits of these two proof test methods are experimentally demonstrated on two different composite systems; one an aramid-epoxy composite, the other a graphite-epoxy composite.

Background on Composite Tensile Failure Mechanism

A rational attempt to improve composite reliability may start with an understanding of its failure process. Through the work of Rosen [1, 2], composite failure process under tension is known to be microscopically sequential starting with failures of the very weak fibers at low load levels. The loads carried by the broken fibers are transferred via the matrix to the neighboring intact fibers, thereby producing a micro-redundancy as illustrated in figure 1a

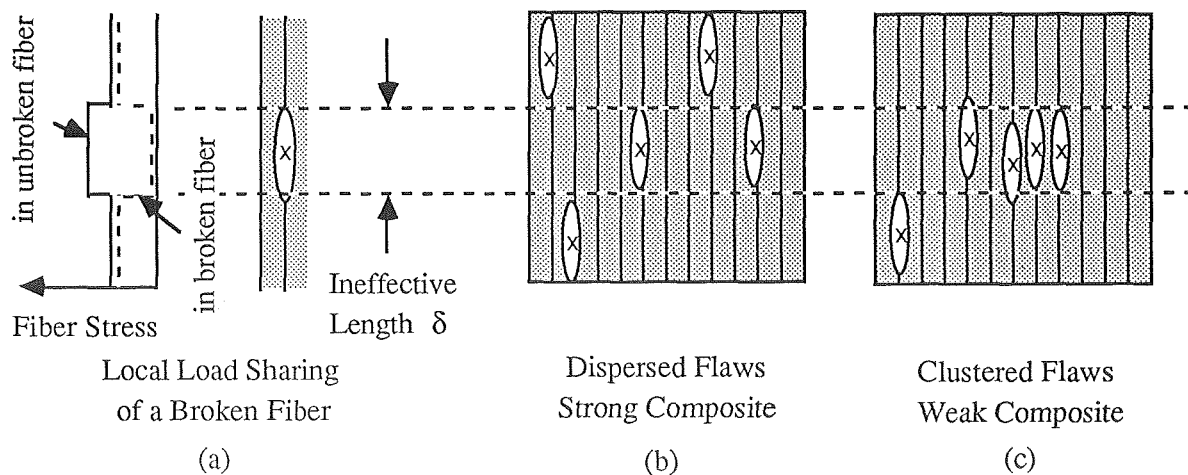


Figure 1. Local Load Sharing around broken fibers cumulating to flaw clustering

This process initiates from spatially dispersed sites. As the externally applied load continues to increase, more failure sites are created which leads to clustering and ultimately, catastrophic failure. The longitudinal distance along the fiber required to transfer the stress from one broken fiber to its neighboring unbroken fiber, termed the ineffective length, is estimated by Rosen [1] to be:

$$\delta = \left\{ \left(V_f^{-\frac{1}{2}} - 1 \right) \frac{E_f}{G_m} \right\}^{\frac{1}{2}} \cosh^{-1} \left\{ \frac{[1 + (1 + \phi)^2]}{2[1 - \phi]} \right\} d_f \quad (1)$$

where:

V_f is the volume fraction of fiber

E_f is the modulus of fiber

G_m is the shear modulus of matrix

ϕ is the fiber load sharing efficiency; a fractional value below which the fiber is considered to be ineffective

d_f is the fiber diameter

It can be calculated from fiber filament strength statistics that local fiber failure occurs at load levels considerably below the macroscopic catastrophic failure load. For a graphite composite at a typical service stress level, there already exists 3 to 4 fiber failure sites per cm^2 of a single layer of lamina. Even for a moderately sized structure, the number of failure sites add up to millions throughout the structure. The strength of a specific structure ultimately depending on the chanced dispersion or clustering of the inherent failure sites as illustrated in figures 1b and 1c. The chance clustering and the resulting stress concentration from local load sharing have been modeled by Harlow and Phoenix [3,4] using a recursive analysis of the permutations and combinations of the fiber failure sequences and the stress concentrations associated with each configuration. The probability of failure due to nominal far field loads and the local load sharing stress concentrations among adjacent failure sites are partitioned by the ineffective length δ . The Harlow-Phoenix Local Load Sharing model can be used to predict the probability of failure of the composite if the constituent fiber strength statistic and the ineffective length δ are both known. The mathematical structure of this model is of a modified Weibull form and it predicts that statistically weak composite samples typically have a larger number of adjacent break clusters which reduce the macroscopic strength.

It follows immediately that the mechanistic principle for a proof test is to eliminate adjacent breaks, thereby eliminating any substandard weak composite samples. With this understanding of the composite failure process in tension, it is now appropriate to re-examine the proof test as a method for improving composite reliability.

Background on Proof Test

The mechanical proof tests consist of applying a pre-load to a structure prior to putting the structure into service. The proof test load level may be the same or higher than the service load level. The underlying premise of the proof test is that any unacceptably weak structures (in load bearing capacity) are eliminated by the pre-load. The remaining structures which passed the proof test are assumed to have sustained no permanent damage during the pre-load excursion; thus assuring the reliability of those specific structures in subsequent service. Stated in probability terms, all the structures before and after the proof test are idealized to belong to the same population with a probability of failure modeled by :

$$\begin{aligned}
 F_1(\sigma) &\equiv \text{Cumulative probability of failure at service conditions } \leq \sigma \\
 F_2(\sigma_p) &\equiv \text{Cumulative probability of failure at proof test conditions } \leq \sigma_p \quad (2) \\
 \sigma_p &\equiv \text{Stress level at proof test} \\
 F_p(\sigma) &\equiv \text{Cumulative probability of failure after proof test at } \sigma_p
 \end{aligned}$$

Under the idealized assumption that no permanent strength reducing damage has been incurred during the pre-loading, the post-proof-test population is identical to the pre-proof-test population and the cumulative probability of failure after the proof test is simply conditioned to the probability of survival during the proof test:

$$F_p(\sigma) = \begin{cases} 0, & \sigma < \sigma_p \\ \frac{F_1(\sigma) - F_2(\sigma_p)}{1 - F_2(\sigma_p)}, & \sigma \geq \sigma_p \end{cases} \quad (3)$$

When the condition of the proof test is the same as the service condition, $F_1 = F_2$, equation (3) reduces to the usual definition of conditional probability. In this investigation, we explored the proof test environment for F_2 in order to enhance the post proof test reliability. For the purposes of graphical representation of the effect of the proof test, and without loss of generality, the Weibull distribution is selected to represent the probability of failure function for a composite structure before the proof test:

$$F_i(\sigma) = 1 - \exp\left\{-\left(\frac{\sigma}{\beta_i}\right)^{\alpha_i}\right\}; \quad i=1,2 \quad (4)$$

The cumulative probability of failure before and after the idealized proof test are shown in figure 2a and repeated in linearized weakest link coordinates in figure 2b

under the transformations:

$$F^* = \ln(-\ln(1 - F))$$

$$\sigma^* = \ln \sigma \quad (5)$$

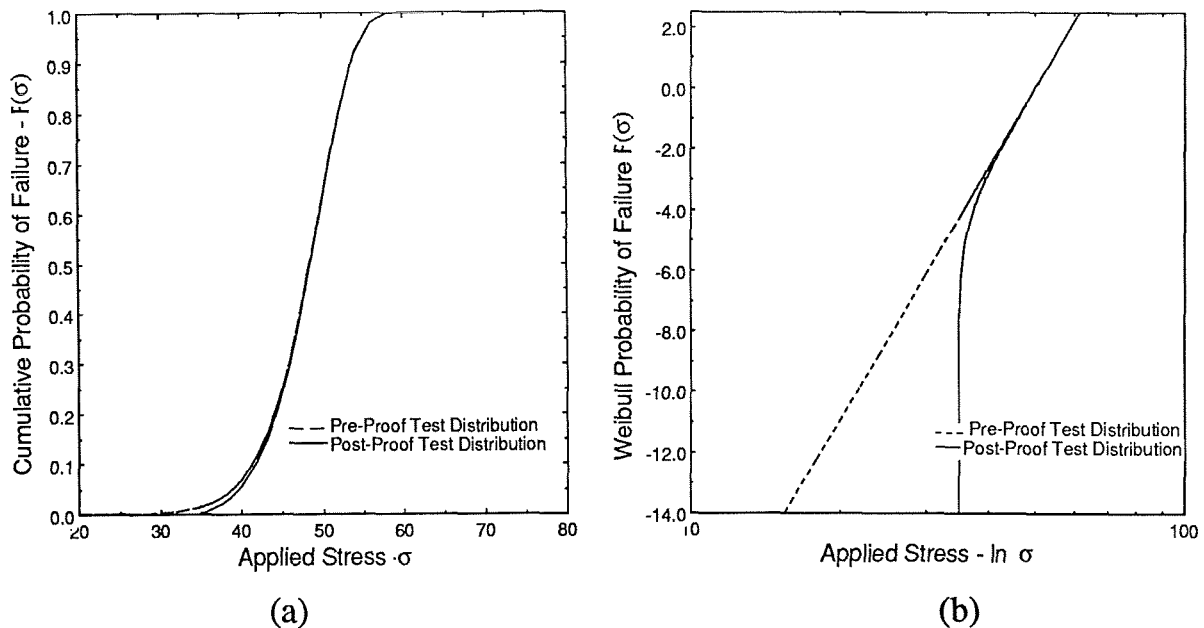


Figure 2. Effect of idealized proof test with truncated lower tail.

The effect of an *idealized* proof test is graphically illustrated by noting that at any stress level, the post proof test probability of failure (at high stresses) is always equal to or (at low stresses) less than the pre-proof test probability of failure. The beneficial effects can be observed from either graphical representation. However, the transformed linear representation (figure 2b) has the added advantage that the effect at lower stress levels is visually magnified. This idealized model is applicable to the proof test of a perfectly brittle material where micro-damage, such as flaw growth, is completely absent. In this case, the sample surviving the proof test is guaranteed to be capable of sustaining at least the proof test load level in service. On the other hand, if the idealized no-permanent-damage assumption is *not* true, then the samples which survive the proof test will be weakened. An example is in the of proof testing of a time or history dependent material with flaw growth. This weakening is most severe for samples which have marginally passed the proof test but because of flaw growth, will result in a higher probability of failure following the proof test as illustrated in figures 3a and 3b, again with the transformed representation (figure 3b) clarifying the lower tail effects. Since failure below service stress is the main concern, the weakest link transformation representation is used here to present and discuss the experimental data in order to observe and assess the beneficial or detrimental effects of the proof testing.

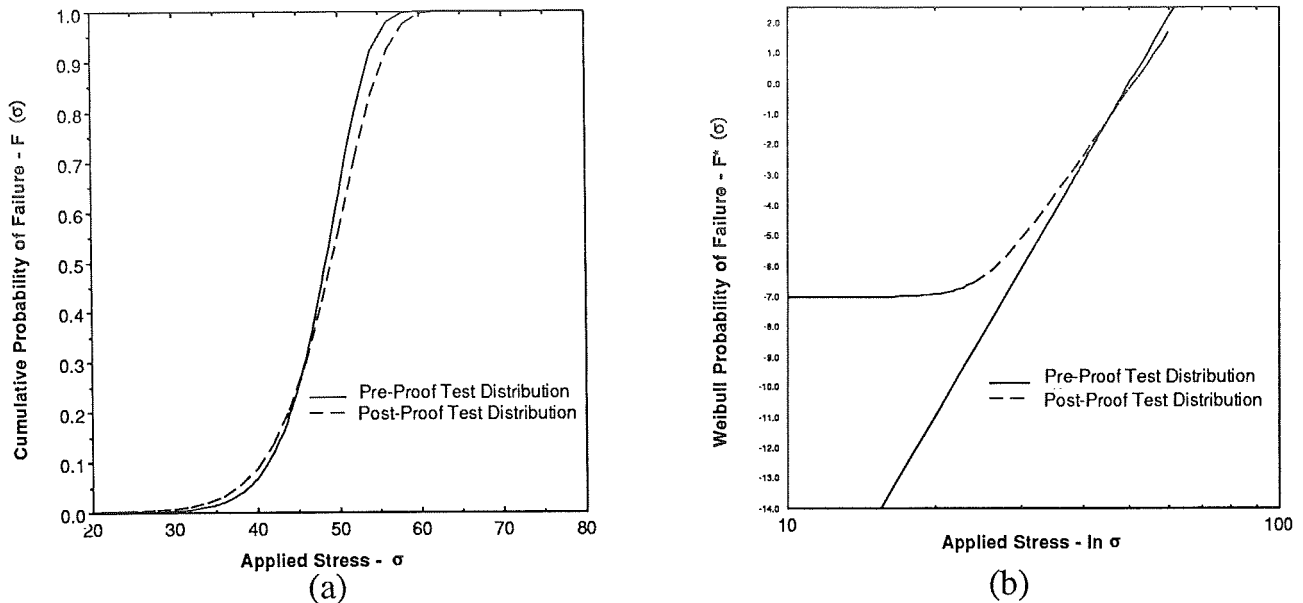


Figure 3. Effect of proof test resulted in damage to lower tail.

The main focus of interpretation of the experimental results herein is whether a particular proof test method is *beneficial*, which results in data *below* the original distribution; or *detrimental*, which results in data *above* the original distribution.

The linearity of experimental data (or lack thereof) is not the main focus; linearity simply suggests that over the range of experimental observations (number of samples tested), the failure process can be represented by the classical Weibull distribution (Eq. 4). In fact, the Local Load Sharing model which best represents the composite failure process is known to be a modified Weibull function which is not linear over a wide probability range. The subject of mathematical modeling of the post proof test distribution will not be discussed.

Proof Test Guideline for Composites

One important result of the local load sharing model is that weak composite samples have an inherently higher number of adjacent fiber breaks (clustered failure sites). It follows immediately that the mechanistic principle for the proof test is to *eliminate adjacent fiber breaks thus eliminating those unacceptable weak composite samples*.

The composite sequential failure process with local fiber failures at low loads directly contradicts the idealization that no permanent damage sites are sustained during proof load. Therefore, conventional proof test methods for homogeneous metals are not applicable for composites. Pre-loading composite articles above service-load levels is sure to cause more local fiber failures while the accompanying stress concentrations induce (otherwise avoidable) additional clustering and weakening of the composite after it has

survived the proof test. Therefore, a beneficial proof test for composites must seek out the weak fibers (whose breakages are inevitable during service) but without creating the accompanying stress concentrations thus avoiding excessive fiber breakages and clustering. The physical parameters which make this condition possible can be inferred from the composite failure model. The Harlow-Phoenix Local Load Sharing model suggests that by increasing the ineffective length, the probability of clustering is reduced, particularly for the weak (lower tail) composites. It follows that if the ineffective length can be increased during the proof test, then the weak composite will be eliminated while the surviving composites will not be damaged by clustering. This can be physically accomplished by two methods.

Method 1: Proof Test for Cured Composites

This first method applies to a composite that has already been processed and whose matrix has polymerized or hardened. Equation (1) indicates that the ineffective length, δ is inversely proportional to the shear modulus of the matrix. For a polymeric matrix composite, the shear modulus of the matrix is temperature dependent and decreases drastically above T_g (the glass transition temperature). Thus, when the composite is proof tested above its glass transition temperature, the reduction in matrix shear modulus leads to an equivalent (effective) increase of ineffective length, which in turn reduces the stress concentration of the broken fibers. As a result, auto-clustering is averted and only composite samples with inherently clustered weak sites are eliminated by the proof load.

The method is experimentally verified on an aramid-epoxy composite. Composite sample configuration was a matrix impregnated strand with a gauge length of 10 inches. Each sample consisted of a Kevlar 49 bundle with 267 filaments impregnated in a DER332/T403 epoxy/hardener matrix. The epoxy matrix had a glass transition temperature centered at 70° C with full rubbery modulus reached by 100° C.

The effects of proof test carried out at glass transition temperature are explored by examining the life of the composite under sustained load (the stress rupture life). The life data for the same sustained load level (8.29 kg) are used for several proof test conditions. The baseline for comparison is sample life without the pre-loading proof test. This is shown in figure 4 presented in weakest link transformation (Eq.5) with time to fail as the random variable. This graphical format is used because of the exposition of the lower weak tail (short life statistics). The model fitted to the data is the two parameter Weibull distribution with the parameters estimated by the maximum likelihood estimator. It should be noted that there is additional scatter at the lower tail (six points) with a significantly shorter life than that predicted by the two parameter Weibull model.

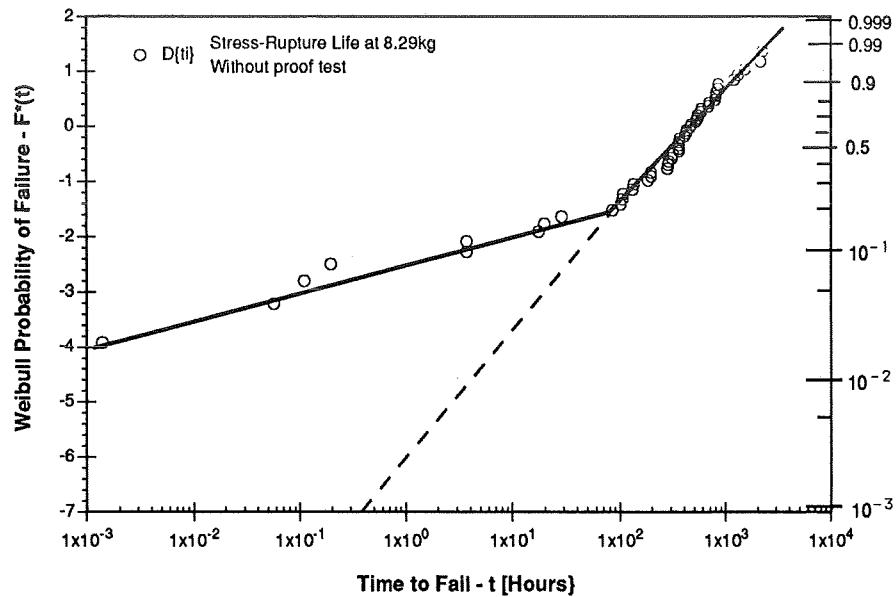


Figure 4. Life of aramid-epoxy composite under sustained load(8.29 kg).

Proof loads at room temperature (23°C) were applied to a second set of samples. Proof load levels were chosen to eliminate 10% of the lower tail. The surviving samples were tested in stress rupture at the same load level (8.29 kg) as the baseline data. The life data are presented in figure 5 with the base line model also presented for comparison. We note that weak lower tail samples recur even after survival of the proof load. This is believed to be caused by those samples with marginal strength above the proof test level but weakened by flaw clustering induced during the proof test which caused the shortening of life under subsequent loading.

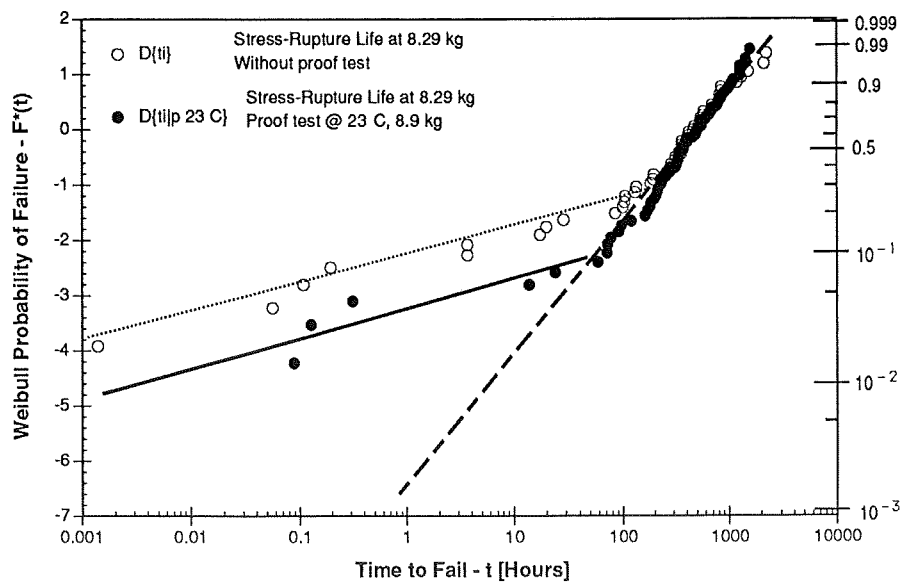


Figure 5. Life of aramid-epoxy composite under sustained load(8.29 kg) after survival of preload (8.93 kg) at 23°C .

Proof loads were applied to a third set of samples at an elevated temperature (70°) to eliminate 10 % of the lower tail. The surviving samples were slowly cooled back to 23°C then tested in stress rupture. This third set of life data is presented in figure 6.

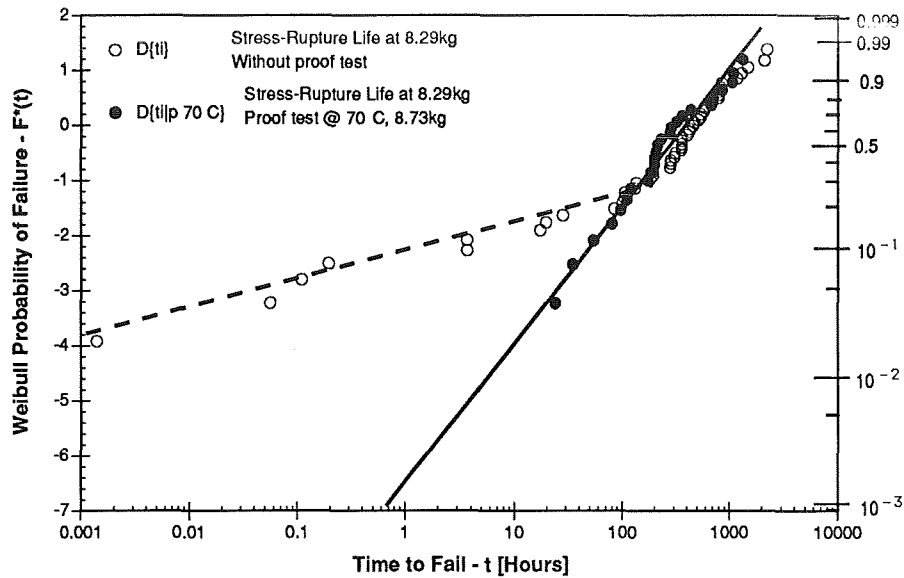


Figure 6. Life of aramid-epoxy composite under sustained load(8.29 kg) after survival of preload (8.73 kg) at 70°C.

Note that the lower tail in life is now totally eliminated. This data substantiates the mechanism that the decrease in matrix shear modulus simultaneously increases the ineffective length and decreases the stress concentration. Both of these parameters minimized flaw clustering thus averting permanent damage during the proof test.

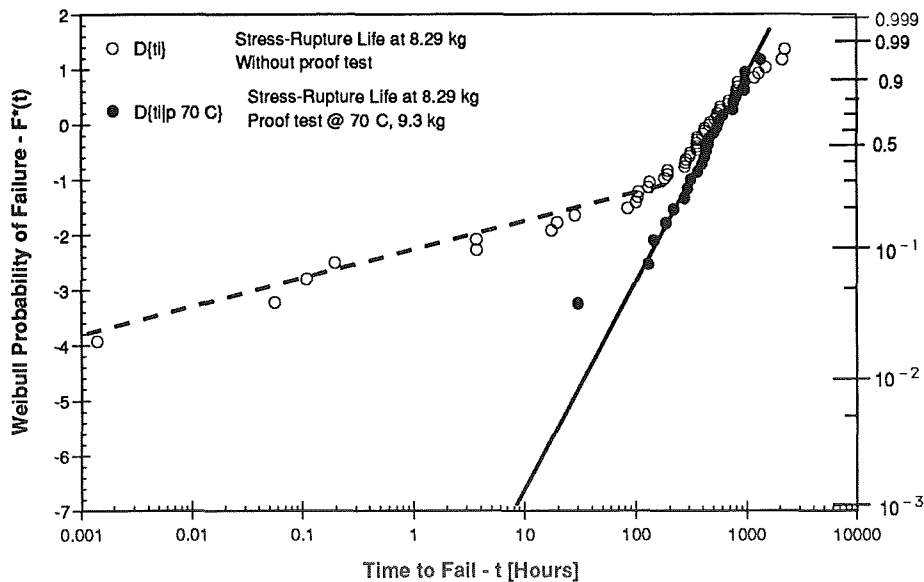


Figure 7. Life of aramid-epoxy composite under sustained load(8.29 kg) after survival of high preload (9.3 kg) at 70°C.

This proof test method is further confirmed on a fourth set of samples where the proof load level was increased to eliminate the lower 50% of the samples at 70°C. The life data are presented in figure 7. We observed that the stress life is further increased as predicted by conditional probability that samples survived elevated temperature proof tests were not damaged.

This proof test method is relevant to the acceptance of composite structures when the level of reliability at a prescribed service condition must be certified.

Method 2 Proof test during processing

This method consists of proof testing the matrix impregnated fiber bundle before the complete polymerization. The physical rationale behind this method is that when the matrix is in the liquid state, the composite behaves as a bundle without a matrix, and load sharing stress concentration is absent and therefore, no unnecessary failure sites are created during the proof test. The trade-off is that, in the uncured state, the ineffective length is the same as the gauge length of the pre-load. This was thousands of times longer than the ineffective length for a polymerized epoxy. The large ineffective length prevents the elimination of *all* the weak fiber sites along the fiber filament and the post proof test benefit is not as complete. However, this can be optimized by proof testing at the matrix partially polymerized state where the ineffective length is decreased. This method has the added benefit that upon curing, the matrix has a measured healing influence on the broken fiber sites.

This proof test method is experimentally verified by performing strength tests on graphite-epoxy samples respectively with and without pre-loading during processing. Samples were of the strand configuration with 10 inch gauge length. AS4 graphite bundles with 3000 filaments were impregnated in a DER332/T403 epoxy/hardener matrix.

Two groups of samples were prepared. One group of samples were allowed to cure without proof load. The second group of samples was allowed to cure for 19 hours at room temperature which brought the epoxy to gel state. These samples were each pre-loaded to 0.9% strain (a level calculated to eliminate the lower 13% of filament flaws at the 10 inch gauge length). After the pre-load, the samples were finally cured at 60°C for 16 hours.

These two groups of samples were individually tested in tension until failure. The strength data for the non-preloaded standard sample and the preloaded sample are graphically presented in figure 8.

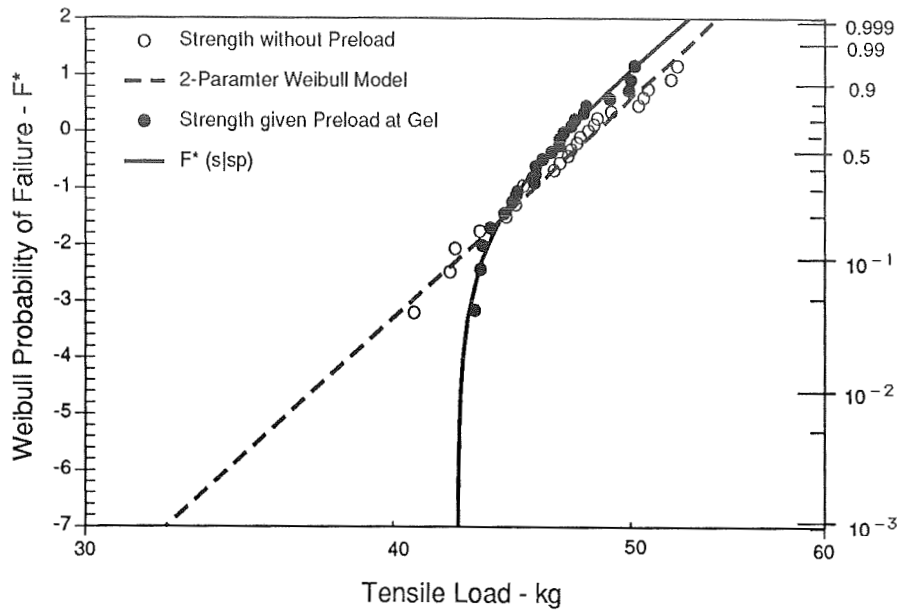


Figure 8. Strength of graphite-epoxy composite verse strength of composite preloaded at gel state during fabrication.

It is clear that the lower tail weak samples were eliminated by the preloading during processing as expected. An unexpected result is that the upper tail is somewhat weaker as compared to the non-preload samples. This could be attributed to fiber misalignment from the dynamic waves of the broken fibers during pre-load. The drawback may be resolved with further development of the processing procedures. In any case, in structural reliability, the upper tail is of relatively minor concern in service conditions. This is further illustrated by the histograms of composite strengths in figure 9. These distribution free histograms indicate that the pre-load before cure composites (shaded histogram) have the lower tail truncated, inferring that the pre-load composite is 100% reliable below the truncation stress level.

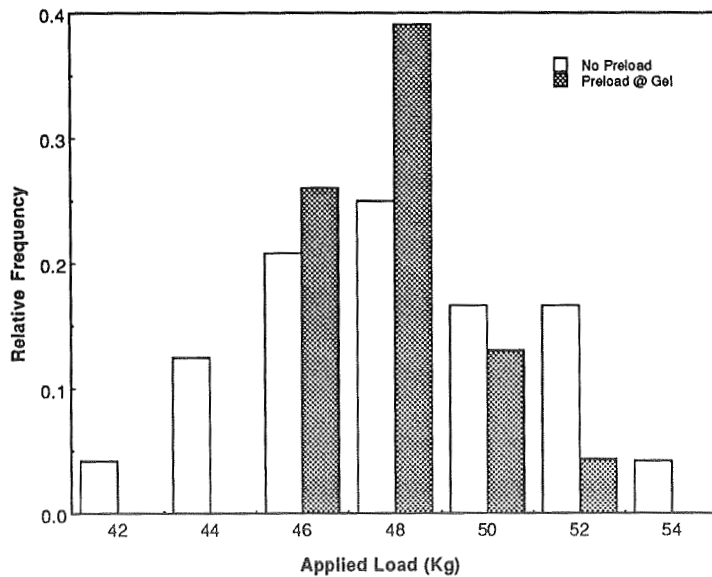


Figure 9. Distribution free strength comparisons of graphite-epoxy composite verse composite preloaded at gel state during fabrication.

This method may be relevant to development of manufacturing processes for very large structures (such as in ship and hulls) and where economic constraints demand zero-reject in manufacturing.

Conclusions

The rationale of applying a proof test to assure composite reliability was examined against the current understanding of the composite failure process in fiber failure dominated tensile failure modes. It was observed that the proof test conditions for composites must be optimized to prevent permanent damage to the samples which survive the proof load. Extensive experimental evidence indicates that proof tests performed in the conventional manner have no beneficial effect, and probably detrimental effects on the composite post-proof test reliability. Two proof test methods were established to prevent permanent damage in terms of excessive fiber breaks and breakage site clustering. The first method involved the proof test of already fabricated composite samples at the glass transition temperature. This method is relevant to certification and acceptance of composite structures. The improvement was experimentally demonstrated on an aramid composite to be over 5 orders of magnitude over an original reliability level of 0.999. The second method consisted of preloading the fiber bundle during fabrication before the complete polymerization of the matrix. This method is relevant to development of zero-reject manufacturing processes. The improvement was experimentally demonstrated on a graphite-epoxy composite to be over 30% at a reliability level of 0.999. At higher reliability levels, the improvement is even more dramatic.

References

1. Rosen, B.W., "Tensile Failure of Fibrous Composites," *Journal American Institute of Aeronautics and Astronautics*, Vol.2 no.11, pp.1985-1991, Nov.1964.
2. Rosen, B.W., "Mechanics of Composite Strengthening," *Fiber Composite Materials*, American Society for Metals, Metals Park, Ohio, pp.37-75, 1965.
3. D.G. Harlow and S.L. Phoenix, "The Chain-of-Bundles Probability Model For the Strength of Fibrous Materials I: Analysis and Conjecture," *J. Composite Materials*, Vol.12, pp. 195-214, April 1978.
4. D.G. Harlow and S.L. Phoenix, "The Chain-of-Bundles Probability Model For the Strength of Fibrous Materials II: A Numerical Study of Convergence," *J. Composite Materials*, Vol.12, pp. 314-334, July 1978.

omit

**Materials and Processes Used for
Bonded Repairs of F/A-18 Advanced Composite
Honeycomb Sandwich Structures**

Douglas R. Perl
Naval Aviation Depot North Island

THIS PAGE INTENTIONALLY BLANK

Page intentionally left blank

Page intentionally left blank

526-24

51394

78

NAVY COMPOSITE MAINTENANCE AND REPAIR EXPERIENCE

T.M. Donnellan, R.C. Cochran, E.L. Rosenzweig
and R.E. Trabocco
Naval Air Development Center
Warminster, PA

Abstract

The Navy has been a strong proponent of composites for aircraft structure. Fleet use of composites started with the F-14 in the early 1970's and has steadily increased. This experience base provides sufficient information to allow an evaluation of the maintenance performance of polymer composites in service.

This presentation will summarize the Navy's experience with maintenance of composite structure. The general types of damage experienced in the fleet as well as specific examples of composite damage to aircraft will be described. The impact of future designs on supportability is also discussed.

Introduction

The U.S. Navy has been a leader in the implementation of composites on weapons systems. The current fleet aircraft all have composite materials in the structure. The F-14 was the first aircraft to use a high performance composite material. The F/A-18 design dramatically increased the level of composites usage. The performance requirements of the AV-8B drove the design to composite materials. Finally, the V-22 represents the largest percentage of composite structure on any military aircraft. The Navy has fielded composite aircraft for approximately 20 years. This experience has provided an excellent database for the evaluation of the service performance of a number of material types and structural designs.

This paper will address the current state of composite supportability in the fleet. A general description of the types of problems experienced with composites will be provided followed by a summary of specific aircraft maintenance experience. Finally, the challenges which the fleet faces with support of emerging designs and issues that must be addressed to make them more supportable will be described. The information is drawn from a report on composites supportability recently completed by the Navy (1).

Generic Composite Component Performance

The Navy's experience with fielded composite systems has been very positive. Carbon, glass and kevlar based composites have been used. The composite components have performed extremely well. It is important to emphasize that no composite component damage has ever been found to have caused an aircraft crash.

A number of the maintenance actions performed in the fleet have been documented in the 3M system. The term "3M" is an acronym for the Navy's Maintenance, Management and Materiel System as defined in OPNAV 4790.2E. The purpose of this system is to serve as a historical data base for all maintenance actions. Because of the volume of information that is stored in the system, it is a valuable tool for accessing and evaluating reliability and maintainability among other parameters. Data are entered into the system by squadron and IMA maintenance personnel. The depots do not currently input into the system. A VIDSMAF or Visual Information Display System/Maintenance Action Form is completed by maintenance personnel. Data are transcribed from this form to the 3M system. The system does have some deficiencies. Malfunction codes for structural components are based upon metallic aircraft and are therefore irrelevant for composites. Composites have a unique set of damage types or failure modes and repair dispositions which are not currently being addressed. This makes it difficult to interpret what the problem was and what disposition was taken.

The primary concern of fielded systems continues to be corrosion and fatigue of metal components. In the mid 1970's, the Navy and Air Force identified the potential for galvanic coupling between aluminum and graphite materials. Composite designs used since this time have attempted to minimize the galvanic corrosion through use of barrier plies and sealants. In general this has been successful. There have been composite driven corrosion problems which have occurred and caused considerable aircraft down-time. One recent example is the corrosion of aluminum substructure on the F/A-18 caused by a galvanic couple to a composite skin through a silver filled epoxy adhesive. The solution involved disassembly of the component, removal of the corroded metal, and reinstallation with a barrier adhesive. It is extremely important that the corrosion testing of all bi-material couples be investigated.

The Navy has had considerable experience with honeycomb structure. Honeycomb structure is ideally suited for stability critical components. The stiffness per unit weight of this structure is superior to that of any other concept. However, honeycomb structures negatively impact aircraft maintainability. For example, the largest single problem with the composite structures used on the F-14 was the degradation of the aluminum honeycomb core substructure on the horizontal stabilizer. The solution for this problem was the removal of the core and reinstallation of additional core material. Improved treated core material and adhesives coupled with enhanced manufacturing techniques greatly reduced the maintenance requirements of similar structure used on the F/A-18. There are still problems with honeycomb structure which are related to the damage intolerance of the structure. Fleet experience has shown that the structure is susceptible to handling damage. This fact was responsible for the elimination of honeycomb from current generation aircraft. Future applications of

honeycomb structure will be dependent on strong requirements for the specific properties that these structures provide.

A significant proportion of the problems encountered with composite materials can be traced to the brittle nature of the resin used in the material. The 3501-6 resin system has been used on all of the epoxy based composite components installed on aircraft. The resin brittleness leads to cracking in the resin. This cracking occurs primarily when loads are applied in directions which cause fracture via resin dominant modes. The two common observations are microcracking which in extreme circumstances may progress through the thickness of the composite and delamination of the plies of the structure. The Navy's experience has shown that the damage that occurs can be introduced by many different mechanisms. Identification of damage in composites is difficult because of the fracture behavior of the material which is characterized by delaminations and cracks that are not visible on the surface. Internal stresses from processing, thermal cycling, poor manufacturing processes, and mishandling have all been found to cause defects in composite structures. Microcracking and delamination in composites can reduce strength and stiffness. In honeycomb structure, it provides a path for moisture intrusion into the core. Moisture has been found to cause dramatic weight increases in some commercial aircraft components which used kevlar composite-nomex honeycomb construction. It also causes corrosion in metallic cores. Since most of the cracking is internal, it is difficult to find with conventional inspection techniques.

Damage to composite components can be produced during initial assembly. The F/A-18, AV-8B and A-6 have all encountered fit-up problems upon assembly of skin structure to the substructure. One result has been delamination in the skin or substructure caused by out-of-plane bending and shear loading in the composites. These problems resulted from the basic design or by manufacturing procedures. The causes of the poor fit include location on fasteners in seal groove areas, failure to tool to all mating surfaces, tool wear, and material springback upon release from the tool. The short term solution has been to shim the structures to improve the fit. Future aircraft designs must improve tooling concepts and structural design to minimize this form of damage.

Handling damage has been observed on all aircraft. Usually, the damage is associated with the operation of aircraft in very restricted space. There has been a considerable amount of damage found on the F/A-18 horizontal stabilizers. Improvements in the aircraft materials and designs could reduce the amount and the severity of the damage incurred. One feature of handling damage is that it is so catastrophic that it is easy to find.

Other causes for component damage exist which although less destructive can lead to more difficult maintenance actions. The F/A-18 and the AV-8B both have a number of composite access doors. The frequent removal and reinstallation of fasteners in these doors eventually results in oversized holes and produces out-of-plane loads which have been found to cause delamination in the composite around the hole. Since the delamination occurs within the laminate, there is no visible indication of damage at the surface.

In addition, aircraft occasionally are impacted by runway debris which produces limited delamination in the composite components with little visible indication of damage. The strakes and gun pods on the

undercarriage of the AV-8B have experienced considerable surface and edge damage.

Finally, exposure to high temperatures has produced heat damage in composites. Composites are formulated to operate in moderate temperature environments (-65°F to 450°F). Exposure to temperatures in excess of the material thermal limit results in delamination, cracking, and blistering of the material. The exposure can occur due to improper prediction of component operating temperatures. For example, an engine access door on the AV-8B which was designed to function at 375°F actually was exposed to temperatures in excess of 650°F. This problem has been remedied by replacement of the composite component with a metal one. In normal aircraft application, the exposure can result from close proximity to other aircraft.

Fleet Experience

F-14 Aircraft

Extensive corrosion has been experienced in the untreated 2024 honeycomb used in the stabilator. In general the corroded honeycomb core is removed and the covers are rebonded on a new sheet of machined honeycomb. The Navy is trying to qualify phosphoric acid anodized and primed honeycomb core and a new toughened assembly adhesive like FM 300 to replace MB 329. These design changes will improve corrosion resistance and moisture seal integrity respectively.

The Navy recently sponsored Grumman to develop and validate flush, step-lap-joint, boron/epoxy repair concepts to expand depot level repair concepts from 2 to 8 inch damage, a low cost, rapid and safe cold-wall autoclave repair method was demonstrated to localize the application of heat only to the damaged area.

F/A-18 Aircraft

A major concern is handling damage to thin skin (i.e., honeycomb sandwich) damage prone structures in areas susceptible to damage (i.e., flaps, rudders, landing gear doors and horizontal stabilizers). These structures appear to be more prone to damage than comparable metal designs. However, repair of these structures is greatly simplified compared to metal structures due to three factors: simple abrasive surface preparation in place of acid etch and chemical treatment required for metals, easy damage removal, and improved tailorability (e.g., tapered and scarfed patches and lighter materials) facilitate weight and balance requirements. The F-18 control surfaces are weight and balance critical by design. No mass was added forward of hinge points to provide counter-balance and narrow flutter margins exist.

Another major concern is with fastener hole wear and edge damage in access doors. The turtle back doors behind the cockpit and the thick monolithic wing access doors aft of the torque box experience this problem frequently. Damage is due to a frequent need for access, the over-torquing of fasteners during installation causing delamination, the failure to install grommets to aid in alignment and reduce hole wear and the necessity to pry off doors with sharp objects.

Thick monolithic structures like wing skins are infrequently damaged by handling abuse because they possess high levels of impact

resistance (energy levels to induce incipient damage) and are not located in damage prone areas. Damage prone areas are located low on the aircraft, near frequent maintenance areas and on the aircraft perimeter.

The second most frequent cause of damage is overheating of the component. Overheating originates from several sources, deck fires, hung ordinance, jet blast and malfunctioning heating blankets, controllers and operators. There is no technique available to rapidly assess overheat damage prior to disposition. Several repair scenarios have lead to overheat problems.

AV-8B Aircraft

The AV-8B has no honeycomb sandwich structure so the service experience differs somewhat from the F-18 composites. The AV-8B is also a VSTOL aircraft and has been subject to more frequent crash landings on a per aircraft basis than the F-18. Recent causes of crashes include engine out landings, night taxi off of established runways and a nose wheel steering problem, including collapse of the gear. Composite structures sustaining damage include: the nose cone and forward fuselage, severed outboard wings and tips, severed horizontal stabilizers and crushed strakes. These structures have been replaced or repaired using engineered splicing style repairs specifically developed for the damage area. A recent fan blade failure ruptured the fuel tank and sparked a fire which engulfed the wing and center fuselage.

In the past the aircraft has sustained numerous bird strike incidents especially when at MCAS Cherry Pt. Damage was sustained to the nose cone, and pressure bulkhead, engine air inlet and wing leading edge. Typical dispositions are remove and replace actions.

Due to design deficiencies the Auxiliary power unit (APU) exhaust door has sustained overheat damage and has been replaced with a titanium door. Similarly the epoxy strake fairings have sustained overheat damage and the inboard trailing edge flap have also experienced frequent overheat damage due to nozzle exhaust impingement. A titanium heat-shield/doubler has been added to the vulnerable areas. Similar to the F-18, the AV-8B has experienced hole wear and edge damage. Early Milson fastener designs resulted in rapid hole wear on removable panels. The AV-8B strakes and strake fairings have been prone to stone and handling damage due to their location on the aircraft.

The AV-8B has experienced frequent manufacturing defects in the form of included materials in the covers and delaminations resulting from cover to substructure mismatch in the wing and horizontal stabilizer during assembly. Assembly delaminations have also been noted over pylon support fittings, along seal grooves and around the front metallic hoist fittings. Several of these deficiencies are being corrected. Acoustic fatigue is a problem for some fuselage panels aft of the nozzles and buffet fatigue to fasteners along the trailing edge of the horizontal stabilizers. The frequency of impact induced damage is relatively low, likely due to the form of composite construction. Also repair procedures are predominantly bolted, quick and simple.

V-22 Aircraft

The period of V-22 service experience has been brief. The bismaleimide engine access doors have experienced rapid hole wear and edge damage. Metal doubler strips are being added to reduce hole wear, but a more serious effort needs to be directed at redesign/material selection as corrective actions. Early in the program fan blade and fuel system failures resulted in fires in the IR suppressor causing damaged mixing ducts and overheat damage. Disposition of damaged components was by removal and replacement. Corrective actions included installing a new fuel drain vent and replacing the Torlon fan blade with a metallic blade. Composite components have also sustained handling damage in the form of delaminations and penetrations from impact with workstands and tools on engine access doors, flaperons and landing gear doors. Hole wear and receptacle problems have been reported for some quick disconnect fasteners. Part of the problem was due to over-torquing and part is due to a design deficiency. Alternative quick disconnect fasteners are being evaluated.

Repair concepts are currently under development for 24 regions of the V-22 aircraft where new materials and unique forms of construction are being applied.

Future Navy Aircraft Needs

The fleet's experiences with support of composite components provide useful insight into improvements that could be made on future aircraft. The quality of the fabricated composite components has a significant impact on fleet readiness. Surprisingly, manufacturing quality of composites has declined as the technology has matured. Quality affects all aspects of process sensitive composites manufacturing. The fabrication of high quality components will improve supportability and fleet readiness.

The design complexity of the aircraft also impacts supportability. Since the repair concepts used are dependent on the structural design, the support of the system becomes more difficult as complexity increases. For example, there are a number of stiffener configurations that can be used in a given structure. Not only can different shapes be used, but also different size stiffeners with modified angles or radii can be incorporated. This places a great logistics burden on the fleet since this myriad of substructural components must be held in stock. Obviously, in many cases the use of specially designed substructure is required in order to meet weight requirements and operational goals. The fact that selection of multiple types of structural designs will negatively affect the Navy's ability to effectively field these systems must be taken into consideration during the system design phase.

Another characteristic of composite design which has impacted supportability has been the assembly processes used in production. The machining process used to mate composite skins to the component substructure must be performed with hard tools which determine the location of the substructure and fasteners in a repeatable process.

Currently the fastener hole locations can vary. The result of this is the skin and substructure become specific to a particular component. Only a limited number of composite components have been made interchangeable. Major component replacement has to be performed with the existing substructure and the original tooling at the manufacturer's facility. Less complex structure can be replaced at the component level at depot installations. This is a logistics burden on the fleet since replacement parts must be purchased and stocked. Also, the replacement parts must be matched to the existing structure, drilled and trimmed. This costly process occurs because of the custom nature of these structural components. The time associated with purchase, acquisition, and preparation of the part is down-time for the aircraft. An effort to produce fully interchangeable parts must be initiated as part of the acquisition program.

Another aspect of supportability addresses the accessibility of structure for repair procedures employed to restore structural integrity. Ideally, repair actions should be performed in an eight hour time period. However, most repair actions take considerably longer. The principal difficulty encountered in performance of repair actions has been in gaining access to the damaged zone. In most cases, repairs must be performed with single side access from the component surface. Inspection of the inside of the component to determine substructure damage is difficult. Completion of the repair process is also hindered because back side sealing or support plate alignment is difficult. As repair designs are driven to flush outer mold line requirements, this problem will increase in importance. Future designs must allow adequate access to the internal structure of components which are expected to require repair actions.

There is a considerable amount of effort being directed towards the development and demonstration of new repair concepts. Most of the work has focused on conventional repair concepts aimed at the restoration of structural integrity to damaged components. Emerging and future Navy aircraft will incorporate low observables (LO) technology in both the materials and the designs used. Based on fleet experience, it is extremely likely that this LO structure will be damaged in service. The repair action required to restore performance may have to restore strength or signature or both. In order for the Navy to take full advantage of the unique capabilities that these structures afford, more effort must be directed towards the establishment of a maintenance system capable of supporting these aircraft.

Finally, the majority of development work performed on field repair of composite structures has concentrated on small, relatively simple damage. A limited number of components have had large, complex damages which have had to be shipped to depots for engineered repairs. This process is time consuming and labor intensive. Although sufficient for peacetime operations, the process of depot repair would not be practical for fast turnaround during wartime scenarios. There is a movement towards field level repair of larger damage sizes through the depot engineering disposition (DED) process at North Island. The need exists for a dedicated program to address the support required for battle damage repair processes.

References

1. T. M. Donnellan, Navy Council on Materials and Structures Report on Composites Supportability, NADC Report 91083-60 Aug 1991.

1. Report No. DOT/FAA/CT-92/25, I*		2. Government Accession No.		3. Recipient's Catalog No.	
4. Title and Subtitle NINTH DoD/NASA/FAA CONFERENCE ON FIBROUS COMPOSITES IN STRUCTURAL DESIGN				5. Report Date September 1992	
				6. Performing Organization Code	
7. Author(s) Joseph R. Soderquist, Lawrence M. Neri, and Herman L. Bohon, Compilers				8. Performing Organization Report No. DOT/FAA/CT-92/25, I	
9. Performing Organization Name and Address Federal Aviation Administration Technical Center Atlantic City International Airport, NJ 08405				10. Work Unit No. (TRAIS)	
				11. Contract or Grant No.	
12. Sponsoring Agency Name and Address Federal Aviation Administration Department of Defense National Aeronautics and Space Administration				13. Type of Report and Period Covered Proceedings November 4-7, 1991	
				14. Sponsoring Agency Code ACD-210	
15. Supplementary Notes Joseph R. Soderquist, Federal Aviation Administration, Washington, DC. Lawrence M. Neri, FAA Technical Center, Atlantic City Int'l Airport, NJ. Herman L. Bohon, Galaxy Scientific Corporation, Hampton, Virginia.					
16. Abstract This publication contains the proceedings of the Ninth DoD/NASA/FAA Conference on Fibrous Composites in Structural Design held at Lake Tahoe, Nevada, during November 4-7, 1991. Presentations were made in the following areas of composite structural design: perspectives in composites, design methodology, design applications, design criteria, supporting technology, damage tolerance, and manufacturing. *Volume I of III					
17. Key Words Composite Aircraft Design Composite Design Applications Composite Design Criteria NASA Advanced Composite Technology			18. Distribution Statement For Early Domestic Dissemination REVIEW for general release November 30, 1994		
19. Security Classif. (of this report) Unclassified		20. Security Classif. (of this page) Unclassified		21. No. of Pages 572	22. Price